Experimental Studies Focused on the Pore-Scale Aspects of Heavy Oil and Bitumen Recovery Using the Steam Assisted Gravity Drainage (SAGD) and Solvent-Aided SAGD (SA-SAGD) Recovery Processes

by

Omidreza Mohammadzadeh Shanehsaz

A thesis
presented to the University of Waterloo
in fulfilment of the
thesis requirement for the degree of
Doctor of Philosophy
in
Chemical Engineering

Waterloo, Ontario, Canada, 2012

Author’s Declaration

I hereby declare that I am the sole author of this thesis. This is a true copy of the thesis, including any required final revisions, as accepted by my examiners.

I understand that my thesis may be made electronically available to the public.

Abstract

Increasing energy consumption and continuous depletion of hydrocarbon reservoirs will result in a conventional oil production peak in the near future. Thus, the gap between the global conventional oil supplies and the required amount of fossil fuel energy will grow. Extensive attempts were made during the last three decades to fill this gap, especially using innovative emerging heavy oil and bitumen production technologies. Most of these recovery methods have been developed in Canada, considering the fact that Canada and Venezuela have the largest deposits of heavy oil and bitumen throughout the world. The horizontal well drilling technology opened a new horizon for the recovery of heavy oil and bitumen. Most of the in-situ recovery techniques, including Steam Assisted Gravity Drainage (SAGD) recovery method, take advantage of horizontal injection and production wells. The vacated pores in the reservoir are filled mainly either with steam or with a mixture of steam and solvent vapour in the case of the SAGD and Solvent Aided SAGD (SA-SAGD) recovery methods, respectively. The use of long horizontal wells combined with the reduced viscosity of the produced oil allows economic production with limited amount of bypassed residual oil in the invaded region.

The macro-scale success of the SAGD recovery technique is greatly affected by its pore-scale performance. It is beneficial to understand the pore-level physics of the SAGD process in order to develop mathematical models for simulating field-scale performance. Available commercial reservoir simulators cannot describe pore-level mechanisms of the SAGD process including mechanisms related to the fluid-flow as well as heat-transfer aspects of the process. A systematic series of flow visualization experiments of the SAGD process using glass-etched micromodels was developed to capture the pore-level physics of the process using qualitative analysis. With the aid of image processing techniques, the pore-scale performance of the SAGD process was qualitatively and quantitatively investigated. The main objective of Chapter 2 of this thesis is to address the relevant pore-scale mechanisms responsible for the in-situ oil mobilization and drainage in a conventional SAGD process. Transport processes, occurred in a conventional SAGD process at the pore-level including fluid flow and heat transfer aspects, were mechanistically investigated and documented. The qualitative analysis of the results revealed that near a well-established oil-steam interface, gravity drainage takes place through a thick layer of pores, composed of about 1-6 pores in thickness, within the mobilized region. The drainage of

the mobile oil takes place due to the interplay between gravity and capillarity forces near this mobilized region. In-situ mobilization of bitumen was found to be as a result of both conductive and convective elements of the local heat transfer process. Moreover, the phenomenon of water-in-oil emulsification at the interface was also demonstrated which is due to the local steam condensation and spreading characteristics of water droplets over the oil phase in the presence of a gas phase. Other pore-scale aspects of the process such as drainage displacement as well as film-flow drainage mechanisms of the mobile oil, localized entrapment of steam bubbles as well as condensate droplets within the mobile oil continuum due to capillarity phenomenon, sharp temperature gradient along the mobilized region, co-current and counter-current flow regimes at the chamber walls, condensate spontaneous imbibition followed by mobile oil drainage, and snap-off of liquid films are also illustrated using these pore-level studies. The second objective of Chapter 2 is to quantitatively analyze the production performance of the SAGD process based on the micro-scale measurements. Our pore-scale experiments revealed that the rate of pore-scale SAGD interface advancement depends directly on the pore-scale characteristics of the employed models and the pertaining operating conditions. The average sweep rate data were correlated using an analytical model proposed by Butler (1979, 1981, 1991) and a pore-scale performance parameter was defined for the SAGD process. The measured horizontal sweep rates of the SAGD process at the pore-scale are in good agreement with the theory predictions provided by the performance parameter. In addition, the effect of different system variables on the ultimate recovery factor of the SAGD experiments were investigated and it was found that higher permeability values and lower in-situ oil viscosities lead to higher ultimate recovery factor values for a particular SAGD trial. Moreover, the Cumulative Steam to Oil Ratio (CSOR) data were scaled and a reasonably good fit for the experimental data was achieved by defining a scaling parameter.

Although the SAGD process offers several inherent advantages including high ultimate recovery, stable oil production rates, reasonable energy efficiency, and high stable sweep efficiency, there are some drawbacks associated with the SAGD process such as high energy consumption, high levels of CO_2 emission, and usage of large quantities of fresh water which make this process uneconomical in reservoirs with thin net pay, low matrix porosity and thermal conductivity, and low initial pressure. The most promising route for improving the SAGD performance appears to

be the co-injection of a light hydrocarbon solvent with steam in the context of the Solvent Aided SAGD (SA-SAGD) process. The pore-level aspects of the SA-SAGD process are not yet understood to the extent of incorporating the pore-scale physics into mathematical models. The main objective of Chapter 3 of my thesis is to mechanistically investigate the SA-SAGD process at the pore-level to enlighten the unrecognized pore-scale physics of the process. A methodical set of pore-scale SA-SAGD experiments were designed and carried out with the aid of glass micromodels. The methodology used in this set of the SA-SAGD trials was similar to that of the pore-scale SAGD experiments described in Chapter 2. Normal Pentane and Normal Hexane were used as the steam additives. The pore-level events were recorded on a real-time basis and then analyzed using the image processing techniques. According to the qualitative results, it was obtained that all the condensate and gaseous phases flow simultaneously in the mobilized region composed of about 1-4 pores in thickness. Heat transfer mechanisms at the pore-scale include conduction as well as convection. The mechanisms responsible for the mass transfer at the pore-level include molecular diffusion as well as convection. The mobile oil drains as a result of two active mechanisms of film flow as well as direct capillary drainage displacements at the pore-scale. Due to the near miscible nature of the displacement process, the residual oil left behind in the invaded portion of the micromodels was negligible and asphaltene precipitation and plugging was found to be a temporary phenomenon. The second objective of Chapter 3 is to quantify the pore-scale production performance of the SA-SAGD process using the flow visualization experiments. The horizontal SA-SAGD interface advancement velocity was chosen to be the indicator of the pore-scale performance of the process. It was found that addition of n-C_6 as the steam additive was more effective than n-C_5 in terms of enhanced pore-scale interface advancement as well as achieving higher ultimate recovery factor when all the other experimental variables are unchanged. The higher the solvent concentration in the injection mainstream is, the higher would be the pore-scale sweep rate as well as the ultimate recovery factor of the process. When oil type with lower in-situ viscosity was used, higher sweep rates as well as higher ultimate recovery factors values were achieved compared to the trials in which the more viscous bitumen was employed as the oil type. In addition, a scaling parameter composed of porous media properties was found by which the pore-scale interface advancement velocity and the ultimate recovery factor of the SA-SAGD trials were scaled when all other experimental variables remain unchanged.

In Chapter 4 of this thesis, the production performance of the SAGD and SA-SAGD processes were demonstrated and compared at the macro-scale under controlled environmental conditions. A 2D physical model was designed and fabricated and Athabasca bitumen was used as the oil type. According to the experimental results, it was obtained that the average mobile oil as well as dead oil production rates are reasonably constant over the course of the SAGD and SA-SAGD trials. As far as the SAGD experiments are concerned, there is a linear correlation between the mobile oil production rates and the square root of the porous media permeability when all the other experimental variables remain unchanged. In addition, the Steam to Oil Ratio (SOR) values of the SAGD trials correlate reasonably well with the inverse of the square root of permeability when all the other experimental variables are fixed. By introducing the solvent additive to the injection mainstream of the SAGD process, it was found that enhancements of about 18% and 17% were observed in the mobile oil and dead oil production rates of the SAGD process respectively. In addition, the SOR values of the SA-SAGD process was reduced by about 35% compared to that of the SAGD process. Finally, an advanced photomicrography unit with an integrated image processing software was used in order to investigate size of the enclosed water condensate droplets in the continuum of the mobile oil produced during the course of the SAGD and SA-SAGD experiments. The captured microscopic snapshots were analyzed using the image processing techniques and some representative average values of the water condensate droplet sizes were reported for the corresponding SAGD and SA-SAGD trials.

Acknowledgements

I would like to thank my supervisor and teacher, Professor Ioannis Chatzis for his supervisory approach, critical thinking, and continuous support during the course of my PhD program. I have learned a lot from his personal manner, methodical thinking, and professional conduct.

Thank you to Professor Jon Sykes, Professor Mario Ioannidis, and Professor Ali Elkamel for serving as my PhD advisory committee members and providing support during my studies.

Special thanks goes to Professor Maurice B. Dusseault for his continuous support and fruitful discussions about the recovery technologies of the unconventional hydrocarbon resources.

I would like to express my appreciation to Microelectronics Heat Transfer Laboratory (MHTL), Department of Mechanical and Mechatronics Engineering – University of Waterloo, especially Professor Richard Culham (MHTL director), Professor Peter Teertstra, and Mr. Elmer Galvis for providing continuous support during the course of the visualization studies.

I would like to thank the Department of Chemical Engineering technical staff for providing assistance during my studies especially Mr. Ravindra Singh and Mrs. Jennifer Moll. I am also grateful of the technical assistance provided by staff of Engineering Student Shop and Engineering Machine Shop, especially Mr. John Boldt, Mr. Karl Janzen, Mr. Rick Forgett, Mr. Jorge Cruz, and Mr. Kwai Chan. The administrative help and support provided by Mrs. Liz Bevan, Mrs. Rose Guderian, Mrs. Ingrid Sherrer, and Mrs. Denise Mueller during my teaching appointment at the Department of Chemical Engineering is greatly appreciated.

Many thanks to my supportive friends at the University of Waterloo and my colleagues in Porous Media Laboratory for their assistance, support, and friendship during my stay in Waterloo.

The financial supports provided by National Iranian Oil Company (NIOC), Natural Sciences and Engineering Research Council of Canada (NSERC), Professor Ioannis Chatzis, and Department of Chemical Engineering – University of Waterloo are gratefully acknowledged.

My sincere gratitude goes to my wife, Maryam, and my parents for their unconditional and endless love and support.

This thesis is dedicated to my wife, *Maryam*, and my parents *Akram* and *Asghar*

Table of Contents

List of Figures

List of Tables

Nomenclature

Variables and Parameters

A	Cross sectional area (cm^2)
cos	Cosine
C_p	Specific heat capacity ($J.kg^{-1}.K^{-1}$)
CWE	Cold Water Equivalent
CSOR	Cumulative Steam to Oil Ratio
CAPEX	Capital Expenditure
D	Average diameter (cm)
d	Differential operator
	Also diameter (cm)
E_b	Total emissive power of a black body (Wm^{-2})
F_{12}	View factor
g	Acceleration of gravity ($cm\ s^{-2}$)
h	Capillary height (cm)
H	Enthalpy ($J.kg^{-1}$)
K	Permeability of porous medium (Darcy)
Kn	Knudsen number
k_B	Stefan–Boltzmann constant ($W\ m^{-2}\ K^{-4}$)
L	Length (cm)
m	slope of the straight line
$\dot{m}$	Mass flow rate ($kg.s^{-1}$)
MW	Molecular Weight ($g.mol^{-1}$)
n	gas number density (m^{-3})

N_A	Avogadro's number (mol^{-1})
OPEX	Operating Expenditure
P	Pressure (psig)
Q	Volumetric flow rate ($cm^3.s^{-1}$)
q_{12}	Net radiation exchange between the two surfaces (W)
$\dot{Q}_{loss}$	Heat losses to the surrounding environment (W)
r	Capillary tube radius (cm)
	Also pore body radius (mm)
RF	Recovery factor
RR	Rate of Return
S	Spreading coefficient ($mN.m^{-1}$)
	Also saturation (vol/vol)
SolOR	Solvent to Oil Ratio (vol/vol)
SOR	Steam to Oil Ratio (vol/vol)
SP GR	Specific Gravity
T	Temperature (°C)
t	Time (min)
U	Velocity element normal to the interface ($cm.s^{-1}$)
VLE	Vapour Liquid Equilibria
$\bar{V}_1$	molar volume ($cm^3.mol^{-1}$)
$\bar{v}_p^{SAGD}$	Average SAGD interface advancement velocity at the pore-scale (pores/min also mm/min)
$v_p^{SA-SAGD}$	Average SA-SAGD interface advancement velocity at the pore-scale (pores/min also mm/min)
W	Width (mm)
x	Location (mm)

	Also mole fraction in the liquid phase
Y	mole fraction in the vapour phase

Greek Letters

α	Thermal diffusivity of the reservoir ($m^2.s^{-1}$)
δ	Pore-scale thickness (mm)
Δ	difference operator
ε	Emissivity of a particular surface
θ	Contact angle (°)
	Also repose angle with the subscript of "r" (°)
λ	Mean free path (m)
	Also latent heat of condensation (kJ/kg)
μ	Viscosity (cP)
ν	Interface advancement velocity (pores/min or mm/min)
	Also kinematic viscosity (cSt)
ρ	Density (g/cm^3)
σ	surface tension ($mN.m^{-1}$)
	Also Stefan-Boltzmann constant ($W\ m^{-2}\ K^{-4}$)
φ	Porosity (vol/vol)
ω	Solvent concentration (mass fraction)

Subscripts

A	Advancing
adv	Advancing

b—LO	Interface between the bitumen-filled pores and the mobile live oil film
b—Mobilized_region	Interface between the bitumen-saturated pores and the mobilized region
c	Denotes capillary in capillary pressure (i.e. P_c)
c, imb	Imbibition capillary rise in a tube
DO	Dead oil
E	Etching
etch	Etching
eq	Equivalent diameter or radius
i	Component “i" in a mixture
in	Inlet face
liquid	Liquid phase
LO	Live oil
LO—Mobilized_region	Interface between the mobile live oil film and the mobilized region
LO—V	Interface between the mobile live oil film and the vapour-invaded pores
m	Mobilized region
Mobilized_region—V	Interface between the mobilized region and the vapour-filled pores
Mobilized_region—S	Interface between the mobilized region and the steam-invaded pores
or	Residual oil
out	Outlet face
p	Pore body
PE	Pore body etching
pl	Pseudo-liquid mixture
rec	Receding
ref	Reference state
S	Steam or steam temperature

Sat	Saturation state
SC	Sub-cooled
Sol	Solvent phase
Steam	Steam phase
T	Pore constriction
TE	Pore throat etching
toluene-air	Toluene-air fluid pair
Water-air	Water-air fluid pair
W/O	Water over oil

Superscripts

dr	Drainage
imb	Imbibition
L	Liquid
LO	Live oil
P	Pore body
pore body	Pore body space
S	Steam phase
T	Pore throat
vap	Vapour
W	Water phase
*	Mobile live oil film

1. Introduction

1.1. Background

Heavy oil and bitumen are of great economic importance to Canada. The quantity of oil in place in the form of bitumen in Canada is as great as that of the conventional crude oil in the Middle East and it is a major technical challenge to utilize this vast resource efficiently and economically. A recent estimate of the recoverable volume represents only 12% of the volume of bitumen in place, based on the available economic conditions. However, there is considerable potential for this percentage to increase as advances are made in the recovery technologies. Recently, the reserves are estimated to be 28.3 billion cubic meters, made up of only 5.6 billion cubic meters in the surface-mineable areas and 22.7 billion cubic meters for the deeper areas. This total volume is sufficient to satisfy demand for crude oil, at current rates, for approximately 250 years in Canada (National Energy Board of Canada 2006).

Thermal recovery techniques have been proved to be effective methods for recovery of heavy oil, extra heavy oil, and bitumen considering their in-situ upgrading potential as well as economic considerations. Among the vast spectrum of thermal recovery techniques, the Steam Assisted Gravity Drainage (SAGD) is a suitable recovery method, especially for the Canadian and Venezuelan unconventional viscous hydrocarbon resources because of their unique unconsolidated lithology and their associated high vertical permeability.

The original concept of SAGD recovery method was proposed by Butler and his colleagues in late 1970's by taking advantage of the traditional steam flooding experiences and the newly developed horizontal well technology. The novel idea behind the SAGD method has been developed and modified by Butler and co-workers in a number of publications (Butler, McNab, and LO, 1979 and 1981; Butler and Stephens, 1981; Butler, 1991, 1994, 1998, 2001, 2004). A schematic of a vertical cross-section in typical SAGD process, perpendicular to the horizontal extension of the paired wells is shown in Figure 1.1. As it is schematically depicted in this Figure, the SAGD recovery technique involves drilling two horizontal wells parallel to each other near the bottom part of the pay zone with a vertical spacing from each other. Steam is injected under constant injection pressure through the upper well (injector) while water

condensate and draining mobile oil are produced from the lower production well. Oil movement towards the producer is caused by the resultant action of gravity and capillarity forces. Injected steam would form a continuously growing steam-saturated zone called “steam chamber”, which is the interface between the hot steam phase and cold bitumen phase. Steam condenses at the boundaries of the steam chamber, hence giving the latent heat of condensation to the cold bitumen to reduce its viscosity. The mobile oil and water condensate move approximately parallel to the steam chamber/bitumen interface towards the producer. Using this recovery technique, heavy oil or bitumen can be extracted in a systematic manner with very high ultimate recovery factor values which are significantly greater than those achieved using the conventional steam flooding processes in which heated oil is moved by pushing it with the hot injected fluids.

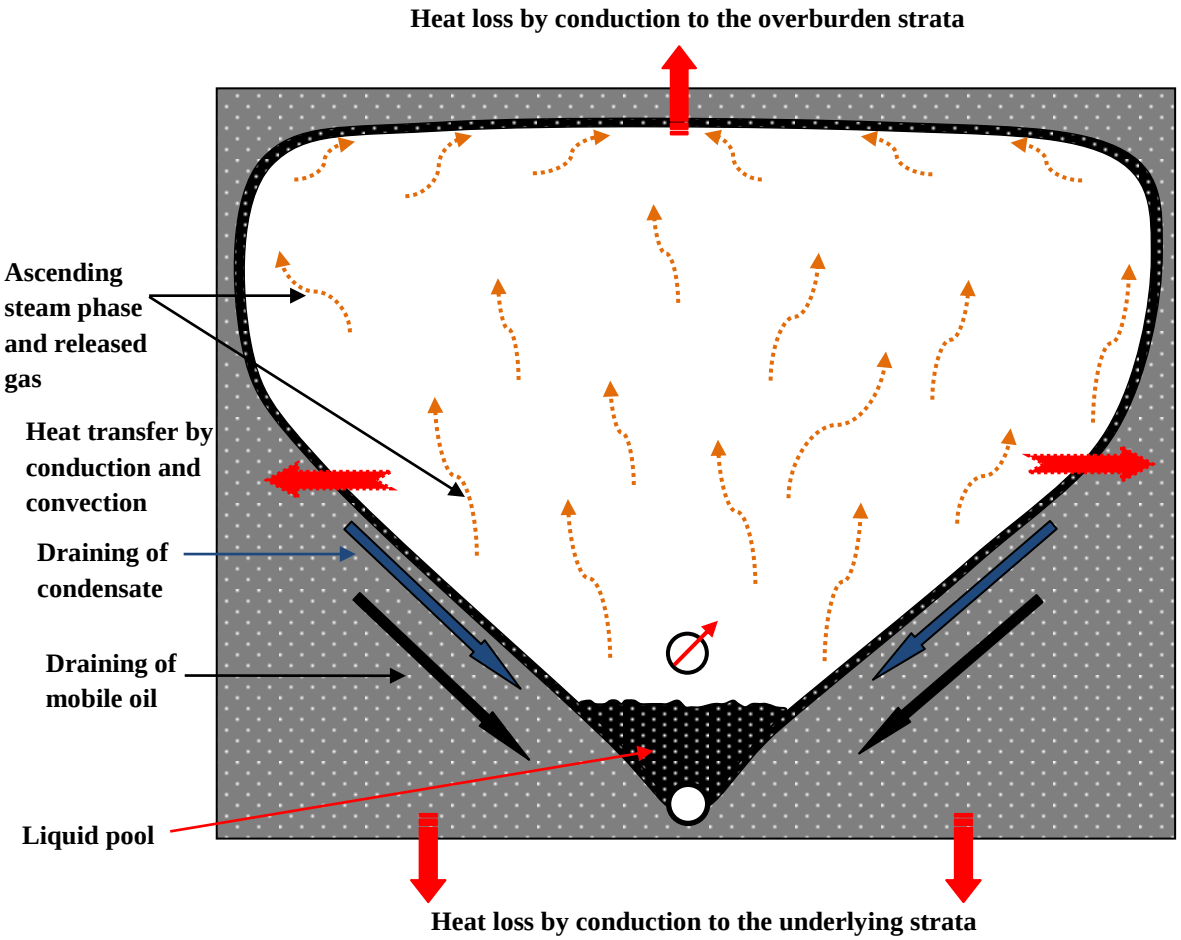

Figure 1.1: Conceptual flow diagram of the SAGD process

Using gravity forces for oil production prevents the possible differential fingering that occurs when the viscous crude oil is pushed with a less viscous fluid (gas, steam, or water at corresponding flooding processes). As far as the overall development of this gravity-dominated process is concerned, each particular SAGD pattern would progress through four successive typical stages which are depicted in Figure 1.2. These stages are classified based on the relative growth of the steam-saturated zone as follows:

a) Establishing an early communication between the paired horizontal wells (Figure 1.2.b),
b) Vertical encroachment of the steam chamber (Figures 1.2.c and 1.2.d),
c) Outward (i.e. lateral) spreading of the steam chamber (Figures 1.2.d and 1.2.e), and
d) Falling-down phase of the steam chamber leading to reservoir depletion (Figure 1.2.f).

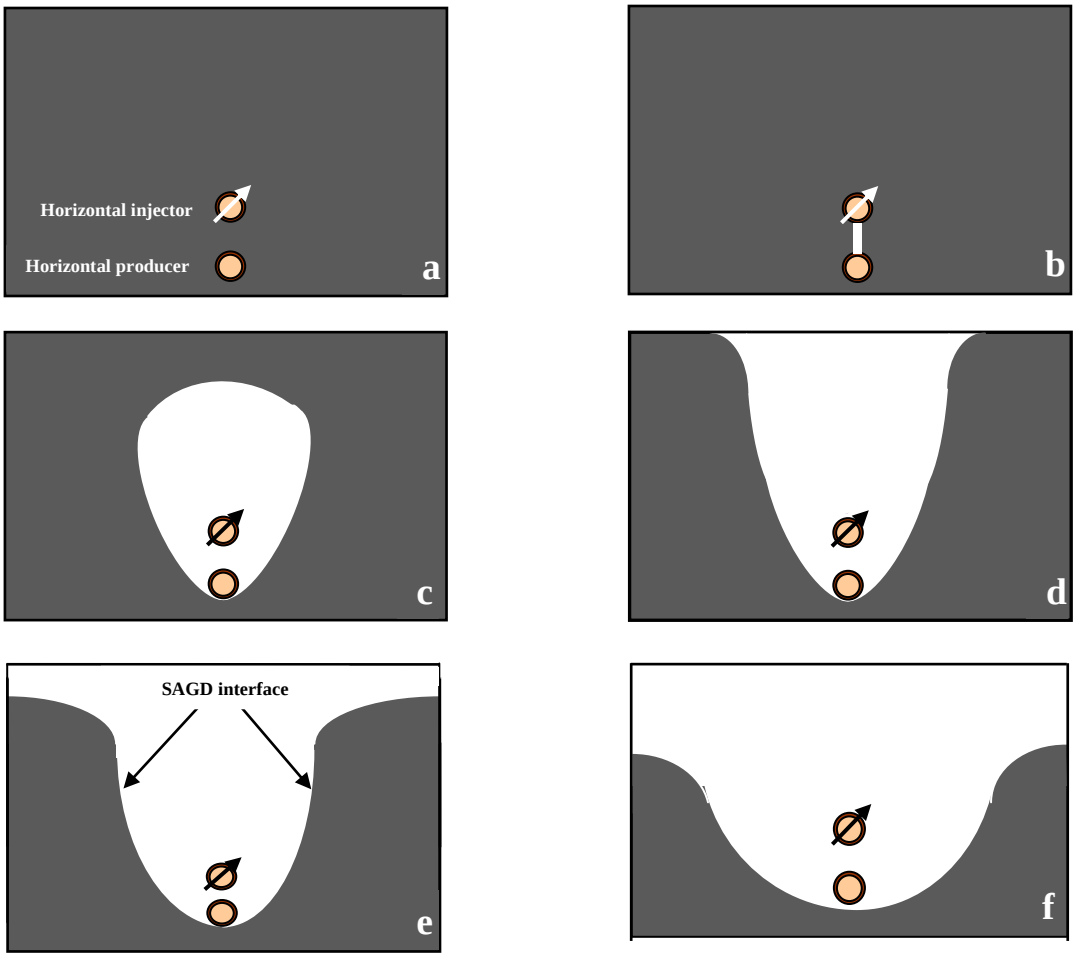

Figure 1.2: Different stages of the development of the SAGD process

High final recovery values as well as economical oil production rates are achievable using the SAGD recovery technique based on the extensive laboratory and field trials. However, there are still some issues related to the high energy requirements of the process, excessive thermal energy losses within the reservoir, CO_2 generation, and expensive surface water treatment facilities.

Considering the drawbacks of the conventional SAGD process, some modifications and even alternative recovery processes were proposed to enhance the overall performance of the SAGD process such as use of non-condensable gas along with the injected steam phase in a so-called Steam And Gas Push (SAGP) process to reduce the amount of heat loss to the overburden (Butler, 1999 and 2002, Butler et al, 2000a, 2000b, 2001) and also low pressure SAGD (Jiang, Butler, and Yee, 1998). On the other hand, an alternative solvent-based recovery method called Vapour Extraction (VAPEX) process was proposed. In the VAPEX process, a hydrocarbon solvent is injected at a pressure below the dew point into the oil layer in place of steam using a well configuration similar to the SAGD process. Mass transfer by diffusion mechanism of solvent into bitumen is responsible for the dilution of bitumen which results in attaining low viscosity in the conventional VAPEX process. The duration of this phenomenon in VAPEX is slower compared to diffusion of heat that causes viscosity reduction in the SAGD process in production in the region near the bitumen interface. The VAPEX process suffers from lower oil production rates compared to the SAGD process. However, the VAPEX process could be beneficial because of the lower energy requirements, lower CO_2 emissions, possible *in-situ* upgrading, and minimizing the cost of water treatment (Butler and Mokrys, 1991).

One modification of the SAGD process uses the idea of adding some steam additives to the injected stream in order to further reduce the bitumen's viscosity as well as to lower the SAGD's energy cost. This method, so-called Solvent Aided SAGD (i.e. SA-SAGD) process has been extensively studied in the literature under different commercial names (Nasr and Isaacs, 2001; Nasr et al, 2002 and 2003; Nasr and Ayodele, 2005; Nasr et al, 1991; Zhao, 2004; Zhao et al, 2005; Gupta et al, 2002, 2003, and 2005; Gupta and Gittins, 2005 and 2006; Boyle et al, 2003; McCormack, 2007). The SA-SAGD processes offer the combined advantages of a conventional SAGD and a conventional VAPEX process by reducing the inherent bitumen viscosity with the aid of solvent dilution and steam heating. Other advantages of the hybrid SAGD processes

include increased recovery potential compared to that of the VAPEX process, reduced energy requirements compared to that of the SAGD process, and possibly *in-situ* upgrading.

1.2. Motivation

Although the SAGD process looks straightforward at the first glance, there are still several concerns regarding the concept itself, as well as pertaining theories and actual oil recovery mechanisms. Aside from the extensive laboratory and numerical simulation studies, as well as pilot-scale and field-scale trials conducted to study the performance, technical aspects, economical issues and feasibility of this recovery technique, there are still numerous challenges which have remained unsolved. One can divide the inherent ambiguities associated with the SAGD process into two main groups of micro-scale (i.e. pore-level) and macro-scale issues. A vast series of these challenging topics have been pointed out in an excellent review paper published by Al-Bahlani and Babadagli (2009). According to this article, a main challenging group of these concerns is related to the lack of understanding of the actual physics of the SAGD process, particularly at the pore-scale.

It is evident that this lack of knowledge is present in both micro- and macro-scale aspects of the process to the extent at which the predicted SAGD process performance obtained from different resources (such as regular scaling up procedures of the experimental data, relevant analytical models, and numerical reservoir simulations) would not be verified by the attributed pilot tests and field trials. Considering the fact that the macro-scale success of this recovery technique is greatly affected by the pore-scale events and microscopic recovery efficiency, the first objective of this thesis is to mechanistically study the pore-scale aspects of the SAGD process by which some of the challenging micro-scale issues of this recovery method could be resolved. It is believed that with a detailed and precise review process and documentation of the events happening at the pore-level during the SAGD process, the associated micro-scale recovery mechanisms could be enlightened to the extent of incorporating these mechanistic findings into the mathematical models and numerical simulators. As the available commercial numerical simulators cannot handle pore-level mechanisms of the SAGD process, both in fluid flow aspect as well as heat-transfer related topics, it would be beneficial if one can consider the pore-level physics of the SAGD process in order to mathematically model or numerically simulate the field-

scale performance. Visualization experiments using glass-etched micromodel at the controlled environmental conditions were selected for this purpose. SAGD experiments using these micromodels were performed for qualitative and quantitative measurements.

Despite the general acceptance of the SA-SAGD process as an effective alternative of the SAGD recovery scheme and hence its progressive pilot-scale trials and field implementations, no effort was made up to the time this PhD study was undertaken in order to investigate the pore-scale features of the SA-SAGD process, particularly focusing on the heat- and mass-transfer related aspects, pertaining micro-scale recovery mechanisms, and the effect of system parameters on the process performance at the pore-level. As the overall scheme of the SA-SAGD process is quite similar to that of the SAGD process in terms of the injection and production patterns, vapour chamber growth, and fluid flow concepts in porous media, it is believed that the previously employed experimental methodology for the SAGD experiments could also be used to qualitatively and quantitatively investigate the pore-level aspects of the SA-SAGD process. As a result, the second objective of this research was defined to qualitatively and quantitatively study the performance of the SA-SAGD process at the pore-scale. Visualization experiments with the aid of glass micromodel prototypes of porous media at the controlled environmental conditions were selected for the purpose of fulfilling this objective.

The last objective of this thesis is to demonstrate the macro-scale performance of the SAGD and SA-SAGD processes using 2D physical model under controlled environmental conditions. A 2D cross-sectional model was designed and fabricated, and these two processes were conducted using the unconsolidated glass-bead packed porous media under controlled environmental conditions. The production performance of the SAGD process was studied extensively in the literature with the aid of scaled physical models; however, there are limited experimental data available regarding the production performance of the SA-SAGD process at the macro-scale. This objective is fulfilled focusing on comparisons made between the production performance, energy requirements, and microscopic state of the produced emulsions associated with these two major heavy oil and bitumen recovery methods.

1.3. Structure of the thesis

This thesis is prepared in four separate Chapters. Chapter one deals with the introductory materials about the heavy oil and bitumen resources and reserves, along with some information about the recovery technologies of these unconventional hydrocarbon resources. The other three Chapters are focused on the major research objectives of my PhD program. Each Chapter has its own statement of the problem, introductory materials, literature review, experimental aspects, results and discussion of results, and concluding remarks. Chapter 2 covers the pore-scale experimental studies focused on the SAGD process performance. In Chapter 3, the pore-level performance of the SA-SAGD process is discussed. Finally, Chapter 4 deals with the macro-scale performance of the SAGD and SA-SAGD processes. All the references are listed at the end of the thesis.

2. Mechanistic Investigation and Performance Evaluation of the SAGD Process Using Pore-Scale Experimental Studies

2.1. Overview

Successful application of gravity drainage process, facilitated with steam injection, using horizontal wells in various field tests, especially within Canada, indicates that high recovery factor and also economical steam to oil ratios are achievable. Steam Assisted Gravity Drainage (SAGD) recovery scheme was theoretically developed, pilot tested, and commercialized in Canada. However, there are still several technical challenges to be solved in this process. The pore-scale events of heavy oil recovery in the SAGD process were not understood prior to this investigation to the extent of developing new mathematical models that incorporate pore-level physics for simulating the SAGD process. Investigation of the physics of fluid distribution and flow behavior in porous media for the SAGD process at the pore-scale was expected to result in significant improvement in understanding the observed macroscopic phenomena. For instance, in-situ water in oil emulsification process, pore-scale characteristics of emulsion propagation, drainage and adsorption of water condensate droplets, different heat transfer mechanisms occurring at the micro-scale, drainage mechanisms of the mobile oil, and some other pore-scale aspects of the process have profound effects on the macro-scale SAGD production characteristics. Unfortunately, none of these pore-scale phenomena can be incorporated properly in available commercial numerical simulation packages.

A systematic series of flow visualization experiments of the SAGD process using micromodels of capillary networks etched on glass plates was developed in this thesis to capture the pore-level physics of the process using qualitative and quantitative analysis. The glass micromodels were initially saturated with heavy oil. All the pore-level SAGD experiments were carried out in a vacuum chamber in order to reduce the excessive heat loss to the surrounding environment while steam was injected under different superheating levels. Local temperatures along the model's height and width were recorded on a real time basis. The pore-scale events were recorded using digital photo capturing techniques. The captured snap-shots were analyzed using image processing procedures and the pore-scale events were documented properly. The relevant pore-scale mechanisms responsible for the in-situ oil mobilization and drainage in a conventional

SAGD process were addressed. Transport processes occurred in a conventional SAGD process at the pore-level including fluid flow and heat transfer aspects were investigated and documented.

According to this study, the steam chamber propagation behavior was found to be influenced by the randomly-distributed fingering nature of the unstable invading steam front near the mobile oil-steam chamber interface. This fingering phenomenon happens within a region of a few pores near the bitumen-filled pores that attain mobility due to heat transfer. This region is called mobilized region at the pore-scale. The extent of steam fingering phenomenon was seen to be severe during the vertical growth stage of the steam chamber where the buoyant front of the steam phase is protruding through the pores containing a continuum of cold bitumen, especially near the topside of the steam chamber. The steam fingering phenomenon was also observed during the outward propagation of the steam chamber at the proximity of its side wings. Simultaneous co-current and counter-current flow of different acting phases were observed near the lateral sides of the steam chamber, which are responsible for the horizontal expansion of the invaded region. In addition, several fluid flow regions were demonstrated in a typical expanding SAGD pattern in which different acting phases (i.e. steam, draining condensate, and mobile oil) flow under the action of gravity and capillary forces. These visualization experiments helped to determine the approximate thickness of these flow zones, and to understand the drainage behaviour and fluid flow regimes of different fluid phases within each particular pore-level fluid flow zone under the pertaining experimental conditions. In addition, several interfacial regions associated with these flow zones were also defined and characterized at the pore-level.

The qualitative analysis of the results also revealed that near a well-established oil-steam interface, gravity drainage takes place through a layer of pores, composed of 1-6 pores in thickness in the direction perpendicular to the interface, within the mobilized region. The interplay between gravity and capillarity forces results in the drainage of the mobile oil near this pore-scale mobilized region. Mobilization of the bitumen was found to be as a result of both conductive and convective elements of the local heat transfer process. Moreover, the visualization results demonstrated the phenomenon of water in oil emulsification at the interface which is an important characteristic of a typical SAGD process at the pore-scale. Following local steam condensation in the interfacial region of the SAGD process at the pore-scale, the

phenomenon of emulsification was hypothesized to be interpreted by the interfacial thermodynamic approach of non-spreading characteristics of water over oil in the presence of a gas phase. This approach, which is based on the entrapment process of the water condensate droplets within the continuum of the draining mobile oil, was also experimentally verified using this pore-scale study of the SAGD process. The extent of emulsification depends directly to the temperature gradient between the steam phase and cold bitumen.

Other pore-scale phenomena are also illustrated using these pore-level visualization studies such as capillary drainage displacement and film-flow drainage mechanisms of the mobile oil, localized entrapment of steam bubbles and condensate droplets within the mobile oil continuum, sharp temperature gradient along the mobilized region, co-current and counter-current flow regimes at the chamber walls, spontaneous imbibition of condensate followed by mobile oil drainage, steam condensation at the interface due to temperature gradient, and snap-off of liquid films. It is believed that these findings, along with the detailed quantitative analysis of the process performance improve our understanding about the relevant physics of the process. This work will form a reliable basis for the development of realistic modeling procedures of the SAGD process.

Parametric sensitivity analyses were performed in order to quantitatively evaluate the SAGD process performance at the pore-level within the range of experimental conditions. SAGD interface advancement velocities at the pore-scale were measured and correlated with system parameters such as operating temperature, macroscopic and pore-scale properties of porous media, and heavy oil properties within the range of experimental conditions. It was concluded that the average sweep rate of each particular SAGD experiment within the range of experimental conditions is a direct function of the permeability of the model, and inversely proportional to the porosity of the model times the viscosity of the oil phase at the operating temperature. The permeability and porosity of the glass micromodels are controlled primarily by several pore-scale dimensions of each particular porous pattern such as pore-to-pore distance, pore throat size, and depth of etching in the pore body as well as pore throat regions. In-situ oil viscosity is also a strong function of the operating (i.e. steam) temperature.

In this Chapter, qualitative and quantitative results of the pore-scale SAGD experiments are presented in detail based on the visualization experiments at the controlled environmental conditions.

2.2. Micro-Scale Challenges of the SAGD Process

According to the mass of articles found in the literature, the experimental aspects related to the utilization of steam heating to produce heavy oil under gravity drainage process are limited to those which are conducted using scaled physical models. These results were used to acquire better understanding of the overall physics of the process, as well as to predict intended field-scale performances based on the empirical scaling-up procedures. It is believed that the macro-scale production performance of a typical SAGD process depends significantly on the pore-level drainage mechanisms, so it is vital to capture the actual physics of this recovery process at the pore-level using relevant mechanistic studies. A series of pore-scale events are believed to have major contribution in the macro-scale performance of the SAGD process. These events include but not limited to the following:

a) Local fluid mixing at the pore bodies,
b) Snap-off mechanism of the invading fluids,
c) Local conduction-convection heat transfer,
d) Pore-scale immiscible displacement of the mobile oil by injected steam as well as water condensate,
e) Local dilution effect as a result of pore-scale mass transfer and dispersion in case a solvent is co-injected along with the steam phase in the Solvent Assisted SAGD process, and
f) Micro-scale emulsion formation and flow along the drainage path.

It would be beneficial to critically analyze and document the pore-level phenomena associated with this process in order to qualitatively understand the relative contribution of each of these pore-scale events in the overall drainage scheme. As mentioned earlier, numerous experimental attempts have been conducted so far to quantify, optimize, and investigate the macro-scale performance of the SAGD process. However, there were still some uncertainties especially about the micro-scale performance of this process which were needed to be addressed properly. Our

methodical study approach elucidates the drainage mechanisms and pore-level performance of the SAGD process with the aid of pore-scale visualization experiments under controlled environmental conditions. Some of these uncertainties associated with the SAGD process at the pore-level are discussed briefly in this section.

2.2.1. Steam Chamber Development

The drainage performance of a typical SAGD process is a strong function of the steam chamber occurrence and its development following the start-up stage. This stage has received a great deal of attention in scientific texts; however, there are still some complexities regarding the development stages of the steam-saturated zone. For example, it was primarily believed that the steam chamber is extended all the way from the injector well down to the producer (Butler 1991). It was a challenge controlling the process to the extent of avoiding steam breakthrough from the producer. However, recent studies of the steam chamber development highlighted that there is a pool of liquid phase above the producer, avoiding steam channeling and breakthrough from the producer (Gates and Chakrabarty, 2005; Gates et al, 2005). Complexities of this form exist in different stages of steam chamber development which is shown schematically in Figure 1.2. To name a few, a number of these complications are listed here:

a) Probable co-current and counter-current local flow of different draining and invading phases,
b) Local heat transfer mechanisms within the steam chamber and at its proximity,
c) Creation of local water-in-oil emulsion at the pore-level,
d) Steam condensation phenomenon near the pore-level SAGD interface,
e) Drainage mechanisms of the mobile liquid phases leading to both lateral and vertical encroachment of the steam chamber, and
f) Vertical rise of the steam phase by fingering.

These phenomena have strong ties with the pore-scale events of the steam chamber development which are discussed later in this Chapter based on our visualization experiments.

2.2.2. Steam Fingering Phenomenon

The original theory of steam chamber vertical rise was hypothesized by Butler considering velocity equilibrium conditions between invading and draining phases, through an arbitrary control volume within the steam chamber (Butler, 1987 and 1994). The conceptualized Butler's theory of rising steam fingers during the vertical encroachment of the steam chamber is schematically shown in Figures 2.1.a and 2.1.b. The flat-front vertical encroachment style of the steam chamber was discredited both by experimental results using scaled physical models (Butler, 1991 and 1994) as well as numerical simulation of actual field trials (Ito and Ipek, 2005; Ito et al, 2004; Ito and Suzuki, 1996). It is believed that the steam fingering phenomenon during the vertical encroachment of the steam chamber happens as a result of buoyancy forces (Al-Bahlani and Babadagli, 2009). Although the steam chamber is stable at its bottom part near the injection well due to continuous nature of the steam injection, buoyant steam phase near the topside of the steam chamber has an inherently unstable interface with the thick, cold, and stagnant continuum of oil on the top. The hypothetical approach of steam fingering at the elemental scale near the topside of the steam chamber is shown in Figure 2.1.b. It is likely that the topside of the chamber would be dome-shaped, having a lot of steam fingers in it (Butler, 1991). According to the literature, there is still doubt about the possibility of steam fingering in the outward direction, i.e. spreading phase of the steam chamber (Al-Bahlani and Babadagli, 2009). In the next sections, it is presented that our visualization experiments facilitated the means to systematically examine the possibility and extent of steam channeling and fingering through the mobilized region ahead of the pore-scale SAGD interface.

2.2.3. Fluid Flow Regimes and Drainage Mechanisms

An overall SAGD pattern could be divided into different flow zones where interacting fluid phases are flowing under the action of gravity, buoyancy, and capillarity forces in the absence of excessive viscous force. One could categorize these flow zones as:

a) Flow zone near the pore-scale SAGD interface along the side wings of the steam chamber,
b) Flow zone within the steam saturated zone far from the pore-scale SAGD interface, and
c) Flow zone in the proximity of the apparent pore-scale SAGD interface towards the topside of the steam chamber.

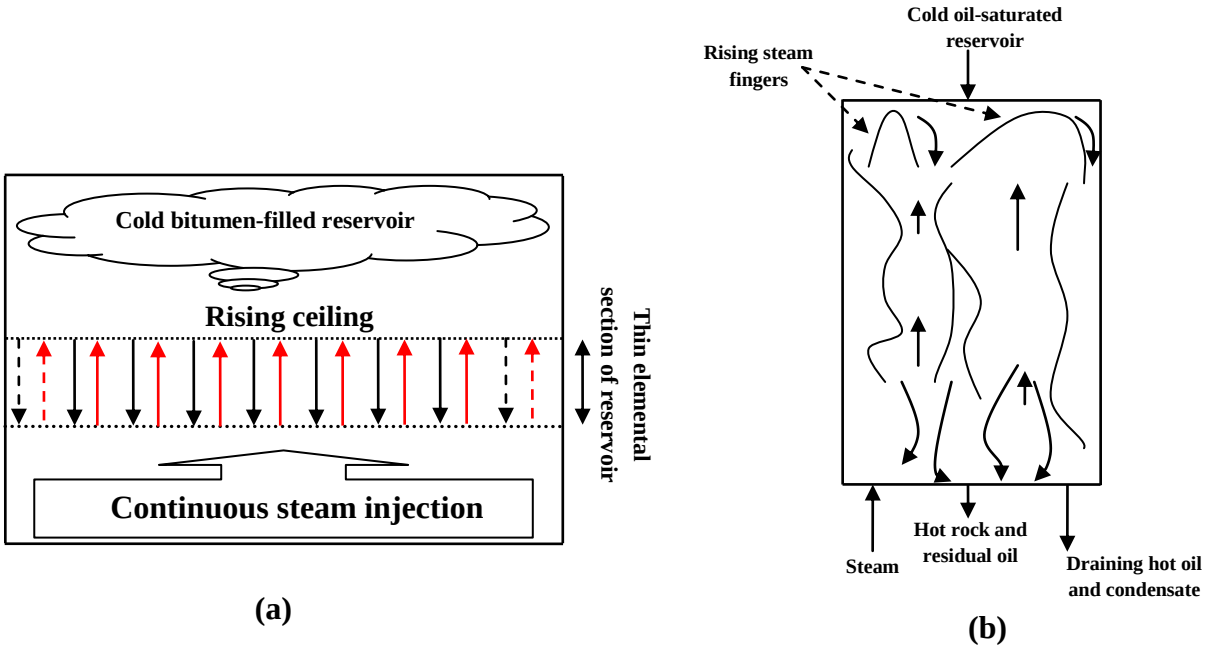

Figure 2.1: (a) Countercurrent flow of rising steam and falling oil and condensate (modified from Butler, 1994), and **(b)** Hypothetical diagram of rising steam fingers (Modified from Butler, 1987).

The common terminologies used for the SAGD front advancement, namely as co-current and countercurrent steam front propagation, have been repeatedly used in scientific texts dealing with this recovery technique (Butler, 1987, 1991 and 1994; Chung and Butler, 1987; Nasr et al, 2000). It is believed that one of the most complex fluid flow regimes of a typical SAGD process could be seen near the pore-scale interface along the lateral extensions of the steam chamber. In this particular steam chamber location, both thermally-mobilized oil and water condensate phases drain along the lateral extension of the steam chamber toward the producer. The drainage phenomenon is facilitated with both capillary and gravity forces acting to the body masses of the draining liquids. Mobile oil cannot drain towards the interior of the steam chamber due to capillary forces. The water condensate phase is being formed due to the local heat transfer between steam and the mobile oil at the pore-scale. There is a tendency for the water condensate phase to spontaneously imbibe through the pores already occupied by the mobile oil in the presence of the steam phase rather than draining back in the form of water films into the steam chamber as a result of capillary forces. On the other hand, steam phase is rising upwards inside the steam chamber at the proximity of its lateral extension. One could argue that a counter-

current front propagation is responsible for the lateral expansion of the steam chamber. However, pore-scale results of our visualization experiments revealed that a much more complex fluid-flow pattern exists near the pore-scale SAGD interface, at the proximity of the lateral extension of the steam chamber which will be discussed later.

As far as the fluid flow through the steam chamber is concerned, steam is the main flowing fluid phase ascending vertically towards the pattern's topside constraint. As the residual oil saturation within the chamber is practically nil, the oil relative permeability within the steam chamber is zero (Butler, 1991 and 1994; Walls, 2003). In the case of partial steam condensation within the steam chamber, the evolved condensate could drain counter-currently with respect to steam. The steam phase condensing in the water-filled pores near the SAGD apparent interface would drain parallel to the pore-scale SAGD interface due to the capillary forces. As a result, it seems unlikely that much of the mobile oil drain directly through the steam chamber and, even if it does, it finally drains into the interface located down gradient and re-joins the main draining oil stream (Butler, 1991 and 1994). Likewise the fluid flow regime at the proximity of the lateral extension of the steam chamber boundaries, our pore-scale results obtained from the conducted visualization experiments revealed more insight into the fluid flow pattern within the steam saturated zone which is discussed in detail later.

Lastly, one would expect a counter-current steam front encroachment near the topside of the steam chamber at the proximity of the pore-scale SAGD interface due to the rising state of the steam phase under the steam fingering scheme of flow and draining nature of the mobile oil and water condensate flow along the apparent interface. Due to the specific design of our visualization experiments, it was not possible to look precisely into this particular fluid flow pattern. Overall, the steam interface advancement is due to a combination of both co-current and counter-current flow patterns.

2.2.4. Emulsification at the Pore-Scale

The subject of "emulsification phenomenon" during the SAGD process was covered in the literature based on the experiments conducted using scaled physical models as well as field-scale data (Chung and Butler, 1987 and 1989; Noik et al, 2005; Sasaki et al, 1996, 1999, 2001 and

2002). According to the field-scale trials of the SAGD process, the produced liquid is in the emulsion state composed of mobile oil and water. This emulsion phase is either stable or unstable depending on the physicochemical characteristics of the interacting liquids as well as process operating conditions. The overall SAGD process performance is a trade-off between an increase in the draining liquid viscosity as a result of in-situ emulsification and a decrease in the produced liquid viscosity as a result of continuous steam heating. The success of a conventional SAGD process in terms of mobile oil production depends on the following simultaneous events:

a. Viscosity reduction of the produced liquids and in-situ stagnant bitumen as a result of incessant steam heating, and at the same time,

b. Increase in the dynamic viscosity of the in-situ W/O emulsion as a result of emulsification process itself, as well as continuous increase in the water volume fraction (i.e. water content) of the developed emulsion. This viscosity increase continues until the emulsion would be produced at the production side, or when the associated water content of the emulsion reaches to its equilibrium (i.e. final) value, whichever is sooner.

It is also believed that the mechanistic aspects of the emulsion creation at the pore-level depend directly on the spreading characteristics of the interacting fluids. Once the injected steam contacts the cold bitumen-saturated pores, it would likely condense as soon as the local temperature drops below the dew point temperature at that particular operating pressure. Very fine water droplets produced at the chamber interface due to condensation would move likely into the continuum of the mobile oil phase. This microscopic invasion of very fine water droplets, whose sizes are in the range of 0.005 to 0.01 mm in diameter, into the bitumen-filled region would likely create water-in-oil emulsions which drain under the resultant of gravity-capillary forces interaction (Sasaki et al, 2002). This emulsification is illustrated schematically in Figure 2.2.a considering a plane interface. As it is shown in this Figure, the steam phase is in contact with a falling film of the mobile oil. Although it is theoretically expected that the steam chamber temperature stabilizes after initial chamber development due to the continuous steam injection into the SAGD pattern, it is also expected to have a temperature gradient at the SAGD interface and nearby area where the mobile oil would drain toward the production side. The state of in-situ viscosity of the draining emulsion is not yet fully understood. The viscosity of draining

bulk oil films, containing isolated droplets of water, could decrease as it drains down-gradient because it approaches region of higher temperature. Another possible scenario is that the associated emulsion viscosity could increase while it drains in the direction of gravity as a result of an increase in its water content due to further local emulsification phenomenon. Suppose that steam phase condenses on the plane surface of falling mobile oil film at t = 0 as shown in Figure 2.2.a The resulting water droplets would be buried within the pool of the mobile oil continuum through an engulfing process, due to negative spreading coefficient of water on oil in the presence of a gas phase. These enclosed and isolated water droplets would drain downwards along with the falling oil film by the combined effect of drag force between the water droplets and the falling oil film and the gravity forces. As time goes on, the cumulative amount of the trapped water droplets, originated from the steam condensation process at the cold oil face, tends to increase within the oil film while the draining oil approaches toward the production end.

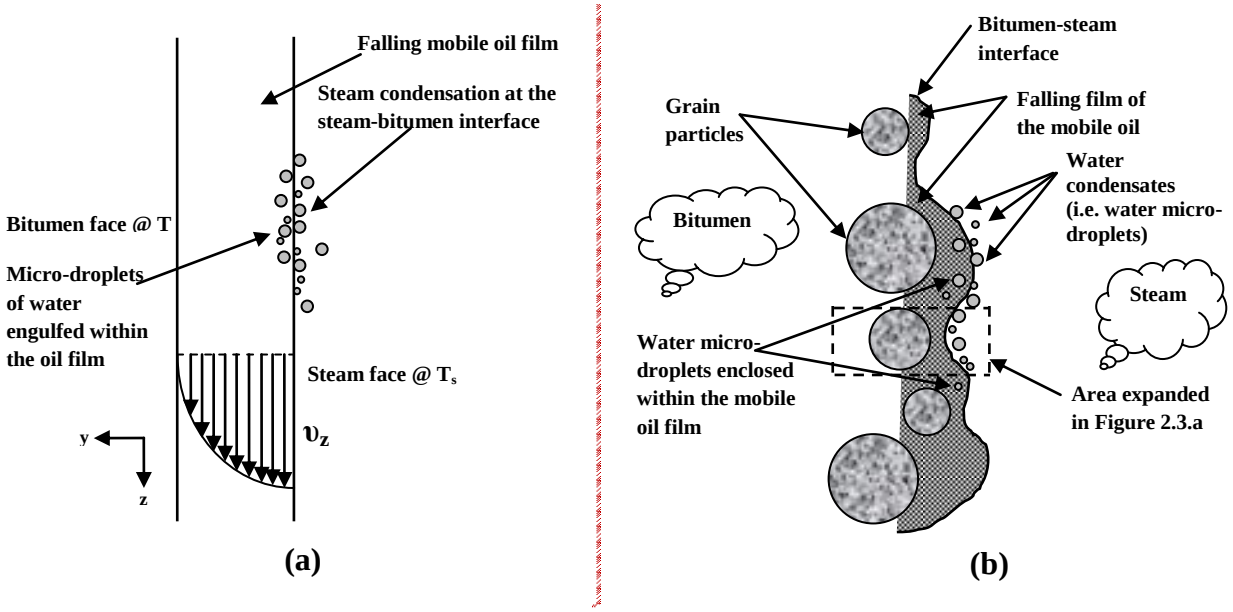

Figure 2.2: Schematic representation of the hypothesis describing the steam condensation process and water droplets engulfment within the draining mobile oil film at the **(a)** planar steam-bitumen interface, and, **(b)** porous media interface.

Another hypothetical view of the microscopic emulsion creation during the SAGD recovery scheme with focus on the pore-scale bitumen-steam interface is presented in Figures 2.2.b and 2.3.a. As it is shown in these two Figures, the falling film of the mobile oil forms an interface between the cold region containing bitumen and hot region (i.e. steam chamber). The grains

could be either covered with water or oil depending on the initial saturation and preferential wettability of the porous medium. As it is demonstrated in these Figures, similar phenomenon could happen at the porous media interface as that of the plane interface (Figure 2.2.a); the water condensate droplets are formed at the apparent SAGD interface by the action of thermal gradient, they would be enclosed by the surrounding oil continuum, and then could be dragged along towards the production side by the falling film of the mobile oil. As steam condensation at the apparent SAGD interface proceeds, the latent heat of condensation transmitted to the colder oil face would effectively mobilize it. On the other hand, microscopic invasion of water micro-droplets through the mobile oil boundaries would result in increased apparent viscosity due to the local emulsion creation. According to our experimental results, it is evident that reduction of viscosity because of heat transfer is much more pronounced than the viscosity increase as a result of local emulsification. The dotted rectangular area in Figure 2.2.b is expanded in Figure 2.3.a to schematically show the details of the water in oil emulsion creation at the pore level.

As it will be discussed further in the "Qualitative Analysis of the Experimental Results" section of this Chapter, the condensate droplets encounter different flow patterns over their tortuous draining path toward the production well. They could coalesce to form larger-sized trapped water droplets under specific circumstances and still drain by gravity. The condensate cannot form a continuous film of water over the falling oil-film though, which is the main idea behind the schematic representation of spreading phenomenon shown as Figure 2.3.b. As it is illustrated in Figure 2.3.b., a water droplet is formed at the top of a falling film of the mobile oil following a thermal gradient-induced condensation process. This droplet of water cannot spread spontaneously over the oil film as the spreading coefficient of water over oil in the presence of a gas phase is negative. As a result, it would be dragged by the falling oil film toward the production well. As time goes on, some of these separate condensate droplets would be engulfed (i.e. buried) by the continuously falling film of the mobile oil and would form the water-in-oil (W/O) emulsion phase. Our experimental results also elucidated that there is a high level of local mixing at the proximity of the apparent SAGD interface at the pore-level due to high thermal gradient, sudden thermodynamic phase change, instability of the interfaces associated with the invading phase which causes sudden jumps over their average position (i.e. Haines jumps), simultaneous flow of different three phases, and snap-off mechanism. This high level of local

mixing phenomenon enhances the heat transfer process locally as well as drains the mobile oil in a gravity-dominated process. It is worthwhile to note that the details of dynamic nature of the local mixing phenomenon and the extent of pore-scale mixing near the interfacial area could be studied best from motion pictures and movies recorded during the experiments.

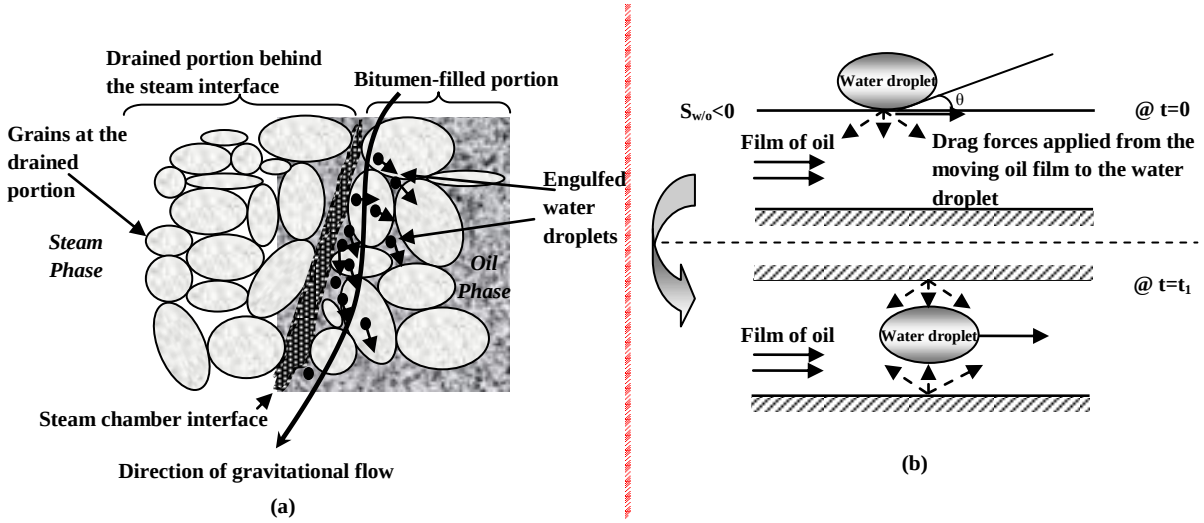

Figure 2.3: Schematic representation of **(a)** pore-scale emulsion creation in the SAGD process focusing on the near interface events (Modified from Sasaki et al, 2002), and, **(b)** engulfing phenomenon at the pore-scale.

The mobile oil along with the enclosed water droplets establish drainage pathways either through the previously drained pores, which may have already been filled with water condensate, under an immiscible co-current frontal advancement, or through the pores which have already been drained by upward-moving steam under an immiscible counter-current displacement. In either of these two cases, the degree of enclosure of water droplets within the continuum of the mobile oil could be increased. For example, if the first scenario happens, pore-level contact of the draining mobile emulsion with the water phase that has already filled the pores could cause possible drag and entrapment of more water droplets within the draining mobile emulsion. If the draining mobile emulsion tends to counter-currently flow against ascending steam phase (or enter a pore whose volume is already occupied by the steam phase), there is still the possibility of excessive heat transfer beyond the condensation limit, followed by steam condensation at the mobile oil-steam interfacial region. This could also increase the rate of enclosure of water droplets inside the draining mobile oil continuum. Water micro-droplets would be likely dispersed through the

draining mobile oil to form a relatively non-homogeneous water-in-oil emulsion at the pore-level. The rate of in-situ emulsification and size of the entrapped water droplets within the mobile oil could be a function of different operational and in-situ factors such as degree of superheating of the injected steam, original temperature of initial bitumen in place, operating pressure in either superheating or saturated states of the injected steam, presence of connate water saturation, injected steam quality, and convective nature of the drainage process near the well-shaken mobilized region. Of particular interest could be the in-situ rheological behaviour of the developed emulsion phase through known-structure synthetic porous media. It is evident that the rheological and dynamic properties of emulsion would be different from those of water and mobile oil, so are their associated viscosity magnitudes.

2.3. Experimental Setup and Model Preparation for the SAGD Visualization Experiments

2.3.1. Model Design and Preparation

Different glass-etched micromodels with fully-characterized pore structures were designed and fabricated to conduct the SAGD visualization experiments. Micromodels are made to replicate porous media in order to visualize capillary and transport processes at the pore level. Micromodels are generally small in size, with inlet and outlet hole(s) drilled into the flow system to facilitate injection and production of chemical substances, as well as to create and maintain a steady flowing system. One efficient form of micromodels that helps to quantify basic transport phenomena could be composed of simple porous networks of fixed-geometry of pore bodies connected by pore throats. The medium employed to create micromodels can be glass, silicon, or even polymers, and the pore network can be either etched or created from a monolayer of substrate. Micromodels are built out of transparent materials to be able to see-through, making it feasible to visually investigate the ongoing process with the aid of captured photos /movies using image processing techniques (Chatzis, 1982; Chatzis et al, 1983; Wan et al, 1996; Feng et al, 2004).

Two dimensional glass micromodels have been used widely to demonstrate fluid flow through porous media for petroleum engineering applications. Glass-etched micromodel preparation procedure, which is based on the photo-fabrication process, originally came from the printed-

circuit technology used in electromagnetic and electrical circuits industry. Considering advances made, it is relatively easy to make 2-D pore network models of even heterogeneous pore size and interconnections within transparent media such as glass. Since the porous structure is only one pore deep, and the surrounding solids walls are all made of glass in a glass micromodel, it is feasible to observe the fluids as they flow along the pore channels and interact with each other. Another benefit of employing such a transparent porous model is the possibility of studying how the geometry of the porous network would affect the fluid flow patterns and also the trapping of the fluids within the network of pores. Various pore patterns including rock-look-alike and geometric patterns can be designed and etched (Sohrabi et al, 2000 and 2007). The choice of pore network pattern is normally made based on the objective of the visualization study. If the objective of micromodel experiments is to generate quantitative data for mathematical modeling of a physical fluid flow process, geometric patterns are preferable as they have pores with definite shapes and sizes. It is not necessarily a general rule, as one could find a mass of qualitative approaches of pore-scale studies in the literature, performed using glass micromodels with geometrically quantified porous structures. On the other hand, rock-look-alike pore patterns are normally derived from porous rock thin sections and as a result, could resemble the real morphology and pore structure of the real porous medium. However, it is much more difficult to mathematically model the transport processes within this type of porous structure as the pore shape, size, connectivity, tortuosity, and other pore-scale dimensions of the porous pattern do not have uniform trends and behaviour.

In our visualization experiments, the etched porous patterns were fully characterized in terms of physical dimensional properties as well as detailed porous pattern characteristics. This detailed characterization will be used for quantitative pore-scale analysis of the process performance. Table 2.1 contains a summary of the micromodels characteristics in terms of the model dimensions as well as the porous pattern properties. The general micromodel pattern geometry is schematically shown in Figure 2.4.a. A close-up of one of the employed glass micromodels is also presented in Figure 2.4.b. Line-source scheme of injection and production was designed for the micromodels in order to facilitate early development of the steam chamber. As a result, the experiments cover the lateral encroachment stage of the steam chamber propagation. Thanks to the symmetry of the geometrical pattern of a typical SAGD process, a high permeable trough

was designed at one side of the etched pattern to experimentally simulate only half of the process scheme. This ditch-like channel, which is relatively large in size (and hence permeability) comparing to the pores, was made along the entire height of the model adjacent to the pore network, to simulate a vertical line source of steam injection (i.e. left side of the micromodel in Figure 2.4.b which is covered entirely by strips of aluminum foil). A production hole was drilled at the bottom part of the trough in order to facilitate the gravity drainage process, providing sufficient drainage height above it. Each micromodel was fitted inside a model holder and then was placed vertically to enforce the gravity-dominated flow scheme. Each micromodel was first saturated with bitumen thoroughly at elevated temperature of a convection oven (60°C) and under a backup pressure (i.e. high-pressure air line over the warm bitumen supply or using a syringe pump). The bitumen-filled micromodel was then brought into the lab environment to represent the initial experimental conditions.

Table 2.1: Physical and pore-scale characteristics of the glass micromodels

Model Name	DC1	DL1	OC-1	OM1	OM2
Physical dimensions					
Length (mm)	304.00	304.00	304.00	301.00	301.00
Pattern length (# of pores)	190	149	149	150	150
Width (mm)	141.00	100.00	100.00	101.00	101.00
Pattern width (# of pores)	89	49	49	50	50
Pore-scale dimensions					
Depth of etching* (μm)	127.70 ± 0.80	250.20 ± 0.90	125.3 ± 1.7	118.90 ± 1.70	196.80 ± 6.60
Pore body width (mm)	1.31	2.04	1.38	2.00	2.00
Pore throat width (mm)	0.49	0.67	0.45	0.30	0.30
Particle size (mm)	1.11	0.99	1.59	1.20	1.20

*: Depth of etching at the pore body space

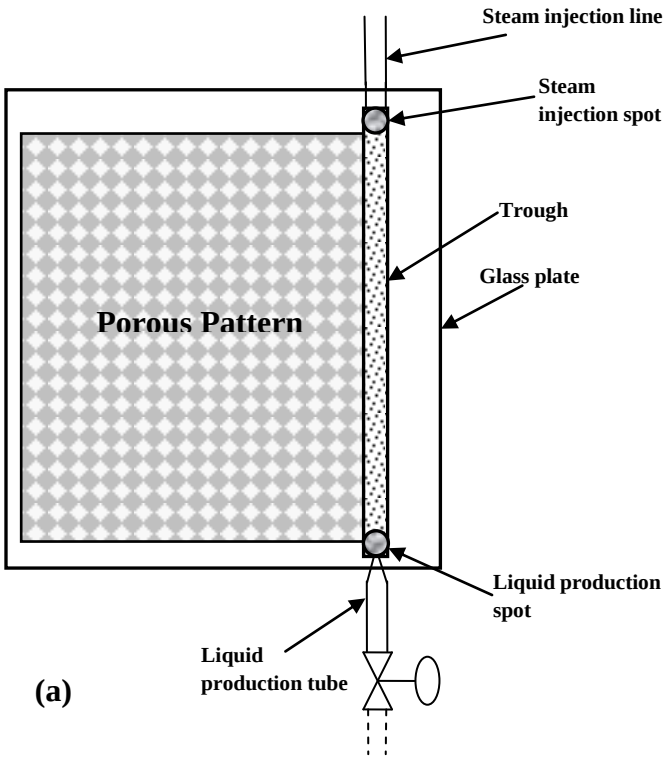

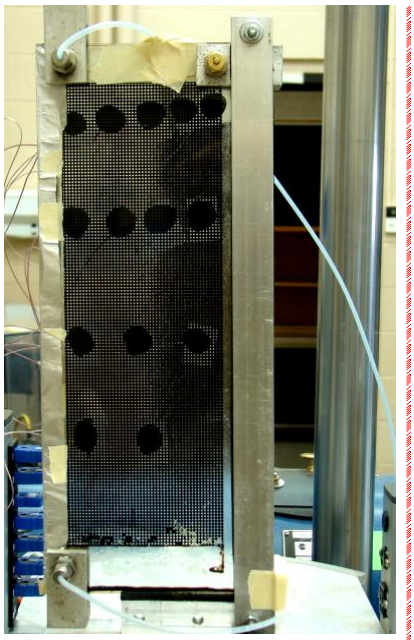

(b)

(c)

Figure 2.4: (a) Micromodel pattern geometry consisting of injector, producer, and trough, **(b)** A close-up of glass micromodel saturated with bitumen just before the SAGD experiment, and, **(c)** A snap shot of the employed vacuum test rig

2.3.2. Experimental Setup

Figure 2.5 schematically shows the process flow diagram for the visualization experiments of the SAGD process. A closed loop steam generation and injection system was used to play the role of steam supply facilities. All the connecting flow lines were heated / insulated to provide steam at superheated condition and also to avoid steam condensation within the transfer lines. The micromodel was then connected to the steam supply flow line at the top (i.e. injection spot). Steam was allowed to enter the micromodel at the top, and fill the trough all the way down on one side of the pore network. In order to mobilize the oil within the pores adjacent to the trough, it was needed to apply a start-up process, i.e. injection of steam through the injection line and producing it directly from the production spot. This procedure involved injecting fresh steam phase to the pores attached to the injection groove; hence initialized the mobilization process of the viscous oil. The production metering valve was closed in order to avoid any steam breakthrough from the production port. In other words, a finite head of the drained liquids (i.e. water condensate at the beginning and drained emulsions afterwards) was maintained continuously inside the production line to prevent steam channeling. This column of liquid was drained occasionally using the production metering valve in order to let the system to uptake as much steam as it required for the ongoing gravity-dominated process. Visualization experiments of the SAGD process at the lab conditions suffer from the excessive heat loss from the model (which is almost at the steam temperature) to the surrounding environment (i.e. at lab temperature). As a result of this heat loss, a considerable fraction of the injected steam, which is supposed to condense on the cold face of bitumen would then be condensed to make up for the above-mentioned temperature difference.

To facilitate an effective steam heating of the bitumen-saturated micromodel in the absence of an undesired heat loss, a vacuum test rig capable of providing down to 10^{-6} torr of vacuum pressure was used. The vacuum chamber operates with a combination of a mechanical and a diffusion pump. Figure 2.4.c provides a snap shot of the employed vacuum test rig. All the visualization tests were carried out at the vacuumed environment within the air pressure range of $5\times10^{-6} – 10^{-4}$ torr. According to the heat loss calculations (presented later in this Chapter), it is believed that the amount of heat loss from the glass surface into the surrounding environment through the convection mechanism would be negligible at this very low range of air pressure. The only heat

loss mechanism that might be of great importance at these low magnitudes of vacuum pressure is the radiation heat transfer which could be lowered by covering the hot spots of the micromodel with shiny reflective thin films such as strips of aluminum foil. It could also be lowered further by covering the portions of the inverted bell jar (that might not be needed from the visibility point of view) with the same shiny layers. Operating the SAGD experiments at low values of environmental air pressure not only prevents the steam phase to condense as a result of excessive undesired heat loss, but also allows it to transfer its latent heat of condensation only to the cold bitumen face where it is supposed to do so.

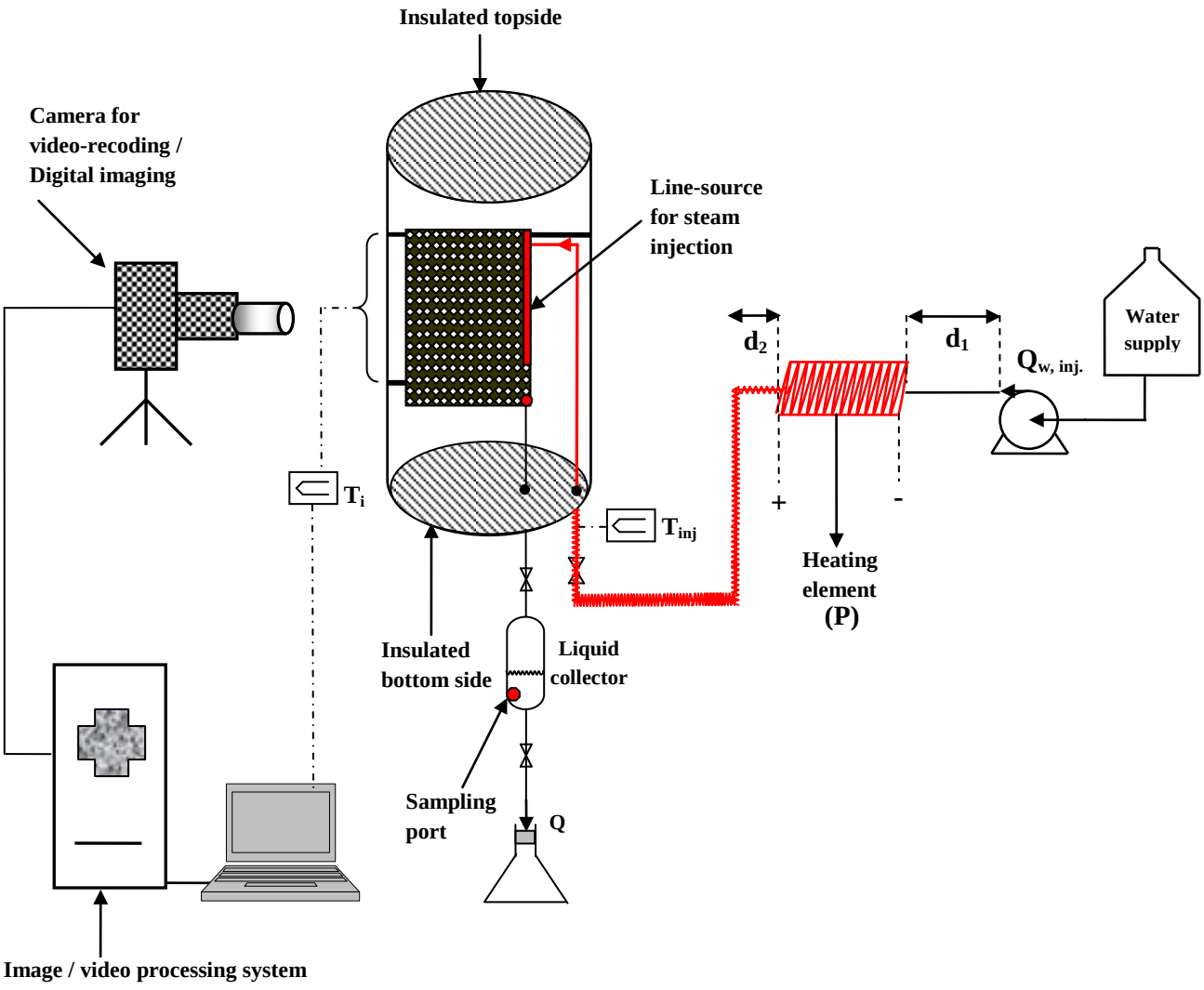

Figure 2.5: Schematic representation of the process flow diagram for the visualization experiments of the SAGD process at the pore-scale

2.3.3. Properties of Crude Oil

In this research, Cold Lake bitumen was used as the oil phase whose properties are summarized in Table 2.2. The viscosity – temperature relationship of bitumen was measured by Hatch Ltd (2009) using Physica Modular Compact Rheometers (Anton Paar), and is shown in Figure 2.6. The Cold Lake bitumen viscosity was correlated to temperature using a power law correlation in the form of:

$$\mu(T) = aT^b \tag{2.1}$$

in which T is the operating temperature (°C) and μ is the viscosity of bitumen (cP). Using these units, the parameters in Eq 2.1 were obtained as a = 91,673,411,565 and b = -4.26.

Table 2.2: The physical properties of Cold Lake bitumen

Density versus temperature	
Bitumen density (g/cc)	*Temperature (°C)*
1.012	15
1.001	22
0.997	40
0.978	70
SAPA analysis	
Fraction	*Mass %*
Saturates	22.4
Aromatics	30.8
Polars	29.4
Asphaltenes	17.4
Main elemental characterization	
Element	*Mass percent*
Carbon	83.62
Hydrogen	9.57
Nitrogen	0.39
Sulphur	5.25
Viscosity at 30°C	47,000cp
Molecular weight	557 g/mol

The C_{100} hydrocarbon analysis of Cold Lake bitumen was carried out by Maxxam Analytics (2006) and is presented in Figure 2.7. The compositional characteristics of the employed oil are presented in the form of cumulative weight percent of the successively increasing carbon numbers in the bitumen sample. It is worthwhile to note that the normalized weight percent of the Hectane plus component (i.e. C_{100}^{+}) and also heavy metals as well as non-hydrocarbon components are 10.4 and 0.6 wt% respectively. According to the viscosity value of bitumen at 30°C (i.e. 47,000 cP) and the exponential decline of viscosity versus temperature as predicted by Eq 2.1 or Figure 2.6, it is evident that the mobile oil viscosity would be around that of water at about 375°C.

2.4. Qualitative Analysis of the Experimental Results

In this section, the qualitative analysis of the SAGD visualization results is presented in order to mechanistically investigate the pore-scale performance of the SAGD process. It took some time for each particular experiment to pass the transient phase of the displacement process during which excessive amounts of the injected steam was condensed in the flow lines and in the micromodel in order to warm up the system and create an early communication between injection and production ports. Steam was injected at atmospheric pressure to avoid viscous-dominated oil drainage. During these SAGD visualization experiments, a temperature range of 100 – 120 °C was achieved depending on the operating conditions and injection rates of each particular SAGD trial. The observed pore-scale phenomena of the SAGD process during the flow visualization experiments were recorded in video format as well as photographs taken at various stages of the process to document the microscopic events. Pore-level phenomena on close-up view were captured using a Canon video camera with appropriate combinations of three close-up focusing lenses (numbers 2, 3, and 4). This made it possible to have a particular focused region in view, containing a few pores as could be seen in Figures presented in this section.

Pore-scale flow visualization of the SAGD process reveals several mechanisms happening in the vicinity of the apparent bitumen-steam interface. In this section, a series of pore-scale visualization events is reported and relevant mechanistic study of these events is also provided.

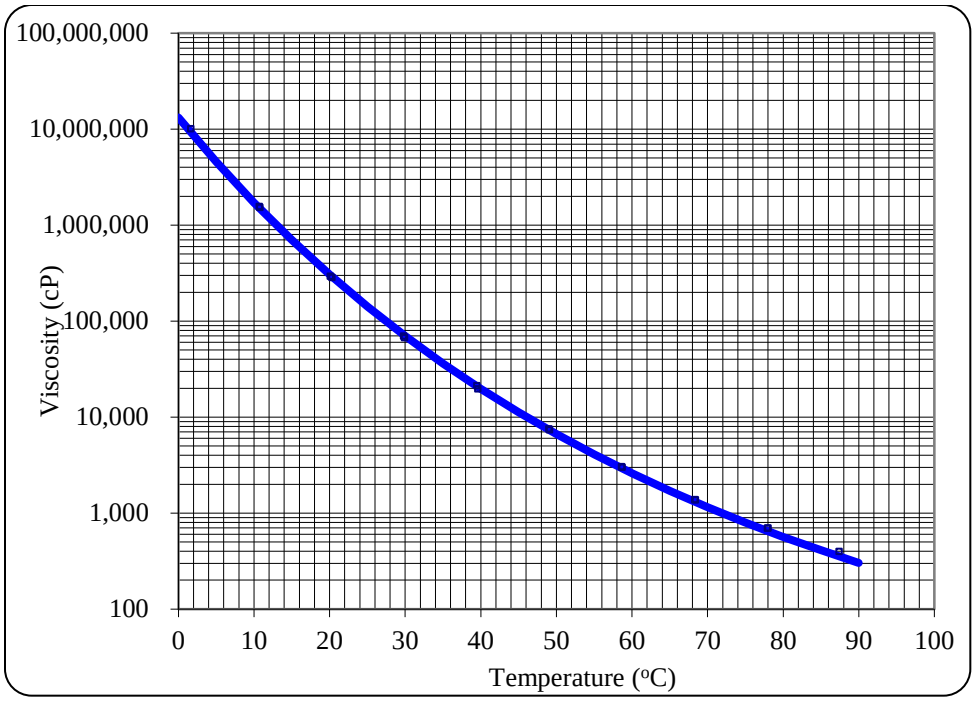

Figure 2.6: Viscosity – temperature relationship for Cold Lake bitumen

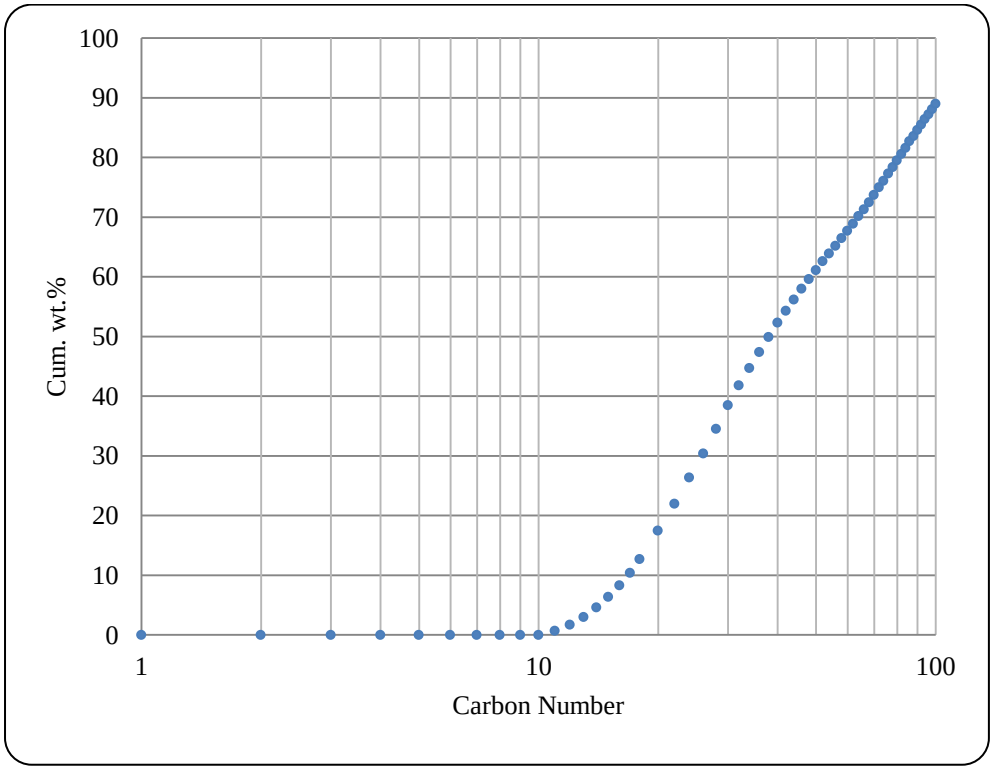

Figure 2.7: C_{100} hydrocarbon analysis for Cold Lake bitumen

2.4.1. Pore-Scale Events Analysis: Early Development of the Steam Chamber and Subsequent Lateral Encroachment

As it was stated before, the presence of high permeable trough extended at one side of the micromodels not only eases the saturation stage of the micromodel with heavy oil, but also provides an early communication between injection and production ports. During the early lateral development of the steam chamber, bitumen present in the pores adjacent to the high permeable trough achieved mobility as soon as steam was introduced into the model. Local invasion of steam into these pores is the first sign of steam chamber lateral development at the pore scale. This phenomenon, which is supported by the temperature gradient, could be seen in two successive pictures shown as Figures 2.8 and 2.9. Mobile oil drained out of these pores and steam invaded through them following the sequential behaviour of pore drainage during an immiscible displacement process (Chatzis and Dullien, 1983).

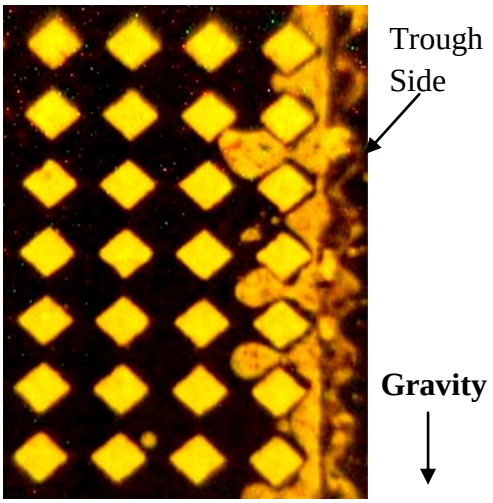

Figure 2.8: Lateral development of the steam chamber initialization by early steam invasion from trough to the adjacent pores.

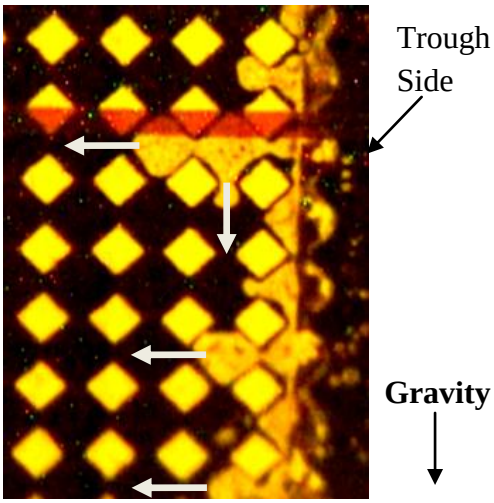

Figure 2.9: The same location as Figure 2.8, but at a later time frame (i.e. 3 minutes later).

During the early stages of the lateral movement of the steam chamber, the steam chamber could be defined by the continuum of the steam invaded pores which is dendritic in nature. These pores are well interconnected from the steam flow point of view; however, there is the possibility of steam condensation at the tip of each contact point of steam-invaded pores with bitumen-filled

pores. This local condensation could happen either in a pore constriction, or within the entire pore body. In Figure 2.10, the early development of the steam chamber and different flow zones in the vicinity of the apparent SAGD interface are shown. The pores adjacent to the pore-level interface drain preferentially in the direction of gravity, and form dead-end type of structure. As a result, the drainage of the oil films could then be re-directed, which could lead potentially to creation of peaks-and-valleys configuration of flow pathways at the apparent SAGD interface such as those pointed out with red arrows. The presence of peaks-and-valleys type of interfacial pattern could be avoided if continuous films of the mobile oil exist at the pore scale, flow down gradient just ahead of the apparent interface, and fill the localized valleys to the extent of creating a relatively smooth apparent interface extended vertically under the action of gravity. This is discussed further in detail later when different drainage displacement mechanisms at the pore level are explained. These localized peaks and valleys are formed at the uneven apparent SAGD interface (i.e. red dotted curve) just behind a relatively thick layer of pores that form the so called "mobilized region".

2.4.2. Pore-Scale Events Analysis Within the Mobilized Region

The mobilized region contains thermally-mobilized oil, droplets of water condensate, and also steam phase which are flowing simultaneously parallel to the apparent interface. In this region, the varying thickness (i.e. in the order of 1-6 pores ahead of the apparent SAGD interface) at different particular elevations is shown by dotted purple arrows in Figure 2.10. Most of the convective nature of the SAGD process in the vicinity of the apparent interface as well as severe local mixing at the pore-scale could be observed in the mobilized region. Different acting forces are contributing to the simultaneous fluid flow within this mobilized region, namely gravity, capillarity, and buoyancy forces in the absence of excessive viscous force. This region is formed due to the presence of temperature gradient at the pore-scale and it clearly has an oriented structure, in which three different fluid phases are flowing parallel to the apparent SAGD interface. Here, the pore-level SAGD interface is defined as the apparent demarcation line (or surface when the 3D skeleton of the porous structure is concerned) between the steam phase and the oil phase at the microscopic level. Unlike the limited drainage depth of the live oil in the VAPEX process at the pore-scale, which is in the order of 1-2 pores (James, 2009; James et al, 2008), our visualization results revealed that the thickness of the SAGD mobilized region (i.e.

"δ_m" in Figure 2.11) is 2-3 times thicker compared to the drainage depth of the live oil in the VAPEX process. This is due to the considerably higher value of thermal diffusivity compared to the molecular diffusion coefficient. This point could also be verified knowing the fact that the oil phase within 1-5 pores away from the apparent SAGD interface is also being mobilized as a result of temperature gradients. This issue would be backed up with gravitational drainage of the enclosed droplets of water within the continuum of the oil phase right behind the apparent SAGD interface when the pore-scale emulsification aspects are being discussed in later sections.

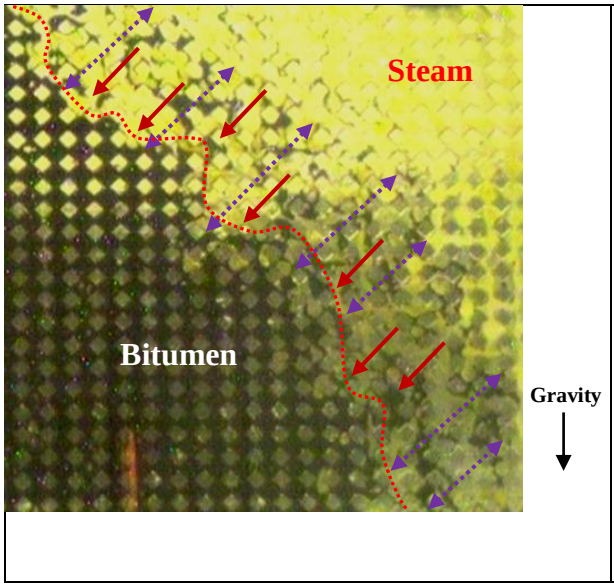

Figure 2.10: Visualization of the skeleton of the apparent SAGD interface, steam flow pathways, and the mobilized region.

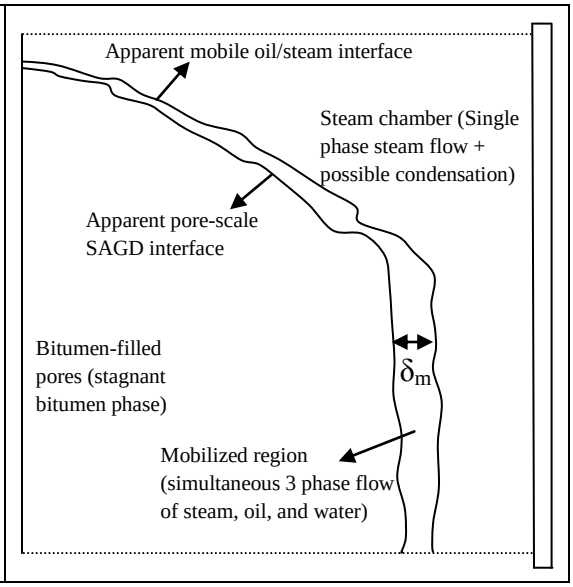

Figure 2.11: Schematic diagram of the pore-level fluid flow zones in a typical SAGD process according to the flow visualization results

Transport mechanisms involved in a typical SAGD process include heat transfer by conduction, mixing of steam and condensate phases with the heavy oil, and gravity drainage of the viscosity-reduced oil along with the water condensate. The mobile oil, as well as the water condensate within the mobilized region, would drain by the action of gravity when gravity forces overcome the capillary and possible viscous forces. The predominant factor is the reduction of viscous drag due to the exponential reduction in inherent viscosity upon steam heating. The role of gravity forces and capillary forces depends on the individual pore-scale mechanisms. According to our flow visualization experiments, there are different pore-level fluid flow zones in a typical SAGD

process which are schematically presented in Figure 2.11. These zones can be characterized as follows:

a) Steam chamber in which steam is the predominant flowing phase. However, there is the possibility of steam condensation followed by condensate movement if the condensate saturation provides enough relative permeability value.

b) Bitumen-filled pores: This zone is the stagnant zone in which in-situ bitumen viscosity is still beyond the mobilization limit. Heat is transferred to this zone by a combination of conduction and convection mechanisms.

c) Mobilized region: In this region, simultaneous three phase flow of the mobile oil, steam, and water phases is observed.

The apparent pore-level SAGD interface is a hypothetical demarcation line (or surface when 3D skeleton structure is concerned) separating bitumen-filled pores from the mobilized region. Apparent mobile oil-steam interface is the other hypothetical 1D or 2D boundary of the mobilized region, ahead of the apparent pore-level SAGD interface.

Figures 2.12 and 2.13 present closer pore-level views of the mobilized region. Figure 2.12 shows the direct contact of steam and oil just at the apparent SAGD interface, i.e. all the pore bodies below this particular location contain only oil phase. Red arrow shows the vertically-oriented film flow drainage of the mobile oil in the presence of the steam phase. One can clearly note the distribution of all three flowing phases within this pore-scale snapshot. Figure 2.13 shows the mobilized region (to the right), apparent SAGD interface, and oil-saturated pore bodies (to the left) behind the apparent pore-level SAGD interface. It is clear that some small bubbles of the steam phase are trapped within the draining mobile oil (i.e. behind the interface to the left), which are pointed out by thin red arrows. In addition, enclosure of small droplets of water condensate is also evident within the continuum of the mobile oil just behind the apparent pore-level SAGD interface (shown by thick white arrows). Continuous drainage of these trapped steam bubbles and water condensate droplets is an evidence to the fact that oil phase behind the apparent pore-level SAGD interface (i.e. within a limited distance in the order of 1-5 pore body dimensions) is mobile enough to drain by gravity forces.

One could clearly observe the state of microscopic fluids distributions within the mobilized region with a quick look at Figure 2.14. As it is evident in all of these snapshots, steam phase (i.e. "S") invades through the core part of the pores as the only truly non-wetting phase, and interacting liquids attach to the grain solids (i.e. "G") whenever applicable as the wetting phases. Spreading characteristics of oil over water (i.e. "W") at the pore-scale is evident. In addition, liquid films of oil tend to keep their capillary continuity along two adjacent grain particles. Areas within dotted ellipses show the local engulfment of tiny water droplets inside the oil phase.

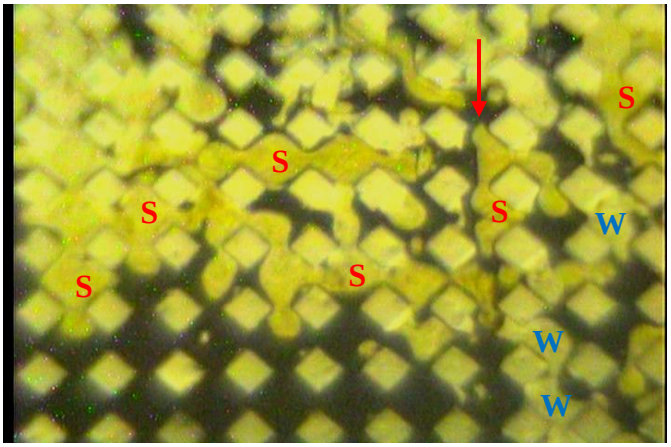

Figure 2.12: A closer look at the pore-level mobilized region

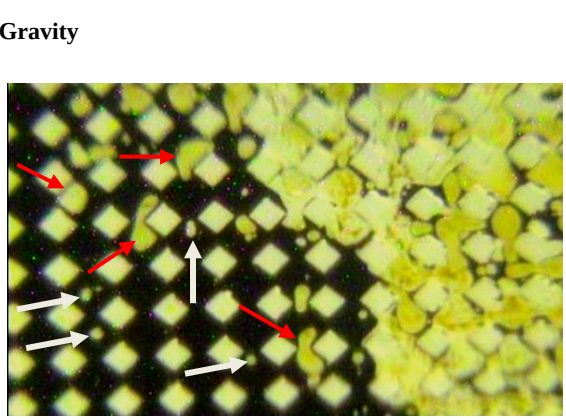

Figure 2.13: Oil phase mobility behind the apparent pore-level SAGD interface

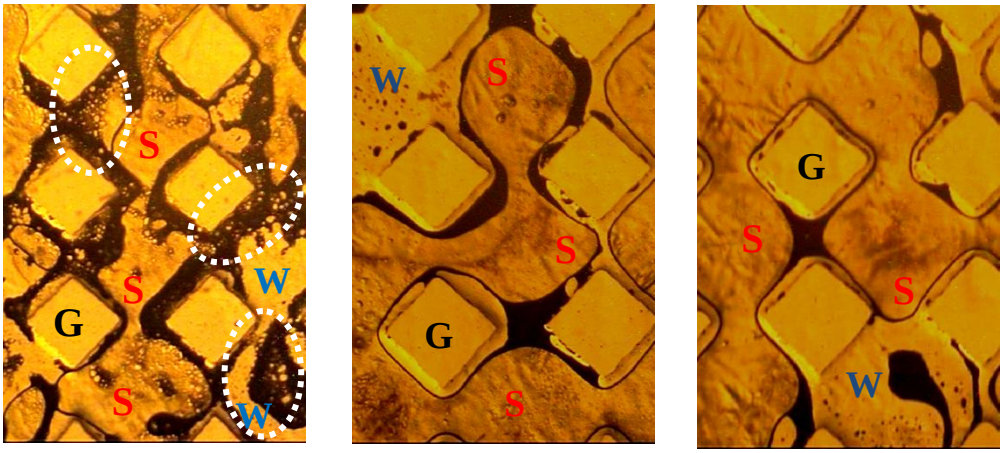

Figure 2.14: State of fluids distributions within the mobilized region at the microscopic scale

2.4.3. Pore-Scale Drainage Mechanisms

According to the flow visualization results, two pertaining drainage mechanisms are responsible for pore-scale sweep efficiency of a typical SAGD process, namely: 1) capillary drainage displacement, and 2) bulk film-flow type of oil drainage. These two simultaneous mechanisms are acting within the mobilized region and also through a few pores just behind the apparent SAGD interface, displacing the mobile oil by gravity drainage.

2.4.3.1. Capillary Drainage Displacement Mechanism

Under this displacement mechanism, a finite volume of the mobile oil, which can be considered as a continuum compared to the slim films of oil within the mobilized region, would drain both within and behind the mobilized region, in a distance composed of 1-5 pores from the apparent SAGD interface, by direct drainage displacement. The steam phase invades through the pores according to the typical sequence of the drainage type displacement of a wetting phase by an invading non-wetting phase at the pore scale (Chatzis and Dullien, 1983). Meanwhile, this direct drainage displacement is facilitated with the aid of gravity force in the absence of excessive viscous force. As it was mentioned earlier, there is a local mixing within the mobilized region during the course of a typical SAGD process. This local mixing enhances the convective element of the overall drainage displacement at the pore-scale. This type of displacement is pointed out by white arrows in Figure 2.9. In addition, Figure 2.15 provides a series of pore-scale events including sequential drainage displacement of oil (wetting phase) by the non-wetting steam phase over a 6-minutes time period. As the oil in contact with steam is heated to the extent of being mobile, it is convenient to observe drainage of several pores consecutively along the extension of the apparent pore-scale SAGD interface. As depicted in Figure 2.15, steam is displacing oil downwards along the yellow arrows shown in one of the snapshots (i.e. ”b”) and the oil phase within all these pore columns drain simultaneously under the action of gravity. The same process is also observed in Figure 2.16 which shows the capillary drainage displacement phenomenon along the facing-down red arrows, just behind the mobilized region (i.e. red dotted rectangular area). It is clear that all three interacting phases are flowing simultaneously within the tiny portion of the mobilized region which is shown in Figure 2.16 (i.e. condensate: light blue arrows, steam: white arrows, and draining oil: vertically-extended white ellipse).

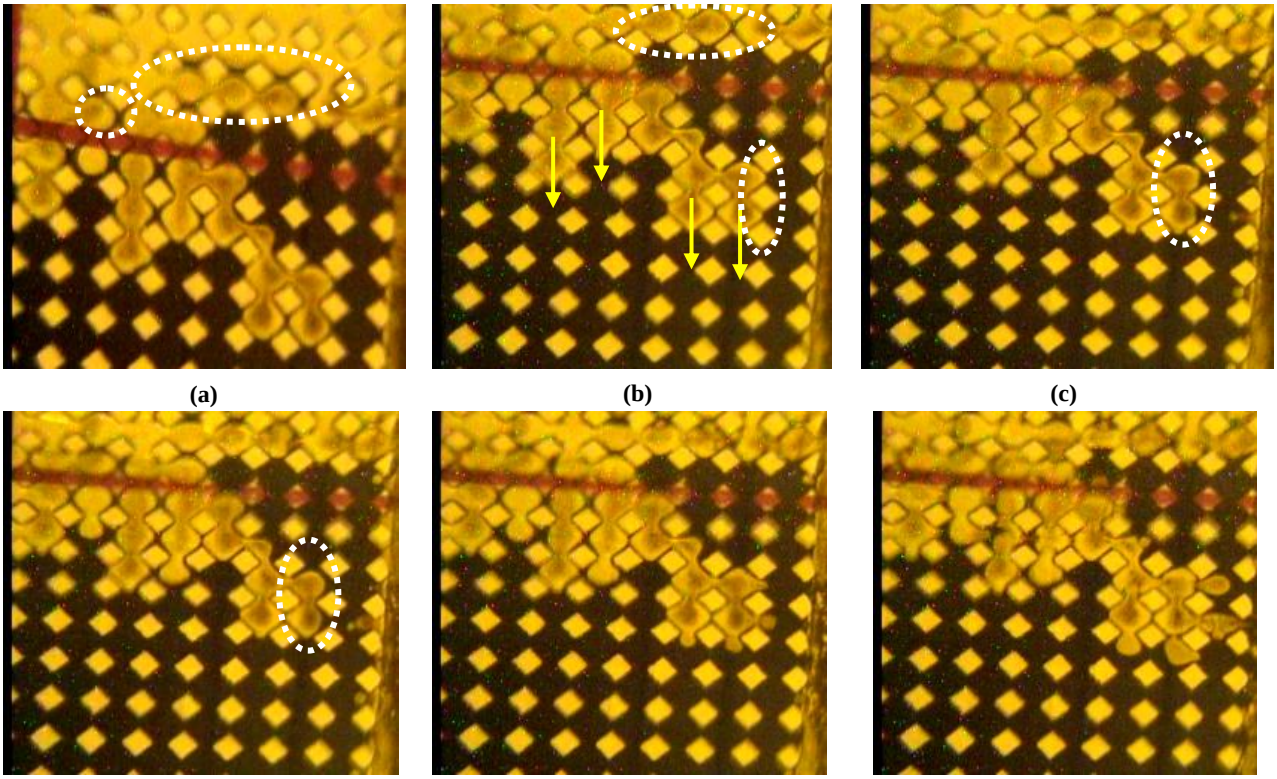

Figure 2.15: Sequence of pore drainage under direct capillary drainage displacement of the wetting phase (i.e. oil) by the invading non-wetting phase (i.e. steam) as well as film-flow type of drainage displacement at the pore-scale

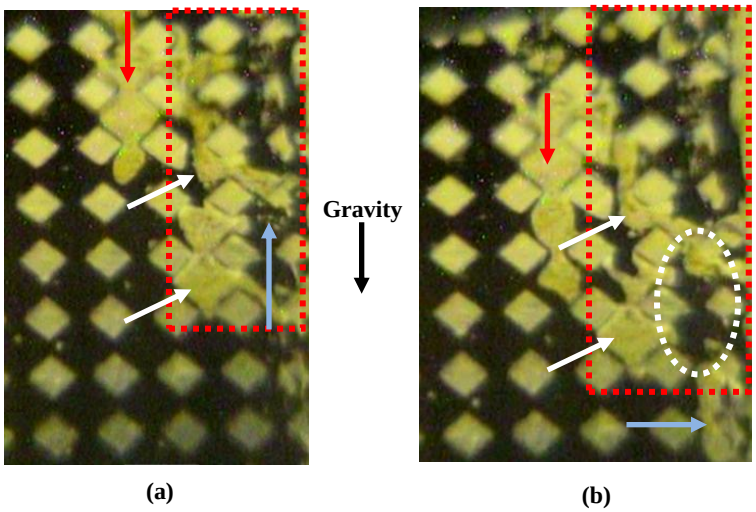

Figure 2.16: Capillary drainage displacement of the wetting phase (i.e. oil) by the invading non-wetting phase (i.e. steam) at the pore-scale

2.4.3.2. Film-Flow Drainage Displacement Mechanism

The film flow drainage displacement mechanism is an effective pore-scale displacement mechanism within the mobilized region and also inside the steam-saturated zone to a lesser extent. The oil films left behind in the steam invaded region periodically form loop structures involving bulk oil films in steam invaded pores. If these films keep their inherent flow continuity over the limited distance of their extension, there is possibility of drainage under film flow drainage displacement. The drainage rate of these closed-loop oil films is lower than that of the bulk oil flow within the pores under the direct drainage displacement mechanism. This is because of the reduced hydraulic conductivity of the thin oil films within the steam invaded pores. The high degree of local mixing associated with the mobilized region usually does not allow sufficient extended flow continuity for the draining oil films, resulting in small contribution of the film-flow drainage component in the overall drainage scheme of the mobilized region. Figure 2.15 shows some degree of film-flow type of drainage where thin films of oil left behind within the steam invaded pores (i.e. top portions of all the snap shots which are indicated by horizontal white dotted ellipses in pictures “a” and “b”) are draining under the film-flow type of displacement over the internal surface of the pore bodies in the presence of the non-wetting phase. As time proceeds, one can observe the periodic thickening and thinning of the bulk oil films next to the leading edge of the invading steam (i.e. white dotted vertically-extended ellipses in pictures “b”, “c”, and “d”, Figure 2.15). This proves the presence of the film-flow drainage mechanism at those locations up until the last snapshot (Figure 2.15.f) at which there are fewer closed-loop draining films in the invaded region.

2.4.4. Emulsion Creation at the Pore – Scale

Our flow visualization experiments support the hypothesis regarding emulsification at the pore-scale during the course of the conventional SAGD process. The invading steam phase could condense locally as a result of heat transfer either within the mobilized region (i.e. ahead of the apparent pore-scale SAGD interface and behind the steam-mobilized oil interface) or at the apparent pore-scale SAGD interface (i.e. apparent interface between the bitumen phase and the mobilized oil region). Liquid condensate could be seen either within the mobilized region or at the apparent SAGD interface. According to the non-spreading characteristics of water over oil in

presence of a gas phase, local enclosure of water droplets within the continuum of the mobile oil behind the apparent SAGD interface would form the localized water in oil emulsification. In Figure 2.17, three snapshots are shown regarding the state of in-situ emulsification in the SAGD process. Figure 2.17.a shows the local entrapment of a large number of water micro-droplets within the continuum of the mobile oil at the pore-scale. The selected area is one pore-body-dimension distance away from the apparent SAGD interface. Figure 2.17.b presents the engulfment of two individual water droplets inside the pool of oil with a distance equivalent to three-pore-dimensions from the apparent SAGD interface. Figure 2.17.c also demonstrates the microscopic enclosure process of a number of small condensate droplets at the left side of the picture which were detached from the bulk column of the condensate phase formed at the top of the oil-filled pores.

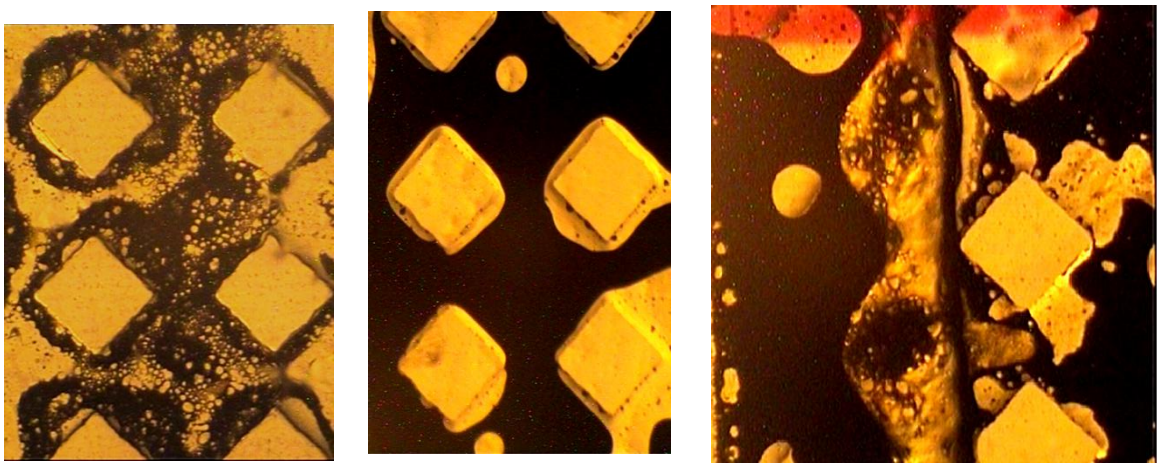

(a) **(b)** **(c)**

Figure 2.17: State of in-situ emulsification during the SAGD process at the pore-scale obtained from flow visualization experiments

The longitudinal distance behind the apparent SAGD interface at the pore-level over which the water condensate droplets invade is referred to as the depth of enclosure (i.e. depth of engulfment). According to the SAGD visualization results, this depth of enclosure for the isolated water condensate droplets within the continuum of the mobile oil can reach up to 5 pores behind the apparent SAGD interface. The temporarily trapped droplets of water condensate are carried along by the surrounding continuum of the mobile oil down gradient. These isolated droplets may coalesce if their enclosure density is high enough, i.e. large number of engulfed

condensate droplets would be trapped within the reduced-viscosity oil continuum. In addition, they should overcome the associated film pressure of the tiny mobile oil films in between in order to be able to coalesce to each other. Due to the convective nature of the drainage process within the mobilized region, it was observed that both condensate droplets and also small steam bubbles become entrapped within the continuum of the mobile oil just behind the apparent SAGD interface. One of the mechanisms responsible for small steam bubbles being trapped within the bulk of the mobile oil is the snap-off phenomenon at the pore-scale. Figures 2.13 and 2.18 (both right and left pictures) present three sample snapshots in which the entrapment of the small condensate droplets as well as finite-pores-extended steam bubbles are demonstrated behind the apparent SAGD interface at the pore-scale.

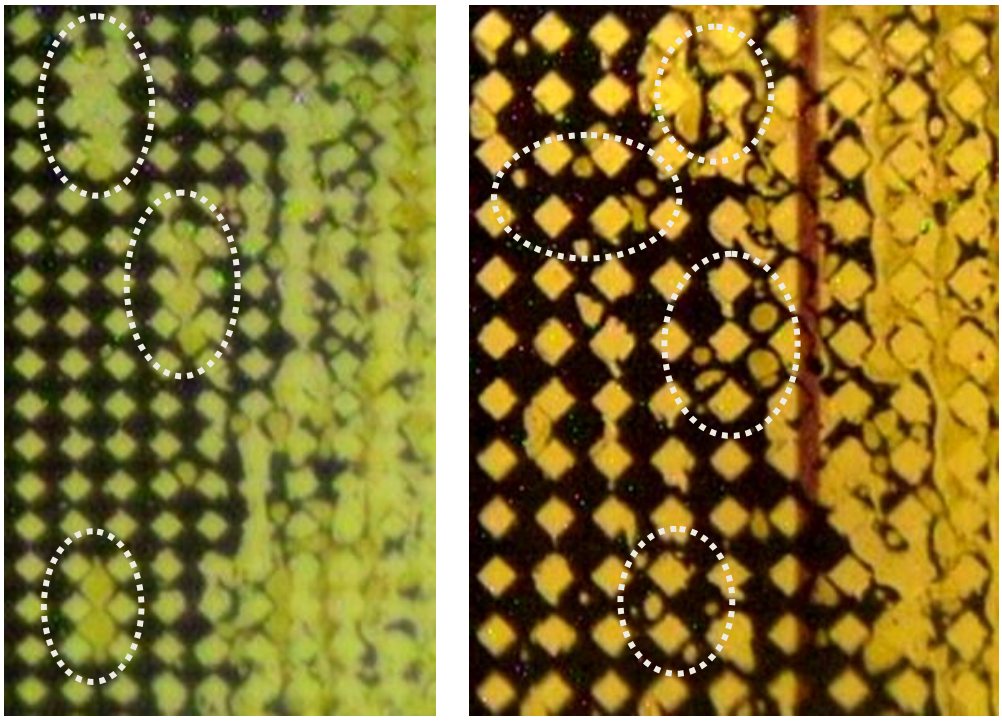

Figure 2.18: Entrapment of small steam bubbles as well as water condensate droplets behind the apparent SAGD interface within the draining mobile oil

2.5. Quantitative Analysis of the Experimental Results

In addition to the qualitative results of our SAGD visualization experiments presented in section 2.4, an effort was made to quantitatively analyze the SAGD process performance at the pore-

level. The quantitative results obtained in this study using 2D micromodel type of porous media cannot be extended to the real case 3D porous structure where pores are more interconnected with higher pore coordination number and film flow respectively. The extent of film flow as well as pore connectedness is higher in a 3D skeleton of porous structure compared to the 2D pore networks. However, parametric sensitivity analysis could be performed in order to investigate the effect of porous media properties, operating conditions, and fluid properties on the measurable process performance parameters at the pore-scale.

Five different glass micromodels were used in this study with different pore-structure characteristics and macro-scale petrophysical properties. The horizontal interface advancement velocity was chosen as a measure of the SAGD process performance at the pore-scale. All the glass-etched micromodels were thoroughly characterized with respect to pore-scale dimensions, model dimensions, porosity, and permeability. The motion pictures and movies taken during each particular SAGD visualization trial were reviewed frame by frame, and the interface advancement velocities were measured at selected fixed vertical elevations along the model height. The parametric sensitivity analysis of the SAGD process performance was performed and then cross-checked with analytical solution proposed by Butler (1979, 1981).

2.5.1. Characterization of the Glass-Etched Micromodels

The five employed glass-etched micromodels were entirely characterized in order to know the pore-scale as well as macroscopic model dimensions, permeability, and porosity. A brief description of the characterization procedure is presented in this section.

2.5.1.1. Model Physical Dimensions

Model dimensions were measured using a precision ruler with accuracy of ±0.5 mm. Length of the porous pattern embedded between the glass plates is presented both in unit length and in number of pores and is defined as the “Model Length”. As well, “Model Width” is defined as the width of the porous pattern embedded between the two glass plates, and it is also presented in both the length unit and also in terms of the number of pores.

2.5.1.2. Porosity

Porosity of a glass-etched micromodel is defined as the model pore volume divided by the model bulk volume. The model pore volume was measured using the saturation method and is defined as the difference between the weighs of the model at two stages of saturated and dry conditions, divided by the saturating liquid density. Model bulk volume was calculated knowing the width and length of the porous pattern and average depth of etching. The following equation presents the porosity calculation for each glass micromodel:

$$\varphi = \frac{Pore\ Volume}{Bulk\ Volume} = \frac{(Weigh\ of\ saturated\ model - Weigh\ of\ dry\ model)/\rho_{Liquid}}{(L \times W)_{Porous\ Pattern} \times \delta_{Etching}} \quad (2.2)$$

2.5.1.3. Depth of Etching

This parameter could be measured directly using profilometer. It can also be characterized using a cumbersome and destructive method of measurement in which the glass micromodel is impregnated thoroughly with epoxy resin, and then the model is sectioned at particular locations. The pore-scale dimensions of the resulting sections could then be measured under the microscope. In the absence of this direct measurement technique, average depth of etching could be calculated using capillarity concepts (Ioannidis et al 1991, Dullien 1992). According to the concept of capillary imbibition of a wetting liquid into a porous medium, the imbibition process is controlled by the average (i.e. equivalent) radius of capillary spaces. In other words, pore body radius is the controlling factor for the imbibition process. Figure 2.19 shows the concept of capillary rise of a wetting liquid in a vertically-standing cylindrical capillary tube.

The physics of wetting phase imbibition into a capillary tube is expressed mathematically in the form of Laplace Equation of Capillarity in which imbibition capillary pressure is directly proportional to the surface tension of the wetting liquid (σ) as well as the advancing contact angle (θ_A), and is inversely proportional to the tube diameter (r). The Laplace Equation of capillarity for capillary rise of a wetting liquid in a cylindrical capillary tube is as follows:

$$P_c^{imb} = \frac{2\sigma Cos\theta_A}{r} \tag{2.3}$$

For capillary rise in a tube, the above imbibition capillary pressure would be balanced by the gravitational force applied to unit mass of the advancing wetting liquid phase:

$$P_c^{imb} = \Delta\rho g h_{c,\,imb} \tag{2.4}$$

One can re-write the Laplace Equation of capillarity for a porous medium with average pore body diameter size D_P by replacing the capillary tube diameter "r" in Equation 2.3 with an equivalent pore body radius of $r_{eq}^{pore\ body}$ which is defined as the equivalent radius of a capillary tube that has the same imbibition capillary pressure as the imbibition capillary pressure required to empty a pore body in the micromodel. The Laplace Equation of Capillarity for such a porous medium can be written as:

$$P_c^{imb} = \frac{2\sigma Cos\theta_A}{r_{eq}^{pore\ body}} \tag{2.5}$$

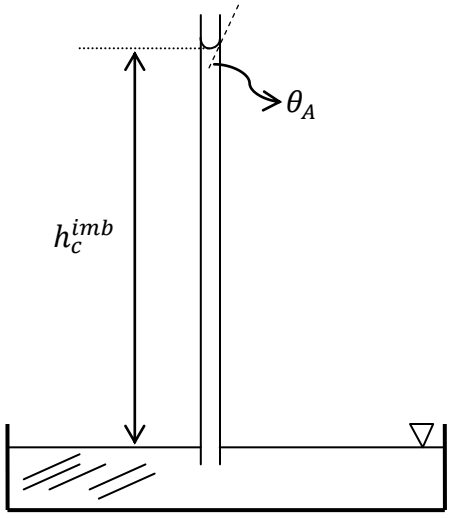

Figure 2.19: Capillary rise of a wetting liquid in a vertically-standing cylindrical capillary tube

Combining Eq's 2.4 and 2.5 results in:

$$h_{c,\,imb} = \frac{4\sigma Cos\theta_A}{\Delta\rho g D_p} \tag{2.6}$$

or:

$$D_p = \frac{4\sigma Cos\theta_A}{\Delta\rho g h_{c,\,imb}} \tag{2.7}$$

in which "$h_{c,\,imb}$" is the height of capillary imbibition of the wetting liquid in a capillary tube of radius "r", "σ" is the surface tension of liquid, "θ_A" is the advancing contact angle, "$\Delta\rho$" is the density difference of the acting fluid phases, and $D_P = 2r_{eq}^{pore\ body}$. For the case of capillary rise of a wetting liquid in a glass micromodel, one can use Equation 2.7 to estimate an equivalent pore body size radius.

Figure 2.20 displays a pore-scale schematic diagram of the dimensions associated with the pore bodies and pore throats of a particular homogeneous porous pattern. In this Figure, depth of etching of pore body and pore throat regions are demonstrated by "δ_{PE}" and "δ_{TE}" respectively. In addition, pore body and pore throat widths are shown by "W_p" and "W_T" respectively.

The equivalent radius of curvature could be related to the principal radii of curvature using the following Equation (Dullien 1992):

$$\frac{2}{r_{eq}^{pore\ body}} = \left[\frac{1}{Pore\ body\ radius} + \frac{1}{Radius\ of\ etching\ in\ the\ pore\ body}\right] \tag{2.8}$$

Substituting the parameters into Equation 2.8 based on the schematic diagram shown in Figure 2.20 results in:

$$\frac{2}{r_{eq}^{pore\ body}} = \frac{2}{W_P} + \frac{2}{\delta_{PE}} \tag{2.9}$$

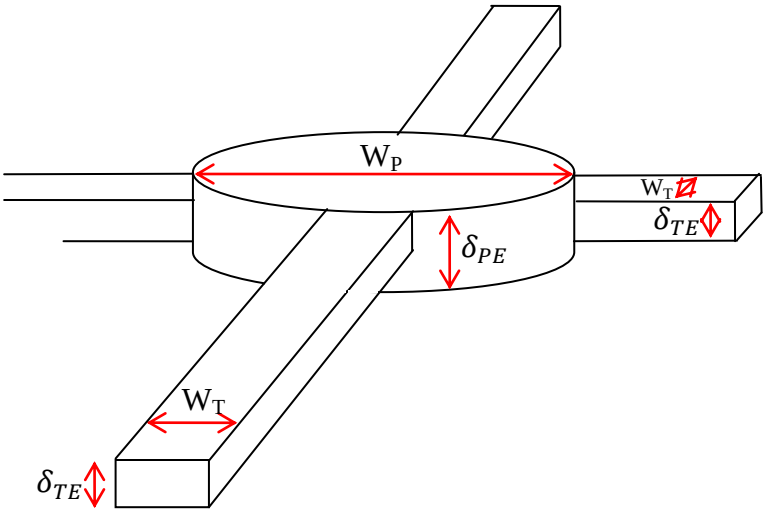

Figure 2.20: Schematic diagram of pore-scale dimensions in a porous pattern with minimal pore size variability

in which "δ_{PE}" is the depth of etching in the pore body region and "W_P" is the pore body width. Equation 2.9 can be solved for the depth of etching in the pore body region as follows:

$$\delta_{PE} = \left(\frac{1}{r_{eq}^{pore\ body}} - \frac{1}{W_P} \right)^{-1} \tag{2.10}$$

If the pore body width would be replaced by the pore throat width, Eq. 2.10 results in calculating the depth of etching in the pore throat region. The calculated depth of etching could then be used in order to calculate the cross sectional area perpendicular to the flow direction. In other words, the cross sectional area across the width of the model is taken as $A = W \times \delta_{PE}$ in which "W" is the width of the model.

2.5.1.4. Permeability

Permeability is the measure of flow conductivity through a particular porous medium, and is measured in units "Darcy" with the dimension of "area". This porous medium's property could

be measured having flow properties (i.e. volumetric flow rate, "Q", the corresponding pressure drop gradient, "$\frac{\Delta P}{L}$", and cross sectional area perpendicular to the flow direction, "A") and fluid properties (fluid viscosity, "μ") using the Darcy equation as follows:

$$Q = \frac{KA}{\mu} \times \frac{\Delta \mathrm{P}}{\mathrm{L}} \qquad \text{and} \qquad K = \frac{Q\mu L}{A\Delta P} \tag{2.11}$$

The permeability of a glass micromodel could be measured using two different methods, namely: a) constant-head permeability measurement, and b) free-imbibition interfacial advancement method.

a) Constant-Head Permeability Measurement

In this method, a constant head of a known liquid (i.e. toluene or water) with known hydrostatic head difference (i.e. ρgh) is maintained over the inlet-exit face of the micromodel, and the liquid flow rate through the porous medium (i.e. "Q") is measured under the constant liquid head at the steady state conditions. Following successive different values of liquid head which results in corresponding hydrostatic pressure gradients across the model, different corresponding flow rate values would be obtained. As a result, the model permeability could be calculated using a plot of "Q" versus "$\frac{\Delta P}{L}$" whose slope would be "$\frac{KA}{\mu}$". It is worthwhile to note that the cross sectional area is the area subject to (i.e. perpendicular to) flow which could be obtained having the average value of the depth of etching of the micromodel.

b) Permeability Measurement using Free-Imbibition Interface Advancement Method

The permeability measurement of a glass micromodel using free-imbibition interface advancement method is also based on the Darcy's equation of fluid flow through porous media and the notion is described in terms of an average imbibition pressure. In this method, the position of the imbibing liquid-air interface is monitored with time. In this transient permeability measurement method, the threshold capillary height of imbibition of a wetting liquid in a glass micromodel is related to the transient position of the liquid interface height. The instantaneous

interface advancement pore velocity of liquid in the glass micromodel during a free imbibition process ($v_p(x,t)$) is related to the transient location of liquid interface through the model using the following equation:

$$v_p(x,t) = \frac{dx}{dt} \tag{2.12}$$

In a free imbibition process without trapping, the imbibing liquid flows through the pore channels based on an average imbibition capillary pressure driving force according to Darcy's law:

$$v(x,t) = \frac{K}{\mu} \times \frac{\Delta P}{x(t)} = \frac{K}{\mu} \times \frac{\bar{P}_{c,imb}}{x(t)} \tag{2.13}$$

in which $v(x,t)$ is the instantaneous Darcy velocity, "K" is the average micromodel permeability, "μ" is the liquid viscosity, x(t) is the average of instantaneous liquid interface locations in the model, and $\bar{P}_{c,imb}$ is a time-averaged dynamic free imbibition capillary pressure governed mainly by the average pore body dimension and is approximated by:

$$\bar{P}_{c,imb} = \frac{4\sigma Cos\theta_A}{D_P} = \Delta\rho g h_{c,\,imb} \tag{2.14}$$

in which "D_p" is the average pore body diameter, $h_{c,\,imb}$ is the average imbibition capillary height of liquid in the model, and $\Delta\rho$ is the density difference between the test liquid and air.

Considering the fact that the pore velocity is related to Darcy velocity by $v_p(x,t) = \frac{v(x,t)}{\phi}$, one can combine equations 2.12 to 2.14, and separate the variables to obtain the following equation:

$$x(t)dx = \frac{K}{\mu\phi}\bar{P}_{c,imb}dt \qquad \text{or} \qquad x(t)dx = \frac{K}{\mu\phi}\Delta\rho g h_{c,\,imb}dt \tag{2.15}$$

Integrating both sides of the above equations results in:

$$x^2(t) = \frac{2Kt}{\mu\phi}\bar{P}_{c,imb} \quad \text{or} \quad x^2(t) = \frac{2Kt}{\mu\phi}\Delta\rho g h_{c,\,imb} \tag{2.16}$$

A plot of "$x^2(t)$" versus time would be a straight line with the slope "m" which is defined as:

$$m = \frac{2K}{\mu\phi}\bar{P}_{c,imb} \quad \text{or} \quad m = \frac{2K}{\mu\phi}\Delta\rho g h_{c,\,imb} \tag{2.17}$$

Having the slope of the straight line, the glass micromodel permeability could be calculated using the following Equations:

$$K = \frac{m\mu\phi}{2\bar{P}_{c,imb}} \quad \text{or} \quad K = \frac{m\mu\phi}{2\Delta\rho g h_{c,\,imb}} \tag{2.18}$$

For the case of the micromodels used in the SAGD visualization studies, the imbibition tests were performed using both water and toluene; however, the interface advancement permeability measurement was carried out using toluene only as the solid surface should be perfectly wetted by the liquid and this characteristic is met more strongly with toluene than water.

2.5.1.5. Pore-Structure Dimensions of the Micromodels

In order to thoroughly characterize a glass micromodel, it is required to measure the pore-scale dimensions in addition to the macroscopic properties of the model. These parameters include:

a) Pore to pore distance: This is the distance from the centre of one pore body to the centre of the next pore body, or the distance from the centre of one pore throat to the centre of the next adjacent pore throat. Pore to pore distance is equal to the pore throat width plus the particle size for a particular pore geometry.

b) Pore body width: It is the width of pore body which contributes to the storage capacity of that particular pore. Depending on the geometry of the solid grains, this dimension could be a constant or variable parameter for a given porous structure. This parameter also controls the

imbibition process of a wetting phase as it is the widest flow path for an invading wetting phase through a porous pattern.

c) Pore throat width: This parameter determines the width of a particular pore constriction and could be a constant parameter for a given homogeneous porous pattern. This dimension controls the drainage process of a particular porous structure as it is generally the narrowest flow path for the invading non-wetting phase.

d) Particle size: This dimension determines the size of the solid particles embedded within a porous structure, and would be a constant value for a particular homogeneous porous medium composed of geometrical-shaped solid particles.

e) Diffusion distance: This dimension refers to the distance between the centre of a particular pore to the edge of another neighbouring pore. The defining factor that determines the limits of a particular pore is the associated pore throat length. If a particular pore structure contains a finite pore throat length, the diffusion distance is defined as the distance from the centre of a particular pore to the half-way distance of the neighbouring finite pore throat length. On the other hand, if the pore throat length is negligible for a particular porous pattern, then the diffusion distance is measured from the centre of a particular pore up until reaching to the entry point (or entry line) of the neighbouring pore. Another definition for the diffusion distance is presented as half of the particle width plus the width of the pore throat. In the solvent aided processes of heavy oil and bitumen recovery such as SA-SAGD and VAPEX, this dimension signifies the distance over which the solvent phase should diffuse from one pore in order to reach the neighbouring adjacent pore. For the condensing and non-condensing modes of the VAPEX process, it was concluded that the larger the diffusion distance is, the smaller would be the interface advancement through a particular micromodel (James, 2009).

f) Flow path length: It is the maximum flow path length for a particular fluid phase from one pore to the one below it when the nature of the flow at the pore-level is assumed to be film flow type of drainage displacement.

g) Pore throat length: This dimension determines the length of a particular pore constriction, and its magnitude depends on the shape of the solid grains which form the corresponding shape of the pore throats. It could either be comparable in size with the pore throat width, or be negligible depending on the particular solid grain shape.

Based on the materials presented in sections 2.5.1.1 to 2.5.1.5, all the five employed glass micromodels were characterized. Table 2.3 shows a summary of the characterization results for all the five models. This table contains:

i. Schematic of the pore-scale pattern etched on the glass surface with associated pore-scale dimensions,
ii. Magnitudes of the pore-scale dimensions (i.e. described in section 2.5.1.5) measured using the printed pattern mask or the magnified high-resolution images captured from the glass micromodels itself,
iii. Depth of etching calculated using both the pore-body and pore-throat dimensions according to the procedure described in section 2.5.1.3,
iv. Macroscopic dimensions of the porous patterns associated with the glass micromodels
v. Porosity of the glass micromodels measured according to the procedure described in section 2.5.1.2,
vi. Permeability of the glass micromodels calculated based on the procedures described in section 2.5.1.4

Considering the specific design of the glass micromodels used in our visualization studies, there is a discrepancy between the measured permeability values using the two techniques described in section 2.5.1.4. As it was stated before, a high permeable trough was etched alongside the porous pattern in each micromodel to ease the initialization stage of the SAGD process. For such a specific pattern design, the high-permeable trough plays an important role in fluid flow when the constant-head permeability measurement procedure is used to measure the permeability of the glass micromodel. This is even more highlighted considering the fact that the trough was etched more than the porous pattern for some of these micromodels, hence achieved significantly higher permeability values compared to the equivalent permeability of the porous structure. In the constant-head permeability measurement method, the glass micromodel is entirely filled with the

working fluid, so the measured permeability includes a combination of trough permeability as well as porous structure permeability. Consequently, the equivalent permeability of the porous structure is expected to be much less than the value measured using the constant-head permeability measurement procedure if this technique was used for calculating the permeability of such a specific micromodel design.

Table 2.3: Characterization of the Micromodels used in the SAGD Visualization Experiments

	Micromodels				
	OC-1	**DL-1**	**DC-1**	**OM-1**	**OM-2**
	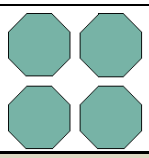	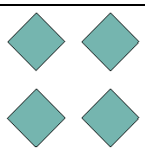	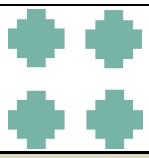	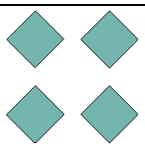	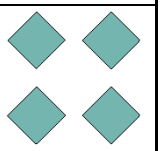
Pore Dimensions (mm)					
1) Pore to Pore	2.04	2.04	1.60	2.00	2.00
2) Pore Body Width	1.38	2.04	1.31	2.00	2.00
3) Pore Throat Width	0.45	0.67	0.49	0.30	0.30
4) Particle Size	1.59	0.99	1.11	1.20	1.20
5) Diffusion Distance	1.25	1.36	1.05	1.15	1.15
6) Flow Path	2.61	2.13	1.93	1.81	1.81
7) Pore Throat Length	0.66	n/a	0.29	n/a	n/a
Depth of Etching (mm)					
Pore Body, δ_{etch}^{P}	0.1253 ± 0.0017	0.2502 ± 0.0009	0.1277 ± 0.0008	0.1189 ± 0.0017	0.1968 ± 0.0066
Pore Throat, δ_{etch}^{T}	0.0928 ± 0.0002	0.0830 ± 0.00003	0.0735 ± 0.0010	0.0943 ± 0.0015	0.1165 ± 0.0035
Porous Media Dimensions					
Length, L (mm)	304	304	304	301	301
Length, L (# pores)	149	149	190	150	150
Width, W (mm)	100	100	141	101	101
Width, W (# pores)	49	49	89	50	50
Pore Volume (ml)	1.6	2.4	2.0	1.1	1.9
Porosity, φ (Fraction)	0.42	0.32	0.37	0.30	0.32
Permeability, K (D)					
Constant Head Method	120.86	272.79	87.08	292.86	310.97
Interface Advancement	56.16 ± 3.10	94.61 ± 2.49	34.13 ± 1.02	77.83 ± 4.85	92.42 ± 3.74

The adverse effect of trough permeability on the measured permeability value of the glass micromodel can be avoided to a great extent when interface advancement permeability measurement method is used. In this method, the model permeability is measured based on the instantaneous position tracking of the advancing wetting liquid interface through the porous medium. The wetting liquid prefers imbibing into the porous structure spontaneously rather than entering into the trough due to the very high capillary pressure associated with the high-permeable trough. Therefore, the permeability value measured using this technique represents the porous structure permeability rather than an average permeability value associated with porous pattern and trough. Although all the glass micromodels were characterized using both permeability measurement methods, the permeability values obtained using the free-imbibition interface advancement method were considered as the representative permeability values of the glass micromodels.

Looking at the data presented in Table 2.3, it is evident that the selected models had variability in macroscopic as well as pore-scale properties. For instance, model DL-1 had the highest permeability which is as a result of having the highest pore body width, pore throat width, and depth of etching (in the pore body) among the other four micromodels. Models DL-1 and OM-2 are examples of a porous network with high permeability and negligible pore throat length. In fact, model DL-1 exhibits higher permeability value due to higher pore throat width, pore body width, and more importantly depth of etching compared to those of OM-2 model. Models OM-1 and OM-2 are two identical models except for the depth of etching. These two models were fabricated in order to investigate the effect of the depth of etching on the pore-level SAGD process performance when all the other pore-scale properties of the porous media were kept identical. The higher magnitude of the depth of etching in OM-2 is responsible for higher porosity and permeability values of this model compared to those of OM-1 model.

Model OM-1 has higher pore body width, but lower pore throat width compared to OC-1 model, hence providing slightly higher permeability for OM-1 considering the fact that the depths of etching (i.e. in pore body and pore throat regions) are almost the same for these two models. It confirms the fact that depth of etching, especially in the pore body region, and also the pore body width are two important factors controlling the permeability of these porous networks. The same

point can be concluded comparing the properties of DC-1 and OC-1 micromodels. It is evident that OC-1 has larger pore bodies, diffusion distance, pore throat length, and also comparable depths of etching which all make its permeability higher than that of DC-1 model. Permeability of the glass micromodels were measured directly based on the information of the depth of etching, which was calculated indirectly from the imbibition or drainage tests.

Models DL-1, OM-2, and OM-1 have negligible pore throat length values, resulting in minimizing the flow path lengths as well as the diffusion distances. The flow path length is an important pore-scale property of a porous medium that affects the extent of the film flow drainage displacement. As far as the effect of the porous medium on the type of drainage displacement is concerned, the smaller the flow path length is, the more probable would be the occurrence of the bulk oil film flow type of drainage displacement at the pore-scale. Diffusion distance is an important pore-scale dimension that greatly affects the diffusion process at the pore-level when a solvent phase diffuses into the oil phase from a pore to the neighbouring pore through the porous network. The significance of this parameter is therefore more pronounced when a solvent-based extraction process is chosen to recover heavy oil and bitumen. Minimizing the diffusion distance of a particular porous network by reducing the associated pore throat length would help the solvent phase to diffuse faster over a shorter distance into the oil phase, resulting in greater sweep rate at the pore-scale.

The physical constants which were used in order to characterize the glass micromodels are presented in Table 2.4. The schematic pore-scale pattern structure used to construct OC-1 micromodel is schematically presented in Figure 2.21. Table 2.5 contains the calculation details of the pore-scale dimensions of OC-1 micromodel based on the pore-scale dimensions identified in Figure 2.21.

The details of the imbibition and drainage tests performed using both water and toluene to calculate the depth of etching of OC-1 micromodel are presented in Table 2.6. Both the constant water head and advancing toluene interface permeability measurement techniques were used in order to calculate the permeability of OC-1 model and the data are presented in Tables 2.7 and 2.8 respectively. The plots used in order to calculate the OC-1 micromodel permeability based on the two noted experimental techniques are shown in Figures 2.22 and 2.23.

Table 2.4: Physical constants used in the glass micromodels characterization

Physical Constants	
$\theta_{water\text{-}air,\ adv}$ (^{o})	7
$\theta_{water\text{-}air,\ rec}$ (^{o})	0
$\sigma_{toluene\text{-}air}$ (dynes/cm)	8.1
$\sigma_{water\text{-}air}$ (dynes/cm)	72
$\theta_{toluene\text{-}air}$ (^{o})	0
g (cm/s^2)	981
ρ_{water} (g/cm^3)	1
ρ_{air} (g/cm^3)	0.01
$\rho_{toluene}$ (g/cm^3)	0.866
μ_{water} (cP)	1
$\mu_{toluene}$ (cP)	0.58

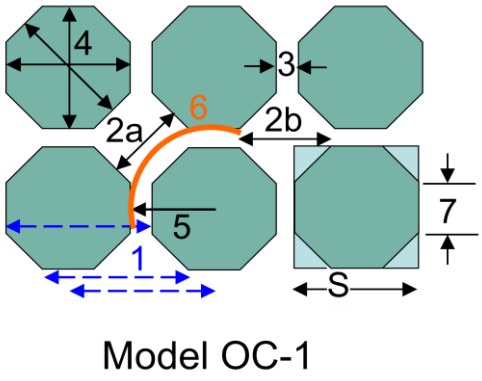

Figure 2.21: Schematic pore-scale structure of the OC-1 glass micromodel (Courtesy of James, 2009)

Table 2.5: OC-1 model dimensions

Microscopic Dimensions	
Pore Dimensions (mm)	
(1) Pore to Pore (3) + (4)	0.04
(2a) Pore Body	1.28
(2b) Pore Body (1) - (7)	1.38
(3) Pore Throat Width	0.45
(4) Particle Size	1.59
(5) Diffusion Distance 0.5*(4) + (3)	1.245
(6) Flow Path 0.25*(2πr) + (7) 0.5*π*(5) (7)	2.61
(7) Pore Throat Length S/2.414 (4)/ .414	0.66
Macroscopic Dimensions	
Length (mm)	304
Length (# pores)	149
Width (mm)	100
Width (# pores)	49

Table 2.6: Capillary heights for Model OC-1							**Average values**		
Horizontal Distance from Left edge (cm)	**Water Imbibition h_c^{imb} (cm)***	**Water Drainage h_c^{dr} (cm)***	**Toluene Imbibition h_c^{imb} (cm)***	**Water Imbibition h_c^{imb} (cm)**	**Water Drainage h_c^{dr} (cm)**	**Toluene Imbibition h_c^{imb} (cm)**	**Water Imbibition (cm)**	**Water Drainage (cm)**	**Toluene Imbibition (cm)**
0	13.5	21.1	6.0	13.8	21.5	6.3			
1	12.5	19.6	6.0	12.6	19.3	6.3			
2	10.6	19.8	6.0	10.8	19.4	6.1			
3	11.9	18.6	6.0	11.7	19.0	5.9			
4	12.6	19.5	6.0	12.3	18.8	5.9			
5	11.8	19.5	5.8	11.2	19.2	5.9			
6	11.8	19.3	5.8	11.6	19.1	5.8			
7	11.4	18.9	5.8	11.0	19.0	5.8			
8	10.9	18.2	5.8	11.2	18.8	5.7			
9	9.9	18.3	5.6	9.5	18.5	5.5			
9.8	10.1	17.2	5.6	9.7	17.7	5.5			
h_c^{avg} (cm)	11.55	19.09	5.85	11.40	19.12	5.88	**11.47**	**19.10**	**5.87**
Statistical Analysis for h_ϵ^{avg} (cm)	11.55 ± 0.65	19.09 ± 0.60	5.85 ± 0.09	11.40 ± 0.73	19.12 ± 0.54	5.88 ± 0.16	11.47 ± 0.14	19.1 ± 0.03	5.87 ± 0.03
r_{eq} (cm)	0.01134	0.008	0.01134	0.01148	0.00769	0.01129	**0.01141**	**0.00769**	**0.01131**
Statistical Analysis for r_{eq}^{ave} (cm)							0.01141 ± 0.00014	0.00769 ± 0.00001	0.01131 ± 0.00005
δ_{etch} (cm)	0.01244	0.00928	0.01244	0.01262	0.00927	0.01238	**0.01253**	**0.00928**	**0.01241**
Statistical Analysis for δ_{etch}^{ave} (cm)							0.01253 ± 0.00017	0.00928 ± 0.00002	0.01241 ± 0.00006
A_x (cm^2)	0.124	0.093	0.124	0.126	0.093	0.124	**0.125**	**0.093**	**0.124**
Statistical Analysis for A_x^{ave} (cm^2)							0.125 ± 0.002	0.093 ± 0.000	0.124 ± 0.001
P_c (g/cms^2)			4968.0			4991.1			**4979.5**
Statistical Analysis for P_c^{ave} ($g/cm\ s^2$)									4979.5 ± 22.7

*: Courtesy of James, 2009

Table 2.7: Constant water head permeability measurements: OC-1 MM

Water Head (cm) Head Loss (mm)	Trial 1* 113.9 0	Trial 2* 102.4 0	Trial 3* 93.4 0	Trial 4 108.6 0
Time (s)	**Mass (g)**	**Mass (g)**	**Mass (g)**	**Mass (g)**
0	0.00	0.00	0.00	0.00
20	0.65	0.60	0.52	0.62
40	1.35	1.22	1.01	1.31
60	2.05	1.84	1.52	1.94
80	2.75	2.47	2.04	2.63
100	3.46	3.09	2.58	3.32
120	4.16	3.71	3.08	3.96
140	4.88	4.33	3.61	4.68
160	6.09	4.95	4.14	5.57
Q (cm^3/s)	**0.0357**	**0.0309**	**0.0257**	**0.0336**
R^2	0.9934	1.000	0.9999	0.9980
$\Delta P/l$ ($g/cm^2.s^2$)	**3675.5**	**3304.4**	**3014.0**	**3504.5**
Slope (Q vs. $\Delta P/l$) ($cm^5.s/g$)	**1.51421E-05**			
R^2	0.9916			
K^{imb} (Darcy)	**120.86**			

*: Courtesy of James, 2009

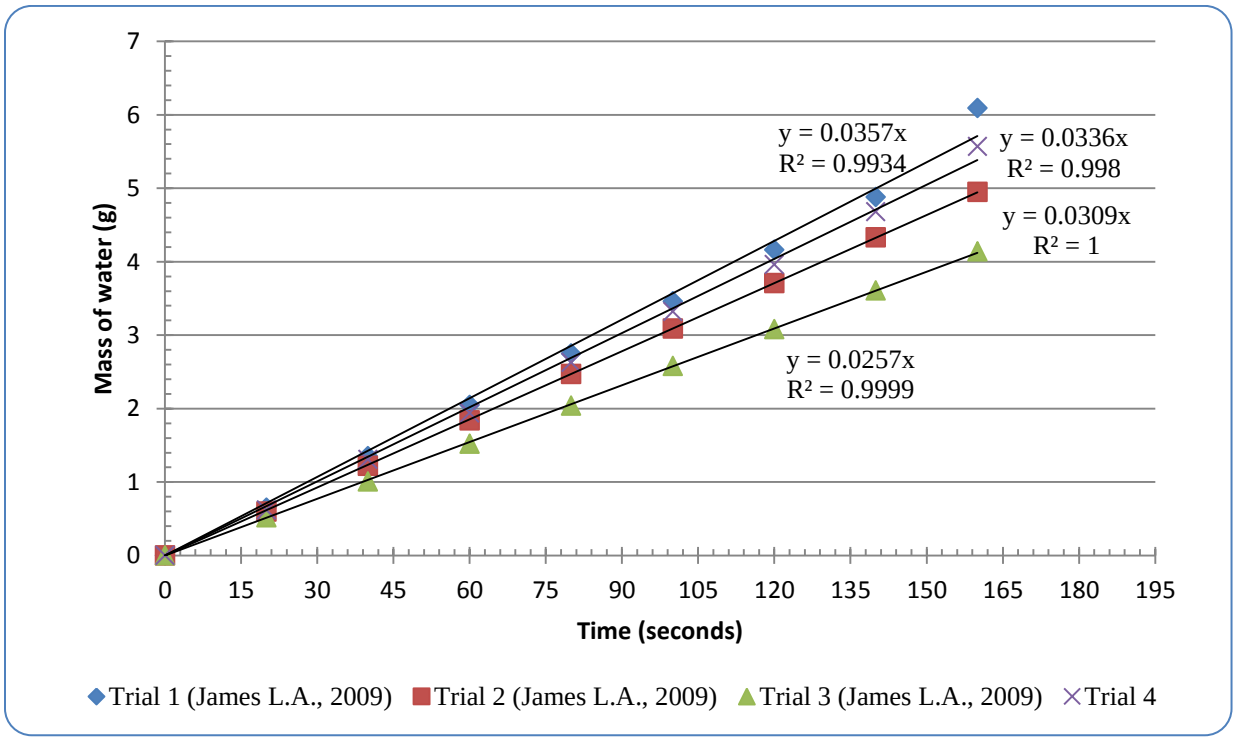

Figure 2.22: Constant water head permeability measurement for OC-1 glass micromodel

Table 2.8: Advancing interface permeability measurements (with Toluene) for OC-1 MM

Trial 1*			Trial 2*			Trial 3		
Time (s)	**Interface Position (cm)**	**X^2 (cm^2)**	**Time (s)**	**Interface Position (cm)**	**X^2 (cm^2)**	**Time (s)**	**Interface Position (cm)**	**X^2 (cm^2)**
26	5.0	25.00	10	2.6	6.76	12	3.1	9.61
40	7.0	49.00	34	4.5	20.25	18	3.7	13.69
55	8.5	72.25	49	7.0	49.00	29	4.2	17.64
68	10.0	100.00	61	8.5	72.25	38	5.4	29.16
77	11.5	132.25	75	10.0	100.00	46	6.7	44.89
91	13.0	169.00	82	11.0	121.00	57	8.2	67.24
103	14.0	196.00	94	12.5	156.25	69	9.6	92.16
			112	13.5	182.25	79	10.9	118.81
			124	14.5	210.25	92	12.6	158.76
						109	13.9	193.21
						119	14.5	210.25
						128	15.6	243.36
						135	16.4	268.96
slope (cm^2/s)		**2.2756**			**2.1495**			**2.3695**
R^2		**0.9848**			**0.9949**			**0.9934**
K (D)		**56.43**			**53.30**			**58.75**

K_{avg} (D)	**56.16**
Statistical Analysis for K_{avg} (D)	**56.16 ± 3.10**

*: Courtesy of James, 2009

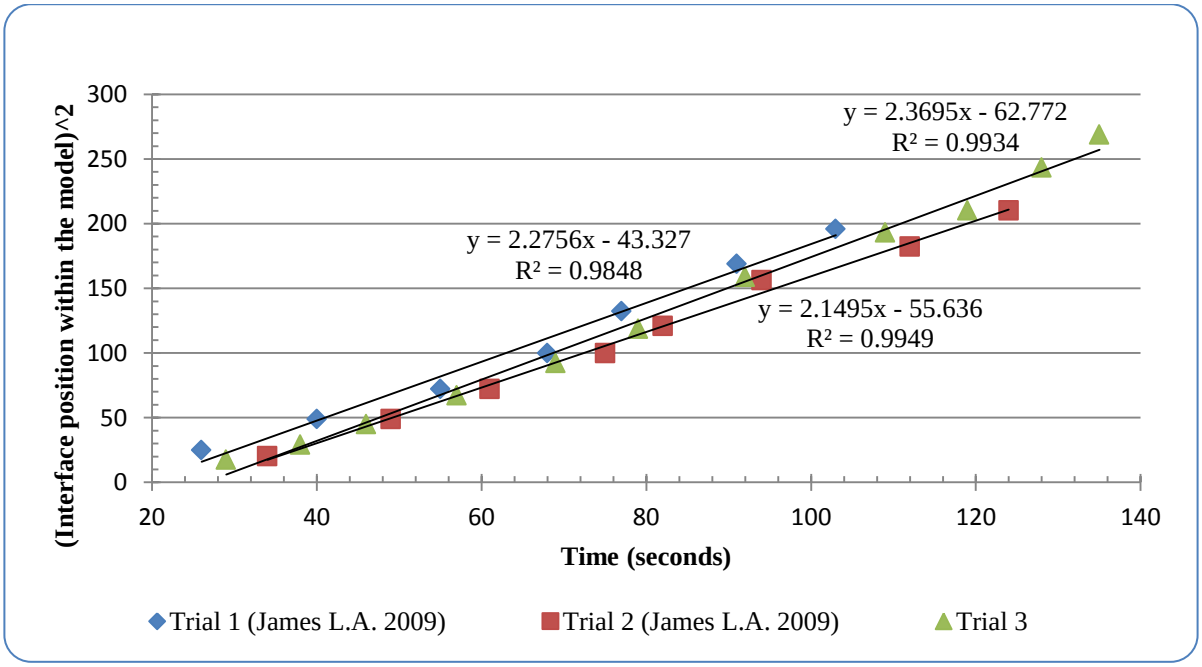

Figure 2.23: Advancing interface permeability measurements with toluene for OC-1 MM

The details of the pore-scale dimensions of DL-1 glass micromodel are summarized in Table 2.9. Using the description provided in the left column of this Table, one can step by step calculate the pore-scale dimensions of DL-1 micromodel based on the schematic pore-scale pattern of this model that is shown in Figure 2.24. In Table 2.10, the details of the imbibition and drainage tests performed using both water and toluene are presented in order to calculate the depth of etching of this glass micromodel using the procedures presented earlier. Tables 2.11 and 2.12 contain the data obtained during permeability measurements of DL-1 micromodel using constant water head as well as advancing toluene interface methodologies respectively. In addition, Figures 2.25 and 2.26 show the plots used in order to calculate DL-1 micromodel permeability using the two noted experimental techniques.

Table 2.9: DL-1 model dimensions

Pore-Scale Dimensions	
Pore Dimensions (mm)	
(1) Pore to Pore (3) + (4b)	2.04
(2a) Pore Body	1.91
(2b) Pore Body (2b) = (1)	2.04
(3) Pore Throat Width	0.67
(4a) Particle Size	0.99
(4b) Particle Size	1.37
(5) Diffusion Distance 0.5*(4b) + (3)	1.36
(6) Flow Path 0.25*(2πr) 0.5*π*(5)	2.13
(7) Pore Throat Length	n/a
Macroscopic Dimensions	
Length (mm)	304
Length (# pores)	149
Width (mm)	100
Width (# pores)	49

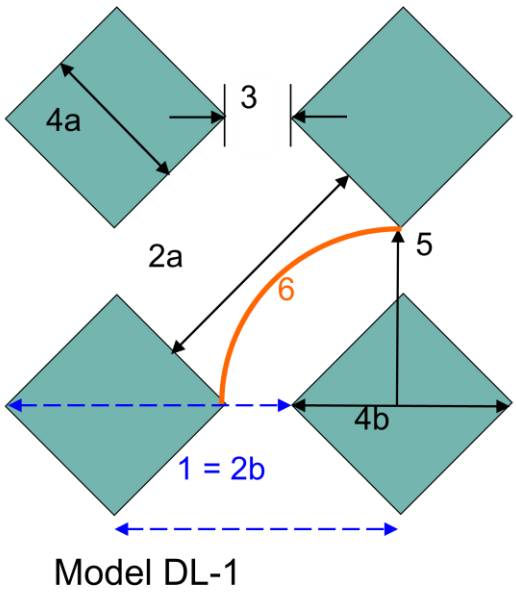

Figure 2.24: Schematic pore-scale pattern of DL-1 glass micromodel (Courtesy of James, 2009)

Table 2.10: Capillary heights for model DL-1									**Average Values**		
Horizontal Distance from Left edge (cm)	**Water Imbibition h_c^{imb} (cm)***	**Water Drainage h_c^{dr} (cm)***	**Toluene Imbibition, h_c^{imb} (cm)***			**Water Imbibition h_c^{imb} (cm)**	**Water Drainage h_c^{dr} (cm)**	**Toluene Imbibition, h_c^{imb} (cm) Reference Height=73 cm**	**Water Imbibition**	**Water Drainage**	**Toluene Imbibition**
			Reference Height = 70.9 cm	**Reference Height = 80.8 cm**	**Reference Height = 89.0 cm**						
0	5.2	15.7	5.8	5.5	6.7	5.1	16.0	5.9			
1	5.4	17.9	6.5	6.3	7.6	5.4	17.7	6.6			
2	5.7	18.8	6.9	6.7	7.5	5.9	18.3	6.9			
3	5.9	19.0	7.2	7.1	7.6	5.8	18.9	7.3			
4	6.0	19.8	7.3	7.2	7.6	5.9	19.8	7.3			
5	5.5	20.0	7.1	7.1	7.7	5.8	19.8	7.2			
6	6.3	21.0	7.4	7.7	7.8	6.5	20.6	7.5			
7	6.0	21.5	7.5	7.7	7.7	5.9	21.8	7.8			
8	6.2	21.4	7.4	7.8	7.9	5.8	21.6	7.4			
9	6.3	21.7	7.5	7.9	8.0	6.5	21.4	7.7			
9.8	6.7	22.5	7.5	8.0	8.0	6.4	22.7	7.8			
h_c^{avg} (cm)	5.93	19.94	7.31			5.91	19.87	7.35	**5.92**	**19.90**	**7.33**
Statistical Analysis for h_c^{avg} (cm)	5.93 ± 0.26	19.94 ± 1.18	7.31 ± 0.21			5.91 ± 0.26	19.87 ± 1.19	7.35 ± 0.34	5.92 ± 0.02	19.90 ± 0.06	7.33 ± 0.04
r_{eq}^{ave} (cm)	0.02209	0.00737	0.00908			0.02216	0.00739	0.00903	**0.02212**	**0.00738**	**0.00906**
Statistical Analysis for r_{eq}^{ave} (cm)									0.02212 ± 0.00007	0.00738 ± 0.00002	0.00906 ± 0.00005
δ_{etch}^{ave}(cm)	0.02498	0.00828	0.00954			0.02506	0.00831	0.00948	**0.02502**	**0.00830**	**0.00951**
Statistical Analysis for δ_{etch}^{ave} (cm)									0.02502 ± 0.00009	0.00830 ± 0.01150	0.00951 ± 0.00005
A_x^{ave} (cm^2)	0.250	0.083	0.095			0.251	0.083	0.095	**0.250**	**0.083**	**0.095**
Statistical Analysis for A_x^{ave} (cm^2)									0.250 ± 0.001	0.080 ± 0.006	0.095 ± 0.001
P_c (g/cm s^2)			6202.2					6237.0			**6219.6**
Statistical Analysis for P_c (g/cm s^2)											6219.6 ± 34.0

*: Courtesy of James, 2009

Table 2.11: Constant water head permeability measurements: DL-1 micromodel						
Water Head (cm) **Head Loss (mm)**	**Trial 1*** **126.6** **2**	**Trial 2*** **119.5** **2**	**Trial 3*** **114.2** **2**	**Trial 4*** **107.0** **2**	**Trial 5** **124.7** **0**	**Trial 6** **113.6** **0**
Time (s)	**Mass (g)**	**Mass (g)**	**Mass (g)**	**Mass (g)**	**Mass (g)**	**Mass (g)**
0	0.00	0.01	0.00	0.00	0.00	0.00
20	3.77	4.03	3.97	3.46	3.82	3.88
40	8.31	8.12	7.92	6.90	8.21	7.78
60	12.71	12.28	11.74	10.41	12.54	11.66
80	17.29	16.42	15.57	13.83	17.06	15.23
100	21.98	20.61	19.44	17.35	21.69	19.28
120	25.96	24.61	23.27	20.76	25.76	22.98
140	30.31	28.73	27.08	24.26	29.93	26.89
160	34.73	32.80	30.83	27.64	34.13	30.75
180	39.11	36.83	34.61	31.00	38.92	34.47
Q (cm^3/s)	**0.2167**	**0.2050**	**0.1933**	**0.1728**	**0.2144**	**0.1919**
R^2	0.9996	1.0000	0.9999	1.0000	0.9996	0.9999
$\Delta P/l$ ($g/cm^2.s^2$)	**4085.3**	**3856.2**	**3685.2**	**3452.9**	**4024.0**	**3665.8**
slope (Q vs $\Delta P/l$) ($cm^5.s/g$)	**6.8251E-05**					
R^2	0.9837					
K^{imb} (Darcy)	**272.79**					

*: Courtesy of James, 2009

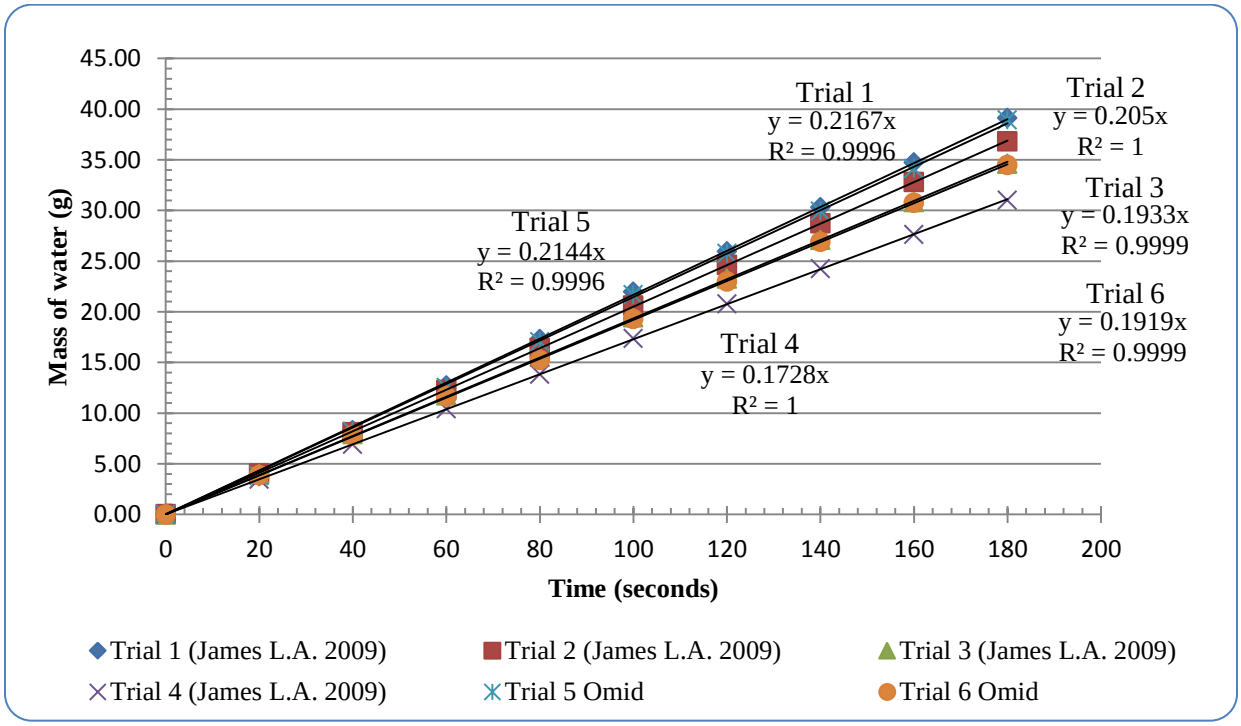

Figure 2.25: Constant water head permeability measurement for DL-1 glass micromodel

Table 2.12: Advancing interface permeability measurements (with Toluene) for DL-1 MM

Trial 1*			Trial 2*			Trial 3		
Time (s)	Interface Position (cm)	X^2 (cm^2)	Time (s)	Interface Position (cm)	X^2 (cm^2)	Time (s)	Interface Position (cm)	X^2 (cm^2)
20	10.0	100.00	25	10.2	104.04	20	10.3	106.09
25	11.4	129.96	30	11.2	125.44	25	10.8	116.64
30	12.6	158.76	35	12.3	151.29	30	12.3	151.29
35	13.4	179.56	40	13.4	179.56	35	13.1	171.61
40	14.4	207.36	45	14.2	201.64	40	13.9	193.21
45	15.2	231.04	50	14.9	222.01	45	14.7	216.09
50	16.3	265.69	55	16.0	256.00	50	15.7	246.49
55	17.6	309.76	60	16.8	282.24	55	17.3	299.29
60	18.4	338.56	65	17.8	316.84	60	17.8	316.84
65	19.7	388.09	70	18.8	353.44	65	18.6	345.96
70	20.3	412.09	75	19.8	392.04	70	19.6	384.16
75	21.2	449.44	80	20.7	428.49	75	20.7	428.49
80	21.9	479.61	85	21.3	453.69	80	21.5	462.25
85	23.3	542.89	90	22.2	492.84	85	22.6	510.76
90	23.7	561.69	95	22.8	519.84	90	23.1	533.61
95	24.1	580.81	100	23.5	552.25	95	23.8	566.44
100	24.8	615.04	105	24.1	580.81	100	24.2	585.64
105	25.7	660.49	110	24.7	610.09	105	25.4	645.16
110	26.2	686.44	115	25.5	650.25	110	25.9	670.81
115	26.9	723.61	120	26.0	676.00	115	26.4	696.96
120	27.3	745.29	125	26.9	723.61	120	26.8	718.24
125	27.8	772.84	130	27.3	745.29	125	27.6	761.76
130	28.1	789.61	135	27.7	767.29	130	27.8	772.84
135	28.7	823.69	140	28.2	795.24	135	28.2	795.24
140	29.1	846.81				140	28.7	823.69
slope (cm^2/s)		**6.5149**			**6.2594**			**6.3942**
R^2		**0.9968**			**0.9980**			**0.9959**
K (D)		**97.15**			**93.34**			**93.34**

K_{avg} (D)	**94.61**
Statistical Analysis for K_{avg} (D)	94.61 ± 2.49

*: Courtesy of James, 2009

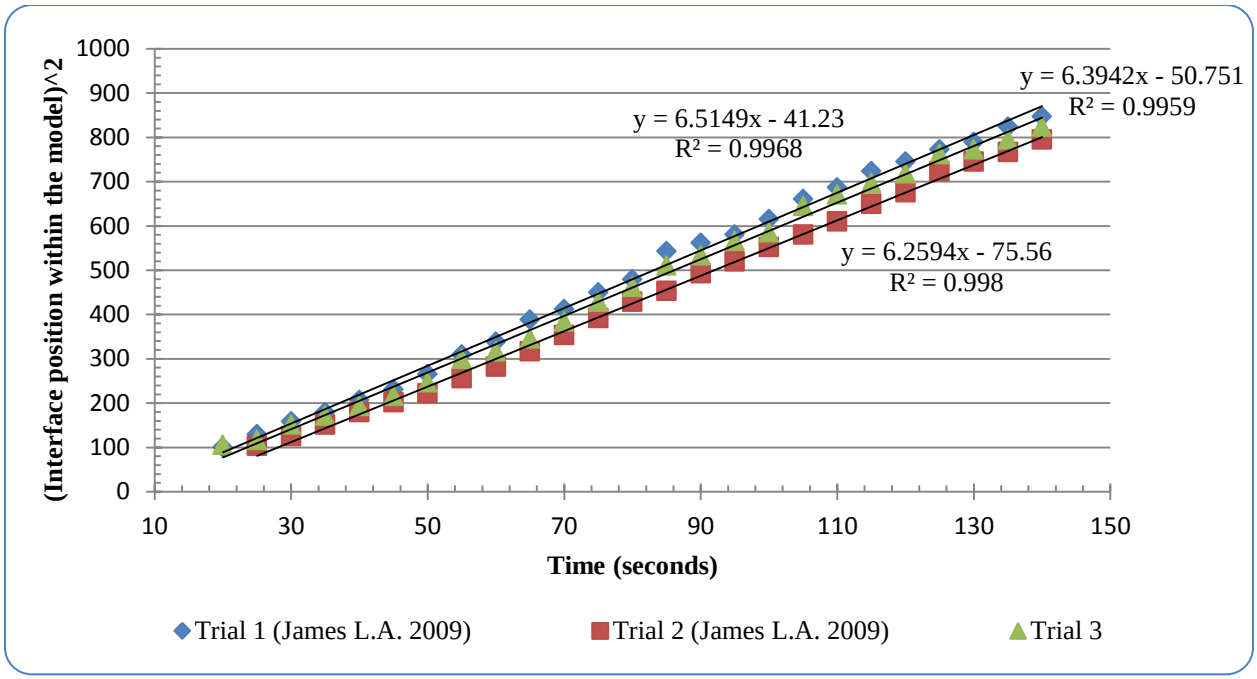

Figure 2.26: Advancing interface permeability measurements with toluene for DL-1 MM

In Table 2.13, the details of the pore-scale dimensions of DC-1 glass micromodel are presented along with the calculation methodology (i.e. left column of the Table) of each of these pore-scale dimensions based on the schematic pore-scale pattern of this model that is shown in Figure 2.27. Tables 2.14 and 2.15 contain the data obtained during permeability measurements of DC-1 micromodel using constant water head as well as advancing toluene interface permeability measurements respectively. In addition, Figures 2.28 and 2.29 show the plots used in order to calculate DC-1 micromodel permeability using the two noted experimental techniques. Table 2.16 contains the details of imbibition and drainage tests performed using both water and toluene in order to calculate the depth of etching of DC-1 glass micromodel using procedure presented earlier.

Table 2.13: DC-1 model dimensions	
Model Dimensions	
Pore Dimensions (mm)	
(1) Pore to Pore (3) + (4)	1.60
(2a) Pore Body	1.34
(2b) Pore Body (1) - (7)	1.31
(3) Pore Throat Width	0.49
(4) Particle Size	1.11
(5) Diffusion Distance 0.5*(4) + (3)	1.045
(6) Flow Path 0.25*(2πr) + (7) 0.5*π*(5) + (7)	1.93
(7) Pore Throat Length	0.29
Macroscopic Dimensions	
Length (mm)	304
Length (# pores)	190
Width (mm)	141
Width (# pores)	89

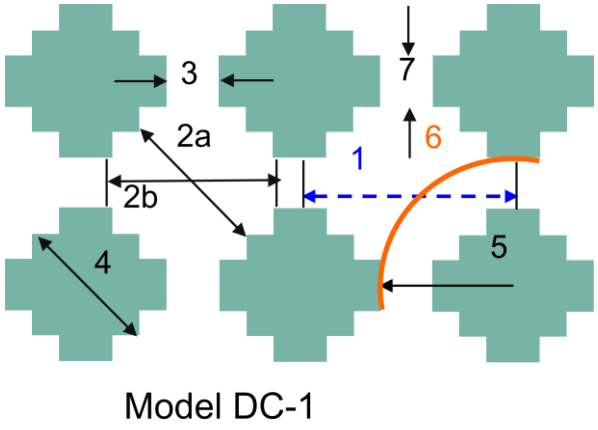

Figure 2.27: Schematic pore-scale pattern of DC-1 glass micromodel (Courtesy of James, 2009)

Table 2.14: Constant water head permeability measurements: DC-1 MM

Water Head (cm) **Head Loss (mm)**	**Trial 1*** **114.1** **0**	**Trial 2*** **102.5** **0**	**Trial 3*** **89.3** **0**	**Trial 4** **112** **0**	**Trial 5** **95.6** **0**
Time (s)	**Mass (g)**	**Mass (g)**	**Mass (g)**	**Mass (g)**	**Mass (g)**
0	0.00	0.00	0.00	0.00	0.00
20	0.94	0.84	0.75	0.91	0.83
40	1.89	1.66	1.49	1.82	1.57
60	2.88	2.49	2.23	2.94	2.48
80	3.88	3.32	2.99	3.83	3.16
100	4.87	4.14	3.71	4.81	4.06
120	5.86	5.00	4.46	5.74	4.86
140	6.86	5.83	5.17	6.76	5.71
160	7.87	6.67	5.91	7.96	6.60
Q (cm^3/s)	**0.0489**	**0.0416**	**0.0370**	**0.0486**	**0.0408**
R^2	0.9998	1.0000	0.9999	0.9988	0.9994
ΔP/l ($g/cm^2.s^2$)	**3682.0**	**3307.6**	**2881.7**	**3614.2**	**3085.0**
slope ($Q_{corrected}$ vs ΔP/l) ($cm^5.s/g$)		**1.4968E-05**			
R^2		0.9622			
K^{imb} (Darcy)		**87.08**			

*: Courtesy of James, 2009

Table 2.15: Advancing interface permeability measurements (with Toluene) for DC-1 micromodel

Trial 2*			Trial 4*			Trial 5*			Trial 6			Trial 7		
Time (s)	**Interface Position (cm)**	**X^2 (cm^2)**	**Time (s)**	**Interface Position (cm)**	**X^2 (cm^2)**	**Time (s)**	**Interface Position (cm)**	**X^2 (cm^2)**	**Time (s)**	**Interface Position (cm)**	**X^2 (cm^2)**	**Time (s)**	**Interface Position (cm)**	**X^2 (cm^2)**
0	0.0	0.00	0	6.8	46.24	0	4.8	23.04	0	0.0	0.00	0	5.2	27.04
5	2.5	6.25	5	7.5	56.25	5	5.5	30.25	5	6.8	46.24	5	6.0	36.00
10	3.0	9.00	10	8.2	67.24	10	5.9	34.81	10	7.9	62.41	10	6.8	46.24
15	4.0	16.00	15	8.4	70.56	15	6.1	37.21	15	8.5	72.25	15	7.2	51.84
20	5.2	27.04	20	8.9	79.21	20	6.6	43.56	20	9.2	84.64	20	7.5	56.25
25	5.4	29.16	25	9.3	86.49	25	7.0	49.00	25	9.6	92.16	25	8.1	65.61
30	6.0	36.00	30	9.8	96.04	30	7.5	56.25	30	10.1	102.01	30	8.3	68.89
35	6.5	42.25	35	10.3	106.09	35	8.0	64.00	35	10.5	110.25	35	8.8	77.44
40	7.3	53.29	40	10.9	118.81	40	8.5	72.25	40	11.0	121.00	40	9.2	84.64
45	7.5	56.25	45	11.3	127.69	45	9.0	81.00	45	11.2	125.44	45	9.7	94.09
50	7.8	60.84	50	11.7	136.89	50	9.3	86.49	50	12.3	151.29	50	10.1	102.01
55	8.0	64.00	55	12.2	148.84	55	9.8	96.04	55	12.6	158.76	55	10.4	108.16
60	8.3	68.89	60	12.5	156.25	60	10.4	108.16	60	12.7	161.29	60	10.7	114.49
65	9.1	82.81	65	12.7	161.29	65	10.9	118.81	65	12.9	166.41	65	11.2	125.44
70	9.5	90.25	70	13.0	169.00	70	11.4	129.96	70	13.2	174.24	70	11.5	132.25
75	10.3	106.09	75	13.5	182.25	75	12.0	144.00	75	13.6	184.96	75	11.9	141.61
80	10.5	110.25	80	13.9	193.21	80	12.7	161.29	80	14.0	196.00	80	12.6	158.76
85	11.2	125.44	85	14.0	196.00	85	13.3	176.89	85	14.3	204.49	85	13.3	176.89
90	11.6	134.56	90	14.4	207.36	90	13.5	182.25	90	14.8	219.04	90	13.6	184.96
95	12.3	151.29	95	14.9	222.01	95	14.1	198.81	95	15.3	234.09	95	14.4	207.36
100	12.6	158.76	100	15.2	231.04	105	14.7	216.09	100	15.5	240.25	100	14.8	219.04
105	13.1	171.61	105	15.7	246.49	110	15.2	231.04	110	16.6	275.56	110	15.3	234.09
110	13.5	182.25	110	16.1	259.21	120	16.0	256.00	120	16.9	285.61	120	15.9	252.81
115	13.9	193.21	120	16.6	275.56	130	16.5	272.25	130	17.2	295.84	130	16.3	265.69
120	14.3	204.49	130	17.0	289.00	140	17.2	295.84	140	18.6	345.96	140	16.9	285.61
125	14.6	213.16	140	18.2	331.24	150	18.1	327.61	150	18.9	357.21	150	17.5	306.25
135	15.0	225.00	150	18.6	345.96	160	18.7	349.69	160	19.6	384.16	160	18.2	331.24
145	15.8	249.64	160	19.3	372.49	170	19.5	380.25	170	20.1	404.01	170	18.8	353.44
155	16.4	268.96	170	20.4	416.16	180	20.4	416.16	180	20.5	420.25	180	19.5	380.25
165	17.5	306.25	180	20.9	436.81	190	21.0	441.00	190	21.0	441.00	190	20.3	412.09

Table 2.15 (cont.): advancing interface permeability measurements (with Toluene) for DC-1 micromodel

Trial 2*			Trial 4*			Trial 5*			Trial 6			Trial 7		
Time (s)	**Interface Position (cm)**	**X^2 (cm^2)**	**Time (s)**	**Interface Position (cm)**	**X^2 (cm^2)**	**Time (s)**	**Interface Position (cm)**	**X^2 (cm^2)**	**Time (s)**	**Interface Position (cm)**	**X^2 (cm^2)**	**Time (s)**	**Interface Position (cm)**	**X^2 (cm^2)**
175	18.5	342.25	190	21.5	462.25	200	21.6	466.56	200	21.7	470.89	200	20.9	436.81
185	19.0	361.00	200	21.9	479.61	210	22.0	484.00	210	22.1	488.41	210	21.6	466.56
195	19.5	380.25	210	22.4	501.76	220	22.5	506.25	220	22.8	519.84	220	22.2	492.84
205	20.0	400.00	220	23.0	529.00	230	23.0	529.00	230	23.2	538.24	230	22.8	519.84
215	20.5	420.25	230	23.3	542.89	240	23.5	552.25	240	23.5	552.25	240	23.2	538.24
225	21.2	449.44	240	23.5	552.25	250	23.8	566.44	250	24.2	585.64	250	23.7	561.69
235	21.6	466.56	250	24.0	576.00	260	24.3	590.49	260	24.6	605.16	260	24.2	585.64
245	22.4	501.76	260	24.2	585.64	270	24.5	600.25	270	24.9	620.01	270	24.6	605.16
255	23.1	533.61	270	24.6	605.16	280	24.6	605.16	280	25.3	640.09	280	24.9	620.01
270	23.8	566.44	280	25.5	650.25	290	25.2	635.04	290	25.8	665.64	290	25.5	650.25
285	24.2	585.64	290	25.5	650.25	300	25.6	655.36	300	26.2	686.44	300	25.8	665.64
300	24.7	610.09	300	26.3	691.69	310	26.1	681.21	310	26.5	702.25	310	26.4	696.96
315	25.3	640.09	310	26.6	707.56	320	26.5	702.25	320	27.5	756.25	320	26.9	723.61
330	26.0	676.00	320	27.2	739.84	330	26.9	723.61	330	27.9	778.41	330	27.3	745.29
345	26.5	702.25	330	27.4	750.76	340	27.3	745.29	340	28.2	795.24	340	27.7	767.29
360	27.6	761.76	340	27.7	767.29	350	27.5	756.25	350	28.3	800.89	350	28.0	784.00
375	28.5	812.25	350	28.2	795.24	360	28.1	789.61	360	28.6	817.96	360	28.5	812.25
390	29.0	841.00	360	28.6	817.96	370	28.7	823.69	370	28.8	829.44	370	29.0	841.00
			370	28.9	835.21	380	29.2	852.64	380	29.1	846.81	380	29.6	876.16
			380	29.3	858.49	390	29.7	882.09	390	29.5	870.25	390	30.2	912.04
			390	29.7	882.09				400	29.7	882.09	400	30.6	936.36
Slope (cm^2/s)		2.3110			2.1915			2.2853			2.1819			2.3608
R^2		0.9984			0.9982			0.9969			0.9986			0.9986
K (D)		**34.81**			**33.01**			**34.42**			**32.86**			**35.56**
K_{avg} (D)		**34.13**												
Statistical Analysis for K_{avg} (Darcy)		34.13 ± 1.02												

*: Courtesy of James, 2009

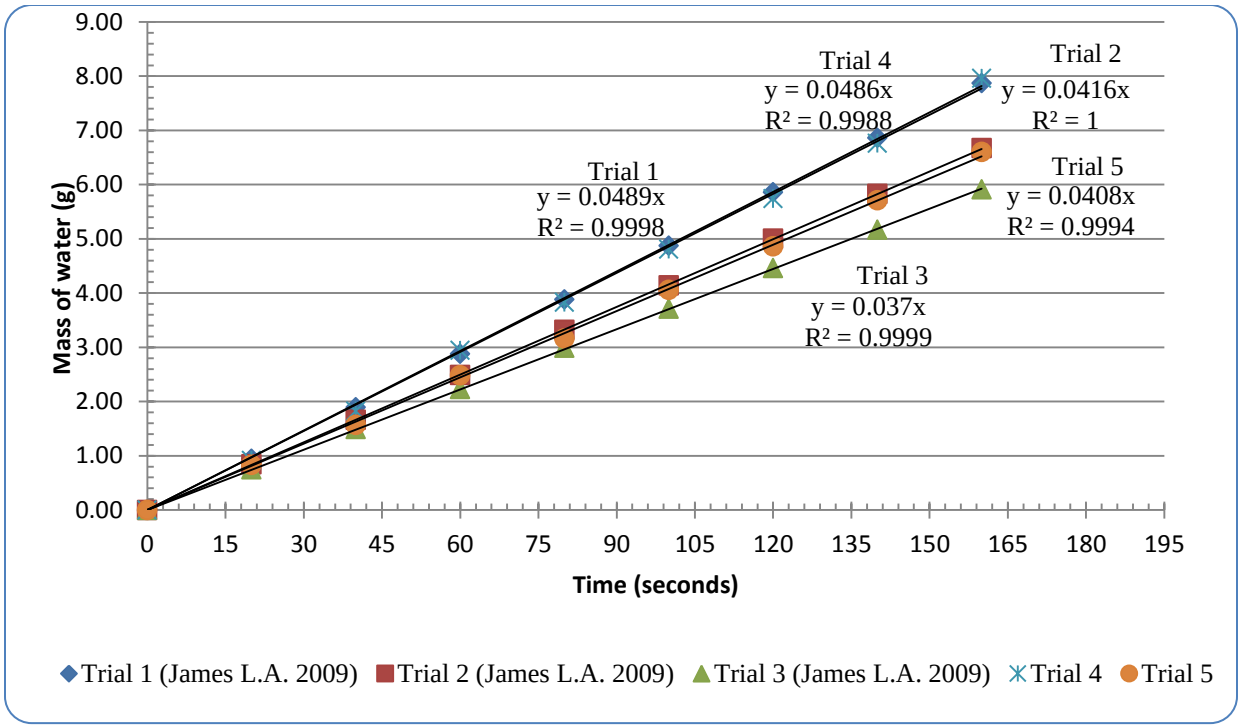

Figure 2.28: Constant water head permeability measurement for DC-1 glass micromodel

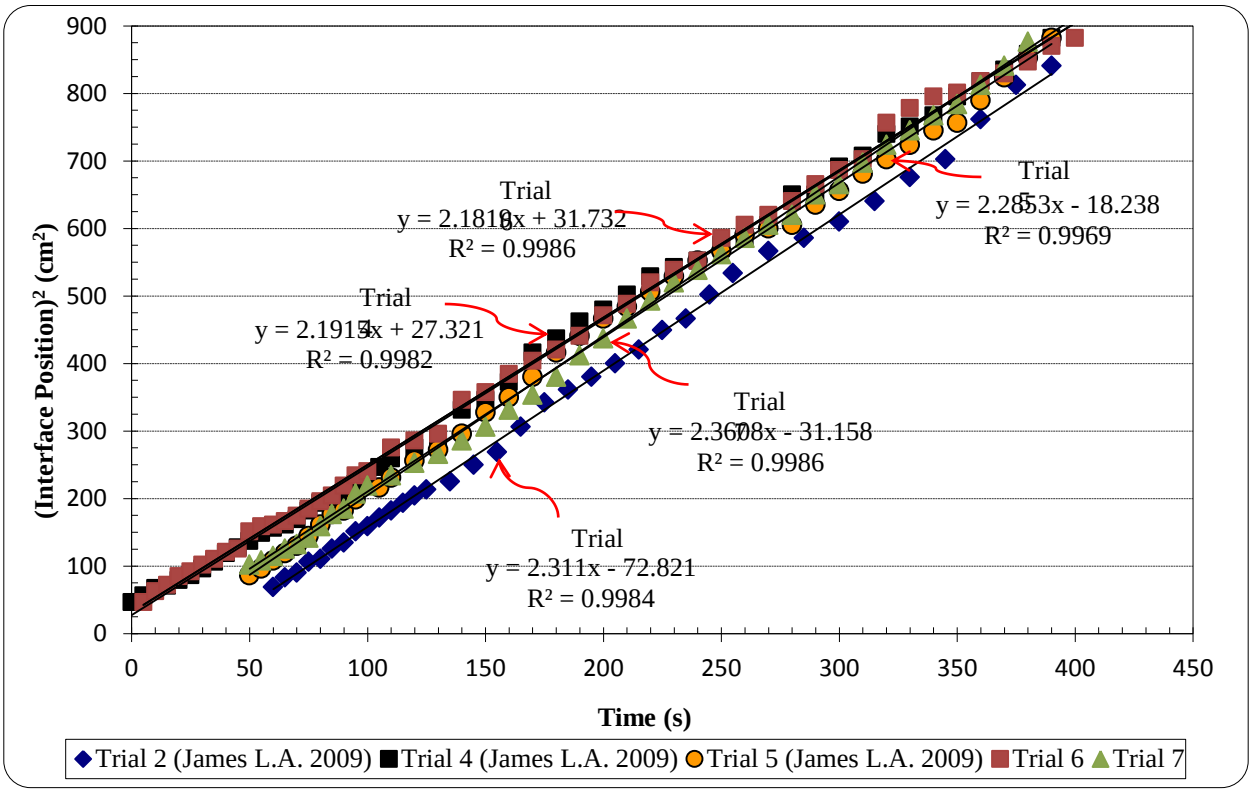

Figure 2.29: Advancing interface permeability measurements with toluene for DC-1 MM

Table 2.16: Capillary heights for Model DC-1									Average Values		
Horizontal Distance from Left edge (cm)	**Water Imbibition h_c^{imb} (cm)***	**Water Drainage h_c^{dr} (cm)***	**Toluene Imbibition, h_c^{imb} (cm)***			**Water Imbibition h_c^{imb} (cm)**	**Water Drainage h_c^{dr} (cm)**	**Toluene Imbibition h_c^{imb} (cm) Ref Height = 79 cm**	**Water Imbibition**	**Water Drainage**	**Toluene Imbibition**
			Ref Height = 70.7 cm	**Ref Height = 81.5 cm**	**Ref Height = 88.8 cm**						
0	11.8	24.4	7.1	7.5	8.2	11.9	24.8	7.6			
1	11.8	24.2	7.7	8.0	8.6	11.7	24.6	7.9			
2	10.0	23.8	8.0	7.9	8.7	10.8	24.1	7.9			
3	11.3	22.5	7.8	8.1	8.7	11.0	23.2	7.7			
4	12.1	22.6	8.1	8.2	8.3	11.6	22.8	8.0			
5	11.7	23.4	8.1	8.3	8.3	11.8	22.9	8.4			
6	11.5	22.5	8.1	8.2	8.6	11.3	22.7	8.1			
7	11.8	22.0	8.3	8.2	8.4	12.0	22.3	8.1			
8	10.7	22.1	8.3	8.5	8.5	11.2	22.4	8.6			
9	10.3	23.1	9.6	8.6	8.6	10.5	23.6	8.8			
10	10.3	23.3	10.0	8.9	8.7	10.4	23.8	8.7			
11	10.5	22.5	8.7	9.6	8.7	10.4	22.6	9.3			
12	11.8	22.6	8.8	8.7	8.6	11.8	22.8	8.6			
13	11.3	22.5	8.9	8.7	8.9	11.0	22.4	8.4			
13.8	11.1	21.1	9.1	8.6	8.2	11.6	21.9	8.3			
h_c^{avg} (cm)	11.20	22.84	8.52			11.27	23.13	8.29	**11.23**	**22.98**	**8.41**
Statistical Analysis for h_c^{avg} (cm)	11.20 ± 0.34	22.84 ± 0.44	8.52 ± 0.15			11.27 ± 0.28	23.13 ± 0.44	8.29 ± 0.23	11.23 ± 0.07	22.98 ± 0.28	8.41 ± 0.22
r_{eq}^{ave} (cm)	0.01169	0.00643	0.00779			0.01162	0.00635	0.00801	**0.01165**	**0.00639**	**0.00790**
Statistical Analysis for r_{eq}^{ave} (cm)									0.01165 ± 0.00007	0.00639 ± 0.00008	0.00790 ± 0.00021
δ_{etch}^{ave} (cm)	0.01281	0.00741	0.00827			0.01272	0.00730	0.00851	**0.01277**	**0.00735**	**0.00839**
Statistical Analysis for δ_{etch}^{ave} (cm)									0.01277 ± 0.00008	0.00735 ± 0.00010	0.00839 ± 0.00023
A_x (cm^2)	0.181	0.104	0.117			0.179	0.103	0.120	0.180	0.104	0.118
Statistical Analysis for A_x^{ave} (cm^2)									0.180 ± 0.001	0.104 ± 0.001	0.118 ± 0.003
P_c (g/cm s^2)			7229.0					7037.4			**7133.2**
Statistical Analysis for P_c (g/cm s^2)											7133.2 ± 187.7

*: Courtesy of James, 2009

In Table 2.17, the details of the pore-scale dimensions of OM-1 glass micromodel are presented. Focusing on the descriptions made in the left column of this Table, one may calculate each of these pore-scale dimensions based on the schematic pore-scale pattern of this model that is shown in Figure 2.30. The details of the imbibition and drainage tests performed using both water and toluene to calculate the depth of etching of OM-1 glass micromodel are presented in Table 2.18. Tables 2.19 and 2.20 contain the data obtained during permeability measurements of OM-1 micromodel using constant water head as well as advancing toluene interface permeability measurement techniques respectively. In addition, Figures 2.31 and 2.32 show the plots used in order to calculate OM-1 micromodel permeability using the two noted experimental techniques.

Table 2.17: OM-1 model dimensions

Model Dimensions	
Pore Dimensions (mm)	
(1) Pore to Pore (3) + (4b)	2.00
(2a) Pore Body	1.63
(2b) Pore Body (1) - (7)	2.00
(3) Pore Throat Width	0.30
(4b) Particle Size	1.68
(4a) Particle Size	1.20
(5) Diffusion Distance 0.5*(4) + (3)	1.15
(6) Flow Path 0.25*(2πr) + (7) 0.5*π*(5) + (7)	1.81
(7) Pore Throat Length	0.00
Macroscopic Dimensions	
Length (mm)	301
Length (# pores)	150
Width (mm)	101
Width (# pores)	50

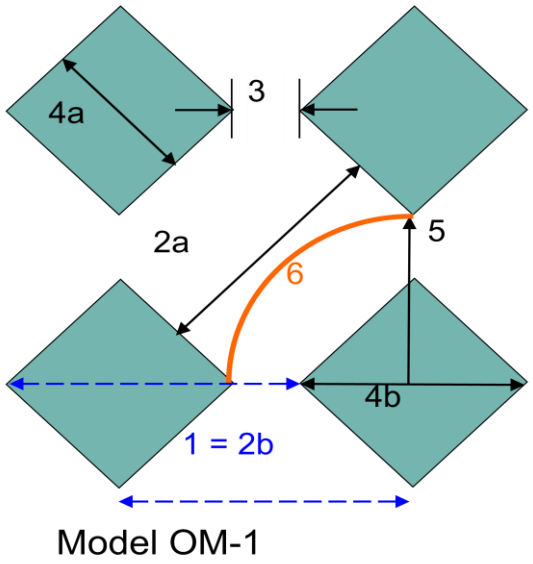

Figure 2.30: Schematic pore-scale pattern of OM-1 glass micromodel

Table 2.18: Capillary heights for model OM-1							**Average Values**		
Horizontal Distance from Left edge (cm)	**Water Imbibition h_c^{imb} (cm)**	**Water Drainage h_c^{dr} (cm)**	**Toluene Imbibition, h_c^{imb} (cm)**		**Water Imbibition h_c^{imb} (cm)**	**Water Drainage h_c^{dr} (cm)**	**Water Imbibition**	**Water Drainage**	**Toluene Imbibition**
			Reference Height = 71.2 cm	**Reference Height = 81.3 cm**					
0	10.6	17.8	6.2	5.8	10.8	17.6			
1	10.9	18.2	6.4	6.3	11.0	18.0			
2	11.1	18.6	6.5	6.5	11.3	18.4			
3	11.2	19.4	6.7	6.6	11.3	18.9			
4	11.6	19.9	6.7	6.6	11.5	19.4			
5	11.9	20.4	7.0	6.9	11.8	20.0			
6	12.0	21.1	7.2	7.0	12.3	20.8			
7	12.2	21.8	7.3	7.2	12.5	21.6			
8	12.3	22.4	7.5	7.6	12.6	22.3			
9	12.5	22.9	7.7	7.9	12.8	22.8			
10	12.8	23.6	7.9	8.2	13.0	23.5			
h_c^{avg} (cm)	11.74	20.55	7.01	6.96	11.90	20.30	**11.82**	**20.43**	**6.99**
Statistical Analysis for h_c^{avg} (cm)	11.74 ± 0.42	20.55 ± 1.16	7.01 ± 0.33	6.96 ± 0.42	11.90 ± 0.46	20.30 ± 1.20	11.82 ± 0.16	20.43 ± 0.25	6.99 ± 0.04
r_{eq}^{ave} (cm)	0.01116	0.00715	0.00947	0.00953	0.01100	0.00724	**0.01108**	**0.00719**	**0.00950**
Statistical Analysis for r_{eq}^{ave} (cm)							0.01108 ± 0.00015	0.00719 ± 0.00009	0.00950 ± 0.00006
δ_{etch}^{ave} (cm)	0.01198	0.00936	0.01006	0.01013	0.01180	0.00951	**0.01189**	**0.00943**	**0.01009**
Statistical Analysis for δ_{etch}^{ave} (cm)							0.01189 ± 0.00017	0.00943 ± 0.00015	0.01009 ± 0.00007
A_x^{ave} (cm^2)	0.121	0.094	0.102	0.102	0.119	0.096	**0.120**	**0.095**	**0.102**
Statistical Analysis for A_x^{ave} (cm^2)							0.120 ± 0.002	0.095 ± 0.002	0.102 ± 0.001
P_c (g/cm s^2)			5947.7	5909.1					**5928.4**
Statistical Analysis for P_c (g/cm s^2)									5928.4 ± 37.8

Table 2.19: Constant water head permeability measurements for OM-1 MM					
	Trial 1	**Trial 2**	**Trial 3**	**Trial 4**	**Trial 5**
Water Head (cm)	**133.8**	**126.4**	**115.2**	**105**	**136.2**
Head Loss (mm)	**2.2**	**2.2**	**2.4**	**2.2**	**2.3**
Time (s)	**Mass (g)**	**Mass (g)**	**Mass (g)**	**Mass (g)**	**Mass (g)**
0	0.00	0.00	0.00	0.00	0.00
10	1.40	1.37	1.24	1.18	1.45
20	3.38	3.17	2.97	2.35	3.55
30	5.51	5.37	5.11	4.39	6.18
40	7.44	6.95	6.22	5.68	8.33
50	9.58	8.68	7.86	6.78	10.12
60	11.64	10.31	9.76	8.53	11.76
70	13.24	12.04	10.97	9.88	13.38
80	15.13	13.97	12.55	11.96	15.16
90	17.02	15.34	14.06	13.57	16.55
100	18.67	17.66	16.03	15.12	18.74
120	22.28	20.73	19.59	18.22	22.62
140	25.82	24.44	23.13	21.78	25.90
160	29.48	27.87	26.54	24.97	30.05
180	33.49	31.45	29.56	28.02	33.59
Q (cm^3/s)	**0.1861**	**0.1740**	**0.1628**	**0.1527**	**0.1879**
R^2	0.9993	0.9996	0.9985	0.9967	0.9984
DP/l ($g/cm^2.s^2$)	**4360.7**	**4119.5**	**3754.5**	**3422.1**	**4438.9**
slope (Q vs DP/l) ($cm^5.s/g$)	**3.5161E-05**				
R^2	0.9907				
K^{imb} (Darcy)	**292.86**				

Table 2.20: Advancing interface permeability measurements (with Toluene) for OM-1 Model

Time (s)	Trial 1 Interface Position (cm)	X^2 (cm^2)	Time (s)	Trial 2 Interface Position (cm)	X^2 (cm^2)	Time (s)	Trial 3 Interface Position (cm)	X^2 (cm^2)
15	8.6	73.96	15	8.3	68.89	15	9.1	82.81
20	9.4	88.36	20	9.1	82.81	20	9.8	96.04
25	10.3	106.09	25	10.0	100.00	25	10.5	110.25
30	11.1	123.21	30	10.8	116.64	30	11.1	123.21
35	11.9	141.61	35	11.6	134.56	35	11.8	139.24
40	12.4	153.76	40	12.3	151.29	40	12.6	158.76
45	13.1	171.61	45	13.4	179.56	45	13.2	174.24
50	13.8	190.44	50	14.1	198.81	50	14.3	204.49
55	14.7	216.09	55	14.8	219.04	55	15.1	228.01
60	15.5	240.25	60	15.7	246.49	60	15.8	249.64
65	16.7	278.89	65	16.4	268.96	65	16.5	272.25
70	17.5	306.25	70	17.3	299.29	70	17.3	299.29
75	18.2	331.24	75	18.0	324.00	75	18.2	331.24
80	18.7	349.69	80	18.7	349.69	80	19.1	364.81
85	19.3	372.49	85	19.5	380.25	85	19.8	392.04
90	20.0	400.00	90	20.4	416.16	90	20.6	424.36
95	20.6	424.36	95	20.9	436.81	95	21.1	445.21
100	21.1	445.21	100	21.6	466.56	100	21.8	475.24
105	21.7	470.89	105	22.1	488.41	105	22.5	506.25
110	22.2	492.84	110	22.6	510.76	110	22.9	524.41
115	22.8	519.84	115	23.3	542.89	115	23.6	556.96
120	23.3	542.89	120	23.7	561.69	120	24.1	580.81
125	23.8	566.44	125	24.0	576.00	125	24.7	610.09
130	24.4	595.36	130	24.4	595.36	130	25.2	635.04
135	25.0	625.00	135	24.9	620.01	135	25.8	665.64
140	25.4	645.16	140	25.5	650.25	140	26.3	691.69
145	25.9	670.81	145	26.2	686.44	145	26.8	718.24
150	26.3	691.69	150	26.7	712.89	150	27.4	750.76
155	26.7	712.89	155	27.3	745.29	155	27.9	778.41
slope (cm^2/s)		**4.9152**			**5.0873**			**5.4701**
R^2		**0.9990**			**0.9983**			**0.9993**
K (Darcy)		**74.18**			**76.77**			**82.55**

K_{avg} (D)	**77.83**
Statistical Analysis for K_{avg} (D)	77.83 ± 4.85

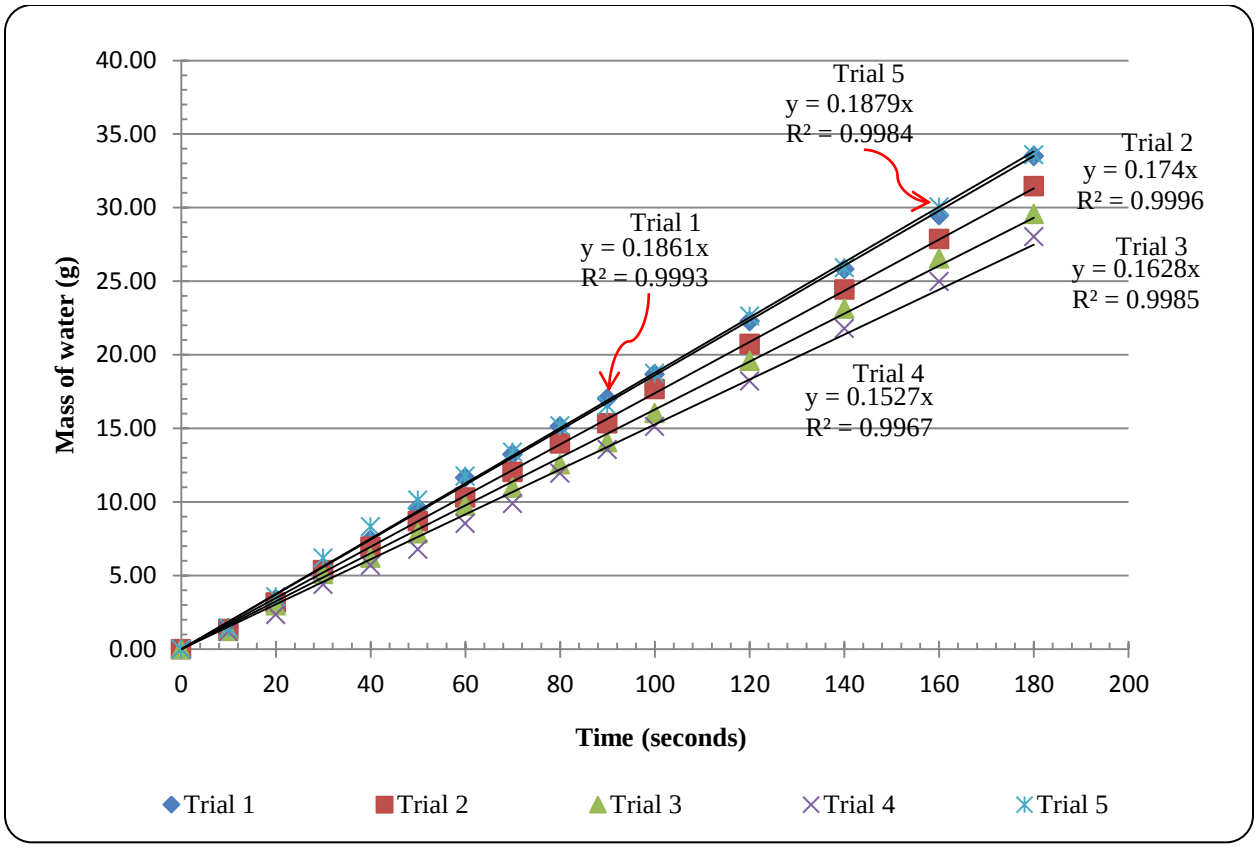

Figure 2.31: Constant water head permeability measurement for OM-1 glass micromodel

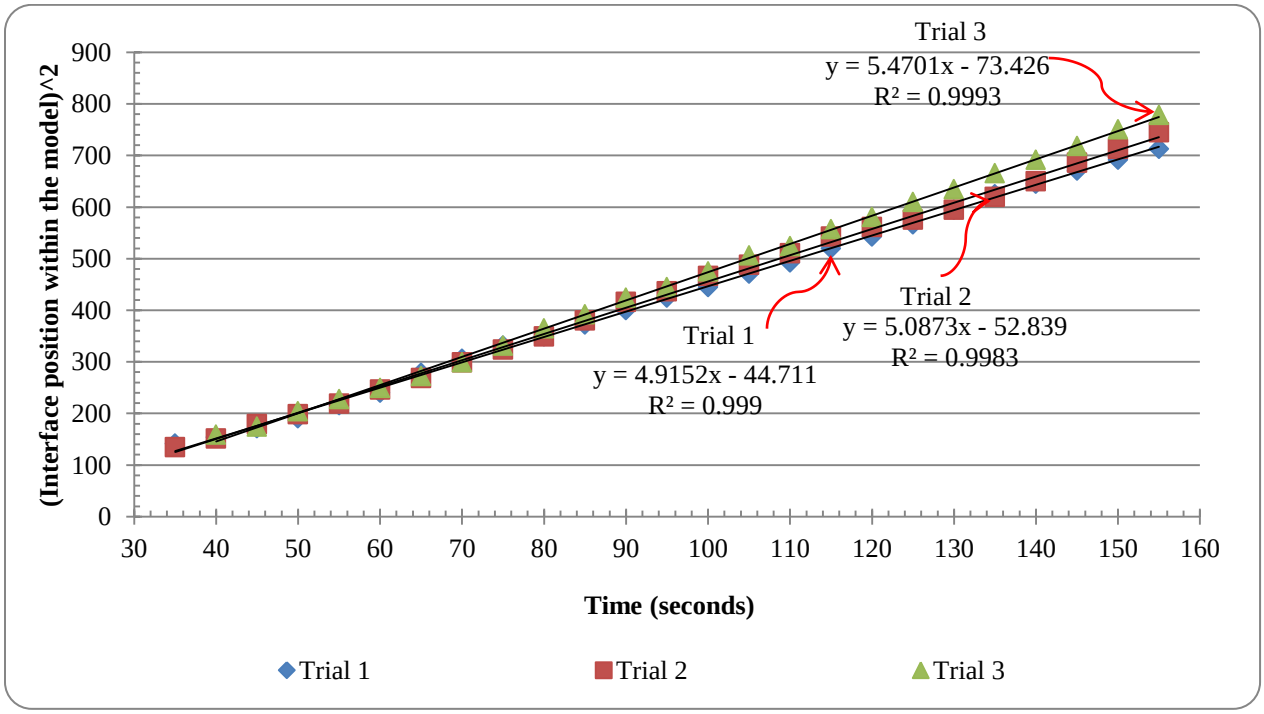

Figure 2.32: Advancing interface permeability measurements with toluene for OM-1 MM

In Table 2.21, the details of the pore-scale dimensions of OM-2 glass micromodel are presented, along with the formulation by which these pore-scale dimensions could be calculated (i.e. left column of the Table) based on the schematic pore-scale pattern of this model that is shown in Figure 2.33. Table 2.22 contains the details of the imbibition and drainage tests performed using both water and toluene in order to calculate the depth of etching of OM-2 glass micromodel. In Tables 2.23 and 2.24, the data obtained during permeability measurements of OM-2 micromodel using constant water head as well as advancing toluene interface permeability measurement methods are presented respectively. In addition, Figures 2.34 and 2.35 show the plots used in order to calculate OM-2 micromodel permeability using the two noted experimental techniques.

Table 2.21: OM-2 model dimensions

Model Dimensions	
Pore Dimensions (mm)	
(1) Pore to Pore (3) + (4b)	2.00
(2a) Pore Body	1.63
(2b) Pore Body (1) - (7)	2.00
(3) Pore Throat Width	0.30
(4b) Particle Size	1.68
(4a) Particle Size	1.20
(5) Diffusion Distance 0.5*(4) + (3)	1.15
(6) Flow Path 0.25*(2πr) + (7) 0.5*π*(5) + (7)	1.81
(7) Pore Throat Length	0.00
Macroscopic Dimensions	
Length (mm)	301
Length (# pores)	150
Width (mm)	101
Width (# pores)	50

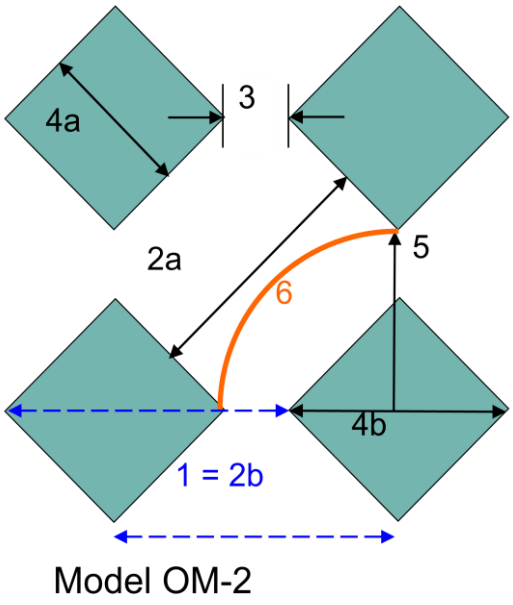

Figure 2.33: Schematic pore-scale pattern of OM-2 glass micromodel

Table 2.22: Capillary heights for model OM-2							**Average Values**		
Horizontal Distance from Left edge (cm)	**Water Imbibition h_c^{imb} (cm)**	**Water Drainage h_c^{dr} (cm)**	**Toluene Imbibition, h_c^{imb} (cm)**		**Water Imbibition h_c^{imb} (cm)**	**Water Drainage h_c^{dr} (cm)**	**Water Imbibition**	**Water Drainage**	**Toluene Imbibition**
			Ref Height = 71.8 cm	**Ref Height = 82.4 cm**					
0	6.2	15.9	5.2	5.1	6.5	15.5			
1	6.4	16.3	5.3	5.2	6.7	15.8			
2	6.7	16.6	5.5	5.5	6.7	16.2			
3	6.8	16.9	5.6	5.7	7.0	16.5			
4	7.1	17.2	5.8	5.9	7.4	16.8			
5	7.2	17.5	6.0	6.3	7.5	17.3			
6	7.5	17.7	6.2	6.6	7.9	17.4			
7	7.8	18.0	6.3	6.8	8.2	17.9			
8	8.1	18.8	6.6	7.3	8.2	18.5			
9	8.4	19.5	6.9	7.4	8.5	18.7			
10	8.6	19.8	7.3	7.5	8.7	19.4			
h_c^{avg} (cm)	7.35	17.65	6.06	6.30	7.57	17.27	**7.46**	**17.46**	**6.18**
Statistical Analysis for h_c^{avg} (cm)	7.35 ± 0.48	17.65 ± 0.75	6.06 ± 0.40	6.30 ± 0.52	7.57 ± 0.46	17.27 ± 0.74	7.46 ± 0.22	17.46 ± 0.37	6.18 ± 0.23
r_{eq}^{ave} (cm)	0.01782	0.00832	0.01095	0.01054	0.01729	0.00851	**0.01756**	**0.00841**	**0.01074**
Statistical Analysis for r_{eq}^{ave} (cm)							0.01756 ± 0.00052	0.00841 ± 0.00018	0.01074 ± 0.00040
d_{etch}^{ave} (cm)	0.02001	0.01147	0.01174	0.01127	0.01934	0.01183	**0.01968**	**0.01165**	**0.01150**
Statistical Analysis for δ_{etch}^{ave} (cm)							0.01968 ± 0.00066	0.01165 ± 0.00035	0.01150 ± 0.00046
A_x^{ave} (cm^2)	0.202	0.116	0.119	0.114	0.195	0.119	**0.199**	**0.118**	**0.116**
Statistical Analysis for A_x^{ave} (cm^2)							0.199 ± 0.007	0.118 ± 0.003	0.116 ± 0.005
P_c (g/cm s^2)			5145.4	5346.0					**5245.7**
Statistical Analysis for P_c (g/cm s^2)									5245.7 ± 196.6

Table 2.23: Constant water head permeability measurements for OM-2 MM

	Trial 1	Trial 2	Trial 3	Trial 4	Trial 5
Water Head (cm)	**131.3**	**124.5**	**111.6**	**107**	**137.2**
Head Loss (mm)	**2**	**2**	**2.2**	**2.3**	**2.5**
Time (s)	**Mass (g)**	**Mass (g)**	**Mass (g)**	**Mass (g)**	**Mass (g)**
0	0.00	0.00	0.00	0.00	0.00
10	1.62	1.42	1.35	1.22	1.94
20	3.95	3.54	2.83	2.39	4.15
30	5.87	5.69	4.69	4.23	6.67
40	7.83	7.57	6.03	5.75	8.68
50	10.31	9.19	7.47	6.89	11.27
60	12.57	11.25	9.28	8.64	13.11
70	14.27	12.88	11.03	9.96	15.23
80	16.21	14.83	12.24	12.06	17.17
90	18.15	16.87	14.24	13.84	19.52
100	20.05	19.15	15.45	15.46	21.85
120	23.57	22.28	18.66	18.59	26.05
140	27.18	26.12	22.49	21.82	29.67
160	31.54	29.74	25.15	25.00	33.13
180	35.88	33.82	28.48	28.23	38.22
Q (cm^3/s)	**0.1987**	**0.1869**	**0.1571**	**0.1540**	**0.2133**
R^2	0.9990	0.9996	0.9992	0.9971	0.9988
DP/l ($g/cm^2.s^2$)	**4279.2**	**4057.6**	**3637.2**	**3487.3**	**4471.5**
slope (Q vs DP/l) ($cm^5.s/g$)	**6.1806E-05**				
R^2	0.9914				
K^{imb} (Darcy)	**310.97**				

Table 2.24: Advancing interface permeability measurements (with Toluene) for OM-2 micromodel

Trial 1			Trial 2			Trial 3		
Time (s)	**Interface Position (cm)**	**X^2 (cm^2)**	**Time (s)**	**Interface Position (cm)**	**X^2 (cm^2)**	**Time (s)**	**Interface Position (cm)**	**X^2 (cm^2)**
15	7.5	56.25	15	7.6	57.76	15	7.2	51.84
20	8.7	75.69	20	8.7	75.69	20	8.4	70.56
25	9.9	98.01	25	9.7	94.09	25	9.3	86.49
30	11.2	125.44	30	10.8	116.64	30	10.6	112.36
35	12.3	151.29	35	11.6	134.56	35	11.5	132.25
40	12.9	166.41	40	12.5	156.25	40	12.2	148.84
45	13.7	187.69	45	13.5	182.25	45	13.4	179.56
50	14.4	207.36	50	14.3	204.49	50	14.1	198.81
55	15.4	237.16	55	15.3	234.09	55	15.1	228.01
60	16.2	262.44	60	16.1	259.21	60	15.9	252.81
65	16.9	285.61	65	16.7	278.89	65	16.5	272.25
70	17.6	309.76	70	17.3	299.29	70	17.0	289.00
75	18.4	338.56	75	18.2	331.24	75	17.8	316.84
80	19.2	368.64	80	18.9	357.21	80	18.5	342.25
85	19.8	392.04	85	19.7	388.09	85	19.4	376.36
90	20.5	420.25	90	20.3	412.09	90	20.0	400.00
95	21.1	445.21	95	21.0	441.00	95	20.7	428.49
100	21.8	475.24	100	21.7	470.89	100	21.4	457.96
105	22.5	506.25	105	22.3	497.29	105	21.9	479.61
110	23.2	538.24	110	23.1	533.61	110	22.4	501.76
115	23.6	556.96	115	23.6	556.96	115	22.7	515.29
120	24.3	590.49	120	24.3	590.49	120	23.2	538.24
125	24.9	620.01	125	24.8	615.04	125	23.8	566.44
130	25.4	645.16	130	25.3	640.09	130	24.4	595.36
135	25.9	670.81	135	25.9	670.81	135	25.0	625.00
140	26.4	696.96	140	26.4	696.96	140	25.5	650.25
145	26.9	723.61	145	26.9	723.61	145	26.2	686.44
150	27.3	745.29	150	27.4	750.76	150	26.7	712.89
155	27.8	772.84	155	27.9	778.41	155	27.3	745.29
slope (cm^2/s)		**5.2332**			**5.2863**			**4.9436**
R^2		**0.9983**			**0.9974**			**0.9980**
K (D)		**93.83**			**94.79**			**88.64**

K_{avg} (D)	**92.42**
Statistical Analysis for K_{avg} (D)	92.42 ± 3.74

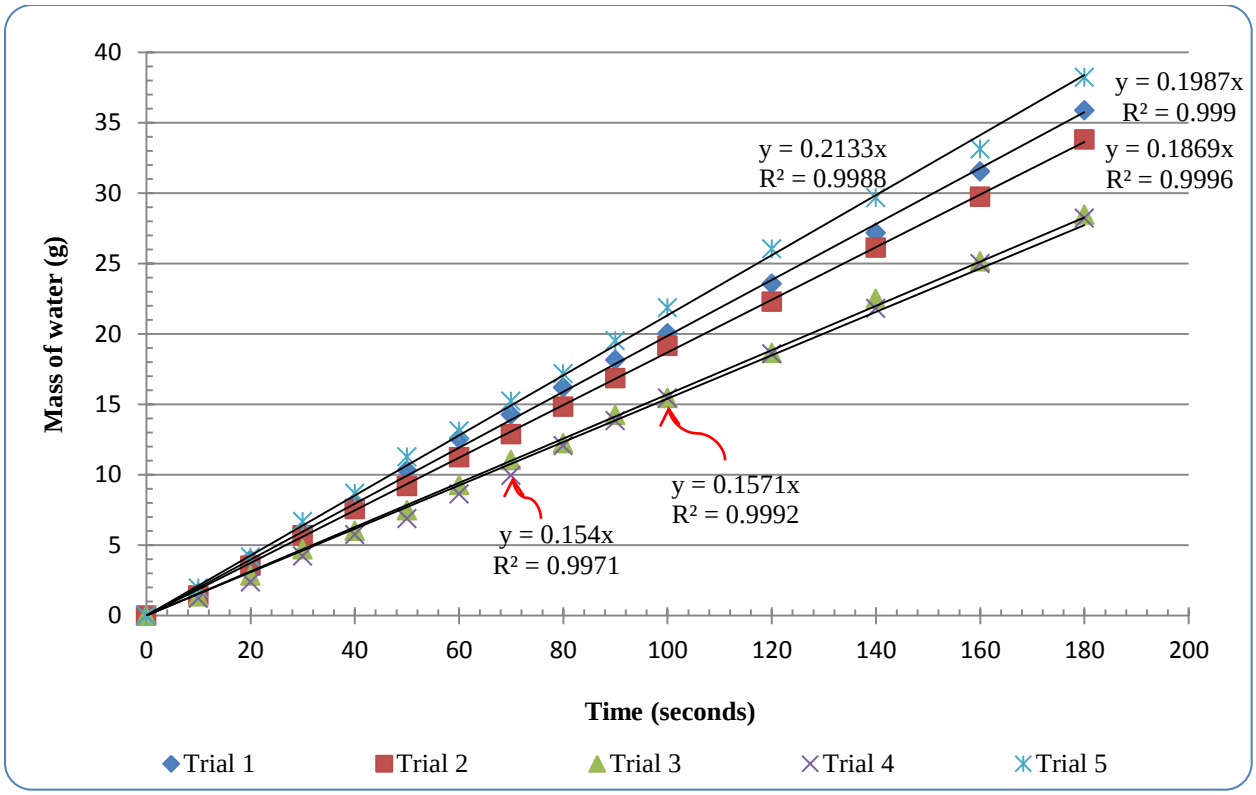

Figure 2.34: Constant water head permeability measurement for OM-2 glass micromodel

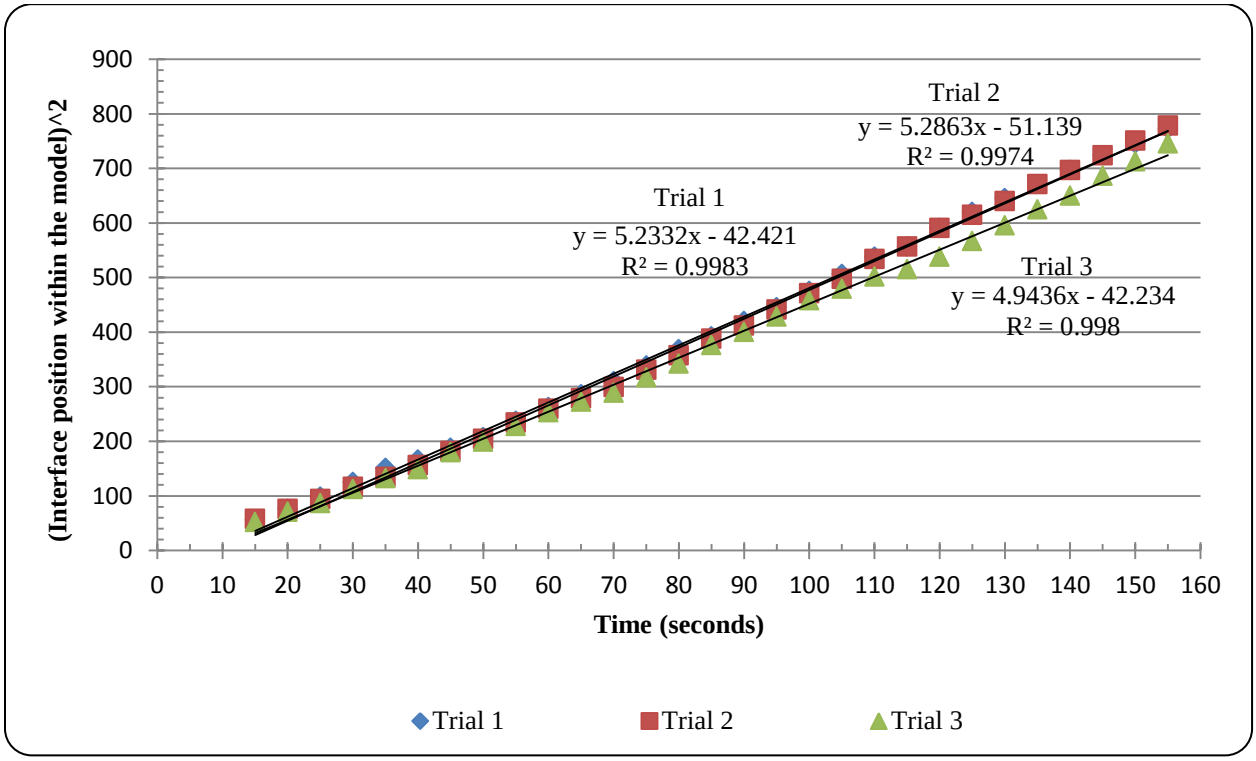

Figure 2.35: Advancing interface permeability measurements with toluene for OM-2 MM

2.5.2. Heat Loss Analysis of the SAGD Visualization Experiments at the Pore-Scale

A high-precision vacuum test rig, operating with two mechanical and diffusion pumps and capable of lowering the pressure down to 10^{-6} torrs was used in our pore-scale SAGD visualization tests in order to reduce the excessive heat loss from the micromodels to the surrounding environment. In this section, I am going to examine whether the use of this vacuum chamber was effective in reducing the overall heat loss of SAGD experiments in glass micromodels or not. The overall heat loss to the surrounding environment consists of two elements: heat loss by convection as well as heat loss by radiation. It is believed that the extremely low values of vacuum pressure enabled us to minimize the convective heat loss to the extent that it could be ignored compared to the radiation heat loss based on the experimental conditions. Secondly, a heat balance was carried out for all the employed micromodels based on the range of operational conditions examined in our visualization experiments. The overall heat balance for each glass micromodel under experimental conditions of each particular SAGD trial was used in order to calculate the energy requirements of the SAGD experiments. Continuous tracking of the SAGD interface at the pore-scale enabled us to determine the amount of steam (i.e. in terms of mass of Cold Water Equivalent, CWE) which is condensed as a result of heat loss at each particular stage of the process. Consequently, an average cumulative Steam to Oil Ratio (SOR) was calculated for each SAGD experiment which displays the amount of CWE consumed in order to produce the mobile oil during the process time.

2.5.2.1. Convective Heat Loss Prevention using Extremely-Low Vacuum Conditions

It is inevitable to experience heat losses to the surrounding environment during thermal recovery of heavy oil and bitumen. Heat loss increases the energy requirements of a thermal recovery method in the context of increased need to heat carrying agent (i.e. steam in the case of the SAGD process). It is believed that ignoring the heat losses occurred when the SAGD process is experimenting in the lab conditions could adversely affect the quantitative and qualitative results acquired due to the excessive steam condensation. During drainage of the mobile oil from an experimental model which is exposed to an active SAGD scheme, the overall heat loss increases with process time (i.e. the more oil is drained out of the model, the more depleted area is available for the heat loss). Therefore, it is intended to minimize the amount of overall heat loss

across the system boundaries with the aid of heat loss prevention techniques. One can utilize effective vacuum conditions in order to control heat losses to the environment. Use of an effective vacuum environment can significantly limit different heat transfer mechanisms. For instance, it is believed that a vacuum pressure of 0.01 torr or less is required for significant reduction of the heat loss through conduction mechanism (Roth 1990). Moreover, to establish an insulating vacuum jacket for minimizing the convective element of the heat transfer, it is required to achieve an extremely low vacuum pressure of about 1×10^{-6} torr (Guyer 1999).

There are two different approaches to study the properties of fluids as well as to treat their dynamics namely as continuum and statistical mechanics. Fluids are composed of molecules which collide with one another and solid objects. The continuity assumption considers fluids to be continuous. That is, properties such as density, pressure, temperature, and velocity are taken to be well-defined at infinitely small points, and are assumed to vary continuously from one point to another. However, the discrete, molecular nature of a fluid is ignored in the continuum mechanics. Those problems for which the continuity assumption does not give answers of desired accuracy are solved using statistical mechanics. In order to determine whether to use conventional fluid dynamics (a sub-discipline of continuum mechanics) or statistical mechanics, the Knudsen Number is evaluated for the system of problem at hand. Problems with Knudsen numbers at or above unity must be evaluated using statistical mechanics for reliable solutions as the mean free path of a molecule is comparable to a length scale of the problem, so the continuum assumption of fluid mechanics is no longer a good approximation for such a system (Gird, 1994).

The Knudsen number (Kn) is a dimensionless number defined as the ratio of the molecular mean free path length to a representative physical length scale, such as radius of a body in a fluid etc., according to the following equation:

$$Kn = \frac{\lambda}{L} \tag{2.19}$$

in which "λ" is the mean free path (L^1) and "L" is the representative physical length scale (L^1). Based on the numerical value of the Knudsen number, the fluid flow dynamics can be divided

into four regimes: continuum (Kn<0.01), slip ($0.01 \leq Kn < 0.1$), transitional ($0.1 \leq Kn < 10$), and free molecular ($Kn \geq 10$). If the mean free path of a molecule is comparable to a length scale of the problem, the continuum assumption of fluid mechanics is no longer a good approximation.

The effects of molecular structure are quite different in gases and liquids. The spacing between liquid molecules is approximately 10 times less that of the gases as liquids' density is about 1000 times of the gases'. As a result, the concept of mean free path is not defined for liquids as is defined for the gases. However, Bridgman (1923) suggested that the lattice spacing (δ) in liquids may be used as a measure similar to the mean free path in gases. In a liquid, lattice spacing is proportional to the liquid molar volume according to the following relationship:

$$\delta \propto \left(\frac{\bar{V}_1}{N_A}\right)^{1/3} \tag{2.20}$$

in which "$\bar{V}_1$" is the molar volume and "N_A" is the Avogadro's number. The lattice space for water is 0.3 nm as a reference for all the liquid phases.

In gas dynamics, however, the ratio of the molecular mean free path "λ" to some characteristic length "L" is a measure of the Knudsen number. The characteristic length chosen will depend on the problem under consideration. It may be, for example, the diameter of a pipe, or an object immersed in a flow, or the thickness of a boundary layer or a shock wave. In our system of a glass micromodel at the centre of an inverted-bell type of vacuum chamber, the characteristic length can be assumed to be the distance between the glass micromodel and the glass wall of the inverted-bell chamber. The magnitude of the Knudsen number determines the appropriate gas dynamic regime. When the Knudsen number is small compared to unity (i.e. in the order of Kn ≤ 0.1), the fluid can be treated as a continuous medium and described in terms of the macroscopic variables such as velocity, density, pressure, and temperature. In the transition flow regime, for Knudsen numbers of the order of unity or greater, a microscopic approach is required, wherein the trajectories of individual representative molecules are considered, and macroscopic variables are obtained from the statistical properties of their motions. In both internal and external flows, for Kn ≥ 10, intermolecular collisions in the region of interest are much less frequent than

molecular interactions with solid boundaries, and can be ignored. Flows under such conditions are termed collision-less or free molecular. In the range $0.1 \leq Kn \leq 1.0$, which is known as the slip flow regime, it is sometimes possible to obtain useful results by treating the gas as a continuum, but allowing for discontinuities in velocity and temperature at the solid boundaries (Gird, 1994).

In physics, the mean free path of a particle is the average distance covered by a particle between successive similar collisions with other moving particles such as elastic collisions of molecules in a gas phase. The concept of mean free path is met in all fields of science and is classified by the events which take place. This concept is useful the most in the systems which can be treated statistically, and is most frequently used in the theoretical interpretation of transport phenomena in gases and solids, such as diffusion, viscosity, heat conduction, and electrical conduction. Based on the kinetics theory, the mean free path could be calculated with the following relationship:

$$\lambda = \frac{k_B T}{\sqrt{2}\pi d^2 p} \tag{2.21}$$

in which "λ" is the mean free path of a particular particle, "d" is the effective hard shell diameter of the particles which depends on the type of gas and is typically in the range of $2\text{-}6\times10^{-10}$ m (Gird, 1994), "k_B" is the Boltzmann's constant ($k_B = 1.38066\times10^{-23}$J/K), and total gas pressure, "p", and temperature, "T", are expressed in Pa and K units respectively.

For an ideal gas, the gas number density (i.e. the number of molecules per unit volume of the ideal gas, "n") could be related to the gas inherent pressure and temperature, "p" and "T" respectively, according to the following equation:

$$n = \frac{p}{k_B T} \tag{2.22}$$

Combining equations 2.21 and 2.22 yields to:

$$\lambda = \frac{1}{\sqrt{2}\pi d^2 n} \tag{2.23}$$

Equation 2.23 can also be presented in terms of the Avogadro's number (N_A) and the Universal gas constant (R) as follows:

$$\lambda = \frac{RT}{\sqrt{2}\pi d^2 N_A p} \tag{2.24}$$

As a result, the following relations could be expressed to calculate the Knudsen number for an ideal gas:

$$\mathrm{Kn} = \frac{RT}{\sqrt{2}\pi d^2 N_A p L} = \frac{1}{\sqrt{2}\pi d^2 n L} \tag{2.25}$$

Considering the case of air molecules within the vacuum chamber in our pore-scale SAGD visualization experiments, their attributed mean free path increases as the number of air molecules decreases in a unit volume. This increase in the mean free path increases the Knudsen number; hence the continuum approach for predicting the thermal characteristics of air would not be applicable. The characteristic dimension of the problem in hand in our pore-scale SAGD visualization experiments is defined as the average distance of the micromodel from inner surface of the vacuum glass bell jar. If the mean free path of air molecules is in the order of this characteristic dimension of the system, the convective element of the heat transfer could be ignored. In other words, the convective heat transfer coefficient of the residual air phase within the vacuum chamber becomes insignificant.

Two optimistic and pessimistic scenarios are defined here based on the maximum and minimum possible values of the mean free path for the air molecules inside the vacuum chamber considering the range of operating parameters provided in Table 2.25. If the mean free path of the air molecules would like to be at maximum, the gas number density should be minimal. Minimum value of the gas number density could be attributed to operating the system at minimum pressure and maximum temperature. To obtain this most optimistic value for the mean

free path of the air molecules, the calculations are conducted considering the lower range of the reported gas molecular size. In contrast, one can calculate the most pessimistic value (i.e. smallest possible value) of the mean free path of the air molecules by maximizing the number density (i.e. at maximum operating vacuum pressure and minimum experienced temperature) and assuming the upper range of the reported hard shell diameter of the gas molecules.

Table 2.25: Range of operating parameters for the vacuuming procedure to control the excessive heat loss during our pore-scale SAGD experiments

Vacuum pressure inside the environmental chamber, torr	$5\times10^{-6} - 10^{-4}$
Air temperature within the vacuum chamber, °C	34 – 44
Hard sphere diameter of air molecule, m	$2\times10^{-10} - 6\times10^{-10}$
Estimated mean free path, m	0.1989 – 36.9616

Considering the calculated mean free path of the air molecules based on the operating conditions presented in Table 2.25, it is evident that even the most pessimistic estimate (i.e. smallest value) of the mean free path of the air molecules is greater than the distance between the micromodel and inner side of the glass bell jar of the vacuum chamber, which is in the order of 17-19cm. It is concluded that the convective element of heat loss from the micromodel to the surrounding environment can be ignored within the range of operating conditions of our visualization experiments. In other words, the employed heat loss prevention technique was successful in minimizing the overall heat loss of the SAGD visualization experiments.

2.5.2.2. Details of the Radiation Heat Loss Analysis

In this section, details of the heat loss analysis of our SAGD visualization experiments are presented based on the concept of radiation heat loss from a hot surface to the surrounding environment. This analysis was used in order to estimate the additional injection flux of water required to take care of the radiation heat loss during the design stage of our SAGD visualization experiment. The problem statement is how to calculate the radiation heat loss from a hot inner surface enclosed in a much colder outer surface. The simplest example of an enclosure is one

involving two surfaces that exchange radiation only with each other. Such a two-surface enclosure is shown schematically in Figure 2.36.

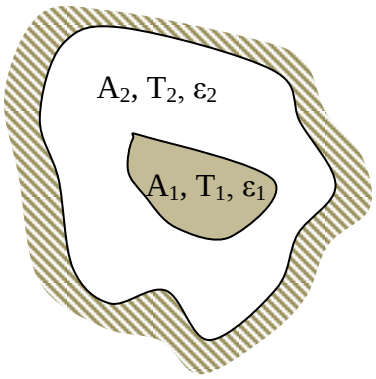

Figure 2.36: The two-surface enclosure

Since there are only two surfaces, the net rate of radiation transfer from surface 1, q_1, must be equal to the net rate of radiation transfer to surface 2, q_2. The total radiation heat transfer between these two surfaces can be written in terms of the total resistance to radiation exchange between surfaces 1 and 2 which is comprised of the two surface resistances and the geometrical resistance. The net radiation exchange between surfaces could be expressed as (Incropera F.P. and DeWitt D.P., 2002):

$$q_{12}|_{radiation} = \left(\frac{1-\varepsilon_1}{\varepsilon_1} + \frac{A_1+A_2-2A_1F_{12}}{A_2-A_1(F_{12})^2} + \left(\frac{1-\varepsilon_2}{\varepsilon_2}\right)\frac{A_1}{A_2}\right)^{-1} A_1\sigma(T_1^4 - T_2^4) \qquad (2.26)$$

in which "q_{12}" is the net radiation exchange between the two surfaces, "T_1" and "T_2" are the temperature of surfaces 1 and 2, "σ" is the Stefan-Boltzmann constant, "ε_1" and "ε_2" are the emissivity of surfaces 1 and 2, "A_1" and "A_2" are the surface areas of surfaces 1 and 2, and "F_{12}" is the view factor.

A reasonable approximation of the state of our glass micromodels inside an outer inverted glass bell jar could be presented in the form of a small convex object in a large cavity. This enclosure of special diffuse gray surfaces is presented as one specific radiation mode by Incropera and

DeWitt (2002) and was formulated considering a series of assumptions. For instance, the area of the hot surface is considered to be negligible compared to that of the surrounding environment, hence $\frac{A_1}{A_2} \cong 0$. In addition, as the single hot spot is fully surrounded by the large cavity, the View Factor, F_{12}, could be considered as unity. Subsequently, the net radiation heat loss between the hot and cold surfaces under these circumstances would be expressed as:

$$q_{12}|_{radiation} = \sigma A_1 \epsilon_1 (T_1^4 - T_2^4) \tag{2.27}$$

The total area subject to the radiation heat loss would be twice the overall model area (and not the porous pattern area) as the glass conductivity makes the whole model at the steady state temperature during each SAGD trial. The calculated heat loss is based on the exposure of 100% emptied model, filled with the steam phase either at the saturation or superheated temperature, to the surrounding environment (i.e. vacuumed area). This heat loss is equivalent to the case of 100% recovery of initial oil in place. It is evident that during each experimental trial, the amount of radiation heat loss would be proportional to the invaded area of the model filled with the steam phase at each particular depletion stage.

Total emissive power of a black body can be calculated by the following relationship:

$$E_b = \sigma T^4 \tag{2.28}$$

in which "T" is the absolute temperature of the body. The emissivity could be defined as the spectral, directional emissivity in the form of $\epsilon_{\lambda,\theta}(\lambda, \theta, \phi, T)$ at the surface temperature of "T". It is the ratio of the intensity of the radiation emitted at the wavelength "λ" and in the direction of "θ" and "ϕ" to the intensity of the radiation emitted by a black body at the same values of "T" and "λ" according to the following relationship:

$$\epsilon_{\lambda,\theta}(\lambda, \theta, \phi, T) = \frac{I_{\lambda,e\,(\lambda,\theta,\phi,T)}}{I_{\lambda,b\,(\lambda,T)}} \tag{2.29}$$

As a result, the total hemispherical emissivity could be defined as the ratio of the total emissive power at temperature "T" to the total emissive power of a black body:

$$\varepsilon(T) = \frac{E(T)}{E_b(T)} \tag{2.30}$$

in which "E(T)" is the heat flux (i.e. emissive power) in kW/m^2. Some sample values of the emissivity coefficient would be 0.90-0.95 for glass window and 0.82 for Pyrex at 300K surface temperature, and 0.06, 0.06, and 0.07 for bright aluminum foil at 100, 200, and 300K respectively.

In order to calculate the total radiation heat loss from the hot surface of the glass micromodel to the colder surface of the glass bell jar of the vacuum chamber, two optimistic and pessimistic scenarios are defined based on the operating conditions of our pore-scale SAGD visualization experiments. The pessimistic radiation heat loss is calculated based on maximizing the total heat loss considering the range of operating conditions, assuming that the entire glass micromodel is filled with steam phase at its maximum experienced steady state superheating temperature, the glass jar temperature is at its minimum value, and maximum emissivity coefficient for the glass surface would be considered. On the other hand, the minimum probable amount of the radiation heat loss (i.e. the optimistic value) can be calculated based on the prevailing operating conditions of our pore-scale visualization experiments of the SAGD process, assuming that the glass micromodel is thoroughly filled with saturated steam phase, the glass bell jar temperature is at the maximum experienced value, and the emissivity coefficient for the glass surface would be the minimum amount based on the values proposed in the open literature. Table 2.26 contains a summary of the calculation steps for all the micromodels used in our pore-scale SAGD visualization experiments.

Table 2.26: Radiation heat loss calculations for the employed glass micromodels in our SAGD visualization experiments					
Constants					
Stefan–Boltzmann constant (σ), $\frac{W}{m^2K^4}$				5.670×10^{-8}	
Emissivity of glass micromodel surface (ϵ_1) at 300K				0.90 – 0.95	
Glass Micromodels	*OC-1*	*DC-1*	*DL-1*	*OM-1*	*OM-2*
Temperature range of the micromodel surface, °C	65 – 128	58 – 116	62 – 118	66 – 116	61 – 114
Temperature range of the glass bell jar of the vacuum chamber, °C	32 – 56	29 – 54	32 – 58	34 – 57	31 – 55
Model length, cm	35.00	35.00	35.10	35.60	35.60
Model width, cm	12.10	16.00	12.00	12.80	12.80
Surface area (A_1), cm^2	423.50	560.00	421.20	455.68	455.68
Total surface area = $2*A_1$	847.00	1120	842.40	911.36	911.36
Pessimistic radiation heat loss, W	78.587	88.072	66.874	68.889	68.275
Optimistic radiation heat loss, W	33.067	45.341	31.650	34.914	36.240

2.5.2.3. Details of the Overall Heat and Mass Balance

Considering the calculations presented in section 2.5.2.2, one can write the overall simultaneous heat and mass balance for the micromodel system to figure out how much volume of the water condensate during each particular run is originated only by means of the radiation heat loss, and how much volume of the produced water condensate can be considered as the true cold water equivalent of the consumed steam (i.e. SOR, in terms of its Cold Water Equivalent, CWE) required for the in-situ oil mobilization. Hence, the energy intensity of each particular SAGD trial based on the steam requirements for each unit volume of the produced oil can be calculated.

Unfortunately, the produced volume of the mobile oil phase could not be measured quantitatively because of the fact that the overall pore volume of each employed glass micromodel is extremely small; hence measuring the very small volume of the produced oil was not practical considering available measuring devices. However, the calculations presented in this section could be used in order to figure out the total amount of the produced water condensate originated only from the excessive heat loss. This volume should be subtracted from the total injected volume of water to

calculate the cold water equivalent of the actual steam to oil ratio for each particular SAGD trial. Continuous tracking of the apparent pore-scale SAGD interface helped to determine the ratio of the invaded area to the total area at each particular time step during the process time. This enables us to calculate the cumulative water condensate produced due to the heat loss up until each particular drainage stage. Based on this procedure, the cumulative water condensate produced as a result of heat loss at the end of each trial was also calculated. Deducting this volume of the produced water condensate from the total water condensate collected at the end of each experiment determines the amount of steam used, in terms of CWE injected, in order to mobilize the in-situ bitumen to the extent of achieving ultimate recovery factor values reported at the end of each particular SAGD trial.

In the absence of the convective element of the heat loss, one can write the overall heat balance for a system whose schematic flow chart diagram is presented in Figure 2.37 with focus on the inlet and outlet mass and heat streams.

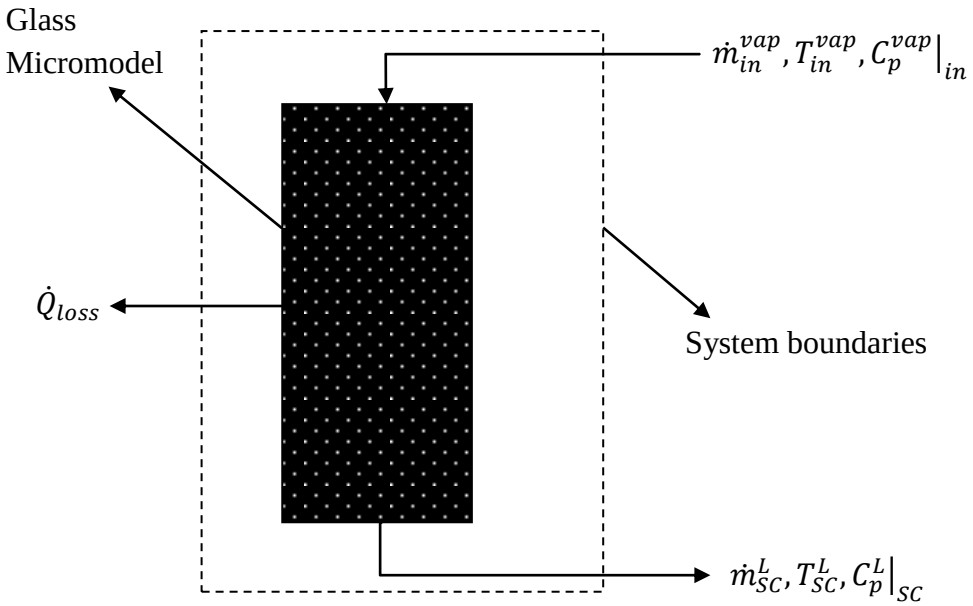

Figure 2.37: Schematic flow diagram of a particular glass micromodel for the purpose of heat balance in our pore-scale SAGD visualization experiments

One can write the enthalpy balance for the entire system considering the inlet and outlet streams and conservation of enthalpy within the system boundaries as:

$$H_{in} - H_{out} = \dot{Q}_{loss} \tag{2.31}$$

in which $\dot{Q}_{Loss}$ is the total heat loss from the model to the surrounding environment in the form of radiation heat loss, and H_{in} and H_{out} are the input and output enthalpies.

The input and output enthalpies can be expanded using a reference state enthalpy, so Eq. 2.31 could be written in the expanded form of:

$$\dot{m}_{in}^{vap}\left(H_{in}^{vap} - H_{ref.}^{vap}\right) = \dot{m}_{SC}^{L}\left(H_{SC}^{L} - H_{ref.}^{vap}\right) + \dot{Q}_{loss} \tag{2.32}$$

in which H_{in}^{vap}, H_{SC}^{L}, and H_{ref}^{vap} are the enthalpies associated with the inlet vapour phase at the corresponding temperatures, sub-cooled liquid condensate phase, and an arbitrary reference-state vapour phase respectively. In addition, $\dot{m}_{in}^{vap}$ and $\dot{m}_{SC}^{L}$ are the mass flow rates of the inlet steam phase and that of the outlet sub-cooled water condensate phase respectively.

The mass balance over the system boundaries reveals that:

$$\dot{m}_{in}^{vap} = \dot{m}_{SC}^{L} = \dot{m} \tag{2.33}$$

in which the inlet vapour mass flow rate ($\dot{m}_{in}^{vap}$) would be considered in terms of the equivalent cold liquid injection rate of the inlet phase.

Substituting Eq (2.33) into Eq (2.32) with some simplifications cancels out the terms containing the reference vapour phase enthalpy from both sides of the equality, and leads to the following simple form of:

$$\dot{m}\left(H_{in}^{vap} - H_{SC}^{L}\right) = \dot{Q}_{loss} \tag{2.34}$$

Adding and subtracting a "H_{sat}^{vap}" into the LHS of Eq (2.34) results in:

$$\dot{m}\left(H_{in}^{vap} - H_{sat}^{vap}\right) + \dot{m}\left(H_{sat}^{vap} - H_{SC}^{L}\right) = \dot{Q}_{loss} \quad (2.35)$$

Considering the fact that $H_{sat}^{vap} = H_{sat}^{L} + \lambda$, Eq (2.35) leads to:

$$\dot{m}\left(H_{in}^{vap} - H_{sat}^{vap}\right) + \dot{m}\left(H_{sat}^{L} - H_{SC}^{L}\right) + \dot{m}\lambda = \dot{Q}_{loss} \quad (2.36)$$

in which λ is the enthalpy of condensation at the operating pressure condition and H_{sat}^{vap} is the enthalpy of the vapour phase at the saturation temperature corresponding to the overall operating pressure.

Expanding the enthalpy parameters in terms of specific heat capacities and temperatures converts Eq (2.36) into a more broadly used format of:

$$\dot{m}\left(C_p^{vap}\big|_{in} T_{in}^{vap} - C_p^{vap}\big|_{sat} T_{sat}^{vap}\right) + \dot{m}\left(C_p^{L}\big|_{sat} T_{sat}^{L} - C_p^{L}\big|_{SC} T_{SC}^{L}\right) + \dot{m}\lambda = \dot{Q}_{loss} \quad (2.37)$$

in which T_{in}^{vap}, T_{sat}^{vap}, T_{sat}^{L}, and T_{SC}^{L} are the superheated vapour temperature at the inlet side, saturated vapour temperature at the corresponding operating pressure, saturated liquid temperature at the corresponding operating pressure, and temperature of the sub-cooled liquid phase at the outlet side respectively. Moreover, the average specific heat capacity values of liquid and vapour phases are defined based on their associated stream temperatures.

In case if the rate of change of the specific heat versus temperature would be close to linear, the magnitude of the specific heat at the average temperature could be used instead according to the following relationship:

$$\dot{m}\, C_p^{vap}\big|_{\frac{T_{in}^{vap}+T_{sat}^{vap}}{2}} \left(T_{in}^{vap} - T_{sat}^{vap}\right) + \dot{m}\, C_p^{L}\big|_{\frac{T_{SC}^{L}+T_{sat}^{L}}{2}} \left(T_{sat}^{L} - T_{SC}^{L}\right) + \dot{m}\lambda\big|_{T_{sat}} = \dot{Q}_{loss} \quad (2.38)$$

Otherwise, one should calculate the area under the curve of the specific heat capacity versus temperature in case if "C_p" variation versus temperature could not be considered as linear:

$$\int_{T_{sat}^{vap}}^{T_{in}^{vap}} \dot{m}\, C_p^{vap} dT + \int_{T_{SC}^{L}}^{T_{sat}^{L}} \dot{m}\, C_p^{L} dT \; + \; \dot{m}\lambda|_{T_{sat}} = \dot{Q}_{loss} \tag{2.39}$$

With a quick look over the steam table, it is evident that the isobaric specific heat capacity of steam at the operating temperature range of our SAGD visualization experiments changes linearly with temperature which satisfies using Eq (2.38) as the governing equation to calculate the overall heat transfer of the process. This Eq is written below based on the fluids present in the SAGD flow system:

$$\dot{m}\, C_p^{s}\big|_{\frac{T_{in}^{S}+T_{sat}^{S}}{2}} (T_{in}^{s} - \; T_{sat}^{s}\,) + \dot{m}\, C_p^{w}\big|_{\frac{T_{SC}^{W}+T_{sat}^{W}}{2}} (T_{sat}^{W} - \; T_{SC}^{w}) + \; \dot{m}\lambda|_{T_{sat}} = \dot{Q}_{loss} \tag{2.40}$$

in which "T_{in}^{S}" is the superheated steam inlet temperature, "T_{sat}^{S}" is the steam saturation temperature at the corresponding operating pressure, "$C_p^{s}\big|_{\frac{T_{in}^{S}+T_{sat}^{S}}{2}}$" is the specific heat capacity of steam at a temperature equivalent to the average of superheated steam temperature at the inlet side and that of the saturated steam at the corresponding operating pressure, "$C_p^{w}\big|_{\frac{T_{SC}^{W}+T_{sat}^{W}}{2}}$" is the water condensate specific heat capacity at a temperature equivalent to the average of sub-cooled water temperature at the outlet side and that of the saturated water phase at the corresponding operating pressure, "T_{sat}^{W}" is the water phase saturation temperature at the corresponding operating pressure, and "T_{SC}^{w} " is the sub-cool temperature of the water condensate.

As a result, one could isolate the mass flux of water required to satisfy the radiation heat loss when the entire sides of the micromodel are exposed (i.e. the maximum possible radiation heat loss from the micromodel):

$$\dot{m} = \frac{\dot{Q}_{loss}}{\left\{ C_p^{s}\big|_{\frac{T_{in}^{S}+T_{sat}^{S}}{2}} (T_{in}^{s} - T_{sat}^{s}) + C_p^{w}\big|_{\frac{T_{SC}^{W}+T_{sat}^{W}}{2}} (T_{sat}^{W} - T_{SC}^{w}) + \lambda|_{T_{sat}} \right\}} \tag{2.41}$$

in which “s” denotes the steam phase and “w” represents the water phase.

Table 2.27 presents the parameters required to calculate the mass flux of water, which is needed to take care of the radiation heat loss when the entire surfaces of the micromodel are exposed to the vacuumed environment. At each set of the operating temperatures, the mass flux is calculated based on two slightly different Equations presented earlier (Eq’s 2.37 and 2.41). It is evident that the results obtained using these two equations are in very good agreement with each other. For each particular micromodel, range of the steam temperature was considered from the dry saturated steam temperature (100°C) to maximum experienced superheating temperature. Two different scenarios were defined in order to calculate the maximum and minimum required water mass influx to compensate the radiation heat loss for each particular glass micromodel. In an optimistic scenario, the minimum amount of water mass influx is calculated in such a way that the model is assumed to be working at the lowest possible operating temperature. However, a pessimistic scenario was defined to express the highest magnitude of the water influx required to compensate for the radiation heat loss if the superheated steam is injected into the model. All the heat loss experiments were carried out under atmospheric conditions of operating pressure.

2.5.3. Interface Advancement Velocity at the Pore-Scale: Experimental Results

In this section, results of the SAGD interface advancement velocity measurement at the pore-scale are presented and analyzed. In addition, the experimental results are cross checked with the analytical model proposed by Butler (1979, 1981). The rate of interface advancement is a representative of oil production or sweep efficiency at the micro-scale, hence it could be considered as the economic viability of the SAGD process for a particular porous medium. In order to determine the interface advancement velocity, the temporary position of the apparent SAGD interface (i.e. pore-scale interface between the oil-saturated pores and the steam-saturated ones) was tracked, and the interface advancement velocity was measured along the width of the micromodel in each particular SAGD experiment. The surface of each micromodel was divided into cell blocks using a marker to ease the interface position recognition and tracking within the porous network. This procedure was quite helpful especially in the case of our flow visualization experiments during which recording the pore-scale events through the thick glass wall of the vacuum chamber was obstructing the visibility.

Table 2.27: Heat loss analysis for the employed micromodels in the SAGD visualization experiments	
OC-1 Micromodel	
Steam temperature range, °C	100 to 128
Water condensate temperature range, °C	86 to 100
$\dot{m}\|_{pessimistic}$, g/min (from Eq 2.37)	1.997
$\dot{m}\|_{pessimistic}$, g/min (from Eq 2.41)	1.987
$\dot{m}\|_{optimistic}$, g/min (from Eq 2.37)	0.854
$\dot{m}\|_{optimistic}$, g/min (from Eq 2.41)	0.856
DC-1 Micromodel	
Steam temperature range, °C	100 to 116
Water condensate temperature range, °C	84 to 100
$\dot{m}\|_{pessimistic}$, g/min (from Eq 2.37)	2.246
$\dot{m}\|_{pessimistic}$, g/min (from Eq 2.41)	2.241
$\dot{m}\|_{optimistic}$, g/min (from Eq 2.37)	1.166
$\dot{m}\|_{optimistic}$, g/min (from Eq 2.41)	1.170
DL-1 Micromodel	
Steam temperature range, °C	100 to 118
Water condensate temperature range, °C	84.5 to 100
$\dot{m}\|_{pessimistic}$, g/min (from Eq 2.37)	1.705
$\dot{m}\|_{pessimistic}$, g/min (from Eq 2.41)	1.700
$\dot{m}\|_{optimistic}$, g/min (from Eq 2.37)	0.815
$\dot{m}\|_{optimistic}$, g/min (from Eq 2.41)	0.817
OM-1 Micromodel	
Steam temperature range, °C	100 to 116
Water condensate temperature range, °C	83.6 to 100
$\dot{m}\|_{pessimistic}$, g/min (from Eq 2.37)	1.755
$\dot{m}\|_{pessimistic}$, g/min (from Eq 2.41)	1.752
$\dot{m}\|_{optimistic}$, g/min (from Eq 2.37)	0.897
$\dot{m}\|_{optimistic}$, g/min (from Eq 2.41)	0.900

Table 2.27 (Cont.): Heat loss analysis for the employed micromodels in the SAGD visualization experiments	
OM-2 Micromodel	
Steam temperature range, °C	100 to 114
Water condensate temperature range, °C	83 to 100
$\dot{m}\|_{pessimistic}$, g/min (from Eq 2.37)	1.740
$\dot{m}\|_{pessimistic}$, g/min (from Eq 2.41)	1.737
$\dot{m}\|_{optimistic}$, g/min (from Eq 2.37)	0.931
$\dot{m}\|_{optimistic}$, g/min (from Eq 2.41)	0.933

A sample of the SAGD pore-scale interface advancement versus time for model DL-1 in one of our visualization experiments is presented in Figure 2.38. As it can be seen in this Figure, the temporary position of the SAGD interface seems uniform from a macroscopic perspective when the overall height of the porous pattern skeleton is considered; however, if one focuses on the position of the apparent pore-scale SAGD interface using the magnified views of the porous pattern containing a few pores in a picture frame, it is evident that the position of the SAGD interface can vary by several pores ahead or behind the position of the interface at the macro-scale. This is because of the fact that the mobile oil drains through a tortuous pathway at the pore-scale due to the immiscible nature of the displacement. At each particular elevation (i.e. within each cell block marked on the surface of the micromodel), the position of the interface was measured at each particular row of pores, and the average of these positions within each particular cell block was reported as the average temporary position of the interface at that particular time frame. Due to the unstable nature of the frontal advancement in the top portion of the models, the top 15-20 pores were neglected to look at when the interface advancement velocities were calculated.

As it was stated before, thermocouples were attached to the glass surface of the micromodels along the height of the porous pattern in order to provide a real-time temperature map during each particular SAGD experiment. For instance, in RUN No. 8 in which DL-1 Model was used (above Figure), 15 thermocouples were attached to the surface of the glass micromodel. The distribution of the surface thermocouples in this trial is schematically shown in Figure 2.39. The

real-time temperature data were collected using an automated data acquisition unit. The temperature data collected during one of our SAGD trials, whose interface advancement versus time was presented in successive snapshots of Figure 2.38, is shown in Figures 2.40.a to 2.40.o respectively. According to the thermocouple arrangement displayed in Figure 2.39, it is evident that thermocouples T1, T2, T3 and T4, which were located at the top row within the first 1-30 pores from the top of Model DL-1, as well as thermocouples T5, T9, T12 and T14, which were attached adjacent to the trough on the most right hand side column of the thermocouples, show the early development of the steam chamber by recording temperatures close to that of the developing steam chamber while other thermocouples show significantly lower local temperatures close to the initial temperature of the glass micromodel. Table 2.28 contains the collected temperature data for this particular SAGD experiment at the time intervals shown in Figure 2.38.

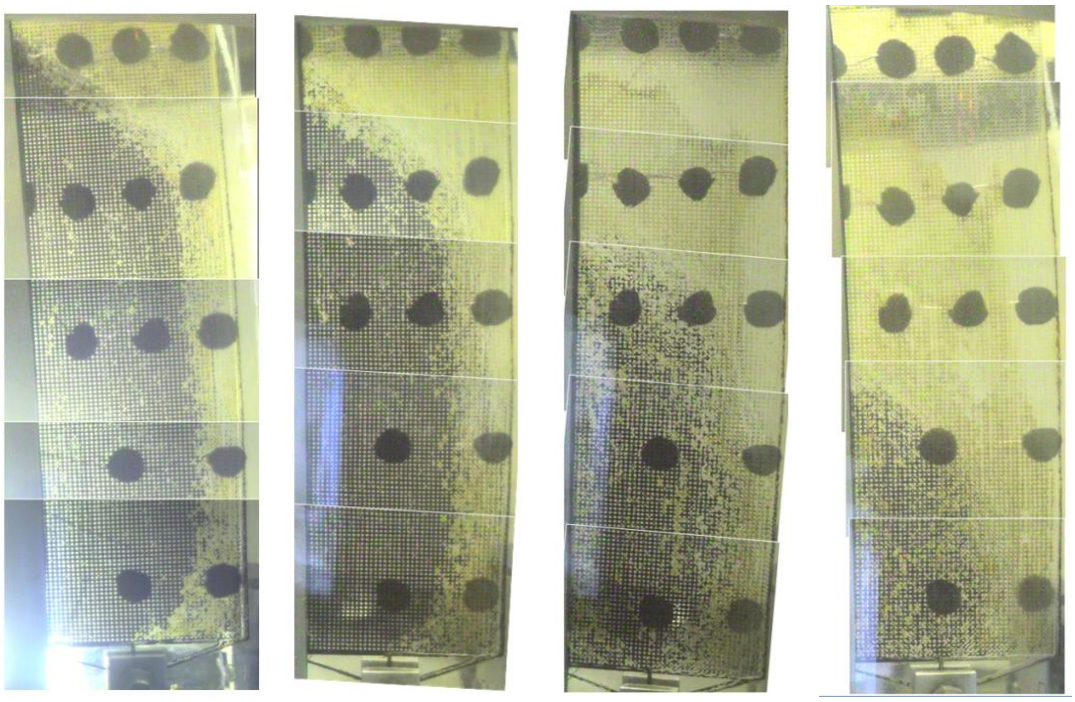

(a) 45 min **(b) 65 min** **(c) 90 min** **(d) 124 min**

Figure 2.38: SAGD interface advancement in RUN No. 8 (Model DL-1)

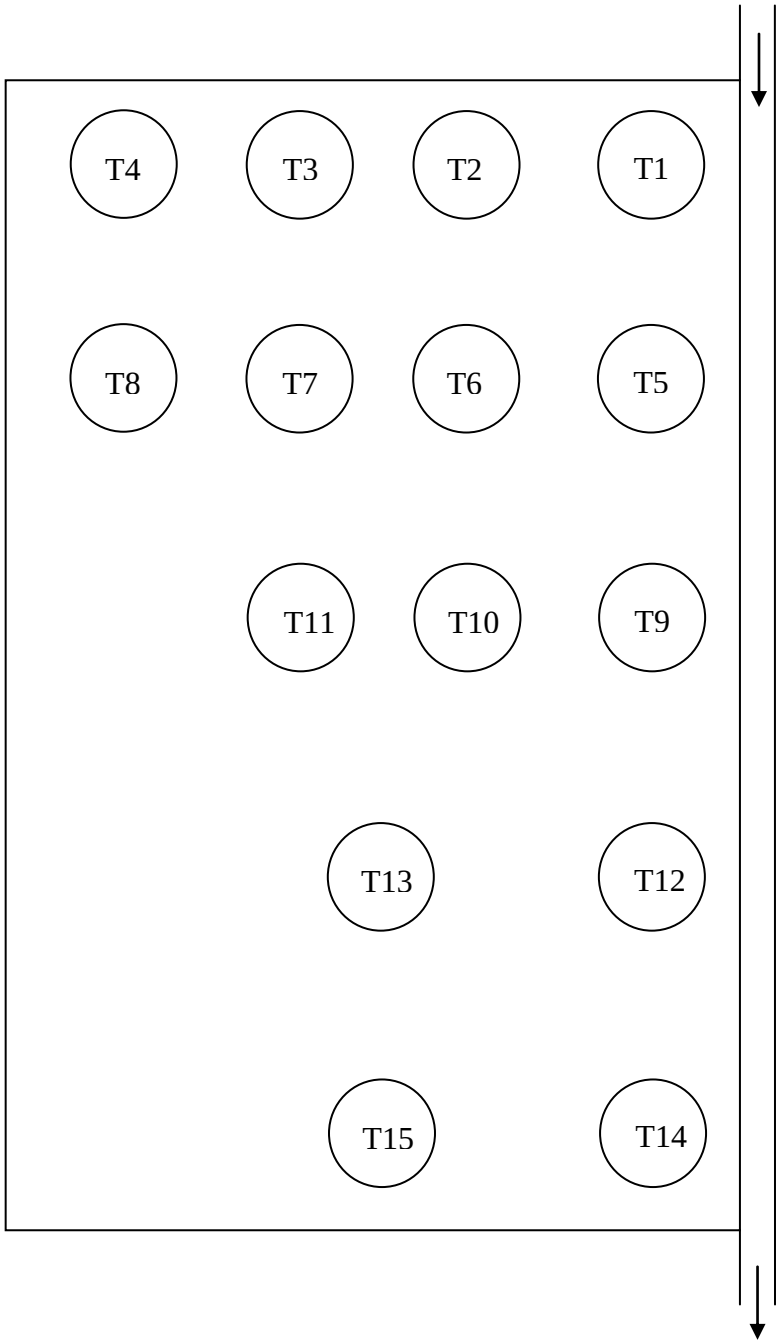

Figure 2.39: The distribution of surface thermocouples along the height of Model DL-1 in RUN No. 8 of the SAGD visualization experiments

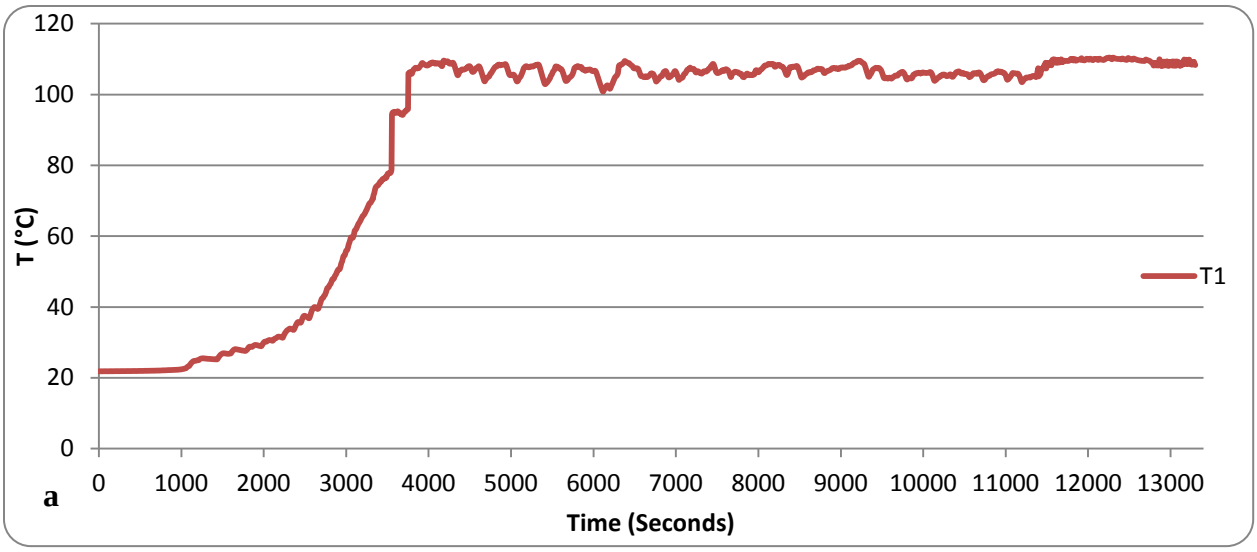
120
100
80
60
40
20
0
T (°C)
0 1000 2000 3000 4000 5000 6000 7000 8000 9000 10000 11000 12000 13000
Time (Seconds)
T1
a

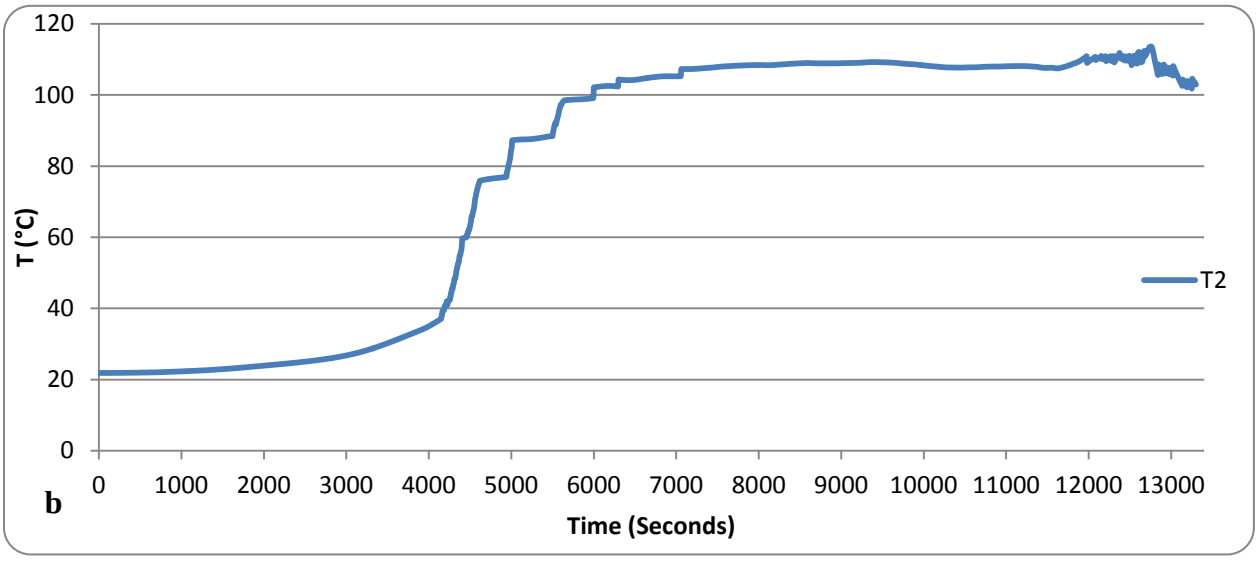
120
100
80
60
40
20
0
T (°C)
0 1000 2000 3000 4000 5000 6000 7000 8000 9000 10000 11000 12000 13000
Time (Seconds)
T2
b

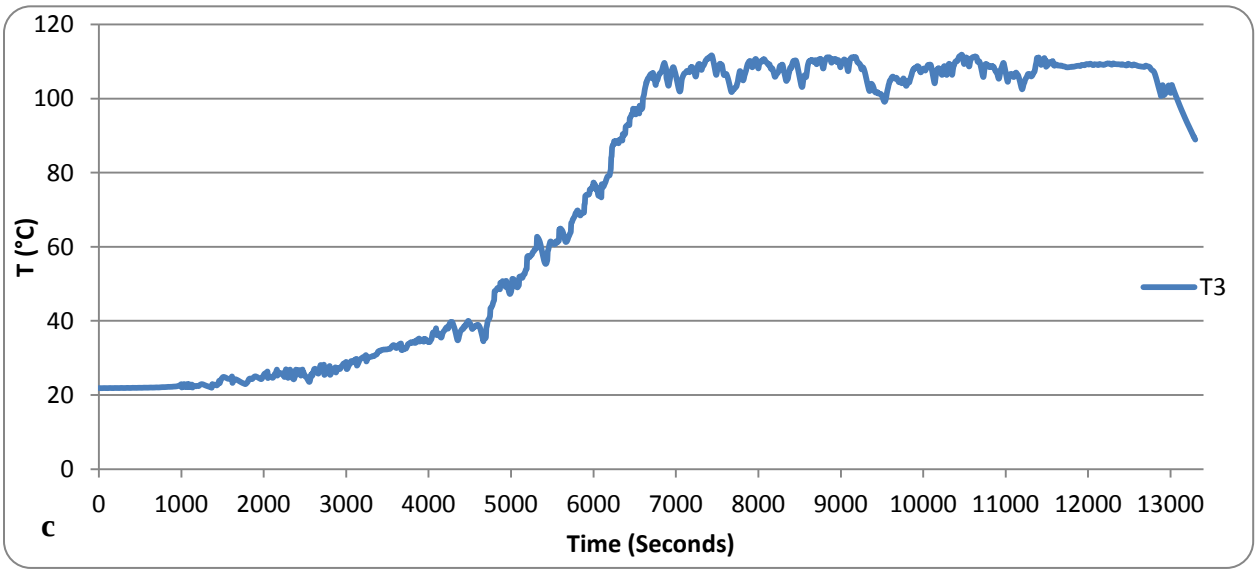
120
100
80
60
40
20
0
T (°C)
0 1000 2000 3000 4000 5000 6000 7000 8000 9000 10000 11000 12000 13000
Time (Seconds)
T3
c

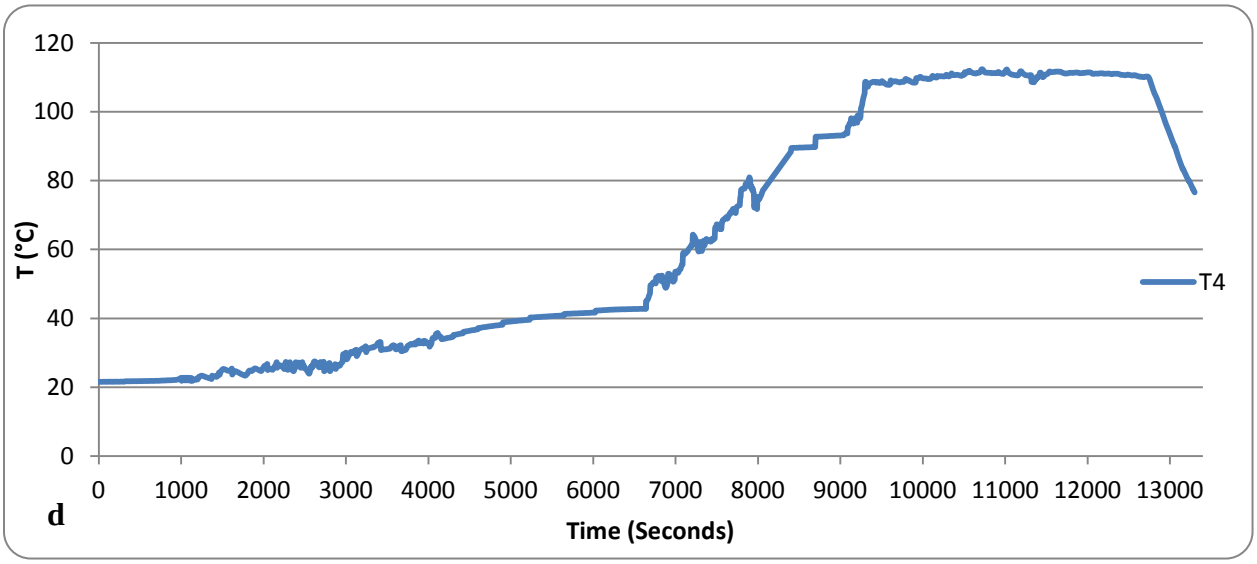
120
100
80
60
40
20
0
T (°C)
0 1000 2000 3000 4000 5000 6000 7000 8000 9000 10000 11000 12000 13000
Time (Seconds)
T4

d

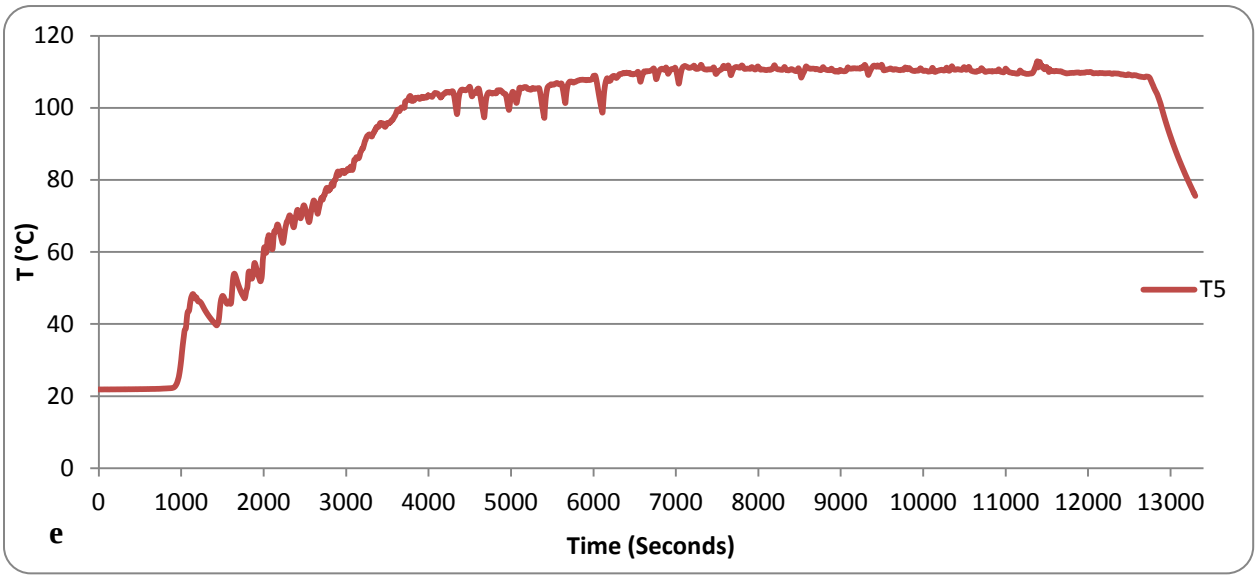
120
100
80
60
40
20
0
T (°C)
0 1000 2000 3000 4000 5000 6000 7000 8000 9000 10000 11000 12000 13000
Time (Seconds)
T5

e

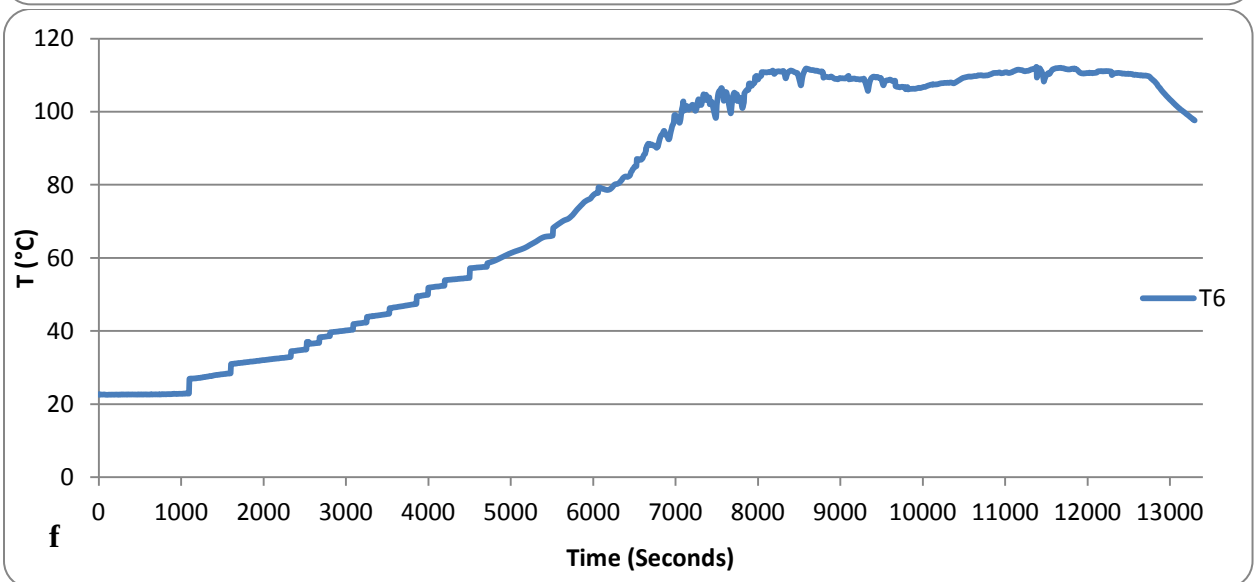
120
100
80
60
40
20
0
T (°C)
0 1000 2000 3000 4000 5000 6000 7000 8000 9000 10000 11000 12000 13000
Time (Seconds)
T6

f

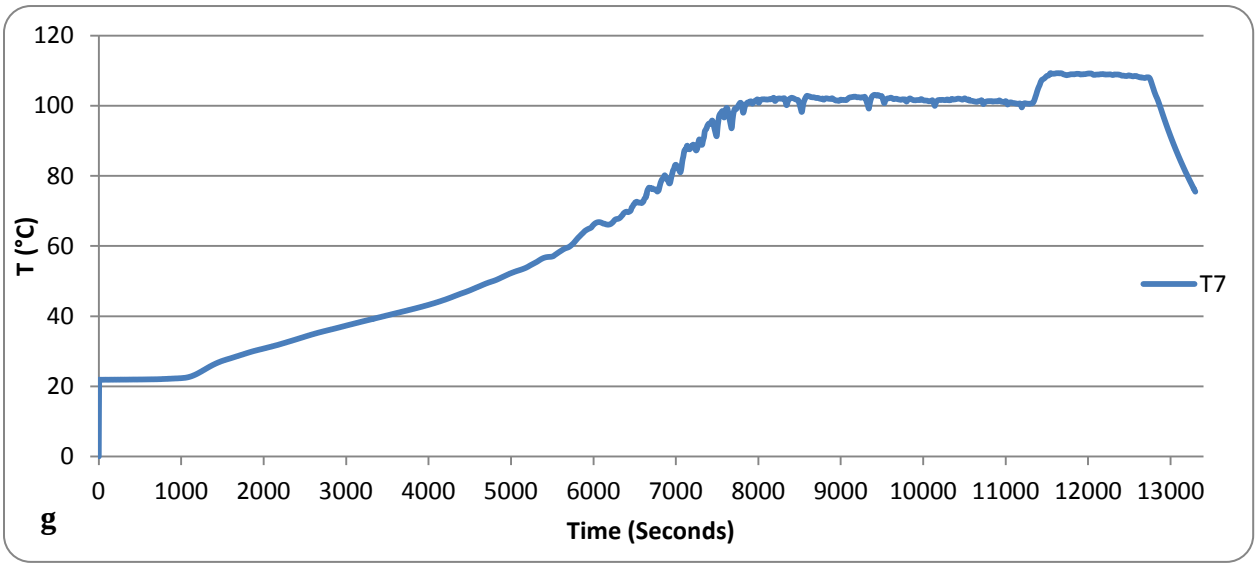
120
100
80
60
40
20
0
T (°C)
0 1000 2000 3000 4000 5000 6000 7000 8000 9000 10000 11000 12000 13000
Time (Seconds)
T7
g

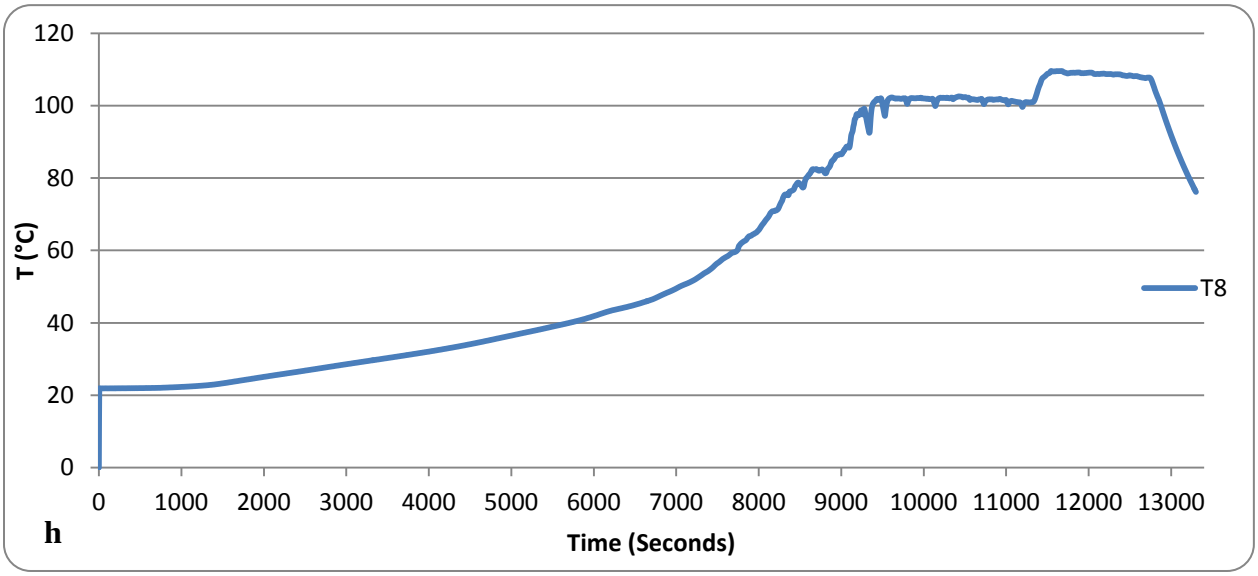
120
100
80
60
40
20
0
T (°C)
0 1000 2000 3000 4000 5000 6000 7000 8000 9000 10000 11000 12000 13000
Time (Seconds)
T8
h

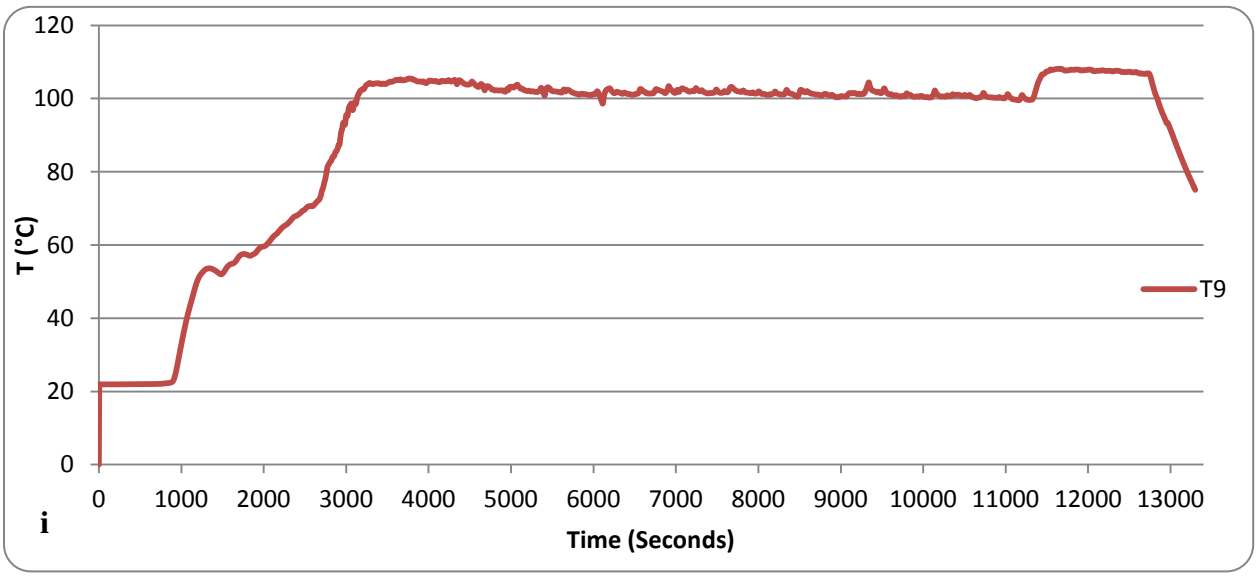
120
100
80
60
40
20
0
T (°C)
0 1000 2000 3000 4000 5000 6000 7000 8000 9000 10000 11000 12000 13000
Time (Seconds)
T9
i

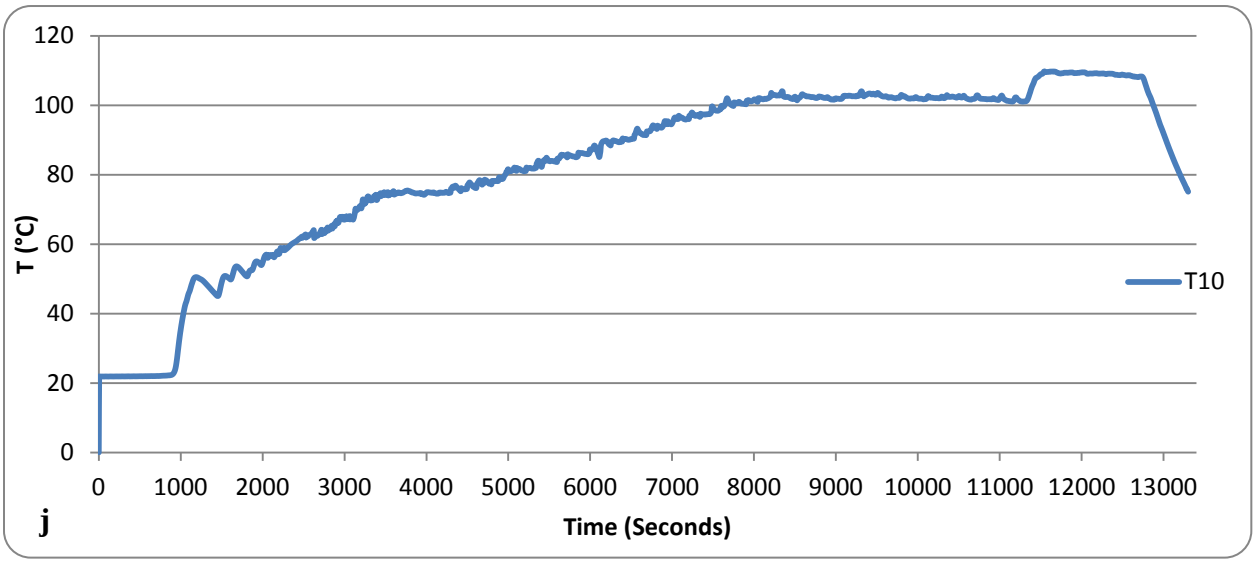
120
100
80
60
40
20
0
T (°C)
0
1000
2000
3000
4000
5000
6000
7000
8000
9000
10000
11000
12000
13000
Time (Seconds)
T10

j

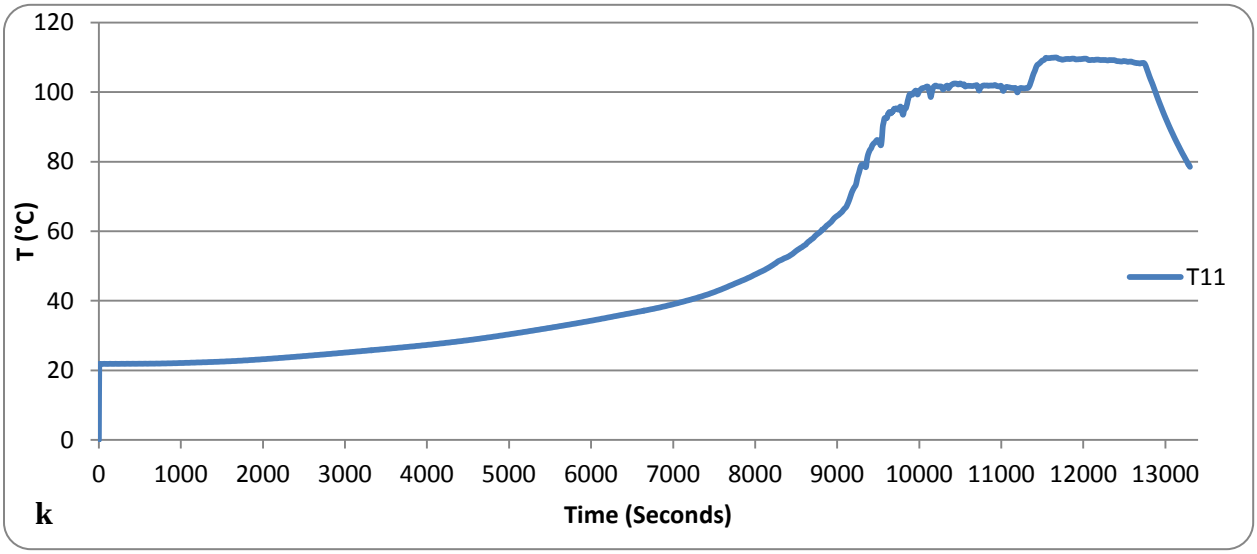
120
100
80
60
40
20
0
T (°C)
0
1000
2000
3000
4000
5000
6000
7000
8000
9000
10000
11000
12000
13000
Time (Seconds)
T11

k

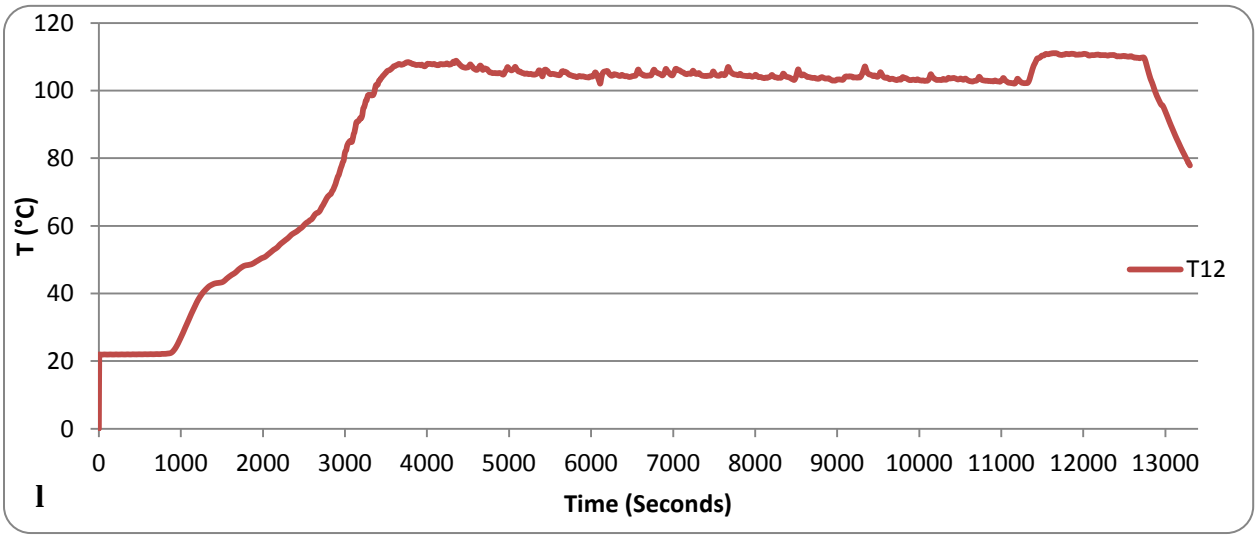
120
100
80
60
40
20
0
T (°C)
0
1000
2000
3000
4000
5000
6000
7000
8000
9000
10000
11000
12000
13000
Time (Seconds)
T12

l

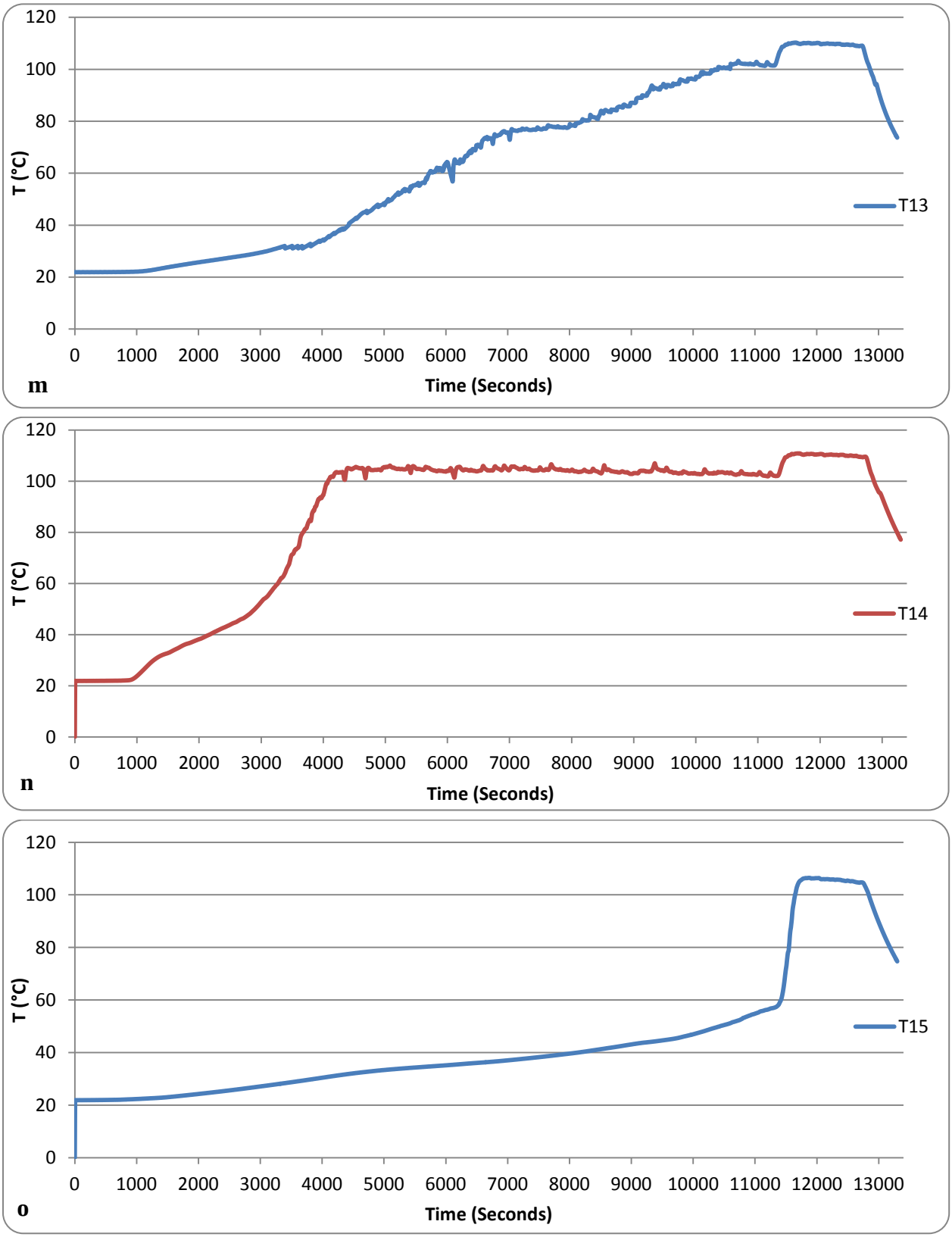

Figure 2.40: Surface temperatures measured along the height of Model DL-1 in RUN No. 8 of the SAGD visualization experiments

Table 2.28: Temperature data collected during RUN No. 8 of the SAGD visualization experiments				
Labview Time (sec)	6600	7800	9300	11300
Process Time (min)	45	65	90	124
Thermocouple No.	Temperature (°C)			
T1	105.03	105.51	107.61	104.85
T2	104.61	108.29	109.18	108.04
T3	100.03	105.99	106.36	106.32
T4	39.29	40.75	108.65	110.65
T5	109.11	111.78	111.64	109.53
T6	87.26	102.22	108.24	111.38
T7	72.66	99.22	101.74	100.62
T8	45.68	62.29	96.33	100.95
T9	102.01	102.02	102.43	99.66
T10	92.23	100.77	103.89	101.11
T11	36.89	45.45	79.20	101.17
T12	105.42	104.76	105.03	102.22
T13	72.78	77.84	92.00	101.47
T14	105.48	104.58	104.82	102.05
T15	36.15	39.04	44.02	57.02

According to the data presented in the second column of Table 2.28 and Figure 2.38.a, the steam chamber is in its early development stage at the labview time of 6600 seconds, and only the thermocouples adjacent to the trough (T1, T5, T9, T12, and T14) as well as three of the four top-structure thermocouples (T1, T2, and T3) show steam temperature.

In the next snapshot taken 20 minutes later, it is evident that the steam chamber is propagating laterally and more thermocouples are now involved with the invaded region, showing the superheated steam temperature. According to Figure 2.38.b, thermocouple T6 shows the mobilized region temperature (i.e. 102.22 °C) at that particular elevation along the height of the micromodel. In addition, thermocouple T10 shows the temperature of the mobile oil right behind the mobilized region, and it is evident that the mobile oil temperature, a few pores behind the SAGD interface, is very close to that of steam. In this Figure, thermocouples T7, T8, T11, T13, and T15 are still in the oil-saturated region and their associated temperature readings decreases by increasing their relative distance from the SAGD interface. It is also clear that the thickness of the mobilized region is higher in Figure 2.38.b compared to the previous snapshot.

Figure 2.38.c shows the development of the SAGD process in later times of the process at which the first two rows of the thermocouples show the invaded region temperature (i.e. superheated steam temperature in the steam chamber). The SAGD interface has just passed the position associated with T10 thermocouple, so it shows the superheated steam temperature at this particular time frame. Thermocouple T11 is still within the mobilized region, hence showing a temperature considerably lower than that of the steam chamber. Although T12 and T14 thermocouples show the steam temperature, their neighbouring thermocouples (i.e. T13 and T15 respectively) show the temperature of the oil-filled pores well behind the apparent SAGD interface. It is also evident that the thickness of the mobilized region is being wider compared to its associated thickness in the two previous snapshots.

Figure 2.38.d shows the developed SAGD chamber in which all the thermocouples except one show the steam chamber temperature. Even thermocouple T13 which has just been passed by the SAGD interface shows the superheated steam temperature. T15 is the only thermocouple that is still in the un-invaded portion of the glass micromodel, hence showing a temperature well below that of the steam phase (i.e. 57.02 °C).

In order to present the effect of pore-scale and macroscopic properties of the glass micromodels on the pore-scale SAGD interface advancement velocity, five of our visualization trials were selected. In addition, two more SAGD experiments were selected in order to investigate the effect of operating temperature on the pore-scale performance of the SAGD process. For each trial, the average position of the SAGD interface within each cell block was carefully tracked versus time. Figure 2.41 presents the average SAGD interface position, along the width of all five employed micromodels within particular cell blocks, which was measured versus process time. Based on the data trends presented in Figure 2.41, it is evident that the average position of the SAGD interface changes linearly with time. It is concluded that for each particular micromodel, the pore-scale sweep rate of the SAGD process within each particular cell block could be considered to be a constant value. Extending this conclusion to the full height of the SAGD interface along the height of each particular micromodel recommends that the SAGD interface advancement velocity could be considered a constant value under prevailing operational conditions. This procedure was performed for every particular cell block in all five

micromodels which were introduced in Table 2.3, and an average interface advancement velocity per cell block was obtained accordingly. In order to calculate an overall interface advancement velocity for each micromodel, the arithmetic averaging technique was used between particular average sweep rates per every cell block. The calculated average sweep rate for each micromodel in terms of number of pores swept away per unit time was translated to interface advancement velocity in unit length per unit time using two pore-scale dimensions of pore-to-pore distance and pore body width of each particular porous pattern. These results are presented in Table 2.29. As it is evident from the data presented in this Table, it was tried to select the trials in which the average operating temperatures of the SAGD process (i.e. steam temperature within the invaded zone) are close to each other in such a way to make the sweep rate data independent of the oil viscosity at the steam temperature. As a result, the interface advancement velocity would then only be affected by the pore-scale and macro-scale properties of the glass micromodels.

Considering the operating temperatures of the SAGD trials presented in Table 2.29 and the fact that the employed fluids were also the same for all these trials, it could be concluded that the drainage rate would be a function of permeability of the glass micromodel. In other words, the higher the permeability is, the higher would be the drainage rate when all other experimental variables are kept constant. The interface advancement velocity is a measure of the mobile oil drainage rate. As a result, the SAGD sweep rate at the pore-scale and the average sweep rate for the entire height of the micromodel are strong functions of permeability. This is in agreement with our experimental results. Considering the interface advancement velocity data presented in the last three rows of Table 2.29 and the measured permeability values of these models presented in Table 2.3, it is evident that the models with higher permeability exhibit higher SAGD sweep rate under prevailing experimental conditions. The SAGD process performed in Model DL-1 which has the highest permeability value among others (94.61 D) had the highest average sweep rate of 0.576 mm/min, while Model DC-1 with minimum permeability value of 34.13 D exhibits the lowest interface advancement rate of 0.170 mm/min.

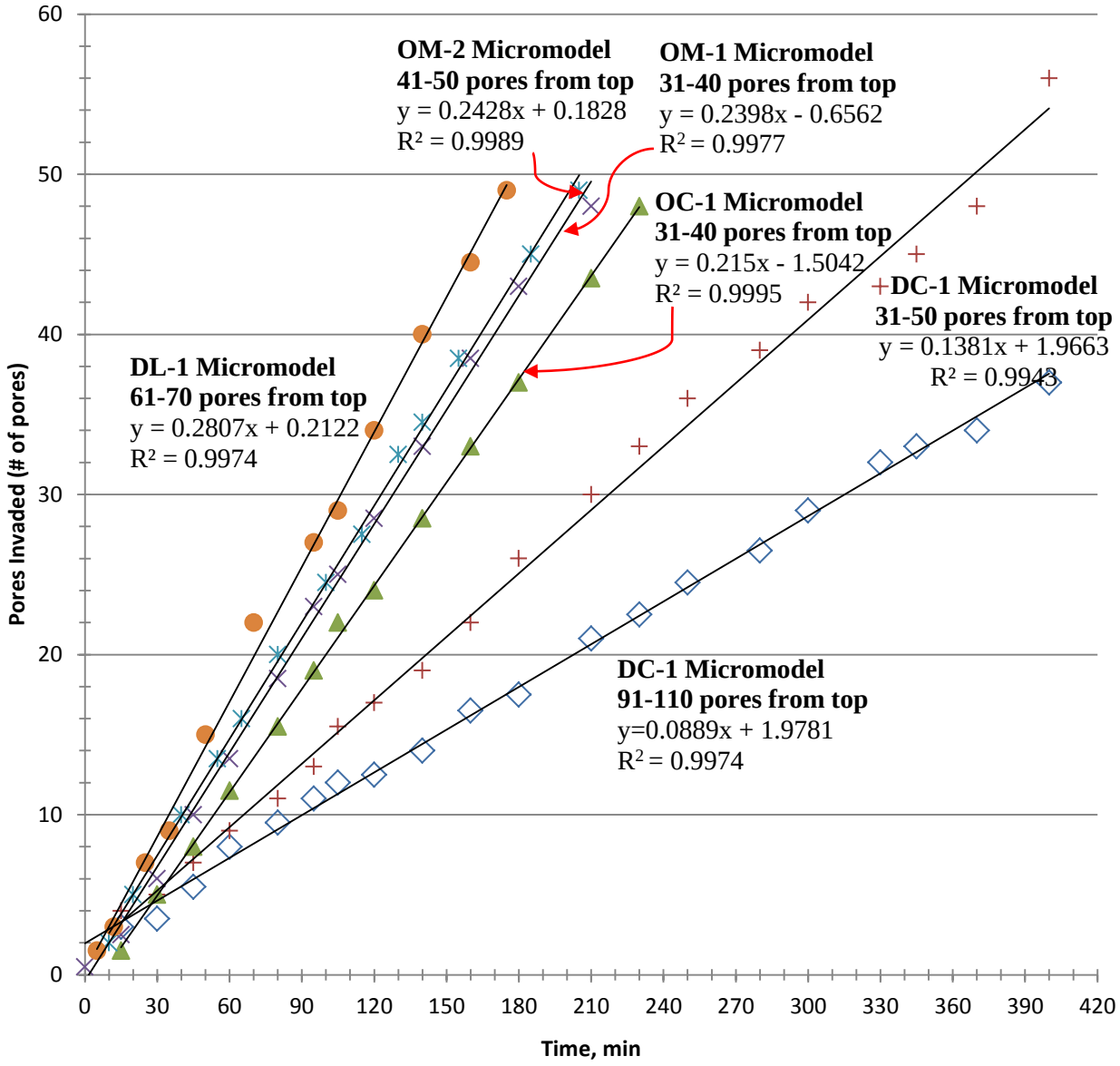

Figure 2.41: SAGD interface advancement in five different micromodels

Table 2.29: SAGD interface advancement velocity based on the visualization experiments

	Micromodels				
	OC-1	**DL-1**	**DC-1**	**OM-1**	**OM-2**
	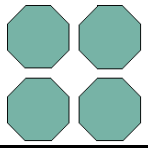	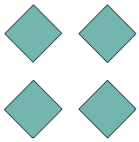	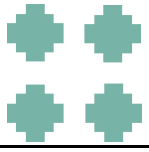	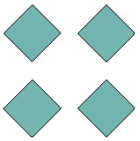	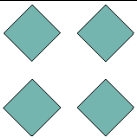
Average temperature in the invaded zone (°C)	101.20	103.10	102.40	101.70	103.80
RUN No.	6	3	7	1	2
Location in Model	**Interface advancement velocity (pores/min)**				
21-30 pores from top	n/a	n/a	n/a	n/a	n/a
31-40 pores from top	**0.215**	0.331	**0.138**	**0.240**	0.264
41-50 pores from top	0.209	0.316		0.233	**0.243**
51-60 pores from top	0.197	0.306	0.125	0.228	0.238
61-70 pores from top	0.181	**0.281**		0.224	0.232
71-80 pores from top	0.174	0.277	0.108	0.219	0.226
81-90 pores from top	0.166	0.268		0.216	0.221
91-100 pores from top	0.157	0.260	**0.089**	0.209	0.215
101-110 pores from top	0.145	0.253		0.201	0.209
111-120 pores from top	0.136	0.249	0.071	0.195	0.202
121-130 pores from top	n/a	n/a		n/a	n/a
131-140 pores from top	n/a	n/a	n/a	n/a	n/a
141-150 pores from top	n/a	n/a	n/a	n/a	n/a
151-160 pores from top			n/a		
161-170 pores from top			n/a		
171-180 pores from top			n/a		
181-190 pores from top			n/a		
Average interface velocity values for each micromodel					
(pores/min)	0.176±0.018	0.282±0.019	0.1059±0.024	0.218±0.010	0.228±0.012
Using Pore to Pore distance (mm/min)	0.358	0.576	0.1695	0.437	0.456
Using Pore Body Width (mm/min)	0.242	0.576	0.1388	0.437	0.456

In order to figure out the effect of mobile oil viscosity on the rate of the SAGD interface advancement, two different pore-scale SAGD trials are considered which both were conducted with the same micromodel. Figure 2.42 presents the temporary SAGD interface positions in Model OM-1 with two different operating temperatures of 101.70 and 116.35 °C measured at the same elevation (i.e. within the same cell block) while all other experimental variables were kept constant. It is evident that at this particular elevation through the model (31-40 pores from top), a 69.30% increase in the sweep rate was observed with almost 14.40% increase in the operating temperature of the SAGD process under prevailing experimental conditions and model properties. It is obvious that the model would be drained sooner when the in-situ oil viscosity at steam temperature is lower as it is observed in the form of shorter process time of the SAGD trial with higher operating temperature. The SAGD interface position was tracked versus time in these two experiments at different elevations from the topside of the OM-1 Model, and an average sweep rate was then calculated at every elevation (i.e. cell block) based on the procedure shown in Figure 2.42. These data are summarized in Table 2.30. In order to figure out a representative sweep rate for the SAGD process in OM-1 micromodel at each of these two operating temperatures, an arithmetic averaging technique was employed over the interface advancement velocities reported in Table 2.30. This average sweep velocity of the SAGD interface was reported in terms of the number of pores per minute of the process time, as well as the unit of length per minute of the process time with the aid of pore-to-pore distance and pore body width dimensions of the OM-1 porous pattern.

According to the data presented in Table 2.30, it is clear that the average SAGD interface advancement velocity in Model OM-1 increased by about 73.6% when the operating temperature was increased from 101.70 to 116.35 °C. It seems that superheating the steam phase prior to injecting into the model can significantly enhance the pore-scale sweep rate and as a result, the oil drainage rate under the SAGD recovery scheme.

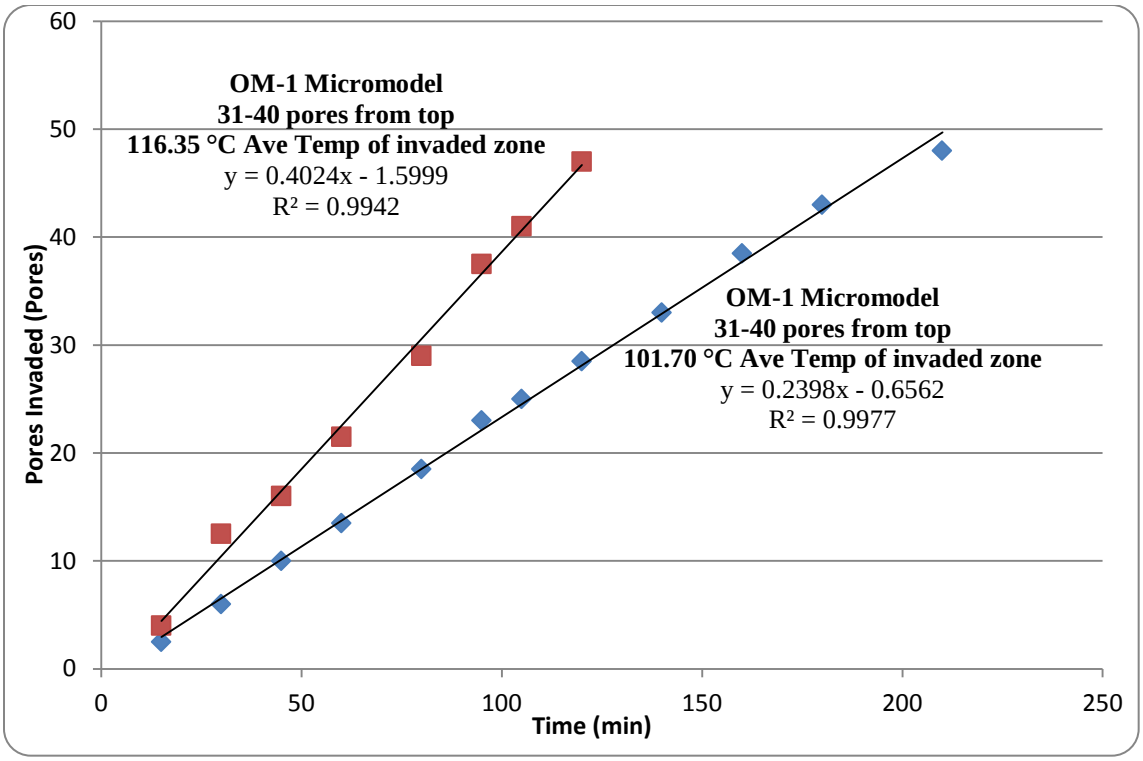

Figure 2.42: Pore-scale SAGD interface advancement in Model OM-1

The same conclusion can be obtained by looking into Figure 2.43 which shows the temporary position of the SAGD interface versus time in OM-2 Model at two different operating temperatures of 103.40 and 110.20 °C. All other system parameters were kept constant in this case and the position of the SAGD interface was tracked at the same elevation (41-50 pores from the top) in these two trials. It is quite evident that at this particular elevation through the porous pattern skeleton, the sweep rate at the higher operating temperature of 110.20 °C (i.e. 0.3352 pores/min) is about 38% more than that of the SAGD trial at the steam temperature of 103.40 °C. The SAGD interface was also tracked in other cell blocks along the height of the model, and an average sweep rate was calculated for each particular cell block based on the procedure followed in Figure 2.43. The details of these pore-scale interface velocities are presented in Table 2.31. An arithmetic averaging technique was used to calculate the average SAGD interface advancement velocity in terms of the number of pores invaded per unit process time through the entire model at each corresponding operating temperature. This representative average sweep rate was also translated to the unit length invaded per minute of the process time using two pore-scale

dimensions of pore-to-pore distance and pore body width obtained from the detailed pore-scale characterization of OM-2 Model.

According to the information presented in Table 2.31, it is evident that increasing the degree of superheat of steam from 103.40 to 110.20 ℃ was responsible for about 31% increase in the sweep rate of the SAGD process under prevailing experimental conditions and model properties. This point also signifies the importance of steam superheating in the overall pore-scale performance of the SAGD process.

Table 2.30: SAGD interface advancement velocity in Model OM-1

OM-1 Micromodel	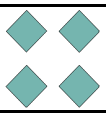	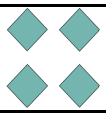
Average temperature in the invaded zone (°C)	101.70	116.35
RUN No.	1	4
Location in Model	**Interface advancement velocity (pores/min)**	
21-30 pores from top	n/a	n/a
31-40 pores from top	**0.240**	**0.402**
41-50 pores from top	0.233	0.398
51-60 pores from top	0.228	0.392
61-70 pores from top	0.224	0.386
71-80 pores from top	0.219	0.380
81-90 pores from top	0.216	0.373
91-100 pores from top	0.209	0.365
101-110 pores from top	0.201	0.359
111-120 pores from top	0.195	0.352
121-130 pores from top	n/a	n/a
131-140 pores from top	n/a	n/a
141-150 pores from top	n/a	n/a
Average interface velocity values		
(pores/min)	0.218±0.010	0.379±0.011
Using Pore to Pore distance (mm/min)	0.437	0.757
Using Pore Body Width (mm/min)	0.437	0.757

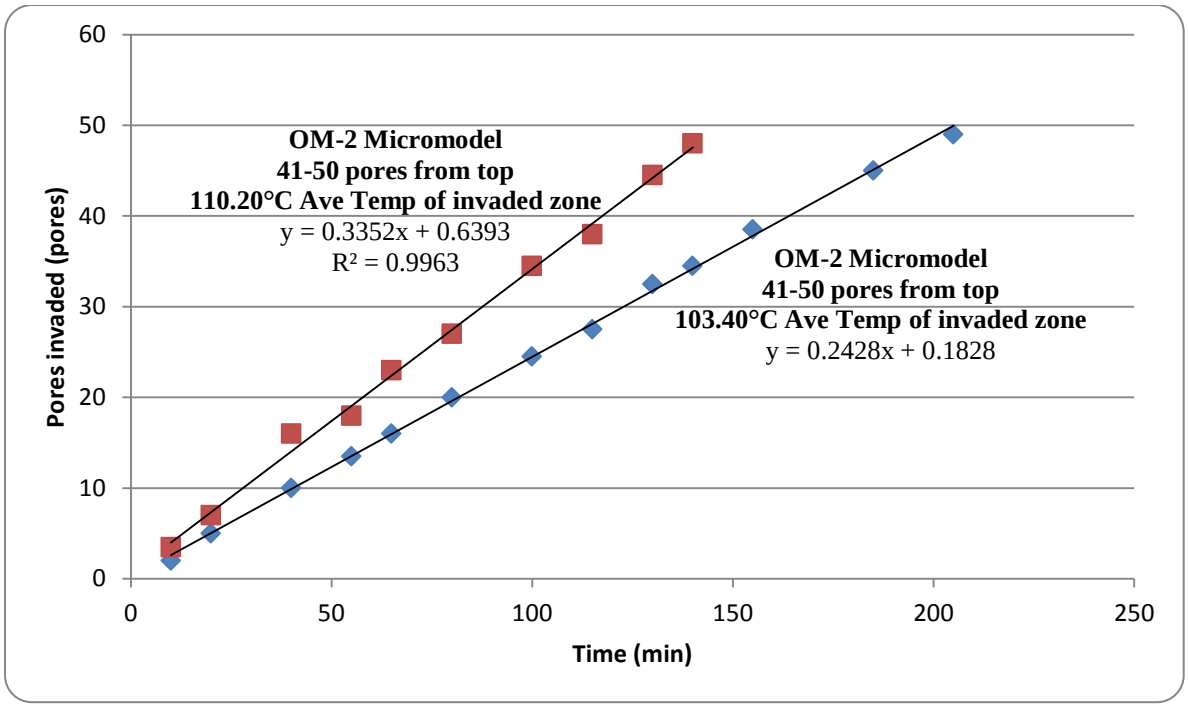

Figure 2.43: Pore-scale SAGD interface advancement in Model OM-2

The pore-scale SAGD process performance for models DL-1, OM-1, and OM-2 is compared in Figure 2.44. These three models have the same pore-scale pattern with very close micro-scale properties. Model OM-2 has higher permeability compared to model OM-1. Consequently, when the SAGD process was performed at a higher temperature of 103.80 °C in model OM-2 compared to that of 101.70 °C in model OM-1, the pore-scale sweep rate should be higher in the former compared to the latter. This point is evident in Figure 2.44 by comparing the data series 1 and 2. It is clear that the interface advancement velocity in RUN 2 even at lower elevation (i.e. less drainage height) is higher than that of RUN 1. This is verified by the data presented in Table 2.29. The same conclusion cannot be made by comparing RUN 4 and RUN 5 in which similar models were used. Although OM-2 has higher permeability compared to OM-1, RUN 5 has less pore-scale interface velocity compared to that of RUN 4 because of higher operating temperature of the latter compared to the former case. In order to make the sweep rate data independent of the interface elevation along the height of the porous skeleton for these two trials, the sweep rate of RUN 5 at 31-40 pores from top of the model is extracted from Table 2.31 (i.e. 0.396) which is still lower than that of trial No. 4 at the same elevation. Comparing the representative average

interface advancement velocity of these two trials using Tables 2.30 and 2.31 also reveals the fact that RUN 4, with an average sweep rate of 0.379 pores/min, is more effective than RUN 5 with an average sweep rate of 0.300 pores/min. It appears that the effect of viscosity reduction due to higher operating temperature in RUN 4 dominates the permeability effect in RUN 5.

Table 2.31: SAGD interface advancement velocity in Model OM-2

OM-2 Micromodel	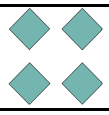	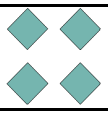
Average temperature in the invaded zone (°C)	103.80	110.20
RUN No.	2	5
Location in Model	**Interface advancement velocity (pores/min)**	
21-30 pores from top	n/a	n/a
31-40 pores from top	0.264	0.396
41-50 pores from top	**0.243**	**0.335**
51-60 pores from top	0.238	0.311
61-70 pores from top	0.232	0.298
71-80 pores from top	0.226	0.285
81-90 pores from top	0.221	0.272
91-100 pores from top	0.215	0.270
101-110 pores from top	0.209	0.267
111-120 pores from top	0.202	0.262
121-130 pores from top	n/a	n/a
131-140 pores from top	n/a	n/a
141-150 pores from top	n/a	n/a
Average interface velocity values		
(pores/min)	0.228±0.012	0.300±0.028
Using Pore to Pore distance (mm/min)	0.456	0.599
Using Pore Body Width (mm/min)	0.456	0.599

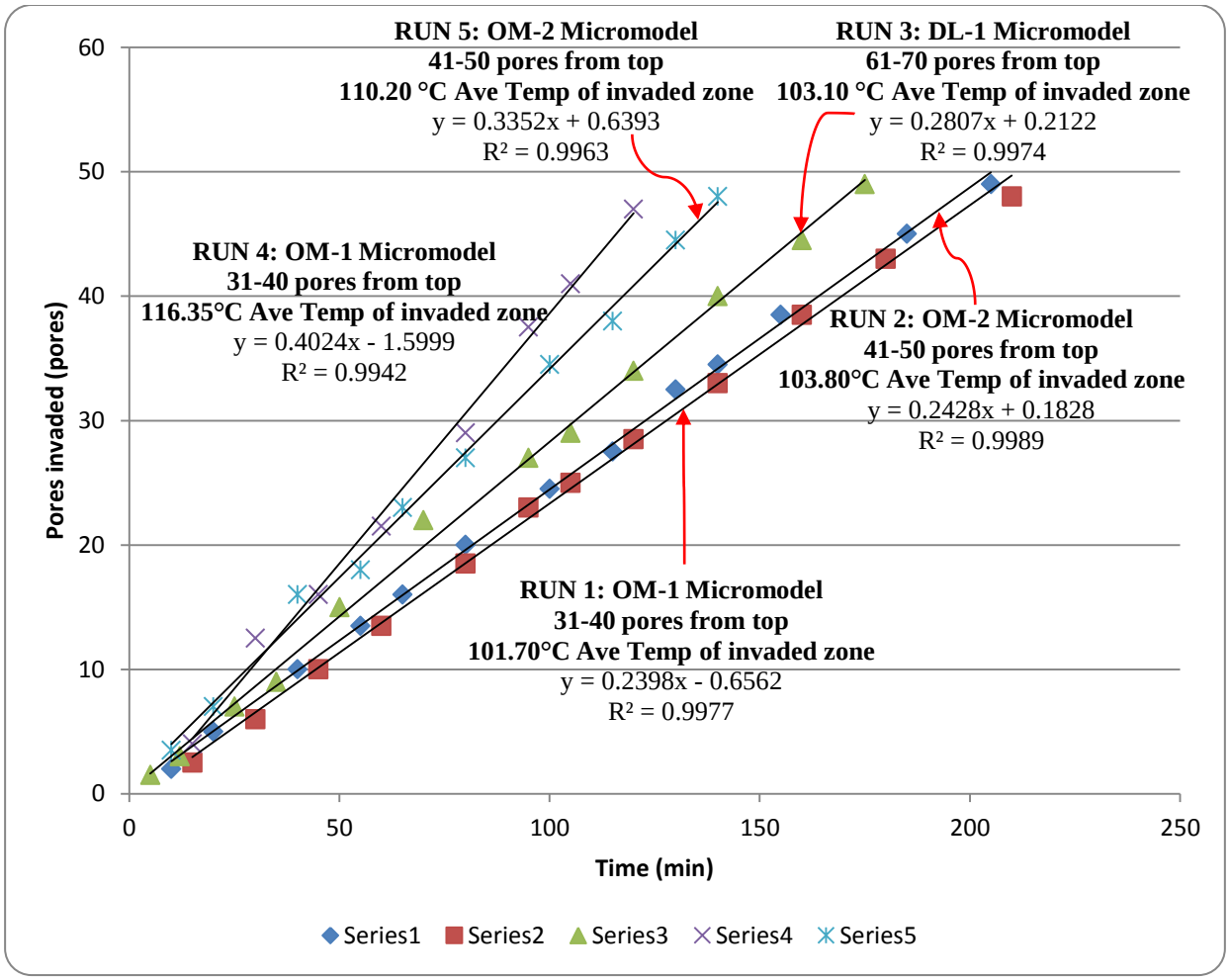

Figure 2.44: Pore-scale SAGD sweep rate in Models DL-1, OM-1, and OM-2

According to Figure 2.44, the pore-scale performance of the SAGD process in DL-1 (i.e. RUN 3) could also be compared to the other trials presented in this Figure. For instance, RUN 3 has higher sweep rate than those of RUN 2 and RUN 1 in which OM-1 and OM-2 micromodels were used. Comparing RUN 3 and RUN 2 which were performed at almost similar operating temperatures, it is evident that higher permeability value of DL-1 compared to that of OM-2 results in higher interface advancement velocity in DL-1 model even at lower elevations. It is also obvious that higher model permeability and higher steam temperature in RUN 3 results in much more sweep rate in this trial even at lower elevations compared to that of RUN 1. These conclusions could also be verified by looking into the average sweep rate of these three models at their corresponding experimental run numbers from Table 2.29 in which DL-1 has the highest

interface velocity (i.e. 0.576 mm/min) followed by OM-2 (i.e. 0.456 mm/min) and OM-1 (0.436 mm/min) respectively under pertaining operating conditions. However, pore-scale SAGD performance in DL-1 model (RUN 3) was obtained to be weaker than those in OM-1 and OM-2 models at their corresponding elevated operating temperatures as presented by RUN numbers 4 and 5 in Figure 2.44 respectively. Even though OM-1 and OM-2 permeabilities are less than that of DL-1, it seems that the additional viscosity reduction due to higher operating temperatures in these two trials affects their pore-scale performance to the extent of achieving higher interface advancement velocities compared to that of the RUN 3. Even considering the sweep rate of RUN 3 at higher elevations would also verify this observation. In fact, RUN 3 sweep rate is 0.675 and 0.645 mm/min at 31-40 and 41-50 pores from the top of the model respectively (refer to Table 2.29). On the other hand, the average sweep rate within 41-50 pores from the top of OM-2 model in RUN 5 is 0.670 mm/min, and that of RUN 4 within the 31-40 pores from the top of OM-1 model is 0.804 mm/min. As a result, it is clear that the interface advancement velocities in models OM-1 and OM-2 at higher operating temperatures are higher than that of model DL-1 at similar elevations from the top of this model but lower operating temperature.

2.5.4. Production Characteristics of the SAGD Process at the Pore-Scale: Experimental Results

2.5.4.1. Ultimate Recovery Factor (RF)

As it was stated previously, the production rates of our pore-scale SAGD experiments could not be measured directly due to very small storage capacity of the glass micromodels. A back-calculation procedure is presented in this section in order to analyze the production characteristics of some of our pore-scale SAGD experiments with the aid of SAGD interface advancement data. The SAGD interface was closely tracked versus time during our pore-scale SAGD visualization experiments. The pore-level interface advancement velocity for each SAGD experiment at particular elevations along the height of the glass micromodel was found to be constant. As the total height of each glass micromodel can be considered as an infinitesimal portion of a real world field-scale SAGD interface, it is obvious that the variation of the horizontal velocity of interface along the height of each micromodel is not significant. Therefore, an arithmetic averaging technique was used to calculate a representative horizontal interface

advancement velocity in terms of the number of pores invaded per unit time or unit length per unit time for each particular pore-scale SAGD experiment.

The calculated horizontal interface advancement velocity along with the pore-scale snapshots was used in order to calculate the invaded area at each particular timeframe during the life of each individual SAGD experiment. The fraction of area swept away was defined as the ratio of the swept area by the total area of a glass micromodel at each particular timeframe within the lifespan of each SAGD experiment. It was obtained that the fraction of area swept varies linearly with process time for each SAGD experiment. An average oil production rate could then be calculated over the entire production history of each particular SAGD experiment by multiplying the slope of the fraction of area swept-process time plot by the pore volume of each particular micromodel. The cumulative oil produced at the end of each SAGD experiment was calculated in two ways. It can be obtained by multiplying the average oil production rate by the process time. In addition, each micromodel was weighed before and after the experiment, and the total volume of oil produced can be calculated within the accuracy range of the weight measurements. The latter method could also be used in order to calculate the ultimate recovery factor of each particular SAGD experiment.

In section 2.5.3, seven SAGD experiments were considered for the purpose of parametric sensitivity analysis of the horizontal interface advancement velocity. These SAGD trials were also considered in this section in order to analyze their associated production characteristics in terms of the ultimate recovery factor. Figure 2.45 displays the temporary location of the SAGD interface at different elevations along the height of Model DL-1 in RUN No. 3 of the SAGD visualization experiments. The high-permeable trough is located at the right hand side of Figure 2.45 extended along the entire height of the micromodel. At each particular timeframe, the invaded area of the model could be obtained by calculating the area over the curve to the right in Figure 2.45 using trapezoidal rule.

Plotting the fraction of the invaded area versus time yields in a straight line, and the average oil production rate over the entire process time could be estimated from the slope of this straight line. Following this procedure, the oil production rate was calculated to be 0.01160 cm^3/min. The ultimate recovery factor for this trial can also be calculated by dividing the product of average oil

production rate by the process time over the DL-1 model pore volume. This ultimate recovery factor could be cross checked with the recovery factor values obtained using direct measurement technique of weighing the model before and after each trial. As the RF value obtained using the interface advancement velocity considerations is subject to some human error when the SAGD interface was tracked over the process time, the RF values associated with pre- and post-trial weighing of the model were considered to be the more accurate numbers. This procedure was carried out for the seven SAGD trials introduced in section 2.5.3, and the results are summarized in Table 2.32.

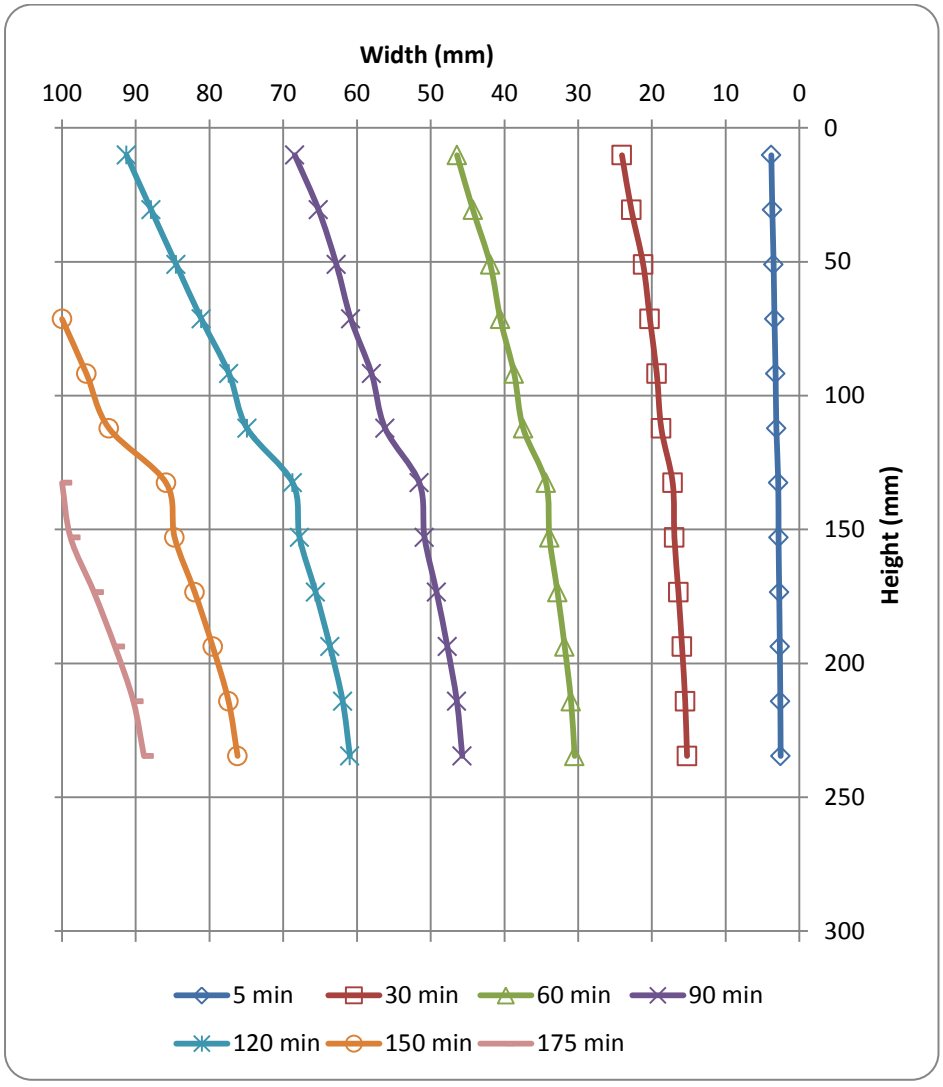

Figure 2.45: Temporary position of the SAGD interface along the height of DL-1 Model in RUN No. 3 of the SAGD visualization experiments

Table 2.32: Production performance calculations of the pore-level SAGD experiments							
Model	RUN No.	K (D)	Process time (min)	Operating temperature (°C)	RF (%)		% Relative Difference
					Interface tracking	Direct measurement	
DL-1	3	94.61	175	103.10	84.6	80.0	5.83
OM-2	2	92.42	205	103.40	74.4	70.4	5.61
OM-1	1	77.83	210	101.70	72.4	71.2	1.60
OM-2	5	92.42	140	110.20	69.9	68.2	2.51
OM-1	4	77.83	120	116.35	71.0	72.0	-1.36
DC-1	7	34.13	400	102.40	34.9	33.1	5.40
OC-1	6	56.16	230	101.20	70.0	69.7	0.53

As it is depicted in Table 2.32, all the RF values obtained using the interface advancement tracking procedure are slightly higher (within 6%) than those measured directly using pre- and post-trial model weighing techniques except for RUN No. 4 in which the interface tracking method underestimates the RF value. The RF values obtained using these two procedures are in good agreement with each other. One can study the effect of porous media properties on the ultimate recovery factor of the pore-scale SAGD experiments with focusing on the data presented in Table 2.32 at similar operating temperature. It is evident that the models with higher magnitudes of permeability exhibit higher values of ultimate RF considering the process time over which each particular experiment was conducted. For instance, Model DL-1 with the highest level of permeability possesses the highest RF value of 80% during a process time which is the lowest among those reported in Table 2.32. On the other hand, Model DC-1 with the lowest permeability value of 34.13D achieved only 33.1% recovery factor during 400 min process time.

It is also possible to figure out the effect of operating temperature on the ultimate recovery factor of the SAGD process based on the data presented in Table 2.32. One can compare the ultimate RF values of RUN No's 2 and 5 in which OM-2 was employed as the porous medium at two levels of degrees of superheat, 103.40 and 110.20 °C respectively. It is clear that the ultimate recovery factor of the former trial is slightly higher (i.e. 2.2%) than that of the latter experiment; however, the comparable RF value for the SAGD trial at higher degrees of steam superheat was achieved during much less process time than that of RUN No. 2. If trial No. 5 would have been continued to the extent of process time associated with RUN No. 2, extremely higher RF values

could be achieved. The same result could be concluded by looking into the SAGD ultimate RF values reported for RUN No's 1 and 4 in which OM-1 micromodel was used at two different levels of operating temperature. It is evident that RUN No 4 with about 15 °C higher operating temperature achieved slightly higher RF value compared to its corresponding trial at lower steam temperature. The enhanced productivity of RUN No 4 compared to RUN No 1 is more pronounced considering the fact that the former trial has extremely shorter process time duration compared to the latter one (i.e. 120 min vs. 210 min respectively). Consequently, the higher the degrees of superheat is, the more enhanced would be the performance of the SAGD process in terms of the ultimate recovery factor.

2.5.4.2. Cumulative Steam to Oil Ratio (CSOR)

The volumetric measurements carried out during the pore-scale SAGD experiments were also used in order to determine the energy requirements of the SAGD process in terms of the cumulative steam to oil ratio (CSOR). The cumulative amount of water produced in each SAGD experiment was measured during different stages of the process such as start-up stage, early development of the steam chamber, and chamber propagation stage. The instantaneous steam injection rate, in terms of Cold Water Equivalent (CWE) injection rate, was adjusted during the process time in order to achieve a relatively constant steam temperature in the invaded area of the porous pattern in the presence of continuously growing heat loss from the model to the surrounding environment. The cumulative steam injected during each particular SAGD trial was obtained by multiplying the instantaneous steam injection rate by the time duration over which each particular injection rate was maintained constant. There was a good agreement between the cumulative water produced and the cumulative steam injected in terms of the CWE during every stage of the SAGD trials. The instantaneous SAGD interface position along the height of each micromodel was determined for each SAGD trial. Considering the fraction of the area swept with respect to the total area and the heat loss calculations performed in section 2.5.2.3, the contribution of the produced water condensate, originated from the heat loss, in the cumulative steam injected in terms of the CWE was determined at the end of each particular pore-scale SAGD experiment. The cumulative steam to oil ratio, in terms of the injected Cold Water Equivalent (CWE) per volume of the oil produced, can then be calculated using net cumulative produced water volume and the cumulative oil produced for each particular SAGD trial.

In sections 2.5.3 and 2.5.4.1, seven SAGD experiments were considered for the purpose of parametric sensitivity analysis of the horizontal interface advancement velocity as well as ultimate RF values respectively. These SAGD trials were also considered in this section in order to analyze their associated energy requirements in terms of the CSOR values. Table 2.33 summarizes the CSOR data for these selected SAGD trials along with some other general information regarding each particular experiment.

Table 2.33: Energy requirements calculations for the pore-level SAGD experiments

Run No.	Model	Runtime (min)	Operating Temperature (°C)	Cum. Oil produced (cm^3)	Cum. steam injected (cm^3 of CWE)	Cum. steam needed for heat loss (cm^3 of CWE)	Net steam consumed (cm^3 of CWE)	CSOR
6	OC-1	230	101.20	1.11	81.95	70.75	11.20	10.05
7	DC-1	400	102.40	0.66	95.17	86.38	8.79	13.28
3	DL-1	175	103.10	1.92	77.20	65.88	11.32	5.90
1	OM-1	210	101.70	0.78	74.75	67.54	7.21	9.20
2	OM-2	205	103.40	1.34	78.82	70.83	7.99	5.97
4	OM-1	120	116.35	0.79	51.55	47.07	4.48	5.66
5	OM-2	140	110.20	1.30	54.97	48.61	6.36	4.91

According to the data provided in Table 2.33, one can study the effect of model permeability on the CSOR values of the SAGD process when all other experimental variables remain reasonably unchanged. It was tried to select SAGD experiments whose operating temperatures were reasonably similar to each other (i.e. RUN No's 1, 2, 3, 6, and 7). This makes the CSOR results for these trials to be nearly independent of the steam temperature. Figure 2.46 displays the variation of the CSOR versus model permeability for the SAGD trials 1, 2, 3, 6, and 7 in which 5 different micromodels were employed. As it is depicted in this Figure, the higher the permeability value is, the less would be the corresponding CSOR value. In addition, there is a good linear correlation between the CSOR and model permeability as is displayed in Figure 2.46.

In addition, two more experiments at higher degrees of steam superheat were selected in order to investigate the effect of operating temperature on the CSOR values. Focusing on the trial numbers 1 and 4 in Table 2.33 in which OM-1 model was used as the porous medium at two different degrees of steam superheat, it is observed that the CSOR value is reduced by almost

63% as a result of an increase in the steam temperature to the extent of 14.70 °C. The same conclusion can also be made considering RUN NO's 2 and 5 in which OM-2 model was employed. It is evident that following an almost 7 °C rise in the operating temperature, the CSOR value was decreased by about 22%. In conclusion, the higher the operating temperature of the SAGD process is, the less would be the associated value of the CSOR.

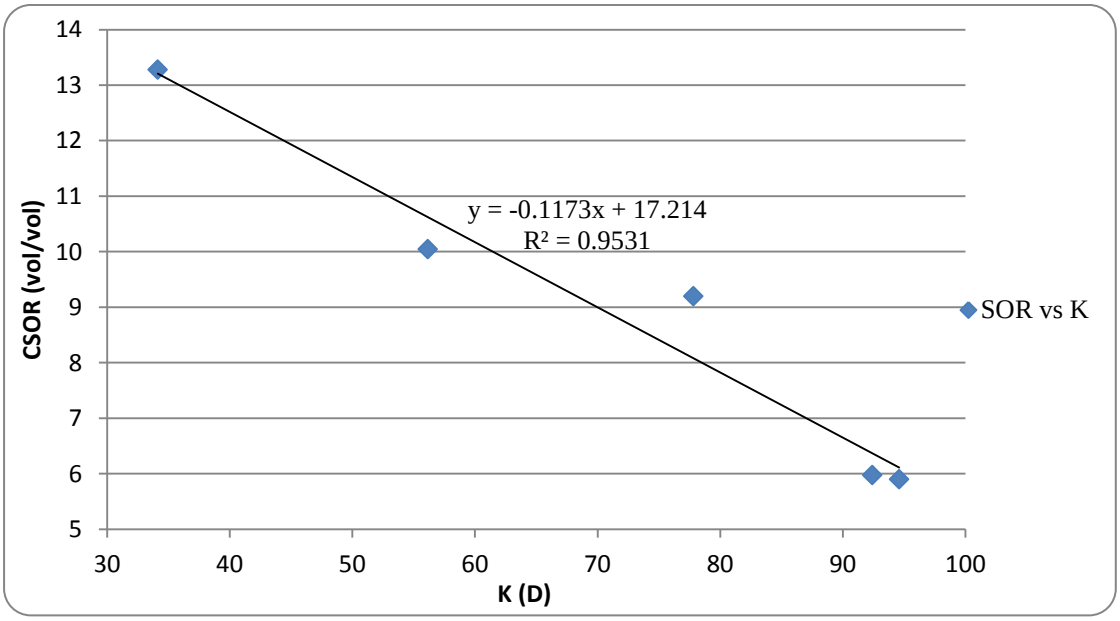

Figure 2.46: Effect of porous media permeability on the CSOR value based on the pore-level SAGD visualization experiments

2.5.5. Experimental Results Validation based on the Butler's Theory

A conceptual model was primarily proposed by Butler et al (1979 and 1981) and was developed further through subsequent publications (Butler and Stephens, 1981; Butler 1985, 1991, and 1994) in order to estimate the drainage rate of the mobile oil under the SAGD recovery process. In this section, the theory is discussed briefly to figure out how the drainage rate of the mobile oil and the steam chamber interface velocity in the horizontal direction are being affected by the reservoir rock and fluid properties. The parametric sensitivity analysis will then be performed in order to quantify the effect of different affecting parameters (i.e. model permeability and porosity, oil viscosity at steam temperature) on the horizontal sweep rate of the SAGD process as

well as on the CSOR based on our SAGD visualization experiments. Finally, the experimental results are being validated by the theory.

According to the original theory describing the fluid flow concept of the SAGD process, the heated oil by steam flows approximately parallel to the condensation surface (i.e. apparent SAGD interface) down gradient towards the production well. This point was also verified with the results of our visualization experiments. Figure 2.47 shows the magnified view of an infinitesimal control volume taken at the apparent interface between the oil and steam phases. It is assumed that the kinematic viscosity of the oil phase is "υ" at a distance "ξ" from the apparent SAGD interface. This heated oil is draining with the volumetric flow rate of "dq" through the tiny element whose thickness in the direction perpendicular to the paper is unity. As a result, the apparent SAGD interface, whose repose angle with horizontal direction is "θ_r", advances from left to right with a velocity of "U" perpendicular to the condensation surface. The horizontal and vertical interface advancement velocities would be defined as $\left(\frac{\partial x}{\delta t}\right)_y$ and $\left(\frac{\partial y}{\delta t}\right)_x$ respectively.

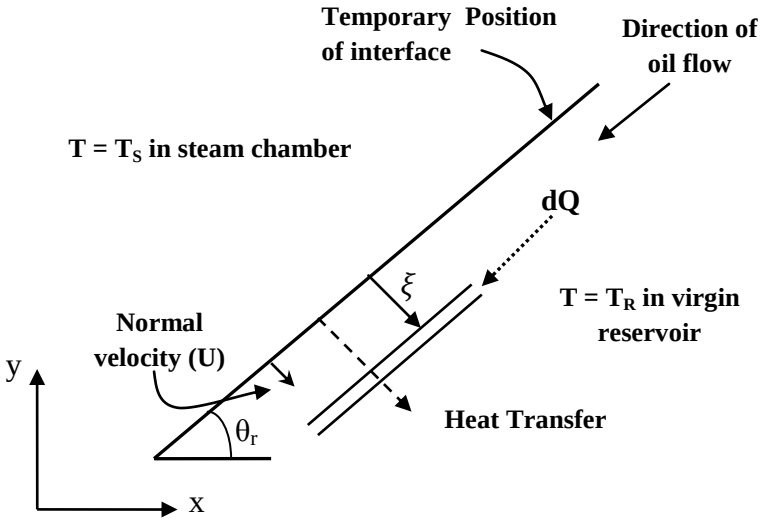

Figure 2.47: Small Free Body Diagram (FBD) of steam chamber interface (Modified from Butler 1991)

There are a series of assumptions which should be considered if the following derivation is going to be used in order to develop a relation for the horizontal interface advancement velocity. These assumptions are:

- Steam pressure should be assumed constant inside the steam chamber. This assumption is valid so far the steam injection at constant pressure is maintained through the injection well.
- Steam was assumed to be the only flowing phase within the chamber. In our visualization experiments, as long as a good treatment of the heat loss prevention was performed, steam was the only flowing phase within the invaded pores of the porous network; however, due to the excessive heat loss at moderate environmental vacuum pressures, water condensate was also draining through the invaded pores of the micromodels ahead of the apparent SAGD interface.
- Oil phase is assumed to be at its residual saturation inside the steam chamber.
- Heat transfer ahead of the steam chamber through the cold bitumen is assumed to be dominated by the conduction mechanism under constant reservoir thermal diffusivity. According to some numerical simulation studies performed on the heat transfer and drainage aspects of the SAGD process, it was concluded that conduction is not the only contributing heat transfer mechanism behind the SAGD interface (Ito 1998 and 2004; Ito and Suzuki, 1996; Ito and Singhal 1999; Ito et.al, 2004; Ito and Ipek, 2005). According to our SAGD visualization experiments, small droplets of water condensate as well as small bubbles of the steam phase invade through the continuum of the mobile oil behind the apparent SAGD interface following an engulfment process at the pore-scale. Due to the extensive pore-scale mixing within the mobilized region, this pore-level intrusion could be translated in the form of convective element of heat transfer ahead of the apparent SAGD interface trough the mobile oil-filled pores.
- The only driving force for fluid flow towards the production well was assumed to be gravitational force. In the absence of excessive viscous pressure drop especially across the interface, this assumption seems to be valid in a conventional SAGD process.

- As Darcy equation was selected to model the fluid flow through porous media, all the primary assumptions related to this equation were explicitly accepted during the course of the SAGD process modeling.

- One of the major shortcomings of this flow modeling of the SAGD process is that presence of capillary forces was ignored. Considering the capillary force as one of the important driving forces in a typical SAGD process would affect the predicted smooth interface shape. In fact, the apparent SAGD interface at the pore-level has an irregular shape in nature. In case if capillary force was considered in the transport processes' modeling of the SAGD process, the amount of microscopic heat transfer would be extended, and because water condensate tends to occupy the smaller-sized water-wet pores, the mobile oil phase would move towards the larger pores easier than predicted. It is true that the effect of microscopic irregularities of the apparent SAGD interface at the pore-scale could be ignored at the macroscopic level. For instance, the SAGD interface could be considered as a smooth distinction line between the oil phase and the invading steam phase when the drainage process of the mobile oil from a physical model under the SAGD process is concerned. This is because of the fact that at the macro-scale, the thickness of the mobile oil layer is too large compared to the thickness of the steam-bitumen transition zone. However, these irregularities associated with the shape of the apparent SAGD interface at the pore-scale are important regarding the fingering effect of the invading steam phase and also when the bypassed regions of the un-drained bitumen are considered during the course of the pore-level studies of the SAGD process.

According to Darcy's law, the differential volumetric flow rate of the mobile oil through the infinitesimal element could be defined as:

$$dq = \frac{kA\Delta\rho g sin\theta_r}{\mu} \tag{2.42}$$

in which "K" is the absolute permeability, "$\Delta\rho$" is the density difference between the acting fluid phases (i.e. steam and the mobile oil), and "A" is the cross sectional area perpendicular to the drainage flow of the mobile oil.

As the steam density is negligible compared to that of the oil phase, and simplifying the area subject to flow which is equal to ($d\xi \times 1$), Eq 2.42 would be simplified to:

$$dq = \frac{kgsin\theta_r}{\nu} d\xi \tag{2.43}$$

in which "ν" is the kinematic viscosity of the mobile oil phase.

If the reservoir is unheated, the differential drainage rate of the cold bitumen at the initial reservoir temperature (T_R) was considered to be a finite value which can be represented by:

$$dq_R = \frac{kgsin\theta_r}{\nu_R} d\xi \tag{2.44}$$

The difference between Eq's 2.43 and 2.44 quantifies the flow rate increase as a result of steam heating:

$$dq^* = dq - dq_R = kgsin\theta_r \left(\frac{1}{\nu} - \frac{1}{\nu_R}\right) d\xi \tag{2.45}$$

Integrating Eq 2.45 results in:

$$q = kgsin\theta_r \int_0^\infty \left(\frac{1}{\nu} - \frac{1}{\nu_R}\right) d\xi \tag{2.46}$$

In order to solve the integral in Eq 2.46, one should know the viscosity-temperature relationship for the in-situ bitumen. For most of the bitumen types in Canada, this relationship could be expressed as:

$$\frac{\nu_S}{\nu} = \left(\frac{T - T_R}{T_S - T_R}\right)^m \tag{2.47}$$

In which "ν" and "ν_s" are kinematic viscosity of bitumen at the virgin reservoir temperature and steam temperature respectively, and "m" is an empirical constant which is of the order of 3-4 for Canadian bitumen.

If the major heat transfer mechanism ahead of the steam chamber is assumed to be conduction, the temperature distribution ahead of the interface could be related to the interface velocity according to the following equation (Butler, 1991):

$$\frac{T-T_R}{T_S-T_R} = e^{-\frac{U\xi}{\alpha}} \tag{2.48}$$

As it was described earlier, our visualization experiments revealed that this assumption is not widely accepted in the literature. The pore-scale intrusion of small droplets of water condensate as well as small bubbles of steam through the continuum of the mobile oil could transfer heat under the convection mechanism into the oil region based on direct visualizations presented in this thesis. Consideration of the convective element of the heat transfer makes this analogy much more complicated and no study was found in the literature that deals with the inclusion of the convection heat transfer mechanism in the quantification of the drainage rate of the SAGD process.

Combining Eq's 2.47 and 2.48, one can obtain a simplified relationship for "υ" (i.e. $\nu = \nu_S e^{mU\xi/\alpha}$), and then it can be plugged into Eq 2.46. Following the integration procedure, Eq 2.46 would result in:

$$q = \frac{kg\alpha \sin\theta_r}{m\nu_S U} \tag{2.49}$$

Using trigonometric relationships, "U" can also be defined as:

$$U = -\left(\frac{\partial y}{\partial t}\right)_x \cos\theta_r \tag{2.50}$$

The negative sign in Eq 2.50 is because of the fact that $\left(\frac{\partial y}{\partial t}\right)_x$ is negative. Substituting Eq 2.50 in Eq 2.49 and defining $\tan\theta_r = \frac{\sin\theta_r}{\cos\theta_r} = \frac{(\partial y/\partial t)_x}{(\partial x/\partial t)_y} = \frac{\partial y}{\partial x}$, Eq 2.49 would be summarized as:

$$q = -\frac{kg\alpha\frac{\partial y}{\partial x}}{m\nu_s\left(\frac{\partial y}{\partial t}\right)_x} \tag{2.51}$$

so:

$$-\frac{\frac{\partial y}{\partial x}}{\left(\frac{\partial y}{\partial t}\right)_x} = \frac{m\nu_s q}{kg\alpha} \tag{2.52}$$

The instantaneous horizontal position of the interface with respect to time (i.e. horizontal velocity of the SAGD interface at a particular elevation) can be defined as:

$$\left(\frac{\partial x}{\partial t}\right)_y = -\frac{\left(\frac{\partial y}{\partial t}\right)_x}{\frac{\partial y}{\partial x}} \tag{2.53}$$

Combining Eq's 2.52 and 2.53 results in:

$$\left(\frac{\partial x}{\partial t}\right)_y = \frac{kg\alpha}{m\nu_s q} \tag{2.54}$$

The drainage rate of the mobile oil for half of the SAGD pattern per unit length of the horizontal well was defined by the following equation (Butler, 1979):

$$q = \sqrt{\frac{2\phi\Delta S_o kg\alpha(h-y)}{m\nu_s}} \tag{2.55}$$

Plugging in the equivalent of "q" from Eq 2.55 into Eq 2.54 and simplifying the relationship results in the following equation for the horizontal SAGD interface advancement velocity:

$$\left(\frac{\partial x}{\partial t}\right)_y = \sqrt{\frac{kg\alpha}{2m\nu_s\phi\Delta S_o(h-y)}} \tag{2.56}$$

Considering the theory of gravity drainage presented above, one can further analyze the experimental results obtained during the course of our SAGD visualization experiments.

2.5.5.1. Interpretation of the SAGD Interface Advancement Velocity Data Using the Theory of Gravity Drainage

The theory of gravity drainage described in section 2.5.5 can be used in order to elucidate some important aspects of the SAGD interface advancement at the pore-scale. Considering Eq 2.56, it is evident that the rate of SAGD interface advancement in the horizontal direction is independent of the process time, i.e. the horizontal sweep rate is constant at each particular elevation. This point was also verified by the results of our SAGD visualization studies presented in section 2.5.3. According to Eq 2.56, if the SAGD trials would have been carried out in models with the same thermal properties and with the same in-situ bitumen, the horizontal interface advancement velocity at similar elevations should be proportional to the square root of permeability, and inversely proportional to the square root of porosity times the oil kinematic viscosity at the steady-state steam temperature.

Table 2.34 contains the operating conditions, oil properties at operating temperature, and physical properties of the employed glass micromodels for different SAGD trials. The parameter presented at the last column of Table 2.34 (i.e. $\sqrt{\frac{k}{\nu_s\phi}}$) was extracted from the theory of gravity drainage described in section 2.5.5 when the thermal properties of the porous media are the same, and similar oil properties were also assumed between different trials. This correlation coefficient is called the "SAGD performance parameter" at the pore-scale for our visualization experiments. It is evident that the higher the numerical value of this parameter is, the higher would be the horizontal SAGD interface advancement velocity. In Figure 2.48, the representative

interface advancement velocity for the SAGD trials 1 to 7 in both pores/min and mm/min units are plotted against the correlation coefficient described above. It is evident that an acceptable correlation exists between the SAGD pore-scale velocities and the SAGD performance parameter at the pore-scale defined based on the theory of gravity drainage.

Table 2.34: Parameters affecting the horizontal sweep rate of the SAGD interface based on Eq 2.56 and results of the SAGD visualization experiments at the pore-scale

Run No.	Model	k (D)	φ (%)	T_S (°C)	μ_o (cP)	ρ_o (g/cc)	ν_o (cSt)	$\bar{v}_p^{SAGD}$ (pores/min)	$\bar{v}_p^{SAGD}$ (mm/min)	$\sqrt{\frac{k}{\nu_s \phi}}$ [$\times 10^{-3}$ $s^{1/2}$]
3	DL1	94.61	32	103.10	243.425	0.957	254.405	0.282	0.576	1.078
2	OM2	92.42	32	103.40	240.431	0.957	251.321	0.228	0.456	1.072
1	OM1	77.83	30	101.70	258.023	0.958	269.435	0.218	0.437	0.981
7	DC1	34.13	37	102.40	250.593	0.957	261.786	0.106	0.1695	0.594
6	OC1	56.16	42	101.20	263.497	0.958	275.069	0.176	0.358	0.697
5	OM2	92.42	32	110.20	183.300	0.953	192.386	0.300	0.599	1.225
4	OM1	77.83	30	116.35	145.445	0.949	153.219	0.379	0.757	1.301

The experimental results of run numbers 1-5 are presented in Figure 2.41 and details of the calculations are also presented in Table 2.29. As it is evident from the information presented in Table 2.29, the measured horizontal sweep rates of the performed SAGD processes in different models follow the logic proposed by the theory of gravity drainage. Run number 3 (i.e. DL-1 Model) has the highest SAGD pore-scale performance parameter while Run number 7 (i.e. DC-1 Model) has the lowest one. This is in agreement with the sweep rate data presented in Table 2.29.

Run numbers 2 and 5 in which model OM-2 was used as the porous medium could also be compared together based on the defined SAGD pore-scale performance parameter whose magnitude for run number 5 is higher than that of run number 2, so is its horizontal sweep rate at each particular elevation. This increase in the sweep rate is a direct result of the higher operating temperature of the SAGD process in run number 5 compared to that of run number 2 (refer to Table 2.31 and Figure 2.43). The same conclusion can be made by comparing SAGD pore-scale performance parameter of run numbers 1 and 4 in which model OM-1 was used as the porous

medium. According to Table 2.34, run number 4 achieves significantly higher performance parameter compared to run number 1, so its pore-scale interface advancement velocity should be higher than that of run 1 which is the case as could be seen in Table 2.30 and Figure 2.42.

The performance trends presented in Figure 2.44 could also be justified with the defined SAGD performance parameter and its numerical values presented in Table 2.34. As it is presented in Figure 2.44, RUNs 4 and 5 possess the first and second highest slopes compared to the other three presented trials, and this is in agreement with the numerical values of their performance parameter presented in Table 2.34 (i.e. 1.301 and 1.225 respectively). These two trials are followed by RUN 3 with the third highest performance parameter of 1.078 in which DL-1 model was used. The lowest sweep rates presented in Figure 2.44 belong to RUNs 2 and 1 in which OM-2 and OM-1 were used respectively at lower operating temperatures. These two trials have the lowest performance parameter as defined in Table 2.34 among the trials presented in Figure 2.44 (i.e. 1.072 and 0.981 for RUNs 2 and 1 respectively).

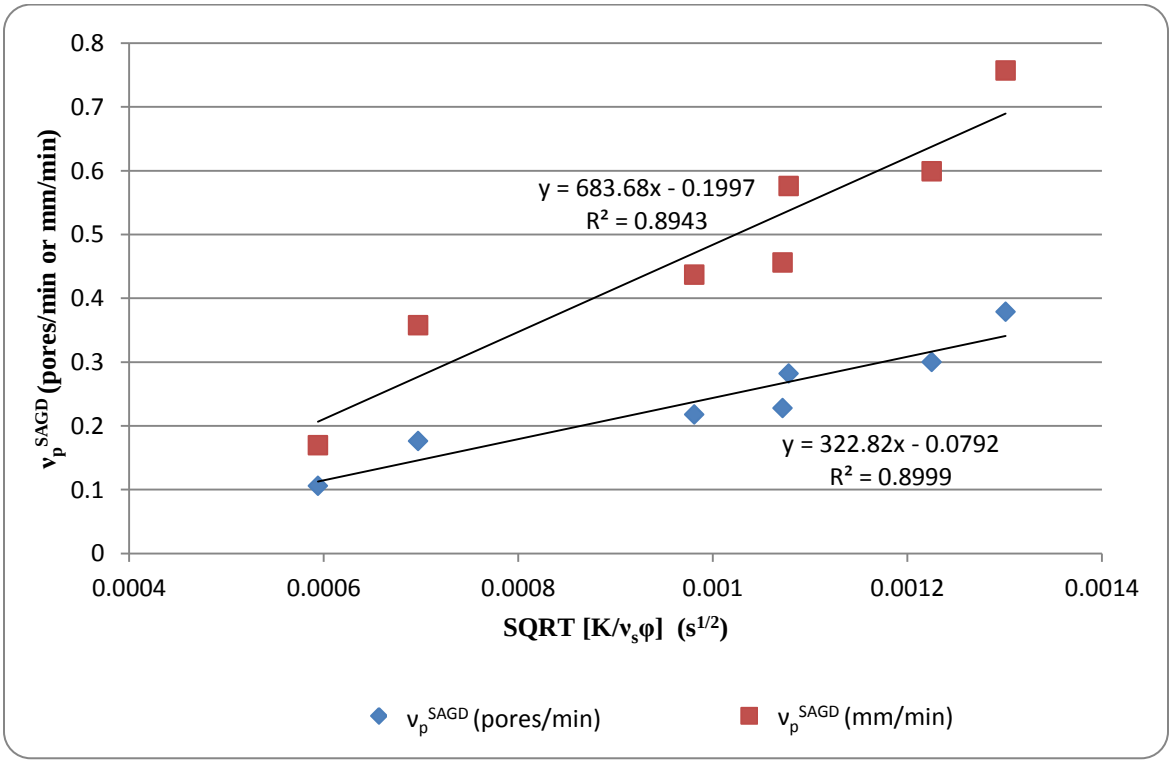

Figure 2.48: Correlation between the SAGD interface advancement velocities and the SAGD performance parameter at the pore-scale defined based on the theory of gravity drainage

2.5.5.2. Analysis of the CSOR Values based on the Theory of Gravity Drainage

In section 2.5.4.2, the cumulative steam to oil ratio for 7 SAGD experiments were calculated based on the volumetric measurements as well as interface advancement tracking at the pore-level. Table 2.33 contains the data used in order to calculate the CSOR values. In order to collapse the CSOR data associated with SAGD RUN No's 1 to 7 into a single graph, it is required to define a correlation coefficient to accommodate for the variations in experimental parameters such as permeability, porosity, and operating temperature. According to the theory of gravity drainage in a conventional SAGD process, the CSOR is proportional to the square root of kinematic oil viscosity at the steam temperature and is also inversely proportional to the square root of porosity multiplied by permeability when all other experimental variables remain unchanged.

Table 2.35 contains some information about the pore-level SAGD experiments including operating conditions, model properties, and calculated CSOR values. The last column in Table 2.35 is the scaling parameter by which the CSOR data of these SAGD trials were collapsed into a single graph as is depicted in Figure 2.49. As it is evident in Figure 2.49, all the CSOR values fit into a single graph reasonably regardless of their associated variabilities such as differences in the porous media properties as well as operating temperature. It turns out that the proposed scaling parameter is able to provide a very good linear correlation with the diverse range of the CSOR values when all other experimental variables remain unchanged.

Table 2.35: Parameters affecting the CSOR values of the SAGD process based on the gravity drainage theory and the SAGD visualization experiments at the pore-scale

Run No.	Model	k (D)	φ (Fraction)	T_S (°C)	μ at T_s (cP)	ρ at T_s (g/cc)	ν @ T_s (cSt)	CSOR (vol/vol)	$\sqrt{\frac{k\phi}{\nu_s}}$ [$\times 10^{-3}$ $s^{1/2}$]
3	DL1	94.61	0.32	103.10	243.425	0.957	254.405	5.90	0.345
2	OM2	92.42	0.32	103.40	240.431	0.957	251.321	5.97	0.343
1	OM1	77.83	0.30	101.70	258.023	0.958	269.435	9.20	0.294
7	DC1	34.13	0.37	102.40	250.593	0.957	261.786	13.28	0.220
6	OC1	56.16	0.42	101.20	263.497	0.958	275.069	10.05	0.293
5	OM2	92.42	0.32	110.20	183.300	0.953	192.386	4.91	0.392
4	OM1	77.83	0.30	116.35	145.445	0.949	153.219	5.66	0.390

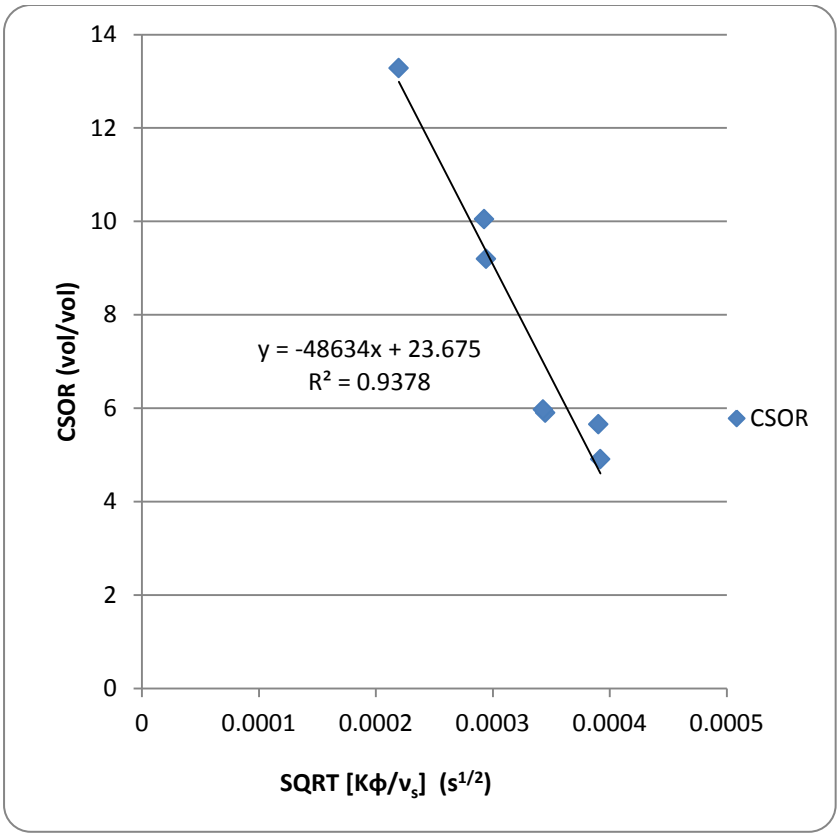

Figure 2.49: CSOR values versus the correlation coefficient for SAGD RUN No's 1 to 7

2.6. Conclusions

A series of flow visualization experiments were conducted using glass etched micromodels to mechanistically investigate the pore-scale aspects of the SAGD process. This visualization study indicates that:

- Periodic condensation of steam at the apparent pore-scale SAGD interface causes condensate build up ahead of the interface which is an indicator of the local heat transfer mechanism of the process at the pore-level. Direct drainage displacement of this condensate by the invading steam phase enhances local pore-scale mixing within the mobilized region ahead of the apparent pore-scale SAGD interface. Moreover, pores which are already filled with the mobile oil are cleaned up by a combined effect of direct drainage displacement of oil by condensate as well as by steam, and film-flow drainage displacement.

- Simultaneous three phase flow of steam, water condensate, and mobile oil was observed within the mobilized region, ahead of the apparent SAGD interface. Steam could be considered as the only truly non-wetting phase during this gravity drainage process. A series of simultaneous co-current and counter-current flow of phases is responsible for lateral encroachment of the steam-saturated zone.

- Periodic rupture of the oil films results in complete oil mobilization with very limited residual phase within the steam invaded zone.

- Small steam pockets, which remain in contact with the mobile oil-filled pores for long periods of time, enhance the local heat transfer process ahead of the apparent interface, followed by local steam condensation. The engulfment process of the water condensate droplets within the continuum of the mobile oil is responsible for the local water in oil emulsification at the pore level.

- According to the heat loss analysis performed in this section, it is concluded that the heat loss from the micromodels was only due to the radiation heat transfer mechanism. In other words, the employed heat loss prevention technique was successful in minimizing the convective element of the heat loss to the extent that it could be ignored at examined extremely-low environmental vacuumed conditions.

- Horizontal interface advancement velocity of the SAGD interface was measured in selected trials. It was found that the sweep rate is constant over the course of the process time at particular elevations along the height of the models. The magnitudes of the interface advancement velocities for different runs were correlated based on an analytical model proposed by Butler (1979, 1981, 1991) and a scaling parameter, so-called "SAGD performance parameter at the pore-scale" was defined based on this theory as well as quantitative results of our visualization experiments. The measured horizontal sweep rates of the SAGD process at the pore-scale are in good agreement with the theory predictions provided by the performance parameter.

- The ultimate recovery factors of the SAGD experiments were calculated using two approaches of direct measurement technique as well as SAGD interface tracking over the process time. The calculated values of the ultimate RF using these two methods are in good

agreement with each other. The effect of different experimental variables on the magnitude of the ultimate RF was also investigated. It was found that higher permeability values and lower in-situ oil viscosities lead to higher values of the ultimate recovery factor for a particular SAGD trial.

- For selected SAGD trials, the cumulative oil produced and cumulative steam injected were used in order to calculate the cumulative steam to oil ratio based on the volumetric measurements over the process time of each particular SAGD process. The analysis of heat loss was an integrated part of calculating the CSOR values in order to correct the total volume of steam injected for the volume which was consumed to cover the radiation heat loss from the model to the environment. A scaling parameter ($\sqrt{\frac{k\phi}{\nu_s}}$) was defined based on the theory of gravity drainage applied for the case of the SAGD process in order to correlate the CSOR values with the experimental variables. An acceptable linear correlation was obtained by plotting all the CSOR values versus the scaling parameter over the entire range of the experimental variables.

3. Insights into the Pore-Level Physics of the Solvent-Aided Steam Assisted Gravity Drainage (SA-SAGD) Process

3.1. Overview

Attempts were made to reduce the energy requirements of the SAGD projects through thermal and solvent hybrid processes. The augmented process brings superior features to the SAGD process in terms of reduced energy requirement, enhanced produced oil quality, and also improved oil recovery. The pore-level recovery mechanisms of the hybrid SAGD process has not been investigated in the literature. The main objective of this Chapter is to mechanistically investigate and document the pore-scale events in a hybrid SAGD process using glass micromodel type of porous media. The glass micromodels used in this study were the same as those used in the pore-scale mechanistic studies of the SAGD process described in detail in Chapter 2. As the general scheme of the hybrid SAGD process is similar to that of the SAGD process, similar process flow schemes were systematically used to investigate the pore-level mechanisms and performance of the Solvent-Assisted SAGD (SA-SAGD) process. Different additives (normal pentane and normal hexane) were added to steam prior to injecting into the models. Local temperatures along the model's height and width were measured and collected on a real time basis using a data acquisition system. Experiments were conducted in an inverted-bell vacuum chamber to reduce the excessive heat loss to the surrounding. An integrated data acquisition and control system was used to control, monitor and adjust the environmental vacuum pressure. The pore-scale events were videotaped and the recorded video and captured snapshots were analyzed thoroughly using image processing techniques. The relevant pore-scale mechanisms responsible for the in-situ oil mobilization and drainage in a SA-SAGD process were addressed. Transport and capillary phenomena at the pore-level in such a process were qualitatively documented including fluid flow, and heat and mass transfer aspects of the process.

The qualitative analysis of the results indicate that the gravity drainage process takes place within a pore-scale region, composed of 1-5 pores in thickness, in the direction perpendicular to the apparent oil-vapour mixture interface. This pore-scale region is called the SA-SAGD mobilized region. The interplay between gravity and capillary forces results in the drainage of the viscosity-reduced oil, whose viscosity was significantly reduced as a result of combined heat

and mass transfer at the micro-scale. Heat transfer is believed to take place through both conductive and convective mechanisms. The solvent content of the injected vapour mixture diffuses into the oil, hence reduces its viscosity following dilution as a result of molecular diffusion as well as convection. The visualization results demonstrated the coexistence of water-in-oil and solvent-in-water emulsification at the interface because of the local condensation of both steam and the solvent vapour. The extent of emulsification depends directly on the temperature gradient between the gaseous mixture and the mobile oil phase. Water in oil emulsion is believed to be formed due to the non-spreading nature of water over the mobile oil phase in the presence of a gas phase. When the solvent in the injected vapour mixture condenses in-situ over the colder bitumen surface, it could form another emulsion phase involving the solvent and water. The water condensate is the continuous phase of this emulsion due to its larger volume contribution.

Asphaltene precipitation was also observed when the condensed solvent reached the bitumen interface. Two pore-level displacement mechanisms were found responsible for mobilization of the diluted live oil, namely, 1) capillary drainage displacement, and 2) film-flow drainage displacement. As the nature of the process involves partially miscible displacements, the extent of film-flow drainage of the mobile oil was also significant. Other pore-scale phenomena include localized entrapment of steam and solvent vapour within the continuum of the mobile oil due to capillary forces followed by their subsequent condensation, relatively sharp temperature gradient along the mobilized region, snap-off of liquid films, steam and solvent vapour condensation at the interface because of the temperature gradient, and capillary instabilities.

Parametric sensitivity analyses were performed in order to quantitatively evaluate the SA-SAGD process performance at the pore-level within the range of experimental conditions using glass micromodels. Horizontal advancement velocity of the apparent SA-SAGD interface at the pore-scale was measured and then correlated with system parameters such as operating temperature, macroscopic and pore-scale properties of porous media, and heavy oil properties within the range of experimental conditions. As in the case of the SAGD process performance at the pore-scale, it was found that the representative sweep rate of the SA-SAGD interface at the pore-scale is a function of permeability and porosity of the model and kinematic viscosity of oil at the steam

temperature. It was also found that the sweep rate has some functionality with the pore-scale dimension of diffusion distance. This dimension determines the ease of diffusion of the solvent phase from one pore into the oil phase in the neighbouring pore at the micro-scale. This conclusion is in agreement with the one derived for the pore-scale performance of the VAPEX process (James, 2009). It is clear that the permeability and porosity of the glass micromodels are controlled primarily by a series of pore-scale dimensions such as pore-to-pore distance, pore throat size, pore body size, and depth of etching in the pore body and pore throat regions. In-situ oil viscosity is also a strong function of the operating temperature.

In this Chapter, qualitative and quantitative results of the SA-SAGD trials at the pore-scale are presented in detail based on the mechanistic visualization experiments at the controlled environmental conditions of extremely-low vacuum pressure.

3.2. History of the Solvent Aided SAGD Processes: Literature Review

It was believed that co-injection or alternate injection of a solvent along with steam could be an appropriate alternative for the steam-only processes. The idea of solvent additives in steam injection was introduced by Farouq Ali and Abad (1976). Mokrys and Butler (1993) compared the performance of the SAGD process with that of the SA-SAGD process and concluded that use of propane resulted in 30% reduction in steam requirements of the process. They also recovered about 99% of the injected propane at the end of the SA-SAGD process in the blow-down stage.

Use of propane as the light hydrocarbon additive in the steam phase was well studied in the literature (Gotie et al, 2001; Mamora et al, 2003; Fergusen et al, 2001; Rivero J.A. and Mamora, 2002). According to these studies, a preliminary start-up stage was conducted in which superheated steam injection resulted in creation of a limited hot region, especially at the proximity of the injection well. This preliminary injection procedure reduced the start-up duration of the process. Steam and propane were then co-injected which resulted in enhanced production performance and reduced energy requirements of the solvent aided thermal process.

Considering general aspects of the SA-SAGD processes including solvent selection criteria, operational conditions and injection scheme, these hybrid SAGD processes could be divided into three main categories which are briefly described in this section.

3.2.1. Expanding Solvent-Steam Assisted Gravity Drainage (ES-SAGD)

This method was proposed and patented by Nasr and Isaacs (2001) as a modification to the conventional SAGD method. This process was successfully field-tested and the results were promising in enhancing the Oil to Steam Ratio (OSR) and recovery rates, thus reducing the energy intensity and water requirements of the process compared to a conventional SAGD process. In this recovery technique, a small concentration of condensable hydrocarbon additive is co-injected along with the steam phase in a conventional SAGD pattern. There are some screening criteria to select the suitable solvent: for example, the boiling point temperature should match that of the steam phase at the operating chamber pressure. The higher the solvent carbon number is, the higher the vaporization temperature would be. This allows operators to select the appropriate steam additive among the hydrocarbon solvents. The steam additive should be kept in the gaseous state when traveling from the injection well until reaches the bitumen surface.

Experimental and numerical simulation studies proved that as the condensable hydrocarbon solvent becomes of heavier molecular weight, the resulting recovery performance is better; however, there is a local maxima in the production performance curve of the ES-SAGD process, as schematically demonstrated in Figure 3.1 (Nasr and Isaacs, 2001; Nasr et al, 2002 and 2003; Nasr and Ayodele, 2005; Nasr et al, 1991). In this Figure, the oil drainage rates are schematically plotted as a function of the difference between the steam temperature and solvent vaporization temperature. It is evident that the lower the temperature difference, the more effective the added solvent is. Solvents whose vaporization temperatures locate their local position on the curve between the two vertical dotted lines in Figure 3.1 appear to be more effective than the others. Thus the temperature difference range of the (-x) ºC to (+x) ºC could be considered as the favorable "ΔT_{Vap}" for the solvent and the steam phases in the ES-SAGD process.

3.2.2. Steam Alternating Solvent (SAS) Process

The SAS process involves alternate injection of steam and solvent phases using the same well configuration as that of the SAGD process. The idea is to replace the large amounts of steam injection in the SAGD process with solvent injection. Higher oil production rates with lower energy requirements can be achieved using this recovery scheme. The dew point temperature of the solvent should be somewhere between the initial reservoir temperature and the steam temperature. According to the schematic diagram of the SAS process presented in Figure 3.2, this process has a cyclic nature, starting with a certain start-up period (part a). The steam injection period (part c) will continue until the heat loss to the surrounding starts to increase, and then it is followed up by the solvent injection cycle (part b). The solvent injection cycles would then be stopped to prevent further temperature drop in the chamber.

The overall performance of the SAS process was verified with both experimental and simulation studies (Zhao, 2004; Zhao et al, 2005). Experimental studies of the SAS process revealed that this process results in lower average oil production rates than those of the analogous SAGD process. However, numerical simulation results revealed that it is feasible to achieve average oil production rates and cumulative oil production comparable with, or even higher than those of the conventional SAGD process. This is due to the enhanced mobility of the live oil attained at the interfacial region in the SAS process compared to that of the conventional SAGD process. Although the mobile oil viscosity is lower in the conventional SAGD compared to that of the SAS process, the oil relative permeability is more enhanced in the SAS process as a result of substantially lower water saturation compared to the conventional SAGD process.

Numerical simulation results showed that only a portion of the swept area of the SAS process is at the steam temperature and there are significant temperature variations within the depleted region (Zhao, 2004; Zhao et al, 2005). Presence of irregularities in the temperature distribution within the invaded area of a SA-SAGD process was also observed during the course of the visualization experiments in my study. Although some localized spots within the invaded area reach the injection temperature in a typical SA-SAGD process especially during the outward encroachment of the chamber, there were still significant temperature gradients near the mobilized region. Due to this relatively sharp temperature gradient across the interfacial region

of the SA-SAGD process (i.e. in the order of 30-40 °C obtained in our visualization experiments under prevailing operational conditions), the solvent content of the injected phase tends to move ahead of the steam phase and condense over the bitumen surface based on its lower dew point temperature compared to that of steam. It is also possible to experience some pore-level temperature gradients even through the invaded area. This is due to a series of parameters such as presence of bypassed oil region, presence of clogged pores with precipitated asphaltene, localized entrapment of the water condensate ahead of the mobilized region, and the heat loss from the invaded region to the surrounding environment.

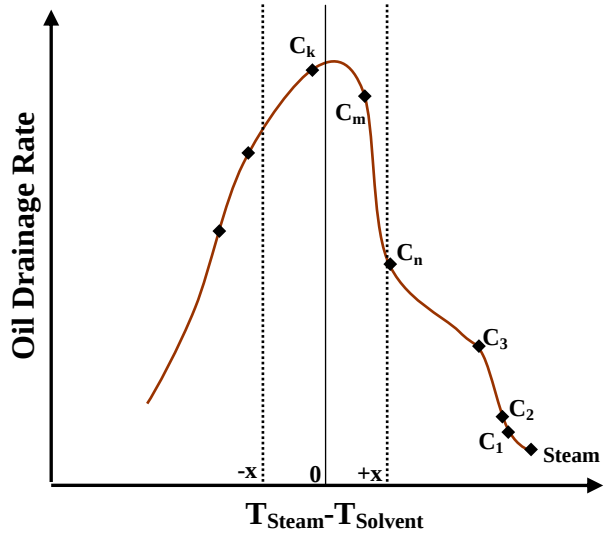

Figure 3.1: Schematic representation of the ES-SAGD process performance as a function of the vaporization temperature difference (Modified from Nasr and Ayodele, 2005; Nasr et al, 2002)

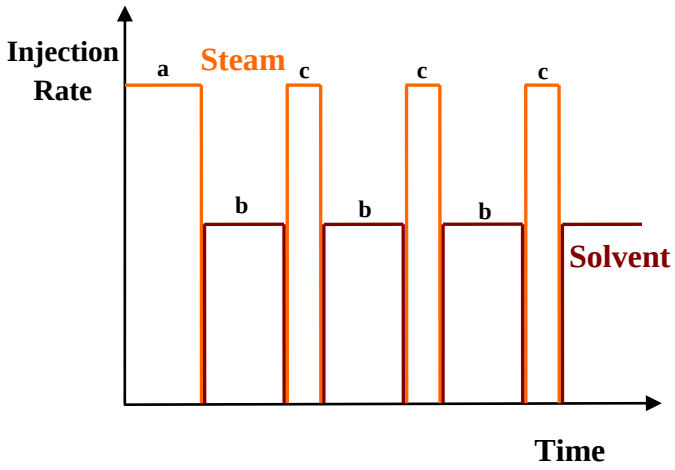

Figure 3.2: SAS injection process pattern (Modified from Zhao 2004)

3.2.3. Solvent Aided Process (SAP)

The main purpose of this process is to add small amounts of light hydrocarbon solvent (such as propane or butane) into the steam phase in a conventional SAGD configuration and use the combined effects of solvent dilution along with the thermal heating. The injection procedure is initiated with the conventional SAGD start-up phase in which steam is circulated through the

horizontal well pair. Co-injection of steam-solvent mixture is started after expiry of a certain initial period in the life of the normal SAGD cycle, first to commence an initial communication between the paired horizontal wells and second to allow for the development of initial steam chamber. The solvent-steam mixture should be injected in the vapour state with sufficient thermal energy content such that most of the solvent in the chamber remains in the vapour phase as it moves with the steam phase toward the condensation front. Although other solvent-aided modifications of the SAGD process also enhance its overall performance, it seems that SAP performance is better in comparison, based on the numerical simulation studies as well as field implementation of the process (Gupta et al, 2002, 2003, and 2005; Gupta and Gittins, 2005, 2006; Boyle et al, 2003; McCormack, 2007).

There are some limitations in other modifications of the SAGD and VAPEX processes, which challenge their technical merits as well as their economic viability. For example, in the case of the ES-SAGD process, it was suggested that a hydrocarbon solvent (or a mixture of solvents), whose condensation characteristics match that of the steam phase at the operating conditions, is co-injected with the steam phase. However, a simple light hydrocarbon solvent could be used in SAP instead of expensive solvent mixtures, without any need to match the condensation-vaporization characteristics of the solvent and steam phases. Moreover, it is unnecessary to support the chamber pressure with a non-condensable gas in SAP as it is required in some variations of the VAPEX process.

The SAP was successfully field tested and promising results regarding the increased production rates as well as reduced steam requirements compared to those of the conventional SAGD process were achieved based on the pilot tests and the numerical simulations (Gupta et al, 2002, 2003, and 2005; Gupta and Gittins, 2005, 2006). Numerical simulation studies showed that higher production rates could be achieved using lighter hydrocarbon solvents and also larger solvent to steam ratios at the injection side. In addition, the lighter the solvent and the higher its concentration is, the lower would be the energy intensity of the SAP.

3.3. Experimental Aspects of the SA-SAGD Visualization Experiments

3.3.1. Model Design and Preparation

It was decided to follow similar procedures for the pore-scale visualizations studies of the SA-SAGD process as those performed for the pore-level mechanistic studies of the SAGD process described in Chapter 2. Three glass-etched micromodels were used in these experiments and the detailed characterization of these models is presented in section 2.5.1. A summary of the important characteristics of these models is presented in Table 2.1. A close-up of one of these models (i.e. DL-1 Model) is also presented in Figure 2.4.a. Details of design and saturation steps of these models are discussed in section 2.3.1.

3.3.2. Experimental Setup

The process flow diagram of our SA-SAGD visualization experiments at the pore-scale is schematically presented in Figure 3.3. A closed-system capable of generating steam and solvent vapour and subsequent injection of the vapour mixture into the micromodels was designed and assembled as the injection supply facilities. All the tubing connections were either heated or insulated to maintain a vapour mixture of steam and solvent under superheated conditions and also to avoid the injected gaseous mixture from being condensed within the transfer lines. Liquid water and liquid solvent phases were pumped under pre-determined volume fractions using high-precision, low discharge rate FMI LAB Pump (Models RP-G400 and RP-SY) and an ISCO Pump accordingly. A band heater and a coil heater were used to generate the gaseous phases. The heaters' input powers were set based on the volumetric pumping rates of the liquids in such a way to generate superheated vapour state at their outlet lines. The superheated steam and superheated solvent vapour were then mixed together in an injection line while being heated to maintain the superheating state of the gaseous mixture. The micromodel was then connected to the supply flow line of the superheated gaseous mixture at the injection spot. The gaseous mixture was allowed to enter the micromodel at the top and to fill the trough all the way down on one side of the pore network. A preliminary start-up procedure was implemented at the beginning of each experiment in order to mobilize the oil phase within the pores adjacent to the trough. During this start-up phase, only steam was injected through the injection line and it was then produced directly from the production end. During this period, steam is introduced to the

pores connecting to the trough which are still filled with bitumen. After a while, the production metering valve was closed to avoid steam breakthrough from the production port. Injecting the solvent vapour into the steam injection line was then started and continued up until the end of the SA-SAGD process. To avoid any gaseous mixture from escaping out of the micromodel, a finite head of the drained liquids (i.e. condensed steam at the beginning, and water condensate and mobile live oil when the process proceeded) was accumulated continuously inside the ⅛" Teflon tube production line. This prevented the breakthrough of the vapour phase. This column of the drained liquid in the ⅛" Teflon tube was emptied occasionally by opening the metering valve at the production end.

Visualization experiments of the SA-SAGD process at lab conditions suffer from the excessive heat loss from the model to the surrounding environment. As a result of this heat loss, a considerable fraction of the injected steam and the solvent content which are supposed to condense on the cold surface of bitumen, condense in the invaded region of the porous pattern. This condensation process adversely affects the heat and mass transfer processes at the pore-scale. It results in condensate phase build-up in the invaded region (i.e. steam chamber). As a result, the continuous pathways of the injected vapour towards the interfacial region could be disrupted to the extent that the condensation rate exceeds the drainage rate from the model, hence the process could not be continued anymore. In addition, severe condensation of the solvent vapour phase results in extensive asphaltene precipitation once excess liquid solvent is in contact with the in-situ bitumen. This phenomenon of asphaltene precipitation, which was experienced in four of our visualization experiments, caused extensive pore-scale clogging of the drainage pathways and prevented the mobilized phases to drain in the direction of flow by gravity.

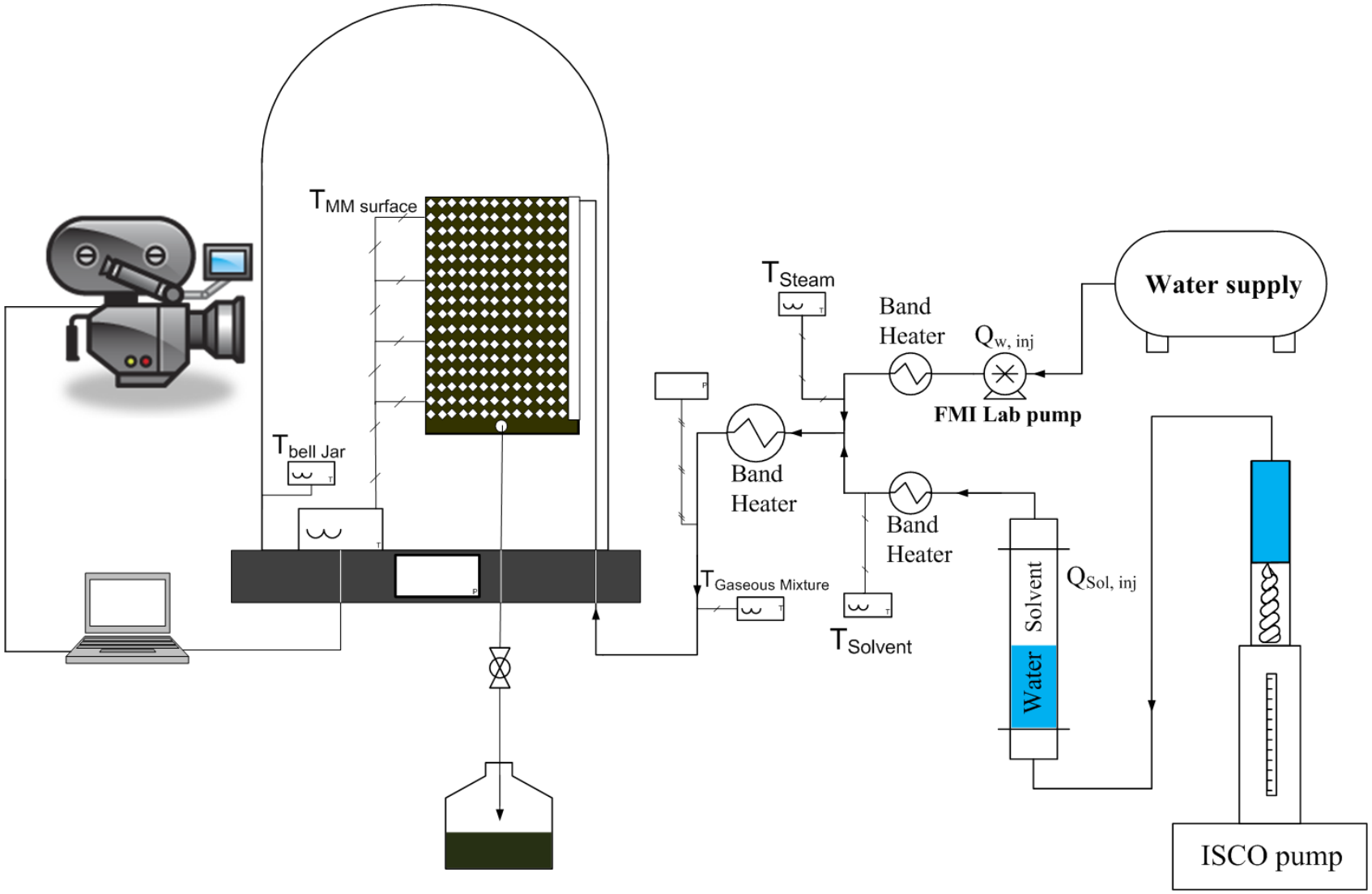

Figure 3.3: Schematic representation of the process flow diagram for the pore-scale visualization experiments of the SA-SAGD process

In order to minimize the excessive heat loss to the surrounding, an inverted-bell vacuum test rig capable of providing a limit of 10^{-6} torr of environmental air pressure was used as an environmental chamber. All the SA-SAGD visualization tests were carried out inside this vacuum test rig to make sure that an effective local heating of the bitumen-saturated micromodel in the absence of an undesired heat loss is performed. The vacuum chamber was operated with a combination of a mechanical and a diffusion pump. A snapshot of the employed vacuum test rig is provided in Figure 2.4.b. The range of operating vacuum pressure inside this chamber was $5\times10^{-6} – 10^{-4}$ torr for our visualization tests. At this extremely-low environmental air pressure, it is believed that the amount of heat loss from the glass surface into the surrounding environment by the convection mechanism is negligible and radiation mechanism of heat transfer is responsible for the heat loss during our experiments. The radiation heat loss mechanism was also reduced by covering the hot spots of the micromodels with strips of aluminum foil. Operating the SA-SAGD experiments at low values of the environmental chamber pressure prevents the condensation of the vapour phase as a result of excessive heat loss within the invaded region of the micromodels. It also allows the steam and the solvent vapour phases to transfer their latent heat of condensation to the cold bitumen surface, where it is intended to take place. This also enhances the mass transfer process between bitumen and the solvent phase by keeping the interface temperature at a higher value.

3.3.3. Operational Conditions and Measured Parameters

The operating temperature of the conducted SA-SAGD experiments is dictated by the solvent properties, its associated concentration in the injection main stream, and the volumetric pumping rates of water and solvent. Table 3.1 contains the range of experimental conditions for the performed SA-SAGD experiments which are categorized according to the type of solvent used in each particular trial.

The observed pore-scale phenomena of the SA-SAGD process during the flow visualization experiments were video recorded. Digital images were captured from video recordings at various stages of the process. The images captured were used to document the microscopic events for this recovery technique. Pore-level phenomena on close-up view were captured using a Canon video camera with appropriate combinations of three close-up focusing lenses (+2, +3, and +4).

This made it possible to have a particular region containing a few pores in view as can be seen in Figures presented in this Chapter. The micromodel was positioned close to one curved side of the inverted bell jar of the vacuum chamber. In order to reduce the reflective problems of the curved glass walls of the chamber and to minimize the parallax, a flat glass or Plexiglas sheet was placed in front of the camera opening to improve image clarity. The micromodel's surface was divided into cell blocks using a pen marker to facilitate the frontal position recognition within the porous structure. This made it feasible to track the interface advancement in terms of the number of pores invaded by the vapour phase. The data collected during each experiment included the following:

a) Continuous tracking of the vapour-bitumen interfacial position: The average position of the interface within each particular cell block, in terms of the number of pores invaded, versus experimental runtime was measured.

b) Video-recording the overall shape of the vapour-bitumen interface for the entire model. Digital images were taken whenever appropriate.

c) The pore-scale events were continuously video-recorded / digitally imaged.

d) Volumetric rate of solvent and steam injection were closely monitored in terms of pumping volume of the cold liquids versus time.

e) The surface temperature of the glass micromodels were continuously monitored on a real-time basis using surface thermocouples at 15 local positions along the surface. The temperature data was collected using a data acquisition system for each particular trial.

f) The vacuum pressure applied as an environmental housing was continuously monitored.

g) Final recoveries of liquids for some experiments were measured.

h) Temperature of the generated vapour mixture (i.e. steam and solvent vapour) at the injection side was continuously monitored.

i) The operating pressure of the vapour injection line was monitored on a real time basis.

Table 3.1: Range of operating conditions for the visualization experiments using the SA-SAGD process	
Vacuum properties	
Vacuum pressure (torr)	$5\times10^{-6} - 10^{-4}$
Operating conditions	
Total operating pressure (atm)	1
Operating temperature (°C)	101-110
Solvent content in the injection main stream	
Normal pentane	5% and 15% (vol/vol)
Normal hexane	5% and 15% (vol/vol)
n-C_5 properties	
Molecular mass, g/mol	72.15
Normal boiling temperature, °C	36
Liquid density, g/cm³	0.626
Relative vapour density to air	2.5
Molecular mass, g/mol	72.15
n-C_6 properties	
Molecular mass, g/mol	86.18
Normal boiling temperature, °C	68
Liquid density, g/cm³	0.6548
Relative vapour density to air	3.0
Molecular mass, g/mol	86.18

3.3.4. Design of Experiments

The objective of conducting these pore-scale SA-SAGD visualization experiments was twofold: firstly, it was intended to mechanistically investigate the pore-scale aspects of the process based on the qualitative analysis of the results using image analysis techniques. Secondly, the pore-scale performance of the SA-SAGD process was quantified using parametric sensitivity analysis of the process variables. It was planned to correlate the pore-scale advancement velocity of the SA-SAGD interface with porous media properties, both macroscopic and pore-scale ones, as well as fluid properties. To achieve the latter objective, it is required to design the experiments accordingly considering appropriate design method and affecting system variables. Focusing on

the nature of the experiments in which several experimental factors affect the outcome of the process, the factorial experimental design approach was selected. It was expected that the SA-SAGD sweep rate at the pore-level would be a function of solvent type, solvent concentration in the injecting stream, porous media properties, and oil properties. Therefore, four major factors of solvent type, solvent volume fraction in the injected stream, porous media properties, and oil type with different viscosity values were considered for the SA-SAGD visualization experiments.

Two solvent type levels of normal pentane and normal hexane were considered for the current study. Three glass micromodels, namely, DL-1, OM-1, and OM-2 were used in these experiments. Two solvent volume fractions of 5 and 15 % vol/vol of the injection stream were considered to be the different levels of solvent concentration. As for the oil type, Cold Lake bitumen and Lloydminster heavy oil blend were used in our pore-scale SA-SAGD experiments. Considering all these experimental factors and levels, the pore-scale SA-SAGD experiments were designed as presented in Table 3.2.

The variability in porous media properties includes the combined effect of porosity, permeability, and other pore-scale dimensions. In order to minimize the number of planned experiments, it was tried not to consider the variability in the operating temperature into the design phase of these experiments by running them within an acceptable temperature range. Considering the operating temperature as one of the design factors of these experiments would have significantly expanded the number of required tests. As it is discussed in the quantitative analysis of the SA-SAGD process performance section, the variation in the operating temperature was controlled satisfactorily through the course of our visualization experiments.

Table 3.2: Design of experiments for the pore-level SA-SAGD visualization study

Standard Order	Run No.	Porous Medium	Solvent Type	Solvent Concentration (% vol/vol)	Oil Type
8	1	OM1	n-Pentane	15	CL bitumen
9	2	OM2	n-Pentane	15	CL bitumen
20	3	OM1	n-Pentane	15	L heavy oil
5	4	OM1	n-Hexane	5	CL bitumen
2	5	OM1	n-Pentane	5	CL bitumen
1	6	DL1	n-Pentane	5	CL bitumen
3	7	OM2	n-Pentane	5	CL bitumen
19	8	DL1	n-Pentane	15	L heavy oil
11	9	OM1	n-Hexane	15	CL bitumen
12	10	OM2	n-Hexane	15	CL bitumen
17	11	OM1	n-Hexane	5	L heavy oil
22	12	DL1	n-Hexane	15	L heavy oil
7	13	DL1	n-Pentane	15	CL bitumen
24	14	OM2	n-Hexane	15	L heavy oil
21	15	OM2	n-Pentane	15	L heavy oil
6	16	OM2	n-Hexane	5	CL bitumen
18	17	OM2	n-Hexane	5	L heavy oil
13	18	DL1	n-Pentane	5	L heavy oil
10	19	DL1	n-Hexane	15	CL bitumen
23	20	OM1	n-Hexane	15	L heavy oil
16	21	DL1	n-Hexane	5	L heavy oil
14	22	OM1	n-Pentane	5	L heavy oil
4	23	DL1	n-Hexane	5	CL bitumen
15	24	OM2	n-Pentane	5	L heavy oil

3.4. Qualitative Analysis of the Experimental Results of the SA-SAGD Trials

In this section, the qualitative analysis of the results of our SA-SAGD visualization experiments is presented in order to mechanistically investigate the performance of this heavy oil and bitumen recovery technique at the pore-level. The pore-scale visualization experiments of the SA-SAGD process at the controlled environmental conditions revealed several heat and mass transfer-related mechanisms in the vicinity of the apparent gaseous mixture-bitumen interface.

3.4.1. Pore-Scale Event Analysis: Early Growth of the Vapour Chamber and Its Gradual Outward Development

The presence of the high-permeable trough extended along one side of the micromodels provided the means of establishing early communication between the injection and production ports. All of the performed SA-SAGD experiments were initiated with a start-up period in which steam / steam-solvent was flowing through the high-permeable trough to mobilize the bitumen phase present in the pores connected to the trough, followed by simultaneous steam and solvent vapour injection. As soon as the bitumen phase achieved enough drainage mobility, the steam phase invaded through the vacated space of these pores, hence the early stages of the vapour chamber growth were initiated. Continuation of this localized invasion of the steam phase through these drained pores is the first sign of the early lateral propagation of the steam chamber, which becomes vapour chamber as soon as the gaseous mixture of steam and solvent is injected instead of the steam-only phase. These pore-level phenomena, which are supported by the temperature gradient in the absence of solvent injection during the start-up stage, could be seen in two successive pore-scale snapshots shown in Figure 3.4. Mobile oil drained out of these pores and steam invaded through them following the sequential behaviour of drainage type displacement in a pore during an immiscible displacement process (Chatzis and Dullien, 1983).

Similar to the case of the SAGD chamber development, the steam/solvent chamber in the SA-SAGD process at the pore-level could be defined by the continuum of the gas-invaded pores. The front of this chamber near the bitumen-filled pores is dendritic in nature during the early development stages of the chamber. The invaded pores by the vapour are well interconnected from the gas flow point of view; however, there is possibility of condensation at the tip of each contact point of the gas-invaded pores with the bitumen-filled pores. The local condensation of vapour could happen either in a pore constriction or within the entire pore body, resulting in creation of water condensate droplets or droplets of the liquid solvent. Figure 3.5 shows the development stages of the SA-SAGD vapour chamber when both solvent and steam phases are injected through the injection main stream. One can clearly observe the state of fluid distribution as well as the condensation phenomenon at the pore-scale through these subsequent snapshots. One can find several vertically- and horizontally-oriented pore constrictions which are filled either with the bypassed oil, or with the trapped non-wetting droplets of condensate ahead of the

interfacial region towards the invaded pores. The presence of these condensate droplets acts as a flow barrier which deteriorates the gaseous phase flow towards the interfacial region and hence decreases the rate of micro-scale mass transfer process.

One can recognize the different flow zones present in the vicinity of the apparent SA-SAGD interface. In the case of non-condensing SA-SAGD process, the pores adjacent to the apparent interface drain preferentially in the direction of gravity and form dead-end type of structures. As a result, the drainage of oil films could then be re-directed, which results in the creation of peaks-and-valleys configuration of the flow pathways at the apparent pore-scale interface such as those pointed out with dark red arrows in Figure 3.6. The presence of peaks-and-valleys type of interface pattern, which is presented by the fine-dotted tortuous red curve in Figure 3.6, could be avoided if continuous films of the mobile live oil exist at the pore-scale, as this is the case in the condensing mode of the SA-SAGD process (Figure 3.7). These finite-in-length continuous films of the mobile live oil flow down gradient just ahead of the apparent SA-SAGD interface, and fill the localized valleys to the extent of creating a relatively smooth apparent interface, oriented vertically under the action of gravity. This is shown by the fine-dotted smooth red curve in Figure 3.7. No matter what form is the apparent SA-SAGD interface, it is located just behind a layer of pores composed of 1-5 pores in thickness which is referred to as the "mobilized region".

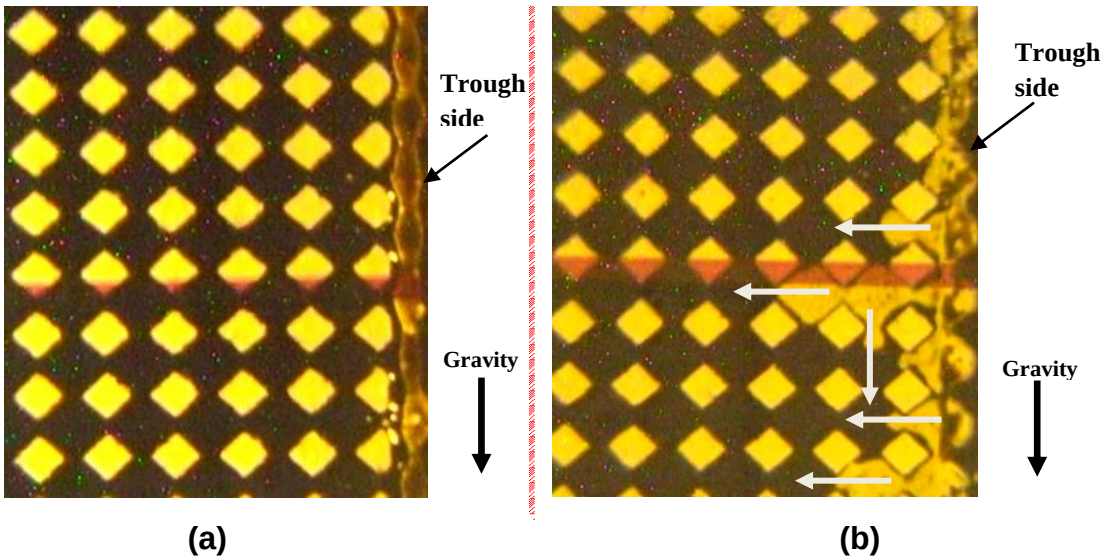

Figure 3.4: Early lateral propagation of the steam chamber during the start-up stage of the SA-SAGD process (RUN No. 19 start-up period, steam-only injection, DL-1 micromodel, average operating temperature of 103.45 °C, time interval: 2 minutes)

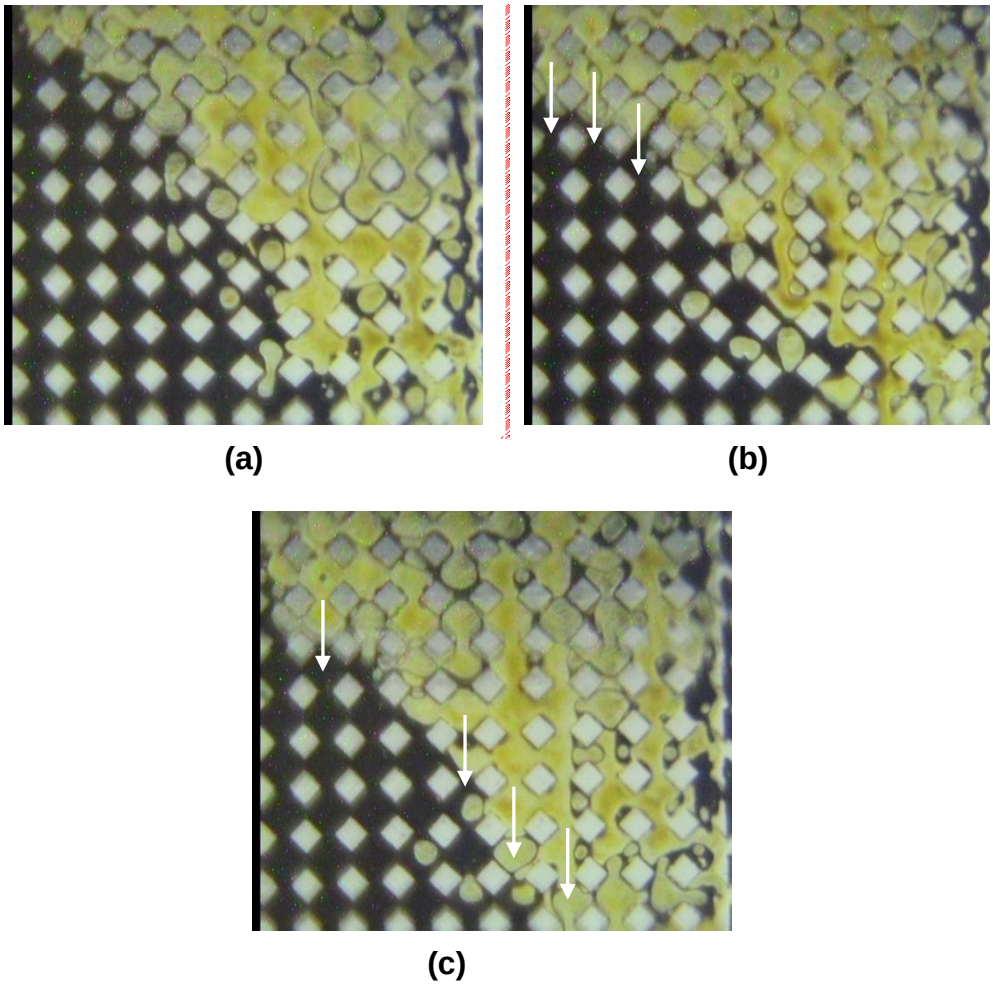

Figure 3.5: Development stages of the steam/solvent chamber in a typical SA-SAGD process at the pore-scale (Run No 1: OM-1 micromodel, n-Pentane as the steam additive at 15% vol/vol, average operating temperature of 103.30 °C, time interval: 240 sec)

3.4.2. Qualitative Pore–Scale Event Analysis within the Mobilized Region

The combined effects of thermal mobilization drive as well as solvent diffusion and convection create the mobilized region in which different interacting fluid phases are flowing simultaneously. The mobilized region contains different fluid phases, including:

a) Gaseous phase: A mixture of steam and solvent vapour, in the form of finite-pores-extended bubbles of the gaseous phase, flow through this region by convection.

b) Liquid phases: These phases include the condensed steam as the main liquid phase and the condensed solvent phase. The condensed solvent could be either in the form of localized liquid solvent in water emulsion phase (i.e. water as the continuous phase and liquid solvent droplets are dispersed due to the volumetric contrast of the liquids), or in the form of small liquid solvent droplets or in the form of finite-pores-extended films of liquid solvent diluting the bitumen phase.

c) Mobile live oil: Presence of this liquid phase depends on the viscosity-reduction process of the bitumen under the simultaneous heat and mass transfer phenomena at the pore-level. This liquid phase drains in the form of finite-pores-extended films of the mobile live oil over the bitumen-saturated pores under the action of gravity.

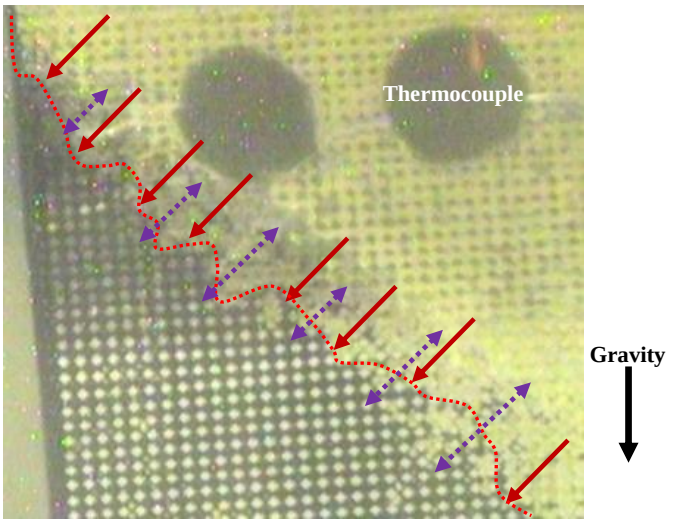

Figure 3.6: Visualization of the skeleton of the non-condensing SA-SAGD interface, flow pathways of the gaseous phase, and the mobilized region (Run No 16: OM-2 micromodel, n-Hexane as the steam additive at 5% vol/vol concentration, average operating temperature: 108.90 °C, time: 9050 seconds).

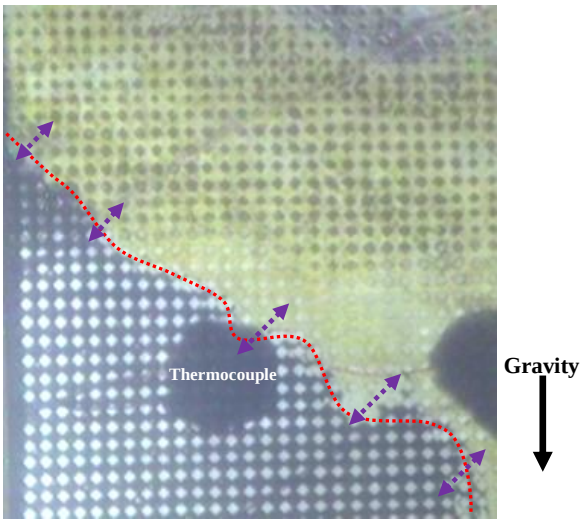

Figure 3.7: Visualization of the skeleton of the condensing SA-SAGD interface, flow pathways of the gaseous phase, and the mobilized region (Run No 10: OM-2 micromodel, n-Hexane as the steam additive at 15% vol/vol concentration, average operating temperature: 101.45 °C, time: 7055 seconds).

The draining phases (i.e. the mobile live oil as well as the water and solvent condensate phases) are flowing downwards and parallel to the apparent pore-scale SA-SAGD interface. The visualization experiments revealed that the thickness of the mobilized region varies at different particular elevations and is in the order of 1-5 pores in depth ahead of the apparent pore-scale SA-SAGD interface. In this region, whose thickness is shown by dotted purple arrows in Figures 3.6 and 3.7, most of the convective nature of the SA-SAGD process is observed to be in the form of intensive pore-scale local mixing in the vicinity of the apparent interface.

The average thickness of the mobilized region depends on several parameters such as operating conditions (i.e. temperature and pressure) as well as the solvent type. Most of the transport processes at the pore-level take place within the thickness of this region, including diffusion and convection mass transfer as well as heat transfer in the form of heat conduction and localized convection. Different acting forces are contributing to the simultaneous fluid flow within this region, namely gravity, capillary, and buoyancy forces in the absence of excessive viscous force. This mobilized region is mainly formed due to the presence of temperature gradient at the pore scale. The interfacial region clearly has an oriented structure, in which different draining fluid phases are flowing parallel to the apparent pore-scale SA-SAGD interface. Unlike the limited drainage depth of the live oil in the VAPEX process, which is in the order of 1-2 pores (James, 2009; James et al, 2008), the presented visualization results reveal that the depth of SA-SAGD mobilized region ($\delta_m|_{SA-SAGD}$) is at least 2 times thicker compared to that seen in the VAPEX process. This is due to the higher magnitude of the thermal diffusivity and convection as a measure of the extent of the heat transfer process, as well as the supplementary contribution of the solvent dilution phenomenon at the SA-SAGD process compared to that of the molecular diffusion only, which is responsible for the local mass transfer aspects of the conventional VAPEX process. This point could also be verified knowing the fact that the oil phase within the pores behind the SA-SAGD apparent interface, in a distance composed of 1-4 pore body widths, is mobilized due to the combined effect of the localized heat and mass transfer. As it is evident in Figure 3.5, the entrapped droplets of condensate and the enclosed bubbles of the gas phase drain within the oil continuum right behind the apparent pore-scale SA-SAGD interface.

Transport mechanisms involved in a SA-SAGD process include heat transfer by conduction and convection, mass transfer by molecular diffusion and convection, convective mixing of the gaseous phases and the liquefied phases with the mobile heavy oil, and gravity drainage of the viscosity-reduced oil along with the water condensate and the liquefied solvent. The mobile live oil and also the liquefied phases drain within the mobilized region by the action of gravity force when it overcomes the capillary and possible viscous forces. The predominant factor for the drainage of bitumen is the reduction of viscous drag due to the exponential reduction of the in-situ bitumen viscosity upon the combinatory effect of steam heating and solvent dilution. The role of gravity force and capillary force depends on the individual drainage mechanisms at the pore-scale. According to our flow visualization experiments, there are different pore-level fluid flow zones in a typical SA-SAGD process which are schematically presented in Figure 3.8. These flow zones were characterized according to the type and thermodynamic state of the fluids flowing in each particular region as:

a) Vapour chamber in which the injected gaseous phases are the predominant flowing phases. There is possibility of condensation through this region, followed by condensate drainage in the direction of gravity.

b) Bitumen-filled pores: Due to high viscosity of bitumen in this region, there is no mobility in these pores. The exact external boundaries of this zone near the vapour chamber could not be easily recognized when a film of the mobile live oil is draining over it. Heat is transferred to this zone across the apparent bitumen – mobile live oil interface by a combination of conduction and convection mechanisms. Engulfed-in-oil droplets of hot water condensate as well as isolated bubbles of the vapour phase are responsible for the convective element of the heat transfer at the pore-scale. Mass transfer by solvent from the gas phase occurs in this zone to a limited depth by the diffusion mechanism.

c) Mobilized region, whose thickness is expressed as $\delta_m\big|_{SA-SAGD}$ in Figure 3.8, is the region in which simultaneous flow of all the acting fluid phases is observed.

d) Mobile live oil film, whose thickness is expressed as $\delta^*\big|_{SA-SAGD}$ in Figure 3.8, is a sub-division of the mobilized region in which layers of the mobile live oil film are draining over the bitumen-filled pores. As soon as this liquid region attains appreciable thickness (i.e. in

the order of 1-2 pores) as a result of the miscibility nature of the SA-SAGD process over time, some small droplets of the condensed steam and solvent, as well as small gaseous bubbles could be enclosed within the thickness of this region and then are being dragged and drained along with the mobile live oil film in the direction of gravity.

The above-mentioned fluid flow zones are separated from each other with hypothetical distinction lines (or distinction surfaces when the 3D skeleton of the pore structure is concerned). According to the schematic diagram presented in Figure 3.8, the following interfaces are present:

- Apparent mobilized region–vapour chamber interface: This is a demarcation line (or demarcation surface) between the vapour invaded pores and the pores within the mobilized region at the microscopic scale.
- Apparent SA-SAGD interface: This is a distinction line (or distinction surface) between the pores in which the live oil phase is draining as a film over the bitumen-saturated pores and the pores in which all the interacting phases are draining simultaneously (i.e. mobilized region). This microscopic interface is defined to be between the mobilized region and the mobile live oil film.
- Apparent bitumen–live oil interface: This demarcation line is defined as the pore-level interface separating the bitumen-saturated pores and the pores in which the mobile live oil is flowing as oil films. It is extremely difficult to distinguish between these two regions even at the magnified pore-level snapshots. The extent of the mobile live oil film flow over the bitumen-saturated pores could cause periodic thickening and thinning of the oil wedge which could be recognized through the pore-scale snapshots and the recorded video.

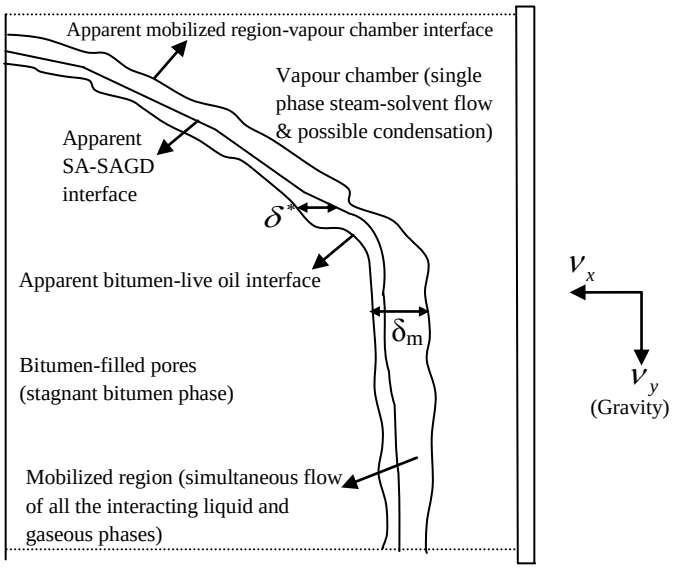

Figure 3.8: Schematic pore-level diagram of fluid flow zones in a typical SA-SAGD process based on our qualitative flow visualization results.

3.4.3. Pore-Scale Drainage Mechanisms

The term "live oil" could be assigned to the oil phase at the pore-level in which one can find a finite concentration of solvent. Part of this live oil could drain as its viscosity is reduced to the extent of mobilization under the action of gravity, which is named "mobile live oil" film, whose thickness is defined as $\delta^*|_{SA-SAGD}$. Figures 3.9 and 3.10 present a closer look at the mobilized region at the pore-level. Figure 3.9 shows the pore-scale contact of the gaseous phase with the oil phase just at the apparent pore-scale SA-SAGD interface, i.e. all the pore bodies below this particular location contain only oil phase. One can see the condensation phenomenon at the tip of the invading gaseous phase, as well as the bypassed oil within some pore throat constrictions. Some of the bypassed oil drains in the form of film flow in the corners of pores which are already invaded by the gaseous phase. In addition, droplets of condensate ahead of the invading gaseous phase are engulfed within the continuum of the mobile oil phase as is indicated by solid red circle in Figure 3.9. The dotted red ellipses show the locations where an isolated droplet of condensate is being formed due to the snap-off mechanism. Tiny bubbles of the gaseous phase could also be encapsulated by the continuum of the mobile oil as are depicted by white arrows in Figure 3.9.

Figure 3.10 shows a closer look at the extension of the mobilized region of the SA-SAGD process. Red arrow shows the vertically-oriented film flow drainage of the mobile live oil in the presence of the gaseous phase. One can clearly see the distribution of all three flowing phases within this pore-scale snapshot. In Figure 3.10, all the aforementioned flow zones of a typical SA-SAGD process at the pore-level could be observed such as the mobilized region followed by the gas-invaded pores to the top right corner of the Figure, the apparent SA-SAGD interface, and the oil-saturated pore bodies behind the apparent pore-scale SA-SAGD interface to the bottom left corner of the Figure. It is clear that some small bubbles of the gaseous phase were trapped within the draining live oil (i.e. beneath the interface to the right), which are pointed out by the thin white arrows. In addition, enclosure of small droplets of condensate is also evident within the continuum of the mobile oil just behind the apparent interface (i.e. thick white arrows). Continuous drainage of these trapped bubbles and droplets is evidence that the oil phase behind the apparent SA-SAGD interface (to the left side of the Figure) within a limited distance in the order of 1-4 pore body widths is mobile enough to drain in the direction of gravity.

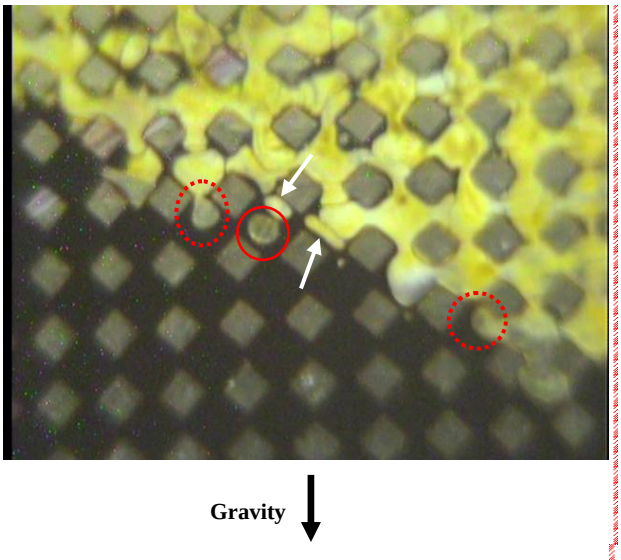

Figure 3.9: Vapour chamber in direct contact with the oil continuum at the pore-level (Run No 6: DL-1 micromodel, n-Pentane as the steam additive at 5% vol/vol concentration, average operating temperature of 106.80 °C, time: 6620 seconds).

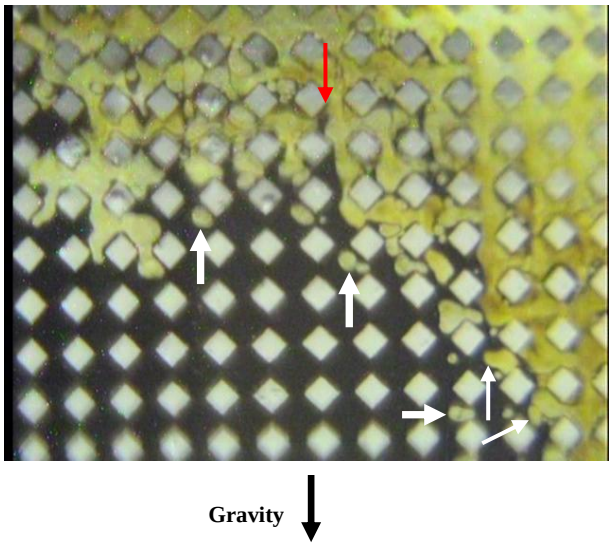

Figure 3.10: A closer look at the pore-level mobilized region of the SA-SAGD process (Run No 23: DL-1 micromodel, n-Hexane as the steam additive at 5% vol/vol concentration, average operating temperature of 108.30 °C, time: 6050 seconds).

According to the flow visualization results, two drainage mechanisms were found responsible for the pore-scale recovery of a typical SA-SAGD process, namely: 1) capillary drainage displacement mechanism, and 2) film-flow drainage mechanism. These two simultaneous mechanisms are responsible for displacing the already-mobile-oil with the aid of gravity and capillary forces within the mobilized region and the invaded area, and also through a limited distance behind the SA-SAGD apparent interface at the pore-scale.

3.4.3.1. Capillary Drainage Displacement Mechanism: This mechanism is responsible for most oil recovery during the SA-SAGD process. Under this displacement mechanism, a finite-pores-extended volume of the mobile live oil drains within the mobilized region ahead of the vapour-filled pores through the direct drainage of oil from the oil-filled pores by the invading gaseous phase according to the typical sequential drainage displacement of a wetting phase by a non-wetting phase at the pore scale (Chatzis and Dullien, 1983). This direct drainage displacement is facilitated with the aid of gravitational force in the absence of excessive viscous forces. The direct invasion of the gaseous phase through the pores which are already filled with the mobile oil creates extensive local pore-scale mixing within the mobilized region just ahead of the apparent SA-SAGD interface. This type of displacement is indicated by white arrows in Figure 3.4. In addition, Figure 3.5 provides a series of pore-scale events including sequential drainage displacement of wetting phase by the invading gaseous non-wetting phase in the direction of the white arrows over a four-minute time period. As the oil in contact with the gaseous phase is already heated to the extent of being readily mobile, consecutive direct drainage of several pores within the interfacial region is observed. This drainage mechanism is also shown in Figure 3.11 through five subsequent pore-level displacement images from snapshot “a” to “e”.

As is depicted in Figure 3.11, the gaseous mixture of steam and n-hexane vapour displaces the already mobile oil in the direction indicated by the thick white arrows. The invading non-wetting phase front is pinched-off in some pores by the snap-off mechanism while displacing the mobile live oil under the direct capillary drainage displacement mechanism. This snap-off phenomenon is due to the unstable nature of the advancing front of the non-wetting phase as well as capillary instabilities caused by the local pore structure (Chatzis and Dullien, 1983). As a result, small bubbles of the gas phase were enclosed within the draining column of the mobile oil. In Figure

3.11, these isolated bubbles of the gaseous phase and engulfed droplets of the condensate are shown by red and yellow arrows respectively. These enclosed phases drain downwards along with the live oil ahead of the invading front of the non-wetting phase. These frequently-occurring pore-scale events enhance the extent of both mass and heat transfer processes. The isolated gas bubbles can re-connect to the bulk of the gaseous phase (i.e. vapour chamber) if they maintain their gaseous state at the time of gas invasion into a pore containing live oil and a gas bubble. Aside from this re-connection scenario, these isolated bubbles could also condense while moving down gradient due to the excessive heat loss. An excessive volume shrinkage phenomenon due to the phase change was also observed which is an indication of the localized heat transfer process at the pore-scale.

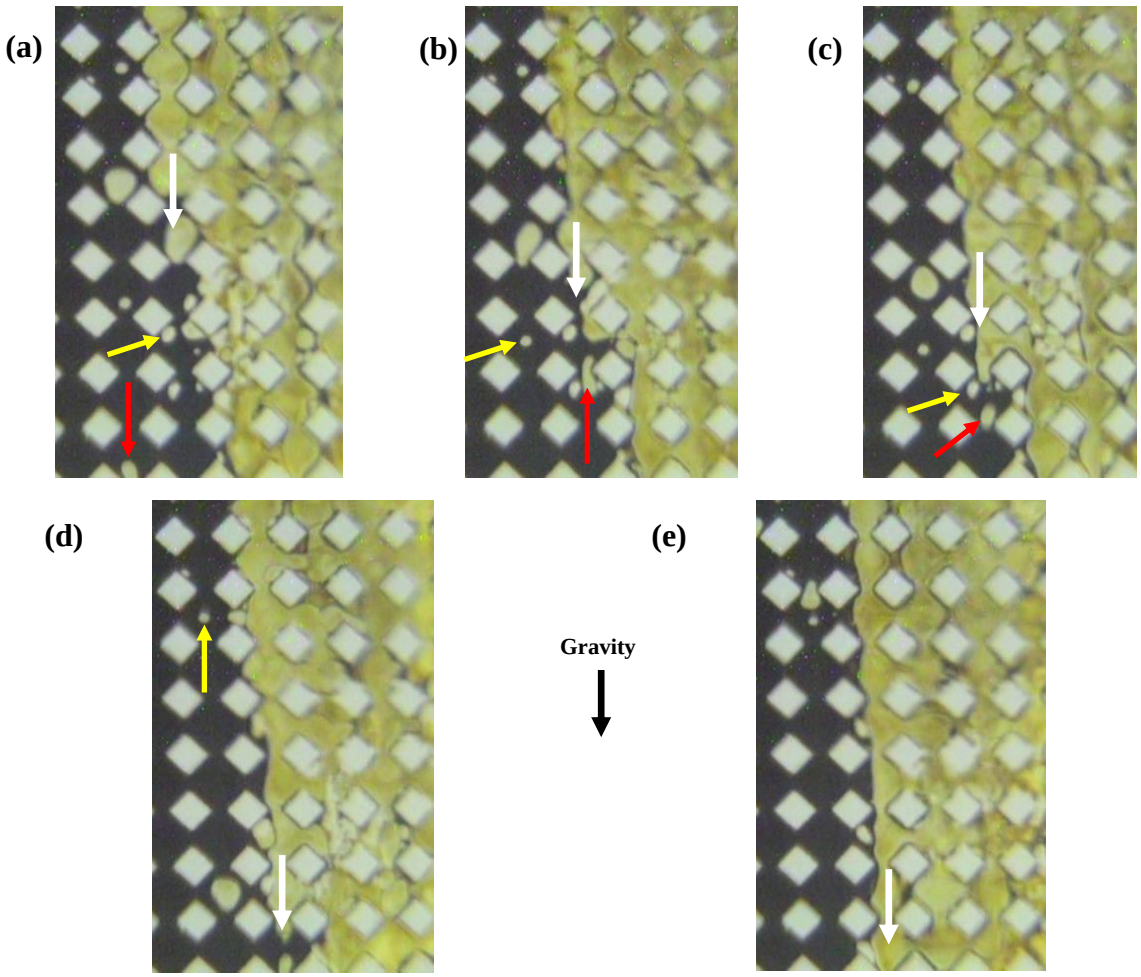

Figure 3.11: Sequential drainage of the wetting phase by the unstable invading front of the non-wetting gaseous phase under the direct capillary drainage displacement mechanism at the pore-level (Run No 23: DL-1 micromodel, n-hexane as the steam additive at 5% vol/vol concentration, average operating temperature of 108.30 °C, time interval: 180 seconds)

If a solvent condensate droplet is enclosed within the continuum of the mobile oil, its volume shrinks as a result of the local mass transfer at the pore-level. The enclosed solvent condensate droplet disappears over time because of the solvent diffusion and convection into the oil phase if an extended-enough drainage path is available within the live oil continuum. On the other hand, if a water condensate droplet is engulfed within the live oil phase, it could propagate within the oil continuum in the form of dispersed water phase in oil, composing the in-situ water in oil emulsion at the pore-scale. Figure 3.12 shows a series of events starting from the encapsulation process of the snapped-off liquid droplet at the pore-level (i.e. red arrow), followed by local mass transfer processes which cause the shrinkage of the enclosed droplet at static conditions where the droplet is stagnant within the pore body (i.e. white arrow). Finally, a coalescence stage exists for some droplets when the contracted condensate droplet is reconnected to the invading liquid front (i.e. yellow arrow).

3.4.3.2. Film–Flow Drainage Displacement Mechanism: The mobile and bypassed oil could drain as a result of film-flow drainage in the corners of the pore space that was already invaded by the gas phase. The extent of the film flow drainage is much more pronounced in a three dimensional porous medium compared to that in a simple 2D porous structure due to the pore interconnectivity and dimensionality. In a typical SA-SAGD process, this type of the drainage mechanism happens in the vicinity of the apparent SA-SAGD interface (i.e. within the mobilized region as well as inside the invaded zone). Periodic formation and rupture of the finite-in-length live oil films within the mobilized region is due to the convective nature of the drainage process at the pore-scale within this region. This factor limits the extent of film flow drainage within the mobilized region. However, one can observe the frequent thickening and thinning of the mobile live oil film in the corners of the gas-filled pores ahead of the apparent SA-SAGD interface within the drained zone of the porous structure. These draining live oil films could alternatively fill some downstream pore bodies or pore throats. As a result, the apparent pore-scale SA-SAGD interface becomes smoother in the form of a vertically-extended type of interface.

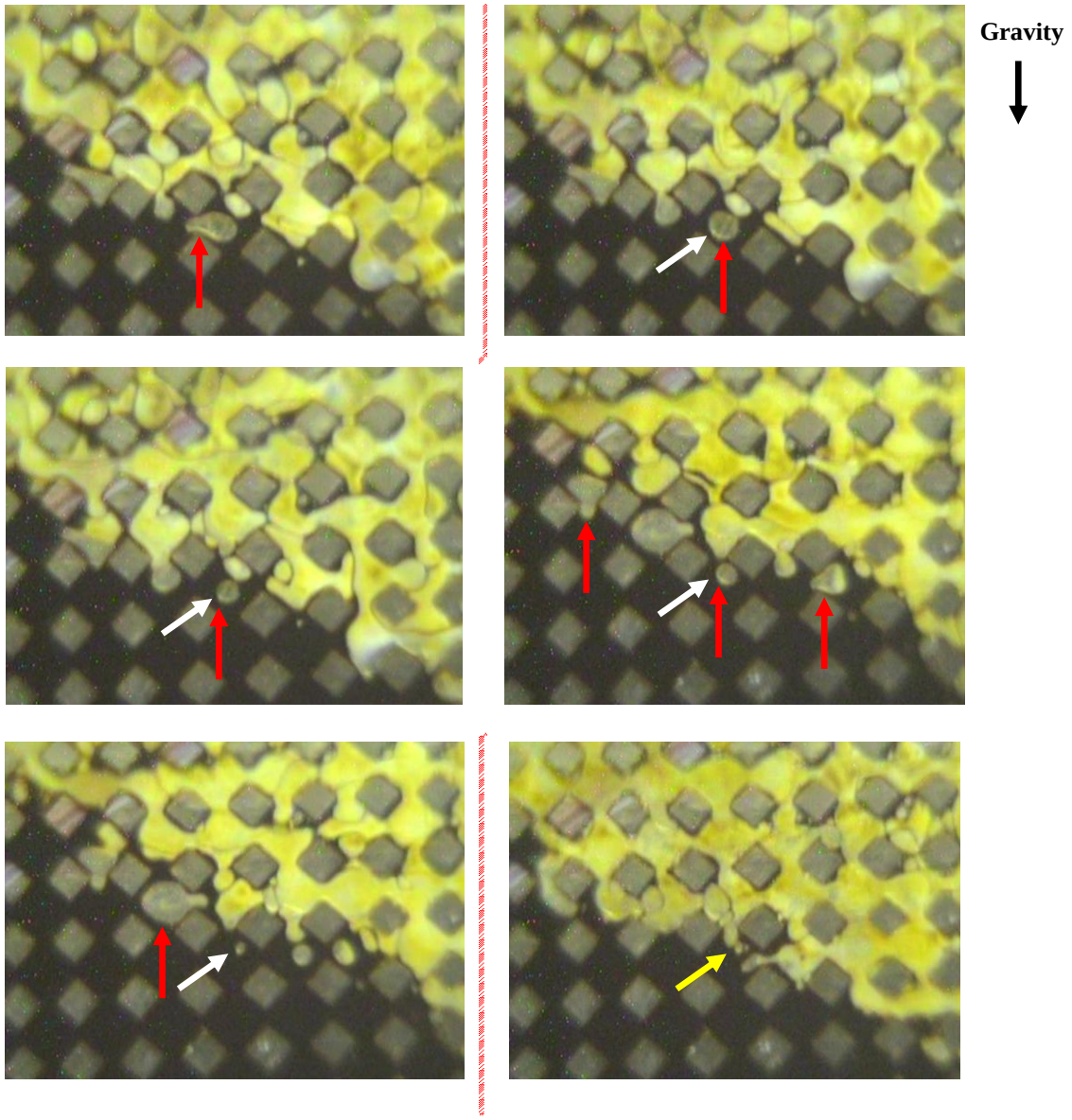

Figure 3.12: Snap-off mechanism occurred at the unstable invading front of the displacing liquid phase, followed by droplet shrinkage phenomenon at the pore-scale due to the local mass transfer process (Run No 6: DL-1 micromodel, n-Pentane as the steam additive at 5% vol/vol concentration, average operating temperature of 106.80 °C, time interval: 320 seconds)

According to the pore-scale observations, momentum transfer at the pore-level does not happen only in one vertical column of pores. Although the apparent SA-SAGD interface at the macro-scale looks like a continuous distinctive line (or surface) between the bitumen-filled pores and the swept region filled with the vapour phase, it contains numerous irregularities at the micro-scale in the form of peaks-and-valleys-type of interface. However, due to the film flow of the

mobile live oil over the apparent pore-scale SA-SAGD interface and the miscibility conditions in this process compared to that of the SAGD process, the extent of tortuousness in the interface is much less in the SA-SAGD compared to that in the SAGD. However, one could still observe some oil-filled pores protruding irregularly into the vapour-filled pores of the swept region of the SA-SAGD process. It is clear that these oil-filled pores contain mobile live oil draining down gradient mainly by the capillary drainage displacement mechanism.

As a result of the film-flow drainage of the mobile live oil in the pores invaded by the gas phase and also through the vertically-oriented mobile-live-oil-filled pore constrictions, the apparent interface between the vapour and the mobile live oil would be re-positioned from the junction of the mobile-live-oil-filled pore throats and the vapour-filled pore bodies to the vertical midway within the pore bodies which were filled previously with the vapour phase. This frequent re-positioning of the interface location, which shows itself in the form of repeated thickening and thinning of the interfacial layer, is evidence of the presence of extensive film-flow drainage at the pore-scale. The pore-scale events of the non-wetting phase bubble and droplet enclosure within the oil continuum during the direct invasion of a pore filled with the mobile live oil by the invading gas phase was described in section 3.4.3.1 where the relevant sequence of pore-level events was analyzed. The same sequence of events is also observed during the film-flow drainage mechanism at the pore-level. A finite bubble of the vapour phase occupying one to several pores or a droplet of the liquefied phase could be truncated as a result of the film-flow of the mobile live oil in the corners of a particular pore, or a series of pores, containing the non-wetting phase. This truncated non-wetting phase is isolated within the surrounding oil phase continuum whose main source is the drained films of oil. Subsequently, the entrapped non-wetting phase undergoes through a shrinkage/disappearance process at the pore-level either in a static or in a dynamic situation. In other words, this trapped non-wetting phase may: a) remain stranded if the drainage velocity of the surrounding mobile oil does not overcome the buoyancy forces applied if it is vapour, or b) flow downwards along with the surrounding mobile live oil. In either of these two cases, the shrinkage/disappearance process happens due to the heat and mass transfer processes at the pore-level. There is also the possibility of reconnection/coalescence of each particular entrapped non-wetting phase either with the continuum of the vapour phase in case it was an isolated vapour bubble or reconnection with the

other enclosed droplets of the liquefied phases in case if it was an isolated liquid droplet. In Figure 3.10, the downward facing red arrow shows the limited extent of film flow within the mobilized region. In addition, Figure 3.13 shows the extent of film-flow of the mobile live oil in the corners of gas-filled pores which leads to pore-refilling by the wetting phase.

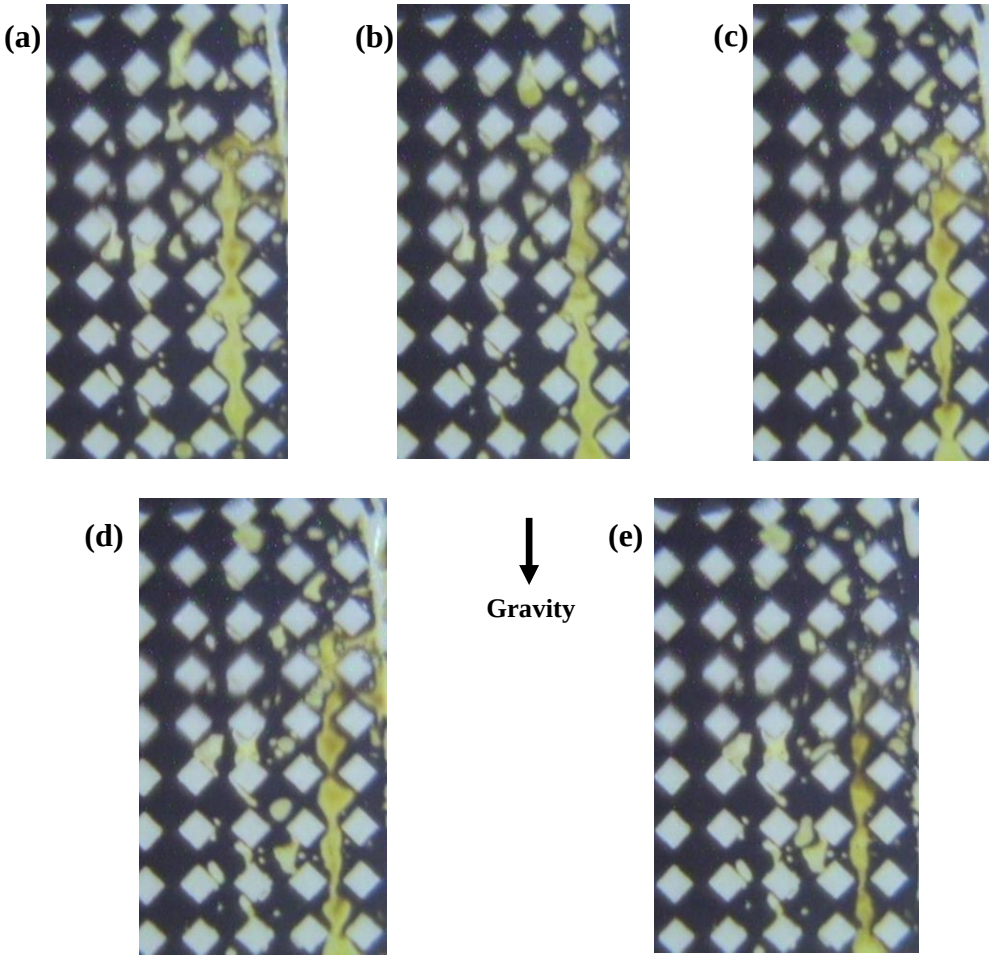

Figure 3.13: Film-flow drainage of the mobile live oil at the pore-scale during a time span of 52 seconds (Run No 16: OM-2 micromodel, n-hexane as the steam additive at 5% vol/vol concentration, average operating temperature: 108.90 °C)

The oil films left behind in the swept region could periodically form loop structures involving finite-in-size oil films within the continuum of the gaseous phase. If these oil films keep their inherent flow continuity over the limited distance of their extension, there is possibility of oil drainage under film flow drainage mechanism within the invaded area. The drainage rate of these

closed-loop oil films is lower than that of the bulk oil within the pores when displaced by the direct invasion of gas. However, the high degree of local mixing associated with the invaded area and the mobilized region as well as the miscible nature of the SA-SAGD process lower the residual oil saturation within the vapour chamber. These two factors usually do not allow sufficient flow continuity for the draining oil films ahead of the apparent SA-SAGD interface within the mobilized region. When these oil films attain enough continuity over their extension within the invaded area, then they are capable of creating some finite-pores-extended regions of mobile live oil within the swept region. The existence of these regions of draining live oil within the vapour chamber depends on the extent of the live oil film flow in the corners of the pores already filled with the vapour phase. The pore-scale mobilization process of these finite mobile live oil regions that appear to be by-passed, takes place through a combination of drainage and imbibition processes. The downwards-moving front of these mobile live oil regions advance down gradient by the imbibition process, imbibing into the vapour-filled pores ahead, while the trailing-end of these structures undergo displacements by the drainage mechanism.

3.4.4. Mass Transfer Mechanisms at the Pore–Scale

For a SA-SAGD process, the dominant pore-scale mobilization mechanism is due to the oil viscosity reduction by heat transfer and gravity drainage. Visualization studies of the SA-SAGD process reveal that there are complex interactions between all the flowing phases draining by gravity in the interfacial region. Mass transfer of the solvent phase into the live oil could take place by molecular diffusion, hydrodynamic mixing caused by capillary phenomena, and convection. It is evident that because of the convective nature of the process, especially within the mobilized region in which there is pore-level convective mixing, the role of the convective mass transfer is greater than that of the molecular diffusion. However, diffusion mass transfer still occurs along the drainage pathways of the flowing live oil phase. It is evident that the mass transfer mechanism in a solvent-aided heavy oil recovery process significantly depends on the thermodynamic state at which the solvent phase is in contact with bitumen. For instance, if the solvent condenses at the bitumen interface, the convection mass transfer from bitumen to the liquid solvent will significantly enhance the process of oil extraction. Depending on the "condensing" or "non-condensing" state of the solvent in contact with the bitumen phase, different mass transfer mechanisms appears to be more important (Rezaei et al, 2010). It is

believed that the overall performance of the SA-SAGD process would be enhanced only if the solvent condenses within the mobilized region ahead of the apparent SA-SAGD interface.

In a solvent aided recovery process, it is generally accepted that the mass transfer is carried out by diffusion and convection of the solvent phase present in the injected vapour phase as it transfers into the heavy oil and vice versa, based on the pore-scale concentration gradient present at the interfacial region. There is an exponential decline in the magnitude of in-situ viscosity of the bitumen phase due to the combined effect of heat and mass transfer. In Figure 3.14, the simultaneous effect of heat and mass transfer on the viscosity of Athabasca-type bitumen is presented (Badamchi-zadeh et al, 2009). It is evident that at constant propane weight fraction in the live oil, the viscosity decreases exponentially with an increase in temperature. It is also clear that at constant operating temperature, increasing the solvent mass fraction in the live oil would decrease the bitumen viscosity. Let's assume that the initial reservoir temperature is around 10°C, close to the typical temperature values of the Athabasca type reservoir. According to this Figure, the in-situ bitumen viscosity at this temperature is around 2,000,000 cP. At 90 °C, the bitumen viscosity is reduced to 300 cP just because of temperature in the absence of solvent dilution. However, if one assumes only 10.1 wt. % of propane in the live oil, the associated viscosity would be approximately 10 cP at 90 °C. This clearly shows the compound effect of heat and mass transfer on the viscosity reduction of bitumen. Each of these two transport processes could profoundly reduce the bitumen viscosity. As a result, the synergistic effects of convective/capillary mixing, and heat and mass transfer enhance the volumetric sweep efficiency of the SA-SAGD process at the pore-scale.

3.4.4.1. Microscopic Solvent Concentration Gradient

As the solvent chemical potential gradient across the interfacial region is the main driving force for the pore-level interfacial mass transfer in a solvent aided process of heavy oil recovery, it is important to analyze it for different typical recovery schemes. Three main in-situ bitumen recovery processes are schematically characterized based on different flow zones present near the interfacial area of each particular process. Figures 3.15.a to 3.15.c schematically show the solvent concentration profile across the interfacial area of three processes of VAPEX, SA-SAGD, and SAGD respectively. According to Figure 3.15.a, the solvent concentration within

the solvent chamber is 100% for the VAPEX process if the injected solvent is pure. There is a dramatic decline in the solvent concentration in the live oil at the live oil-solvent vapour interface ($\omega_{Sol}^{LO}|_{LO-V}$) to that of the live oil at the bitumen-live oil interface ($\omega_{Sol}^{LO}|_{b-LO}$). The former depends on the Vapour-Liquid Equilibria (VLE) of solvent/live oil pair and the k-factor which relates the solvent mole fraction in the vapour phase to the liquid phase solvent mole fraction in the live oil film at the interface, while the latter is close to zero at the stagnant bitumen face. In the VAPEX process, the maximum pressure applied through the invaded region in the absence of an inert gas is the vapour pressure of solvent that corresponds to the operating temperature. The VAPEX process could be categorized into condensing and non-condensing modes depending on the operating pressure and temperature which dictate the thermodynamic state of the solvent phase near the apparent VAPEX interface. In this Figure, the thickness of the live oil film draining over the bitumen-saturated pores is shown by δ^*.

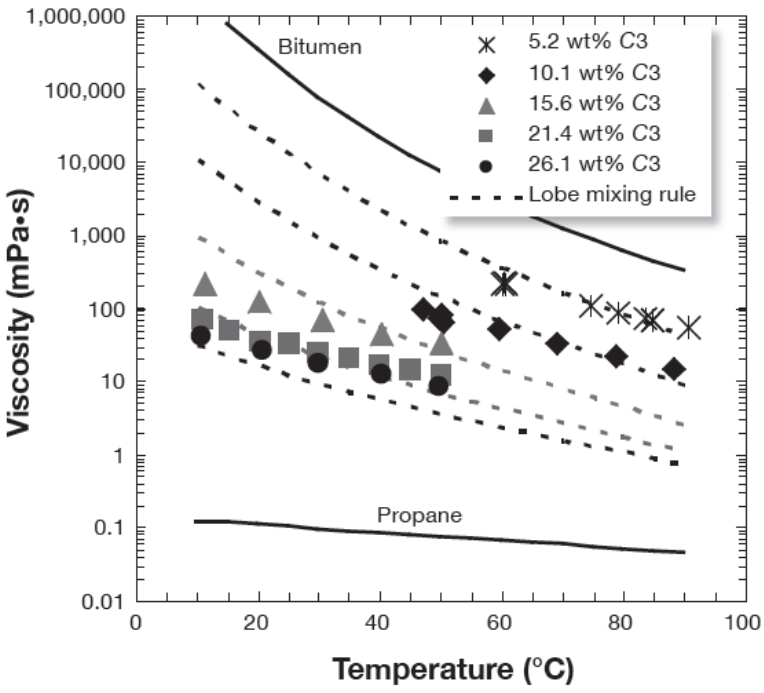

Figure 3.14: Viscosity reduction of Athabasca bitumen as a combined effect of heat and mass transfer (Courtesy of Badamchi-zadeh et al 2009)

Figure 3.15.b shows the schematic diagram of the solvent concentration in a typical SA-SAGD process. In such a process, the solvent concentration in the invaded area is limited to low values of solvent being injected along with the steam phase. As is shown in this diagram, there is a solvent concentration gradient near the mobilized region. This gradient is caused by the temperature gradient in the same region. As a result of this temperature gradient, steam is the first component to condense even before reaching the mobilized region. As a result, the steam concentration of the injected vapour experiences a gradual decline within the mobilized region. On the other hand, solvent concentration in the vapour phase increases significantly near the mobilized region-vapour chamber interface as it is the last component in the vapour phase to condense based on the temperature gradient present within the vapour chamber. Depending on the vapour-liquid equilibria of the solvent-steam-oil system at the apparent interface between the mobilized region and the vapour chamber, the solvent content of the live oil at this interface varies from the solvent content of the vapour phase at this interfacial region. There is a decline in the magnitude of the live oil solvent content from its value at the apparent mobilized region-vapour chamber interface (i.e. $\omega_{Sol}^{LO}\big|_{Mobilized\_region\text{-}V}$) to its value at the apparent mobile live oil film-mobilized region interface (i.e. $\omega_{Sol}^{LO}\big|_{LO-Mobilized\_region}$). This decline in the solvent content value in the live oil is continued, from its magnitude at the apparent mobile live oil film-mobilized region interface ($\omega_{Sol}^{LO}\big|_{LO-Mobilized\_region}$) to its value at the bitumen-mobile live oil film ($\omega_{Sol}^{LO}\big|_{b-LO}$) where the bitumen phase still contains some limited solvent content to the extent at which it could no longer be considered as the "raw bitumen". The finite magnitude of the solvent content of the bitumen phase at the apparent bitumen-mobile live oil film interface causes another decline in the live oil solvent concentration through the bitumen-filled pores. There is not a sharp step-change decline in the concentration of solvent at the apparent mobile live oil film-bitumen interface. The low solvent concentration beyond this interface makes the bitumen more of an "immobile live oil" phase rather than a "raw bitumen" phase. It means that at this low value of solvent concentration and relatively low local temperature, this layer of oil still remains immobile. This immobile live oil phase attains enough mobility upon further solvent and thermal energy propagation within this oil region as time goes on, and will eventually drain under the action of gravity later on.

Figure 3.15.c schematically shows the solvent concentration profile in a typical SAGD process. It is obvious that the concentration of solvent in the injected feed stream is zero. In addition, the mobile oil solvent concentration at the mobilized region-steam chamber interface ($\omega_{Sol}^{LO}\big|_{Mobilized\_region-S}$) as well as its corresponding value at the bitumen-mobilized region interface ($\omega_{Sol}^{LO}\big|_{b-Mobilized\_region}$) is zero.

Figure 3.15.d demonstrates the mole fraction profile for the steam and solvent vapour at a distance close to the interfacial region between the vapour chamber and the mobilized region in a typical SA-SAGD process. Assuming complete mixing of steam and solvent vapour through the invaded region, there would be no solvent concentration gradient within the invaded area except for the near interfacial region. It is clear that the mole fraction of either steam or solvent does not change with position when it is far away from the mobilized region interface where the temperature is constant. Due to the decreasing trend of the temperature profile in the vicinity of the vapour chamber-mobilized region interface, the mole fraction of steam in the gaseous phase decreases while approaching this interfacial region (i.e. position "b" in Figure 3.15.d); however, there is a significant increase in the mole fraction of solvent in the vapour phase in the vicinity of this live oil interface.

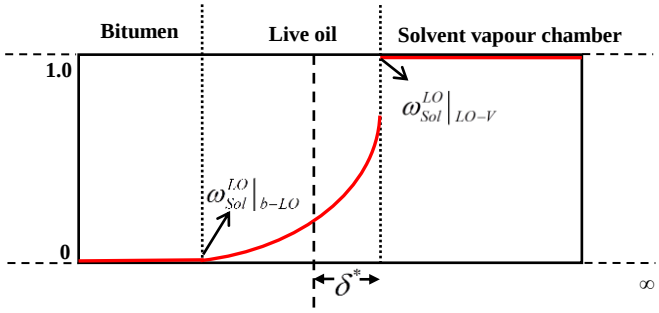

(a)

VAPEX Process

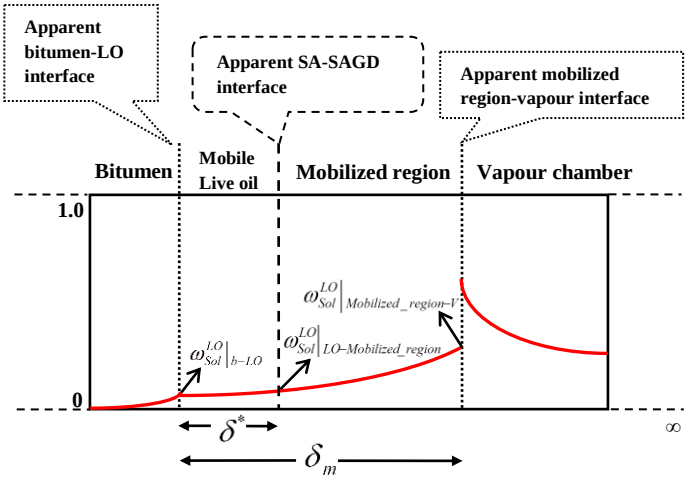

(b) **SA-SAGD Process (Condensing mode)**

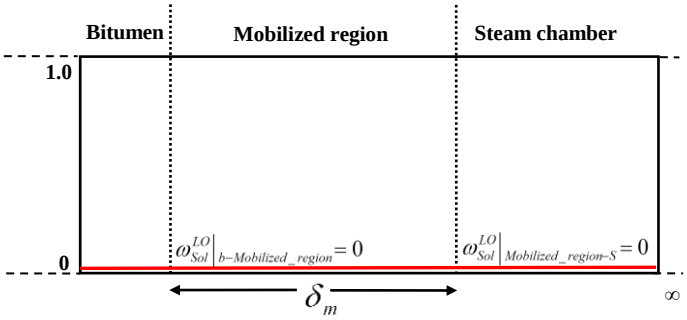

SAGD Process

(c)

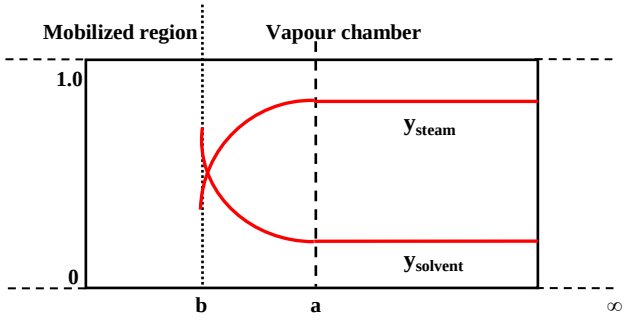

SA-SAGD Process (Condensing mode)

(d)

Figure 3.15: (a-c) Schematic solvent concentration profile across the cross sectional area of the VAPEX, SA-SAGD, and SAGD processes respectively, and (d) Schematic diagram of solvent vapour and steam mole fraction gradients across the cross sectional area of the SA-SAGD process

3.4.4.2.Diffusion Mechanism of Mass Transfer in the SA-SAGD Process at the Pore – Scale

Due to the abrupt solvent concentration gradient at the interfacial region of the SA-SAGD process, mass transfer could take place by molecular diffusion. As the solvent vapour diffuses into the bitumen, a thin film of the live oil phase becomes mobile. The draining live oil then engulfs some bubbles of the entrapped non-wetting phase as a result of several pore-scale mechanisms associated with the snap-off mechanism in the SA-SAGD process which were demonstrated earlier in Figures 3.11 and 3.13. By focusing on the size and shape of these enclosed bubbles, gradual volume shrinkage and possible disappearance along the drainage path is observed. The pore-scale shrinkage/disappearance phenomenon demonstrates the extent of local heat and mass transfer processes. The entrapped gas bubbles tend to disappear with time, which indicates that the local diffusion process enables the complete solubility of the gas pocket into the surrounding live oil continuum. In the SA-SAGD process, it is unlikely to observe pure solvent vapour pockets entrapped within the continuum of the live oil because the limited mole fraction of the injected solvent within the carrying steam phase forms a homogeneous gas mixture. The gradual volume shrinkage process of the entrapped gas bubbles indicates that the process of condensation of the gaseous mixture at the pore-level happens simultaneously with the diffusion mass transfer process of the solvent phase into the live oil. If a sufficiently long drainage path is provided for the entrapped bubbles of the gas mixture, they would likely be fully converted into small isolated droplets of water condensate down gradient. This is true provided that the chance of coalescence of these propagated bubbles are neglected by assuming that the isolated bubbles are independent of each other and remain isolated during their entire drainage path. These phenomena result in the formation of the in-situ water-in-oil emulsion phase. The volume shrinkage phenomenon to produce the isolated condensate droplets due to the local temperature drop and diffusion mass transfer was presented through a series of pore-scale events shown in Figure 3.12.

3.4.4.3. Pore–Scale Convection Mechanism of Mass Transfer in the SA-SAGD Process

In the SA-SAGD recovery method, the convective mass transfer process plays an important role in the overall mass transfer scheme when the solvent phase condenses at the bitumen interface. It is evident that the condensed solvent phase, flowing over the apparent SA-SAGD interface,

strips-off bitumen while draining down gradient by a combination of capillary, convective mass and heat transfer phenomena. The presence of temperature gradient near the interfacial region, which is caused by steam condensation within the invaded region, results in improved bitumen recovery because of the enhanced convection mass transfer from solvent condensate to bitumen and vice versa. The liquid solvent washes away the bitumen-filled pores or pores which are partially filled with bitumen either from top-side, bottom-side, or sideways in the direction of gravity. The draining liquid solvent not only strips bitumen off the bitumen-filled pores, but it also helps to enhance the mixing process of the live oil and the solvent phase at the pore-scale. This was verified clearly in the videos taken from the pore-level phenomena of the SA-SAGD process during the course of the visualization experiments when the draining solvent condensate phase has a lot of bitumen striations running through it.

A nearly perfect vertical interface was observed between the liquid solvent and bitumen at the pore scale when liquid solvent was flowing all over the bitumen-filled pores. This near flat interface, extending through the middle of the pore bodies, is an indication of the extent of miscibility of the solvent condensate with bitumen at the pore-level due to higher solvent concentration near the interface. One can clearly distinguish between the flat interface of the liquid solvent-bitumen fluid pair and the curved interface of the solvent vapour-live oil fluid pair at the pore-scale. Figure 3.16 contains a series of pore-scale snapshots starting from the top left and ending at the bottom right showing that the bitumen phase being stripped away from the bitumen-saturated pores by continuous flow of excess liquid solvent. The presence of a smooth interface at the micro-level is also observed.

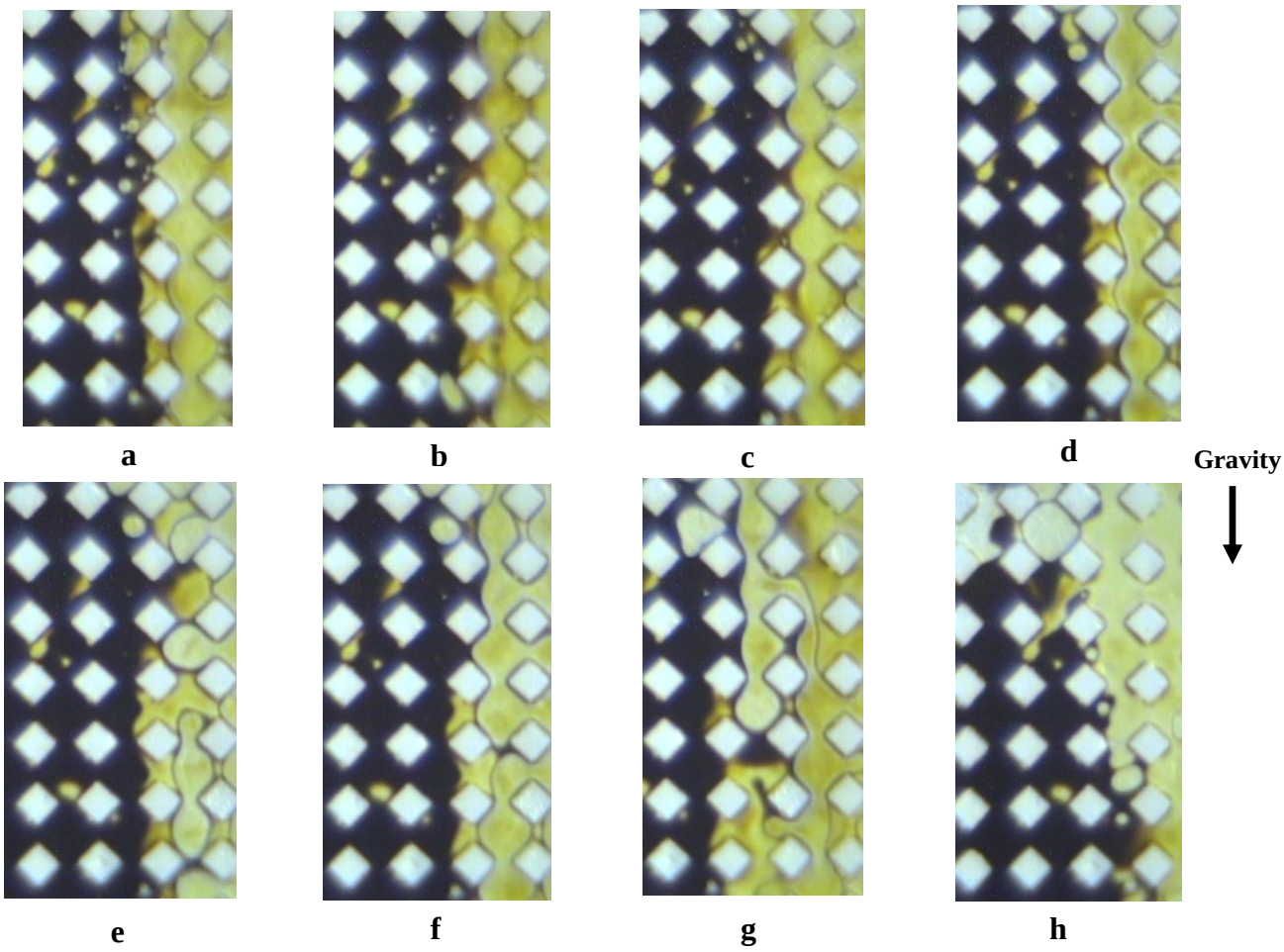

Figure 3.16: Pore-scale stripping of the bitumen phase by solvent condensate is an evidence of the convective mass transfer mechanism during the SA-SAGD process (Run No 19: DL-1 micromodel, n-hexane as the steam additive at 15% vol/vol concentration, average operating temperature of 103.45 °C, time interval: 430 seconds)

3.4.5. Asphaltene Precipitation During the SA-SAGD Process at the Pore – Scale

Asphaltene is the non-volatile end of the asphaltenic crude oil. It has polar molecular characteristics of aromatic structure and often contains heavy metals and nitrogen. Asphaltene is defined as the insoluble fraction of the crude oil in excess volume of normal alkanes such as normal pentane and normal heptane, but it is soluble in excess volume of other solvents such as benzene and toluene at room temperature and atmospheric pressure. Several factors influence the onset of asphaltene flocculation and precipitation from an asphaltenic crude oil in a displacement process, namely temperature, pressure, and compositional changes. However, the temperature

has a weaker effect on the asphaltene precipitation. It is believed that temperature change may weakly affect the process of asphaltene flocculation, and may enhance or inhibit the overall precipitation process. An increase in the concentration of light chain hydrocarbons, such as n-pentane and n-heptane in the excess volume can profoundly enhance the asphaltene precipitation process (Firoozabadi, 1999).

Asphaltene precipitates out of heavy oil and bitumen if the phase equilibrium between the components is disturbed according to operating conditions. Asphaltene precipitation has a profound effect on the viscosity reduction of the heavy oil. The de-asphalting process of the heavy oil and bitumen, which could be an induced phenomenon during the course of any condensing solvent aided process of heavy oil recovery at the pore-scale, could upgrade the heavy oil in-situ to the extent of reducing its inherent viscosity by orders of magnitude. Asphaltene precipitation was observed during the course of the VAPEX process with propane as the solvent when the operating pressure was above the dew point of propane (Mokrys I.J. and Butler, 1993). It was concluded that the propane liquid to oil ratio was required to be greater than 0.35 by mass in order to experience asphaltene precipitation. While in-situ asphaltene precipitation reduces the operating and environmental expenses of thermally or catalytically upgrading processes of heavy oil and bitumen, some issues are raised regarding undesired side effects of the in-situ bitumen upgrading. For instance, in-situ de-asphalting may reduce the permeability, and may have an adverse impact on the oil production as well as the sweep efficiency. In this regard, low permeability values of the formation may be problematic for implementing solvent aided processes because if asphaltene precipitates, it may drastically reduce the permeability or plug the formation.

According to our visualization experiments of the SAGD process at the pore-level, it is unlikely to experience asphaltene precipitation during the SAGD process at the pore-level within the range of experimental conditions. In other words, steam heating of the bitumen phase within the temperature range of 100-130°C did not de-stabilize the asphaltene content of the bitumen to the extent of developing precipitation conditions. However, the extent of asphaltene precipitation was more pronounced during the course of our pore-scale SA-SAGD experiments, especially when the solvent was condensed ahead of the apparent SA-SAGD interface. In these cases, the

swept region contains vertical striations of the precipitated asphaltene where liquid solvent was in contact with bitumen. There were still some localized spots within the invaded region in which limited-length residual oil ganglia were present within the pore bodies ahead of the apparent SA-SAGD interface without any sign of extensive asphaltene precipitation.

As the main drainage driving forces of the SA-SAGD process are based on gravity and capillary forces, we were interested in qualitatively studying the impact of asphaltene precipitation on vertical permeability reduction of the porous media. From our visualization studies of the SA-SAGD process, it turns out that asphaltene could precipitate out of the continuous bitumen phase as soon as it is subjected to the excess amount of the liquid solvent. The precipitated asphaltene can block the pore constrictions as well as randomly selected parts of the pore bodies in a homogeneous structure to the extent of eliminating fluid flow near the blocked region. The gaseous mixture has to re-route in order to reach the bitumen phase, and the draining phases could no longer drain through those clogged flow paths (Figures 3.17.a and 3.17.b). However, it is clear that the pore blockage is not a permanent issue for most of the clogged flow pathways in the SA-SAGD operation as the injected fresh gaseous mixture could open-up the blocked pore constrictions and pore bodies, hence creating randomly-propagated zigzag flow paths through the blocked region. These new openings would remain as accessible flow pathways for the gaseous mixture ahead of the apparent SA-SAGD interface within the swept region, providing continuous flow of steam and solvent towards the bitumen region (Figure 3.17.d). In addition, some asphaltene particles migrate along with the live oil towards the production spot. One of the drawbacks of the fine migration of the mobilized asphaltene particles is the blockage of the production line due to the buildup of asphaltene particles in the production well (Figure 3.17.c).

Precipitation of asphaltene, however, temporarily limits the drainage of the liquid phases through the mobilized region. The chance of the pore-scale mixing of the excess liquid solvent with the oil and potential subsequent asphaltene precipitation and local blockage of the draining pathways exists. The frequent re-shaping of the draining liquid phases while draining within the pores which have been already blocked partly by the precipitated asphaltene is an evidence of the effect of asphaltene precipitation on the scheme of fluid flow through porous patterns, so is the frequent re-sizing of the draining liquid phases as a result of capillary phenomenon of snap-off

mechanism when passing by the clogged section of the pores. Considering the low concentration of solvent vapour in the injected gaseous mixture, which is in the order of 5 to 15 volume percentage, and presented observations regarding asphaltene precipitation at 15% volume content of the feed stream to be solvent vapour, it is apparent that there is no need for high solvent content in the injected gaseous mixture to induce in-situ upgrading of the crude oil in the form of asphaltene precipitation.

The condensing nature of the solvent phase at the pore level, even at low solvent content values of the gaseous mixture in the SA-SAGD process, guarantees asphaltene precipitation and possible in-situ upgrading. The extent of in-situ upgrading is more pronounced in the case of our SA-SAGD processes compared to that of the conventional VAPEX process, even those at higher live oil solvent compositions [i.e. 48% with n-pentane (Rezaei et al, 2010) and 38% with butane (James, 2009; James et al, 2008)]. Although the solvent content of the produced live oil is lower in the SA-SAGD process compared to that of the conventional VAPEX process, it appears that the localized pore-scale liquid solvent concentration in the condensing mode of the SA-SAGD process is high enough to promote asphaltene precipitation. In order to review the process of asphaltene precipitation within the mobilized region of the SA-SAGD process, it would be beneficial to address the schematic diagrams presented in Figures 3.15.b. As was described before, the solvent concentration changes abruptly from its initial value at the gaseous mixture which is the vapour solvent concentration at the invaded area far from the gaseous phase-mobilized region interfacial area, to zero at the raw bitumen side through a series of pore-scale sections called the mobilized region and the mobile live oil film. The mobilized region composes of 1-5 pores in thickness, behind which the mobile live oil film with the thickness of 1-2 pores drains over the pores filled with the solid bitumen phase. The bitumen content of these pores might contain a low level of solvent concentration in it, and therefore, could not be considered as raw bitumen. However, this solvent content is not to the extent at which it could mobilize the bitumen in the direction of gravity and hence the bitumen could not be considered as the mobile live oil. The depth of the mobile live oil film is between 1-2 pores in thickness over which the solvent content of the live oil would be reduced from $\omega^{LO}_{Sol|Mobilized\_region-LO}$ to $\omega^{LO}_{Sol|b-LO}$, and the latter is not necessarily zero as there might be some immobile live oil behind the mobile live oil film. At the mobile live oil film-bitumen interface, there is still some minor solvent concentration

gradient which could lead to solvent diffusion through the bitumen phase. Excess liquid solvent near the apparent SA-SAGD interface could cause asphaltene precipitation ahead of the SA-SAGD interface towards the swept region, especially within the mobilized region.

3.5. Quantitative Analysis of the Results in the SA-SAGD Experiments

In addition to the mechanistic pore-level investigation of the SA-SAGD process performance, it was tried to quantitatively study the performance of this process at the micro-scale based on the measurable system response. Due to extremely-low drainage rate and cumulative production of the mobile live oil in this set of experiments, it was decided to focus on the horizontal advancement of the SA-SAGD interface in order to analyze the performance of such a process at the pore-scale. It is evident that the quantitative results acquired using 2D glass micromodels of porous media cannot be upscaled to the real world cases of fluid flow when 3D porous structure is involved. However, one can figure out the contribution of different system variables on the performance of the SA-SAGD process using parametric sensitivity analysis of the process variables. Similar to most gravity-dominated processes of oil recovery, the mobile oil drainage rate of the SA-SAGD process would be proportional to the permeability of the porous medium, and inversely proportional to the live oil viscosity.

In this study, three different glass-etched micromodels of porous media with fully-characterized pore structure were used; Cold Lake bitumen and Lloydminster heavy oil blend were used as the oil phase, and normal pentane and normal hexane were used as solvent additives to steam. The temporary positions of the SA-SAGD interface were located versus time at different elevations in each cell block along the height of each micromodel. For each particular trial, the SA-SAGD interface advancement velocity was measured accordingly. In this section, details of the quantitative analysis of the SA-SAGD process performance at the pore-scale are discussed.

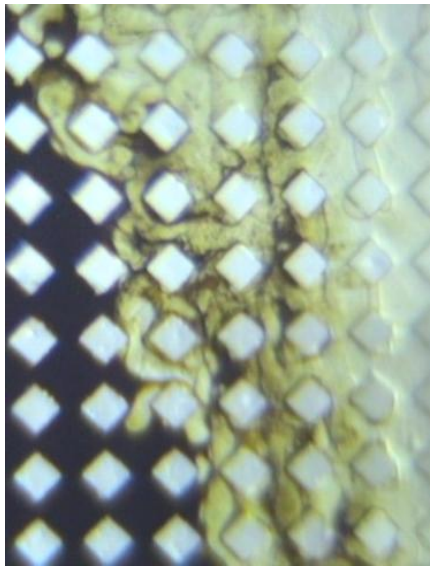

(a) Asphaltene precipitated at the pore-scale within the mobilized region caused re-shaping/re-sizing of the phases flowing past it (Run No 10: OM-2 micromodel, n-hexane as the steam additive at 15% vol/vol concentration, average operating temperature of 101.45 °C, time: 7845 seconds)

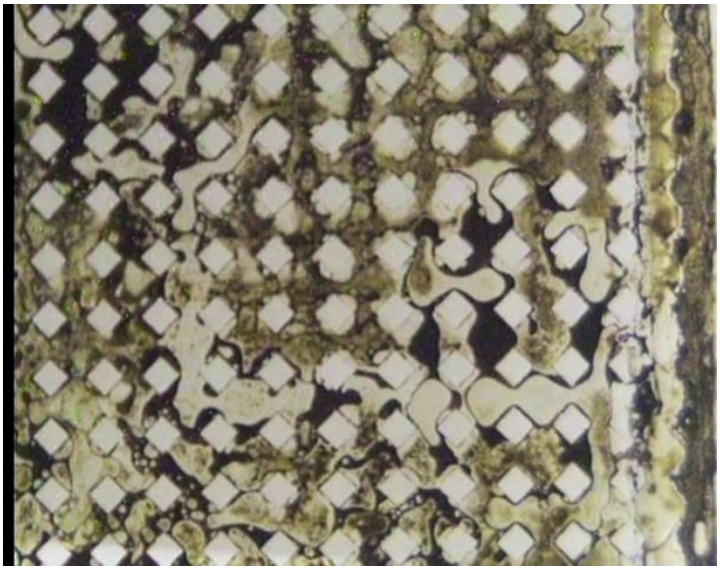

(b) Severe asphaltene precipitation within the mobilized region prevents the gravity drainage process because of the impaired vertical permeability (Run No 9: OM-1 micromodel, n-hexane as the steam additive at 15% vol/vol concentration, average operating temperature of 101.85 °C, time: 8615 seconds)

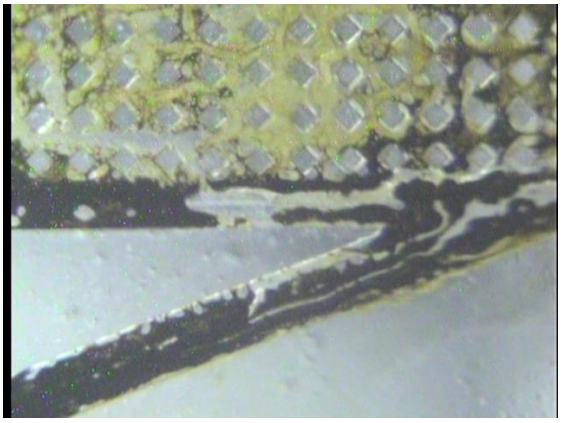

(c) Blockage of the production line as well as down-structured pore space as a result of asphaltene mobilization in the form of fine migration (Run No 13: DL-1 micromodel, n-pentane as the steam additive at 15% vol/vol concentration, average operating temperature of 102.75 °C, time: 8455 seconds)

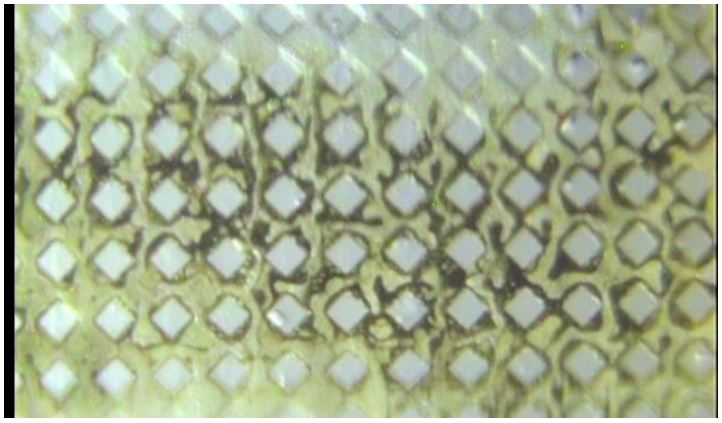

(d) Asphaltene precipitation within the invaded region, followed by re-opening of pores via flow paths due to gas phase invasion through the blocked region (Run No 13: DL-1 micromodel, n-pentane as the steam additive at 15% vol/vol concentration, average operating temperature of 102.75 °C, time: 8230 seconds)

Figure 3.17: State of in-situ asphaltene precipitation as a result of excess solvent condensate near the interfacial region of the SA-SAGD process

3.5.1. Pore-Scale and Macroscopic Properties of Glass-Etched Micromodels

Three different glass micromodels with known pore structures were employed in this study. These micromodels were also used to carry out the pore-scale visualization experiments of the SAGD process. They were thoroughly characterized in terms of pore-level as well as macroscopic dimensions and properties. The characterization procedures were discussed in section 2.5.1. A summary of the model properties was presented in Table 2.3, and the details of the characterization experiments and data analysis were presented in Tables 2.4 to 2.24 and Figures 2.19 to 2.33.

3.5.2. Oil Properties

Cold Lake bitumen and Lloydminster heavy oil blend were used as the oil phase in this study. The bitumen is similar to the one used previously in our SAGD visualization studies discussed in Chapter 2. The physical properties of bitumen are listed in Table 2.2. In addition, the viscosity-temperature relationship and the C_{100} hydrocarbon analysis of this bitumen are presented in Figures 2.6 and 2.7.

The viscosity–temperature relationship of Lloydminster heavy oil blend was measured by Hatch Ltd (2009) using the Paar Physica MCR100 Modular Compact Rheometers (Anton Paar), and is shown in Figure 3.18. The viscosity of Lloydminster heavy oil blend at 35 °C was reported to be 5400 cP. An acceptable exponential trend line was fitted to the experimental data points and is presented in the form of Eq 3.1:

$$\mu = 171403.886e^{-0.099T} \tag{3.1}$$

in which "μ" is the oil viscosity in cP and "T" is temperature in °C.

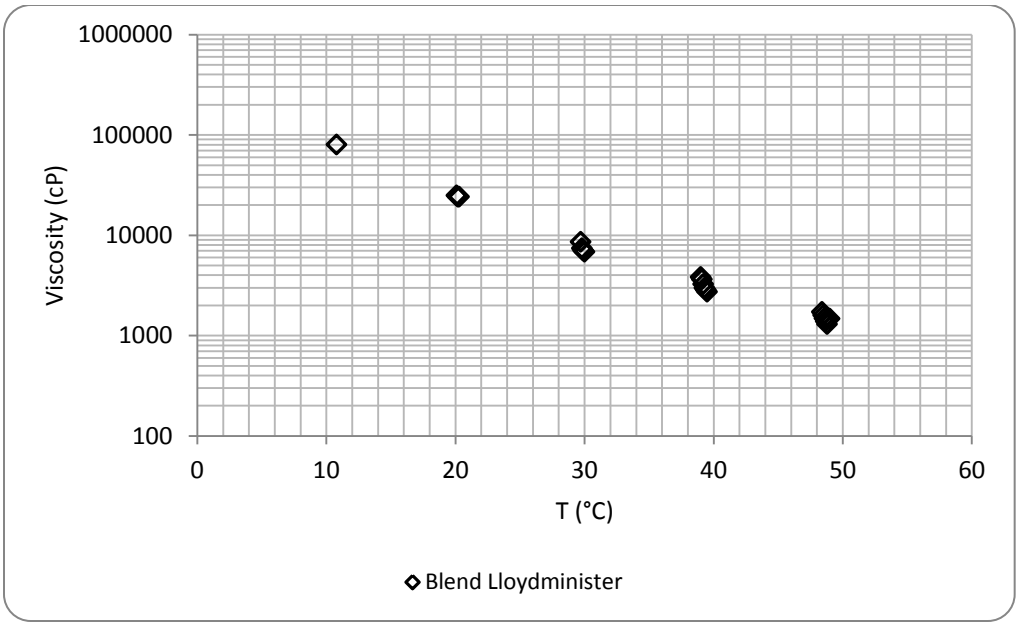

Figure 3.18: Viscosity – Temperature relationship for Lloydminster heavy oil mixture

3.5.3. Effect of Temperature and Solvent Concentration on the Density and Viscosity of Cold Lake Bitumen and Lloydminster Heavy Oil Mixture

The sensitivity of bitumen and heavy oil viscosity to temperature and solvent concentration is analyzed using relevant correlations found in the literature. These predictions are used to analyze the SA-SAGD process performance at the pore-scale in terms of the horizontal interface advancement velocity in the next section.

The presence of solvent in the oil phase at high operating temperatures would alter both density and viscosity of the mobile live oil. Due to the nature of our SA-SAGD visualization experiments and very low storage capacity of the employed micromodels, there is no production data available as far as the rate of oil production as well as solvent content of the produced mobile live oil is concerned. It is reported that the solvent content of the produced live oil from conventional and warm VAPEX processes would be in the range of 0.15 – 0.45 mass fraction of the produced oil (Rezaei, 2010). The solvent content of the produced oil from a typical SA-SAGD process would likely be on the lower range of this spectrum due to the extremely

higher operating temperature of the process which significantly lowers the solvent solubility in the produced live oil. In the absence of the solvent concentration in the live oil data, a solvent content of about 20% mass fraction was assumed to be reasonable value for the produced mobile live oil of the SA-SAGD process. This assumption is just for the sake of calculations in this section to highlight the combined effect of heat and solvent dilution on the viscosity reduction of Cold Lake bitumen and Lloydminster heavy oil blend, and it is not used to analyze the SA-SAGD interface advancement velocity at the pore-scale.

In order to calculate the density of oil-solvent mixture at different solvent content levels and corresponding temperatures, it is required to use an appropriate equation of state or a relevant mixing rule considering the volume change upon mixing of these two compounds. The topic of non-ideality of heavy oil-solvent mixtures has been addressed in the literature (Firoozabadi, 1999; Madrazo, 1960; Luo et al, 2007; Wen et al, 2003, 2004 and 2005; Wen and Kantzas, 2006) and it is currently an active research topic at the University of Calgary. Due to the volume contrast between the heavy oil and bitumen molecules and those of paraffinic solvents, the density calculations for such a mixture would be affected by volume shift parameters. In the absence of detailed characterization of the employed oil types and also volume shift parameters, extensions of ideal-solution mixing method was considered as the simplest way to correlate mixture volumetric properties such as density.

An ideal liquid solution is a hypothetical mixture of liquids in which there is no special force of attraction between the components of the solution and for which no change in internal energy occurs on mixing. Under these circumstances, no change in the character of the liquids is caused by mixing, merely a dilution of one liquid by the other. It is believed that following mixing liquids to generate an ideal solution, there is no heat of mixing effect and the thermodynamic properties are additive. The volume of the ideal solution is the sum of the volumes of the pure liquid components. There is neither shrinkage nor expansion when the liquids are mixed to form an ideal solution (McCain, 1990). Here, it is assumed that the heavy oil–solvent mixture and bitumen–solvent mixture are both binary mixtures and can be considered to be ideal solutions. The following equation can be used to calculate the pseudo-liquid mixture density (Standing, 1981 and 1962; Standing and Katz, 1942):

$$\rho_{pL} = \frac{\sum_{i=1}^{N} x_i MW_i}{\sum_{i=1}^{N} \left({x_i MW_i}/{\rho_i} \right)} \tag{3.2}$$

in which ρ_{pL} is the pseudo-liquid density of mixture, x_i is the mole fraction of each component in the ideal mixture, MW_i and ρ_i are the molecular weight and density of each of the components of the ideal mixture, and N is the number of components in the ideal mixture.

The effect of temperature on the density of Cold Lake bitumen mixture with n-C_5 and n-C_6 is shown in Figures 3.19 and 3.20 respectively. The temperature range was selected based on the operating temperature range that was experienced during the course of our SA-SAGD visualization experiments. The same calculations were also carried out to study the effect of operating temperature on the mixture density of Lloydminster heavy oil with n-C_5 as well as n-C_6 and the results are plotted in Figures 3.21 and 3.22. The raw data of mixture density at different temperature levels are also presented in Tables 3.3 and 3.4. Although the mixture density data were calculated based on 0.1 °C temperature steps, they were reported at 1 °C temperature intervals in these two Tables. In these calculations, the density-temperature relationship for normal pentane and normal hexane were extracted from Perry's handbook (2008) and Yaws' Thermophysical Properties of Chemicals and Hydrocarbons (2010) respectively. The density of water at different temperatures was described by a cubic polynomial (Alley, 2006).

As shown in Figures 3.19 to 3.22, the mixture density is a linear function of temperature in the range of interest. The presence of paraffinic solvents in the mixture reduces the density of the mixture below that of the heavy oil and/or bitumen sample. It is also evident that solvents with lower carbon number (i.e. lighter solvent) reduce the mixture density more than that which is obtained using the heavier solvents. It is concluded that an increase in the solvent concentration in the mixture will decrease the mixture density.

Using the PVT data available for Cold Lake bitumen and Lloydminster heavy oil blend, it is also possible to figure out the combined effect of temperature and solvent concentration on the viscosity of oil-paraffinic solvent mixtures within the range of our experimental conditions. A well-accepted viscosity mixing rule proposed by Shu (1984) was used. The accuracy of this

correlation is very good when dealing with high-viscosity liquids. The Shu correlation was based on a modified Arrhenius mixture viscosity model which was proposed earlier by Lederer as follows (Lederer, 1933):

$$\ln \mu = x_A ln\mu_A + x_B ln\mu_B \tag{3.3}$$

in which μ, μ_A and μ_B are the viscosity of mixture, higher viscosity (i.e. oil) agent, and lower viscosity (i.e. solvent) agent respectively, and x_A and x_B are the compositional parameters for higher viscosity (i.e. oil) and lower viscosity (i.e. solvent) agent as defined by:

$$x_A = \frac{\alpha V_A}{\alpha V_A + V_B} \tag{3.4}$$

$$x_B = 1 - x_A \tag{3.5}$$

in which V_A and V_B are the volume fraction of more viscous (i.e. oil) and less viscous (i.e. solvent) components respectively.

α is an empirical parameter which was defined as:

$$\alpha = \frac{17.04\Delta(SP\ GR)^{0.5237}(\text{SP GR})_A^{3.2745}(\text{SP GR})_B^{1.6316}}{\ln(\frac{\mu_A}{\mu_B})} \tag{3.6}$$

in which $\Delta(SP\ GR) = (SP\ GR)_A - (SP\ GR)_B$, and (SP GR) designates the specific gravity of component A or B. In order to calculate the viscosity of bitumen-solvent mixture and heavy oil-solvent mixture at different operating conditions, Equations 2.1 and 3.1 were used to calculate the bitumen and heavy oil viscosities respectively. The viscosity of normal pentane at different operating conditions was obtained from Yaws' Handbook of Thermodynamic and Physical Properties of Chemical Compounds (2003). The viscosity–temperature variation of normal hexane was obtained from Chemical Properties Handbook (1999). The density-temperature relationship for normal pentane and normal hexane were extracted from Perry's handbook (2008) and Yaws' Thermophysical Properties of Chemicals and Hydrocarbons (2010) respectively. The density of water at different temperatures was described by a cubic polynomial (Alley, 2006).

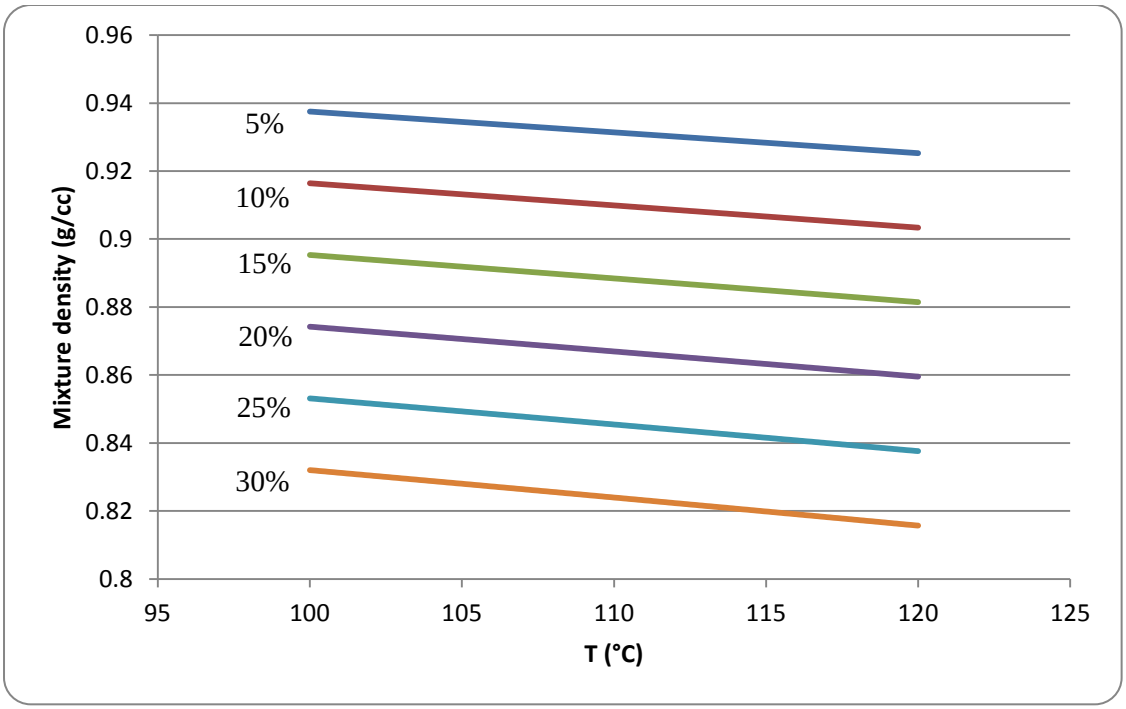

Figure 3.19: The effect of temperature on the mixture density of Cold Lake bitumen and n-C_5 at different solvent volume fractions

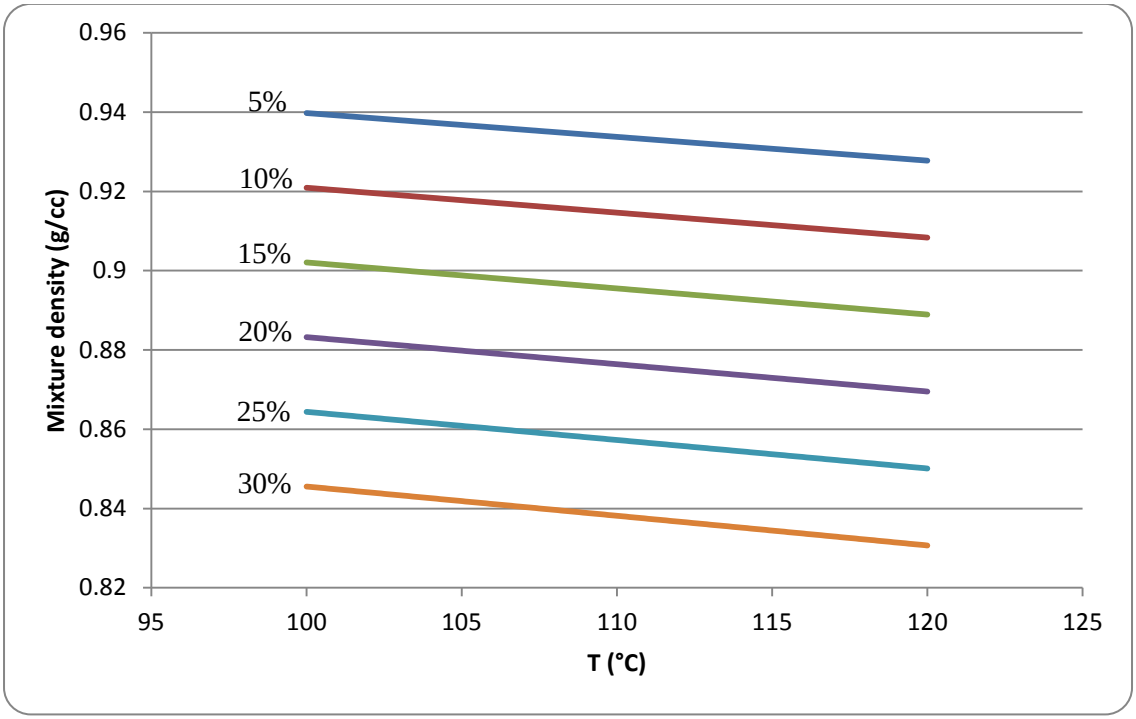

Figure 3.20: The effect of temperature on the mixture density of Cold Lake bitumen and n-C_6 at different solvent volume fractions

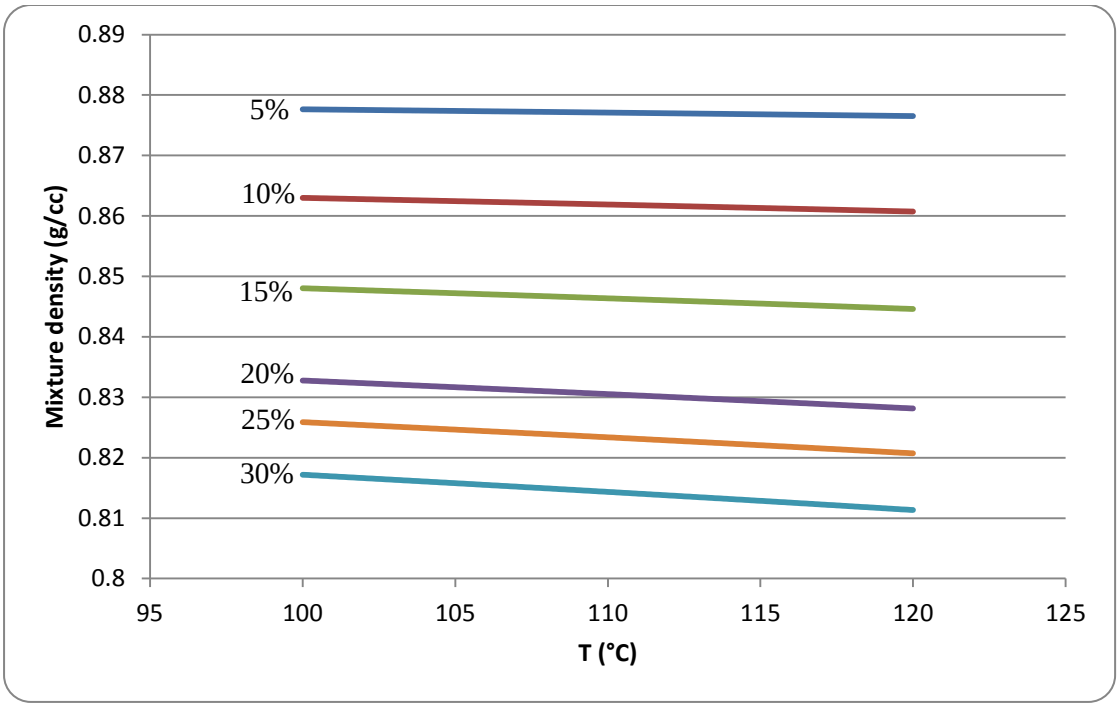

Figure 3.21: The effect of temperature on the mixture density of Lloydminster heavy oil and n-C_5 at different solvent volume fractions

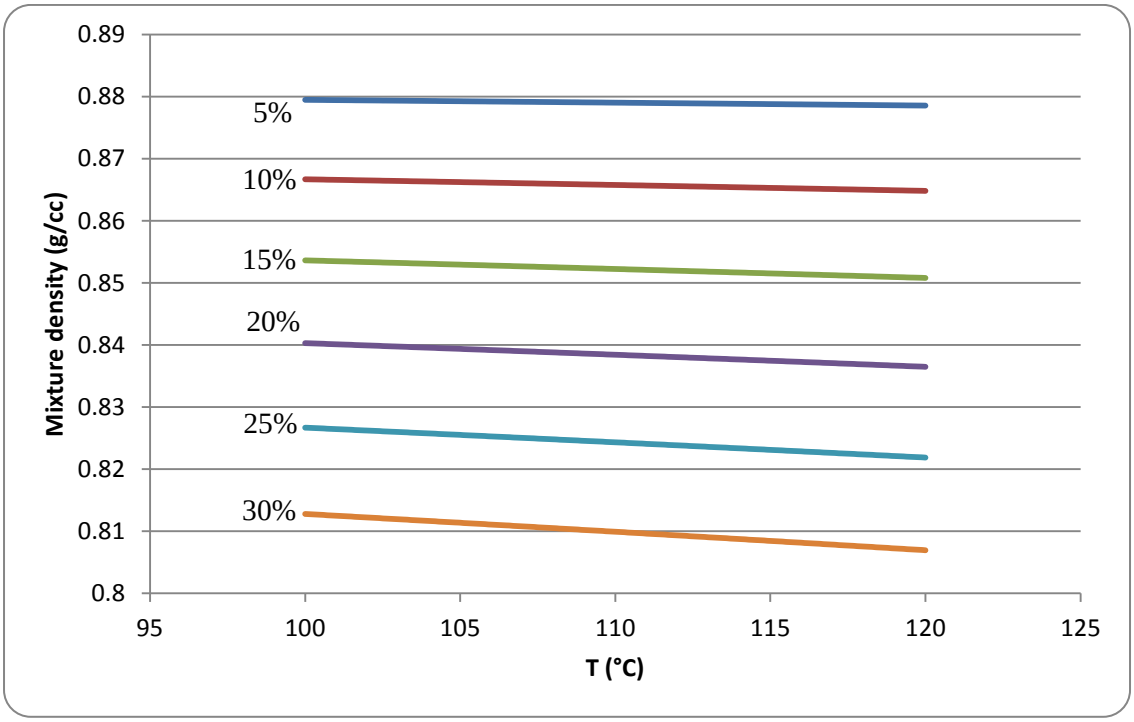

Figure 3.22: The effect of temperature on the mixture density of Lloydminster heavy oil and n-C_6 at different solvent volume fractions

Table 3.3: The calculated density of Cold Lake bitumen-nC_5 and Cold Lake bitumen-nC_6 mixtures at different levels of solvent concentration and operating temperatures

T (°C)	n-C_5 concentration (% vol/vol of mixture)						n-C_6 concentration (% vol/vol of mixture)					
	5	10	15	20	25	30	5	10	15	20	25	30
100.00	0.9375	0.9164	0.8953	0.8742	0.8531	0.8320	0.9398	0.9209	0.9021	0.8832	0.8644	0.8455
101.00	0.9369	0.9158	0.8946	0.8735	0.8524	0.8312	0.9392	0.9203	0.9014	0.8826	0.8637	0.8448
102.00	0.9363	0.9151	0.8940	0.8728	0.8516	0.8304	0.9386	0.9197	0.9008	0.8819	0.8630	0.8441
103.00	0.9357	0.9145	0.8933	0.8720	0.8508	0.8296	0.9380	0.9190	0.9001	0.8812	0.8623	0.8433
104.00	0.9351	0.9138	0.8926	0.8713	0.8501	0.8288	0.9374	0.9184	0.8995	0.8805	0.8616	0.8426
105.00	0.9345	0.9132	0.8919	0.8706	0.8493	0.8280	0.9368	0.9178	0.8988	0.8798	0.8609	0.8419
106.00	0.9338	0.9125	0.8912	0.8699	0.8485	0.8272	0.9362	0.9172	0.8982	0.8791	0.8601	0.8411
107.00	0.9332	0.9119	0.8905	0.8691	0.8478	0.8264	0.9356	0.9165	0.8975	0.8785	0.8594	0.8404
108.00	0.9326	0.9112	0.8898	0.8684	0.8470	0.8256	0.9350	0.9159	0.8968	0.8778	0.8587	0.8397
109.00	0.9320	0.9106	0.8891	0.8677	0.8462	0.8248	0.9344	0.9153	0.8962	0.8771	0.8580	0.8389
110.00	0.9314	0.9099	0.8884	0.8669	0.8454	0.8240	0.9338	0.9146	0.8955	0.8764	0.8573	0.8382
111.00	0.9308	0.9093	0.8877	0.8662	0.8447	0.8231	0.9332	0.9140	0.8949	0.8757	0.8566	0.8374
112.00	0.9302	0.9086	0.8870	0.8655	0.8439	0.8223	0.9326	0.9134	0.8942	0.8750	0.8559	0.8367
113.00	0.9296	0.9079	0.8863	0.8647	0.8431	0.8215	0.9320	0.9128	0.8935	0.8743	0.8551	0.8359
114.00	0.9289	0.9073	0.8856	0.8640	0.8423	0.8207	0.9314	0.9121	0.8929	0.8737	0.8544	0.8352
115.00	0.9283	0.9066	0.8849	0.8632	0.8415	0.8199	0.9308	0.9115	0.8922	0.8730	0.8537	0.8344
116.00	0.9277	0.9060	0.8842	0.8625	0.8408	0.8190	0.9302	0.9109	0.8916	0.8723	0.8530	0.8337
117.00	0.9271	0.9053	0.8835	0.8618	0.8400	0.8182	0.9296	0.9102	0.8909	0.8716	0.8523	0.8329
118.00	0.9265	0.9047	0.8828	0.8610	0.8392	0.8174	0.9290	0.9096	0.8903	0.8709	0.8515	0.8322
119.00	0.9259	0.9040	0.8821	0.8603	0.8384	0.8165	0.9284	0.9090	0.8896	0.8702	0.8508	0.8314
120.00	0.9253	0.9034	0.8814	0.8595	0.8376	0.8157	0.9278	0.9083	0.8889	0.8695	0.8501	0.8307

Table 3.4: The calculated density of Lloydminster heavy oil-nC_5 and Lloydminster heavy oil-nC_6 mixtures at different levels of solvent concentration and operating temperatures

T (°C)	n-C_5 concentration (% vol/vol of mixture)						n-C_6 concentration (% vol/vol of mixture)					
	5	10	15	20	25	30	5	10	15	20	25	30
100.00	0.8776	0.8630	0.8480	0.8328	0.8172	0.8259	0.8795	0.8667	0.8536	0.8403	0.8267	0.8128
101.00	0.8776	0.8629	0.8479	0.8326	0.8169	0.8256	0.8794	0.8666	0.8535	0.8401	0.8264	0.8125
102.00	0.8775	0.8628	0.8477	0.8323	0.8166	0.8254	0.8794	0.8665	0.8533	0.8399	0.8262	0.8122
103.00	0.8775	0.8627	0.8475	0.8321	0.8163	0.8251	0.8793	0.8664	0.8532	0.8397	0.8260	0.8119
104.00	0.8774	0.8626	0.8474	0.8319	0.8161	0.8249	0.8793	0.8663	0.8531	0.8396	0.8257	0.8117
105.00	0.8774	0.8624	0.8472	0.8317	0.8158	0.8247	0.8792	0.8662	0.8529	0.8394	0.8255	0.8114
106.00	0.8773	0.8623	0.8470	0.8314	0.8155	0.8244	0.8792	0.8661	0.8528	0.8392	0.8253	0.8111
107.00	0.8773	0.8622	0.8469	0.8312	0.8152	0.8241	0.8791	0.8660	0.8526	0.8390	0.8250	0.8108
108.00	0.8772	0.8621	0.8467	0.8310	0.8149	0.8239	0.8791	0.8659	0.8525	0.8388	0.8248	0.8105
109.00	0.8772	0.8620	0.8465	0.8308	0.8146	0.8236	0.8791	0.8658	0.8524	0.8386	0.8245	0.8102
110.00	0.8771	0.8619	0.8464	0.8305	0.8143	0.8234	0.8790	0.8658	0.8522	0.8384	0.8243	0.8099
111.00	0.8770	0.8618	0.8462	0.8303	0.8140	0.8231	0.8790	0.8657	0.8521	0.8382	0.8241	0.8096
112.00	0.8770	0.8617	0.8460	0.8301	0.8137	0.8228	0.8789	0.8656	0.8519	0.8380	0.8238	0.8093
113.00	0.8769	0.8615	0.8458	0.8298	0.8135	0.8226	0.8789	0.8655	0.8518	0.8378	0.8236	0.8090
114.00	0.8769	0.8614	0.8457	0.8296	0.8132	0.8223	0.8788	0.8654	0.8517	0.8377	0.8233	0.8087
115.00	0.8768	0.8613	0.8455	0.8294	0.8129	0.8221	0.8788	0.8653	0.8515	0.8375	0.8231	0.8084
116.00	0.8768	0.8612	0.8453	0.8291	0.8126	0.8218	0.8787	0.8652	0.8514	0.8373	0.8229	0.8082
117.00	0.8767	0.8611	0.8451	0.8289	0.8123	0.8215	0.8787	0.8651	0.8512	0.8371	0.8226	0.8078
118.00	0.8766	0.8610	0.8450	0.8286	0.8120	0.8213	0.8786	0.8650	0.8511	0.8369	0.8224	0.8075
119.00	0.8766	0.8608	0.8448	0.8284	0.8116	0.8210	0.8786	0.8649	0.8509	0.8367	0.8221	0.8072
120.00	0.8765	0.8607	0.8446	0.8282	0.8113	0.8207	0.8785	0.8648	0.8508	0.8365	0.8219	0.8069

Figure 3.23 presents the effect of SA-SAGD operating temperature on the viscosity of Cold Lake bitumen, and bitumen-normal pentane mixture with different solvent volume fractions. The same procedure was applied to the mixture viscosity of Cold Lake bitumen and normal hexane at the same solvent volume fraction levels and is shown in Figure 3.24. The selected range of operating temperature was decided based on our visualization experiments and all the calculations were carried out at atmospheric operating pressure condition. As it is evident in these two Figures, the mixture viscosity is more sensitive to temperature at lower solvent content of the mobile live oil. For each particular solvent type and considering a particular solvent content, it is clear that the rate of change of the mixture viscosity with respect to temperature is lower at higher operating temperatures.

The same analogy was used in order to quantify the sensitivity of the Lloydminster heavy oil viscosity to temperature. In addition, the viscosity of heavy oil-nC_5 as well as heavy oil-nC_6 mixtures were also calculated using Shu correlation at different levels of temperature and solvent content of the mobile oil. Figures 3.25 and 3.26 show the viscosity-temperature relationship for Lloydminster heavy oil and also its mixtures with n-C_5 and n-C_6 at different solvent content values respectively. As it is evident from these two Figures, the mixture viscosity at fixed solvent type and solvent content is more sensitive to temperature at lower temperature levels. In addition, the rate of change of the mixture viscosity versus temperature is more pronounced at lower solvent content of the mobile live oil. Comparing Figures 3.25 with 3.23 or Figures 3.26 with 3.24, it can be concluded that the rate of change of mixture viscosity with temperature is steeper in the case of bitumen compared to that of the heavy oil as it is generally expected from the compositional nature of these two oil types.

Considering all these four Figures, another important conclusion can be made: at each particular solvent concentration, oil type, and operating temperature, the solvent with lower carbon number reduces the mixture viscosity more than the heavier solvent. This could be verified using two comparison plots presented as Figures 3.27 and 3.28. Although the difference between the oil and solvent viscosities are significantly high and the major contribution in the mixture viscosity is associated with the oil phase rather than the solvent phase, solvent viscosity still has an influence on the total mixture viscosity. The lighter the solvent is, the lower would be its

viscosity. As a result, the viscosity of mixture would be less with lighter solvent compared to that with heavier solvent.

The calculated viscosity data for bitumen-solvent and heavy oil-solvent mixtures are also provided in Tables 3.5 and 3.6 respectively. It is worthwhile to note that the temperature sensitivity of the mixture viscosity was investigated using 0.1 °C temperature steps; however, only temperature intervals of 1 °C are presented in these Tables.

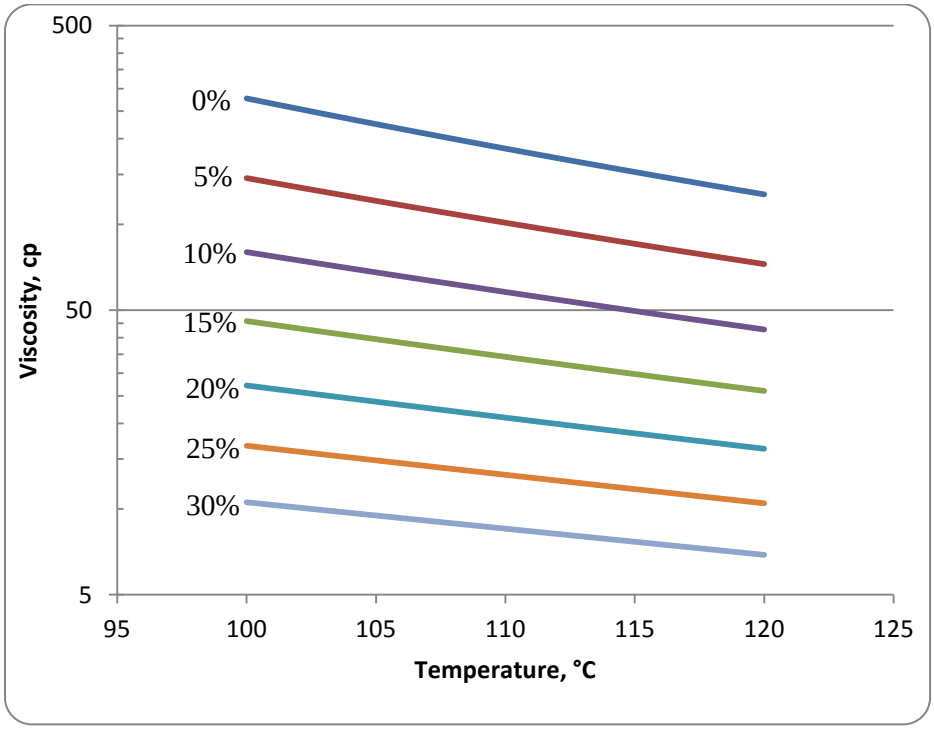

Figure 3.23: The effect of temperature on the dynamic viscosity of Cold Lake bitumen as well as on the bitumen-nC_5 dynamic mixture viscosity at different solvent volume fractions

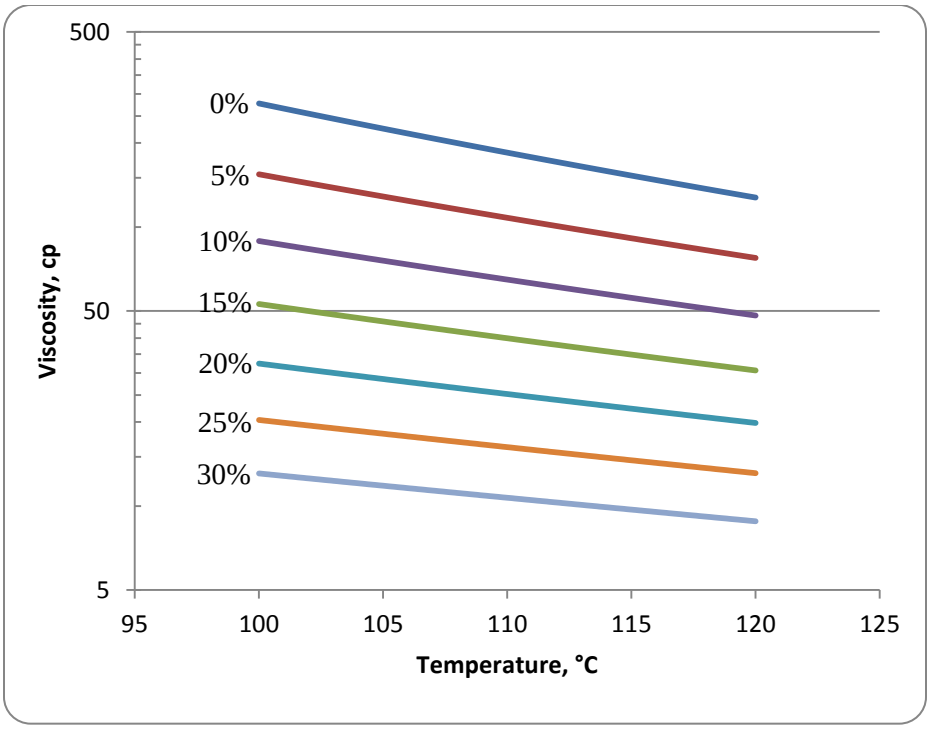

Figure 3.24: The effect of temperature on the dynamic viscosity of Cold Lake bitumen as well as on the bitumen-nC_6 dynamic mixture viscosity at different solvent volume fractions

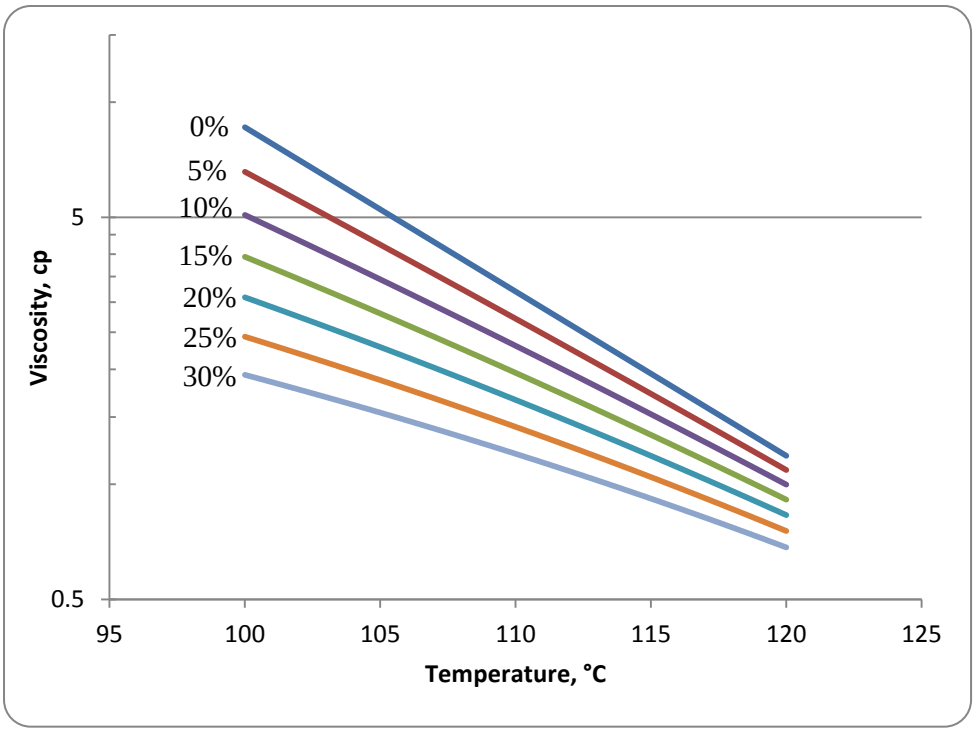

Figure 3.25: The effect of temperature on the dynamic viscosity of Lloydminster heavy oil as well as on the heavy oil-nC_5 dynamic mixture viscosity at different solvent volume fractions

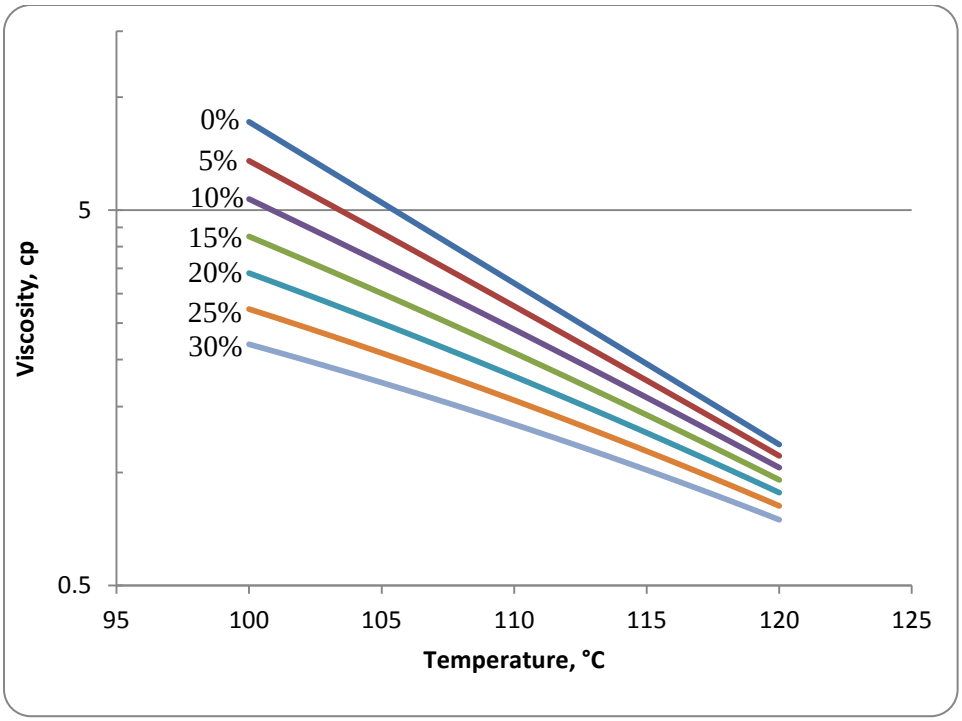

Figure 3.26: The effect of temperature on the dynamic viscosity of Lloydminster heavy oil as well as on the heavy oil-nC_6 dynamic mixture viscosity at different solvent volume fractions

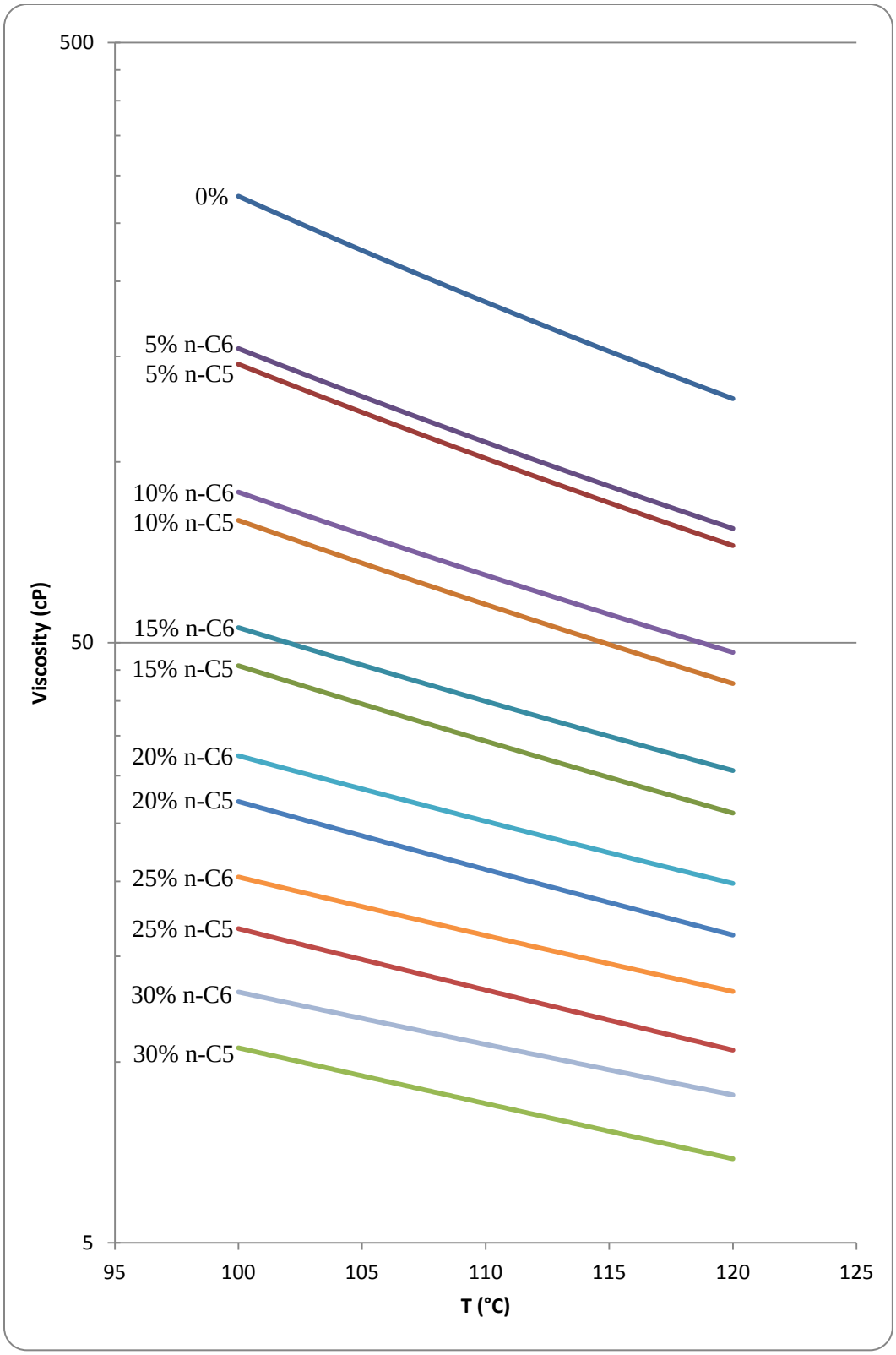

Figure 3.27: Comparison chart between Cold Lake bitumen-nC_5 and Cold Lake bitumen-nC_6 dynamic mixture viscosities at different solvent concentration and temperature levels

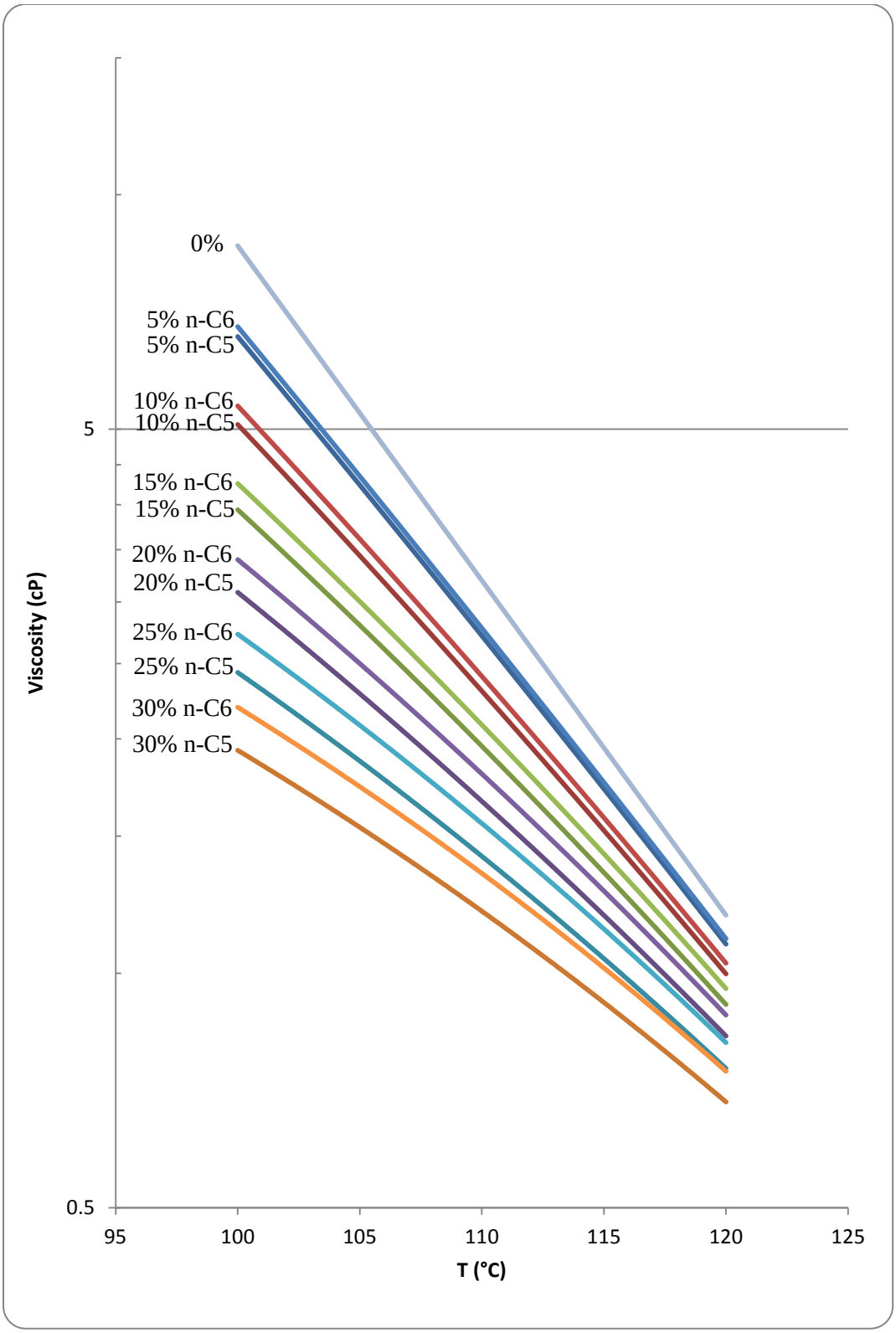

Figure 3.28: Comparison chart between Lloydminster heavy oil-nC_5 and Lloydminster heavy oil-nC_6 dynamic mixture viscosities at different solvent concentration and temperature levels

Table 3.5: The calculated viscosity of Cold Lake bitumen-nC_5 and Cold Lake bitumen-nC_6 mixtures at different levels of solvent concentration and operating temperatures

T (°C)	n-C_5 concentration (% vol/vol of mixture)						n-C_6 concentration (% vol/vol of mixture)					
	5	10	15	20	25	30	5	10	15	20	25	30
100.00	145.51	79.94	45.76	27.18	16.69	10.56	154.51	89.07	52.96	32.40	20.34	13.08
101.00	140.15	77.32	44.42	26.46	16.29	10.34	148.85	86.19	51.44	31.57	19.88	12.82
102.00	135.04	74.81	43.13	25.77	15.91	10.12	143.45	83.42	49.98	30.77	19.43	12.56
103.00	130.15	72.40	41.88	25.10	15.54	9.90	138.28	80.76	48.56	30.00	19.00	12.31
104.00	125.48	70.07	40.68	24.45	15.17	9.69	133.35	78.21	47.21	29.25	18.58	12.07
105.00	121.03	67.86	39.53	23.83	14.83	9.49	128.63	75.75	45.88	28.52	18.16	11.83
106.00	116.74	65.70	38.39	23.21	14.48	9.29	124.10	73.38	44.60	27.81	17.76	11.59
107.00	112.66	63.65	37.32	22.63	14.15	9.10	119.79	71.11	43.38	27.13	17.37	11.36
108.00	108.73	61.65	36.26	22.05	13.82	8.90	115.65	68.92	42.18	26.46	16.99	11.14
109.00	104.98	59.74	35.24	21.49	13.50	8.71	111.68	66.82	41.03	25.82	16.61	10.92
110.00	101.38	57.88	34.25	20.94	13.18	8.53	107.89	64.80	39.93	25.20	16.26	10.71
111.00	97.93	56.11	33.30	20.41	12.88	8.35	104.25	62.84	38.85	24.59	15.90	10.50
112.00	94.63	54.40	32.39	19.90	12.59	8.17	100.77	60.97	37.82	24.00	15.56	10.29
113.00	91.47	52.76	31.50	19.41	12.30	8.00	97.42	59.16	36.81	23.43	15.23	10.09
114.00	88.42	51.16	30.63	18.92	12.02	7.83	94.22	57.42	35.84	22.87	14.90	9.90
115.00	85.50	49.63	29.80	18.45	11.74	7.67	91.14	55.73	34.89	22.33	14.58	9.71
116.00	82.70	48.16	28.99	17.99	11.48	7.51	88.18	54.11	33.98	21.80	14.27	9.52
117.00	80.01	46.73	28.21	17.54	11.22	7.35	85.35	52.55	33.10	21.30	13.98	9.34
118.00	77.42	45.36	27.45	17.11	10.96	7.20	82.62	51.04	32.24	20.80	13.68	9.16
119.00	74.93	44.03	26.71	16.69	10.71	7.05	79.99	49.58	31.41	20.31	13.39	8.98
120.00	72.55	42.75	26.00	16.28	10.47	6.90	77.47	48.18	30.61	19.85	13.11	8.82

Table 3.6: The calculated viscosity of Lloydminster heavy oil-nC_5 and Lloydminster heavy oil-nC_6 mixtures at different levels of solvent concentration and operating temperatures

T (°C)	n-C_5 concentration (% vol/vol of mixture)						n-C_6 concentration (% vol/vol of mixture)					
	5	10	15	20	25	30	5	10	15	20	25	30
100.00	6.57	5.07	3.94	3.09	2.43	1.93	6.77	5.36	4.26	3.40	2.73	2.20
101.00	6.03	4.69	3.68	2.91	2.31	1.85	6.20	4.95	3.97	3.20	2.59	2.10
102.00	5.52	4.35	3.44	2.74	2.20	1.77	5.68	4.58	3.71	3.01	2.45	2.00
103.00	5.06	4.02	3.22	2.58	2.09	1.69	5.20	4.23	3.46	2.83	2.32	1.91
104.00	4.63	3.72	3.00	2.43	1.98	1.61	4.75	3.91	3.22	2.66	2.20	1.82
105.00	4.24	3.44	2.80	2.29	1.87	1.54	4.35	3.61	3.00	2.50	2.08	1.74
106.00	3.88	3.18	2.61	2.15	1.77	1.47	3.98	3.33	2.80	2.34	1.97	1.65
107.00	3.55	2.93	2.43	2.02	1.68	1.40	3.64	3.08	2.60	2.20	1.86	1.57
108.00	3.25	2.71	2.26	1.89	1.59	1.33	3.32	2.84	2.42	2.06	1.75	1.49
109.00	2.97	2.50	2.11	1.78	1.50	1.27	3.04	2.61	2.25	1.93	1.65	1.42
110.00	2.71	2.30	1.96	1.66	1.41	1.20	2.78	2.41	2.08	1.80	1.56	1.34
111.00	2.48	2.12	1.82	1.56	1.33	1.14	2.53	2.22	1.93	1.69	1.47	1.27
112.00	2.27	1.96	1.69	1.46	1.26	1.08	2.31	2.04	1.79	1.57	1.38	1.21
113.00	2.07	1.80	1.57	1.36	1.18	1.02	2.11	1.88	1.66	1.47	1.30	1.14
114.00	1.89	1.66	1.45	1.27	1.11	0.97	1.93	1.72	1.54	1.37	1.22	1.08
115.00	1.73	1.53	1.35	1.19	1.04	0.92	1.76	1.58	1.42	1.28	1.14	1.02
116.00	1.57	1.40	1.25	1.11	0.98	0.87	1.60	1.46	1.32	1.19	1.07	0.96
117.00	1.44	1.29	1.15	1.03	0.92	0.82	1.46	1.34	1.22	1.10	1.00	0.90
118.00	1.31	1.18	1.07	0.96	0.86	0.77	1.33	1.23	1.12	1.03	0.93	0.85
119.00	1.20	1.09	0.99	0.89	0.81	0.73	1.22	1.12	1.04	0.95	0.87	0.80
120.00	1.09	1.00	0.91	0.83	0.75	0.68	1.11	1.03	0.96	0.88	0.81	0.75

As it was described in section 2.5.4, the drainage rate of the SAGD process is inversely proportional to the kinematic viscosity of the mobile oil. In a SAGD process, the viscosity reduction is as a direct result of steam heating. Considering the solvent analogue of the SAGD process to be Vapour Extraction (VAPEX) in which the viscosity reduction is a result of solvent dilution, it could also be shown that the drainage rate inversely varies with kinematic viscosity (Das and Butler, 1998; Yazdani and maini, 2005). As far as the SA-SAGD process is concerned, the in-situ mobilization mechanisms are affected by heat transfer and mass transfer at the pore-scale which is a combination of both SAGD and VAPEX mobilization mechanisms. It could be concluded that for such a gravity-dominated flow whose mobilization mechanisms include both heat and mass transfer, the drainage rate would be inversely proportional to the kinematic viscosity of the mobile live oil.

Having the predicted dynamic viscosity and density of the mobile live oil under prevailing SA-SAGD operational conditions, one can predict the kinematic viscosity behaviour under different temperature and solvent content conditions of the mobile live oil. Figures 3.29 and 3.30 show the effect of temperature on the kinematic viscosity of Cold lake bitumen–nC_5 and Cold Lake bitumen–nC_6 mixtures at different solvent concentrations. In addition, Figures 3.31 and 3.32 present the temperature variation of the Lloydminster heavy oil–nC_5 as well as Lloydminster heavy oil–nC_6 kinematic mixture viscosities at different solvent content of the produced mobile live oil. In order to compare the effect of solvent type on the viscosity reduction of mixtures at different operating conditions, Figures 3.33 and 3.34 are presented here. The kinematic viscosity raw data are also tabulated in Tables 3.7 and 3.8. According to these Figures, it is concluded that for each particular oil type, the kinematic viscosity of the oil-solvent mixture is more sensitive to temperature at lower solvent content of the mobile live oil. In addition, the lighter the solvent is, the lower would be the oil-solvent mixture kinematic viscosity for each particular oil type at each particular operating temperature. Under similar solvent type and concentration conditions, it is believed that bitumen-solvent kinematic viscosity is more sensitive to temperature compared to that of the heavy oil-solvent mixture.

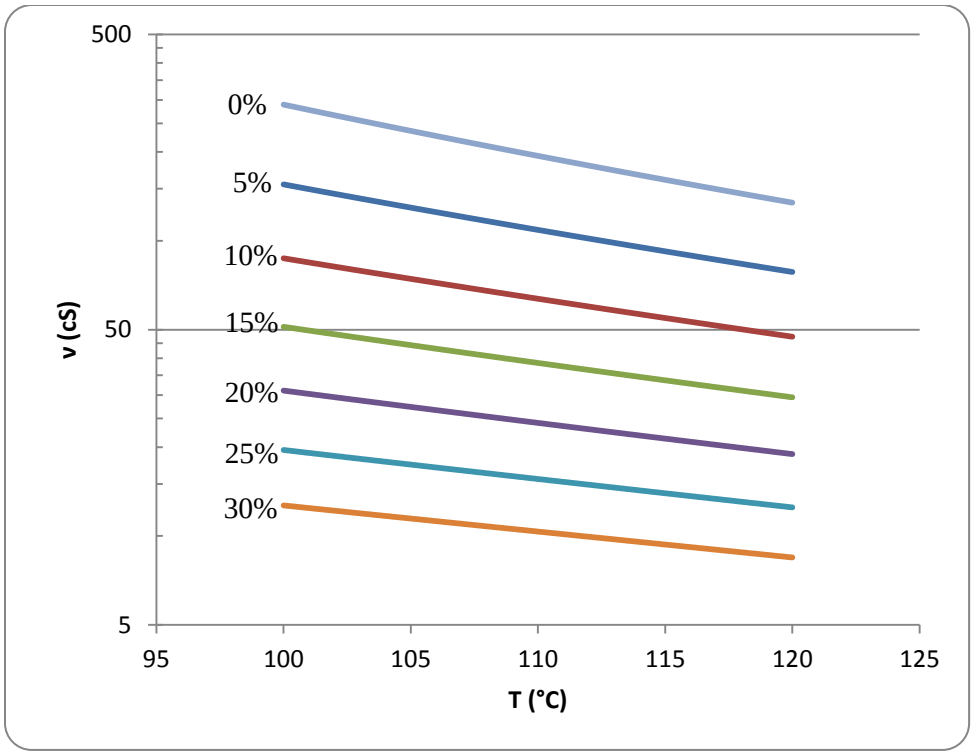

Figure 3.29: The effect of temperature on the kinematic viscosity of Cold Lake bitumen as well as on the bitumen-nC_5 kinematic mixture viscosity at different solvent volume fractions

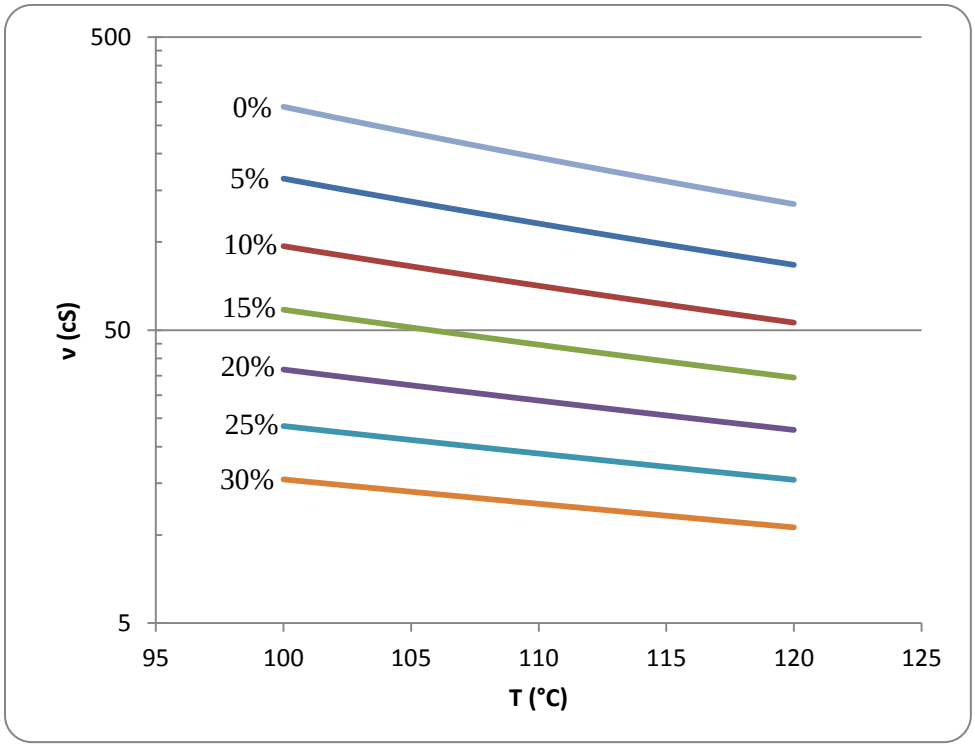

Figure 3.30: The effect of temperature on the kinematic viscosity of Cold Lake bitumen as well as on the bitumen-nC_6 kinematic mixture viscosity at different solvent volume fractions

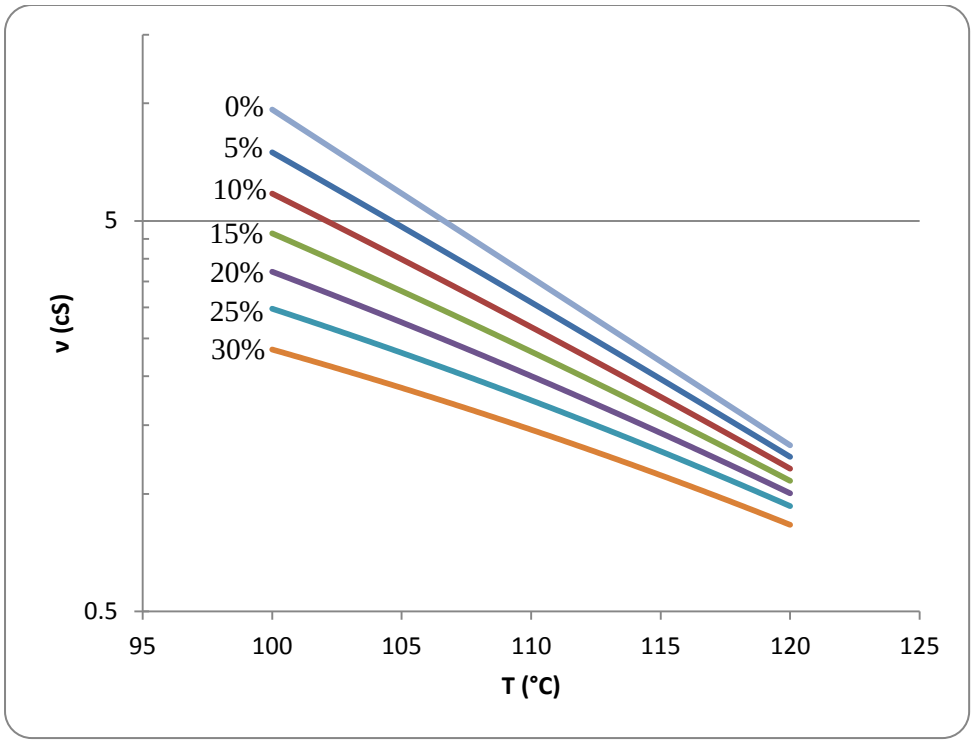

Figure 3.31: The effect of temperature on the kinematic viscosity of Lloydminster heavy oil as well as on the heavy oil-nC_5 kinematic mixture viscosity at different solvent volume fractions

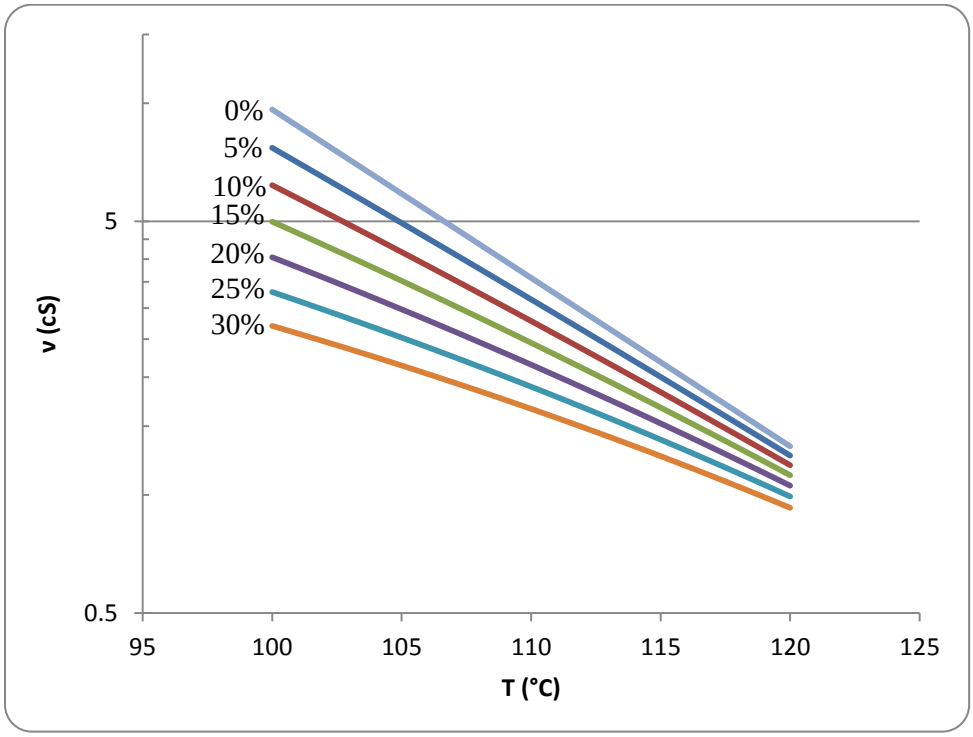

Figure 3.32: The effect of temperature on the kinematic viscosity of Lloydminster heavy oil as well as on the heavy oil-nC_6 kinematic mixture viscosity at different solvent volume fractions

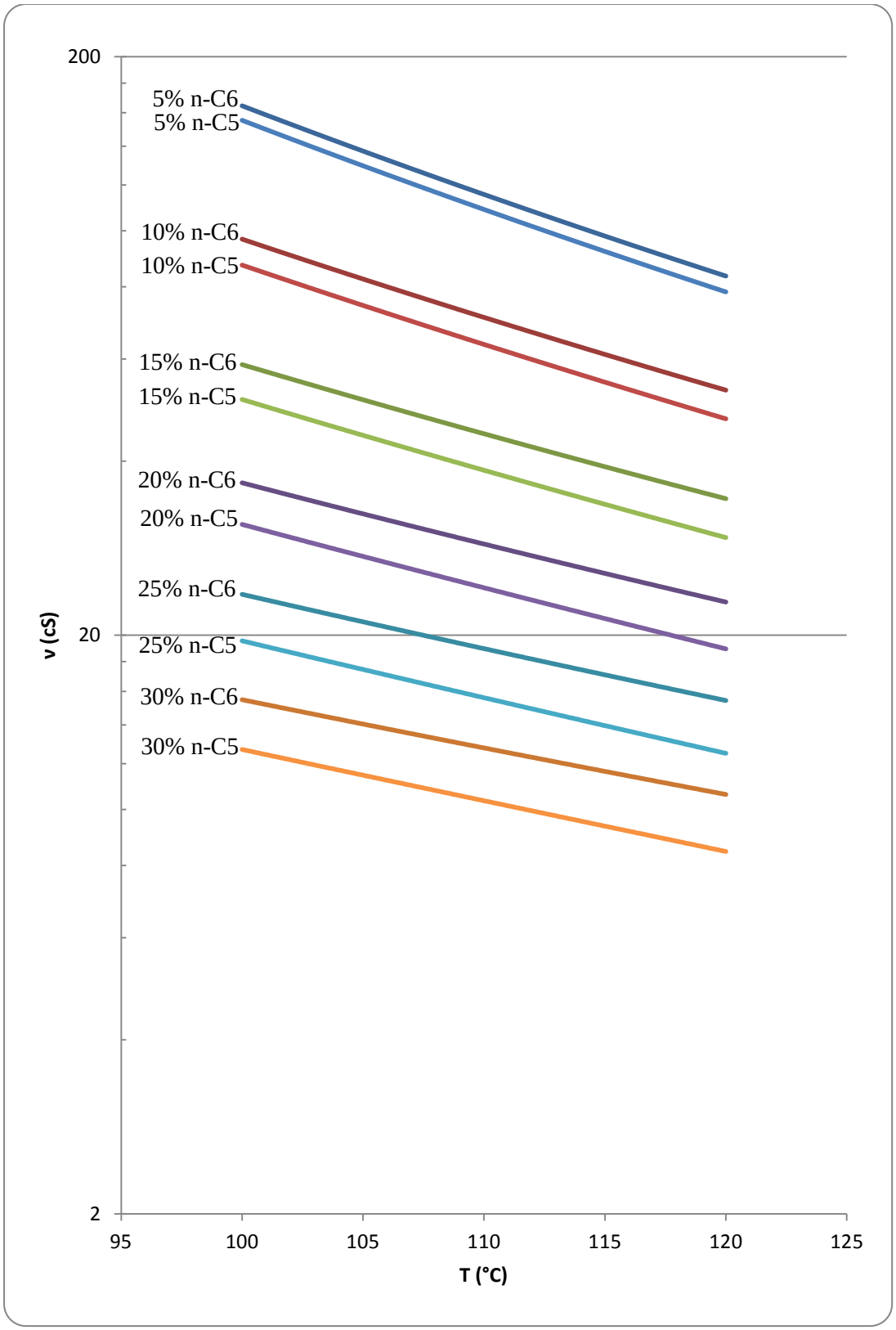

Figure 3.33: Comparison chart between Cold Lake bitumen-nC_5 and Cold Lake bitumen-nC_6 kinematic mixture viscosities at different solvent concentration and temperature levels

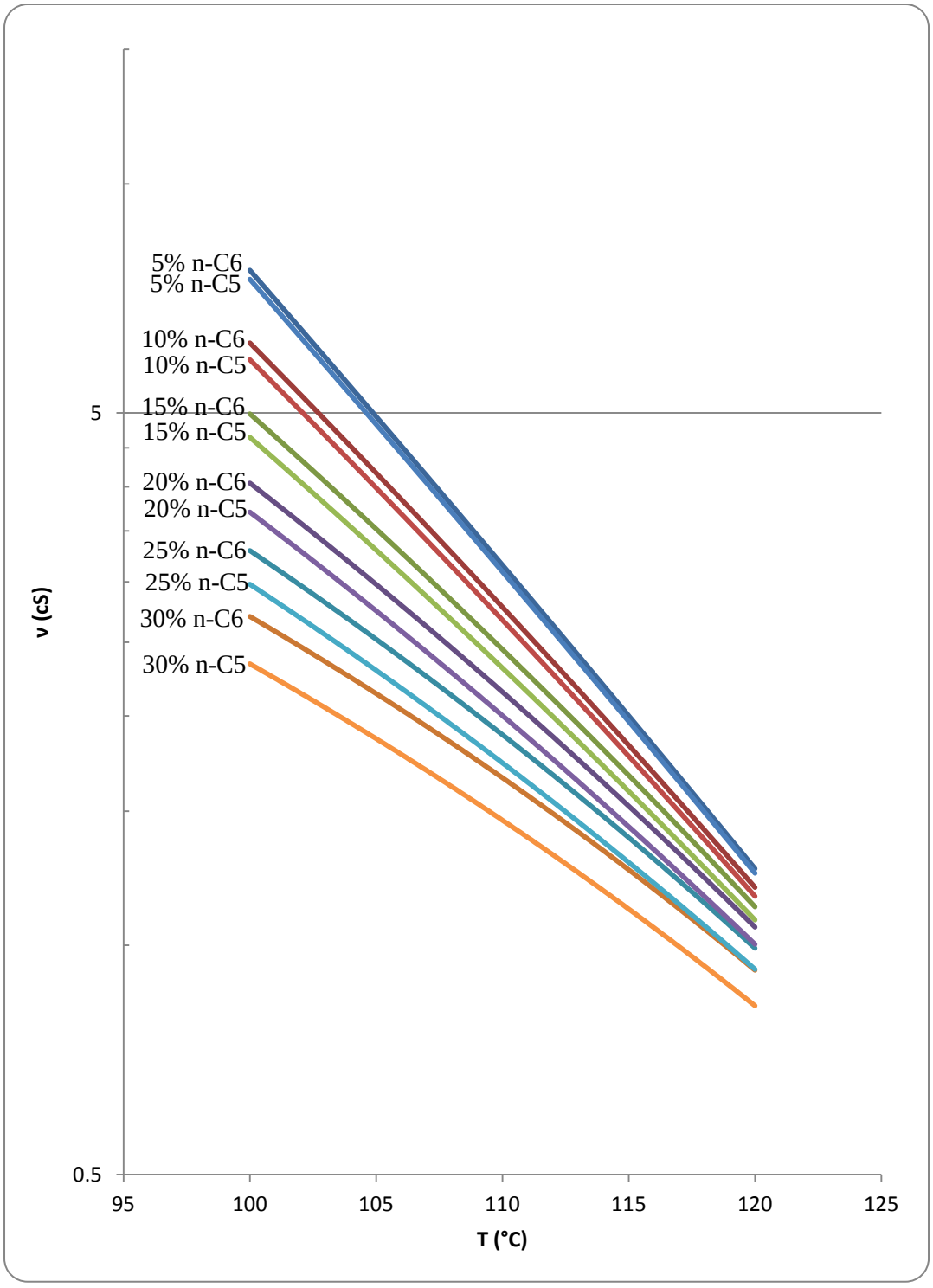

Figure 3.34: Comparison chart between Lloydminster heavy oil-nC_5 and Lloydminster heavy oil-nC_6 kinematic mixture viscosities at different solvent concentration and temperature levels

Table 3.7: The calculated kinematic viscosity of Cold Lake bitumen-nC_5 and Cold Lake bitumen-nC_6 mixtures at different levels of solvent concentration and operating temperatures

T (°C)	n-C_5 concentration (% vol/vol of mixture)						n-C_6 concentration (% vol/vol of mixture)					
	5	10	15	20	25	30	5	10	15	20	25	30
100.00	155.21	87.23	51.11	31.09	19.56	12.69	164.42	96.72	58.71	36.68	23.53	15.47
101.00	149.59	84.44	49.65	30.30	19.12	12.44	158.49	93.65	57.07	35.77	23.02	15.17
102.00	144.23	81.75	48.24	29.53	18.68	12.18	152.83	90.70	55.48	34.90	22.52	14.88
103.00	139.10	79.17	46.89	28.79	18.26	11.94	147.42	87.87	53.95	34.04	22.03	14.60
104.00	134.19	76.68	45.57	28.07	17.85	11.69	142.26	85.16	52.48	33.22	21.56	14.32
105.00	129.51	74.31	44.32	27.37	17.46	11.46	137.31	82.54	51.05	32.42	21.10	14.05
106.00	125.01	71.99	43.08	26.69	17.06	11.23	132.56	80.00	49.66	31.63	20.64	13.78
107.00	120.72	69.80	41.90	26.04	16.69	11.01	128.04	77.59	48.33	30.89	20.21	13.52
108.00	116.59	67.65	40.75	25.39	16.31	10.78	123.69	75.25	47.04	30.15	19.78	13.26
109.00	112.64	65.60	39.64	24.77	15.95	10.57	119.53	73.00	45.79	29.44	19.36	13.01
110.00	108.84	63.61	38.55	24.15	15.59	10.35	115.55	70.84	44.59	28.75	18.96	12.77
111.00	105.22	61.71	37.52	23.57	15.25	10.14	111.72	68.76	43.42	28.08	18.57	12.53
112.00	101.74	59.88	36.51	23.00	14.92	9.94	108.06	66.75	42.29	27.43	18.18	12.30
113.00	98.40	58.11	35.54	22.44	14.59	9.74	104.54	64.81	41.19	26.79	17.81	12.07
114.00	95.18	56.39	34.59	21.89	14.27	9.55	101.16	62.95	40.14	26.18	17.44	11.85
115.00	92.10	54.74	33.67	21.37	13.96	9.36	97.91	61.14	39.11	25.58	17.08	11.63
116.00	89.14	53.16	32.79	20.86	13.65	9.17	94.80	59.41	38.11	25.00	16.73	11.42
117.00	86.30	51.62	31.92	20.36	13.35	8.99	91.81	57.74	37.16	24.44	16.40	11.22
118.00	83.57	50.14	31.09	19.88	13.06	8.81	88.93	56.11	36.22	23.88	16.06	11.01
119.00	80.93	48.70	30.28	19.40	12.78	8.63	86.16	54.54	35.31	23.34	15.74	10.81
120.00	78.41	47.32	29.50	18.95	12.50	8.46	83.51	53.04	34.44	22.82	15.42	10.61

Table 3.8: The calculated kinematic viscosity of Lloydminster heavy oil-nC_5 and Lloydminster heavy oil-nC_6 mixtures at different levels of solvent concentration and operating temperatures

T (°C)	n-C_5 concentration (% vol/vol of mixture)						n-C_6 concentration (% vol/vol of mixture)					
	5	10	15	20	25	30	5	10	15	20	25	30
100.00	7.49	5.87	4.65	3.71	2.98	2.34	7.70	6.18	4.99	4.04	3.30	2.70
101.00	6.87	5.44	4.34	3.50	2.83	2.24	7.05	5.72	4.66	3.81	3.13	2.58
102.00	6.29	5.04	4.06	3.29	2.69	2.14	6.46	5.29	4.35	3.59	2.97	2.47
103.00	5.76	4.66	3.79	3.10	2.55	2.05	5.91	4.89	4.05	3.37	2.81	2.36
104.00	5.28	4.31	3.54	2.92	2.42	1.96	5.41	4.52	3.78	3.17	2.67	2.25
105.00	4.83	3.99	3.30	2.75	2.30	1.87	4.95	4.17	3.52	2.98	2.52	2.14
106.00	4.42	3.68	3.08	2.58	2.17	1.78	4.52	3.85	3.28	2.79	2.38	2.04
107.00	4.05	3.40	2.87	2.43	2.06	1.70	4.14	3.55	3.05	2.62	2.25	1.94
108.00	3.70	3.14	2.67	2.28	1.95	1.61	3.78	3.27	2.84	2.46	2.13	1.84
109.00	3.38	2.90	2.49	2.14	1.84	1.54	3.46	3.02	2.63	2.30	2.01	1.75
110.00	3.09	2.67	2.31	2.00	1.74	1.46	3.16	2.78	2.45	2.15	1.89	1.66
111.00	2.83	2.46	2.15	1.88	1.64	1.39	2.88	2.56	2.27	2.01	1.78	1.57
112.00	2.58	2.27	2.00	1.76	1.54	1.31	2.63	2.36	2.11	1.88	1.67	1.49
113.00	2.36	2.09	1.85	1.64	1.45	1.25	2.40	2.17	1.95	1.75	1.57	1.41
114.00	2.16	1.93	1.72	1.53	1.37	1.18	2.19	1.99	1.81	1.63	1.48	1.33
115.00	1.97	1.77	1.59	1.43	1.28	1.12	2.00	1.83	1.67	1.52	1.38	1.26
116.00	1.80	1.63	1.48	1.34	1.21	1.05	1.83	1.68	1.55	1.42	1.30	1.18
117.00	1.64	1.50	1.37	1.24	1.13	1.00	1.67	1.54	1.43	1.32	1.22	1.12
118.00	1.50	1.38	1.26	1.16	1.06	0.94	1.52	1.42	1.32	1.23	1.14	1.05
119.00	1.36	1.26	1.17	1.08	0.99	0.88	1.38	1.30	1.22	1.14	1.06	0.99
120.00	1.24	1.16	1.08	1.00	0.93	0.83	1.26	1.19	1.12	1.06	0.99	0.93

3.5.4. Interface Advancement Velocity at the Pore–Scale: Experimental Results

In this section, results of the SA-SAGD interface advancement velocity at the pore-scale are presented and analyzed based on our pore-level visualization experiments at the controlled environmental conditions. As it was stated before, the surface of each glass micromodel was divided into cell blocks containing definite numbers of pores per unit area using a pen marker. The full-frame pictures taken over the entire height of the pore network during the SA-SAGD process were analyzed. Each cell block was magnified at particular time intervals using image processing software, and the instantaneous position of the SA-SAGD interface was tracked in each row of pores within each particular cell block. An arithmetic averaging was then carried out in order to determine the average sweep rate of the process at each particular cell block within subsequent time frames. As a result, an average SA-SAGD interface advancement sweep rate was determined for each particular cell block at corresponding time intervals. It was observed that the interface advancement velocity was constant at each particular elevation (i.e. cell block number from the top of the model) along the height of the micromodel. Finally, the determined interface sweep rates at each elevation from the model's top were arithmetically averaged over the height of the porous network to obtain a representative interface advancement velocity for that particular model under prevailing operational conditions. The average SA-SAGD sweep rate for each particular model is represented in terms of the number of pores invaded per unit time. It is also translated to the unit length per process time using two pore-scale dimensions of porous networks, including the pore-to-pore distance and pore body width.

The interface position recognition in our pore-scale SA-SAGD visualization experiments was quite easier than that in the SAGD visualization experiments. This is because of the miscible nature of the SA-SAGD process at the pore-scale in which the width of the mobilized region was thinner (i.e. contains less pores) than that of the SAGD process at the pore-level. This made it easier to identify the boundary between the oil-saturated pores and the vapour-saturated pores. All of our SA-SAGD trials were carried out under condensing mode of operation during which solvent vapour condensed over the surface of bitumen-saturated pores. As a result, there was normally a smooth distinctive line between the vapour-saturated pores and those saturated with bitumen. This made it reasonably easier to locate the SA-SAGD interface and track it versus process time. As it was also pointed out in section 2.5.3, about 10-20 pores from the topside of

each glass micromodel were not considered for the interface advancement position tracking because of the unstable frontal advancement of the vapour phase at the pore-level in this region.

Tables 3.9 to 3.11 summarize the results of measured SA-SAGD interface advancement velocities for three different models of DL-1, OM-1, and OM-2 when both n-C_5 and n-C_6 were used as the solvent and Cold Lake bitumen was employed as the oil type. As the oil type used in our SAGD visualization experiments was the same Cold Lake bitumen sample, the last column(s) of these three Tables contain the results of the pore-scale SAGD interface advancement velocities for the purpose of comparison with those of the SA-SAGD processes. The SA-SAGD sweep rate in pores/min was also converted to mm/min using two pore-scale dimensions of pore-body width as well as pore to pore distance for each particular porous pattern. Tables 3.12 to 3.14 present the results of the SA-SAGD interface advancement velocities for three models of DL-1, OM-1, and OM-2 using both n-C_5 and n-C_6 solvents when Lloydminster heavy oil blend was used as the oil phase. The sweep rate was converted from pores/min to mm/min unit system using the procedure stated above for all three micromodels.

Figures 3.35 to 3.37 present the procedure through which the interface advancement velocity data were calculated for three employed models focusing on particular windows of pores along the height of the porous patterns. These Figures deal with the experimental trials in which Cold Lake bitumen was employed as the oil type. The sweep rates obtained using these three Figures are inserted in bold digits in Tables 3.9 to 3.11. The same procedure was then carried out for all the cell blocks along the height of each particular model, and a representative sweep rate was then calculated for each model under pertaining operating conditions using arithmetic averaging. Figures 3.38 to 3.40 show the interface advancement velocities for three micromodels in trials in which Lloydminster heavy oil blend was used as the oil type. Each of these Figures shows the sweep rate at one particular elevation measured from the topside of the model. The data achieved using these three graphs are presented in bold figures in Tables 3.12 to 3.14. For every employed model, the sweep rates at other elevations along the height of the porous network were calculated accordingly, and are presented in Tables 3.12 to 3.14. For each micromodel, a representative interface advancement velocity was calculated by averaging individual sweep rates along the model's height, and is presented in Tables 3.12 to 3.14 in both pores/min and mm/min units.

Table 3.9: SA-SAGD interface advancement velocity [Model: DL-1, Oil type: Cold Lake bitumen]

Micromodel	**DL-1**	**DL-1**	**DL-1**	**DL-1**	**DL-1**
SA-SAGD Design RUN Number	6	13	23	19	SAGD
	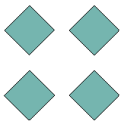	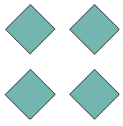	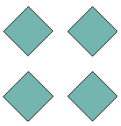	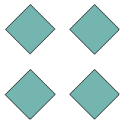	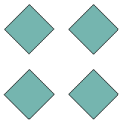
Average temperature in the invaded zone (°C)	106.80	102.75	108.30	103.45	103.10
Solvent Type	n-C_5	n-C_5	n-C_6	n-C_6	N/A
Solvent Concentration (% Vol/Vol)	5	15	5	15	0
Location in the Model	**Interface advancement velocity ($v_p^{SA-SAGD}$), pores/min**				
21-30 pores from top	n/a	n/a	n/a	n/a	n/a
31-40 pores from top	0.360	0.397	0.364	0.431	0.331
41-50 pores from top	0.348	0.379	0.348	0.408	0.316
51-60 pores from top	0.330	0.364	0.333	0.383	0.306
61-70 pores from top	**0.309**	**0.341**	**0.312**	**0.361**	**0.281**
71-80 pores from top	0.297	0.339	0.302	0.356	0.277
81-90 pores from top	0.292	0.326	0.297	0.348	0.268
91-100 pores from top	0.285	0.318	0.288	0.341	0.260
101-110 pores from top	0.282	0.311	0.285	0.336	0.253
111-120 pores from top	0.279	0.308	0.280	0.335	0.249
121-130 pores from top	n/a	n/a	n/a	n/a	n/a
131-140 pores from top	n/a	n/a	n/a	n/a	n/a
141-150 pores from top	n/a	n/a	n/a	n/a	n/a
Average Interface Velocity					
(pores/min)	**0.309±0.020**	**0.343±0.020**	**0.312±0.019**	**0.367±0.022**	**0.282±0.019**
Using Pore to Pore distance (mm/min)	**0.631**	**0.699**	**0.637**	**0.748**	**0.576**
Using Pore Body Width (mm/min)	**0.631**	**0.699**	**0.637**	**0.748**	**0.576**

Table 3.10: SA-SAGD interface advancement velocity [Model: OM-2, Oil type: Cold Lake bitumen]

Micromodel	**OM-2**	**OM-2**	**OM-2**	**OM-2**	**OM-2**	**OM-2**
SA-SAGD Design RUN Number	7	2	16	10	SAGD	SAGD
	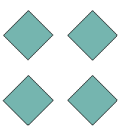	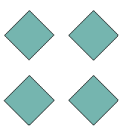	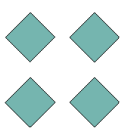	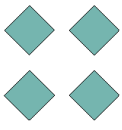	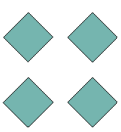	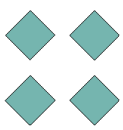
Average temperature in the invaded zone (°C)	107.10	102.10	108.90	101.45	103.40	110.20
Solvent Type	n-C_5	n-C_5	n-C_6	n-C_6	N/A	N/A
Solvent Concentration (% Vol/Vol)	5	15	5	15	0	0
Location in the Model	**Interface advancement velocity ($v_p^{SA-SAGD}$), pores/min**					
21-30 pores from top	n/a	n/a	n/a	n/a	n/a	n/a
31-40 pores from top	0.306	0.411	0.318	0.431	0.264	0.396
41-50 pores from top	**0.283**	**0.327**	**0.284**	**0.358**	**0.243**	**0.335**
51-60 pores from top	0.271	0.323	0.274	0.338	0.238	0.311
61-70 pores from top	0.262	0.309	0.265	0.320	0.232	0.298
71-80 pores from top	0.252	0.303	0.253	0.314	0.226	0.285
81-90 pores from top	0.245	0.288	0.245	0.299	0.221	0.272
91-100 pores from top	0.234	0.282	0.236	0.291	0.215	0.270
101-110 pores from top	0.224	0.275	0.227	0.285	0.209	0.267
111-120 pores from top	0.219	0.270	0.221	0.278	0.202	0.262
121-130 pores from top	n/a	n/a	n/a	n/a	n/a	n/a
131-140 pores from top	n/a	n/a	n/a	n/a	n/a	n/a
141-150 pores from top	n/a	n/a	n/a	n/a	n/a	n/a
Average Interface Velocity						
(pores/min)	**0.255±0.019**	**0.310±0.028**	**0.258±0.020**	**0.324±0.031**	**0.228±0.012**	**0.300±0.028**
Using Pore to Pore distance (mm/min)	**0.510**	**0.619**	**0.516**	**0.648**	**0.456**	**0.599**
Using Pore Body Width (mm/min)	**0.510**	**0.619**	**0.516**	**0.648**	**0.456**	**0.599**

Table 3.11: SA-SAGD interface advancement velocity [Model: OM-1, Oil type: Cold Lake bitumen]

Micromodel	**OM-1**	**OM-1**	**OM-1**	**OM-1**	**OM-1**	**OM-1**
SA-SAGD Design RUN Number	5	1	4	9	SAGD	SAGD
	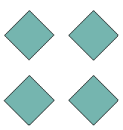	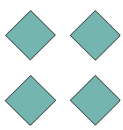	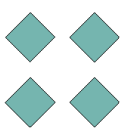	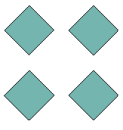	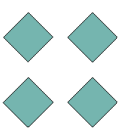	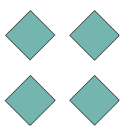
Average temperature in the invaded zone (°C)	106.40	103.30	107.40	101.85	101.70	116.35
Solvent Type	n-C_5	n-C_5	n-C_6	n-C_6	N/A	N/A
Solvent Concentration (% Vol/Vol)	5	15	5	15	0	0
Location in the Model	**Interface advancement velocity ($v_p^{SA-SAGD}$), pores/min**					
21-30 pores from top	n/a	n/a	n/a	n/a	n/a	n/a
31-40 pores from top	**0.272**	**0.282**	**0.270**	**0.324**	**0.240**	**0.402**
41-50 pores from top	0.265	0.277	0.269	0.321	0.233	0.398
51-60 pores from top	0.259	0.272	0.264	0.318	0.228	0.392
61-70 pores from top	0.252	0.269	0.258	0.316	0.224	0.386
71-80 pores from top	0.246	0.265	0.251	0.311	0.219	0.380
81-90 pores from top	0.244	0.259	0.247	0.307	0.216	0.373
91-100 pores from top	0.238	0.255	0.243	0.301	0.209	0.365
101-110 pores from top	0.231	0.249	0.235	0.298	0.201	0.359
111-120 pores from top	0.228	0.244	0.233	0.293	0.195	0.352
121-130 pores from top	n/a	n/a	n/a	n/a	n/a	n/a
131-140 pores from top	n/a	n/a	n/a	n/a	n/a	n/a
141-150 pores from top	n/a	n/a	n/a	n/a	n/a	n/a
Average Interface Velocity						
(pores/min)	**0.248±0.010**	**0.264±0.008**	**0.252±0.009**	**0.310±0.007**	**0.218±0.010**	**0.379±0.011**
Using Pore to Pore distance (mm/min)	**0.497**	**0.527**	**0.504**	**0.620**	**0.437**	**0.757**
Using Pore Body Width (mm/min)	**0.497**	**0.527**	**0.504**	**0.620**	**0.437**	**0.757**

Table 3.12: SA-SAGD interface advancement velocity [Model: DL-1, Oil type: Lloydminster heavy oil blend]

Micromodel	**DL-1**	**DL-1**	**DL-1**	**DL-1**
SA-SAGD Design RUN Number	18	8	21	12
	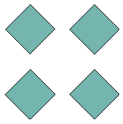	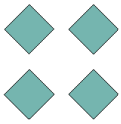	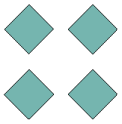	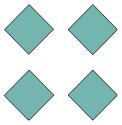
Average temperature in the invaded zone (°C)	105.95	103.50	107.80	103.80
Solvent Type	n-C_5	n-C_5	n-C_6	n-C_6
Solvent Concentration (% Vol/Vol)	5	15	5	15
Location in the Model	**Interface advancement velocity ($v_p^{SA-SAGD}$), pores/min**			
21-30 pores from top	n/a	n/a	n/a	n/a
31-40 pores from top	0.473	0.531	0.540	0.724
41-50 pores from top	0.458	0.511	0.522	0.710
51-60 pores from top	0.445	0.505	0.513	0.698
61-70 pores from top	**0.423**	**0.483**	**0.494**	**0.679**
71-80 pores from top	0.411	0.475	0.479	0.669
81-90 pores from top	0.403	0.467	0.470	0.658
91-100 pores from top	0.397	0.460	0.463	0.650
101-110 pores from top	0.388	0.452	0.455	0.642
111-120 pores from top	0.382	0.445	0.445	0.633
121-130 pores from top	n/a	n/a	n/a	n/a
131-140 pores from top	n/a	n/a	n/a	n/a
141-150 pores from top	n/a	n/a	n/a	n/a
Average Interface Velocity				
(pores/min)	**0.420±0.021**	**0.481±0.019**	**0.487±0.021**	**0.674±0.021**
Using Pore to Pore distance (mm/min)	**0.857**	**0.981**	**0.993**	**1.374**
Using Pore Body Width (mm/min)	**0.857**	**0.981**	**0.993**	**1.374**

Table 3.13: SA-SAGD interface advancement velocity [Model: OM-2, Oil type: Lloydminster heavy oil blend]

Micromodel	**OM-2**	**OM-2**	**OM-2**	**OM-2**
SA-SAGD Design RUN Number	24	15	17	14
	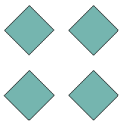	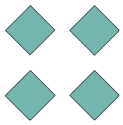	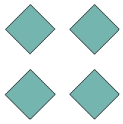	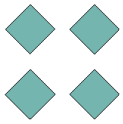
Average temperature in the invaded zone (°C)	107.55	101.75	108.35	102.10
Solvent Type	n-C_5	n-C_5	n-C_6	n-C_6
Solvent Concentration (% Vol/Vol)	5	15	5	15
Location in the Model	**Interface advancement velocity ($v_p^{SA-SAGD}$), pores/min**			
21-30 pores from top	n/a	n/a	n/a	n/a
31-40 pores from top	0.412	0.469	0.445	0.548
41-50 pores from top	**0.390**	**0.441**	**0.421**	**0.516**
51-60 pores from top	0.383	0.430	0.411	0.502
61-70 pores from top	0.379	0.423	0.406	0.496
71-80 pores from top	0.371	0.416	0.399	0.490
81-90 pores from top	0.365	0.410	0.395	0.482
91-100 pores from top	0.360	0.404	0.388	0.477
101-110 pores from top	0.354	0.396	0.381	0.468
111-120 pores from top	0.349	0.390	0.377	0.461
121-130 pores from top	n/a	n/a	n/a	n/a
131-140 pores from top	n/a	n/a	n/a	n/a
141-150 pores from top	n/a	n/a	n/a	n/a
Average Interface Velocity				
(pores/min)	**0.374±0.013**	**0.420±0.016**	**0.403±0.014**	**0.493±0.017**
Using Pore to Pore distance (mm/min)	**0.747**	**0.840**	**0.805**	**0.987**
Using Pore Body Width (mm/min)	**0.747**	**0.840**	**0.805**	**0.987**

Table 3.14: SA-SAGD interface advancement velocity [Model: OM-1, Oil type: Lloydminster heavy oil blend]

Micromodel	**OM-1**	**OM-1**	**OM-1**	**OM-1**
SA-SAGD Design RUN Number	22	3	11	20
	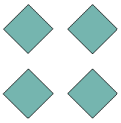	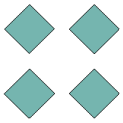	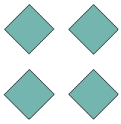	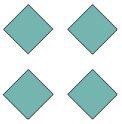
Average temperature in the invaded zone (°C)	107.15	102.90	107.85	101.60
Solvent Type	n-C_5	n-C_5	n-C_6	n-C_6
Solvent Concentration (% Vol/Vol)	5	15	5	15
Location in the Model	**Interface advancement velocity ($v_p^{SA-SAGD}$), pores/min**			
21-30 pores from top	n/a	n/a	n/a	n/a
31-40 pores from top	**0.338**	**0.437**	**0.386**	**0.473**
41-50 pores from top	0.332	0.429	0.379	0.466
51-60 pores from top	0.326	0.425	0.374	0.459
61-70 pores from top	0.321	0.421	0.367	0.455
71-80 pores from top	0.315	0.416	0.363	0.451
81-90 pores from top	0.313	0.411	0.356	0.444
91-100 pores from top	0.308	0.402	0.350	0.440
101-110 pores from top	0.302	0.395	0.344	0.435
111-120 pores from top	0.297	0.390	0.341	0.428
121-130 pores from top	n/a	n/a	n/a	n/a
131-140 pores from top	n/a	n/a	n/a	n/a
141-150 pores from top	n/a	n/a	n/a	n/a
Average Interface Velocity				
(pores/min)	**0.317±0.009**	**0.414±0.010**	**0.362±0.010**	**0.450±0.010**
Using Pore to Pore distance (mm/min)	**0.634**	**0.828**	**0.724**	**0.900**
Using Pore Body Width (mm/min)	**0.634**	**0.828**	**0.724**	**0.900**

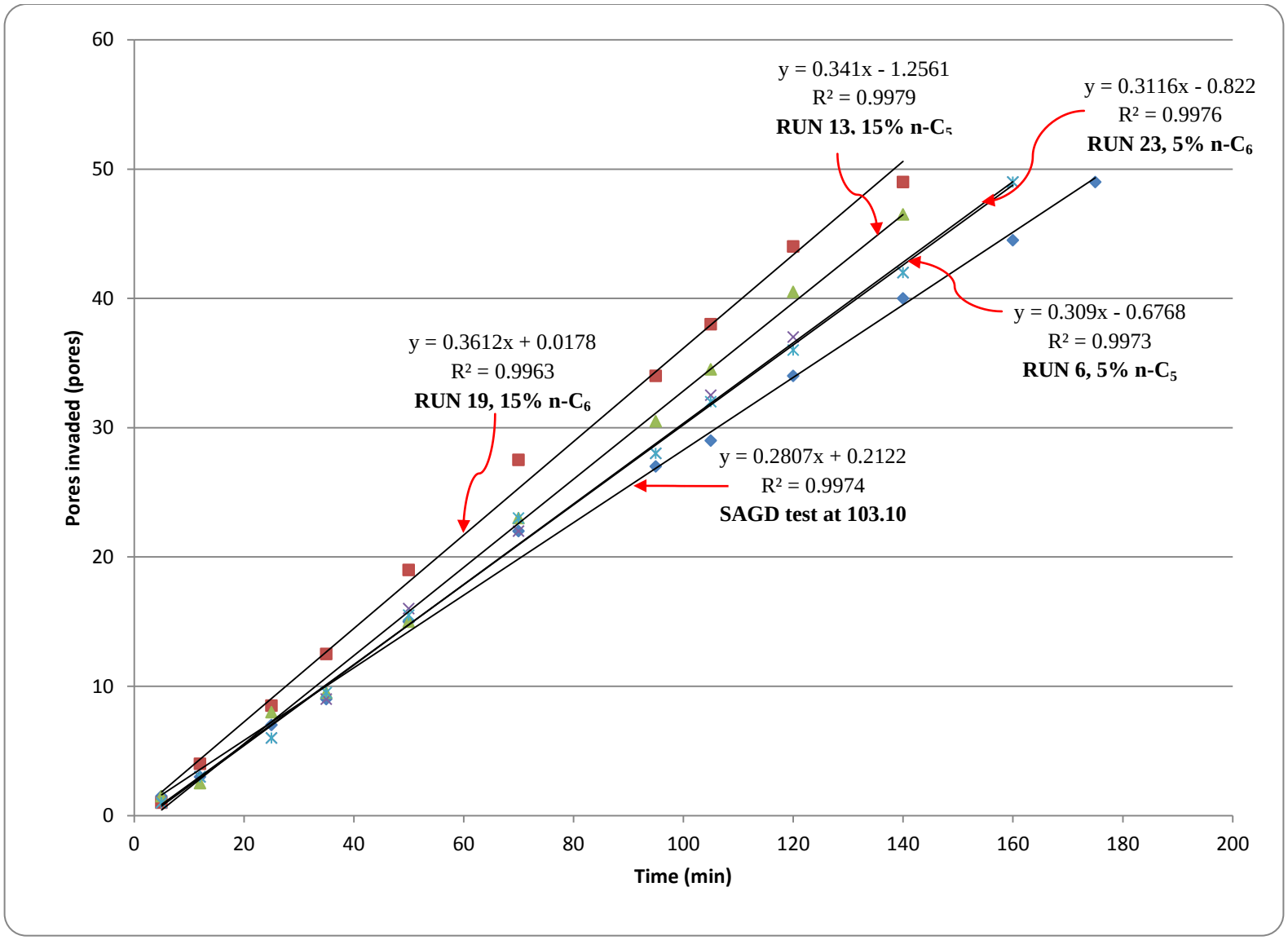

Figure 3.35: Interface advancement velocity for Model DL-1 [61-70 pores from top, Oil type: Cold Lake bitumen]

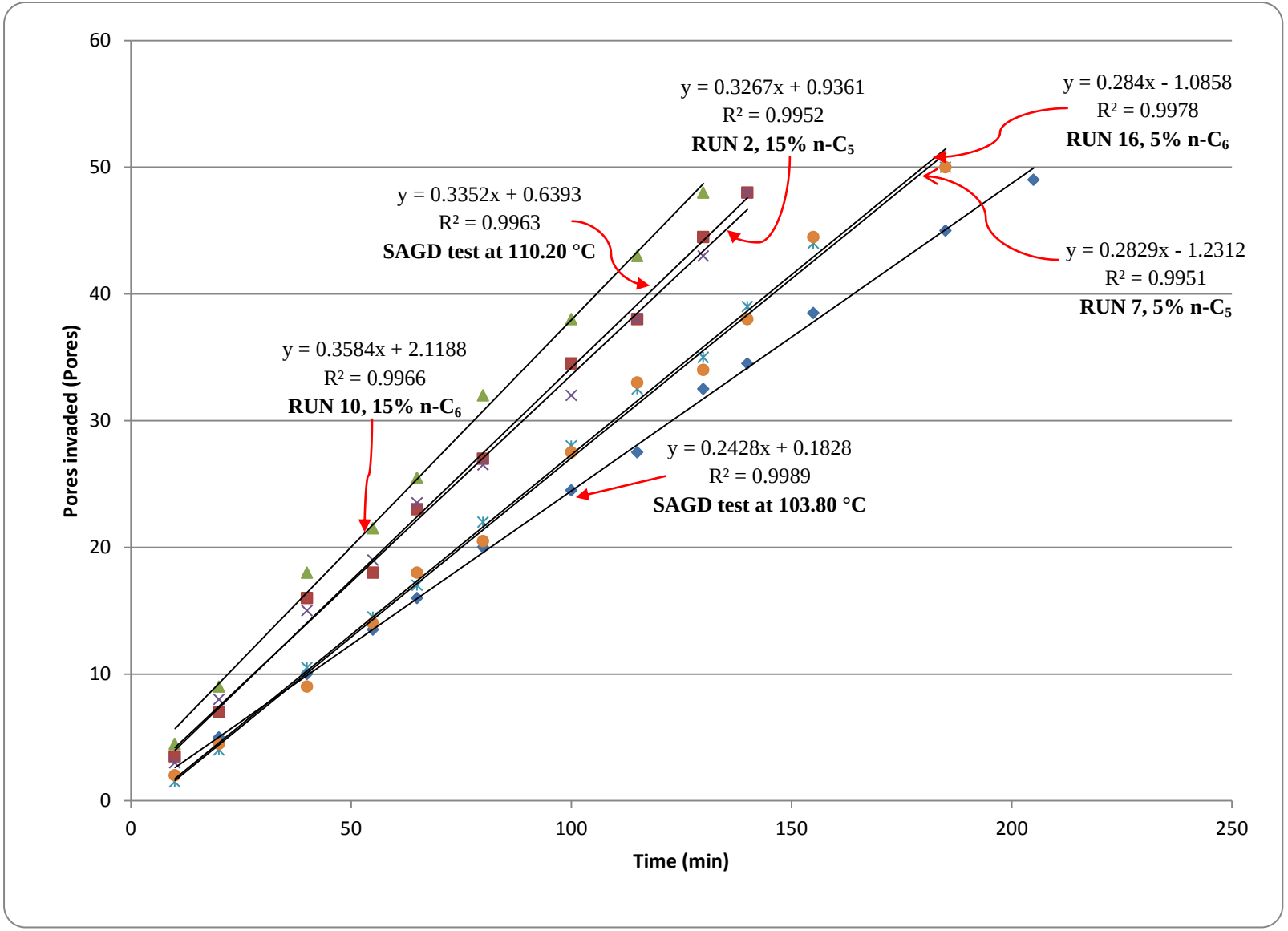

Figure 3.36: Interface advancement velocity for Model OM-2 [41-50 pores from top, Oil type: Cold Lake bitumen]

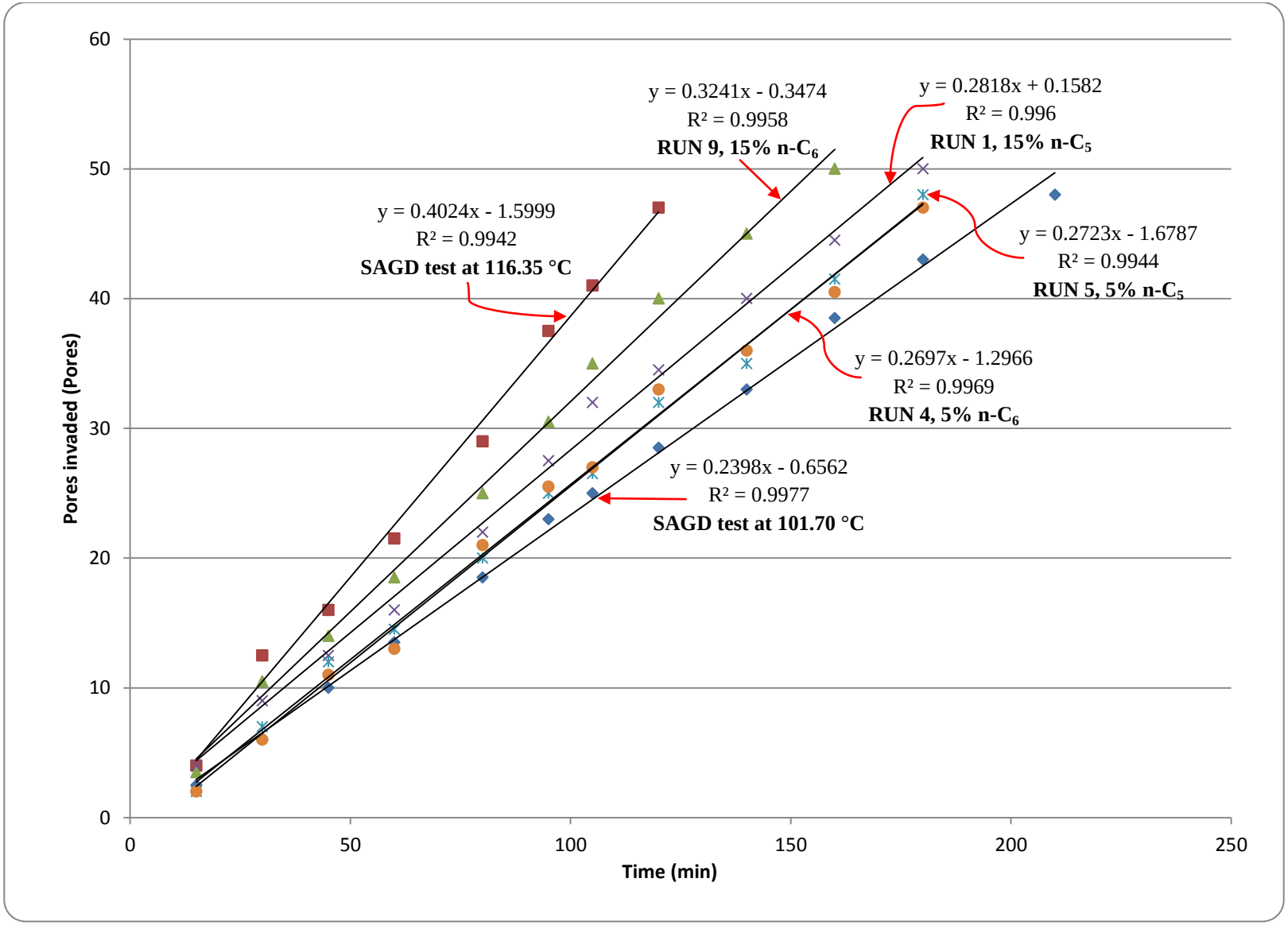

Figure 3.37: Interface advancement velocity for Model OM-1 [31-40 pores from top, Oil type: Cold Lake bitumen]

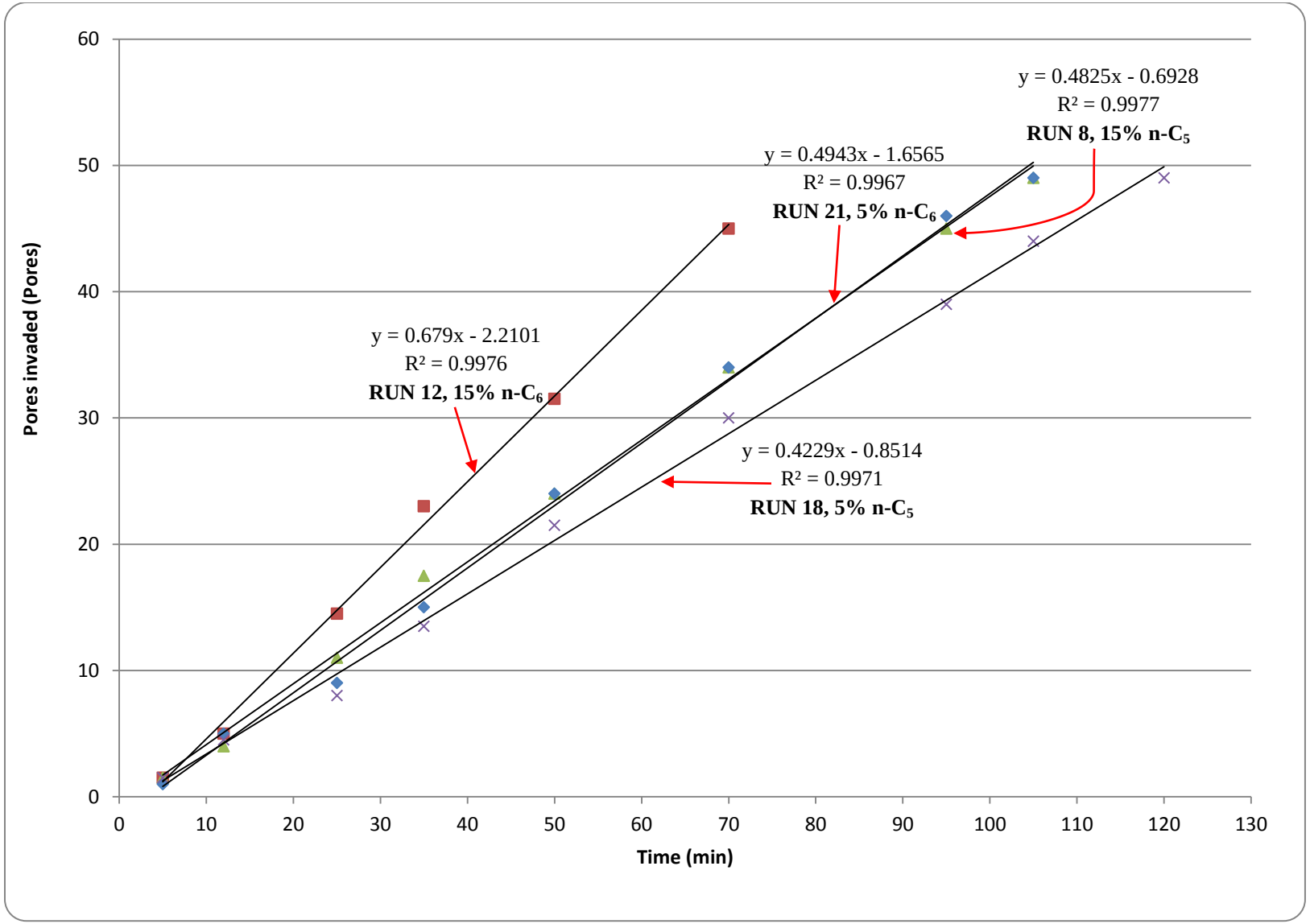

Figure 3.38: Interface advancement velocity diagram for Model DL-1 [61-70 pores from top, Oil type: Lloydminster heavy oil blend]

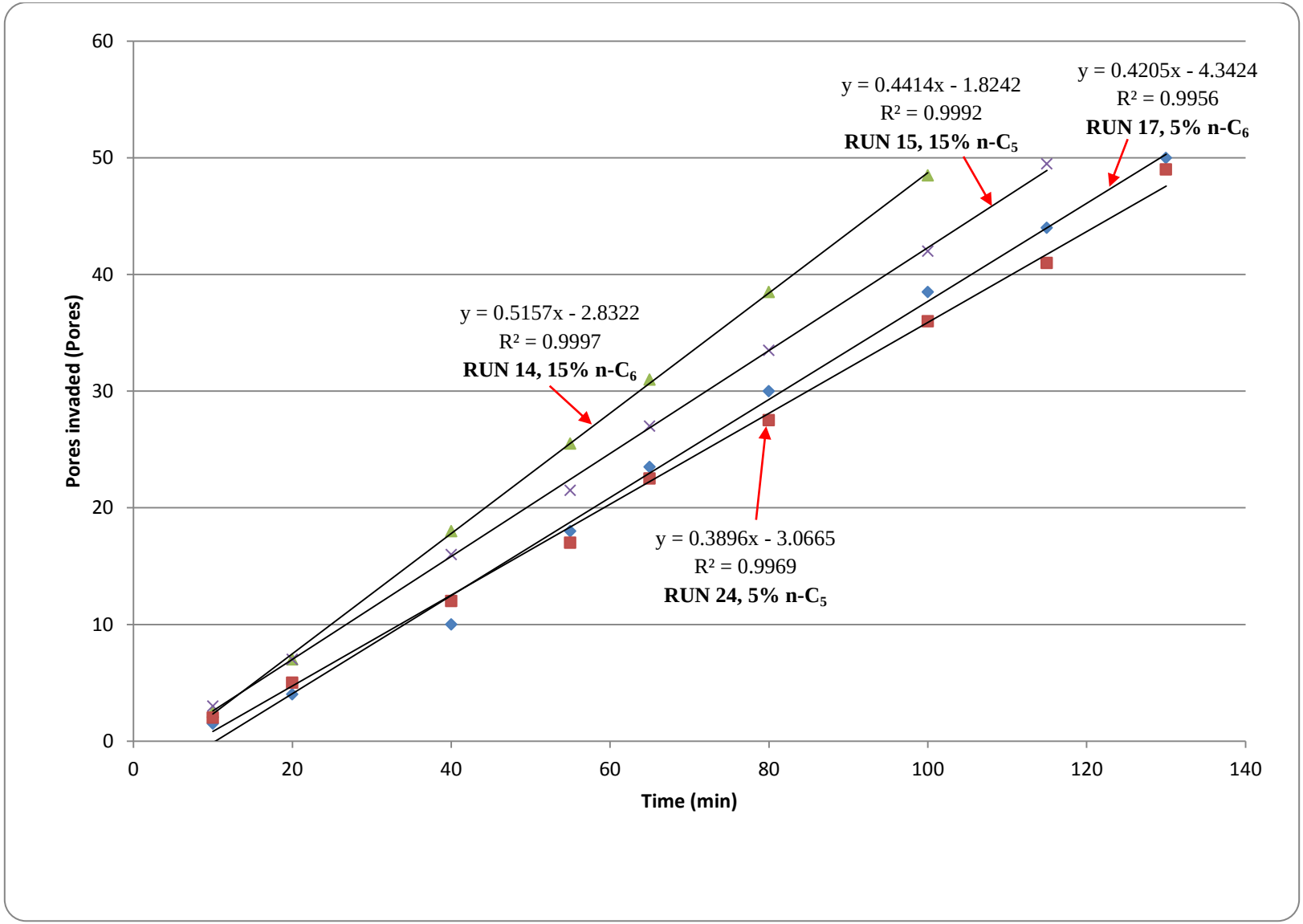

Figure 3.39: Interface advancement velocity diagram for Model OM-2 [41-50 pores from top, Oil type: Lloydminster heavy oil blend]

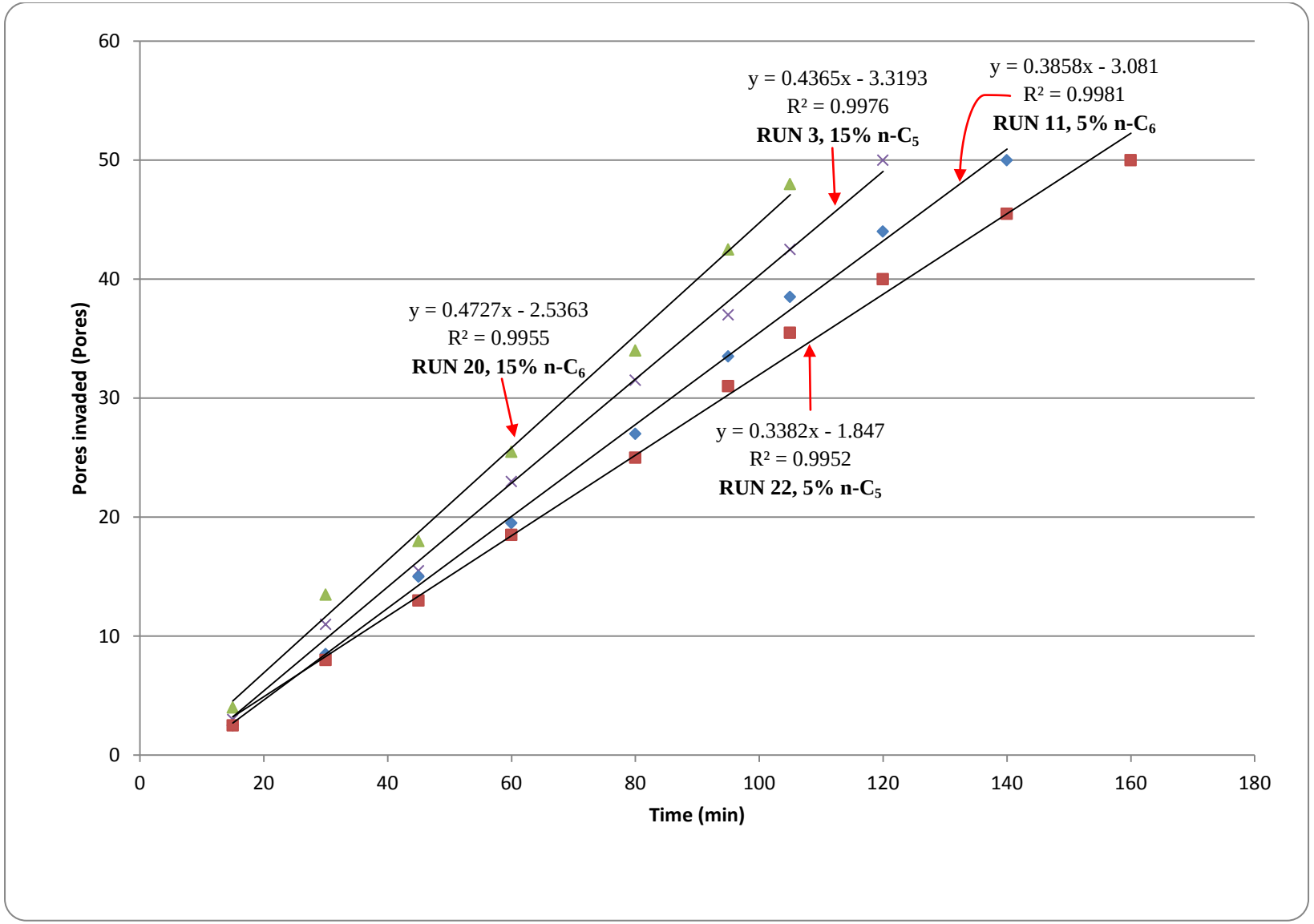

Figure 3.40: Interface advancement velocity diagram for Model OM-1 [31-40 pores from top, Oil type: Lloydminster heavy oil blend]

Table 3.15 contains the volumetric measurements of the injected fluids during our SA-SAGD experiments. The reported steam and solvent injection rates are averaged through the process time over which the pore-scale events were recorded and also the instantaneous position of the interface was tracked. This duration-weighted averaging is based on the instantaneous injection rates of each fluid phase as well as the time interval over which each particular injection rate was maintained. The main purpose of adjusting the injection flow rates was to provide a fairly constant operating temperature in the invaded area of the micromodels during the time span of each trial. It is worthwhile to note that it was tried not to change the injection flow rates frequently to avoid disturbing the steady state mode of the process after the start-up stage was passed. For all of our SA-SAGD trials, except 6 of them, pure steam was injected during the start-up stage. In RUN numbers 5, 6, and 7 (Cold Lake bitumen as the oil type, 5% vol/vol n-C_5 as the steam additive in three different micromodels) as well as RUN numbers 3, 8, and 15 (Lloydminster heavy oil blend as the oil type, 15% vol/vol n-C_5 as solvent in three different models), steam and solvent were co-injected during the start-up stage. The start-up stage was continued for each trial until about 2-3 pores adjacent to the trough were invaded by steam (or steam and solvent mixture). During this stage, some pores at the topside of the models were also emptied by means of randomly-propagated channels of the invading phase. These emptied pores initiated the development of the steam (or steam and solvent mixture) chamber at the pore-scale. The start-up stage was finished for each trial by adjusting the steam injection rate and initiating injection of the solvent phase (or adjusting the solvent injection rate to the appropriate values based on the injection rate of steam for the trials in which solvent was also injected during the start-up stage).

The cumulative steam and solvent injected were calculated by adding up the total volumes of steam or solvent which was injected during the process time. It is worthwhile to mention that the volume contribution of solvent in the injection main stream was kept constant at the predetermined values of 5% or 15% vol/vol during the process time. Each micromodel was weighed just before and also right after the trial using an analytical balance with precision of 0.005 g. Using direct measurement of the mass of oil produced during each SA-SAGD experiment, the recovery factor values were calculated in terms of the mass of oil recovered with

respect to the original oil in place. These values are reported in the 2nd column from right of Table 3.15 for the purpose of comparison.

As it was the case in the production characteristic analysis of the SAGD trials in Chapter 2, the production rates of the pore-scale SA-SAGD experiments could not be measured directly due to very small storage capacity of the employed glass micromodels. A back-calculation procedure was performed in order to analyze the production characteristics of the pore-scale SA-SAGD experiments with the aid of interface advancement data. The SA-SAGD interface was closely tracked versus time during the course of each experiment. The pore-level interface advancement velocity for each particular SA-SAGD trial at particular elevations along the height of each glass micromodel was found to be constant. As the total height of each glass micromodel can be considered as an infinitesimal portion of a real world field-scale SAGD interface, it is obvious that the variation of the horizontal velocity of interface along the height of each micromodel is not significant. Therefore, an arithmetic averaging technique was used in order to calculate a representative horizontal interface advancement velocity in terms of the number of pores invaded per unit time or unit length per unit time for each particular pore-scale SA-SAGD experiment.

The calculated horizontal interface advancement velocity along with the pore-scale snapshots was used in order to calculate the invaded area at each particular timeframe during the life of each individual SA-SAGD experiment. The fraction of the area swept away was defined as the ratio of the swept area by the total area at each particular timeframe within the lifespan of each SA-SAGD experiment. It was obtained that the fraction of area swept varies linearly with the process time for each SA-SAGD experiment. An average oil production rate could then be calculated over the entire production history of each particular SA-SAGD experiment by multiplying the slope of fraction of the area swept vs. process time plot by the pore volume of each particular micromodel. The cumulative oil produced at the end of each SA-SAGD experiment was then calculated by multiplying the average oil production rate by the process time. Consequently, the ultimate recovery factor for each particular SA-SAGD experiment based on the interface advancement tracking procedure was calculated and reported in Table 3.15.

Table 3.15: Volumetric measurements of the SA-SAGD trials

Run No.	Solvent Type and quantity (vol/vol)	Model	Oil Type	$T_{Operating}$ (°C)	$t_{Start-up}$ (min)	$q_{inj,steam}^{start-up}$ (cc/min, CWE)	$q_{inj,solvent}^{start-up}$ (cc/min, CSE)	t_p (min)	$\bar{q}_{inj,steam}$ (cc/min, CWE)	$\bar{q}_{inj,solvent}$ (cc/min, CSE)	q_{cum}^{steam} (cc)	$q_{cum}^{solvent}$ (cc)	RF (%)		
													Interface tracking	Direct	% Relative Difference
19	n-C_6, 15%	DL-1	CL B	103.45	29	1.5	0	140	0.600	0.106	84.00	14.82	88.95	78.09	13.90
10	n-C_6, 15%	OM-2	CL B	101.45	33	1.5	0	130	0.503	0.089	65.39	11.54	68.51	69.07	-0.81
9	n-C_6, 15%	OM-1	CL B	101.85	39	1.5	0	160	0.535	0.094	85.60	15.11	76.72	78.53	-2.30
13	n-C_5, 15%	DL-1	CL B	102.75	32	1.5	0	140	0.515	0.091	72.10	12.72	81.92	75.62	8.33
2	n-C_5, 15%	OM-2	CL B	102.10	33	1.5	0	140	0.485	0.086	67.90	11.98	70.41	70.53	-0.18
1	n-C_5, 15%	OM-1	CL B	103.30	41	1.5	0	180	0.480	0.085	86.40	15.25	74.06	77.85	-4.87
23	n-C_6, 5%	DL-1	CL B	108.30	30	1.5	0	160	0.487	0.026	77.92	4.10	85.68	77.13	11.09
16	n-C_6, 5%	OM-2	CL B	108.90	32	1.5	0	185	0.436	0.023	80.66	4.25	77.80	75.33	3.28
4	n-C_6, 5%	OM-1	CL B	107.40	40	1.5	0	180	0.422	0.022	75.96	4.00	71.35	74.00	-3.59
6	n-C_5, 5%	DL-1	CL B	106.80	24	1.5	0.079	160	0.480	0.025	76.80	4.04	82.64	76.58	7.91
7	n-C_5, 5%	OM-2	CL B	107.10	26	1.5	0.079	185	0.430	0.023	79.55	4.19	76.90	75.07	2.44
5	n-C_5, 5%	OM-1	CL B	106.40	31	1.5	0.079	180	0.417	0.022	75.06	3.95	69.89	72.93	-4.18
12	n-C_6, 15%	DL-1	L HO	103.80	19	1.5	0	70	0.680	0.120	47.60	8.40	77.20	75.62	2.09
14	n-C_6, 15%	OM-2	L HO	102.10	22	1.5	0	100	0.592	0.104	59.20	10.45	77.13	78.00	-1.11
20	n-C_6, 15%	OM-1	L HO	101.60	25	1.5	0	105	0.576	0.102	60.48	10.67	72.92	76.00	-4.06
8	n-C_5, 15%	DL-1	L HO	103.50	13	1.5	0.265	105	0.575	0.101	60.38	10.65	83.83	78.36	6.98
15	n-C_5, 15%	OM-2	L HO	101.75	15	1.5	0.265	115	0.547	0.097	62.91	11.10	75.95	77.91	-2.51
3	n-C_5, 15%	OM-1	L HO	102.90	20	1.5	0.265	120	0.540	0.095	64.80	11.44	77.02	77.68	-0.84
21	n-C_6, 5%	DL-1	L HO	107.80	22	1.5	0	105	0.582	0.031	61.11	3.22	85.42	77.22	10.62
17	n-C_6, 5%	OM-2	L HO	108.35	24	1.5	0	130	0.512	0.027	66.56	3.50	82.22	78.89	4.23
11	n-C_6, 5%	OM-1	L HO	107.85	28	1.5	0	140	0.485	0.026	67.90	3.57	79.01	78.45	0.71
18	n-C_5, 5%	DL-1	L HO	105.95	21	1.5	0	120	0.550	0.029	66.00	3.47	84.61	78.13	8.29
24	n-C_5, 5%	OM-2	L HO	107.55	25	1.5	0	130	0.495	0.026	64.35	3.39	75.96	78.07	-2.70
22	n-C_5, 5%	OM-1	L HO	107.15	30	1.5	0	160	0.430	0.023	68.80	3.62	79.19	79.19	0.00

Figure 3.41 displays the temporary location of the SA-SAGD interface at different elevations along the height of Model OM-1 in RUN No. 1 in which n-C_5 was used as the steam additive at 15% vol/vol concentration and Cold Lake bitumen was used as the oil type. Figure 3.42 also shows the sequential SA-SAGD interface advancement along the Model DL-1 in RUN No. 21 in which n-C_6 at 5% vol/vol concentration was used as the solvent phase and Lloydminster heavy oil blend was used as the oil phase. The high-permeable trough is located at the right hand side of these two Figures extended along the entire height of the micromodels. At each particular timeframe, the invaded area of the model could be obtained by calculating the area over the curve to the right in both Figures using trapezoidal rule.

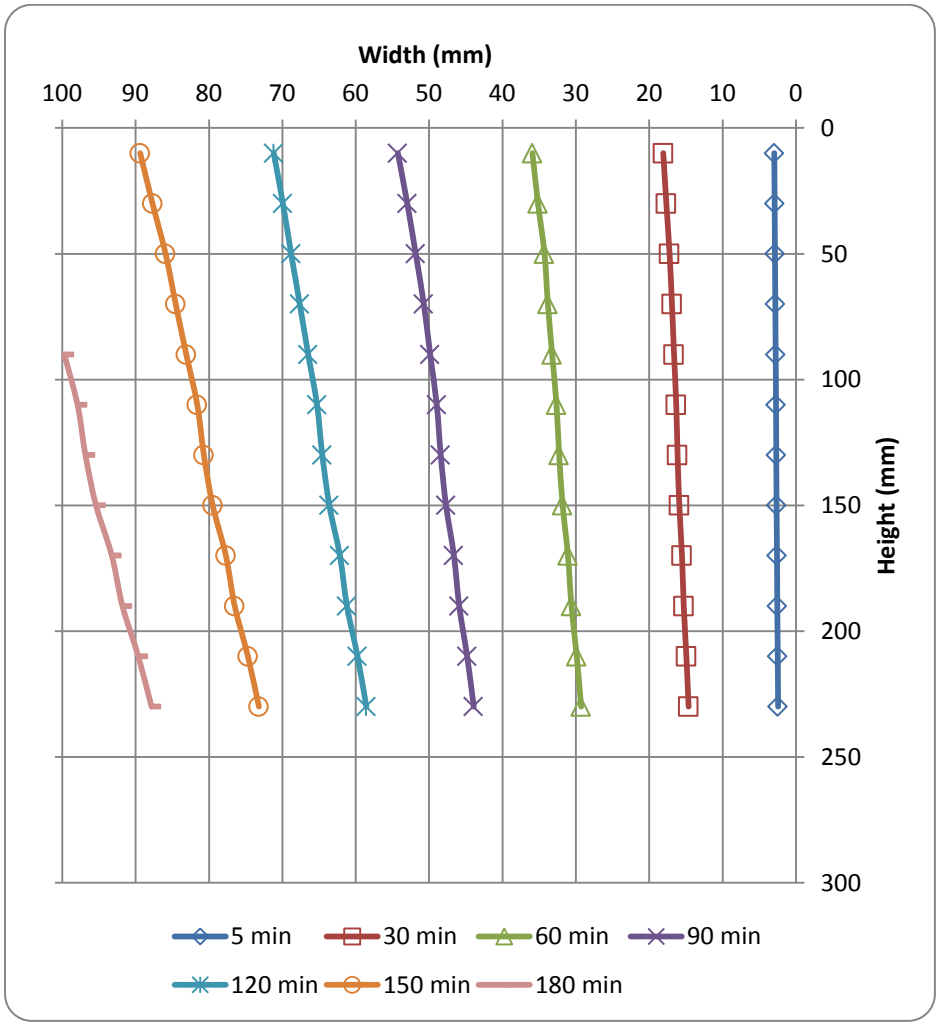

Figure 3.41: Temporary position of the SA-SAGD interface along the height of Model OM-1 in RUN No. 1 (Solvent: 15% vol/vol nC_5, Oil type: Cold Lake bitumen)

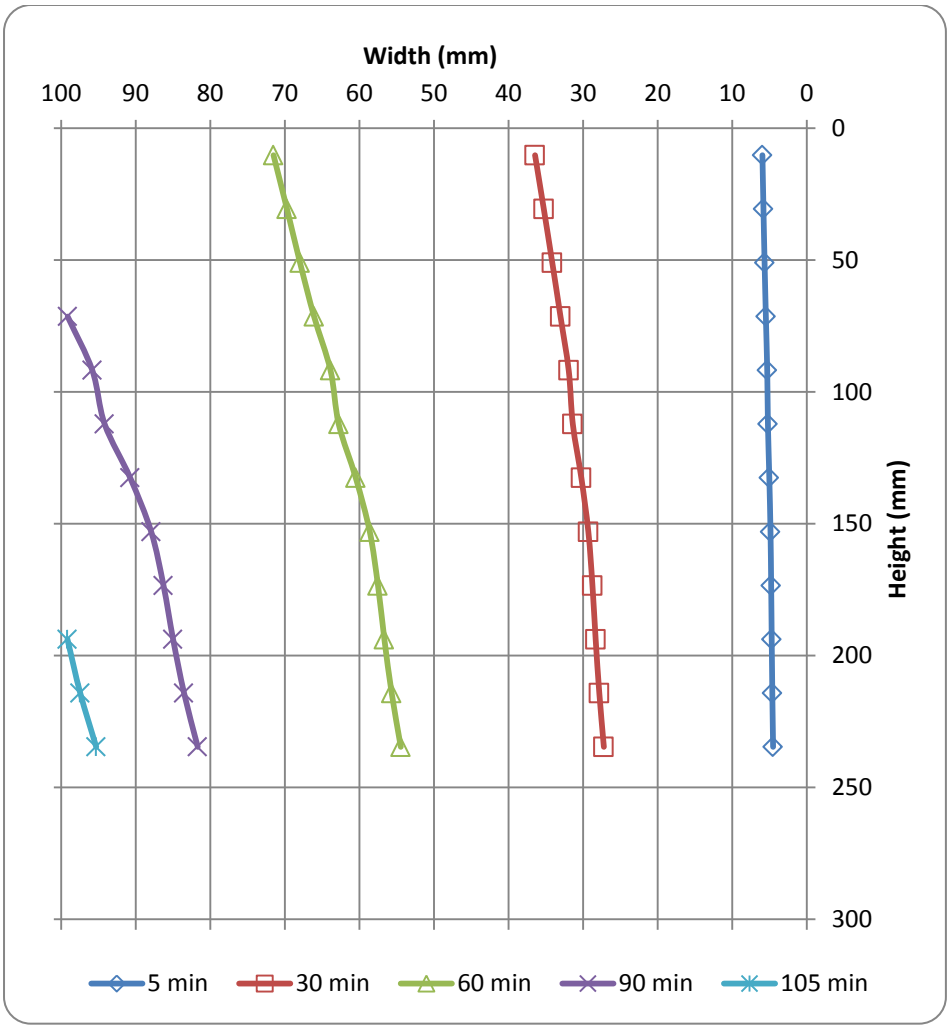

Figure 3.42: Temporary position of the SA-SAGD interface along the height of Model DL-1 in RUN No. 21 (Solvent: 5% vol/vol nC_6, Oil type: Lloydminster heavy oil blend)

Plotting the fraction of the invaded area versus time yields in a straight line, and the average oil production rate over the entire process time could be estimated from the slope of this straight line. Following this procedure, the oil production rate was calculated to be 0.00453 and 0.01953 cm^3/min for RUN No's 1 and 21 respectively. The ultimate recovery factor for these trials can also be calculated by dividing the product of the average oil production rate by the process time over the associated values of micromodel pore volume. This ultimate recovery factor could be cross checked with the recovery factor values obtained using direct measurement technique of weighing the model before and after each trial. As the ultimate RF value obtained using the interface advancement velocity consideration is subject to some human error when the

SA-SAGD interface was tracked over the process time, the ultimate RF values associated with pre- and post-trial weighing of the models were considered to be the more accurate numbers. This procedure was carried out for all the SA-SAGD trials, and the results are summarized in Table 3.15.

3.5.5. Parametric Sensitivity Analysis of the SA-SAGD Experimental Results

In this section, parametric sensitivity analysis of the experimental results are presented based on the design of experiments shown in Table 3.2 to figure out the effect of solvent type, solvent concentration, macroscopic properties of porous media, and oil type on the SA-SAGD interface advancement at the pore-scale, ultimate RF and energy requirements of each particular experiment under prevailing operating conditions.

3.5.5.1. Effect of Solvent Type

Two paraffinic solvents of normal pentane and normal hexane were used in our SA-SAGD experiments. One can study the effect of solvent type on the sweep rate of the SA-SAGD process when all other experimental parameters are kept constant. Generally, normal hexane enhances the pore-scale performance of the SAGD process significantly compared to the baseline SAGD process. Normal pentane, however, enhances the interface advancement rate moderately compared to the matching SAGD process. In general, n-C_6 performs more effective than n-C_5 especially at higher concentrations of solvent when Cold Lake bitumen was used. This point is evident considering Figures 3.35 to 3.37 in which the performance of the SA-SAGD process to recover Cold Lake bitumen using DL-1, OM-2, and OM-1 models were presented respectively in terms of the interface advancement at the pore-scale. It is clear that for each particular model, the sweep rate is higher when normal hexane was injected as the steam additive especially at 15% vol/vol concentration. This point is also verified using representative sweep rate of each micromodel presented in Tables 3.9 to 3.11. In Table 3.16, the average sweep rates of the SA-SAGD experiments as well as the ultimate recovery factor values are categorized based on the solvent type used in each particular trial. According to this Table, SA-SAGD interface advancement rate was enhanced the best at 15% vol/vol n-C_6 concentration trials using OM-1 and OM-2 models (RUN No's 9 and 10 respectively) in which a sweep rate increase of about

42% was seen in both of these two trials compared to those of their corresponding SAGD processes. When DL-1 model was used at higher level of n-C_6 concentration, an increase of about 27% in sweep rate was observed compared to the corresponding baseline.

Table 3.16: Production performance of the SA-SAGD experiments categorized based on the solvent type and concentration

	Solvent Type	**n-C_5**	**n-C_6**
Solvent Concentration		*Representative SA-SAGD Interface Advancement Velocity ($\boldsymbol{v_p^{SA-SAGD}}$, mm/min) and RF (% of OOIP)*	
5% vol/vol	DL-1, CL B	RUN 6: **0.631** @ 106.80 °C RF = **76.58%** in 160 min	RUN 23: **0.637** @ 108.30 °C RF = **77.13%** in 160 min
	DL-1, L HO	RUN 18: **0.857** @ 105.95 °C RF = **78.13%** in 120 min	RUN 21: **0.993** @ 107.80 °C RF = **77.22%** in 105 min
	OM-2, CL B	RUN 7: **0.530** @ 107.10 °C RF = **75.07%** in 185 min	RUN 16: **0.536** @ 108.90 °C RF = **75.33%** in 185 min
	OM-2, L HO	RUN 24: **0.747** @ 107.55 °C RF = **78.07%** in 130 min	RUN 17: **0.805** @ 108.35 °C RF = **78.89%** in 130 min
	OM-1, CL B	RUN 5: **0.496** @ 106.40 °C RF = **72.93%** in 180 min	RUN 4: **0.505** @ 107.40 °C RF = **74.00%** in 180 min
	OM-1, L HO	RUN 22: **0.634** @ 107.15 °C RF = **79.19%** in 160 min	RUN 11: **0.724** @ 107.85 °C RF = **78.45%** in 140 min
15% vol/vol	DL-1, CL B	RUN 13: **0.699** @102.75 °C RF = **75.62%** in 140 min	RUN 19: **0.748** @ 103.45 °C RF = **78.09%** in 140 min
	DL-1, L HO	RUN 8: **0.981** @ 103.50 °C RF = **78.36%** in 105 min	RUN 12: **1.374** @ 103.80 °C RF = **75.62%** in 70 min
	OM-2, CL B	RUN 2: **0.619** @ 102.10 °C RF = **70.53%** in 140 min	RUN 10: **0.648** @ 101.45 °C RF = **69.07%** in 130 min
	OM-2, L HO	RUN 15: **0.840** @ 101.75 °C RF = **77.91%** in 115 min	RUN 14: **0.987** @ 102.10 °C RF = **78.00%** in 100 min
	OM-1, CL B	RUN 1: **0.527** @ 103.30 °C RF = **77.85%** in 180 min	RUN 9: **0.620** @ 101.85 °C RF = **78.53%** in 160 min
	OM-1, L HO	RUN 3: **0.828** @ 102.90 °C RF = **77.68%** in 120 min	RUN 20: **0.900** @ 101.60 °C RF = **76.00%** in 105 min

To study the effect of solvent type on the SA-SAGD performance, let's first look at the higher level of solvent concentration when Cold Lake bitumen was used as the oil type. The SA-SAGD performance enhancement could be observed in all different micromodels. For instance, the experimental set of RUN numbers 19, 10, and 9 with 15% vol/vol n-C_6 were performed using DL-1, OM-2, and OM-1 models respectively. These experiments could be compared one to one with RUN numbers 13, 2, and 1 respectively in which 15% vol/vol nC_5 was used as the steam additive. It is observed that higher sweep rates were achieved to the extent of 7, 4.7, and 17.70% respectively when nC_6 was used as the steam additive. This conclusion could be backed up by comparing the recovery factor values at the end of these trials. According to the data presented in Table 3.16, experiments with n-C_6 as the solvent have slightly higher RF values compared to those with n-C_5 as the steam additive. It is clear that RUN No 19 has almost 2.5% higher final recovery factor compared to its corresponding trial with 15% vol/vol of n-C_5 as the solvent (i.e. RUN No 13). RUN No 2 has a slightly higher RF value compared to that of RUN 10, which is due to the longer process time of former compared to the latter trial. As far as model OM-1 is concerned, it is evident that although the process time of RUN No. 1 (i.e. n-C_5 as the solvent) was 20 minutes longer than that of RUN number 9 (i.e. n-C_6 as the solvent), the latter's RF is still higher than the former's.

It is also interesting that SA-SAGD in OM-2 micromodel with 15% vol/vol concentration of either n-C_6 or n-C_5 as steam additives performs better than the corresponding SAGD process at superheated injection temperature of 110.20 °C. In model OM-1, although the SA-SAGD processes at higher solvent concentration level of 15% vol/vol for n-C_5 and n-C_6 (i.e. RUN numbers 1 and 9 respectively) perform better compared to the corresponding conventional SAGD process at 101.70 °C, one can realize that neither of these two trials provide higher sweep rates than that of the SAGD process at the elevated steam temperature of 116.35 °C.

In the absence of detailed heat loss analysis of the SA-SAGD experiments, it is not possible to determine the corrected values of the steam to oil ratio and also solvent to oil ratio based on the data presented in Table 3.15. However, the cumulative steam consumption (i.e. steam consumed to cover the heat loss plus the net amount of steam consumed to maintain the gravity drainage process) in each of the SA-SAGD trials could be compared qualitatively to figure out what is the

effect of experimental variables on the energy requirements of the SA-SAGD process. It is evident that more steam was consumed on a cumulative basis in the SA-SAGD trials in which nC_6 at 15% vol/vol was used as the steam additive than the corresponding trials with nC_5 as the solvent. It is because of the fact that when the interface advances with higher pore-scale velocities, more swept area is subject to the heat loss which significantly affects the cumulative steam requirements of the SA-SAGD trial. It is evident that SA-SAGD trials with high nC_6 concentrations achieve significantly higher pore-scale interface advancement velocities than those in which 15% vol/vol nC_5 was used. In fact, the cumulative steam consumed is a strong function of the process time, so it might be a good idea to compare the duration-weighted average steam injection rate instead of the cumulative steam consumption when there is a considerable difference between the process times of the corresponding SA-SAGD trials. In addition, steam requirements of each SA-SAGD experiment is a strong function of the operating temperature. The higher the operating temperature, the higher would be the overall heat loss to the surrounding environment. It is obvious that the corresponding SA-SAGD trials at higher levels of solvent concentration were carried out at very close operating temperatures which make the qualitative comparison to be conducted on a common ground.

The effect of solvent type on the pore-scale SA-SAGD process performance could also be investigated at lower levels of solvent concentration when Cold Lake bitumen was used as the oil type. It is clear that SA-SAGD trials with 5% vol/vol n-C_6 have reasonably higher sweep rates compared to their corresponding SAGD trials; however, they provide comparable sweep rates with the ones in which 5% vol/vol n-C_5 was used as the steam additive. For instance, in RUN numbers 23, 16, and 4, n-C_6 solvent with 5% vol/vol concentration was used along with DL-1, OM-2, and OM-1 glass micromodels, respectively. The sweep rates of these trials could be compared to those of RUN numbers 6, 7, and 5 which are the corresponding trials at similar operating conditions and fluid and model properties, except solvent type. It is evident that an insignificant enhancement of about 1-2% in the sweep rate is observed when n-C_6 was used as the steam additive. However, an appreciable pore-scale process enhancement is observed when the sweep rates of these trials are compared to their corresponding baseline SAGD process. It is evident that interface advancement velocities of RUN numbers 23, 16, and 4 in which n-C_6 at lower concentration was added to steam were reasonably higher than those of their

corresponding baseline SAGD trials to the extent of 10.60, 17.50, and 15.60% respectively. As far as the effect of solvent type on final RF is concerned, it is evident that at lower range of solvent concentration, solvent type does not significantly affect the recovery factor values. Focusing on two experimental sets of trial numbers 23, 16, and 4 (i.e. 5% vol/vol n-C_6) and their corresponding trials with 5% n-C_5 as the solvent (i.e. trial numbers 6, 7, and 5), it is clear that the recovery factor values of the experiments with n-C_6 as the solvent are somewhat higher (i.e. to the extent of 1-2%) than those with n-C_5 as the steam additive at similar process time durations.

The start-up stage of the experimental set of RUN numbers 23, 16, and 4 follows the normal steam injection procedure whose duration depends directly on the permeability of the employed porous medium as well as the oil viscosity at steam temperature. However, in the case of SA-SAGD experiments with 5% vol/vol solvent concentration in the injection main stream when Cold Lake bitumen was used as the oil type (i.e. RUN numbers 6, 7, and 5), steam and solvent with the predetermined volume contributions of 95% and 5% vol/vol respectively were co-injected during the start-up stage of the process. It is clear that presence of the solvent phase during the start-up stage of the SA-SAGD process would further reduce the bitumen viscosity, hence shortens the duration of the start-up stage as it is depicted in Table 3.15. On the other hand, due to excessive condensation of the injected vapour phase during the start-up stage of the process for these particular runs, these three trials experienced asphaltene precipitation which was not a dominant operational hassle due to the reasons expressed previously in section 3.4.5. It is obtained that the duration of the start-up stage due to the co-injection of solvent along with the steam phase was decreased to the extent of 21-33%, 23-27%, and 26-32% for RUN numbers 6, 7, and 5 respectively when it is compared with the other corresponding SA-SAGD trials with Cold Lake bitumen as the oil type.

The type of the solvent used appears to have minor effect on the steam requirements of the SA-SAGD trials at lower concentrations of solvent when Cold Lake bitumen was used as the oil type. Based on the data provided in Table 3.15, it seems that almost the same volumes of steam was consumed in RUN numbers 23, 16, and 4 with 5% vol/vol nC_6 as the solvent compared to those consumed in the corresponding trials with 5% vol/vol nC_5 as the steam additive. The major contribution to the cumulative steam consumed comes from the heat loss while the net amount of

steam required to maintain the gravity drainage process plays an insignificant role in the cumulative steam requirements. It appears that similar operating temperatures and process times of these two sets of trials, along with the very close pore-scale interface advancement velocities provide similar energy requirements in terms of the cumulative steam and solvent consumed during these two sets of experiments.

As no SAGD trial was carried out using Lloydminster heavy oil blend as the oil type, the pore-scale performance of the SA-SAGD trials using this type of oil could not be cross examined with corresponding SAGD baselines. According to the interface advancement comparison charts provided in Figures 3.38 to 3.40 and the relevant interface advancement velocity data summarized in Tables 3.12 to 3.14, it is believed that the pore-scale SA-SAGD performance in terms of the interface advancement velocity is enhanced more when n-C_6 was used as the steam additive, provided that all other experimental variables are kept unchanged. This enhancement is more highlighted when SA-SAGD trials with higher solvent content of the injection main stream are concerned. Let's compare the representative sweep rate of the SA-SAGD experiments using different micromodels of DL-1, OM-2, and OM-1 when solvent was added to the steam phase by 15% vol/vol contribution. The corresponding RUN numbers to these experiments are 8 and 12 for DL-1, 15 and 14 for OM-2, and 3 and 20 for OM-1 models when n-C_5 and n-C_6 were used as the steam additives respectively for each particular micromodel. According to the data provided in Table 3.16, it is evident that enhancements of 40, 17.5, and 8.70% in the representative sweep rates were achieved in SA-SAGD experiments with DL-1, OM-2, and OM-1 models respectively upon using hexane over pentane as the steam additive. It is evident that the enhancement made by changing the solvent type is more pronounced when the model permeability is higher.

Focusing on the recovery factor values reported in Table 3.16, it is clear that the final recovery factor of trials 12 and 20, in which DL-1 and OM-1 models were used respectively in the presence of 15% vol/vol of n-C_6 contribution in the feed stream, are slightly less (i.e. in the order of 2-4%) than those of RUN numbers 8 and 3 respectively in which all the operating conditions are the same except the solvent type. It is because of the fact that the latter trials (i.e. RUN numbers 8 and 3) were carried out over longer period of process time (i.e. 50 and 15%

respectively) compared to their corresponding trials with n-C_6 as the steam additive (i.e. RUN numbers 12 and 20). Had the trials with n-C_6 as the solvent been conducted over the same process time duration, significantly higher RF values would have been achieved compared to their corresponding ones with n-C_5 as the solvent. It is also observed that RUN numbers 14 and 15 with OM-2 as the model and n-C_6 and n-C_5 as the steam additives respectively have almost the same recovery factor values of about 78% of OOIP. However, the ultimate RF value of the former trial was achieved during shorter process time (i.e. 15%) compared to that associated with the latter trial in which n-C_5 was used as the steam additive. As a result, it can be concluded that trials with n-C_6 as the steam additive at 15% vol/vol contribution in the injection side have considerably higher ultimate recovery factors compared to those associated with the trials in which n-C_5 was injected along with the steam phase at similar injection concentration. Another interesting point can be observed focusing on the start-up stage duration of the above-mentioned experimental sets. It is evident that the experimental set composed of trial numbers 8, 15, and 3 is the only set of experiments in which solvent (i.e. n-C_5 at 15% vol/vol concentration in the feed stream) was co-injected along with the steam phase during the start-up stage. Comparing the duration of the start-up stage between this set of experiments with those of the corresponding trials with n-C_6 as the solvent (i.e. RUN numbers 12, 14, and 20) reveals that presence of the solvent phase during the initialization stage of the SA-SAGD process accelerates oil drainage from the pores adjacent to the trough, hence cuts down the start-up stage duration of the process by about 25-45%.

In order to investigate the effect of solvent type on the energy requirements of the SA-SAGD process at high level of solvent concentration and Lloydminster heavy oil blend as the oil type, one can focus on the cumulative steam and solvent consumed during the process time of RUN numbers 12, 14, and 20 (i.e. n-C_6 as the solvent) and their corresponding trial numbers of 8, 15, and 3 (i.e. n-C_5 as the steam additive). It is clear that addition of n-C_6 as the steam additive would enhance the pore-scale process performance in terms of increasing the interface advancement velocity; hence the invaded area at each particular timeframe, which is a representative of the extent of heat loss during the SA-SAGD experiments, would be larger if n-C_6 was used as the steam additive. This is also confirmed by the temporal position recognition and tracking of the SA-SAGD interface during the course of the visualization experiments. As a

result, it is expected to consume more steam in the case of using n-C_6 as the solvent phase compared to that of the trials with n-C_5 as the steam additive. This point is confirmed by the data presented in Table 3.15.

The effect of solvent type on the sweep rate of the SA-SAGD process could also be investigated by looking at the trials in which Lloydminster heavy oil was diluted by injecting 5% vol/vol of solvent along with the steam phase. The SA-SAGD interface advancement velocities in RUN numbers 21, 17, and 11 (i.e. n-C_6 as the solvent) can be compared to those of 18, 24, and 22 (i.e. n-C_5 as the solvent) respectively in order to figure out the effect of solvent type on the pore-scale SA-SAGD process performance for three models of DL-1, OM-2, and OM-1 respectively. It was obtained that the former trials have an increase in the order of 15.90, 7.80, and 14.20% in the sweep rate compared to the latter ones respectively. Consequently, it is obvious that normal hexane was able to enhance the pore-scale sweep rate of the SA-SAGD process more effectively than normal pentane at very similar operating conditions and porous media properties when Lloydminster heavy oil blend was used as the oil phase. The superior performance of nC_6-assisted SAGD compared to its n-C_5 counterpart can also be verified by looking into the ultimate RF values of the corresponding trials. Consider RUN numbers 21, 17, and 11 in which n-C_6 was used as the steam additive in three different micromodels. It is observed that these three trials have almost the same ultimate RF values compared to those of their corresponding trials using n-C_5 (i.e. RUN numbers 18, 24, and 22) but at shorter process times.

One could notice the effect of the solvent type on the energy requirements of the SA-SAGD process with focus on the cumulative steam and solvent consumed when only 5% vol/vol solvent concentration was used in order to dilute Lloydminster heavy oil blend. It is observed that normal hexane, even at lower level of concentration, could increase the pore-level interface advancement velocity more than that achieved with n-C_5 as the steam additive. Although this represents itself in terms of increased average steam injection rate for n-C_6-assisted SAGD process compared to the one assisted with n-C_5, the reduced process time of former compared to the latter provides better energy efficiency in terms of reduced (or at least comparable) cumulative steam and solvent consumed over the lifespan of the process.

The enhancement observed in the pore-scale sweep rate of the SA-SAGD process with the aid of n-C_6 as the solvent compared to that of n-C_5 at similar operating conditions can be explained using the concept of solubility of solvent in the live oil phase. It is believed that heavier paraffinic solvent has higher solubility potential in an oil phase provided that all operating parameters and fluid properties remain constant. The effect of solvent type on the pore-scale sweep rate of the SA-SAGD process, when all other experimental variables are kept constant, can be explained qualitatively by considering two theories proposed to describe the performance of SAGD and VAPEX processes in terms of interface advancement velocity and drainage rate. It was previously pointed out that the rate of horizontal interface advancement in the SAGD process is proportional to a so-called "SAGD performance parameter at the pore-scale" which is defined by $\sqrt{\frac{K}{\nu_s \phi}}$ when all other parameters remain unchanged. On the other hand, VAPEX horizontal sweep rate is a function of $\sqrt{\frac{KN_s}{\phi^{\Omega}}}$ assuming all other variables to be unchanged (Das and Butler, 1998; Yazdani and maini, 2005). In this parameter, "K" and "ϕ" are permeability and porosity of the porous medium respectively, "Ω" is cementation factor, and "N_s" parameter is expressed using an integral function which depends directly on the concentration-dependent mutual effective diffusivity of solvent and oil phase and also on the concentration-dependent density of the live oil phase. The "N_s" parameter also depends inversely on the concentration-dependent viscosity of the produced live oil. According to the kinematic viscosity data of oil-solvent mixture presented in Tables 3.7 and 3.8, it is evident that the presence of normal pentane as the solvent in the oil-solvent mixture would reduce the mixture kinematic viscosity slightly more than that of the hexane-oil mixture (i.e. the order of 10-15%) at similar solvent content, temperature, and oil type levels. However, this behavior is observed assuming ideal mixing conditions of oil and solvent at pertaining temperature and solvent content of the mixture which deviates from the reality when it comes to our SA-SAGD visualization experiments. However, due to the lack of knowledge about the solvent content of the produced mobile live oil, it is not possible to draw a solid and quantitative conclusion regarding the effect of solvent type on the process performance using the data presented in Tables 3.7 and 3.8. As the operating temperature of our SA-SAGD trials are not exactly similar to each other, it might even be possible that two corresponding runs with similar solvent content of the main injection stream and rock and fluid

properties except solvent type would have had different solvent content of the produced live oil due to a minor difference in their corresponding operating temperatures.

The actual solvent content of the produced mobile live oil as well as the reliable steam to oil ratio (SOR) data for our SA-SAGD experiments cannot be reported in the absence of heat loss trials as well as the measured solvent content data of the produced live oil. A portion of the injected steam (or steam-solvent mixture for six of our trials) at the operating temperature was consumed to warm up the model during the start-up stage, and it should not be considered for calculation of the SOR data. In addition, another significant portion of the injected vapour mixture was condensed in the model to make for the radiation heat loss from the model to the surrounding environment. As a result, the cumulative produced solvent condensate volume obtained during each SA-SAGD trial could not be used for calculation of the solvent content of the produced live oil. Had the solvent content data of the mobile live oil for every single experiment been known, it would have been possible to scale the interface advancement velocity data using a combination of the operating variables ($\sqrt{\frac{K}{\nu_s \phi}}$). Using this procedure, the effect of other contributing parameters such as effective diffusivity on the pore-scale sweep rate of the SA-SAGD process could have been explained. This procedure could have also helped us to figure out a quantitative theory-based explanation on the effect of solvent type on the SA-SAGD interface velocity at the pore-level. In summary, although the presence of pentane seems to be slightly more effective in reducing the kinematic viscosity of oil-solvent mixture compared to hexane assuming the mixture to be an ideal solution, there are some other parameters which make n-C_6 to be a better solvent for the SA-SAGD process as far as the interface sweep rate is concerned. These parameters include non-ideality of the solvent-oil mixture, the effect of concentration-dependent diffusivity of oil and solvent, variability of solvent content of the produced mobile live oil even at similar solvent content of the injection main stream due to the operating temperature variations between corresponding SA-SAGD trials, and greater solubility of n-C_6 in oil compared to that of n-C_5 at similar operating conditions. The superior performance of normal hexane as the steam additive derived from our visualization experiments is compatible with other published results in the literature of solvent-assisted thermal processes (Gates, 2010; Hosseininejad et al, 2010; Li et al, 2011; Bryan, 2009; Li and Mamora, 2010; Ayodele et al, 2010).

3.5.5.2. Effect of Solvent Concentration

As it was pointed out in the design of experiments section of this Chapter, the paraffinic solvents were mixed with the steam phase prior to injection into the models at two different volumetric concentrations of 5 and 15% vol/vol in the injection main stream. The performance analysis of the SA-SAGD experiments revealed the fact that trials with higher concentration of solvent in the injection feed stream achieve higher pore-scale sweep rates compared to those in which solvent was added into the steam phase with low volumetric contribution. This point was concluded when all the other operating conditions as well as fluid and porous pattern properties were remained unchanged.

One can figure out the effect of solvent concentration on the pore-scale SA-SAGD process performance by looking into the data presented in Tables 3.9 to 3.11 when the solvent-aided thermal process was used to extract Cold Lake bitumen. The production performance data of the SA-SAGD experiments are categorized in terms of solvent concentration in the injection mainstream and are presented in Table 3.16. Model DL-1 was used in order to conduct RUN numbers 6 and 13 using n-C_5 and RUN numbers 23 and 19 with the aid of n-C_6 at low and high levels of solvent concentration for each particular solvent type respectively. According to the data provided in Table 3.16, it is observed that an increase in the interface advancement velocity in the order of 10.80% and 17.50% was achieved by increasing the solvent content level of the injection main stream using n-C_5 and n-C_6 solvents respectively.

The enhanced performance of the SA-SAGD process at higher concentrations of either of these two solvents can also be analyzed by focusing on the ultimate RF values of these trials. According to Table 3.16, it is clear that RUN number 19 has slightly higher RF compared to that of RUN number 23 even at lower operating temperature and shorter process time. On the other hand, the RF value of RUN number 6 is slightly (i.e. about 1%) higher than that of RUN 13, but it is due to the higher operating temperature as well as longer process duration of the trial number 6 in which lower concentration n-C_5 was injected along with the steam phase. It is evident that the enhancement occurred in the sweep rate of the SA-SAGD process as a result of solvent concentration increase is more pronounced when n-C_6 was used as the steam additive.

As far as the duration of the start-up stage is concerned, it is evident that although RUN numbers 19 and 23 have similar start-up stage duration, the initialization period of RUN number 13 is about 34% more than that of RUN number 6. This is because of the fact that the former set of trials were initiated with the same start-up procedure; however, the second set of experiments were commenced with two different start-up methods upon which the trial in which solvent-steam mixture was injected at the start-up stage (i.e. RUN number 6) needed much less initialization effort which manifests itself in the lower duration of the start-up period.

The same trend can also be seen considering the SA-SAGD trials conducted using the other two glass micromodels. As far as the SA-SAGD trials using OM-2 model are concerned, one can compare the sweep rates of RUNs 2 and 10 in which n-C_5 and n-C_6 at 15% vol/vol were used with those of RUN numbers 7 and 16 respectively. It is observed that the sweep rates were increased by 17% and 21% respectively when the solvent concentration in the injection side was increased. Focusing on the ultimate RF values of these trials, it is evident that trials with higher solvent concentration in the injection main stream (i.e. RUN numbers 2 and 10) have lower ultimate RF values compared to their corresponding trials at lower solvent content of the injecting fluids (i.e. trial numbers 7 and 16 respectively). Considering the operating conditions including longer process times as well as higher operating temperatures associated with trials in which solvent concentration is lower, the observed trends are reasonable. As far as the start-up stage is concerned, it is clear that the same discussion mentioned in the previous paragraph (i.e. SA-SAGD trials with DL-1 as the model) is also applicable for the SA-SAGD experiments in which OM-2 is considered as the porous medium. Although RUN numbers 10 and 16 possess similar initialization methods and hence the same start-up durations, it is clear that RUN numbers 2 and 7 follow different initialization procedures, so their start-up durations vary by about 27%.

A similar trend was also observed in the SA-SAGD trials in which OM-1 was used as the porous model. Sweep rate enhancements of about 6.2% and 23% were observed by increasing the solvent content of the injecting fluid between trials 5 and 1 (i.e. n-C_5 as the solvent) and 4 and 9 (n-C_6 as the solvent) respectively. It is clear that the effect of solvent concentration increase on the sweep rate of the SA-SAGD process is more pronounced when n-C_6 was used as the steam

additive. Considering the ultimate RF values presented in Table 3.16, it is evident that both RUN numbers 9 and 1 (i.e. trials with higher injected solvent concentration) achieved higher RF values compared to their corresponding trials with lower concentration of solvent in the injected main stream (i.e. RUN numbers 4 and 5). It is interesting that the former trials achieved enhanced RF values even at lower operating temperatures and shorter process times compared to the latter experiments. As far as the lead time of the SA-SAGD process is concerned, it is clear that similar start-up procedures were implemented in RUN numbers 9 and 4, which resulted in similar initialization periods for these two experiments. However, the start-up stage of RUN number 1 took about 33% longer than that of trial number 5 due to the enhanced warm-up procedure associated with the latter trial as a result of solvent-steam co-injection.

The effect of solvent content of the injecting fluid on the pore-scale sweep rate of the SA-SAGD process can also be studied by analyzing the interface advancement velocities of trials in which Lloydminster heavy oil blend was used as the oil type. For instance, one can compare the sweep rates of RUN numbers 18 and 8 (i.e. n-C_5 as the solvent) or 21 and 12 (n-C_6 as the solvent) and conclude that an enhancement of about 14.50% and 38.50% in the sweep rate is experienced following an increase in the solvent content of the injecting stream respectively when DL-1 was considered as the porous medium. It is clear that the pore-scale sweep rate was benefited more from increasing the solvent concentration of the feed stream whenever n-C_6 was used as the steam additive. The same trend is also observed for the trials in which OM-2 and OM-1 models were used as the porous media. With a quick review over the data presented in Table 3.16, it is concluded that at similar operating conditions and process time span, trials with higher solvent content of the injected fluids possess higher attained (or projected) ultimate RF values. In addition, trial numbers 8, 15, and 3 benefited from shortened lead time due to the effective co-injection of solvent and steam during the start-up stage of the process compared to the other trials introduced in the lower half of Table 3.15.

The enhancing trend of the interface advancement velocity of the SA-SAGD process at the pore-scale upon increasing the solvent concentration in the injecting fluid can be justified with the fact that the mixture viscosity would be reduced further at higher solvent concentrations. Although all of the SA-SAGD trials with 15% vol/vol solvent content of the injecting fluid were carried out at

slightly lower operating temperatures compared to those with 5% vol/vol solvent content, higher sweep rates were still observed in the former trials. It seems that in trials with higher solvent content of the injecting fluid, the more effective dilution phenomenon of the higher-concentration solvent overcomes the slightly lower operating temperature associated with these runs. Moreover, the effective diffusivity term between oil and solvent that plays an important role in the drainage process of the mobile live oil will be improved at higher solvent concentration in the injection main stream. In the absence of the solvent content data of the produced mobile live oil, it is unreasonable to quantitatively compare the high- and low-concentration solvent trials in terms of their associated pore-scale sweep rate. However, the qualitative concluding statements made in this section about the effect of solvent content of the injecting fluid on the SA-SAGD sweep rate still hold validity within the range of our experimental conditions.

3.5.5.3. Effect of Macroscopic Properties of Porous Media

In this section, the effect of macroscopic porous media properties such as porosity and permeability on the pore-scale sweep rate of the SA-SAGD process is described based on our SA-SAGD visualization experiments. As it was discussed before, the horizontal sweep rate of both SAGD and VAPEX processes is proportional to the square root of permeability over porosity for every particular porous medium when all other experimental variables are unchanged. It is evident that the $\sqrt{\frac{k}{\phi}}$ parameter is higher for DL-1 model, followed by OM-2 and OM-1 models respectively. As a result, it is expected that the interface advancement velocity would be the highest in DL-1, followed by that of OM-2 and OM-1 models respectively when all other experimental variables would be the same.

Table 3.17 summarizes the representative sweep rate data and ultimate recovery factor of different SA-SAGD trials performed during our visualization experiments which are categorized based on the type of porous medium at similar levels of oil type (Cold Lake bitumen, CL B, and Lloydminster heavy oil, L HO), solvent type (n-C_5 and n-C_6) and solvent concentration of the feed stream (5% and 15% vol/vol). According to the data presented in this Table, it is clear that when all other experimental variables were fixed (i.e. moving horizontally along each particular

row of Table 3.17), SA-SAGD trials carried out using DL-1 model have the highest sweep rates compared to the other corresponding trials in which OM-2 and OM-1 were used as the porous media. This can be related to the highest $\sqrt{\frac{k}{\phi}}$ value associated with DL-1 model. The next high $\sqrt{\frac{k}{\phi}}$ value belongs to OM-2 model, and it is clear that SA-SAGD trials in which OM-2 model was used as the porous medium have the second highest pore-scale sweep rates when all other experimental variables remain unchanged. As it is evident in the data presented in each particular row of Table 3.17 where the pore-level sweep rates are presented, the operating temperatures of the corresponding trials are reasonably close to each other, hence porosity and permeability of the models are remained as the only major experimental variables of concern.

One can also study the effect of model porosity and permeability on the ultimate recovery factor of our SA-SAGD trials. It is believed that as the model porosity and permeability increases at similar operational conditions and experimental parameters, the expected ultimate recovery factor would be increased. This is in quite agreement with the data presented in Table 3.17. For instance, in the first row where CL bitumen was used as the oil type and n-C_5 was injected at 5% vol/vol of the injection main stream, it is clear that the ultimate RF values reported decreases from left to right where both the $\sqrt{\frac{k}{\phi}}$ parameter as well as the porosity and permeability values decrease accordingly. It becomes more interesting if one notices the process time duration over which the reported ultimate RF values were obtained for the SA-SAGD experiments in the first row of the Table. It is clear that the ultimate RF values of models DL-1, OM-2, and OM-1 were obtained over successively longer periods of the process time in which the operating temperatures are reasonably similar to each other. As a result, the enhancement occurred in the ultimate recovery factor as a result of higher porosity and permeability values would have been more pronounced if all these three trials were upscaled to a common similar process time.

Table 3.17: Average sweep rate of the SA-SAGD experiments categorized based on the model type

Glass Micromodel	**DL-1**	**OM-2**	**OM-1**
K (D)	94.61	92.42	77.83
φ (fraction)	0.32	0.32	0.30
Representative SA-SAGD Interface Advancement Velocity ($\upsilon_p^{SA-SAGD}$, mm/min) and RF (% of OOIP)			
CL B, 5 vol % n-C_5	RUN 6: **0.631 (**106.80 °C) RF = **76.58%** in 160 min	RUN 7: **0.530 (**107.10 °C) RF = **75.07%** in 185 min	RUN 5: **0.496 (**106.40 °C) RF = **72.93%** in 180 min
CL B, 15 vol % n-C_5	RUN 13: **0.699 (**102.75 °C) RF = **75.62%** in 140 min	RUN 2: **0.619 (**102.10 °C) RF = **70.53%** in 140 min	RUN 1: **0.527 (**103.30 °C) RF = **77.85%** in 180 min
CL B, 5 vol % n-C_6	RUN 23: **0.637** (108.30 °C) RF = **77.13%** in 160 min	RUN 16: **0.536 (**108.90 °C) RF = **75.33%** in 185 min	RUN 4: **0.505 (**107.40 °C) RF = **74.00%** in 180 min
CL B, 15 vol % n-C_6	RUN 19: **0.748 (**103.45 °C) RF = **78.09%** in 140 min	RUN 10: **0.648 (**101.45 °C) RF = **69.07%** in 130 min	RUN 9: **0.620 (**101.85 °C) RF = **78.53%** in 160 min
L HO, 5 vol % n-C_5	RUN 18: **0.857 (**105.95 °C) RF = **78.13%** in 120 min	RUN 24: **0.747 (**107.55 °C) RF = **78.07%** in 130 min	RUN 22: **0.634 (**107.15 °C) RF = **79.19%** in 160 min
L HO, 15 vol % n-C_5	RUN 8: **0.981 (**103.50 °C) RF = **78.36%** in 105 min	RUN 15: **0.840 (**101.75 °C) RF = **77.91%** in 115 min	RUN 3: **0.828 (**102.90 °C) RF = **77.68%** in 120 min
L HO, 5 vol % n-C_6	RUN 21: **0.993 (**107.80 °C) RF = **77.22%** in 105 min	RUN 17: **0.805 (**108.35 °C) RF = **78.89%** in 130 min	RUN 11: **0.724 (**107.85 °C) RF = **78.45%** in 140 min
L HO, 15 vol % n-C_6	RUN 12: **1.374 (**103.80 °C) RF = **75.62%** in 70 min	RUN 14: **0.987 (**102.10 °C) RF = **78.00%** in 100 min	RUN 20: **0.900 (**101.60 °C) RF = **76.00%** in 105 min

In some cases, the increasing trend of the ultimate recovery factor from left to right of Table 3.17 at each particular row is not observed due to some inconsistencies present in the process time during which the corresponding ultimate RF values were calculated. For instance in the last row of this Table, it is observed that at similar experimental levels of oil type (L HO) and solvent type and concentration (n-C_6, 15% vol/vol), the reported values of the ultimate RF do not increase by increasing the porosity and permeability values of the employed model. As it was mentioned above, the reason is the inconsistencies present in the duration of the process time. In other words, 75.62% recovery factor in DL-1 model was achieved only during 70 minutes of the

process time; however, model OM-1 with lower $\sqrt{\frac{k}{\phi}}$ parameter achieves 76.00% recovery factor but during 105 minutes of the process time. Considering all other operational parameters and experimental factors to be reasonably constant during both these trials, the recovery factor of DL-1 model would have been enhanced more than that of the OM-1 model if the process had been allowed to continue over similar process time span. Quantitative comparison of the ultimate recovery factor values for this kind of situation requires scaling of the process time to a common similar value between trials of interest.

It is also clear that models with higher permeability need shorter start-up time when all the other parameters remain unchanged. For instance, it is evident that between the trials in which n-C_6 at 15% vol/vol concentration were used as the steam additive, the shortest start-up stage belongs to RUN No 19 (i.e. DL-1 as the model) followed by RUN No's 10 and 9 (i.e. OM-2 and OM-1 as the model respectively) respectively.

3.5.5.4. Effect of the Oil Type

There are two different types of oil used in our pore-scale visualization experiments of the SA-SAGD process namely as Cold Lake bitumen and Lloydminster heavy oil blend whose physical properties were presented in sections 2.3.3 and 3.5.2 respectively. In this section, the effect of employed oil type on the pore-scale SA-SAGD process performance is discussed based on the results obtained during the course of our visualization studies.

Table 3.18 contains the representative pore-scale interface advancement velocities as well as the ultimate recovery factor values for our SA-SAGD experiments which are arranged based on the type of oil used in each particular trial. It is evident that for the SA-SAGD trials at similar model, solvent type, and solvent concentration levels, the sweep rate is significantly higher when the less viscous oil was used. It is clear that Lloydminster heavy oil blend benefited more from the solvent concentration enhancement as well as solvent type change from n-C_5 to n-C_6 than that of Cold Lake bitumen. As the Lloydminster heavy oil viscosity is significantly lower than that of Cold Lake bitumen at every particular solvent type and concentration levels, it seems reasonable

to achieve appreciably higher pore-scale sweep rates in trials in which this lower viscosity oil was used.

Table 3.18: Average sweep rates of the SA-SAGD experiments categorized based on the oil type

Oil Type	**Cold Lake bitumen**				**Lloydminster heavy oil blend**			
Representative SA-SAGD Interface Advancement Velocity and Ultimate Recovery Factor								
Trial Information	**RUN No.**	**$v_p^{SA-SAGD}$ (mm/min)**	**RF (%)**	**Process Time (min)**	**RUN No.**	**$v_p^{SA-SAGD}$ (mm/min)**	**RF (%)**	**Process Time (min)**
DL-1, 5% n-C_5	6	0.631	76.58	160	18	0.857	78.13	120
DL-1, 15% n-C_5	13	0.699	75.62	140	8	0.981	78.36	105
DL-1, 5% n-C_6	23	0.637	77.13	160	21	0.993	77.22	105
DL-1, 15% n-C_6	19	0.748	78.09	140	12	1.374	75.62	70
OM-2, 5% n-C_5	7	0.530	75.07	185	24	0.747	78.07	130
OM-2, 15% n-C_5	2	0.619	70.53	140	15	0.840	77.91	115
OM-2, 5% n-C_6	16	0.536	75.33	185	17	0.805	78.89	130
OM-2, 15% n-C_6	10	0.648	69.07	130	14	0.987	78.00	100
OM-1, 5% n-C_5	5	0.496	72.93	180	22	0.634	79.19	160
OM-1, 15% n-C_5	1	0.527	77.85	180	3	0.828	77.68	120
OM-1, 5% n-C_6	4	0.505	74.00	180	11	0.724	78.45	140
OM-1, 15% n-C_6	9	0.620	78.53	160	20	0.900	76.00	105

It is also observed that almost all of the SA-SAGD experiments with L HO as the oil type achieve significantly higher ultimate recovery factors compared to those carried out using CL bitumen as the oil type. This point is more highlighted considering the fact that the trials with the less viscous oil usually were conducted over shorter process time durations compared to their corresponding trials with the aid of CL bitumen. There are some exceptions to this general trend including experimental pairs of RUN numbers 19 and 12, 1 and 3, and 9 and 20. In the former trial set, it is clear that the reported RF value for RUN number 12 with the less viscous oil was

achieved over a process time whose duration is half of that of its corresponding trial with the high-viscous oil (i.e. RUN number 19). In the other two experimental sets, it is also evident that the ultimate recovery factor values obtained with L HO as the oil type were achieved over appreciably shorter process times (in the order of 60 and 55 minutes respectively) compared to their corresponding trials with CL bitumen as the oil type. It is expected that the experiments with less viscous oil would have achieved much higher recovery factors if they had been allowed to run over extended period of time.

3.6. Conclusions

A methodical series of pore-level flow visualization experiments at the controlled environmental conditions were conducted using glass micromodel prototypes of porous media to mechanistically investigate the pore-scale aspects of the Solvent Aided SAGD process. The general concluding remarks from this study are summarized below:

- Simultaneous flow of steam, solvent vapour, condensate phase, and mobile live oil was observed within the mobilized region, ahead of the apparent SA-SAGD interface. The gas phase could be considered as the only truly non-wetting phase during this gravity drainage process.

- Periodic condensation of steam and solvent vapour at the apparent SA-SAGD interface causes condensate build up ahead of the apparent vapour-liquid interface, indicative of the local heat transfer mechanism of the process at the pore-level. Direct drainage displacement of this condensate by the invading gaseous phase enhances the local pore-scale mixing within the mobilized region ahead of the apparent SA-SAGD interface. Moreover, mobile-oil filled pores are drained by a combination of direct capillary drainage displacement of oil by the condensate as well as by the gas phase, and film-flow type of drainage mechanism.

- Local heat transfer mechanisms at the pore-scale include conduction and convection. Enclosed gas bubbles and engulfed condensate droplets within the continuum of the mobile live oil are responsible for the convective element of heat transfer at the pore-level.

- Mass transfer at the pore-level occurs by diffusion mass transfer as well as convective mass transfer mechanisms. The former is as a result of concentration gradient at the pore-level across the SA-SAGD interface while the latter is caused by capillary displacement mechanism and flow by gravity drainage.

- Periodic formation and rupture of the unstable oil films happen within the invaded area ahead of the apparent SA-SAGD interface as well as inside the mobilized region. These phenomena result in complete oil mobilization with very small amount of residual oil phase remaining within the vapour-invaded zone. In addition, the nearly-miscible nature of the SA-SAGD process helps cleaning up the residual oil in the invaded region.

- Asphaltene precipitation was found to be a temporary phenomenon at the pore-scale due to the local convective mixing as well as partial re-opening of the clogged pores by the injected vapour phase.

- Parametric sensitivity analysis of the experimental results were carried out in order to investigate the effect of different experimental variables on the measurable SA-SAGD process performance indicator at the pore-scale based on our visualization experiments. The SA-SAGD trials were designed in a way to figure out the effect of solvent type, solvent concentration in the injection main stream, oil type, and model properties on the sweep rate of the SA-SAGD process at the pore-level. Horizontal interface advancement which represents the lateral expansion of the SA-SAGD process at the pore-level was measured for every particular experiment at different elevations along the height of the glass micromodels.

- According to the quantitative experimental results, it was found that trials with normal hexane as the solvent have greater pore-level sweep rates compared to the ones in which n-C_5 was used as the solvent, provided that all other experimental parameters remained unchanged. It was also observed that the ultimate recovery factors of the trials with n-C_6 as the solvent were higher than those with n-C_5 as the steam additive, if all the other experimental parameters were fixed.

- Higher solvent content of the injecting fluid phase provided faster interface advancement compared to the trials in which the same solvent was used with less volume contribution to the injected fluids. More concentrated solvent phase within the vapour chamber provides

more effective viscosity reduction and mass transfer, which leads to higher drainage rates of the mobile live oil and provides higher ultimate recovery factor at similar process time durations.

- The lower the in-situ viscosity of the oil is, the higher would be the interface advancement velocity under similar experimental conditions. All the trials in which Lloydminster heavy oil blend was used had greater sweep rates compared to those of the corresponding experiments with Cold Lake bitumen as the oil type when all the other experimental parameters remain unchanged. In addition, under similar circumstances of operating conditions and experimental variables, trials with less viscous oil achieved considerably higher ultimate recovery factor compared to those with higher viscosity oil over similar process time durations.

- Models with higher $\sqrt{\frac{k}{\phi}}$ parameter values had a more effective pore-level sweep efficiency as long as all other variables remain unchanged. This is in agreement with the theory of gravity drainage of viscosity-reduced oil with the aid of either thermal or solvent diffusion. An enhancement in the magnitude of the ultimate recovery factor was also observed as a result of higher $\sqrt{\frac{k}{\phi}}$ parameter under similar operating conditions and experimental variables.

4. Performance Evaluation of the SAGD and SA-SAGD Processes Using Unconsolidated Glass-Bead Packed Prototype of Porous Media at the Macro-Scale

4.1. Overview

Although the main focus of this thesis was to systematically investigate the pore-scale performances of the SAGD and SA-SAGD processes, it was decided to quantify the production performances of these two recovery processes at the macro-scale with the aid of a 2D physical model at the controlled environmental conditions. This set of experiments was carried out to demonstrate how effective these two recovery processes are in terms of production characteristics such as mobile oil and dead oil production rates, energy requirements, and also the properties of the produced water in oil emulsion in terms of the size of the dispersed water condensate droplets in the continuum of the mobile oil.

A 2D physical model of porous media was designed and fabricated for the purpose of implementing thermal and thermal-solvent processes of heavy oil and bitumen recovery. The physical model was packed with different sizes of glass beads to create porous media with different permeability values. Athabasca bitumen was used as the oil phase. All the SAGD and SA-SAGD experiments were performed in an isothermal jacket as the controlled temperature environment to reduce the amount of undesired heat loss from the model to the surrounding environment. In addition, layers of insulating materials attached to wooden frames were used to cover the back and side faces of the packed model to further reduce the heat losses. Steam injection and mobile oil production were performed through well-insulated/heated flow lines in order to avoid steam/steam-solvent condensation and line blockage. All the experiments were conducted under the free uptake flow circulation methodology at atmospheric pressure. For the SAGD experiments, replicate trials were also designed and considered in order to make sure of the repeatability of the experiments.

According to the SAGD experimental results, the average mobile oil production rate as well as that of the dead oil are constant over the course of the process. When all other experimental variables are unchanged except the porous medium permeability, it was found that there is a

linear correlation between the mobile oil production rate and the square root of permeability. The higher the permeability of the porous medium is, the higher would be the amount of water content of the produced mobile oil, but the lower would be the steam to oil ratio. The residual oil saturation in the invaded region of the porous medium was obtained to be about 3 and 4.6% of the total pore volume at the higher and lower permeability levels respectively. Moreover, the state of the dispersed water condensate droplets in the continuum of the produced mobile oil was studied with the aid of an advanced photomicrography system integrated with image processing unit. It was obtained that water condensate droplets with equivalent sizes as small as 5 microns were dispersed in the mobile oil background. Average droplet size values were estimated for both of the permeability levels used in the SAGD experiments based on the image processing of the microscopic snapshots taken from the produced emulsion samples.

One SA-SAGD trial was conducted in order to demonstrate the enhancement made in the production performance of the SAGD process following addition of solvent into the injection mainstream. It was obtained that average mobile oil and dead oil production rates of the SA-SAGD process are relatively constant over the course of the experiment. In the SA-SAGD process, there was an enhancement of about 18% and 17% in the mobile oil and dead oil production rates respectively comparing to the corresponding average values of the SAGD process at the same level of the porous medium permeability. The average water production rate and the SOR values of the SA-SAGD process were about 9% and 35% less than those of the corresponding SAGD trial respectively. The microscopic snapshots of the produced water in oil emulsion were studied with the aid of an advanced photomicrography unit and it was obtained that water condensate droplets with an equivalent size of as small as 5 microns were dispersed in the continuum of the mobile oil. In addition, an average water droplet size range was estimated based on the measurements using image processing techniques.

4.2. Parametric Analysis of the SAGD Process Performance Using Physical Models: Literature Review

An extensive literature review was performed on the subject of performance evaluation of the SAGD process with the aid of physical models of porous media. The experimental investigations of the SAGD process were useful in evaluating different mathematical models developed since

1980 for the purpose of performance evaluation of the SAGD process. Most of the SAGD theoretical studies and mathematical representations were checked and verified against scaled experimental studies; some of these models are actually derived directly based on the experimental results in the form of mathematical representations of the experimental data. In addition, these experimental studies with the aid of scaled physical prototypes of porous media helped researchers to tune numerical models developed during the past 30 years for the purpose of predicting the field-scale performance of the SAGD process.

According to the literature survey conducted about the SAGD recovery technique, there are several experimental studies focusing on the enhancement of the SAGD production performance in terms of increasing the ultimate recovery factor and decreasing the energy requirements. The general approach that was followed in these studies is to figure out the type of major experimental variables which affect the process performance significantly, followed by conducting parametric sensitivity analysis of the SAGD process performance. The main experimental variables were found to be reservoir, fluid and operational parameters. The common hierarchical steps include:

- Scaling up the model (if possible) based on the model dimensions, rock and fluid properties, and particular scaling factors,
- Defining a base case for the purpose of performance comparison by specifying the rate of oil production and also steam to oil ratio (SOR) for a simple horizontal well pair,
- Conducting parametric modifications to enhance the SAGD performance focusing on the oil production rate and SOR.

In this section, an overview of the major experimental studies found in the literature is presented.

4.2.1. Application of Different Well Schemes in the SAGD Process

Different combinations of vertical and horizontal (and even slant) wells can be used for field implementation of the SAGD process. Based on the particular field conditions and economical considerations, one could optimize the types and specific properties of the wells in order to maximize the cumulative production whilst minimizing the overall project costs. The field-scale

economic optimization of the SAGD process includes maximizing the Net Present Value (NPV) and Rate of Return (RR) while minimizing the Capital Expenditure (CAPEX) and Operating Expenditure (OPEX) of the project. Several authors have reported different field-scale decision-making procedures to select the appropriate well type, well design and operating conditions for the purpose of achieving maximum profitability for the SAGD process [Birrell, 2000; Mukherjee et. al., 1994; Edmunds et. al., 1991 and 1994; Hamm and Ong, 1994; O'Rourke et. al., 1997; Komery et. al., 1995; O'Rourke et. al., 1994; Rottenfusser et. al., 1991; Edmunds and Suggett, 1995; Edmunds, 1999; Farouq Ali, 1997]. However, it is necessary to conduct precise experimental procedures to sensitively analyze the performance of different well schemes in a typical SAGD process. A series of these experimental studies are described as follows:

4.2.1.1. Effect of Different Production Well Schemes on the SAGD Process Performance

Two similar series of experimental studies were conducted by Liebe and Butler (1991) and Sawhney et al (1995) to experimentally investigate the effect of various injection-production schemes on a typical SAGD process performance. In both of these studies, the experimental setup consisted of a 3D well-insulated cylindrical scaled model with random glass bead packing to produce a fairly homogeneous porous medium. Thermocouples were used to detect development and growth of the steam chamber along the producer. Vertical wells were used for steam injection and three different production schemes of planar, horizontal and vertical were employed. Two different sets of experiments were conducted to sensitively analyze the effect of operating parameters, fluid properties, and production well scheme on the SAGD process performance indicators including recovery efficiency and steam chamber growth rate. These experiments were scaled up to express the performance of the SAGD process in Cold Lake and Lloydminster type of reservoirs.

The authors concluded that experiments with planar and horizontal production wells showed enhanced performance in terms of higher drainage rate, cumulative production, and ultimate recovery values compared to those with vertical producers provided that all other operating conditions were the same. This result was verified for both scaled model experiments representing the SAGD process performance in Cold Lake and Lloydminster type of reservoirs. The reason is that planar and horizontal wells were extended extensively in the formation, so

their active lengths available for oil drainage were wider compared to that of the vertical producer. However, the drainage area of the vertical producer was just limited to the neighbouring area around the production well. As a result, planar and horizontal producers provide much more effective flow contact with reservoir. In addition, the heated oil should travel less distance horizontally to reach the planar or horizontal production wells compared to the case in which vertical producer is used. It was also observed that the oil recovery value increased as a result of either higher operating pressure or lower initial oil viscosity.

The growth rate of the steam chamber was also affected by the geometry of the production well. It is reported that steam chamber grew much faster when horizontal and planar producers were employed. Considering the fact that steam injection well was vertical in all these trials, the rate of chamber growth was very fast at the top portion of the chamber while it grew very slow near the bottom portion of the chamber.

4.2.1.2. Effect of Different Injection Well Schemes on the SAGD Process Performance

Different injection well schemes were proposed in the literature to enhance the performance of the SAGD process. Of particular interest is the use of horizontal and vertical injection wells.

a) *SAGD Process with Horizontal Injection Well:* In this application, the injector-producer well pairs are drilled from the surface, or from a subsurface tunnel (like the case in UTF project); the well pairs are drilled close together with a definite vertical distance between the horizontal sections of injector and producer. This will allow the inter-well communication and reservoir heating to mobilize the cold bitumen. Under this well configuration, the steam chamber grows upward and sideways from the horizontal injector above the horizontal producer to the top of the reservoir in order to achieve high vertical conformance (Rich Kerr et. al., 2002; Birrell, 2000; Mukherjee et. al., 1994; Edmunds et. al., 1991 and 1994; Hamm and Ong, 1994; and Rottenfusser et. al., 1991). The recovery performance of the SAGD process using horizontal injector and horizontal producer (HI-HP) were investigated extensively in the literature using scaled 2D and 3D models (Nasr et. al., 2003; Nasr and Ayodele, 2005; Butler and Stephens, 1980 and 1981; Butler, 1987; and Butler, 1994).

Determination of the maximum allowable vertical spacing between the paired wells is one of the most crucial steps in implementing the HI-HP SAGD process in an oil field. According to the experimental results and based on the schematic demonstration of the SAGD process presented in Figure 1.2, the steam chamber grows upward and later spreads beneath the overburden. If the reservoir contains oil having an acceptable mobility, it is possible to drill the injector somewhat higher in the pay zone. The only limiting factor governing the vertical distance between the injector and producer is the heavy oil mobility. The mobility should be high enough to allow the initially-developed chamber to move downwards toward the producer during a reasonable time scale. During this stage, there is a displacement of the mobile oil and water condensate to the production well, and with adequate oil mobility, this communication period can be highly productive. In the case of low initial oil mobility, a suitable start-up procedure has to be conducted using simultaneous steam circulation in both injector and producer for a certain period of time. This will mobilize the initially immobile bitumen and create flow communication between the paired wells.

b) *SAGD Process with Vertical Injection Well:* The feasibility of the vertical well SAGD process and its production performance were addressed in the literature by several authors through experimental studies with the aid of scaled physical models (Yongrong Gao et. al, 2002; Rose and Deo, 1995; Liebe and Butler, 1991; and Sawhney et. al, 1995). This mode of the SAGD process has been also implemented in some fields such as Cold Lake project directed by Imperial Oil, Yarega in Russia, Hopco Project in California, Esso Resources and Cold Lake Project, and Sceptre oil project in the Tangleflags field in Saskatchewan (Butler, 1991; Donnelly, 1997 and 1999, Sawhney et. al, 1995; Rose and Deo, 1995; Butler, 2001; and Butler, 1998). In this mode of the SAGD operation, one or more vertical steam injectors are drilled above a horizontal producer, which is landed at the reservoir base. Steam chamber would form along the height of the vertical injectors (i.e. around the perforated interval which is intended to be as near to the producer as possible). There are some incentives behind vertical well-SAGD process such as cheaper and less complicated drilling operations, flexibility over the height of the steam injection wells, and more efficient steam distribution along the horizontal producer in the absence of axial steam pressure drop along the length of the horizontal injector.

It is required to use several vertical injectors in order to obtain the same performance as that obtained using a horizontal injector. The choice of the inter-well spacing is an economic decision; closer spacing gives more rapid production and better Oil to Steam Ratio (OSR); but requires more investment in wells. Effective length of the horizontal producer is the length of a segment along the horizontal extension of the producer that is served by one single steam injector. Experimental results performed by Sawhney et.al (1995) showed an initial approximation for the effective length of the horizontal producer which is in the order of 10 to 30% of the formation thickness. The inter-well spacing can even be extended to the same order as the height of the pay zone considering the economic concerns of the SAGD project especially when these vertical injection wells are available from previous field operations (Sawhney, 1995).

4.2.2. Permeability Enhancement of the Inter-Well Zone in a Conventional SAGD Process

It is believed that the recovery performance of a conventional SAGD process as well as its energy requirements are improved by enhancing the permeability of the inter-well region between paired horizontal wells. Results of the experimental investigations found in the literature show that presence of permeability enhancement in the form of a vertical channel between the paired horizontal wells enhances the production performance and also thermal efficiency of the process (Nasr et. al., 1998; Nasr et. al., 1997; Nasr et. al., 1991; and Vanegas Prada, 2005). This channel enhances the start-up stage of the process by utilizing high permeable pathways for fluid flow between the well, and also help to propagate the heating energy more effective than the typical SAGD process. It was found that the average oil recovery rates were almost the same for both cases, as it is a characteristic of the gravity-dominated process; however, the ultimate recovery of the case with vertical channel was higher as a result of process enhancement.

4.2.3. Effect of Additional Vertical Injector on the SAGD Process Performance

According to the experimental results presented by Nasr et. al. (1991, 1997, and 1998), presence of an additional vertical injector could effectively enhance the production performance of the SAGD process especially during the early stages. This vertical injector allows the steam chamber to be formed faster and more effective than the case of a typical SAGD process. This is due to

the fact that a vertical steam chamber could also form around the vertical injector in addition to that which is a result of the horizontal injection. Therefore, it is possible to enhance the SAGD performance using an existing or a newly drilled vertical well, combined with the typical paired horizontal wells. If an existing vertical well is used, favorable economics could also be expected compared to the case of drilling a new vertical injector.

4.2.4. Effect of the Length of Production Well on the SAGD Process Performance

Optimizing the length of the paired horizontal wells, especially the producer, has been the subject of some experimental, theoretical, and numerical studies in the literature (Edmunds and Gittins, 1993; Nasr et. al, 1991, 1997 and 1998]. According to the experimental results presented by Nasr et.al, increasing the length of the horizontal producer has a direct impact on the SAGD performance, as the longer producer would facilitate the rate of drainage, and the resulting chamber growth would also be more effective as a result of the increased reservoir voidage. The authors concluded that for the case of longer producer, the drainage rate was a little higher than the baseline case of a conventional SAGD process with equi-length producer and injector during the early stages of the process. However, as the steam chamber expanded laterally beyond the length of the injector at the late process time, the oil production rate of the case with longer producer became greater than the base case. The reason is that as the producer length increases, its effective drainage length is also increases which results in higher oil production and chamber growth rates. One major experimental error is observed in this section, which was not addressed properly by the authors. As the length of the longer producer was in the same order of the model length, the model walls could have adverse end effects on the producer endpoint. This issue may negatively affect the measured recovery rates for the case of the longer producer.

4.2.5. Performance Modeling of Single Well SAGD

In this variation of the SAGD process, both the steam injection and liquid production take place through a single extended horizontal well. This single well is landed at the base of the reservoir, and is completed using dual completion techniques in which two separate annular and tubing spaces are designed through one single borehole. Steam is injected into the annular space which is perforated along the length of the horizontal well, whilst liquids are produced from the toe

section of the well. This modification of the SAGD process is applicable in reservoirs in which oil has some in-situ mobility, or the formation thickness is around the cut-off value for the SAGD implementation. A series of experiments were conducted to obtain the technical viability of the single well SAGD process as well as to compare its performance with a conventional SAGD process taken as the comparison baseline (Nasr et. al., 1991 and 1997, Sasaki et. al., 1996 and 1999).

Experimental results showed that single well SAGD production performance could be comparable with that of the conventional SAGD process if the single well would be lengthier (i.e. in the order of 1.5-2 times) than those of the conventional SAGD process. In the single well SAGD process, steam chamber tends to initiate towards the toe of the single well where the production takes place, and then spreads toward the heel of the single well. The well length effect on the production performance of the single well SAGD was also investigated using scaled physical models. It was concluded that long single well SAGD produced more oil than short single well SAGD during the later stages of the experimental duration, but the early experimental response to these cases were almost the same. It is because of the fact that the steam chamber growth over the length of the long single well would be more pronounced during the late experimental duration rather than in its early life span.

4.2.6. Effect of Steam Injection Pressure on the SAGD Process Performance

According to the experimental results presented by Sasaki et. al. (1996 and 1999), steam injection pressure has a direct impact on the recovery performance and steam chamber growth of the SAGD process. The authors used 2D scaled physical models in order to predict the field performance of the SAGD project in PCEJ/CANOS oilfield. From the sensitivity study of the SAGD process performance to the steam injection pressure, the authors concluded that higher steam injection pressure leads to shorter breakthrough time of the steam phase into the production well followed by higher growth rate of the steam chamber. Increasing the steam injection pressure also caused an increase in the pressure difference between the paired horizontal wells, resulting in a more effective pressure-driven driving force for the oil mobilization. Consequently, higher drainage rates were achieved at higher operating pressures.

4.2.7. Effect of Vertical Spacing Between Horizontal Wells on the SAGD Process Performance

The initial stage of production and also steam chamber rise in a conventional SAGD process are sensitive to the relative position of the steam injection well with respect to the production well. To land the horizontal injection well near the centre of the reservoir thickness would have the advantage of supplying steam uniformly in all directions from the injector. According to the experimental results presented by Sasaki et. al. (1996 and 1999), the oil production rate increases when the vertical spacing becomes larger, but the amount of the drainage rate increase would be also a function of the process time. A definite time interval was expressed as the lead time, and was defined as the time required to generate the initial steam chamber between the wells at near breakthrough conditions prior to the vertical expansion of the steam chamber over the injector. The authors concluded that the amount of increase in the steam breakthrough time into the producer is proportional to the square root of the vertical spacing. As a result, using smaller vertical spacing between horizontal wells reduced the lead time during the initial stages of the process, while decreased the production rate after steam breakthrough into the producer during the depleting stage of the SAGD process life.

4.2.8. Effect of Intermittent Steam Stimulation of the Production Well on the SAGD Process Performance

A modification of the conventional SAGD process was proposed by Sasaki et al (1999) which is called “SAGD process with Intermittent Steam Stimulation of the Lower Well” (SAGD-ISSLW). As it is mentioned before in section 4.2.7, conventional SAGD process with larger inter-well vertical spacing had higher production rate after steam breakthrough into the producer during the mature phase of the process. On the other hand, the lead time required to generate a rising steam chamber would also be increased which has a negative impact on the overall process economics. In SAGD-ISSLW application, the process is modified by intermittent stimulation of the producer using steam circulation. According to the experimental results, this method can accelerate the steam chamber growth compared to the usual time consumed in a conventional SAGD process. In other words, the lead time in a SAGD-ISSLW process is considerably shorter than that of a conventional SAGD process. According to the methodology carried out by the authors, the

production well experienced a series of consecutive production and stimulation cycles. The duration of each production and stimulation stage could be specified considering the properties of reservoir rock, in-situ bitumen, and operational considerations.

The performance of the SAGD-ISSLW process was compared to that of the SAGD process in terms of production enhancement, steam chamber growth, and thermal efficiency. It was concluded that the invaded region of the SAGD-ISSLW process was larger and wider than that of the conventional SAGD process in similar timeframes, showing that the rate of steam chamber growth was accelerated due to the intermittent stimulation of the production well. In addition, it was obtained that both the steam breakthrough time into the producer as well as time to reach the maximum production rate were shortened in SAGD-ISSLW process compared to those obtained during the conventional SAGD process. Regarding the production performance, it was obtained that SAGD-ISSLW provided higher production rates compared to those of the SAGD process. On the other hand, SAGD-ISSLW was found to be a less attractive process compared to the conventional SAGD process when the thermal efficiency of the process is concerned. The reported cumulative steam to oil ratio of the SAGD-ISSLW process was increased considerably compared to that of the SAGD process. No specific reason was mentioned in the original paper for this unusual system behavior, but it might be because of the increased heat loss to the side walls of the model, or heat storage inside the scaled model. In addition, no optimization procedure was carried out in order to determine the most suitable duration of the stimulation period within the limits of the experimental conditions. No document was found in the literature about the commercialization of this process, nor about any pilot-scale / field-trial of the SAGD-ISSLW method.

4.3. Performance Evaluation of the SAGD Process Using Numerical Simulation Techniques: Literature Review

When it comes to the performance evaluation of a particular oil recovery technique, numerical simulation and history matching methodologies are the most important disciplines of reservoir engineering. Through the use of numerical codes and computer programming, different transport processes such as flow, heat, and mass transfer would be numerically modeled. Numerical simulation is able to accept complicated and detailed input data structures, but the simulation

results tend to be complicated and it is sometimes difficult to identify which specific features have more influence on the output results. Although numerical simulation is able to accept complicated input data, it tends to be limited to relatively few reservoir recovery mechanisms. It is important to verify the governing mechanisms of different processes for numerical simulation studies in order to achieve reliable simulated results especially with commercial numerical simulators. The predictive accuracy of the numerical simulation techniques is usually improved by making successive modifications to the input data and/or equations if possible in order to closely match the actual performance observed in the field. For in-situ steam projects including the SAGD process and its modifications, the key parameters are steam injection rate, oil production rate and water production rate. No matter which numerical modeling procedure is used, assumptions are made and physical parameters are required as input data. The production data from field operations is also required to confirm and validate the model.

There are always some uncertainties in the input data, which can considerably affect the final performance of the predictive models. Numerical simulation can help us to precisely predict the relative effectiveness of these uncertain data on the process performance. As the general theme of this thesis is based on the understanding of the physics and relevant mechanisms associated with the SAGD and SA-SAGD processes using experimental methodologies either at the pore-level or at the macroscopic scale, it is not intended to focus on the numerical modeling aspects of these two processes. In fact, it was tried to select some unique publications among the mass of literature dedicated to the numerical simulation of the SAGD and SA-SAGD processes, focusing on the mechanistic studies of these two recovery methods with the aid of commercial numerical simulators. The review materials presented in this section also show a qualitative proof of our experimental results obtained during the course of the visualization studies as well as macroscopic SAGD and SA-SAGD processes performance evaluation with the aid of 2D physical model. Most of these numerical simulation studies were carried out using Steam, Thermal, and Advanced Processes Reservoir Simulator (STARS) module of CMG simulation package. It is claimed that STARS is capable of precisely predicting the SAGD and SA-SAGD performances with the aid of confident high-quality input data (Ito et. al., 2004; Ito and Singhal, 1999; Ito and Ipek, 2005; Ito and Suzuki, 1996; Kisman and Yeung, 1995;

Mukherjee et. al., 1995; Edmunds and Suggett, 1995; Edmunds and Gittins, 1993; Hamm and Ong, 1994; and McCormack, 2007).

In this section, some selected studies regarding numerical simulation of the SAGD process are reviewed in order to demonstrate the importance of numerical simulation in performance modeling and prediction of the SAGD process as well as its effectiveness in understanding the mechanisms involved in this dominant heavy oil and bitumen recovery process.

4.3.1. Heat Transfer Mechanisms Ahead of the Steam Chamber Interface

A series of numerical simulation studies were conducted by Ito and colleagues (Ito, Hirata and Ichakawa, 2004; Ito and Singhal, 1999; Ito and Ipek, 2005; and Ito and Suzuki, 1996) in order to validate the performance of the SAGD process in some of the field applications. Numerical parametric sensitivity analysis were performed in all these studies in order to figure out the effect of each process variable on the SAGD performance in terms of enhancement/deterioration of the process performance in comparison to the conventional SAGD process which was considered as the baseline. One of the main results of these studies is about the heat transfer mechanisms in a conventional SAGD process ahead of the steam chamber interface. In contrary to the original theories proposed in the literature to describe the major heat transfer mechanism in a conventional SAGD process to be conduction, these studies revealed that convection heat transfer mechanism plays an important role in the general scheme of heat transport ahead of the steam chamber interface. Defining this new heat transfer mechanism in a typical SAGD process helped the authors to justify their observations during the course of numerical simulation of the SAGD process as well as history matching of some field-scale SAGD projects such as Phases "A" and "B" of the UTF project.

A new recovery mechanism for the SAGD process was proposed by Ito and colleagues based on the convective-conductive heat transfer instead of conduction-only ahead of the steam chamber interface. The authors believed that steam loses its internal thermal energy and finally condenses through **two** different mechanisms; one is by *natural convection* where steam flows into the liquid zone consisting of water condensate and cold oil, then loses its energy by mixing with these cold fluids. When the steam chamber has been maturely developed, condensation through

this new mechanism occurs mainly at the upper part of the reservoir in which fresh steam could create local mixing with in-situ liquids such as cold oil and water condensate. On the other hand, it was also believed that condensation by *thermal conduction* occurs along the entire steam chamber interface at a relatively uniform magnitude. Consequently, water condensate was believed to play an important role in the oil recovery within the interfacial region of the SAGD process. Considering the iso-saturation maps of oil and water condensate as well as the temperature contours ahead of the steam chamber interface, it was concluded that water condensate displaces the oil phase ahead of the steam chamber interface and provides energy to oil by thermal convection.

4.3.2. Effect of Formation Thermal Conductivity on the SAGD Process Performance

Thermal conductivity of the formation rock has a direct impact on the heat transfer mechanisms in the reservoir during the course of the SAGD process. As it was noted in section 4.3.1, Ito and his colleagues proposed a new heat transfer mechanism as of thermal convection for the SAGD process aside from the thermal conduction. A numerical sensitivity analysis was performed on the magnitude of formation thermal conductivities in order to identify the relative importance of convection and conduction heat transfer mechanisms during the SAGD process (Ito and Suzuki, 1996). Following a reduction in the magnitude of thermal conductivity, the amount of water condensate at the steam chamber in the lower part of the reservoir was reduced accordingly. This is as a result of reducing the conduction mechanism of heat transfer at the lower parts of the chamber, while increasing the upward movement of steam towards the topside of the steam chamber. The steam phase would condense at the chamber top, and the condensate loses the thermal energy by convection during a trip from the upper part of the reservoir to the producer. The water condensate phase has sufficient time and distance to be cooled during this trip as a result of the convection heat transfer. However, the water condensate phase developed at the lower parts of the chamber do not have sufficient time and distance to be cooled during the trip towards producer. It was also found that decreasing the thermal conductivity of the formation decreased the steam injectivity, but enhanced the overriding of the steam chamber which supports the theory of presence of the convection mechanism.

The effect of formation thermal conductivity on the production performance and energy requirements of a typical SAGD process was also investigated by Kisman and Yeung (1995) and Mukherjee et al (1995). According to these studies, the daily oil recovery during the early stages of the process decreased significantly upon a decrease in the formation thermal conductivity. The decrease in the oil production was also followed by a gradual improvement in the production performance with respect to time. It shows that the thermal conductivity is an important parameter which considerably contributes to the overall heat transfer of the SAGD process especially during the start-up phase. However, simulation results showed that decreasing the thermal conductivity values reduced the amount of steam injectivity, hence reducing the total energy intensity of the process by enhancing the Oil to Steam Ratio (OSR) values. As the improved OSR values partially compensates for the reduced productivity values, the overall detrimental effect of the reduction in the thermal conductivity is quite moderate.

4.3.3. Temperature Profile Ahead of the Steam Chamber Interface

Numerical simulation makes it possible to obtain the temperature profile at any time step and location throughout the model. Ito and Suzuki (1996) used the predicted temperature profiles ahead of the steam chamber interface to justify their proposed combined heat transfer mechanism for the SAGD process. According to this study, the temperature distribution ahead of the steam chamber interface was shown to have general decreasing convex trends regardless of the horizontal location ahead of the interface where the associated temperature profiles were calculated. Based on the specific shape of the temperature distribution ahead of the steam chamber interface, it was concluded that the main energy transfer mechanism for this region is heat convection; otherwise, if the only heat transfer mechanism ahead of the interface was assumed to be conduction, the associated temperature distributions should have had an exponential decreasing trend over the distance ahead of the interfacial region and concaved-shape temperature profiles would have been expected.

4.3.4. Effect of Formation Geo-Mechanical Changes on the SAGD Process Performance

In order to understand the effect of formation geo-mechanical changes on the SAGD process performance, a series of numerical sensitivity analysis were performed by several authors (Ito,

2004; Ito, 1998; Ito and Suzuki, 1996; Chalaturnyk and Li, 2004). In most of the numerical simulation studies, the formation properties are assumed to be constant and the shear failure and geo-mechanical deformations are totally ignored. However, formation geo-mechanical changes, which are mostly because of the excessive thermal disturbance during the SAGD process, seem to have a significant role in determining the operational conditions. It is obvious that major rock properties such as porosity, permeability, and relative permeability depend on the operating temperature, pressure and their associated changes especially in loose unconsolidated tar sands and bitumen resources. Therefore, it is important to study the effect of shear failure and rock deformation during the course of a thermally-aided process.

According to the simulation results, it was concluded that although the cumulative oil recovery was not changed significantly considering the changes in the petrophysical rock properties, steam chamber shape and growth and also its saturation distribution were changed significantly. Considering the fluid distribution inside the steam chamber and oil and water flow rates in the vertical and horizontal directions, it was concluded that a significant amount of the mobile oil remained in the steam chamber. This oil drained vertically through the steam chamber at an increasing rate approaching towards the bottom of the chamber. Hence, the entire steam chamber became a flow path for oil and a reserve of the mobile oil. This conclusion was considered by the authors to be in contradiction with the preliminary assumptions made during the course of analytical modeling of the SAGD process where it was assumed that the remaining oil saturation in the chamber, which might be different from its residual value, is too small and oil drainage cannot take place through the chamber.

4.3.5. Effect of Operating Conditions and Enhancement Procedures on the SAGD Process Performance

According to the simulation results presented by Kisman and Yeung (1995) and Mukherjee et al (1995), increasing the vertical permeability of the formation (i.e. increasing the k_v/k_h ratio) would definitely enhance the SAGD performance in terms of increasing the production rates and reducing the energy requirements during the early and intermediate stages of the process. However, numerical results showed that the SAGD late-time performance was not as sensitive to the vertical permeability variation as its early-life stage performance.

Effect of permeability heterogeneity on the SAGD process performance due to the presence of impermeable shale barriers was also investigated by the above mentioned authors. The results of the SAGD process performance in homogeneous reservoirs were compared with those in the presence of horizontal shale barriers. The permeability barriers were characterized in terms of their horizontal continuity as well as their associated vertical spacing. For the case of discontinuous lenses of flow barriers with finite lengths and definite spacing, it was found that the daily oil production and the OSR were not affected considerably by the presence of the flow barriers. In fact, presence of small discontinuous barriers might even enhance the performance of the SAGD process by diverting the steam chamber towards other areas where might not be invaded in a homogeneous formation. This phenomena, which was pointed out as "steam detouring", is addressed in the literature by other authors (Ito, Hirata and Ichakawa, 2004; Ito and Singhal, 1999; Ito and Ipek, 2005; Ito and Suzuki, 1996). However, in the case of continuous flow barriers whose horizontal extension exceeds a threshold length, the SAGD process performance was found to be significantly deteriorated in terms of the oil production rate as well as the steam requirements.

Operating pressure of the SAGD process was also considered as one of the operating conditions of interest and it was tried to numerically study the effect of steam injection pressure on the SAGD process performance. According to the numerical simulation studies introduced in this section, operating the SAGD process at higher pressures resulted in enhancing the process performance in terms of both recovery and thermal efficiencies. It is important to note that the final choice for operating pressure depends upon the type of production scheme, in terms of natural flow or artificial lift.

4.3.6. Effect of Presence of Solution Gas and/or Free Gas on the SAGD Process Performance

Heavy oil volatility due to operating conditions of applied recovery methods such as pressure and temperature is a possible concern with regard to production performance. This is because of the fact that presence of the free gas can lower the partial pressure and hence temperature of the steam phase inside the steam chamber at a given operating pressure. On the other hand, free gas evolving from the oil phase could mobilize the bitumen in the areas close to the interfacial region

and it would also reduce the heat loss to the overburden by providing an insulation layer against the heat transfer. According to the numerical simulation studies performed by Kisman and Yeung (1995) and Mukherjee et al (1995), two types of oil with high and low levels of volatility were used in order to investigate the effect of presence of the free gas on the SAGD process performance. It was found that the degree of bitumen volatility does have a strong enhancing effect on the production performance of the SAGD process during the early process life; however, this enhancement was leveled off as the time went by. In other words, greater amounts of bitumen was produced sooner in the presence of the free gas compared to the baseline case in which there was no free gas in the steam chamber.

4.4. Demonstration of the SAGD and SA-SAGD Processes Performances: Experimental Investigation using Physical Packed Model

The last objective of my PhD research was to investigate the macro-scale performance of the SAGD and SA-SAGD processes using physical model of porous media. A two dimensional cross-sectional physical model was designed and fabricated for the purpose of conducting SAGD and SA-SAGD processes at the controlled environmental conditions of constant temperature housing. Both the SAGD and SA-SAGD experiments were carried out at atmospheric operating pressure and the results were collected and analyzed in order to compare the production characteristics and energy requirements of these two analogue bitumen recovery processes. In this section, various aspects of this experimental study are described.

4.4.1. Physical Model: Design and Fabrication

The 2-dimensional physical model is composed of a rectangular o-ringed middle frame, and two front and back plates all made of Lexan Polycarbonate Plexiglas®. This extruded polycarbonate material was chosen because of very high operating temperature rating and high compressive strength. As the walls of the cross-sectional physical model should be considered as no flow boundaries of mass and energy, this type of plastic was chosen because of its very low associated values of thermal conductivity. In order to provide minimum amount of heat transfer across the assumed no-flow boundary, an isothermal housing with uniform elevated temperature compared to that of the environment was employed.

The middle o-ringed frame was sandwiched between the front and back plates. The schematic of the middle plate is displayed in Figure 4.1. As it is evident in this Figure, the middle plate contains a packing port at the top, a perforated injection tube passed along the length of the plate, a steam or steam/solvent injection port, and an excess steam or steam/solvent exit port to the atmospheric condenser.

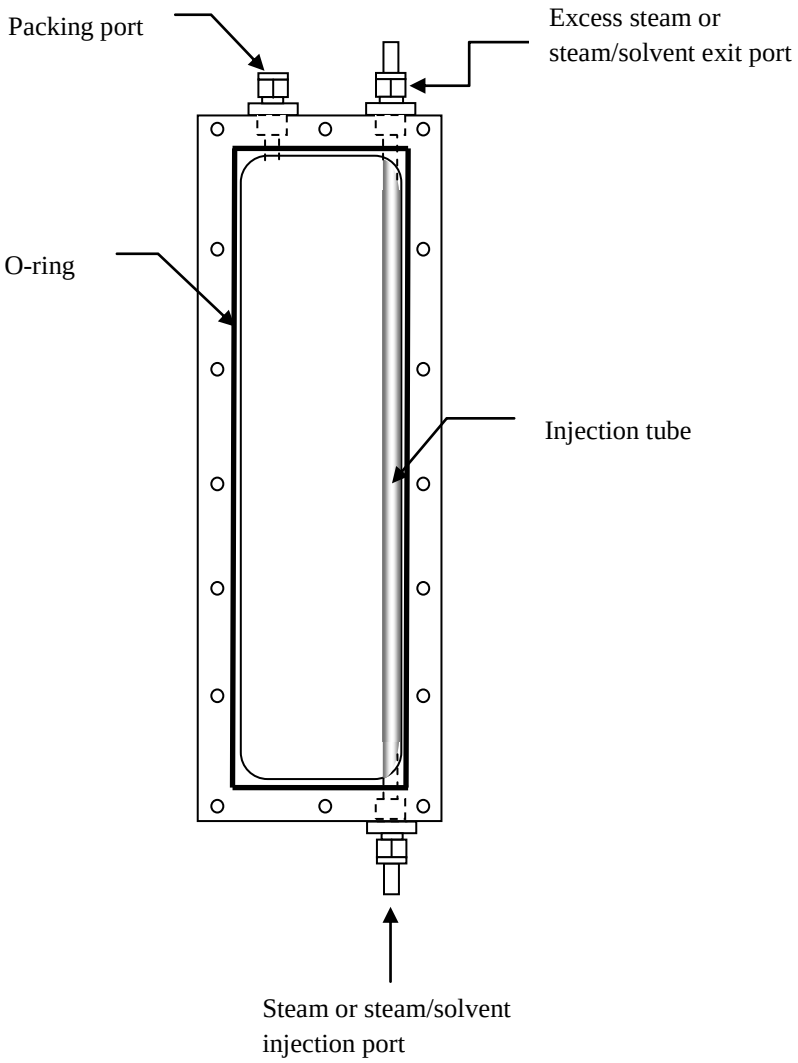

Figure 4.1: Schematic of the middle plate of the 2D physical model (Modified from Rezaei, 2010 with permission)

Figures 4.2 to 4.4 show the map view of the three front, middle and back plates of the physical model. The empty space between the two face windows has the dimensions of 56.83 cm (22.375") length, 13.65 cm (5.375") width, and 1.905 cm (¾") thickness. Consequently, the bulk volume of the empty space is about 1478 cm^3. A production port of the size of 0.635 cm (¼") was tapped in the front window. Ten 0.3175 cm (⅛") thermocouple wells were tapped in the back plate in order to monitor the temperature profiles along the height and width of the porous medium. A packing port of the size of 0.635 cm (¼") was also tapped in the o-ringed frame to ease the packing stage of the physical model. A 0.635 cm (¼") perforated gas injection tube was passed through one side of the o-ringed frame, resembling half of the SAGD or SA-SAGD scheme. This gas injection tube was perforated with increasing density of perforations towards the top of the model in order to compensate for the pressure drop inside the tube, hence providing a more uniform distribution of steam or steam-solvent mixture along the height of the model. The role of the perforated injection tube is to ease the hydraulic communication along the height of the packed model and to facilitate the vertical growth of the steam or steam-solvent chamber towards the top of the packed bed. During the saturation stage of the model, another 0.3175 cm (⅛") solid stainless steel rod was installed inside the gas injection tube. This solid steel rod was used in order to prevent the oil phase from flowing into the gas injection tube through the perforations. A fine wire mesh was wrapped around the perforated gas injection tube to avoid glass beads penetrating through the perforations of the injection tube. The model was reinforced by aluminum bars, enabling it to withstand higher applied pressures during the oil saturating stage. Overall, the physical model design is simple, easy to assemble and to dismantle for the cleaning purposes.

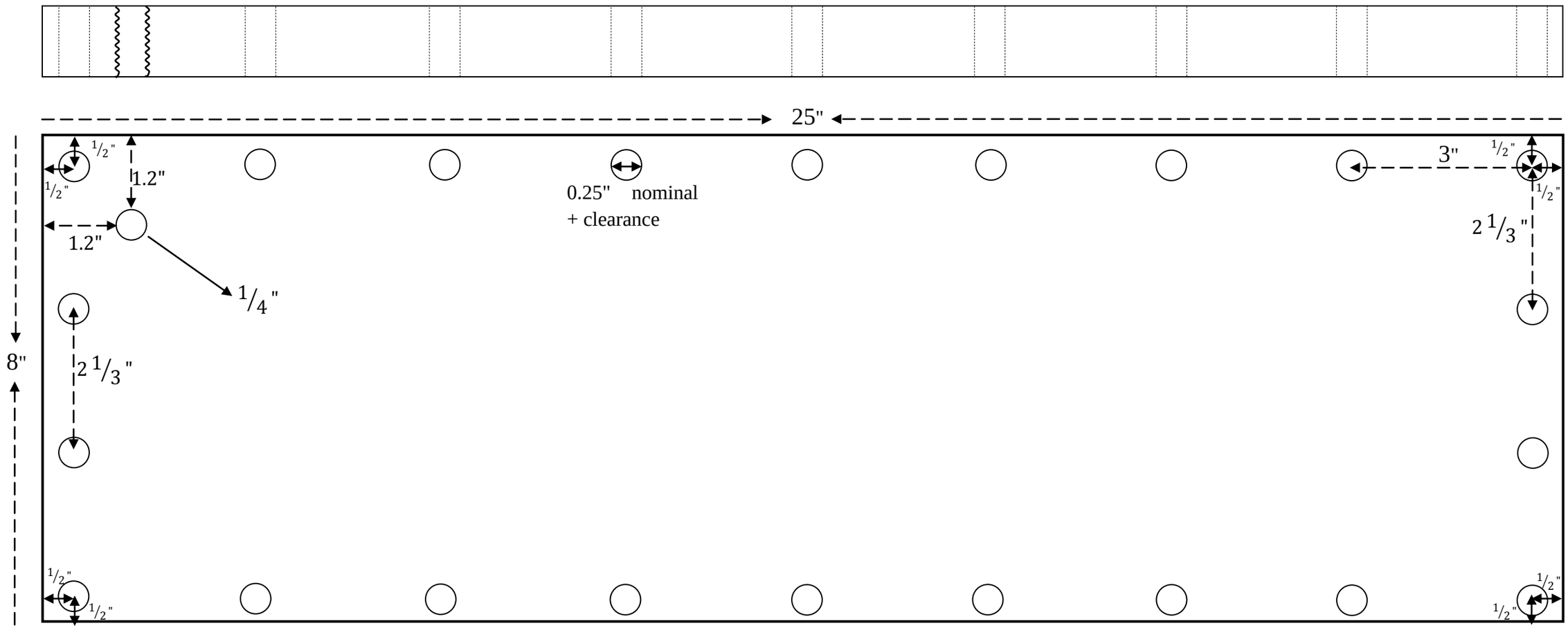

Figure 4.2: Map view of the front plate scheme (0.5" Lexan Polycarbonate sheet)

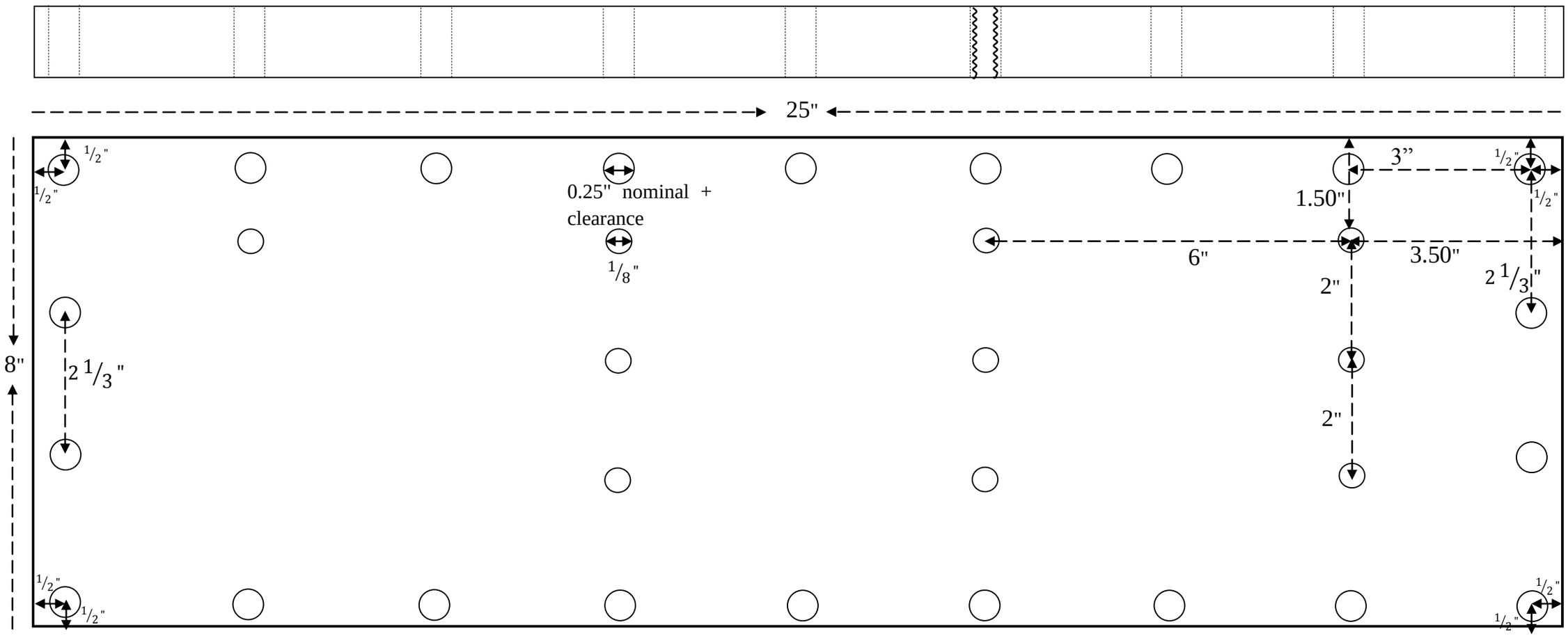

Figure 4.3: Map view of the back plate scheme (0.5" Lexan Polycarbonate sheet)

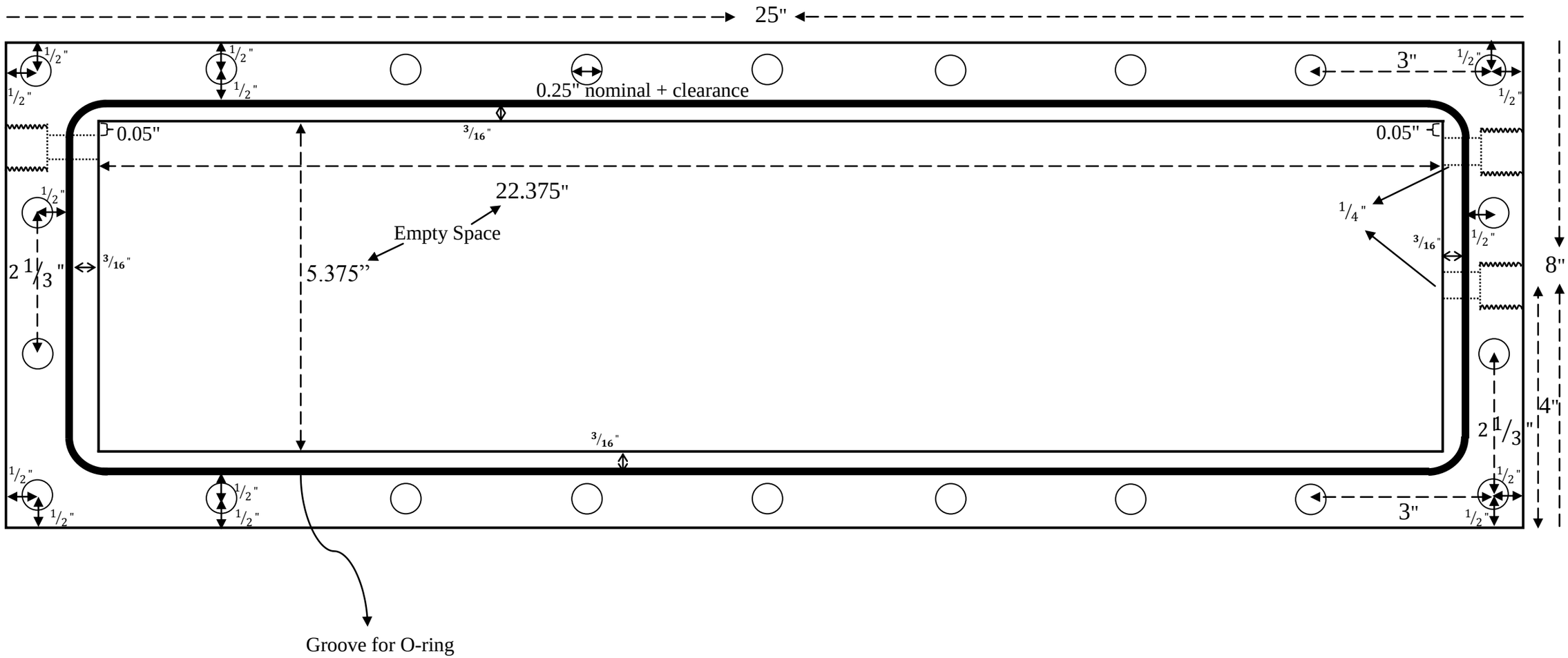

Figure 4.4: Map view of the middle o-ringed frame scheme (0.75" Lexan Polycarbonate sheet)

4.4.2. Experimental Setup and Procedures for the SAGD and SA-SAGD Processes

Both the SAGD and SA-SAGD experiments were carried out at the controlled environmental conditions of isothermal housing, resembling the surrounding constant reservoir temperature. These two processes were conducted based on the free uptake methodology of steam or steam-solvent injection in which the injecting fluid(s) was provided in excess of the amount(s) that was needed to fulfill the gravity-dominated process to ensure that the steam or steam-solvent chamber was propagated entirely along the height of the porous medium.

The schematic process flow diagram of the SAGD experiments using unconsolidated glass-bead packed porous medium is presented in Figure 4.5. For each single experiment, the physical model was packed on a vibrating table to ensure that a homogeneous tight packing of the unconsolidated glass beads was achieved. A leak test was then performed on the packed model to the extent of 20 Psig in order to make sure that the packed model is capable of withstanding moderate injection pressures during the oil saturation stage. The packed model was then connected to a pressure vessel filled with bitumen. Both the packed model and the bitumen container were heated at 50 °C using heating tapes and/or convection oven. A maximum back pressure of 10 Psig was applied on the injection vessel with the aid of a 40-Psig air stream and a back pressure regulator to push the heated oil into the empty packed model. Depending on the temperature of the physical model and the oil injection vessel and also the magnitude of the applied saturating pressure, the saturation stage took between 3-5 hours. The fully saturated model was brought into ambient temperature after the saturation stage to resemble the primary conditions of the SAGD or SA-SAGD experiments. As the thermal processes of heavy oil recovery at the lab conditions suffer from excessive heat losses across the model boundaries, attempts were made in order to reduce the heat loss by conducting the experiments in an isothermally-heated environmental chamber. The packed model was placed inside an isothermal environmental chamber resembling the surrounding reservoir for the 2D cross-sectional porous medium. A high-pressure air stream with the flowing pressure of 40 Psig was passed through a 420 W coiled heater and then was injected into the environmental housing. A thermocouple was installed half way along the height of the environmental chamber in order to monitor the average housing temperature. This thermocouple was housed inside an aluminum tube to prevent the effect of environmental disturbance and air convection on the temperature measurement. The

housing temperature was measured on a real-time basis and the measured data was collected using an automated data acquisition unit. A microprocessor-based temperature/process controller (OMEGA CN 76000) was used in order to maintain the housing temperature extremely close to a predetermined set point. The real-time measured housing temperature was compared against the temperature set point using temperature controller, and the appropriate controlling response was implemented into the coiled heater based on the employed process control schemes. Two different housing temperatures of 50 and 60 °C were used in the heat loss, SAGD, and SA-SAGD trials. In order to provide a more uniform temperature profile along the height of the isothermal housing, the heated air stream was distributed along the height of the housing through a perforated vertical cupper tube with increasing perforation density towards the top of the tube. Two axial AC fans were installed at the ceiling and bottom plates of the isothermal housing in order to provide sufficient air mixing inside the jacket.

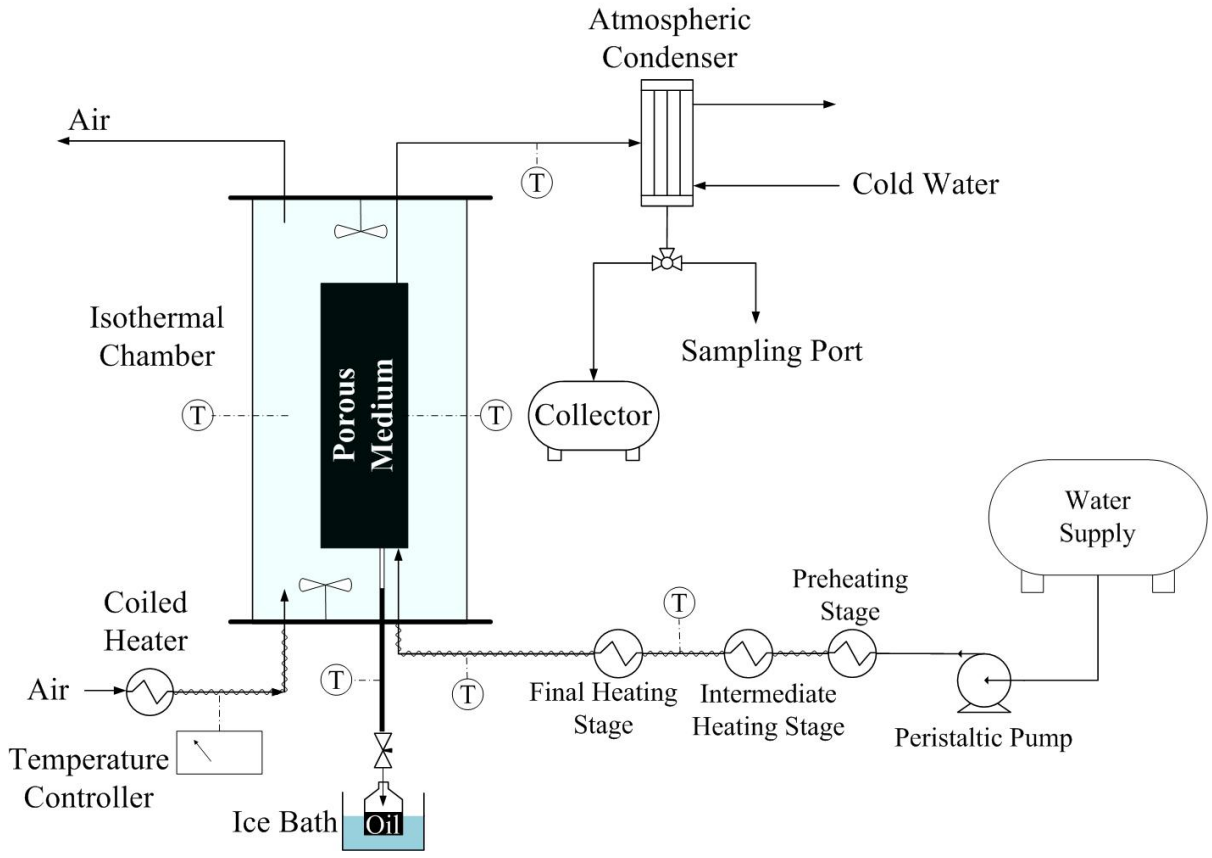

Figure 4.5: Schematic process flow diagram for the SAGD experiments as well as the heat loss experiments using packed physical model at the controlled environmental conditions

In the SAGD experiments, de-aerated de-ionized water was pumped using a peristaltic pump from the water supply through a pre-heating stage (i.e. a 627 W coil heater), intermediate heating stage (i.e. 160 W coil heater), and final heating stage (i.e. a 600 W coil heater) at the steady state heater temperature. The pre- and intermediate-heating stages brought the liquid water close to the saturation temperature. The temperature of the liquid water passing through these two stages was measured using a thermocouple installed into the flow line right after the intermediate heating stage and was collected on a real-time basis using the automated data acquisition unit. The final heating stage provided enough energy for the saturated liquid water to generate superheated steam at the injection side (i.e. lowest position along the height of the perforated gas tube inside the physical model). The three coils in series were used in order to prevent instability in the temperature of the injecting fluid. The temperature of the injected steam at the injection port was measured using a "T" type thermocouple inserted through the perforated gas tube and was collected on a real-time basis using the data acquisition unit. All the steam flow lines were continuously heated to prevent the steam phase being condensed as a result of undesired heat loss during the steam generation and injection process. The steam injection rate, which was controlled by the pumping rate of the cold water from the water supply into the steam generation unit, was adjusted at rates higher than the one that the system could have taken up. As a result, some extra steam was allowed to leave the system from the top of the physical model and to condense in an atmospheric condenser. The condensed steam at the top of the system was collected in a collection vessel and the weight of the water condensate was monitored continuously during the process time. The rate of condensed steam leaving the system from top was used in order to correct the water content of the produced emulsion for the amount of steam which was condensed inside the physical model due to the undesired heat loss to the surrounding environment during the SAGD process. Using this injection scheme, the system was allowed to uptake as much steam as it needed for developing the mobile oil conditions near the bitumen-steam interface in the porous medium. The temperatures of different zones along the height and width of the physical packed model were measured using ten thermocouples inserted into the porous medium, and were collected using the automated data acquisition system. These temperature measurements along with the snapshots taken during the process time helped to monitor the development and lateral expansion of the steam or steam-solvent chamber during the SAGD and SA-SAGD trials respectively.

In these experiments, the produced emulsion was continuously drained out of the model and was collected in a sampling vessel. It was intended to avoid steam breakthrough from the production line during the SAGD process. A needle valve was installed at the production line, and short cut of steam through the production line was prevented by adjusting the position of the needle valve. A certain liquid head of the drained mobile oil was maintained in the production tube above the production valve to avoid the steam phase being produced through the production port. The start-up stage of the SAGD process was initiated by injecting steam into the packed model. Upon mobilization of bitumen in contact with the perforated steam injection tube along the height of the packed model, the lateral spreading phase of the steam chamber was started. The draining mobile oil was allowed to be produced through the production line during the start-up stage of the SAGD process in order to facilitate further lateral encroachment of the steam chamber away from the steam injection line. This procedure allows the bitumen-steam interface to propagate away from the injection tube, hence avoid uncertainties associated with the drainage of the mobile oil close to the wellbore extension. The flow communication between the production end and the line-source injection scheme was eventually accomplished at the end of the start-up phase of the experiment when the mobile oil near the injection line was thoroughly drained. At the end of the start-up stage when the bitumen-steam interface moved 1-2 cm away from the perforated tube, the steady-state drainage phase of the SAGD process was started during which the production rate of the mobile oil was constant throughout the lateral development stage of the steam chamber. It was observed that the production rate of the SAGD process started to fall below that of the steady-state stage of the process when the steam chamber reached the horizontal physical boundaries of the packed model.

In the SA-SAGD experiment, the general flow process diagram was very similar to that of the SAGD trials. The solvent phase (i.e. normal hexane) was pumped using a syringe pump from the solvent container to the injection flow line through a T-section attached just before the pre-heating stage. The liquid mixture was then flowed into the heating stage through which the vapour mixture was formed. The vapour mixture was then passed through the perforated tube along the height of the model. The fluid injection scheme of the SA-SAGD trial was similar to that of the SAGD process in terms of following the free uptake injection strategy. The excess amount of the injected vapour mixture left the model from top to the environmental condenser.

Having followed the noted injection strategy, one can make sure that the model uptakes enough volume of the injecting fluid and the drainage process is governed under the gravity drainage conditions. In addition, this injection strategy ensures the operator that the process is carried out in the absence of pressurizing the model as a result of over-injecting the vapour phase, so the conditions of the gravity-dominated flow are not violated. The production stream control and sampling procedure were similar to that of the SAGD experiments.

4.4.3. Heat Losses to the Surrounding Environment

During the laboratory-scale experimental investigation of heavy oil and bitumen recovery with the aid of thermal recovery methods, energy requirements of each particular recovery process is influenced mainly by the heat losses to the surrounding environment. This energy dissipation, which is originated from the significant temperature gradient between the steady-state operating temperature of the thermal process and that of the surrounding environment, manifests itself in terms of the increased required steam (or solvent or both in the thermal-aided solvent processes of heavy oil recovery) in addition to the amount which is truly needed in order to mobilize the in-situ bitumen under the gravity-stabilized flow conditions.

In the case of the SAGD process using a 2D packed model of porous media, the amount of heat loss to the surrounding environment is proportional to the invaded surface area subject to flow of the high-temperature fluids. As more oil is being recovered from the cross-sectional prototype of porous media, more area is available for the heat losses. As a result, the heat losses increase continuously as a function of the process time for this particular lab-scale study of the SAGD process. In order to control the excessive heat loss to the surrounding environment, the SAGD and SA-SAGD experiments were conducted in the controlled environmental conditions of an isothermally-heated housing. In other words, the available temperature gradient between the steady-state operating temperatures of the SAGD or SA-SAGD processes and that of the surrounding environment was reduced by conducting the experiments in an isothermal housing with constant uniform temperature of 50 °C.

The heat loss experiments were conducted in a similar process flow scheme as that of the SAGD experiments shown in Figure 4.5 except the fact that the porous medium was not saturated with

oil, so the entire porous space was exposed to the steam phase. As a result, the amount of heat loss calculated in the heat loss experiments was the maximum possible heat loss, corresponding to a 100% recovery of the in-situ bitumen. As it was pointed out in sections 4.4.1 and 4.4.2 of this Chapter, 10 similar T-type thermocouples were installed inside the porous medium to measure the real-time temperatures along the height and width of the model. In addition, 5 more thermocouples were installed in different spots of the system to help solving a heat balance over the system. These thermocouples include 5 T-type thermocouples to measure the steam injection temperature in the injection point, temperature of the steam phase leaving the system at the outlet to the atmospheric condenser, liquid condensate temperature, housing temperature, and injecting liquid temperature right after the intermediate heating stage respectively. The inlet flow rate, outlet flow rate, and flow rate of liquid condensate were also measured at the steady-state conditions. These temperature and flow rate measurements enabled us to solve the heat and mass balance for the entire system, and consequently allowed for quantification of the heat loss under pertaining operating conditions. A bourdon pressure gauge was also installed on the porous medium to check the system pressure during the heat loss experiments. Heat loss experiments were performed under different operating modes including housing temperatures of 50° and 60°C, porous medium with and without insulating materials, and also different injection rates of the steam phase. Steam was introduced into the packed model, and model temperature at 10 different measurement spots as well as other noted temperatures were monitored on a real-time basis and were recorded using an automated data acquisition unit. Steam injection process was continued until the model temperature reached the steady state temperature at which all the thermocouples inserted in the porous medium matrix showed a reasonably constant value. At this stage, sampling procedure was performed during which mass of the steam phase entering into the system through the injection spot and also leaving the system via condenser, as well as mass of the liquid condensate produced were measured on a cumulative basis and/or rate basis. The collected data were used in order to calculate the overall heat loss from the packed model into the surrounding environment at the steady state conditions.

Due to the excessive heat loss from the model to the surrounding environment, it was not possible to achieve significant degrees of superheat in the steady-state operating temperature

under the prevailing experimental conditions. Therefore, it was decided to execute the SAGD and SA-SAGD experiments at the operating temperatures close to the system dew point.

4.4.4. Properties of Crude Oil

In this study, Athabasca bitumen was used as the crude oil. The viscosity – temperature relationship of bitumen was measured by Hatch Ltd (2009) using Physica Modular Compact Rheometers (Anton Paar), and is shown in Figure 4.6. The Athabasca bitumen viscosity was correlated reasonably to temperature within the range of the experimental data using the following exponential relationship:

$$\mu = 34{,}051{,}153.686e^{-0.1632T} \tag{4.1}$$

in which "μ" is oil viscosity in cP and "T" is temperature in °C.

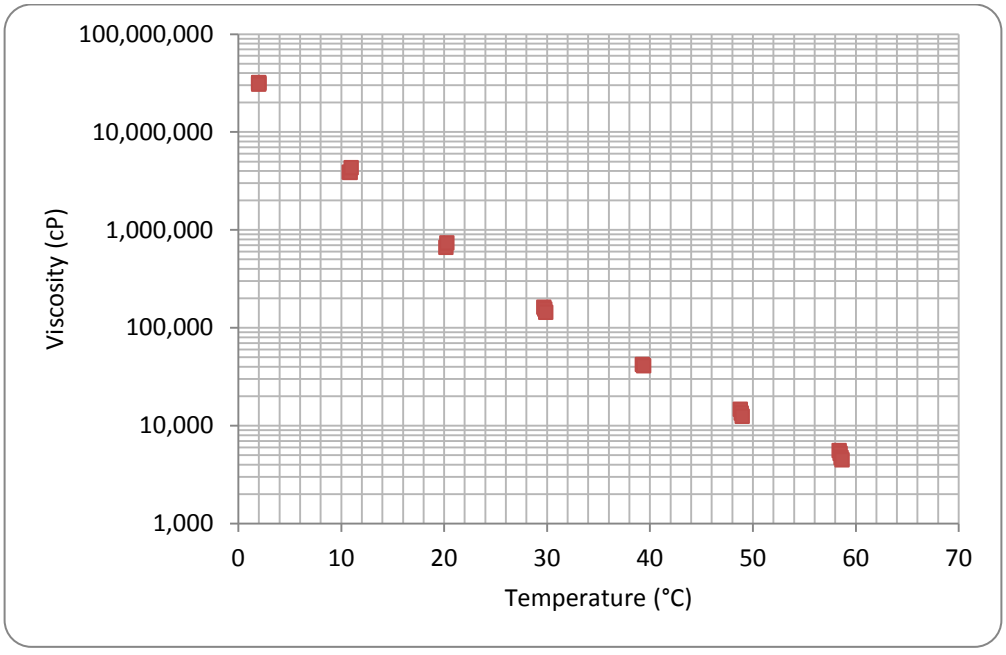

Figure 4.6: Viscosity – Temperature relationship for Athabasca bitumen

4.5. Experimental Results and Discussion

4.5.1. Analysis of the Heat Loss

As it was mentioned in section 4.4.3, different operating modes were considered to calculate the amount of heat loss from the model to the surrounding environment. The heat loss was calculated using the steam temperatures at the inlet and outlet spots, condensate temperature, average steam temperature in the model, and associated flow rates at the corresponding flow streams along the flow circulation system. Figure 4.7 schematically shows the energy and mass flow across the system boundaries.

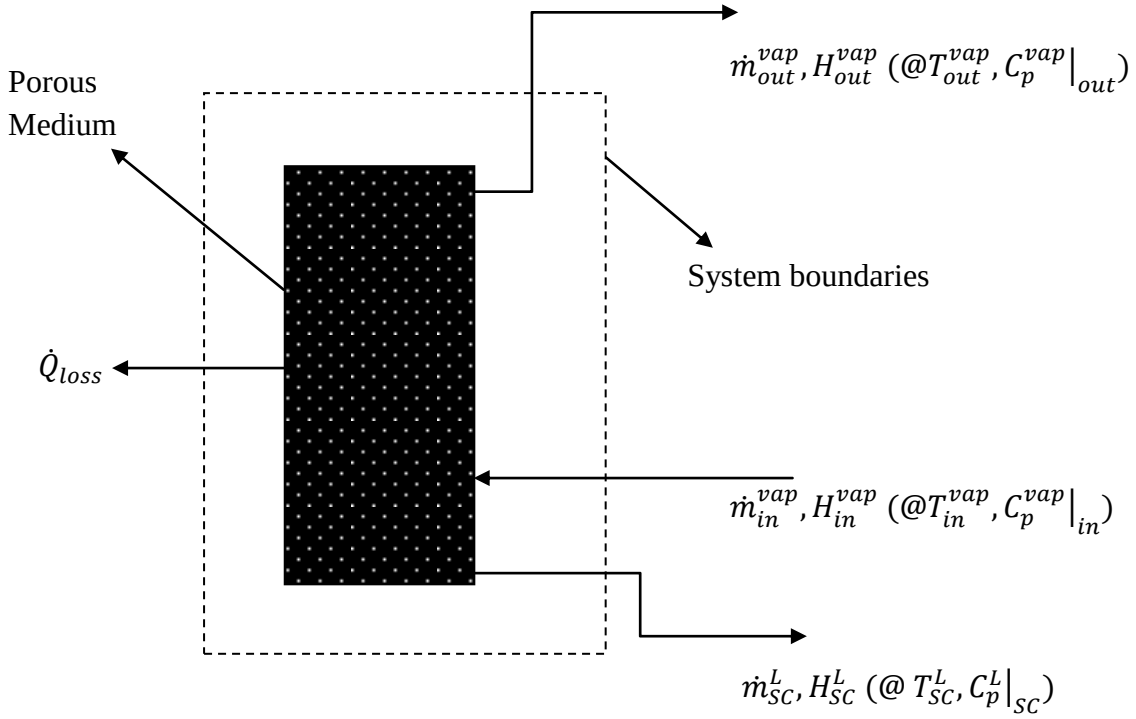

Figure 4.7: Energy and mass flow across the system boundaries during the heat loss experiments

The overall heat loss from the system can be defined as:

$$\dot{Q}_{Loss} = H_{in} - H_{out} \tag{4.2}$$

in which $\dot{Q}_{Loss}$ is the total heat loss from the model to the surrounding environment, and H_{in} and H_{out} are the input and output enthalpies and are defined as:

$$H_{in} = \dot{m}_{in}^{vap}\left(H_{in}^{vap} - H_{ref}^{vap}\right) \tag{4.3}$$

$$H_{out} = \dot{m}_{out}^{vap}\left(H_{out}^{vap} - H_{ref}^{vap}\right) + \dot{m}_{SC}^{L}(H_{SC}^{L} - H_{ref}^{vap}) \tag{4.4}$$

In Equations 4.3 and 4.4, H_{in}^{vap}, H_{out}^{vap}, H_{SC}^{L}, and H_{ref}^{vap} are the enthalpies associated with the inlet and outlet vapour phase at the corresponding temperatures, enthalpy of the sub-cooled liquid condensate phase, and an arbitrary reference-state vapour phase enthalpy respectively. In addition, $\dot{m}_{in}^{vap}$, $\dot{m}_{out}^{vap}$, and $\dot{m}_{SC}^{L}$ are the mass flow rates of inlet and outlet vapour phase and that of the sub-cooled liquid condensate phase respectively.

A simple mass balance across the system boundaries would result in:

$$\dot{m}_{in}^{vap} = \dot{m}_{out}^{vap} + \dot{m}_{SC}^{L} \tag{4.5}$$

Combining Eq.'s 4.2 to 4.5, one can obtain the generalized overall heat loss equation for the system shown in Figure 4.7 as:

$$\dot{Q}_{Loss} = \dot{m}_{out}^{vap}\,\overline{c_p^{vap}}\left(T_{in}^{vap} - T_{out}^{vap}\right) + \dot{m}_{SC}^{L}\,\overline{c_p^{vap}}\left(T_{in}^{vap} - T_{sat}^{vap}\right) + \dot{m}_{SC}^{L}\overline{c_p^{L}}(T_{sat}^{L} - T_{SC}^{L}) + \dot{m}_{SC}^{L}\lambda \tag{4.6}$$

in which λ is the enthalpy of condensation at the operating pressure condition, T_{sat}^{vap} and T_{sat}^{L} are the vapour and liquid saturation temperatures respectively, and the average specific heat capacity values are defined based on the associated stream temperatures.

If the values of the specific heat capacities at the corresponding stream temperatures are close to each other, the average specific heat capacity could be determined by linear regression analysis

and arithmetic averaging of the associated specific heat capacity values; otherwise, the average specific heat capacity would be calculated by plotting the c_p values at the temperature interval of interest and calculating the area under the c_p–T curve using trapezoidal rule. If the former case is followed, Eq 4.6 would be simplified in the form of:

$$\dot{Q}_{Loss} = \dot{m}_{out}^{vap}\left(\frac{c_p^{vap}|_{in}+c_p^{vap}|_{out}}{2}\right)\left(T_{in}^{vap}-T_{out}^{vap}\right)+\dot{m}_{SC}^{L}\left(\frac{c_p^{vap}|_{in}+c_p^{vap}|_{sat}}{2}\right)\left(T_{in}^{vap}-T_{sat}^{vap}\right)+\dot{m}_{SC}^{L}\left(\frac{c_p^{L}|_{sat}+c_p^{L}|_{SC}}{2}\right)\left(T_{sat}^{L}-T_{SC}^{L}\right)+\dot{m}_{SC}^{L}\lambda \quad (4.7)$$

Seven different heat loss experiments were performed in order to study the effect of different variables such as housing temperature, presence of an external insulation coating material on the surface of the packed model, and steam injection flow rate on the magnitude of the overall heat loss from the model to the surrounding environment. It was tried to execute all these heat loss experiments under relatively constant steam injection temperature. This will enable us to quantify the effect of different variables on the overall heat loss in the absence of any significant injection temperature variability.

Figure 4.8 presents the real-time temperature measurement along the surface of the packed model for RUN number 2 of the heat loss experiments. It is evident that the thermocouples embedded inside the matrix of the packed porous medium became exposed to steam temperature based on their proximity to the line-source injection tube extended along the height of the packed model. It is noteworthy that the temperature controller was successfully capable of maintaining a constant temperature with minimum level of fluctuation inside the housing during all the heat loss experiments. In order to measure the steam inlet and outlet flow rates as well as the liquid condensate production rate, a sampling procedure was performed on an instantaneous and/or cumulative basis when all the thermocouples showed the steady state steam temperature (i.e. after about 21,800 seconds for RUN number 2 as indicated in Figure 4.8).

In Table 4.1, the general information and results regarding the heat loss experiments conducted in this study are presented. According to this Table, the experimental variables include housing temperature, presence of insulating materials for the packed model, and steam injection rate.

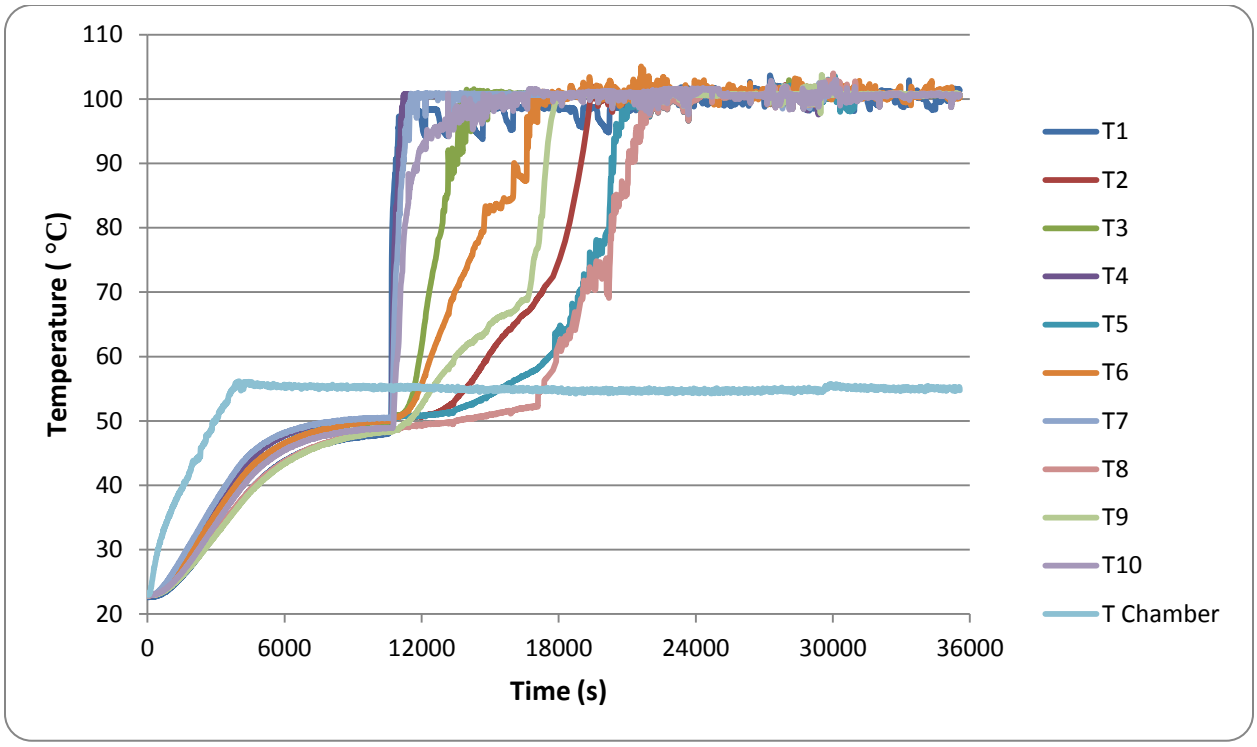

Figure 4.8: Real-time temperature measurement for RUN number 2 of the heat loss experiments

Table 4.1: Summary of the heat loss experiments

Run No	Average operating temperature (°C)	Insulation	Chamber Temperature (°C)	Steam Injection Rate (g/min, CWE)	Heat Loss (W)
1	102.70	NO	50	7.43	165.91
2	103.04	NO	55	7.43	152.10
3	100.34	YES	50	5.36	126.03
4	100.25	YES	50	7.20	138.47
5	100.34	YES	60	5.30	112.12
6	100.21	YES	60	7.30	123.65
7	100.22	YES	60	8.30	127.36

RUN numbers 1 and 2 were conducted with no insulating materials at two different housing temperatures of 50 and 55 °C respectively under relatively similar steam injection temperatures. RUN numbers 3 and 4 were performed under similar conditions of insulation, housing and steam injection temperatures, but at two different steam injection rates of 5.36 and 7.20 g/min, Cold Water Equivalent (CWE) respectively. Run numbers 5, 6, and 7 were carried out at similar

conditions of insulation and steam injection temperature, and at elevated housing temperature of 60 °C, but different steam injection rates of 5.30, 7.30, and 8.30 g/min, CWE respectively. As it is indicated in this Table, the overall heat loss from the model decreased moderately by increasing the housing temperature. Comparing RUN numbers 1 and 2, it is observed that only a 5 °C increase in the housing temperature resulted in about 9% decrease in the total heat loss. The effect of housing temperature on the total heat loss can also be observed by comparing RUN numbers 3 and 5 in which all the other experimental variables remained reasonably unchanged except the housing temperature. It is evident that a 10 °C increase in the housing temperature resulted in about 13% decrease in the overall heat loss. The same trend can also be observed comparing RUN numbers 4 and 6 in which a 12% decrease in the overall heat loss was achieved by 10 °C increase in the housing temperature.

In addition to the isothermal housing, Pyrogel® XT insulation materials attached to wooden cover frames were used to shield the back and side surfaces of the packed model in order to reduce the amount of heat loss to the surrounding environment. One can figure out the effectiveness of the insulating material using the data presented in Table 4.1. Comparing trials 4 and 1 (with and without insulation) reveals that presence of insulating materials reduced the total heat loss by about 20%. One may argue that other inconsistencies in the steam injection temperature and flow rate among these two trials might lead to an overestimation regarding the effectiveness of the insulating materials in reducing the overall heat loss. It is noteworthy to mention that no matter how much degrees of superheat would be attained at the injection spot, the model temperature at the steady state conditions would be very close to the dew point temperature of the gaseous phase (i.e. steam) at the atmospheric operating pressure due to the huge surface area available for the heat loss under prevailing operational conditions. As it will be described in the next paragraph, the injection flow rate of steam would not have a significant effect on the overall heat loss from the system under specific operating conditions of open-flow free-uptake steam injection at atmospheric pressure. Trial 6 can also be reasonably compared against RUN number 2 to figure out the combined effect of higher housing temperature (i.e. in the order of 5 °C) and presence of the insulation materials on the overall heat loss. It is evident that the total heat loss was reduced by about 23% as a result of these two heat loss prevention techniques.

Attempts were also made in order to investigate the effect of steam injection rate on the total amount of heat loss from the system under described experimental conditions. As the system is under atmospheric conditions in the absence of gas phase accumulation and pressurizing, increasing the injection flow rate would mainly manifest itself in the form of a subsequent increase in the rate of steam leaving the system from top to the condenser; thus remains the liquid condensate production rate to be reasonably constant. With a quick look over Eq. 4.7, it is clear that the overall heat loss would not be significantly increased by an increase in the steam injection flow rate under specific operational conditions described earlier. In fact, the production rate of the liquid condensate significantly affects the overall heat loss term as it is the parameter that is being multiplied by the enthalpy of condensation of steam which is the most significant term in magnitude in Eq. 4.7. Any minor error in measuring the liquid condensate production rate even to the extent of a few droplets would considerably affect the heat loss calculations. By comparing RUN numbers 3 and 4, it is evident that the heat loss was only increased by about 10% following a 35% increase in the steam injection rate. In addition, similar comparison can be made considering RUN numbers 5, 6, and 7 in which increasing the steam injection rate by 38% (RUN numbers 5 and 6) and 57% (RUN numbers 5 and 7) resulted in an increase in the overall heat loss by only 10% and 13.6% respectively. Overall, the effect of steam injection rate variation on the total heat loss to the surrounding environment seems not to be a major one under pertaining operational conditions.

4.5.2. The SAGD Process at the Macro-Scale

It was decided to demonstrate the performance of the SAGD process at the macro-scale at constant levels of oil type and steam temperature. Two different SAGD trials were conducted at two different permeability levels with the aid of packing the physical model with BT2 glass beads (i.e. 830 D) or BT3 glass beads (220 D). In addition, two associated replicates were also performed in order to make sure of the repeatability of the process.

4.5.2.1. Production Characteristics of the SAGD Experiments: Mobile Oil Production Rate

Four SAGD experiments (two different trials with 2 associated replicates) were carried out in this phase of the study. In each SAGD experiment, the model was allowed to reach the

isothermal chamber temperature before steam injection is started. The sampling procedure was started when the steam-oil interface moved about 1.5-2 cm away from the line-source injection tube to minimize the near wellbore drainage issues as well as to avoid disturbing the drainage phenomenon of the mobile oil by continuous flow of steam inside the perforated tube. During this production stage which is called the steady state mode of the mobile oil production, it is observed that the production rate remains fairly constant. This stage of production contributes significantly to the overall production of a particular SAGD experiment at the lab-scale. The term "mobile oil" is defined as the volume of the draining oil plus the enclosed droplets of water condensate leaving the model through the production line. The mobile oil samples were collected in individual containers at the pre-determined time intervals and weighed right after being sampled. All samples of the mobile oil were placed in a convection oven for 3 days at elevated temperature of 85-90 °C in order to vaporize all the water content of the samples. The oil remained inside each particular container after being heated is called the equivalent dead oil of that particular sampling duration. Some samples of oil were being taken at the beginning of each experiment directly from the saturation vessel, and were called virgin oil samples. These samples were placed inside the convection oven along with the samples of the mobile oil taken during the experiment for the same period of time. The purpose of having virgin oil samples is to figure out how much of the lighter components of the produced oil is being vaporized during the drying procedure of the mobile oil. It was found that about 8% by weigh of the lighter components of the virgin oil are being vaporized as a result of the drying process inside the convection oven. As a result, mass of the dead oil as well as mass of the water content of each particular sample were corrected to account for the lighter components of the produced oil which were vaporized during the drying process of the mobile oil.

The measured values of the instantaneous mobile oil production rates were transformed into a cumulative basis. Figure 4.9 presents the cumulative mobile oil production plot of the two SAGD trials as well as the corresponding replicates. It is observed that there is a very good linear correlation between the cumulative weigh of the produced mobile oil and the sampling time over the course of all these experiments. This strong linear correlation reveals the fact that the mobile oil production rate remains reasonably constant during the course of the SAGD experiment. It is also observed that there is a very good consistency between the original SAGD trials and the

corresponding replicates proving the reproducibility of the measured experimental data. All the data points were checked against the lab notes collected during the course of each single experiment to ensure that all of them are being supported with appropriate physical rationale. The average mobile oil production rates can be obtained using the slopes of the linear correlations fitted on the experimental data as it is presented in Figure 4.9.

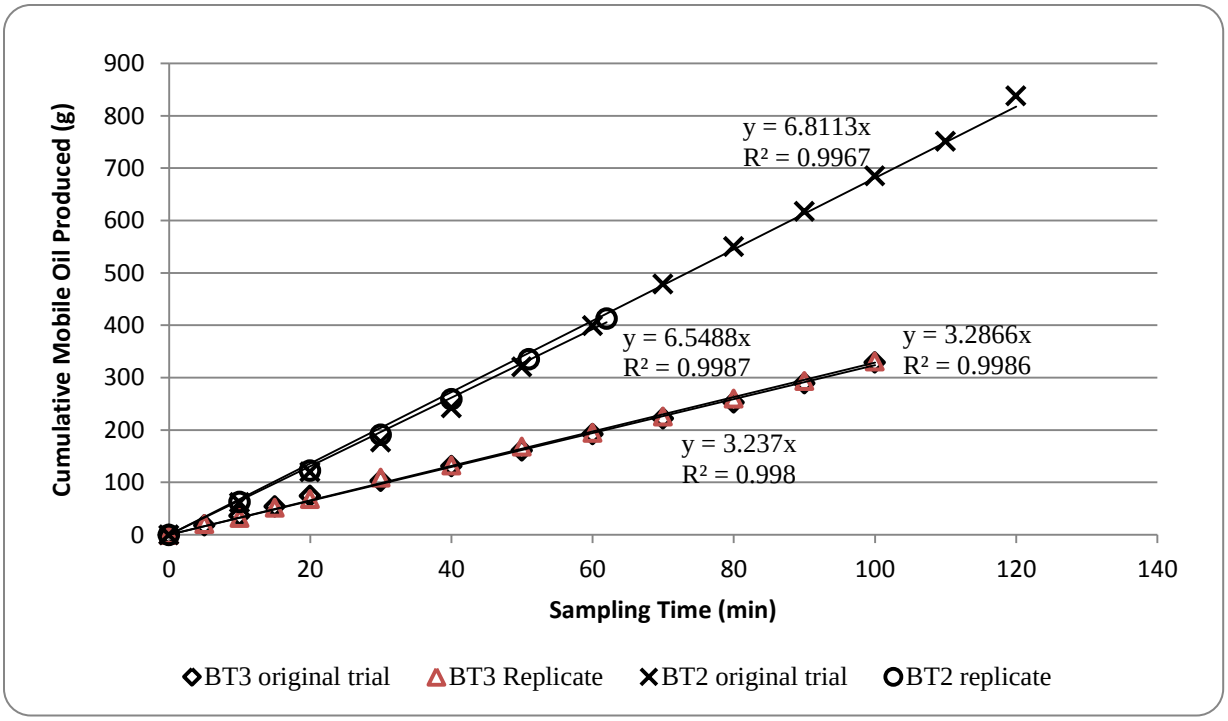

Figure 4.9: Cumulative mobile oil production versus sampling time in the SAGD experiments conducted using two different permeability levels of BT2 and BT3

According to the data presented in Figure 4.9, the average mobile oil production rate of the original SAGD trial in BT2 medium is 6.81 g/min (i.e. 3.58 g/min.cm of the model thickness) which was reproduced with reasonable accuracy to be 6.55 g/min (i.e. 3.44 g/min.cm of the model thickness). As a result, the average mobile oil production rate of the SAGD process in BT2 medium is about 6.68 ± 0.01 g/min based on these two trials under pertaining experimental conditions. In addition, the original SAGD trial in BT3 medium achieved an average mobile oil production rate of 3.24 g/min (i.e. 1.70 g/min.cm of the model thickness) which was repeated with very good accuracy in the associated replicate trial to be 3.29 g/min (i.e. 1.73 g/min.cm of the model thickness). Therefore, the average mobile oil production rate of the SAGD process in

the BT3 matrix based on these two trials is about 3.26 ± 0.00 g/min within the experimental conditions. Comparing the mobile oil production rates of the SAGD process with the rate of the live oil production using the VAPEX process reveals the superiority of the SAGD process with respect to the VAPEX method from the production rate point of view. A recent study was conducted in our porous media lab about the applicability of the VAPEX and Warm VAPEX processes to recover heavy oil and bitumen (Rezaei, 2010). In this study, the production characteristics of the VAPEX and Warm VAPEX processes were studied at different levels of oil type and permeability of the porous medium. Table 4.2 summarizes the highest live oil production rates achieved under the VAPEX and Warm VAPEX processes at the optimum operating temperature. In addition, a summary of the mobile oil production rates of the current SAGD processes are presented for the purpose of comparison.

The mobile oil production rates presented for the SAGD trials are the average values extracted from Figure 4.9. The correlation presented for Athabasca bitumen viscosity – temperature relationship in section 4.4.4 works reasonably good for the provided temperature range of the experimental data measured by Hatch ltd. However, it is not suitable for extrapolating the bitumen viscosity – temperature relationship beyond the range of the viscosity – temperature experimental data. In order to estimate the viscosity of Athabasca bitumen in the desired temperature range, the Mehrotra and Svrcek correlation on the viscosity – temperature relationship of Athabasca bitumen was used as follows:

$$\ln \ln \mu = A + B\ lnT \tag{4.8}$$

in which A = 22.8515, B = -3.5784, "μ" is in cP and "T" is in K.

According to the data presented in Table 4.2, it is evident that at the higher permeability level (i.e. first and forth rows of the Table), the SAGD process is capable of producing mobile oil to the extent of about 5.9 times that of the live oil produced under the Warm VAPEX process. The superior performance of the SAGD process is even more highlighted considering the fact that for the above-mentioned experiments, the in-situ viscosity of Athabasca bitumen at the operating conditions of the corresponding SAGD trial is about 31 times that of the draining live oil in the Warm VAPEX experiment. It is worthwhile to note that when the in-situ viscosities of the oil

phases in these two experiments were compared to each other, the effect of viscosity gain of the mobile oil in the SAGD process because of the in-situ emulsification was not taken into consideration. If one would like to adjust the viscosity of the mobile oil in the SAGD experiment based on the operating temperature as well as presence of dispersed water droplets in the mobile oil rather than just considering the viscosity of Athabasca bitumen at the elevated SAGD operating temperature, the in-situ viscosity of the mobile oil corresponding to the SAGD experiment would have been much more than the value presented in Table 4.2 (i.e. 184.50 cP). The production characteristics of the SAGD experiment at higher permeability level can also be compared against that of the Warm VAPEX experiment in which Lloydminster heavy oil blend was used as the oil type (i.e. rows 4 and 2 in Table 4.2 respectively). Although the in-situ oil viscosity in the SAGD experiment is about 81 times more than that of the live oil in the corresponding Warm VAPEX trial, it is evident that the SAGD process was able to produce mobile oil to the extent of about 4.5 times that of the live oil produced in the corresponding Warm VAPEX experiment. As it was discussed earlier, the viscosity gain of the in-situ mobile oil in the SAGD experiment due to the enclosure of the water condensate droplets was not considered in the comparison made between the performances of these two recovery processes; otherwise, the superiority of the SAGD process over the Warm VAPEX process from the mobile oil production characteristics point of view would have been more elucidated.

Table 4.2: Live/mobile oil production rate data for the Warm VAPEX and SAGD trials

Recovery Process	K (D)	Oil type	μ (cP)	Live/mobile oil production rate per unit thickness of the porous medium (g/min.cm)	Solvent content of the live oil (%)
Warm VAPEX at 43.1 °C*	830	CL B**	5.92	0.598	36.50
Warm VAPEX at 43.3 °C*	830	L HO§	2.28	0.775	33.95
Warm VAPEX at 43.1 °C*	220	CL B**	6.26	0.366	35.84
SAGD at 100.86 °C	830	A B‡	184.50	3.510	NA
SAGD at 101.26 °C	220	A B	180.86	1.715	NA

*: extracted from Rezaei, 2010
**: Cold Lake bitumen
§: Lloydminster heavy oil blend
‡: Athabasca bitumen

According to our experimental results, it is evident that the SAGD process at the lower permeability level was also much more profitable compared to the VAPEX and Warm VAPEX processes from the in-situ oil mobilization and drainage point of view. Comparing the data presented in the third and fifth rows of Table 4.2, it is evident that the SAGD process was able to produce mobile oil to the extent of about 4.7 times that of the live oil produced under the optimum producing conditions of the Warm VAPEX process. Turning a blind eye on the viscosity gain process of the Athabasca bitumen due to the in-situ emulsification of water condensate droplets in the continuum of the mobile oil, the enhanced productivity of the SAGD process would be more highlighted considering the fact that the draining mobile oil in the SAGD experiment was about 29 times more viscous than that of the live oil draining under the corresponding Warm VAPEX process.

The above quantitative comparison between the production performances of the SAGD and Warm VAPEX experiments were conducted assuming that all other experimental variables remain unchanged between the corresponding trials. In order to make sure that this quantitative comparison is performed in a systematic manner, one has to make sure that there is no other contributing parameter adversely affecting the comparison common ground. The first parameter which should be watched out is the height of the porous medium which is 56.83 and 41.91 cm for the SAGD and Warm VAPEX trials respectively. Assuming there was no subsidence happened during each of these two particular tests and the entire height of the porous media was subject to the drainage process during the sideways propagation stage of the steam and/or vapour chamber, the mobile oil production rate of the SAGD experiment should be adjusted for this drainage height difference as this experiment took advantage of a taller pay zone compared to that of the Warm VAPEX process. The other parameter that could negatively affect the production characteristics comparison procedure presented earlier between the SAGD and Warm VAPEX experiments is the in-situ density of the draining oil. Unfortunately, it was not feasible to measure the in-situ oil density at the operating conditions for both of these two sets of the experiments. The in-situ density of the draining live oil under the Warm VAPEX process could have been calculated with reasonable accuracy using the density of normal pentane and cold Lake bitumen at the corresponding operating temperature with the aid of appropriate mixing rules. The density-temperature relationship of Athabasca bitumen is not available. In the absence

of the density data associated with the draining oil phase in these two sets of experiments, it is not feasible to quantify the extent to which the draining oil density could affect the presented comparison methodology regarding the production performances of the SAGD and Warm VAPEX processes.

As far as the effect of permeability of the porous medium on the production characteristics of the mobile oil in the SAGD experiments is concerned, one can use the data presented in Figure 4.9 in the form of the average mobile oil production rate for each particular SAGD experiment at different permeability levels. According to the theory of gravity drainage and its application to the heavy oil recovery using the SAGD process, the mobile oil production rate is a sole function of the square root of permeability of the porous medium when all other experimental variables remain unchanged. It is evident that this is valid for the case of our SAGD experiments in which the ratio of the average production rate of the SAGD trial in the higher permeability medium over that of the lower permeability medium is about 2.048 and the square root of the corresponding permeability ratio is about 1.942 as well. As it is demonstrated in Figure 4.10, there is a very good linear correlation between the mobile oil production rates of both of the SAGD trials and their corresponding replicates and the square root of the model permeability.

4.5.2.2. Production Characteristics of the SAGD Experiments: Dead Oil Production Rate

As it was pointed out previously, the mobile oil samples collected during the course of the SAGD experiments were weighed right after being collected and then placed in a convection oven for at least 3 days at elevated temperature of 85-90 °C in order to vaporize all the water content of the produced emulsion. The dead oil samples were then weighed after being dried and the produced dead oil weighs were converted into a cumulative basis. The weight of the dead oil samples were corrected for the amount of the lighter components of oil which were vaporized in the convection oven during the drying process of the produced emulsions.

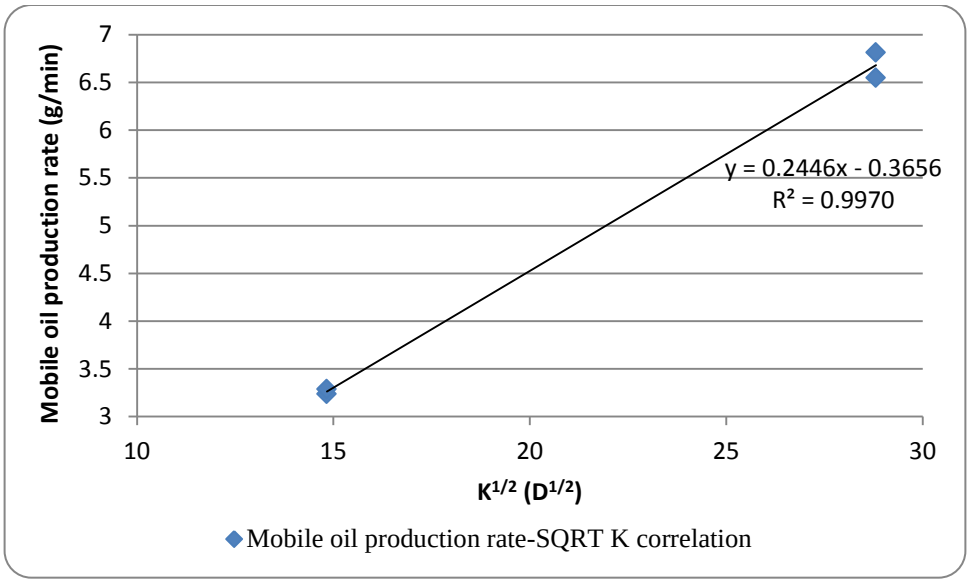

Figure 4.10: Correlation between the mobile oil production rates of the SAGD experiments and the square root of the porous media permeability

Figure 4.11 presents the cumulative plot of the dead oil produced during the course of the two SAGD experiments at different permeability levels along with their associated replicate trials. As it is demonstrated in this Figure, there is a very good linear correlation between the cumulative dead oil production and the sampling time for all the SAGD experiments and their associated trials. It can be concluded that the dead oil production rate for each particular SAGD trial remains reasonably constant during the course of the experiment. In addition, it is observed that there is a very good agreement between each particular SAGD experiment and the associated replicate trial proving the reproducibility of the collected experimental data. For each particular SAGD experiment, the average dead oil production rate can be obtained using the slope of the linear correlations fitted on the experimental data in Figure 4.11.

Table 4.3 contains a summary of the dead oil production rates for our SAGD trials as well those of the Warm VAPEX experiments extracted from Rezaei, 2010. As it was mentioned previously, the selected Warm VAPEX processes in Table 4.3 are the optimum trials with the highest production rates among all other conducted VAPEX experiments at different operating temperatures. The best VAPEX trials from the production characteristics point of view were selected here in order to highlight the superiority of the SAGD process over the optimum

modification of the VAPEX process. As far as the dead oil production rate is concerned, it is obvious that the SAGD process performs much better compared to the Warm VAPEX process.

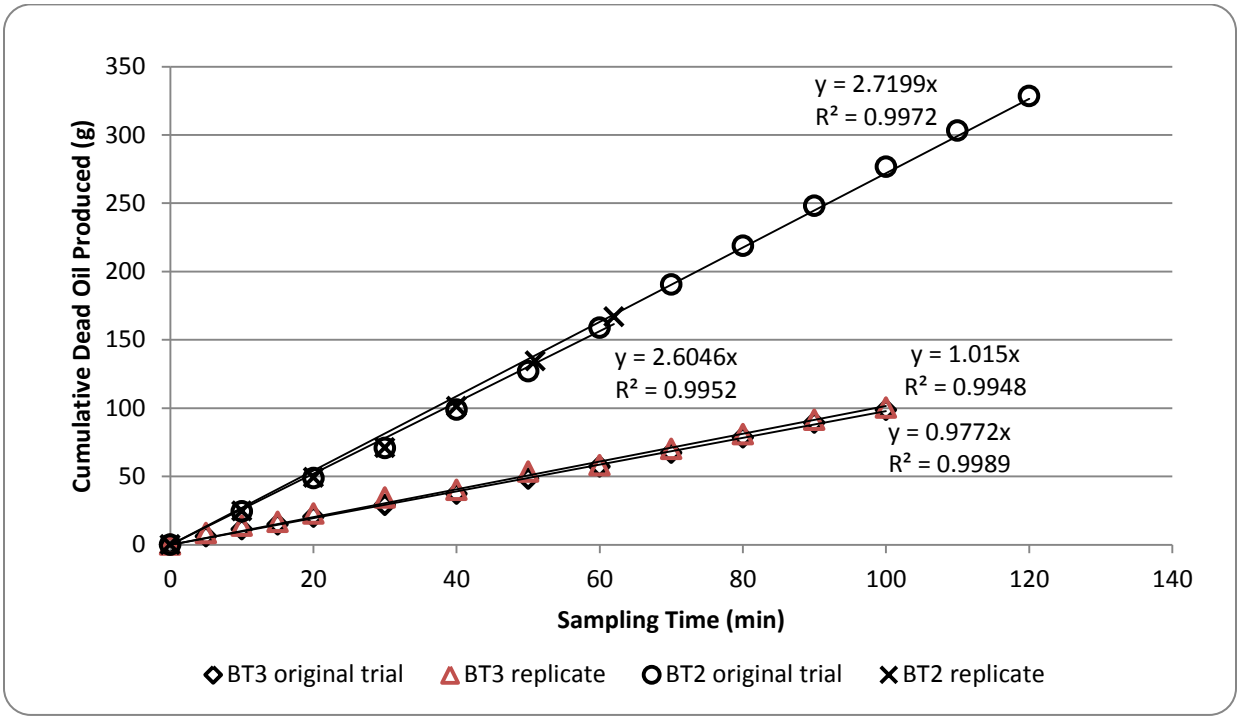

Figure 4.11: Cumulative dead oil production versus the sampling time for the SAGD experiments at two permeability levels of BT2 and BT3

Table 4.3: Dead oil production rate data for the Warm VAPEX and SAGD trials

Recovery Process	K (D)	Oil type	Dead oil production rate per unit thickness of the porous medium (g/min.cm)	Average dead oil production rate (g/min)
Warm VAPEX at 43.1 °C*	830	CL B**	0.387	NA
Warm VAPEX at 43.0 °C*	830	L HO§	0.477	NA
Warm VAPEX at 43.1 °C*	220	CL B**	0.228	NA
Warm VAPEX at 43.1 °C*	220	L HO§	0.282	NA
SAGD at 100.86 °C	830	A B‡	1.398	2.662 ± 0.004
SAGD at 101.26 °C	220	A B‡	0.523	0.994 ± 0.001

*: extracted from Rezaei, 2010
**: Cold Lake bitumen
§: Lloydminster heavy oil blend
‡: Athabasca bitumen

According to the data provided in Table 4.3, it is obvious that the SAGD process at the lower level of permeability is capable of producing dead oil with a rate to the extent of about 2.3 times more than that of the Warm VAPEX process when Cold Lake bitumen was used as the oil type (rows 6 and 3 of Table 4.3 respectively). This ratio was decreased to 1.9 when Lloydminster heavy oil blend was considered as the oil type for the Warm VAPEX experiment (i.e. rows 6 and 4 of Table 4.3 respectively). The enhanced production performance of the SAGD process compared to that of the Warm VAPEX could even be more highlighted considering the dead oil production data at the higher permeability level of the porous medium. At higher permeability level, it is evident that the SAGD process produces dead oil with a production rate to the extent of about 3.6 and 2.9 times those of the Warm VAPEX process when Cold Lake bitumen and Lloydminster heavy oil blend were used as the oil type in the Warm VAPEX experiments respectively.

As far as the effect of permeability of the porous medium on the dead oil production rate of the SAGD process is concerned, it is evident that the higher the permeability is, the higher would be the average dead oil production rate when all the other experimental variables remain unchanged.

Figures 4.12 and 4.13 display how the instantaneous dead oil production rate of the SAGD process per unit thickness of the porous medium at two different permeability levels behaves as a function of the sampling time as well as the sample number respectively. As it is evident in these two figures, the instantaneous production rates of the dead oil for these two trials do not vary significantly over the process time or from sample to sample. This is another indication of the fact that the oil production rate of the SAGD process would be reasonably constant during the spreading phase of the steam chamber, so an average value of the oil production rate could be assigned to any particular SAGD process during the steady state stage of the drainage process.

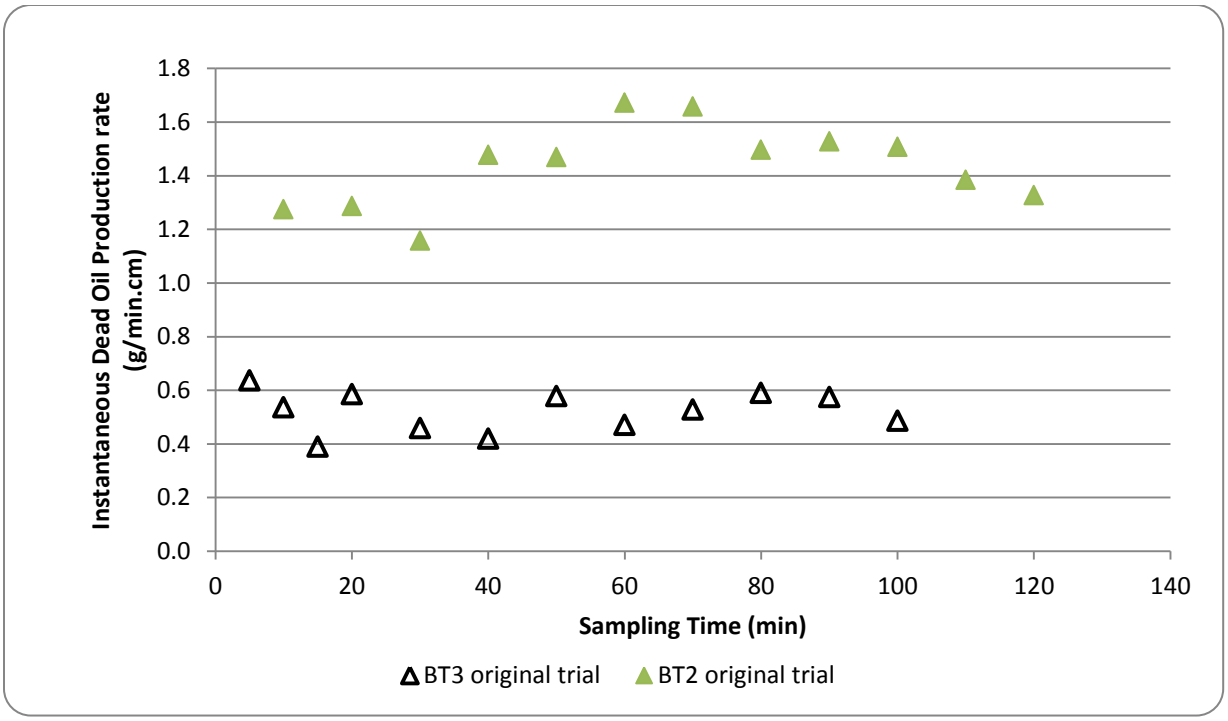

Figure 4.12: Instantaneous dead oil production rate of the SAGD process per unit thickness of the porous medium as a function of the sampling time at two different permeability levels

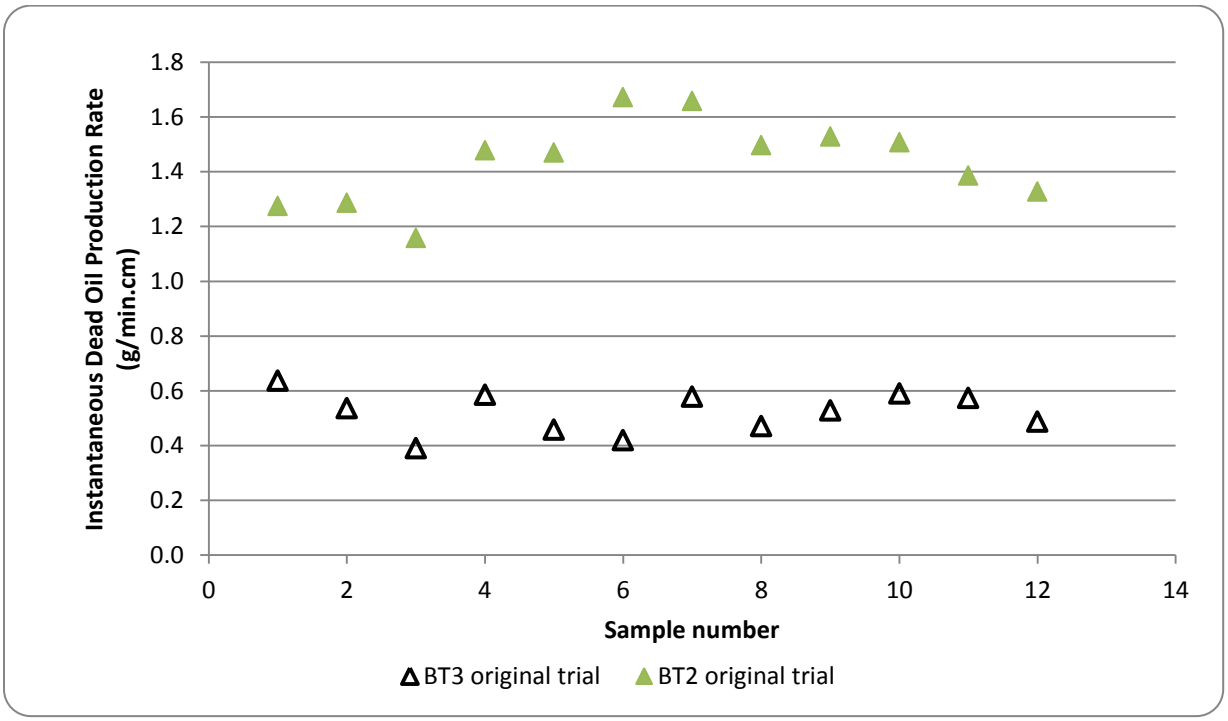

Figure 4.13: Instantaneous dead oil production rate of the SAGD process per unit thickness of the porous medium as a function of the sample number at two different permeability levels

4.5.2.3. Production Characteristics of the SAGD Experiments: Water Content of the Produced Mobile Oil

As it is stated previously, the mobile oil samples collected during the course of the SAGD experiments were placed inside a convection oven at 85-90 °C for at least 3 days in order to vaporize the water content of the mobile oil. The water content of the mobile oil was then corrected accounting for the lighter fractions of the oil phase that were being evaporated during the drying process of the mobile oil. Mass of the water content of the produced mobile oil during the course of the SAGD trials was transformed into the cumulative basis and is presented in Figure 4.14. As it is evident in this Figure, there is a very good linear correlation between the cumulative weigh of the water content of the produced mobile oil and the sampling time for all the SAGD trials. In addition, there is a very good agreement between the water production data associated with the original trials and the replicates showing that the data collected during the course of the SAGD experiments are reproducible.

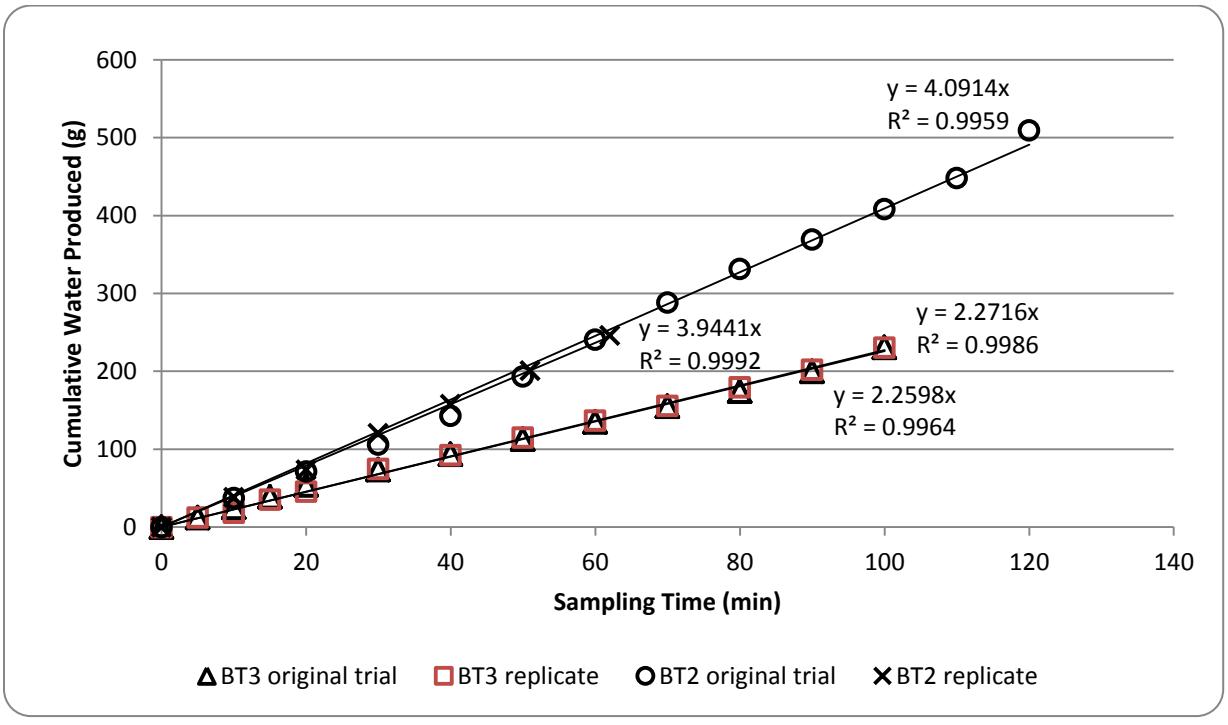

Figure 4.14: Cumulative water produced along with the oil phase versus the sampling time in the SAGD experiments at two permeability levels of BT2 and BT3

Focusing on the linear correlation between the cumulative water produced and the sampling time, one may conclude that the average rate of the water production in each particular SAGD process could be delineated as the slope of the straights lines fitted to the experimental data presented in Figure 4.14. It is worthwhile to note that the water content of the produced mobile oil is not in the form of free continuous water phase, but instead is in the form of very small water droplets emulsified in the continuum of the mobile oil. More details on the state of the produced emulsion from the microscopic point of view is discussed later in this Chapter.

As far as the effect of permeability on the amount of the produced water along with the oil phase in the form of the mobile oil is concerned, it is evident that the higher the permeability of the porous medium is, the higher would be the amount of water content of the produced mobile oil. However, this is not the property of interest as far as the energy consumption of the SAGD process is concerned. Increasing the permeability of the porous medium results in increasing both the dead oil and mobile oil production rates as well as the water content of the produced mobile oil. Here, the weight basis Steam to Oil Ratio (SOR) for each particular SAGD process is defined as the parameter that describes the energy requirements of the SAGD process. This parameter is calculated based on the information regarding the cumulative steam uptake of the model during each particular experiment in terms of the Cold Water Equivalent and the cumulative dead oil production data. Along with the production characteristics of any particular steam-based heavy oil recovery technique, the SOR value determines the feasibility of the recovery process from the technical and economical points of view.

The net cumulative value of SOR for the original SAGD tests performed in BT2 and BT3 permeability levels are calculated to be 1.584 and 2.463 wt/wt respectively. Based on the replicate trials, the average values of SOR were found to be 1.540 and 2.641 wt/wt for the BT2 and BT3 permeability levels respectively. There is a good agreement between the calculated SOR values obtained for the original and replicate SAGD trials. Moreover, one can figure out the effect of porous medium permeability on the average value of SOR for the SAGD process under prevailing experimental conditions. Figure 4.15 presents the linear correlation between the average SOR values of the SAGD trials and the square root of the porous media permeability. It

is observed that for a particular SAGD experiment, SOR is inversely proportional to the square root of permeability when all other experimental variables remain constant.

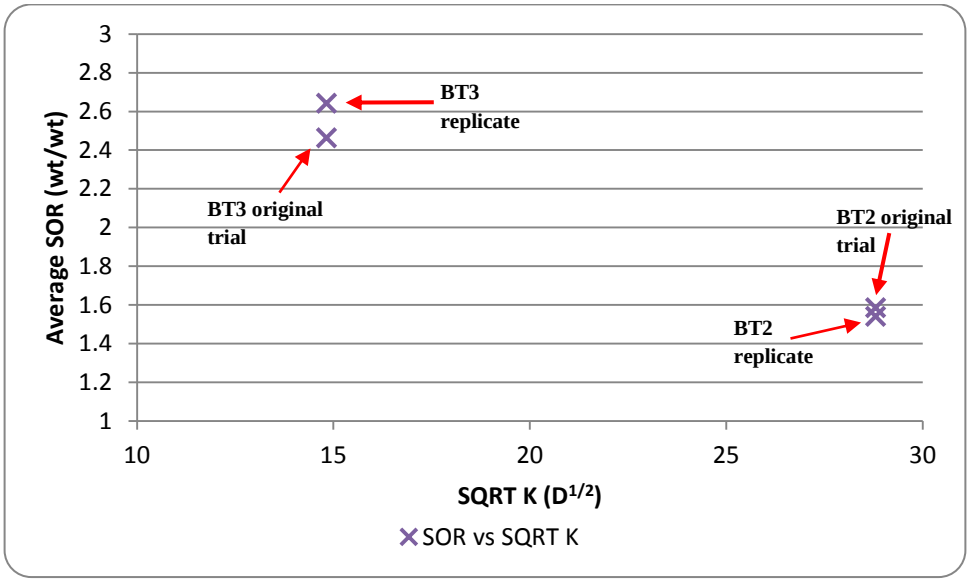

Figure 4.15: Correlation between the average values of SOR in the SAGD experiments and the square root of the porous media permeability

4.5.2.4. Production Characteristics of the SAGD Experiments: Microscopic State of the Produced Emulsion Phase

During the course of the SAGD experiments, the produced mobile oil is in the form of the micro-emulsion of dispersed water droplets in the continuum of the mobile oil. The qualitative pore-scale physics of the emulsion creation and flow in porous media in the context of the SAGD process was studied in Chapter 2 of this thesis. During our macro-scale study of the SAGD process using physical packed model, small-volume samples of the produced mobile oil was collected and placed on transparent glass slides. For each clear slide containing the mobile oil sample, another matching transparent glass slide was placed as the top cover over the sample. Excessive press and push was avoided to somehow preserve the state of the dispersed water droplets close to their original state within the oil continuum. The collected mobile oil samples in-between the glass slides were studied using an advanced photomicrography system (i.e. Olympus Research System Microscope AX70 integrated with automated U-PHOTO Universal Photo System). The autofocus option associated with different optical magnifications of up to

100X enabled us to take magnified snapshots of selected frames containing dispersed droplets of water condensate engulfed in the continuum of the mobile oil. Using an image processing software integrated with this photomicrography system, it was tried to measure the size of these water condensate droplets to have an estimate about the range of the dispersed water droplets.

It was tried to measure a various range of droplet sizes for each particular snapshot, but the image processing was sometimes limited to the clarity of the smaller-sized droplets in higher magnifications. Images of droplets as small as 5 microns in equivalent spherical diameter were captured; however, due to coalescence of some small-sized droplets as a result of environmental instabilities during handling the slides and photomicrography, significantly larger-sized droplets in the order of 150-200 microns were also created which do not seem to be representative of the spectrum of water condensate droplets sizes associated with the in-situ conditions of the SAGD process. Figures 4.16.a to 4.16.k present a series of snapshots taken from the emulsion samples collected during the course of the SAGD experiment in the higher permeability level associated with BT2 glass beads. In Figures 4.17.a to 4.17.f, the water condensate droplets sizes were plotted as a function of the number of the measurements conducted in each particular snapshot. In addition, an arithmetic average droplet size was defined for every particular snapshot for which the size measurements were performed. Within the range of the experimental conditions, it is observed that the average size of the water condensate droplets changes from 15.04±0.34 to 26.75±0.32 microns in the higher permeability medium respectively. As it was mentioned before, measuring the droplets sizes smaller than about 5 microns was not feasible considering the problems associated with focusing as well as clarity of the captured images. For instance, Figure 4.16.k is among a few snapshots that turned to be clear and perfectly-focused in which even the smallest-sized droplets are also visible. In other snapshots such as 4.16.b and 4.16.j, the clarity of the photos made it impossible to exactly measure the size of the smaller droplets.

Figures 4.18.a to 4.18.h display a series of snapshots captured during the course of the SAGD experiment at the lower level of permeability. In addition, Figures 4.19.a through 4.19.e present the distribution of the droplets sizes as a function of the number of measurements made in each particular snapshot.

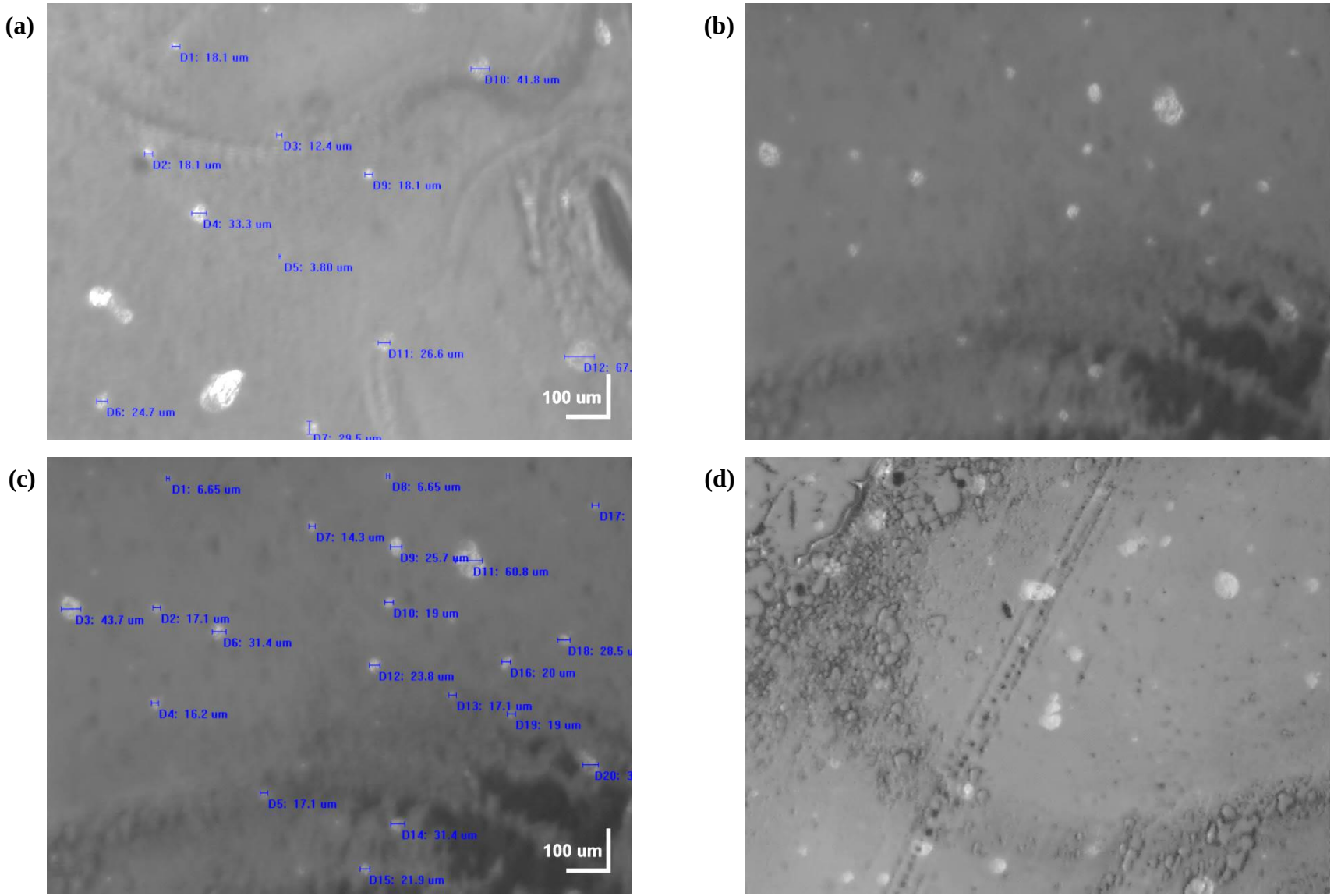

Figure 4.16: Microscopic images of W/O emulsion samples taken during the SAGD experiment at the higher permeability level

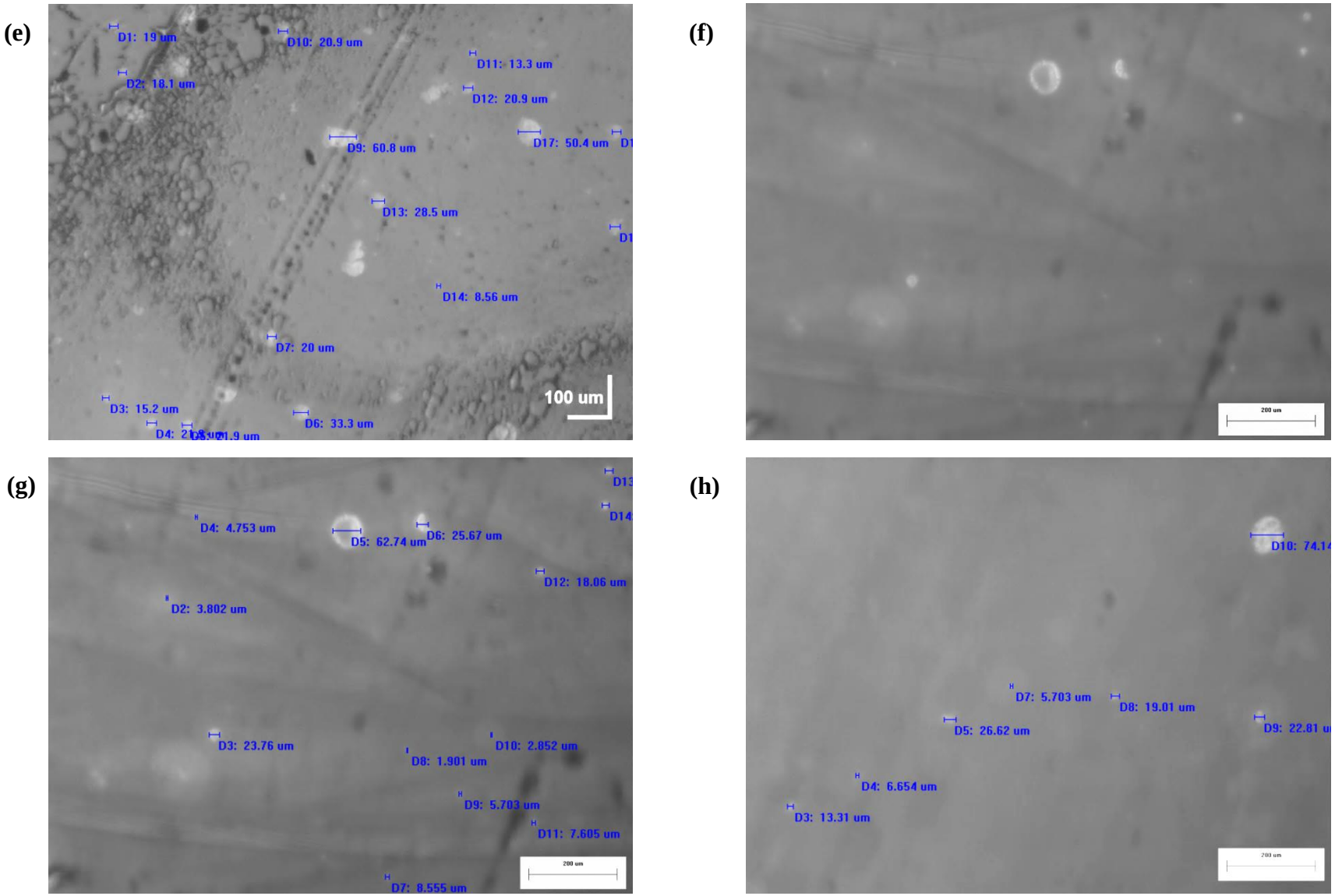

Figure 4.16 (Cont.): Microscopic images of W/O emulsion samples taken during the SAGD experiment at the higher permeability level

(i)

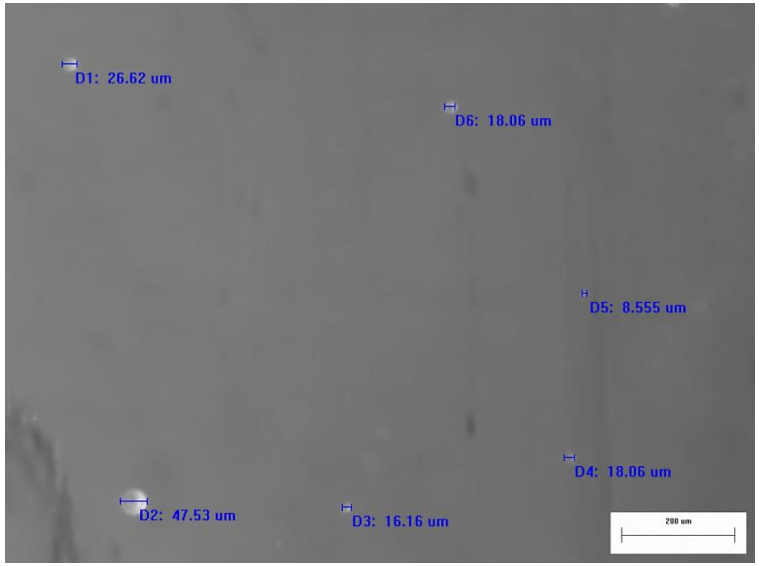

(j)

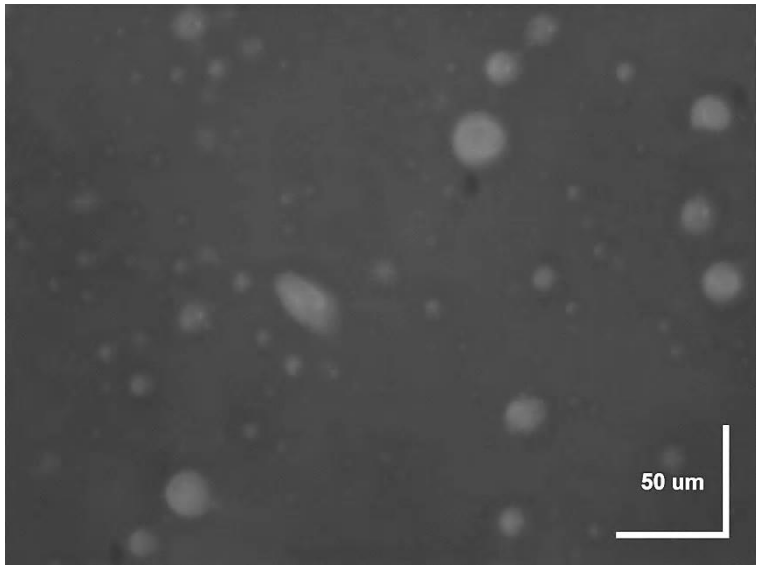

(k)

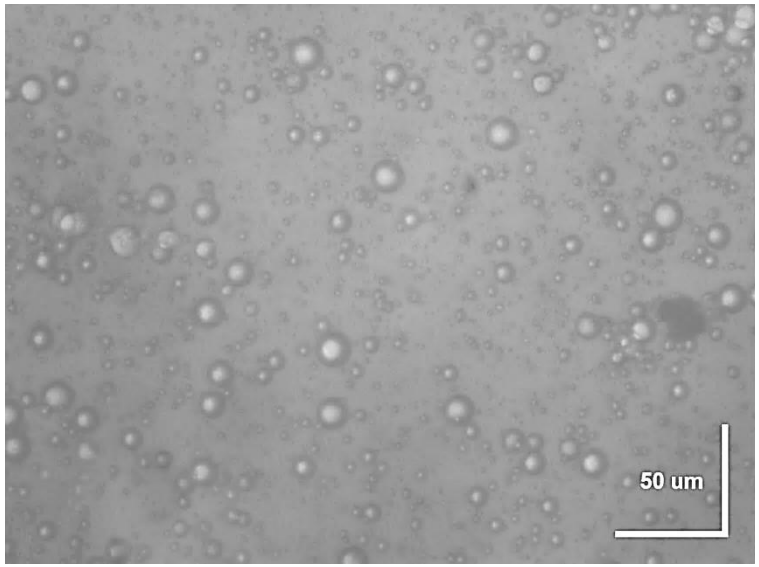

Figure 4.16 (Cont.): Microscopic images of W/O emulsion samples taken during the SAGD experiment at the higher permeability level

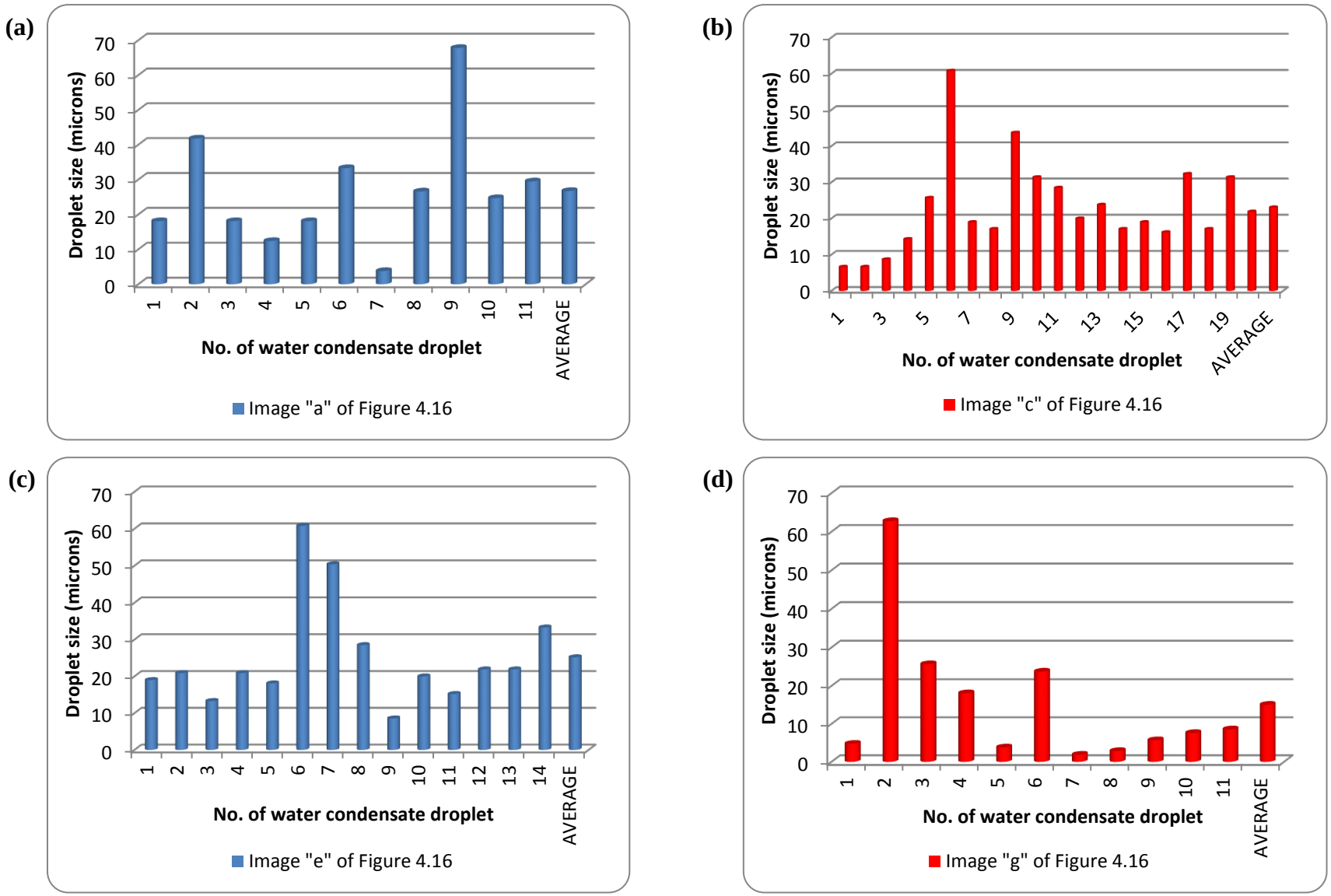

Figure 4.17: Size distribution of the water condensate droplets engulfed in the continum of the mobile oil – SAGD experiment at the higher permeability level

(e)

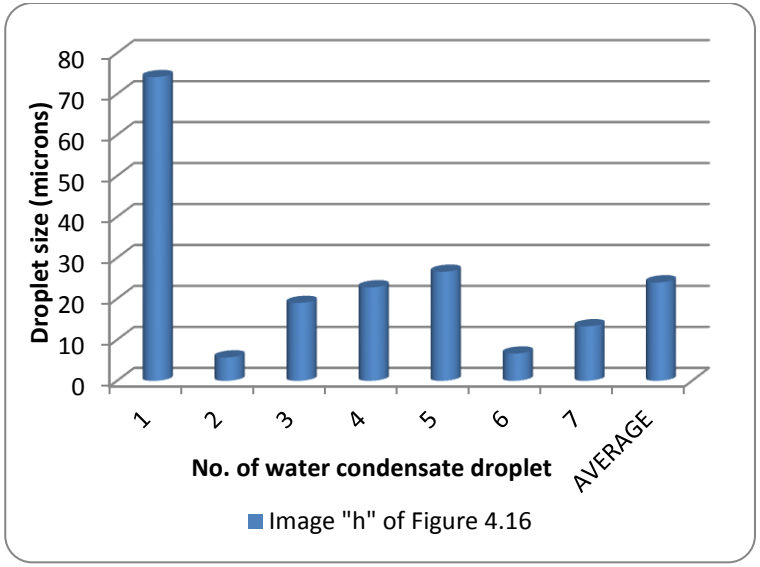

(f)

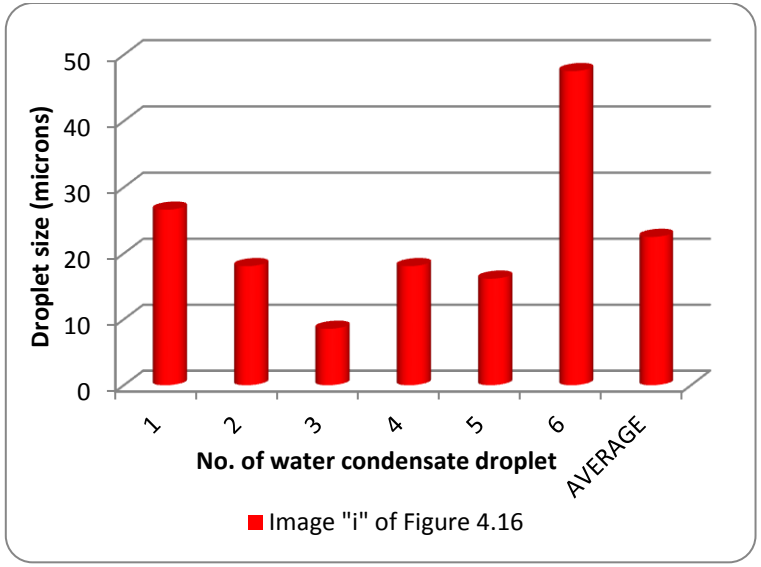

Figure 4.17 (Cont.): Size distribution of the water condensate droplets engulfed in the continum of the mobile oil – SAGD experiment at the higher permeability level

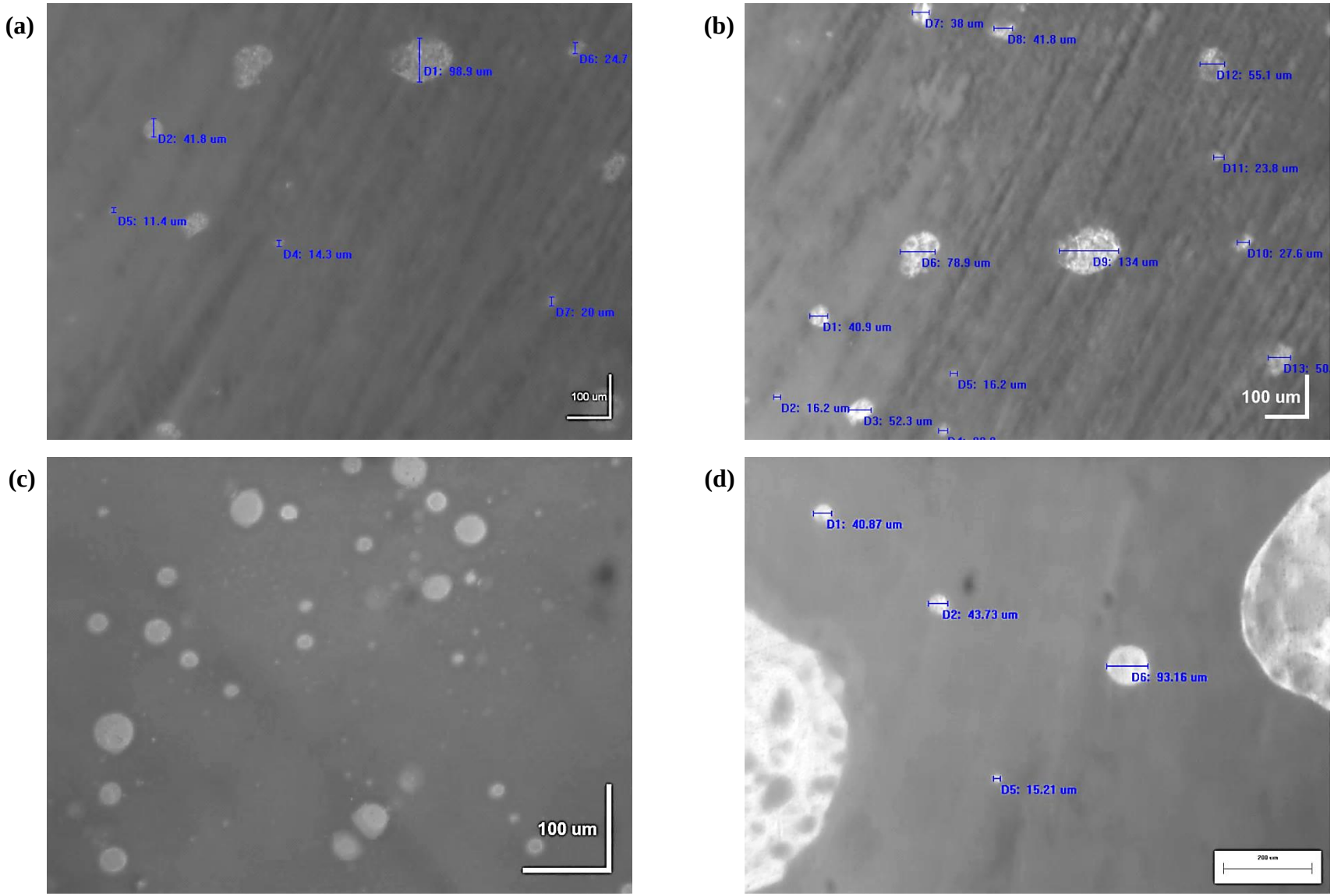

Figure 4.18: Microscopic images of W/O emulsion samples taken during the SAGD experiment at the lower permeability level

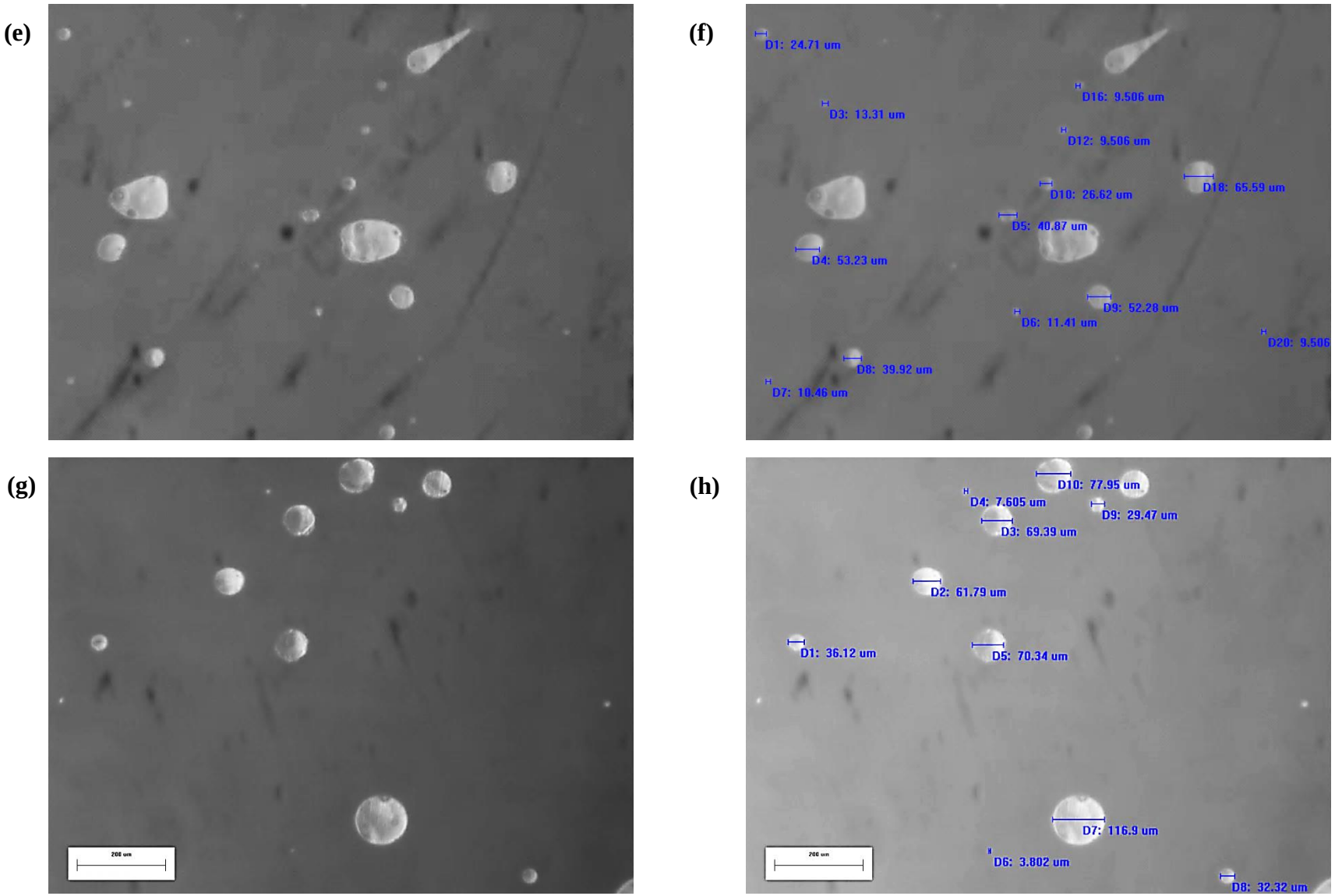

Figure 4.18 (Cont.): Microscopic images of W/O emulsion samples taken during the SAGD experiment at the lower permeability level

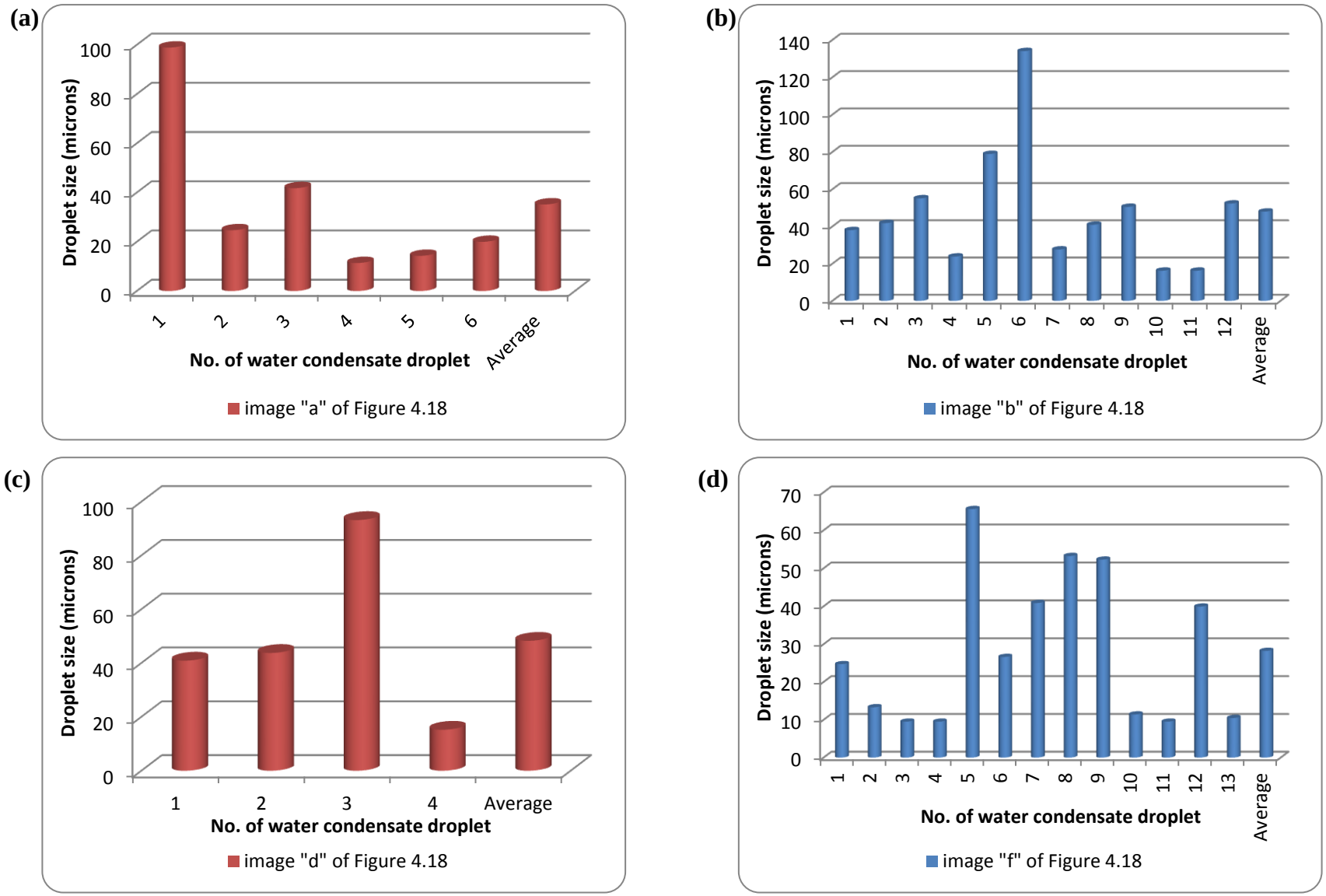

Figure 4.19: Size distribution of the water condensate droplets engulfed in the continum of the mobile oil – SAGD experiment at the lower permeability level

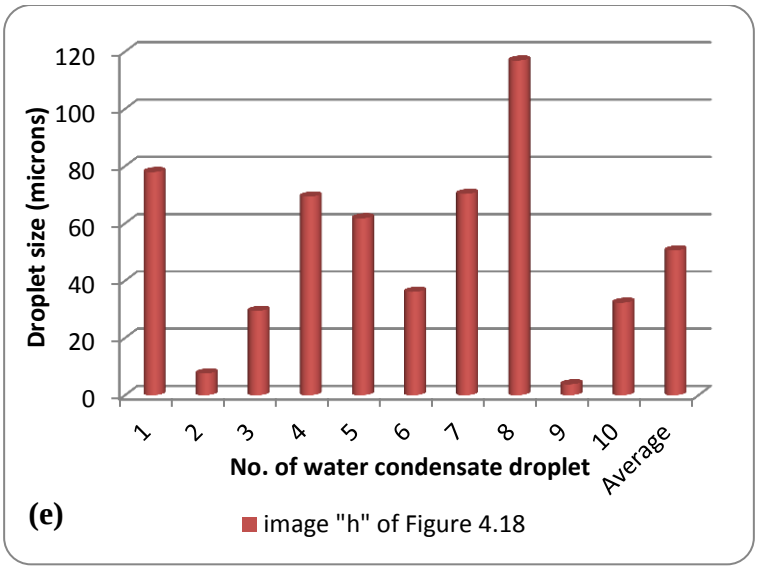

Figure 4.19 (Cont.): Size distribution of the water condensate droplets engulfed in the continum of the mobile oil – SAGD experiment at the lower permeability level

In each of the plots presented in Figure 4.19, an arithmetic average value column represents the average size of the dispersed water condensate droplets within the range of the measurements. As it was the case for the water droplets size distribution in the SAGD test at higher permeability level, the size range reported here for the case of porous medium composed of BT3 glass beads is limited to the capability of capturing clear snapshots from the lower range of the droplet sizes. Within the limits of our experimental conditions and considering the limitations regarding capturing the actual size of the smaller droplets, it was observed that the average size of the water condensate droplets at the lower permeability level changes from 28.22±0.35 to 50.57±0.69 microns. The minimum and maximum droplet sizes measured in the case of lower permeability level were 3.802 and 134 microns respectively. There are very big water droplets present in Figure 4.18.d which clearly do not represent the actual size of an enclosed droplet, and probably were formed because of the coalescence of some nearby condensate droplets.

In general, it is observed that the average size of the water condensate droplets engulfed in the continuum of the mobile oil in the lower permeability medium is relatively larger than that in the higher permeability medium. The reason could be related to the fact that in the lower permeability medium, the residence time of the draining mobile oil would be longer than that of

the higher permeability medium. This prolonged drainage process in the lower permeability medium, along with the high degrees of pore-scale mixing associated with the drainage region of the SAGD process could facilitate coalescence of smaller droplets together to form larger droplets in size. Other factors such as operating conditions, in-situ viscosity of the mobile oil continuum that engulfs the water condensate droplets, pore-size distribution of the porous medium, and some other counterparts could affect the size distribution of the propagating water condensate droplets.

4.5.2.5. Analysis of the Residual Oil

The residual oil left behind in the invaded portion of the model was measured at the end of each experiment when the physical model was dismantled. Samples of the beads taken from the swept area, near the topside of the model, were weighed and then put in the oven at 85-90 °C for at least 3 days to be dried. After the water content of the samples was dried, they were re-weighed and the weight difference was assigned to be the weight of the residual water phase in the invaded region plus any oil that was vaporized (i.e. lighter components of the residual oil) during the drying process. The beads were then thoroughly washed and cleaned with toluene and then methanol and then put in the oven to be completely dried. The clean dried beads were weighed, so that weight of the residual oil left within the pores would be determined. Volume of the residual oil was obtained using the density of the dead oil produced. The residual oil saturation of each particular sample was calculated based on the volume of the residual oil per pore volume of the sample.

Residual oil of a particular sample is defined as:

$$S_{or} = \frac{Volume\ of\ the\ residual\ oil}{Total\ pore\ volume\ of\ the\ sample} \tag{4.9}$$

in which volume of the residual oil and the total pore volume of the sample are determined using the following two equations:

$$Volume\ of\ the\ residual\ oil = \frac{(W_1 - W_2)}{\rho_{DO}} \tag{4.10}$$

$$\varphi = \frac{pore\ volume}{pore\ volume + grain\ volume} \tag{4.11}$$

in which "W_1" and "W_2" are the weight of the glass beads after first-stage drying in the oven (i.e. to vaporize the moisture content) and weight of the glass beads after being washed with toluene and methanol and being dried in the oven respectively, "ρ_{DO}" is the density of the dead oil, and "φ" is the porosity of the glass beads packing.

One may substitute the term "grain volume" in Eq 4.11 with its equivalent in terms of $\frac{m_{beads}}{\rho_{beads}}$ in which "m_{beads}" is the weight of the clean and dried glass beads and "ρ_{beads}" is the density of the glass beads, and then solve Eq 4.11 for the term "pore volume". Substituting the equivalent of "pore volume" from Eq 4.11 and that of "volume of the residual oil" from Eq 4.10 into Eq 4.9 results in:

$$S_{or} = \frac{\left[{(W_1 - W_2)}/{\rho_{DO}}\right]}{\left[\left(\frac{\varphi}{1-\varphi}\right) \times \left(\frac{m_{beads}}{\rho_{beads}}\right)\right]} \tag{4.12}$$

The residual oil saturation is expressed in volume basis. The porosity of the packed models regardless of the size of the glass beads used is about 0.37 under the tight packing scheme with the aid of a vibrating table. For the lower permeability beads (BT3), the residual oil saturation was measured to be 4.60±0.01%. The magnitude of the residual oil saturation at the higher permeability beads (BT2) was measured to be 3.02±0.01%. It is evident that the higher the permeability of the porous medium is, the lower would be the residual oil saturation in the invaded region of the medium.

4.5.3. The SA-SAGD Process at the Macro-Scale

In order to demonstrate the performance enhancement of the SAGD process upon co-injection of steam and a hydrocarbon solvent, it was decided to conduct one SA-SAGD process under similar process configuration as that described for the macro-scale SAGD processes. Athabasca

bitumen was used as the oil type, and normal hexane was used as the steam additive. This SA-SAGD experiment was in fact a continuation of one of the SAGD experiments (the replicate trial with BT2 glass bead as the porous medium packing). The experiment was started up based on the protocol used for initialization of the SAGD experiment, and when the SAGD interface moved about 1.5 cm away from the perforated injection tube, the sampling procedure was started. After about 1 hour of the sampling time during which 6 samples of the mobile oil under the SAGD process were collected, n-C_6 was started to be injected along with the steam phase in the context of a solvent aided thermal process. The solvent mass fraction at the injection mainstream of the process flow scheme was adjusted to be about 17% wt/wt of the total fluids injected. During the first 38 minutes of the SA-SAGD experiment, the steady-state drainage condition was disturbed as a result of addition of solvent to the injection mainstream. In other words, it was observed that the production rate was increased as a result of solvent dilution as well as the thermal effects, but the enhancement was not to the amount that was observed afterwards when the steady state drainage condition of the SA-SAGD process was attained. In this section, production characteristics of the SA-SAGD experiment is discussed.

4.5.3.1. Production Characteristics of the SA-SAGD Experiment: Mobile Oil Production Rate

The sampling procedure and experimental methodology for the SA-SAGD experiment is the same as those described for the case of the SAGD experiments. During the steady state phase of the drainage process, it was observed that the production rate of the SA-SAGD process remained fairly constant with respect to the sampling time. The term “mobile oil” is defined as the volume of the draining oil plus the enclosed water condensate droplets in the form of the W/O emulsion, and the solvent content of the oil phase, all draining out of the model through the production line. The term “dead oil” refers to the volume of the oil left inside the sampling cups after being kept in the convection oven for at least 3 days at 85-90 °C. The cumulative oil produced during the entire process time of the experiment is depicted in Figure 4.20.a while the same data was plotted versus the sampling time in Figure 4.20.b with focus on distinct acting processes including the time interval dedicated to SAGD and SA-SAGD processes as well as the transition period. The purple arrow in Figure 4.20.a shows the time at which the solvent phase was introduced into the injection flow line. It is observed that the cumulative weight of the mobile oil produced

correlated very well with the sampling time during each of the corresponding process durations. As of interest are the linear correlations describing the relationship between the cumulative mobile oil produced and the respective sampling times associated with the SAGD and SA-SAGD processes. These strong linear correlations reveal the fact that the production rates of the mobile oil associated with these two processes are reasonably constant over the course of the sampling time. The slope of these two straight lines show the average mobile oil production rates for these two processes which are 6.55 g/min (i.e. 3.44 g/min.cm of the porous medium thickness) and 7.86 g/min (i.e. 4.13 g/min.cm of the porous medium thickness) for the SAGD and SA-SAGD experiments respectively. Considering the average mobile oil production rate of the SAGD process at the high permeability level to be 6.68 g/min, it is evident that an enhancement of about 17.7% was achieved upon addition of solvent into the steam phase. This enhancement in the production performance of the SA-SAGD process is due to the more effective in-situ viscosity reduction of bitumen with the aid of both heat and mass transfer effects.

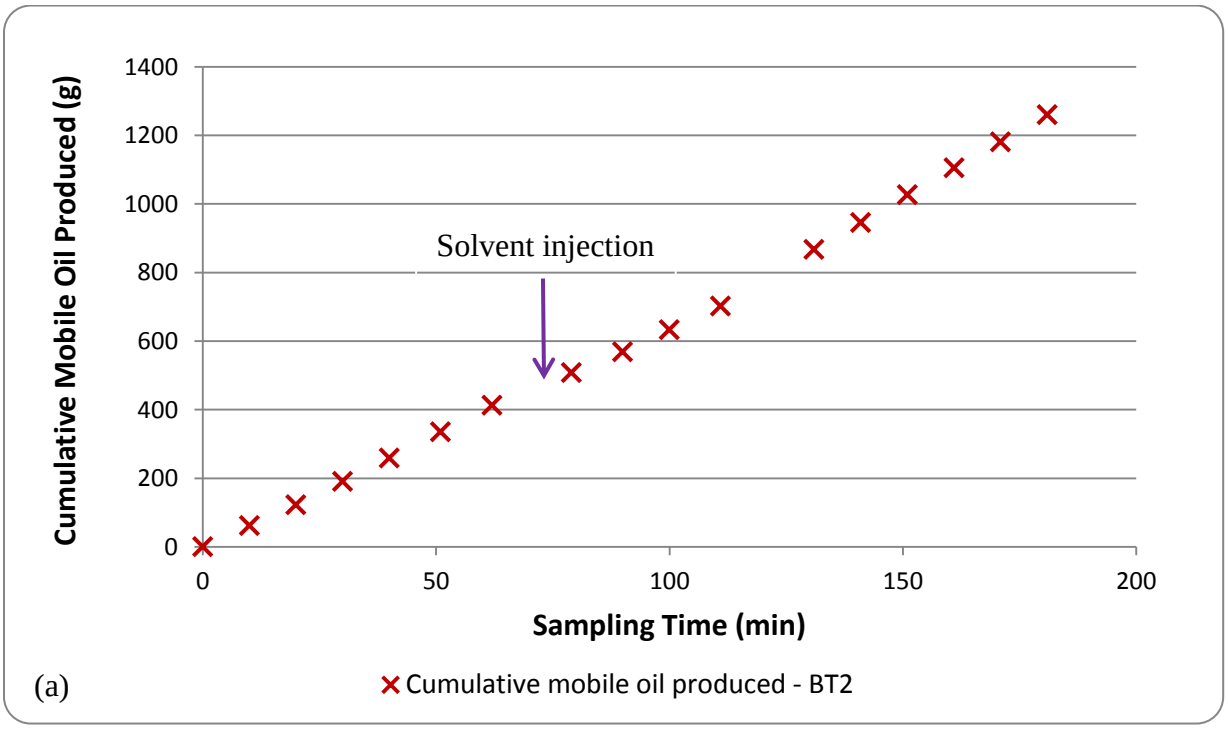

(a)

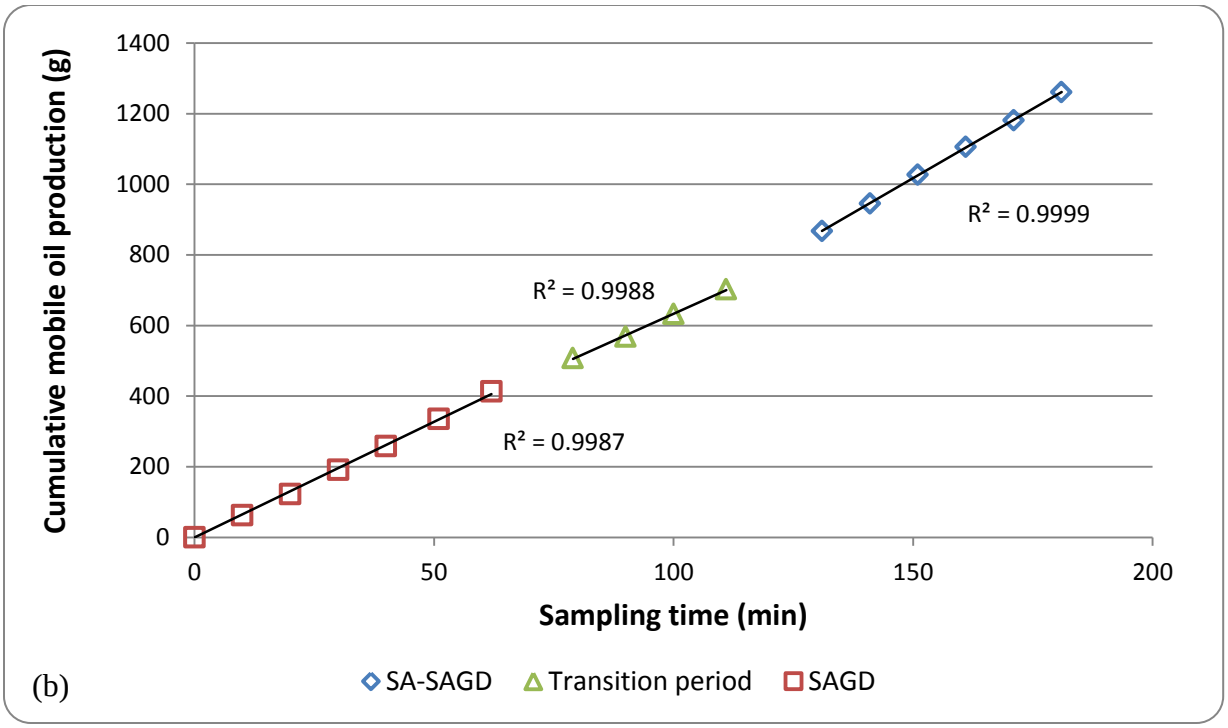

Figure 4.20: Cumulative mobile oil produced versus the sampling time: (a) for the entire experiment, (b) characterized based on distinct acting processes

4.5.3.2. Production Characteristics of the SA-SAGD Experiment: Dead Oil Production Rate

The mobile oil samples produced during the course of the SA-SAGD experiment were placed inside a convection oven at 85-90 °C for at least 3 days to allow the water and solvent content of the samples to be flushed. The dead oil samples were then weighed, and the individual dead oil sample weighs were transformed into the cumulative basis. Figure 4.21 presents the cumulative dead oil production data for the SA-SAGD process, along with the data associated with the transition period as well as the corresponding SAGD portion of the experiment. As it can be seen in this Figure, there is a strong correlation between the cumulative dead oil production data and the sampling time, showing that the average dead oil production rate of the SA-SAGD process can be considered to be a constant value over the process time. According to the data presented in this Figure, the average dead oil production rate of the SA-SAGD portion is about 3.12 g/min (i.e. 1.64 g/min.cm of the porous medium thickness) while that of the corresponding SAGD

experiment is about 2.66 g/min (i.e. 1.40 g/min.cm of the porous medium thickness) which shows an enhancement of about 17.2% in the dead oil production rate upon injecting n-C_6 along with the steam phase.

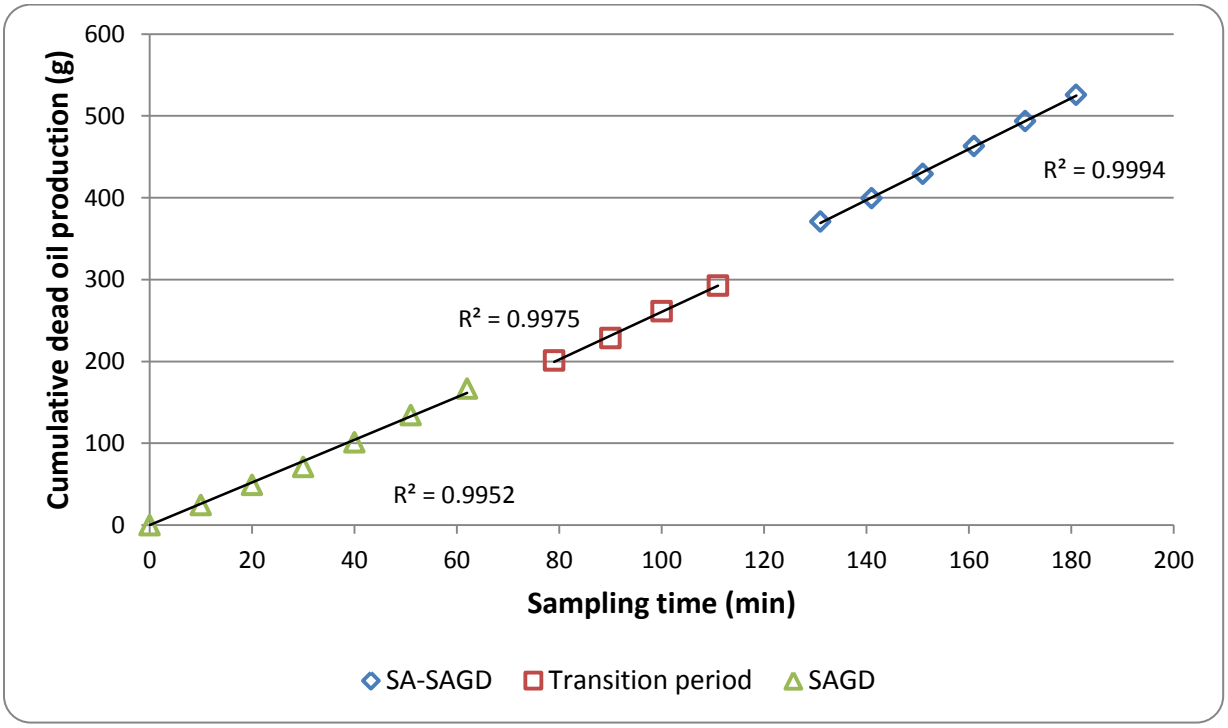

Figure 4.21: Cumulative dead oil produced versus the sampling time for the SAGD, SA-SAGD and the transition time sections of the experiment

Figures 4.22 and 4.23 display how the instantaneous dead oil production rates changed versus either the sampling time or the sample number when the production scheme was changed from SAGD to SA-SAGD passing through the transition period. It is evident that for both the SAGD and SA-SAGD portions of the curve, the dead oil production rate does not vary significantly over the sampling time. As a result, it is reasonable to define an average production rate to identify the drainage performance of each of these two sections over their corresponding sampling times. In addition, the gradual increase in the dead oil production rate from the SAGD portion to the SA-SAGD portion of the curve is quite obvious in these two Figures through the transition time in between.

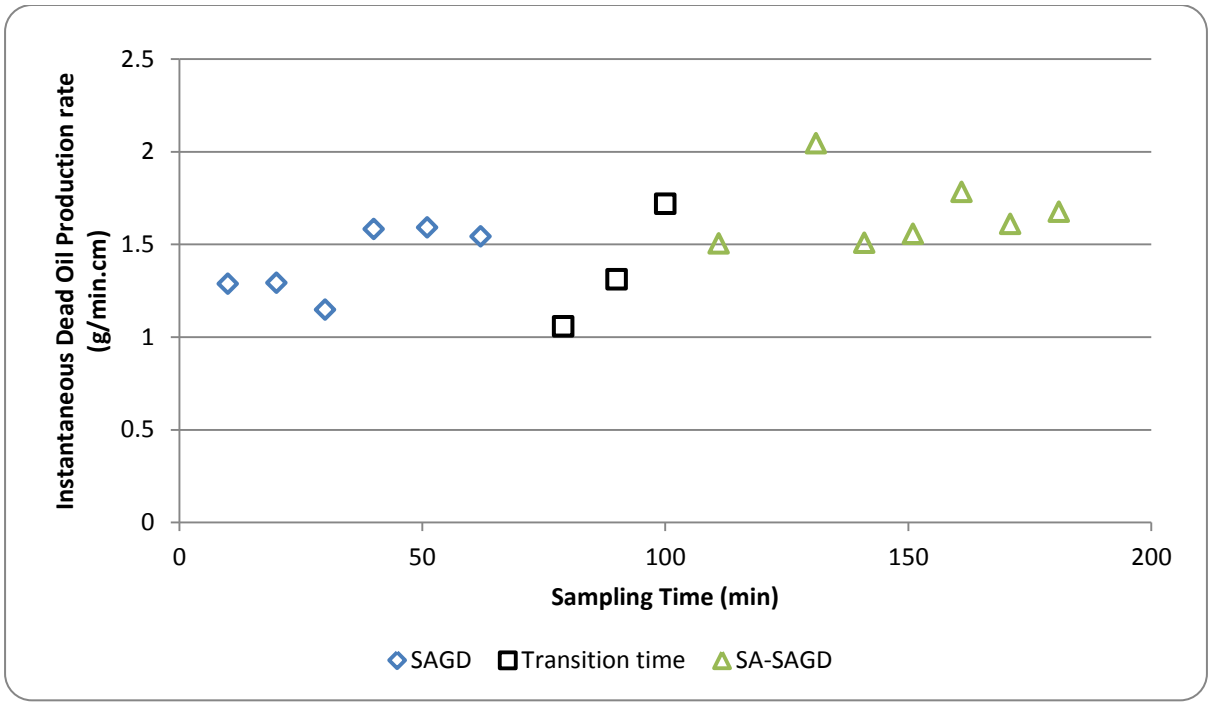

Figure 4.22: Instantaneous dead oil production rate per unit thickness of the porous medium for the SAGD and SA-SAGD portions of the experiment as a function of the sampling time

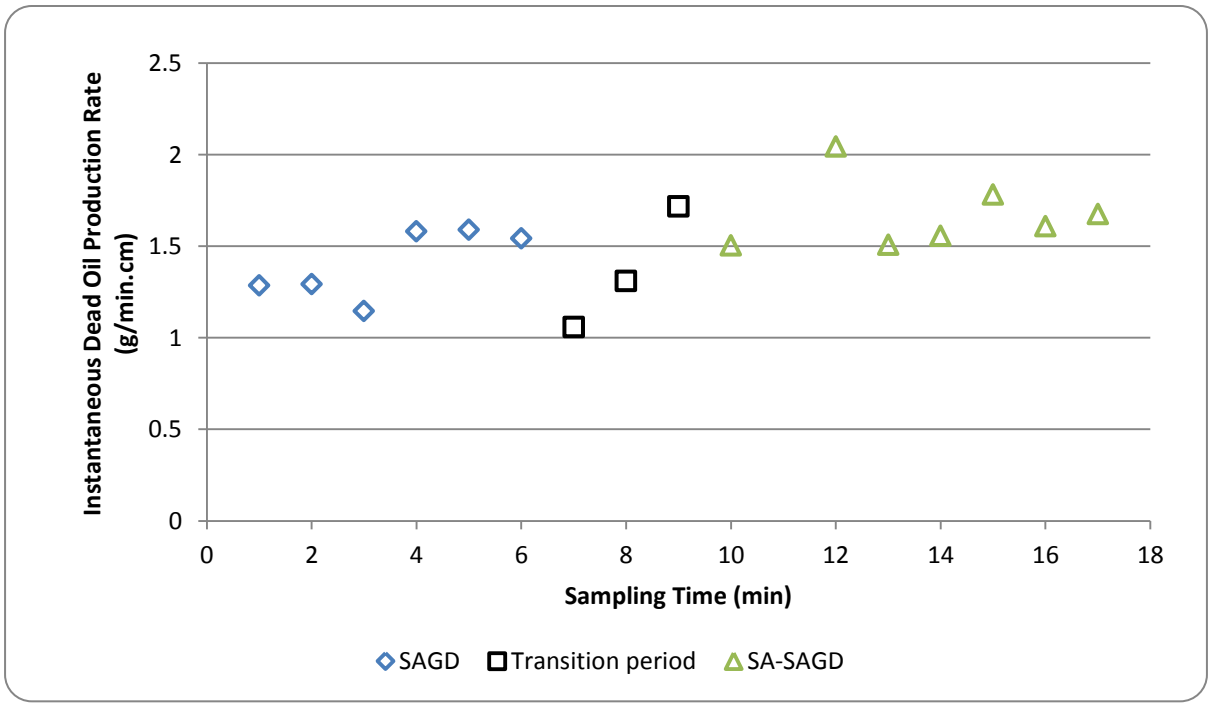

Figure 4.23: Instantaneous dead oil production rate per unit thickness of the porous medium for the SAGD and SA-SAGD portions of the experiment as a function of the sampling time

4.5.3.3. Production Characteristics of the SA-SAGD Experiment: Water Content of the Produced Mobile Oil

Following the drying process of the moisture content as well as the solvent content of the mobile oil samples produced during the SA-SAGD process using a convection oven at 85-90 °C, mass of the water content of the samples were transformed into the cumulative basis and is presented in Figure 4.24. In this Figure, the cumulative water produced is characterized based on the acting process. It is evident that the cumulative water produced correlated very good with the sampling time in both the SAGD and SA-SAGD segments. The average rate of water production using the cumulative data is about 3.68 g/min for the SA-SAGD section of this experiment. Using the original and replicate trials of the SAGD process in the higher permeability level, the average water production rate was calculated to be 4.02 g/min. It is evident that addition of solvent into the injection mainstream of the SA-SAGD process resulted in about 9.25% reduction in the average rate of water production compared to the conventional SAGD trial.

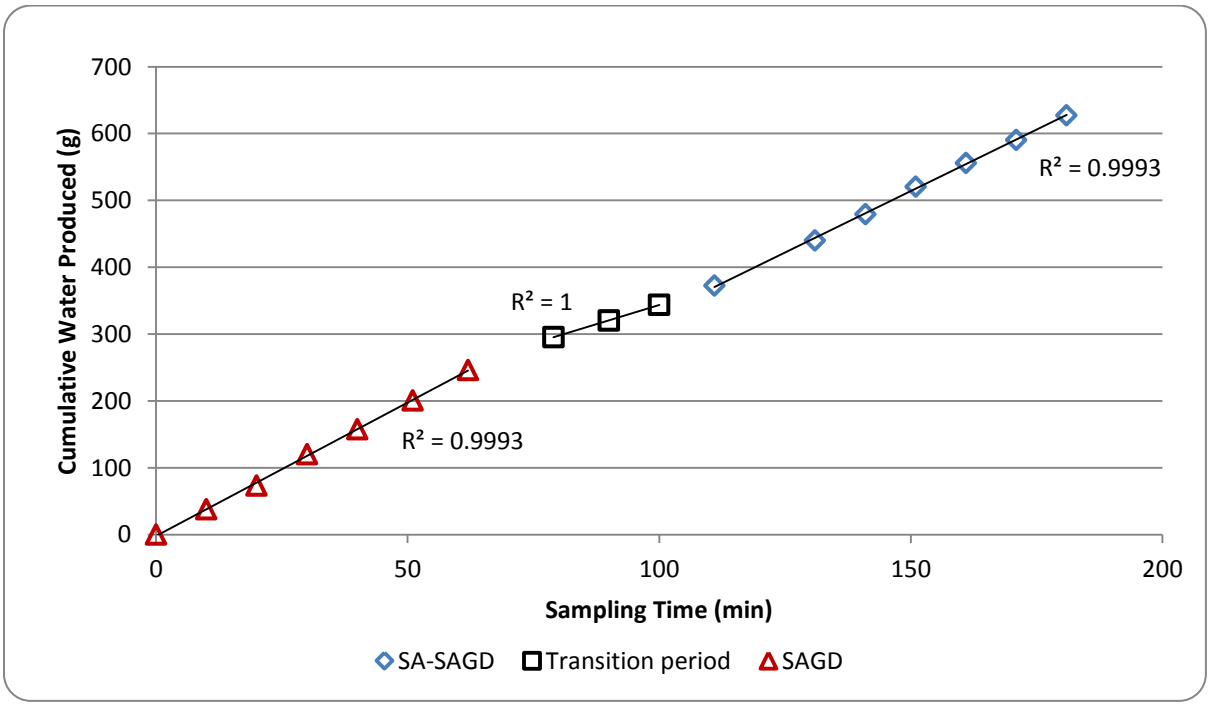

Figure 4.24: Cumulative water produced along with the oil phase versus the sampling time in two different portions of the SAGD and SA-SAGD processes as well as the transition period

One of the advantages of the SA-SAGD process compared to the conventional SAGD process is the lower energy intensity associated with the former process compared to that of the latter one. The energy requirements of the thermal and/or thermal solvent process is expressed in terms of the amount of the steam required to produce one unit volume of the dead oil (i.e. so-called SOR) in terms of the cold water equivalent of steam per volume of the produced dead oil. The numerical values of the SOR for the SAGD and SA-SAGD processes are calculated using the cumulative steam uptake data during respective experiments and the information regarding the cumulative dead oil produced in the corresponding trials. For the SA-SAGD segment of the experiment, the average SOR value was obtained to be 1.137 wt/wt. Comparing the average SOR values of the SA-SAGD and the corresponding SAGD trials reveals that a decrease of about 35.5% in the SOR value is obtained as a result of solvent addition to the injection mainstream in the SA-SAGD process.

4.5.3.4. Production Characteristics of the SA-SAGD Experiment: Solvent Content of the Produced Mobile Oil

A mass balance was conducted focusing on the solvent phase during the course of the SA-SAGD section of the experiment. Mass of the solvent phase leaving the system from top to the condenser was monitored versus time on a cumulative basis. The solvent content of the produced mobile oil was evaporated along with the moisture content of the samples in the convection oven. The contribution of the solvent content in the produced mobile oil samples were determined knowing the average injection flow rate of the solvent phase as well as the average flow rate of the solvent phase in the effluent to the atmospheric condenser. The average concentration of n-C_6 in the produced mobile oil was calculated to be 11.32% wt/wt. In addition, the average solvent to oil ratio (SolOR) was calculated on a weight basis for the SA-SAGD portion of the experiment considering the cumulative solvent uptake and the cumulative dead oil production of this period. The net cumulative SolOR magnitude was calculated to be 0.302wt/wt.

4.5.3.5. Production Characteristics of the SA-SAGD Experiment: Microscopic State of the Produced Emulsion Phase

During the course of the SA-SAGD experiment, small-volume samples of the produced mobile oil were collected for the purpose of the microscopic studies. The procedure followed for the

microscopic studies was the same as that used in the case of the SAGD experiments. The live oil samples were kept and spread between the surfaces of two matching transparent glass slides and were analyzed in terms of the size of the enclosed water condensate droplets in the continuum of the mobile oil using an advanced photomicrography device of Olympus Research System Microscope AX70 integrated with automated U-PHOTO Universal Photo System. Using an image processing software integrated with the photomicrography device, the size of the enclosed water droplets were measured within the accuracy and clarity of the images and the constraints associated with magnifying the snapshots containing very small dispersed phase droplets. Similar to the case of the microscopic image analysis in the SAGD experiments, some big-in-size water condensate droplets in the order of 100-200 microns were observed; however, they were not considered in the droplet size measurement and analysis. Figures 4.25.a to 4.25.k present a series of microscopic snapshots presenting the status of the enclosed water condensate droplets in the background of the mobile oil. Figures 4.25.g and 4.25.h are the same snapshot, one with and the other without the droplet size measurements. Moreover, the droplet size measurements were not performed on images 4.25.i, 4.25.j and 4.25.k; however, the length unit reference is provided in these three snapshots making it possible to estimate the size of the enclosed condensate droplets. Focusing on these three images, one can realize that there are a large number of tiny water condensate droplets whose sizes are smaller than 5 microns engulfed in the mobile oil background. Figures 4.26.a to 4.26.f display plots of the water condensate droplets sizes as a function of the number of the measurements performed in each particular snapshot. An arithmetic average value of the water condensate droplets sizes was presented for every particular micro-scale snapshot for which the droplet size measurement was carried out. According to the plots presented in Figure 4.26, it is obtained that the average size of the water condensate droplets was in the range of 22.82±0.19 to 39.51±0.41 microns. It is clear that the above-mentioned average droplet size value might not be a true representative of the actual size distribution of the enclosed water condensate droplets because the very fine droplet sizes were not considered for the purpose of averaging (i.e. Figures 4.25.i to 4.25.k) and also there is the possibility of droplets coalescence during handling and measurements.

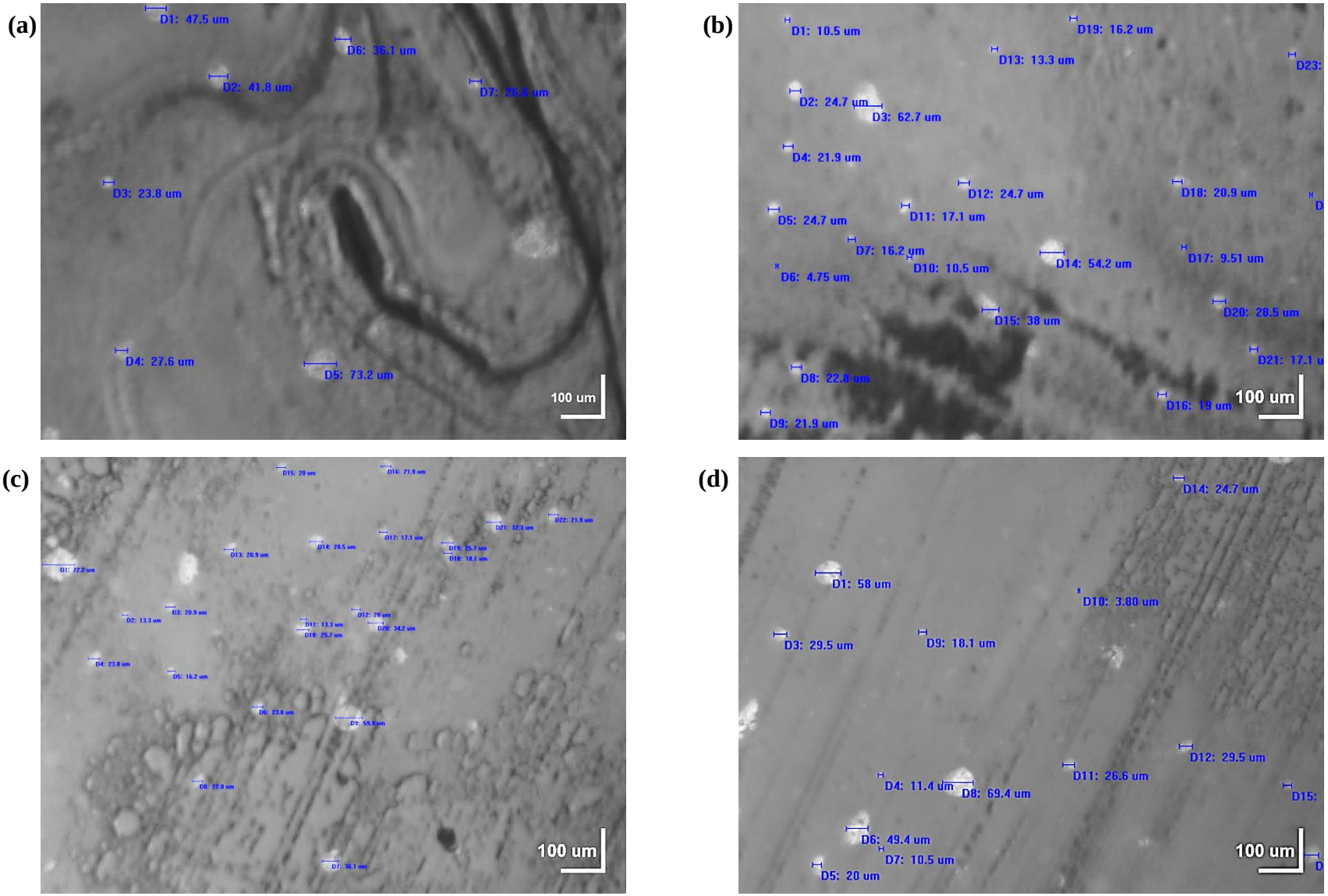

Figure 4.25: Microscopic images of W/O emulsion samples taken during the SA-SAGD experiment

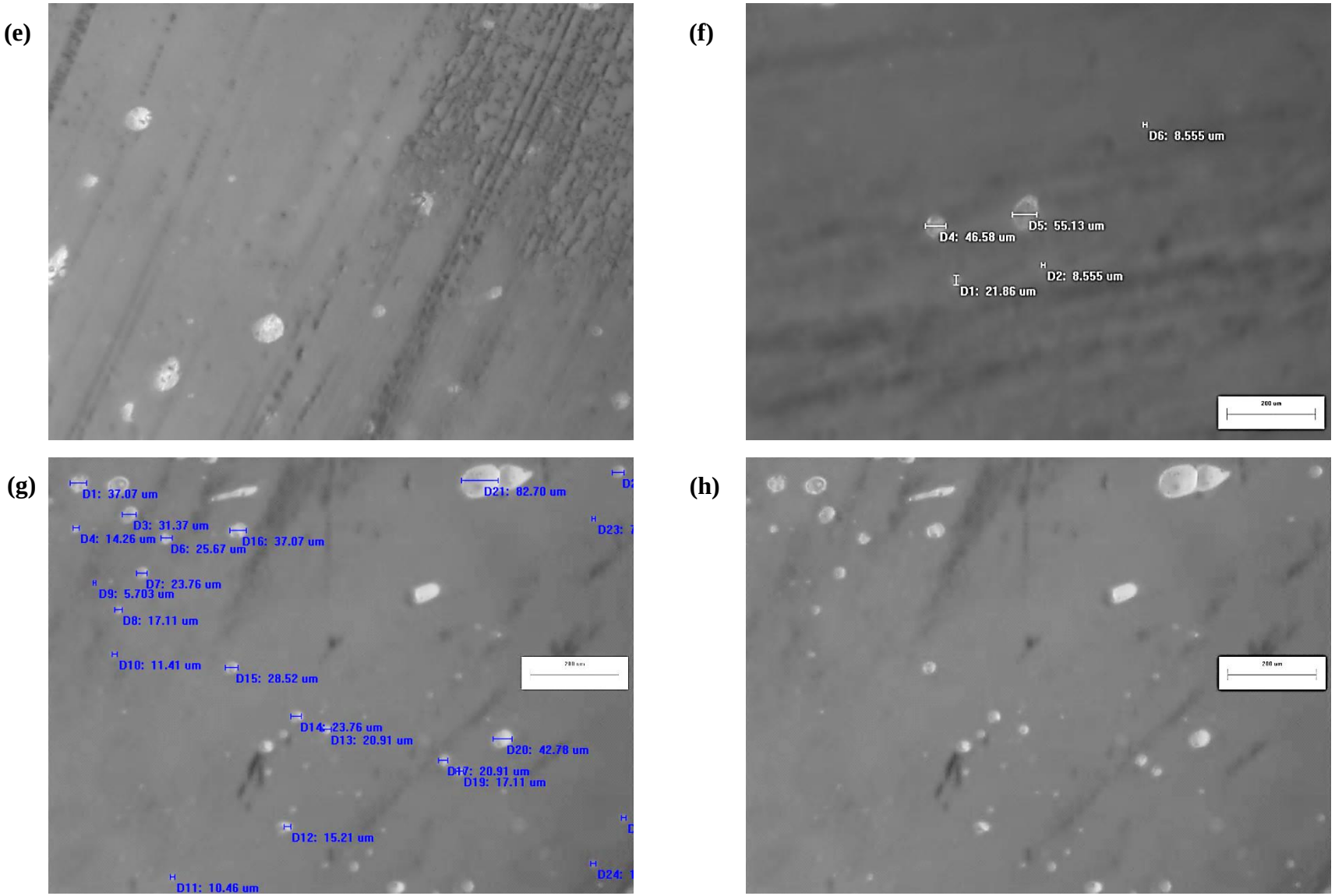

Figure 4.25 (Cont.): Microscopic images of W/O emulsion samples taken during the SA-SAGD experiment

(i)

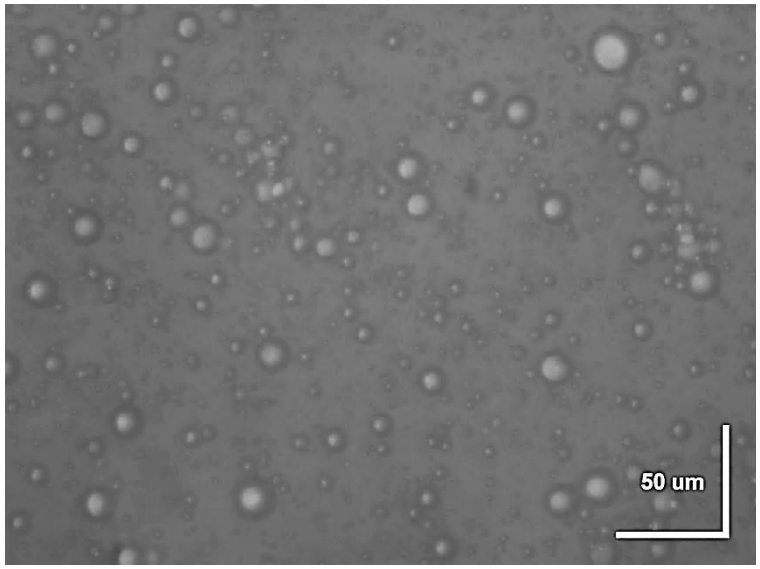

(j)

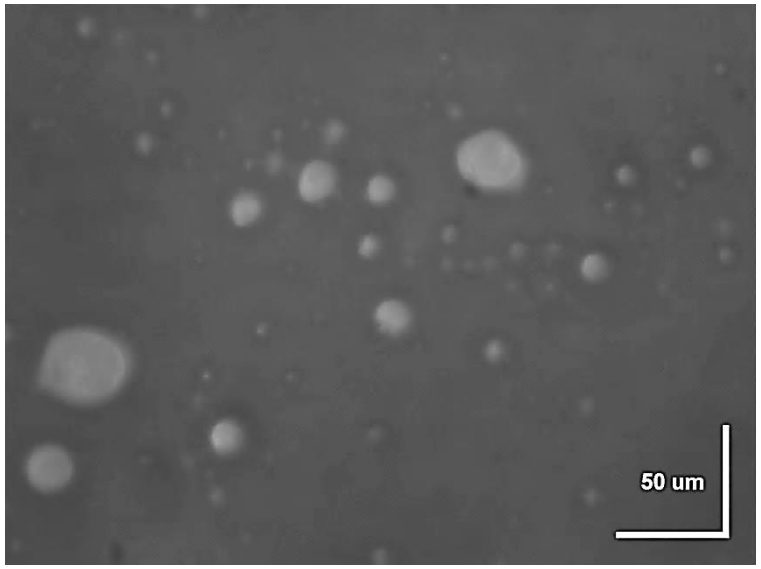

(k)

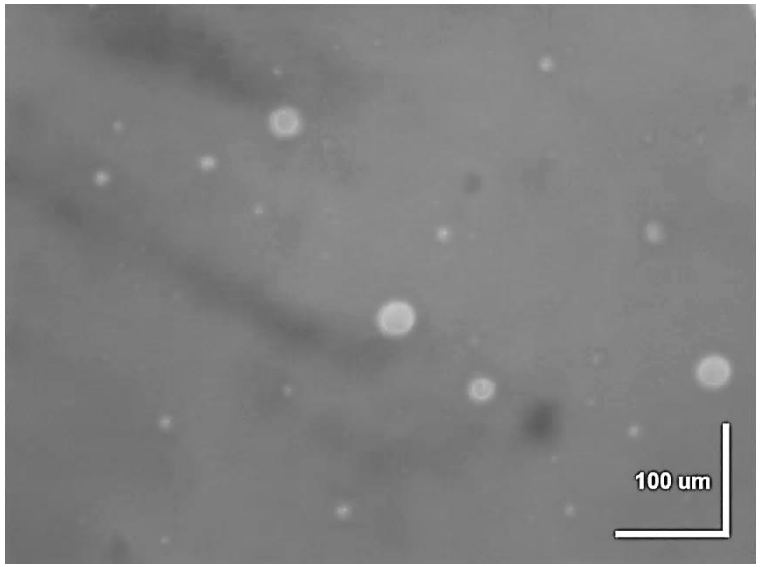

Figure 4.25 (Cont.): Microscopic images of W/O emulsion samples taken during the SA-SAGD experiment

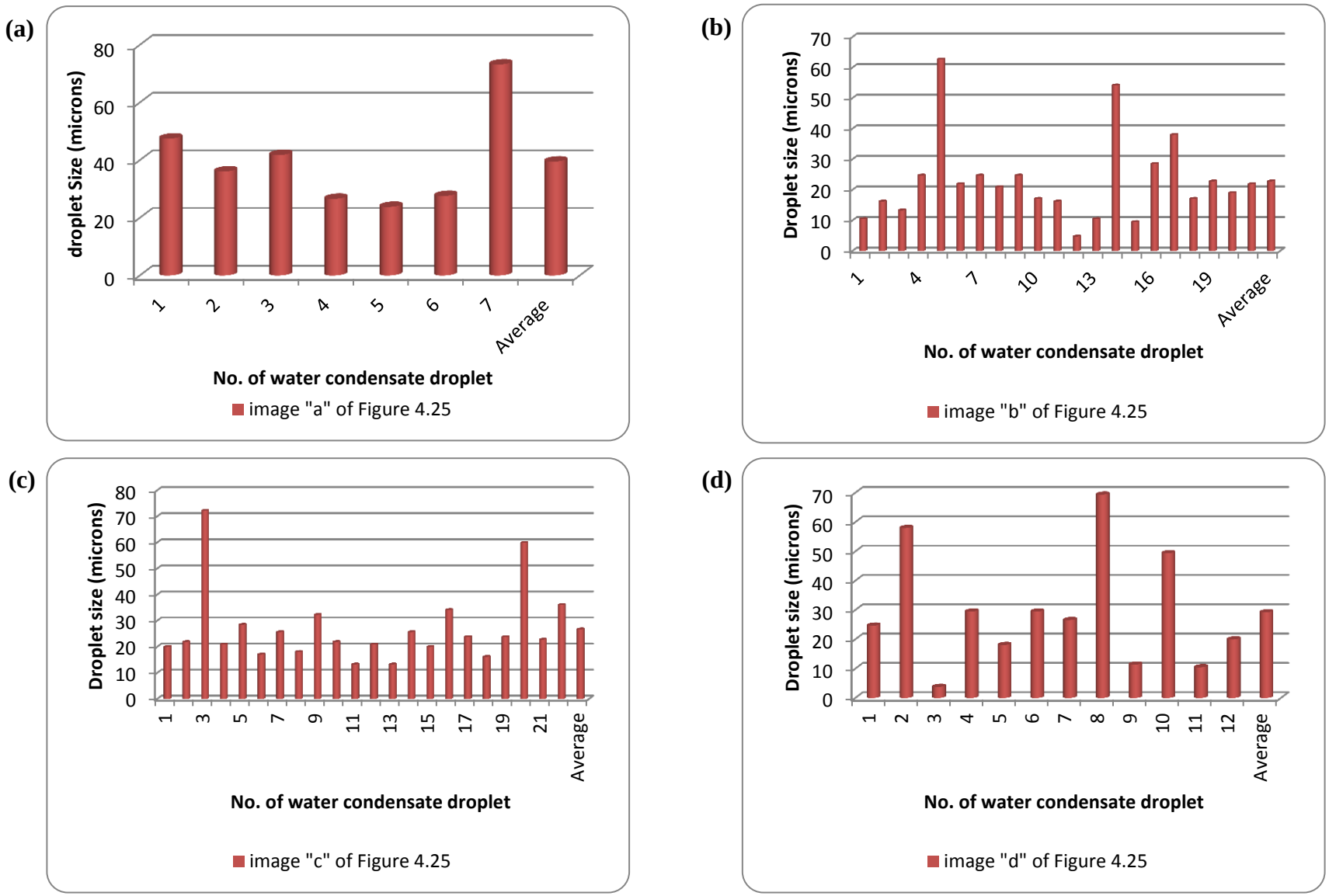

Figure 4.26: Size distribution of the water condensate droplets enclosed in the continum of the mobile oil: SA-SAGD experiment

(e)

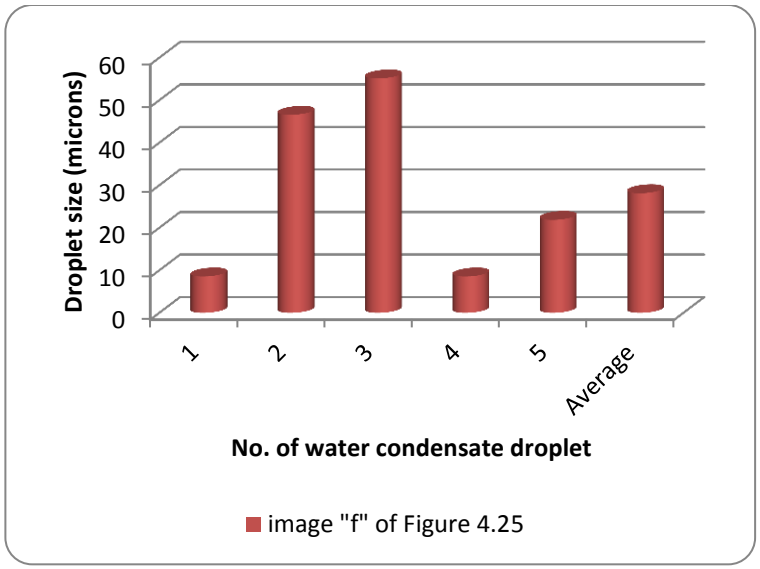

(f)

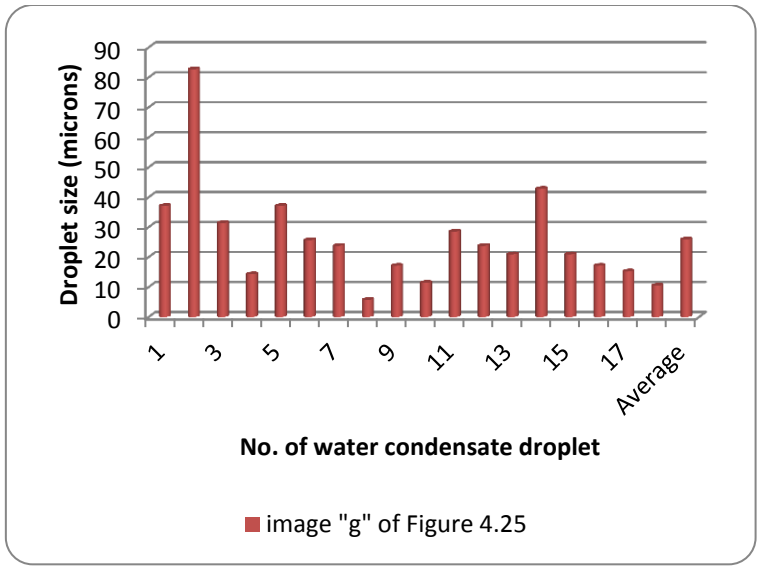

Figure 4.26 (Cont.): Size distribution of the water condensate droplets enclosed in the continum of the mobile oil: SA-SAGD experiment

4.6. Conclusions

In order to investigate and compare the performance of the SAGD and SA-SAGD processes at the macro-scale, a 2-D physical model was designed and fabricated. Four SAGD and one SA-SAGD trials were carried out with the aid of this physical model at the environmental conditions of an isothermal jacket. The following conclusions were drawn from these experimental studies:

- There is a strong linear correlation between the cumulative mobile oil production and the sampling time for all the SAGD and SA-SAGD experiments which proves that the average SAGD and SA-SAGD mobile oil production rates can be considered to be constant values over the corresponding sampling periods.
- The cumulative dead oil produced changes linearly with respect to the sampling time for both the SAGD and SA-SAGD experiments suggesting that the average dead oil production rate of these two processes is constant over their respected sampling time.
- The higher the permeability of the porous medium is, the higher would be the average mobile oil as well as dead oil production rates of the SAGD process. It was also observed that the average mobile oil production rates of the SAGD trials correlates reasonably with the square root of the porous medium permeability when all other experimental variables are unchanged.
- It was observed that the SOR values obtained in the SAGD experiments correlates reasonably with the inverse of the square root of porous medium permeability when all the other experimental parameters remain unchanged.
- For different permeability levels, it was obtained that the produced emulsion phase during the course of the SAGD process contains enclosed water condensate droplets with the equivalent sizes as small as 3 microns. The average size of these engulfed droplets is between 15-25 and 28-50 microns for the higher and lower permeability levels, respectively.

- The residual oil saturation in the invaded region of the SAGD process was measured to be between 3 to 4.6% of the total pore volume for the higher and lower permeability levels respectively.
- In the SA-SAGD process, it was observed that following introduction of solvent into the injection stream, enhancements of about 18% and 17% were achieved in the average mobile oil as well as dead oil production rates compared to those of the SAGD process respectively.
- The average SOR value of the SAGD process was decreased by about 35% when solvent phase was introduced into the injection stream in the context of the SA-SAGD process.
- Using microscopic image analysis of the produced emulsion phase in the SA-SAGD process, it was obtained that there are dispersed water condensate droplets with equivalent sizes of as small as 5 microns in the continuum of the produced mobile oil. The measured average water condensate droplet size was in the order of 22 to 40 microns.

References

1) Al-Bahlani A.M. and Babadagli T. **(2009)** SAGD laboratory experimental and numerical simulation studies: A review of current status and future issues, *J. Pet. Sci. Eng.*, doi:10.1016/j.petrol.2009.06.011

2) Ayodele O. R. et al **(2010)** Testing and history matching ES-SAGD (using Hexane), *Presented at the SPE Western Regional Meeting,* SPE paper number 134002, Anaheim, CA, USA.

3) Badamchi-zadeh A., Yarranton H.W., Svrcek W.Y., and Maini B.B. **(2009)** Phase behaviour and physical property measurements for VAPEX solvents: part I. Propane and Athabasca bitumen, *Journal of Canadian Petroleum Technology*, 48(1), 54-61.

4) Birrell, G.E. and Putnam, P.E. **(2000)** A Study of the influence of reservoir architecture on SAGD steam chamber development at the Underground Test Facility, Northeastern Alberta, Canada, using a graphical analysis of temperature profiles, *Presented at the Petroleum Society's CIPC Conference*, Petroleum Society of CIM Paper No. 2000-104, Calgary, AB, Canada.

5) Boyle, T.B.; Gittins, S.D.; and Chakrabarty, C. **(2003)** The evolution of SAGD technology at East Senlac, *Journal of Canadian Petroleum Technology*, Paper number 2002-300, **42**, 1, Jan.

6) Bridgman P. W. **(1923)** The Thermal Conductivity of Liquids under Pressure, *Proc. Am. Acad Arts Sciences*, **59**, 7, pp. 154-169.

7) Bryan O. **(2009)** ES-SAGD; past, present, and future, *Presented at the SPE International Student Paper Contest at the SPE ATCE,* SPE paper number 129518-STU, New Orleans, Louisiana, USA.

8) Butler R.M., McNab G.S., and Lo H.Y. **(1979)** Theoretical studies on the gravity drainage of heavy oil during in-situ steam heating, *29th Canadian Chemical Engineering Conference*, Sarnia, Ontario, October 1-3.

9) Butler R.M., McNab G.S., and Lo H.Y. **(1981)** Theoretical studies on the gravity drainage of heavy oil during steam heating, *Canadian Journal of Chemical Engineering*, **59**, 455-460.

10) Butler R.M. **(1991)** *Thermal Recovery of Oil and Bitumen*, Prentice Hall Inc., New Jersey.

11) Butler R.M. **(1994)** *Horizontal wells for the recovery of oil, gas and bitumen*, Petroleum Society Monograph Number 2, Canadian Institute of Mining Metallurgy and Petroleum.

12) Butler R.M. **(1994)** Steam-assisted gravity drainage: concept, development, performance, and future, *Journal of Canadian Petroleum Technology (JCPT)*, **32**, 2.

13) Butler R.M. **(1998)** SAGD comes of age, *JCPT*, **37**, 7.

14) Butler R.M. **(2001)** Some recent developments in SAGD, *Distinguished JCPT Author Series*, **40**, 1.

15) Butler R.M. **(2004)** The behaviour of non-condensible gas in SAGD — a rationalization, *JCPT*, **43**, 1.

16) Butler, R.M. and Stephens, D.J. **(1981)** The gravity drainage of steam heated heavy oil to parallel horizontal wells, *Journal of Canadian Petroleum Technology*, Paper No. 81-02-07, April-June.

17) Butler, R.M. **(2002)** The Behavior of Non-condensible Gas in SAGD – A Rationalization, *Petroleum Society's Canadian International Petroleum Conference*, Petroleum Society Paper No.: 2002-117, Calgary, Alberta, Canada, June 11-13.

18) Butler R.M. **(1999)** The Steam and Gas Push (SAGP), *JCPT*, **38**, 3, 54-61.

19) Butler, R.M.; Jiang, Q.; and Yee, C.T. **(2000a)** The Steam and Gas Push – 2, Mechanism Analysis and Physical Model Testing, *JCPT*, **39**, 4, 52-61.

20) Butler, R.M.; Jiang, Q.; and Yee, C.T. **(2000b)** The Steam and Gas Push – 3, Recent Theoretical Developments and Laboratory Results, *JCPT*, **37**, 8, 51-60

21) Butler, R.M.; Jiang, Q.; and Yee, C.T. **(2001)** The Steam and Gas Push – 4, Recent Theoretical Developments and Laboratory Results Using Layered Models, *JCPT*, **40**, 1, 54-61.

22) Butler, R.M. and Mokrys, I.J. **(1991)** A new process (VAPEX) for recovery of heavy oils using hot water and hydrocarbon vapour, *Journal of Canadian Petroleum Technology*, **30**, 1.

23) Butler R.M. **(1987)** Rise of interfering steam chamber, *JCPT*, Paper No.: 87-03-07, **26**, 3, 70-75.

24) Butler, R.M., Stephens, D.J., and Weiss, M. **(1980)** The vertical growth of steam chambers in the in-situ thermal recovery of heavy oils, *Proc. 30th Can. Chem. Eng. Conf.*, 4, 1152-1160.

25) Butler, R.M. **(1998)** SAGD comes of age!, *Distinguished JCPT Author Series*, **37**, 7.

26) Chalaturnyk, R.J. and Li, P. **(2004)** When is it important to consider geo-mechanics in SAGD operations?", *Journal of Canadian Petroleum Technology*, **43**, 4, pp 53-61.

27) Chatzis I., Morrow N., and Lim H.T. **(1983)** Magnitude and detailed structure of residual oil saturation, *SPE J*, April, 311-326.

28) Chatzis I. **(1982)** Photo-fabrication technique of 2-D micromodels, PPRC report No. 82-12, New Mexico Petroleum Recovery Research Centre

29) Chatzis I. and Dullien FAL **(1983)** Dynamic immiscible displacement mechanisms in pore doublets – theory versus experiment, *Journal of Colloid and Interface Science,* **91**, 1, 199-222.

30) Chung K.H. and Butler R.M. **(1987)** Geometrical effect of steam injection on the formation of emulsions in the Steam Assisted Gravity Drainage process, *38th Pet. Soc. Ann. Tech. Meet. Of CIM*, Paper Number 87-38-22, Calgary, Canada, June.

31) Chung K.H. and Butler R.M. **(1989)** In situ emulsification by the condensation of steam in contact with bitumen, *JCPT*, **28**, 1, Jan–Feb.

32) Das S. K. and Butler R. **(1998)** Mechanism of the vapour extraction process for heavy oil and bitumen, *Journal of Petroleum Science and Engineering,* **21**, 2, 43.

33) Donnelly, J. K. **(1997)** Application of Steam Assisted Gravity Drainage (SAGD) to Cold Lake, *JCPT*, Paper No: 97-192.

34) Donnelly, J.K. **(1999)** Hilda Lake, a gravity drainage success, *Presented at the 1999 SPE International Thermal Operations and Heavy Oil Symposium*, SPE paper No 54093, Bakersfield, California, U.S.A.

35) Dullien F. A. L. **(1992)** Porous Media: Fluid Transport and Pore Structure, Second Edition, *ACADEMIC PRESS INC*, ISBN 0-12-223651-3.

36) Edmunds, N.R. and Gittins, S.D. **(1993)** Effective application of Steam Assisted Gravity Drainage of Bitumen to long horizontal well pairs, *JCPT*, **32**, 6, Paper No 93-06-05.

37) Edmunds, N.R., Kovalsky, J.A., Gittins, S.D. and Pannacchioli, E.D. **(1991)** Review of Phase A Steam-Assisted Gravity-Drainage test", *Presented at the SPE International Thermal Operations Symposium*, SPE Paper No. 21529, Bakersfield.

38) Edmunds, N.R., Kovalsky, J.A., Gittins, S.D., and Pennacchioli, E.D. **(1994)** Review of Phase "A" Steam Assisted Gravity Drainage test", *SPE Reservoir Engineering*.

39) Edmunds, N.R. and Suggett, J.C. **(1995)** Design of a commercial SAGD heavy oil Project, *Presented at the International Heavy Oil Symposium*, SPE Paper No. 30277, Calgary, AB, Canada.

40) Edmunds, N.R. **(1999)** On the difficult birth of SAGD, *JCPT Distinguished Author Series*, **38**, 1.

41) Edmunds, N.R. and Gittins, S.D. **(1993)** Effective application of Steam Assisted Gravity Drainage of Bitumen to long horizontal well pairs, *JCPT*, Paper No 93-06-05, **32**, 6.

42) Farouq Ali, S.M. and Abad, B. (**1976)** Bitumen Recovery from Oil Sands using Solvent in Conjunction with Steam, *JCPT*, July-September, 80-90.

43) Farouq-Ali, S.M. **(1997)** Is there life after SAGD?, *JCPT Distinguished Author Series*, JCPT Paper No. 97-06-DAS, **36**, 6.

44) Feng Q., Di L., Tang G., Chen Z., Wang X., and Zou J. **(2004)** The mechanism of Water Alternative Gas displacement in porous media, *14th SPE-IOR Symposium*, SPE Paper Number 89362, Tulsa, OK, Apr 17-21

45) Fergusen, M.A.; Mamora, D.D.; and Goite, J.G. **(2001)** Steam-propane injection for production enhancement of heavy Morichal oil, SPE paper number 69689.

46) Firoozabadi A. **(1999)** Thermodynamics of Hydrocarbon Reservoirs, *McGraw-Hill*, New York, ISBN-13: 978-0070220713.

47) Gates I.D. and Chakrabarty N. **(2005)** Optimization of Steam-Assisted Gravity Drainage in McMurray reservoir, *6th CIPC (56th Pet. Soc. Ann. Tech. Meet.)*, Paper No. 2005-193, Calgary, Canada, June.

48) Gates I. D. **(2010)** Solvent-Aided Steam Assisted Gravity Drainage in thin oil sands reservoirs, *Petroleum Science and Engineering*, DOI: 10.1016/j.petrol.2010.09.003.

49) Gates I.D., Kenny J., Hernandez-Hdez I.L., and Bunio G.L. **(2005)** Steam-injection strategy and energetics of Steam-Assisted Gravity Drainage, *SPE/PS-CIM/CHOA Int. Ther. Opr. and HO Sym.*, SPE Paper number 97742 and PS Paper number 2005-332, Calgary, Canada, November.

50) Gird, G. **(1994)** Molecular gas Dynamics and the Direct Simulation of Gas Flows, *Clarendon Press*, Oxford.

51) Gotie, J.G.; Mamora, D.D; and Ferguson, A.M (**2001)** Experimental study of Morichal heavy oil recovery using combined steam and propane injection, SPE paper number 69566.

52) Green Don W. and Perry Robert H. **(2008)** Perry's Chemical Engineers' Handbook (8th Edition), *McGraw-Hill*.

53) Gupta, S.; Gittins, S.; and Picherack, P. **(2002)** Field implementation of Solvent Aided Process, *Petroleum Society's Canadian International Petroleum Conference*, Calgary, Alberta, Canada, June 11-13.

54) Gupta, S.; Gittins, S.; and Picherack, P. **(2003)** Insights into some key issues with Solvent Aided Process, *Journal of Canadian Petroleum Technology*, **43**, 2, Feb.

55) Gupta, S.; Gittins, S.; and Picherack, P. **(2005)** Field implementation of Solvent Aided Process, *Journal of Canadian Petroleum Technology*, **44**, 11, Nov.

56) Gupta, S.C. and Gittins, S.D. **(2005)** Christina Lake Solvent Aided Process pilot, *Petroleum Society's Canadian International Petroleum Conference*, Calgary, Alberta, Canada, June 7-9.

57) Gupta, S.C. and Gittins, S.D. **(2006)** Christina Lake Solvent Aided Process pilot, *Journal of Canadian Petroleum Technology*, **45**, 9, September.

58) Gupta, S.C. and Gittins, S.D. **(2006)** Effect of solvent sequencing and other enhancements on Solvent Aided Process, *Petroleum Society's 7th Canadian International Petroleum Conference (57th Annul Technical Meeting)*, Calgary, Alberta, Canada, June 13-15.

59) Guyer, E.C. **(1999)** Handbook of applied thermal design, 1st Edition, *CRC Press*.

60) Hamm, R.A. and Ong, T.S. **(1994)** Enhanced Steam Assisted Gravity Drainage-A new horizontal well recovery process for Peace River", *Presented at the International Conference on Recent Advances in Horizontal Well Application*, Calgary, AB, Canada.

61) Hosseininejad M. et al **(2010)** Numerical evaluation of hydrocarbon additives to steam in the SAGD process, *Journal of Canadian Petroleum Technology,* **49**, 9, 42-55.

62) Incropera F.P. and DeWitt D.P. **(2002)** Fundamentals of Heat and Mass Transfer, 5th edition, *John Wiley & Sons Inc.*, ISBN 0-471-38650-2.

63) Ioannidis M., Chatzis I., and Payatakes A. C. **(1991)** A Mercury Porosimeter for Investigating Capillary Phenomena and Micro-displacement Mechanisms in Capillary Networks, *Journal of Colloid and Interface Science,* Vol. 143, No. 1, April.

64) Ito Y. and Ipek G. **(2005)** Steam fingering phenomenon during SAGD process, *SPE/PS-CIM/CHOA Program Committee*, also *SPE Int. Ther. Opr. and HO Sym.*, SPE Paper Number: 97729, Calgary, AB, Canada, November 1-3.

65) Ito Y., Hirata M., and Ichikawa M. **(2004)** The effect of operating pressure on the growth of the steam chamber detected at the Hangingstone SAGD project, *Journal of Canadian Petroleum Technology*, **43**, 1, January.

66) Ito Y. and Suzuki S **(1996)** Numerical simulation of the SAGD process in the Hangingstone oil sands reservoir, *47th Annual Technical Meeting of the Petroleum Society*, Paper Number 96-57, Calgary, AB, Canada, June 10-12.

67) Ito, Y. **(2004)** Discussion of when is it important to consider geo-mechanics in SAGD operations, *JCPT*, Discussion/Response Series, **43**, 8.

68) Ito, Y. **(1998)** To be or not to be: A long term economic decision, *Presented at the 49th Annual Technical Meeting of the Petroleum Society*, The Petroleum Society Paper No 98-38, Calgary, AB, Canada.

69) Ito, Y. **(2004)** Discussion of when is it important to consider geomechanics in SAGD operations?, *JCPT Discussion/Response Series*, Vol. 43, No. 8.

70) Ito, Y. **(1998)** To be or not to be: A long term economic decision, The Petroleum Society Paper No.: 98-38, *Presented at the 49th Annual Technical Meeting of the Petroleum Society in Calgary,* Alberta, Canada.

71) Ito, Y., Hirata, M., and Ichikawa, M. **(2004)** The effect of operating pressure on the growth of the steam chamber detected at the Hangingstone SAGD project, *Journal of Canadian Petroleum Technology (JCPT)*, Vol. 43, No. 1.

72) Ito, Y., and Singhal, A.K. **(1999)** Reinterpretation of performance of horizontal well pilot No. 1 (HWPI), 1980 – 1989, *Journal of Canadian Petroleum Technology (JCPT),* Vol. 38, No. 13.

73) Ito, Y. and Ipek, G. **(2005)** Steam, fingering Phenomenon during SAGD process, SPE/PS-CIM/CHOA Paper No.: 97729, *Presented at the SPE/PS-CIM/CHOA Program Committee, also Presented at the SPE International Thermal Operations and Heavy Oil Symposium held in Calgary*, Alberta, Canada.

74) Ito, Y. and Suzuki, S. **(1996)** Numerical simulation of the SAGD process in the Hangingstone oil sands reservoir, Paper No. 96-57, *Presented at the 47th Annual Technical Meeting of the Petroleum Society in Calgary*.

75) James L.A. **(2009)** Mass transfer mechanisms during the solvent recovery of heavy oil, *PhD thesis*, University of Waterloo.

76) James L.A., Rezaei N., and Chatzis I. **(2008)** VAPEX, Warm VAPEX, and Hybrid WAPEX – The state of enhanced oil recovery for in-situ heavy oils in Canada, Technology Brief, *JCPT*, April.

77) James L.A.; Rezaei N.; and Chatzis I. **(2008)** VAPEX, Warm VAPEX, and Hybrid WAPEX – The state of enhanced oil recovery for in-situ heavy oils in Canada, *JCPT*, April.

78) Jiang, Q.; Butler, R.M.; and Yee, C.T. **(1998)** The Steam and Gas Push (SAGP)-2: mechanism analysis and physical model testing, *Proceedings of the Petroleum Society 49th Annual Technical Meeting,* Paper 98-43, Calgary, Alberta, Canada, June 8-10.

79) Kisman, K.E. and Yeung, K.C. **(1995)** Numerical study of the SAGD process in the Burnt Lake oil sands lease, *Presented at the International Heavy Oil Symposium*, SPE Paper No 30276, Calgary, AB, Canada.

80) Komery, D.P., Luhning, R.W. and O'Rourke, J.C. **(1995)** Towards commercialization of UTF project using surface drilled horizontal SAGD wells, *Presented at the 46th Annual Technical Meeting of the Petroleum Society of CIM,* The Petroleum Society of CIM Paper No. 95-60, Banff, AB, Canada.

81) Lederer, E.L. **(1933)** *Proceeding, World Petroleum Congress*, London, **2**, 526-528 (1933).

82) Li W. et al **(2011)** Light- and heavy-solvent impacts on Solvent-Aided SAGD process: A low-pressure experimental study, *Journal of Canadian Petroleum Technology,* April, 19-30.

83) Li. W. and Mamora D. **(2010)** Numerical simulation of thermal solvent replacing steam under steam assisted gravity drainage (SAGD) process, *Presented at the Western North America Regional Meeting,* SPE paper number 133453, Anaheim, CA, USA.

84) Li. W. and Mamora D. **(2010)** Experimental investigation of solvent co-injection in vapor and liquid phase to enhance SAGD performance, *Presented at the SPE ATCE,* SPE paper number 133277, Florence, Italy.

85) Liebe, H. and Butler, R.M. **(1991)** A study of the use of vertical steam injectors in the steam assisted gravity drainage process, *Presented at the CIM/AOSTRA technical conference*, CIM / AOSTRA paper No 91-32, Banff, AB, Canada.

86) Luo H., Salama D., Kryuchkov S., and Kantzas A. **(2007)** The Effect of Volume Changes Due to Mixing on Diffusion Coefficient Determination in Heavy Oil and Hydrocarbon Solvent System, SPE paper number 110522, *Presented at the 2007 SPE Annual Technical Conference and Exhibition held in Anaheim, CA.*

87) Madrazo A. **(1960)** Liquid density correlation of hydrocarbon systems, *Petroleum Transactions of AIME*, Vol 219.

88) Mamora, D.D.; Rivero, J.A.; Hendroyono, A.; and Venturini, G.J **(2003)** Experimental and simulation studies of steam-propane injection for the Hamaca and Duri fields, SPE paper number 84201.

89) McCain W. D. **(1990)** The properties of petroleum fluids, ISBN-10: 0878143351, *Pennwell Pub*; 2 Sub edition.

90) McCormack, M. E. **(2007)** Design of steam-hexane injection wells for gravity drainage systems, *Petroleum Society's 8th Canadian International Petroleum Conference (58th Annual Technical Meeting),* Paper No. 2007-102, Calgary, Alberta, Canada, June 12-14.

91) McCormack, M. E. **(2007)** Design of steam-hexane injection wells for gravity drainage systems, *Presented at the Petroleum Society's 8th Canadian International Petroleum Conference (58th Annual Technical Meeting),* CIPC Paper No 2007-102, Calgary, AB, Canada.

92) Mehrotra, A.K. and Svrcek, W.Y. **(2009)** Viscosity of compressed Athabasca bitumen, *The Canadian Journal of Chemical Engineering*, **64** (5), 844-847.

93) Mohammadzadeh, O., Rezaei, N., and Chatzis, I. **(2010)** Pore-level Investigation of Heavy Oil and Bitumen Recovery Using Solvent-Aided Steam Assisted Gravity Drainage Process, *ACS journal Energy and Fuels*, **24**, 6327-6345 (DOI: 10.1021/ef100621s).

94) Mohammadzadeh, O. and Chatzis, I. **(2010**) Pore-level Investigation of Heavy Oil Recovery using Steam Assisted Gravity Drainage (SAGD), *Journal of Oil and Gas Science and Technology — Revue de l'IFP Energies nouvelles,* **65**, 6, 839-857 (DOI:10.2516/ogst/2010010).

95) Mokrys, I.J. and Butler, R.M., (**1993)** In-Situ Upgrading of Heavy Oil and Bitumen by Propane De-asphalting: The VAPEX Process, *Production Operations Symposium*, SPE 25452Oklahoma City, OK, 21-23 March.

96) Mukherjee, N.J., Gittins, S.D., Edmunds, N.R., and Kisman, M.E. **(1995)** A comparison of field versus forecast performance of phase "B" of the UTF SAGD project in the Athabaska oil sands, *Presented at the 6th UNITAR International Conference on Heavy Crude and Tar Sands*, Houston, TX.

97) Mukherjee, N.J., Edmunds, N.R., and Gittins, S.D. **(1994)** Impact and mitigation of certain geological and process factors in the application of SAGD at AOSTRA's UTF", *Presented at the Canadian SPE/CIM/CANMET International Conference on Recent Advances in Horizontal Well Applications*, Canadian SPE/CIM/CANMET Paper No. HWC94-51, Calgary, AB, Canada.

98) National Energy Board of Canada **(2006)** Canada's oil sands: opportunities and challenges to 2015, an update, June.

99) Nasr, T.N. and Isaacs, E.E. **(2001)** Process for enhancing hydrocarbon mobility using a steam additive, *US Patent 6,230,814*, May 15.

100) Nasr, T.N.; Beaulieu, G.; Golbeck, H.; and Heck, G. **(2003)** Novel Expanding Solvent-SAGD process, ES-SAGD, *Journal of Canadian Petroleum Technology*, **42**, 1, Jan.

101) Nasr, T.N. and Ayodele, O.R. **(2005)** Thermal techniques for the recovery of heavy oil and bitumen, *SPE International Improved Oil Recovery Conference in Asia Pacific*, SPE Paper 97488, Kuala Lumpur, Malaysia, Dec. 5-6.

102) Nasr, T.N.; Beaulieu, G.; Golbeck, H.; and Heck, G. **(2002)** Novel Expanding Solvent-SAGD process (ES-SAGD), *Petroleum Society's Canadian International Petroleum Conference*, Paper No. 2002-072, Calgary, Alberta, Canada, June 11-13.

103) Nasr, T.N.; Kimber, K.D.; Vendrinsky, D.A.; and Jha, K.N. **(1991)** Process enhancement in horizontal wells through the use of vertical drainage channels and hydrocarbon additives, *Western Regional Meeting*, SPE Paper 21794, Long Beach, California, March 20-22.

104) Nasr T.N., Law D.H.S., Golbeck H., and Korpany G. **(2000)** Counter-current aspect of the SAGD Process, *JCPT*, **39**, 1, January.

105) Nasr, T.N., Golbeck, H., Korpany, G. and Pierce, G. **(1998)** SAGD operating strategies, *Presented at the 1998 SPE International Conference on Horizontal Well Technology*, SPE Paper No 50411, Calgary, Alberta, Canada.

106) Nasr, T.N., Golbeck, H., Korpany, G., and Pierce, G. **(1997)** Steam Assisted Gravity Drainage (SAGD) in horizontal wells: A visualization model study, *Presented at the SPE International Thermal Operations and Heavy Oil Symposium*, SPE Paper No 37521, Bakersfield, California, U.S.A.

107) Noik C., Dalmazzone C., Goulay C., and Glenat P. **(2005)** Characterization and emulsion behaviour of Athabaska extra heavy oil produced by SAGD, SPE paper No.: 97748, *2005 SPE Int. Ther. Opr. and HO Sym.*, Calgary, Alberta, Canada, Nov. 1-3.

108) O'Rourke, J.C., Chambers, J.I., Suggett, J.C. and Good, W.K. **(1994)** UTF project status and commercial potential, *Presented at the 48th Annual Technical Meeting of the Petroleum Society of CIM and AOSTRA*, Paper No. 94 - 405, Calgary, Canada.

109) O'Rourke, J.C., Begley, A.G., Boyle, H.A., Tee, C.T., Chambers, J.I. and Luhning, R.W. **(1997)** UTF project status update May 1997, *Presented at the 48th Annual Technical Meeting of the Petroleum Society*, The Petroleum Society Paper No. 97-08, Calgary, AB, Canada.

110) Rezaei, N., Mohammadzadeh, O., and Chatzis, I. **(2010)** Warm VAPEX: a thermally improved vapor extraction process for recovery of heavy oil and bitumen, *ACS journal Energy and Fuels*, **24**, 5934-5946 (DOI: 10.1021/ef100749z).

111) Rezaei N. **(2010)** Experimental investigations in improving the VAPEX performance for recovery of heavy oil and bitumen, *PhD thesis*, University of Waterloo.

112) Rich Kerr et al **(2002)** The Long Lake project – The first field integration of SAGD and upgrading, *Presented at the SPE International Thermal Operations and Heavy Oil Symposium and International Horizontal Well Technology Conference*, SPE – CIM/CHOA Paper No 79072, Calgary, Alberta, Canada.

113) Rivero, J.A. and Mamora, D.D. **(2002)** Production acceleration and injectivity enhancement using steam-propane injection for Hamaca extra-heavy oil, SPE paper number 75129.

114) Rose, P.E. and Deo, M.D. **(1995)** Steam Assisted Gravity Drainage in oil sand reservoirs using a combination of vertical and horizontal wells, *Fuel*, **74**, 8, 1180 – 1184.

115) Roth, A. **(1990)** Vacuum technology, 3rd Edition, *North–Holland*.

116) Rottenfusser, B. A., Hunt, P. L. and Edmunds, N.R. **(1991)** Applicability of UTF technology to the Athabaska oil sands deposit, *Presented at the CIM / AOSTRA 1991 Technical Conference*, CIM/AOSTRA Paper No. 91-80, Banff, AB, Canada.

117) Sasaki K., Akibayashi S., Yazawa N., and Kaneko F. **(2002)** Microscopic visualization with high-resolution Optical-Fiber Scope at steam chamber interface on initial stage of SAGD process, SPE Paper No. 75241, *SPE/DOE Improved Oil Recovery Symposium*, Tulsa, OK, April 13-17.

118) Sasaki K., Akibayashi S., Yazawa N., Doan Q., and Farouq Ali S.M. **(1999)** Experimental modeling of the SAGD process – Enhancing SAGD performance with periodic stimulation of the horizontal producer", SPE Paper N.: 56544, *SPE Annual Technical Conference and Exhibition*, Houston, TX, October 3-6.

119) Sasaki K. et.al. **(1996)** Experimental study on initial stage of SAGD process using 2-dimensional scaled model for heavy oil recovery, SPE Paper No.: 37089, *2nd International 3-Day Conference on Horizontal Well Technology*.

120) Sasaki K., Akibayashi S., Yazawa N., Doan Q.T., and Farouq Ali S.M. **(2001)** Experimental modeling of the SAGD process — enhancing SAGD performance with periodic stimulation of the horizontal producer, SPE Paper Number 69742, *SPEJ*, March.

121) Sawhney, G.S., Liebe, H., and Butler, R.M. **(1995)** Vertical injection wells for SAGD: a practical option or not?, *Journal of Canadian Petroleum Technology*, Paper No 95-01-06, **34**, 1, 1.

122) Shu, W.R. **(1984)** A viscosity correlation for mixtures of heavy oil, bitumen and petroleum fractions, *SPE Journal*, 277-287.

123) Sohrabi M., Henderson G.D., Tehrani D.H., and Danesh A. **(2000)** Visualization of oil recovery by water alternating gas (WAG) injection using high pressure micromodels – Water-wet systems, *SPE-ATCE*, SPE Paper Number 63000, Dallas, TX, Oct. 1-4.

124) Sohrabi M., Danesh A., and Jamiolahmady M. **(2007)** Visualization of residual oil recovery by near miscible gas and SWAG injection using high-pressure micromodels, *Transport in Porous Media*, **74**, 2, 239-257.

125) Sohrabi M., Danesh A., and Jamiolahmady M. **(2007)** Microscopic mechanisms of oil recovery by near-miscible gas injection, *Transport in Porous Media*, **72**, 3, 351-367.

126) Standing M. B. **(1981)** Volumetric and phase behaviour of oilfield hydrocarbon systems, *SPE*, Richardson, Texas.

127) Standing M. B. **(1962)** Oil-system correlations, P.P. Handbook (ed.), *McGraw-Hill Book Co. Inc.*, New York City.

128) Standing M. B. and Katz D. L. **(1942)** Density of crude oils saturated with natural gas, *Transactions AIME*, **146**, 159.

129) Vanegas Prada, J.W. and Cunha, L.B. **(2005)** Impact of operational parameters and Reservoir variables during the start-up phase of a SAGD process, *Presented at the SPE International Thermal Operations and Heavy Oil Symposium*, SPE/PS – CIM/CHOA Paper No 97918, Calgary, Alberta, Canada.

130) Walls E., Palmgren S., and Kisman K. **(2003)** Residual oil saturation inside the steam chamber during SAGD, *JCPT*, **42**, 1, January.

131) Wan J., Tokunaga T.K., Tsang C., Bodvarsson G.S. **(1996)** Improved glass micromodel methods for studies of flow and transport in fractured porous media, *Water Resources Research*, **32**, 7, 1955-1964.

132) Wen Y., Kantzas A., and Wang G. J. **(2004)** Estimation of Diffusion Coefficients in Bitumen Solvent Mixtures Using X-Ray CAT Scanning and Low Field NMR, PetSoc paper number 2004-064, *Presented at the Petroleum Society's 5th CIPC*, Calgary, AB.

133) Wen Y. and Kantzas A **(2006)** Evaluation of heavy oil/bitumen – solvent mixture viscosity models, *Journal of Canadian Petroleum Technology*, **45**, 4, 56-61.

134) Wen Y., Bryan J., and Kantzas A. **(2003)** Estimation of Diffusion Coefficients in Bitumen Solvent Mixtures as Derived From Low Field NMR Spectra, PetSoc paper number 2003-017, *Presented at the Petroleum Society's CIPC*, Calgary, AB.

135) Wen Y., Bryan J., and Kantzas A. **(2005)** Estimation of Diffusion Coefficients in Bitumen Solvent Mixtures as Derived From Low Field NMR Spectra, *Journal of Canadian Petroleum Technology*, **44,** 4, 29-35.

136) Yaws, Carl L. **(2010)** Yaws' Thermophysical Properties of Chemicals and Hydrocarbons, *Electronic Edition provided by Knovel*.

137) Yaws, Carl L. **(2003)** Yaws' Handbook of Thermodynamic and Physical Properties of Chemical Compounds, *Electronic Edition provided by Knovel*.

138) **Edited by** Yaws, C.L. **(1999)** Chemical Properties Handbook, *McGraw-Hill*.

139) Yazdani A. and Maini B. B. **(2005)** Effect of drainage height and grain size on production rates in the VAPEX process: Experimental study, *SPE Reservoir Evaluation and Engineering Journal*, June.

140) Yongrong Gao, Shangqi Zhang, and Yitang Zhang **(2002)** Implementing Steam Assisted Gravity Drainage through combination of vertical and horizontal wells in a super-heavy crude reservoir with top-water", *Presented at the SPE Asia Pacific Oil and Gas Conference and Exhibition*, SPE Paper No 77798, Melbourne, Australia.

141) Zhao, L. **(2004)** Steam Alternating Solvent process, *SPE International Thermal Operations and Heavy Oil Symposium and Western Regional Meeting*, SPE Paper 86957, Bakersfield, California, March 16-18.

142) Zhao, L.; Nasr, T.N.; Haung, H.; Beaulieu, G.; Heck, G.; and Golbeck, H. **(2005)** Steam Alternating Solvent process: lab test and simulation, *Journal of Canadian Petroleum Technology*, **44**, 9, September.